Научном већу Института за физику Београд

Београд, 5. Јула 2019. године

Предмет:
Молба за покретање поступка за избор у звање научни сарадник

С обзиром да испуњавам критеријуме прописане од стране Министарства просвете, науке и технолошког развоја за стицање звања научни сарадник, молим Научно веће Института за физику Београд да покрене поступак за мој избор у наведено звање.

У прилогу достављам:

1. Мишљење руководиоца пројекта са предлогом чланова комисије за избор у звање
2. Стручну биографију
3. Преглед научне активности
4. Елементе за квалитативну и квантитативну оцену научног доприноса са доказима
5. Списак објављених научних радова и њихове копије
6. Податке о цитираности
7. Уверење о одбрањеној докторској дисертацији

Са поштовањем, др Михаило Савић

Научном већу Института за физику Универзитета у Београду

ПРЕДМЕТ:Мишљење руководиоца пројекта о избору др Михаила Савића у звање научни сарадник

Др Михаило Савић запослен је у Институту за физику у Београду од 2011. године. Ангажован је на пројекту основних истраживања Министарства просвете, науке и технолошког развоја Републике Србије ОИ171002, под називом *Нуклеарне методе истраживања ретких догађаја и космичког зрачења*. У оквиру пројекта бави се истраживањима у физици космичког зрачења и физици високих енергија. С обзиром да испуњава све предвиђене услове за избор у звање научног сарадника, у складу са Правилником о поступку, начину вредновања и квантитативном исказивању научноистраживачких резултата истраживача Министарства просвете, науке и технолошког развоја Републике Србије, сагласан сам са покретањем поступка за избор др Михаила Савића у звање научни сарадник.

За састав комисије за избор др Михаила Савића у звање научни сарадник предлажем:

1. др Димитрије Малетић, виши научни сарадник, Институт за физику у Београду

2. др Александар Драгић, виши научни сарадник, Институт за физику у Београду

3. проф. др Марија Димитријевић-Ћирић, ванредни професор, Физички факултет Универзитета у Београду

Руководилац пројекта

проф. др Иштван Бикит

Стручна биографија др Михаила Савића

Михаило Савић рођен је 31.12.1975. године у Београду, где је завршио основну школу и гимназију. Дипломирао је 2009. године на експерименталном смеру на Физичном факултету Универзитета у Београду. Дипломски рад под насловом "Дигитална обрада сигнала у нуклеарној физици" урадио је под менторством проф др Јована Пузовића. 2011. године завршио је мастер студије на Физичком факултету у Београду и исте године уписао је докторске студије на истој установи.

У периоду од 2009. до 2011. године био је запослен на Физичком факултету у Београду, где је у оквиру катедре за Физику језгра и честица држао рачунске и експерименталне вежбе из неколико предмета. Од 2011. године запослен је на Институту за физику у Београду као члан Нискофонске лабораторије за нуклеарну физику, а на пројекту Министарства просвете, науке и технолошког развоја ОИ171002 "Нуклеарне методе истраживања ретких догађаја и космичког зрачења".

Од 2011. до 2014. године, као члан Београдског SHINE Team-а, био је део NA61/SHINE колаборације. Од 2015. године, као члан Београдског MICE Team-а, део је MICE колаборације.

У оквиру Нискофонске лабораторије за нуклеарну физику радио је на анализи временских серија мионске компоненте секундарног космичког зрачења, пре свега на проблемима везаним за утицај атмосферских параметара на ову компоненту као и на проблематици ефикасности мерења исте.

У оквиру NA61/SHINE колаборације радио је на анализи продукције барионских резонанци, продукцији података, одржавању и надгледању Time-Of-Flight (TOF) поддетектора, калибрацији TOF података, одржавању и развоју софтвера за калибрацију, реконструкцију и геометрију.

У оквиру MICE колаборације радио је на развоју апликације за визуелизацију догађаја (EventViewer) снимљених у оквиру MICE експеримента.

Докторску дисертацију под насловом "Моделовање утицаја атмосфере не мионску компоненту секундарног космичког зрачења", урађену под менторством др Димитрија Малетића, одбранио је 04.07.2019. године на Физичком факултету Универзитета у Београду.

Преглед научне активности др Михаила Савића

Михаило Савић је започео свој научно-истраживачки рад као члан Београдског SHINE тима у оквиру NA61/SHINE колаборације. Радио је на анализи продукције барионских резонанци у сударима снопова протона са фиксном протонском метом на енергијама доступним на SPS акцелератору у CERN-у. Поред тога, радио је на продукцији и репроцесирању података. Такође, као TOF *on-call expert* био је задужен за одржавање и надгледање *Time-Of-Flight* (TOF) под-детектора и калибрацију TOF података. Као SHINE *software developer* радио је на одржавању и развоју софтвера за калибрацију, реконструкцију и геометрију TOF под-детектора.

У оквиру Нискофонске лабораторије за нуклеарну физику ради на анализи временских серија мионске компоненте секундарног космичког зрачења, пре свега на проблемима везаним за утицај атмосферских параметара на ову компоненту као и на проблематици ефикасности мерења исте. На основу података о флуксу космичких миона, мереном у оквиру Нискофонске лабораторије за нуклеарну физику Института за физику Београд, мерених вредности атмосферског притиска и температуре ваздуха и нумерички моделованих температура атмосфере, кориговао је детектовани одброј миона на метеоролошке ефекте применом неколико постојећих метода, од којих је посебно значајан интегрални метод.

Потом ради на успешној имплементацији два нова емпиријска метода за анализу и корекцију метеоролошких ефеката на космичке мионе. Први од новоуведених метода базира се на техници декомпозиције на основне компоненте. Полазни скуп корелисаних метеоролошких варијабли је трансформисан у скуп некорелисаних компоненти. Из добијеног скупа издвојен је подскуп сигнификантних компоненти, које садрже највећи део варијације полазног скупа. Коначно, на основу корелације са детектованим одбројем миона издвојен је подскуп коришћен за анализу. Тиме је број улазних варијабли за анализу редукован са 26 на 5. Помоћу линеарне регресије одређени су одговарајући парцијални температурски коефицијенти, на основу којих је детектовани одброј миона коригован.

Други метод базира се на примени различитих аллгоритама за мултиваријантну регресију имплементираних у пакету TMVA, у оквиру окружења за анализу ROOT. Методи за су тренирани на изабраном подскупу података, где су улазне варијабле представљале атмосферски притисак, температуру на нивоу тла и нумерички моделоване температуре различитих слојева атмосфере, док је излазна варијабла била детектовани одброј. За изабране методе одређени су оптимални параметри. Алгоритми дају предикцију одброја космике који садржи варијацију пореклом само од улазних метеоролошких варијабли, помоћу које је израчунат коригован одброј. На основу критеријума ефикасности и конзистентности, коначно су као најбољи кандидати за примену издвојени методи LD (метод линеарних дискриминантних фукција) и BDTG (метод бинарног гранања са градијентним *boost*-ом).

Осим поменутог, Михаило Савић дао је допринос у другим делатностима у оквиру Нискофонске лабораторије за нуклеарну физику, пре свега у нуклеарној спектроскопији и активностима везаним за мерење радона.

У оквиру MICE колаборације учествовао је у развоју апликације *Event Viewer* у склопу MAUS софтвера за реконструкцију и обраду података. Апликација се користи за визуелизацију догађаја снимљених у оквиру MICE експеримента.

Елементи за квалитативну оцену научног доприноса

1 Квалитет научних резултата

1.1 Значај научних резултата

Најзначајнији научни допринос кандидата представља увођење две нове емпиријске методе за анализу и корекцију метеоролошких ефеката на мионску компоненту секундарног космичког зрачења.

Уведени методи дају карактеристичан допринос по питању ефикасности, односно посебног увида у проблематику. У поређењу са постојећим емпиријским и теоријским методима, у отклањању варијација флукса космичких миона метеоролошког порекла, показали су се најмање једнако ефикасни, а углавном веће ефикасности. Корекција на метеоролошке ефекте је значајно повећала осетљивост апаратуре на периодичне и апериодичне варијације флукса космичког зрачења неатсмоферског порекла, као и прецизност одређивања различитих индиректно мерених варијабли. Ово повећава применљивост експерименталне поставке у проучавању ефеката у физици Сунца и хелиосфере.

Методи су применљиви на било који тип мионских монитора, независно од географске локације или дубине на којој се детектор налази. Додатна предност метода декомпозиције на основне компоненте је једноставна и непосредна примена, која омогућава примену корекције са минималним закашњењем. Компаративна предност уведених мултиваријантних метода је флексибилност и могућност додатне софистикације.

Представљени методи омогућавају једноставну екстензију анализе на шири скуп метеоролошких варијабли, чиме би били укључени додатни ефекти (влажност, динамички притисак и сл.). Такође, постоји могућност примене корекција метеоролошких ефеката на друге типове детектора, као што су неутронски монитори, за које не постоји једноставан теоријски или емпиријски модел. Коначно, демонстриране технике су применљиве за анализу различитих варијација космичког зрачења које нису метеоролошког порекла.

1.2 Параметри квалитета часописа

Кандидат др Михаило Савић објавио је укупно 15 радова у међународним часописима и то:

- 1 рад у међународном часопису изузетних вредности *Physical Review C* (IF=3,881)
- 1 рад у међународном часопису изузетних вредности *Journal of Fusion Energy* (IF=1,886)
- 2 рада у врхунском међународном часопису *The European Physical Journal C* (IF=5,297, IF=5,436)
- 1 рад у врхунском међународном часопису *Astroparticle Physics* (IF=3,425)
- 2 рада у врхунском међународном часопису *Nuclear Instruments and Methods in Physics Research A* (IF=1,362, IF=1,316)

- 1 рад у врхунском међународном часопису *Journal of Instrumentation* (IF=1,656)
- 1 рад у врхунском међународном часопису *Applied Radiation and Isotopes* (IF=1,231)
- 1 рад у истакнутом међународном часопису *Journal of Instrumentation* (IF=1,310)
- 1 рад у истакнутом међународном часопису *Advances in Space Research* (IF=1,529)
- 1 рад у истакнутом међународном часопису *Nuclear Technology and Radiation Protection* (IF=1,159)
- 1 рад у међународном часопису *Nuclear Technology and Radiation Protection* (IF=0,620)
- 1 рад у међународном часопису *Physical Review Accelerators and Beams* (IF=1,413)
- 1 рад у међународном часопису *Nukleonika* (IF=0,760)

Укупан импакт фактор објављених радова је 32.281. Укупан импакт фактор радова ван колаборација је 11.972.

1.3 Подаци о цитираности

Према бази SCOPUS, радови др Михаила Савића цитирани су 29 пута, од тога 16 пута изузимајући аутоцитате.

1.4 Међународна сарадња

Михаило Савић био је члан две међународне колаборације и то:

- NA61/SHINE у периоду од 2011. до 2014. године
- MICE од 2015. године до данас

2 Нормирање броја коауторских радова, патената и техничких решења

Сви радови спадају у категорију експерименталних радова у природно-математичким наукама, тако да се радови са 7 и мање коаутора узимају са пуном тежином, а радови са више коаутора (два чланка са 9 коаутора, један чланак са 8, као и радови са конференција) нормирају се по формули датој у Правилнику о поступку и начину вредновања и квантитативном исказивању научноистраживачких резултата истраживача.

3 Учешће у пројектима, потпројектима и пројектним задацима

Кандидат је од 01.11.2011. године ангажован на пројекту ОИ171002 "Нуклеарне методе истраживања ретких догађаја и космичког зрачења" Министарства просвете, науке и технолошког развоја Републике Србије, под руководством др Иштвана Бикита.

4 Активност у научним и научно-стручним друштвима

4.1 Организација научних скупова

Кандидат је био члан организационог одбора два међународна научна скупа:

- NA61/SHINE Collaboration Meeting (2013. године)
- MICE Collaboration Meeting (2017. године)

4.2 Педагошки рад

У периоду од 2009. до 2012. године Михаило Савић, као сарадник у настави на катедри за Физику језгра и честица Физичког факултета у Београду, држао је рачунске вежбе из предмета Нуклеарна физика, Физика језгра и честица и Нумеричке методе у физици

5 Утицај научних резултата

Утицај научних резултата кандидата описани су у тачкама 1.1 и 1.3 овог одељка, као и у прилогу о цитираности.

6 Конкретан допринос кандидата у реализацији радова у научним центрима у земљи и иностранству

Кандидат је највећи део своје истраживачке делатности реализовао у Институту за физику Београд, а мањим делом на Физичком факултету Универзитета у Београду. Значајно је допринео свим радовима у којима је коаутор, а кључан допринос дао је у два рада у којима је први аутор. Допринос се огледа у обради и анализи података, што подразумева примену нумеричких симулација и имплементацију различитих алгоритама за препарацију, процесирање и анализу података, као и у презентацији и интепретацији резултата и писању радова.

Елементи за квантитативну оцену научног доприноса

Остварени М-бодови по категоријама публикација (радови са колаборација SHINE и MICE нису нормирани)

Категорија	М-бодова по публикацији	Број публикација	Укупно М-бодова	Укупно М-бодова нормирано
M21a	10	2	20	18.333
M21	8	7	56	56
M22	5	3	15	13.571
M23	3	3	9	8.143
M33	1	11	11	9.357
M34	0.5	3	1.5	0.726
M63	1	14	14	11.750
M70	6	1	6	6

Поређење оствареног броја М-поена са минималним условима потребним за избор у звање научног сарадника (урачунавајући радове са колаборација SHINE и MICE)

	Потребно	Остварено
Укупно	16	123.880
M10+M20+M31+M32+M33+M41+M42	10	106.131
M11+M12+M21+M22+M23	6	96.048

Остварени М-бодови по категоријама публикација (без радова са колаборација SHINE и MICE)

Категорија	М-бодова по публикацији	Број публикација	Укупно М-бодова	Укупно М-бодова нормирано
M21a	10	1	10	8.333
M21	8	3	24	24
M22	5	2	10	8.571
M23	3	2	9	5.143
M33	1	11	11	9.357
M34	0.5	3	1.5	0.726
M63	1	14	14	11.750
M70	6	1	6	6

Поређење оствареног броја М-поена са минималним условима потребним за избор у звање научног сарадника (без радова са колаборација SHINE и MICE)

	Потребно	Остварено
Укупно	16	73.880
M10+M20+M31+M32+M33+M41+M42	10	56.130
M11+M12+M21+M22+M23	6	46.048

Списак радова др Михаила Савића

M21a

N, Abgrall, ..., Jokovic Dejan R, ..., Maletic Dimitrije M и др. (2014). "Measurements of production properties of K-S(0) mesons and Lambda hyperons in proton- carbon interactions at 31 GeV/c". у: *PHYSICAL REVIEW C* 89.2. M21a, IF 3,881, с. -.

I, Udovicic Vladimir, Dragic Aleksandar L и др. (2011). "Yield from Proton-Induced Reaction on Light Element Isotopes in the Hydrogen Plasma Focus". у: *JOURNAL OF FUSION ENERGY* 30.6. M21a, IF 1,886, с. 487—489.

M21

Adams, D. и др. (2019). "First particle-by-particle measurement of emittance in the Muon Ionization Cooling Experiment". у: *The European Physical Journal C* 79. M21, IF 5,297.

Savić, M., A. Dragić, D. Maletić и др. (2019). "A novel method for atmospheric correction of cosmic-ray data based on principal component analysis". у: *Astroparticle Physics* 109. M21, IF 3.203, с. 1—11. ISSN: 0927-6505. DOI: https://doi.org/10.1016/j.astropartphys.2019.01.006. URL: http://www.sciencedirect.com/science/article/pii/S0927650518302378.

B, Veselinovic Nikola, Dragic Aleksandar L, Savic Mihailo R и др. (2017). "An underground laboratory as a facility for studies of cosmic-ray solar modulation". у: *NUCLEAR INSTRUMENTS AND METHODS IN PHYSICS RESEARCH SECTION A-ACCELERATORS SPECTROMETERS DETECTORS AND ASSOCIATED EQUIPMENT* 875. M21, IF 1,362, с. 10—15.

N, Abgrall, ..., Cirkovic M и др. (2014). "NA61/SHINE facility at the CERN SPS: beams and detector system". у: *JOURNAL OF INSTRUMENTATION* 9. M21, IF 1,656, с. -.

N, Abgrall, ..., Jokovic Dejan R, ..., Manic D и др. (2014). "Measurement of negatively charged pion spectra in inelastic p plus p interactions at p(lab)=20, 31, 40, 80 and 158 GeV/c". у: *EUROPEAN PHYSICAL JOURNAL C* 74.3. M21, IF 5,436, с. -.

M, Banjanac Radomir, Dragic Aleksandar L и др. (2014). “Variations of gamma-ray background in the Belgrade shallow underground low-level laboratory”. у: *APPLIED RADIATION AND ISOTOPES* 87. M21, IF 1,231, с. 70—72.

N, Abgrall, ..., Grabez Bojana S и др. (2013). “Pion emission from the T2K replica target: Method, results and application”. у: *NUCLEAR INSTRUMENTS AND METHODS IN PHYSICS RESEARCH SECTION A-ACCELERATORS SPECTROMETERS DETECTORS AND ASSOCIATED EQUIPMENT* 701. M21, IF 1,316, с. 99—114.

M22

Asfandiyarov, R. и др. (2019). “MAUS: The MICE Analysis User Software”. у: *Journal of Instrumentation* 14. M22, IF 1,310.

R, Savic Mihailo, Veselinovic Nikola B и др. (2019). “Rigidity dependence of Forbush decreases in the energy region exceeding the sensitivity of neutron monitors”. у: *ADVANCES IN SPACE RESEARCH* 63.4. M22, IF 1,529, с. 1483—1489.

L, Dragic Aleksandar, Udovicic Vladimir I и др. (2011). “The New Set-Up in the Belgrade Low-Level and Cosmic-Ray Laboratory”. у: *NUCLEAR TECHNOLOGY AND RADIATION PROTECTION* 26.3. M22, IF 1,159, с. 181—192.

M23

I, Udovicic Vladimir, Maletic Dimitrije M и др. (2018). “Multiyear Indoor Radon Variability in a Family House - a Case Study in Serbia”. у: *NUCLEAR TECHNOLOGY AND RADIATION PROTECTION* 33.2. M23, IF 0,620, с. 174—179.

M, Bogomilov и др. (2017). “Lattice design and expected performance of the Muon Ionization Cooling Experiment demonstration of ionization cooling”. у: *PHYSICAL REVIEW ACCELERATORS AND BEAMS* 20.6. M23, IF 1,413, с. -.

Z, Filipovic Jelena и др. (2016). “The use of multivariate analysis of the radon variability in the underground laboratory and indoor environment”. у: *NUKLEONIKA* 61.3. M23, IF 0,760, с. 357—360.

M33

Savić, M., A. Dragić, N. Veselinović и др. (2016). “Effect of pressure and temperature corrections on muon flux variability at ground level and underground”. у: с. -.

R, Savic Mihailo, Maletic Dimitrije M и др. (2015). “Pressure and temperature effect corrections of atmospheric muon data in the Belgrade cosmic-ray station”. у: т. 632, с. -.

B, Veselinovic Nikola, Dragic Aleksandar L, Maletic Dimitrije M и др. (2015). “Cosmic Rays Muon Flux Measurements at Belgrade Shallow Underground Laboratory”. у: т. 1645, с. 421—425.

M, Maletic Dimitrije, Banjanac Radomir M и др. (2015). “Correlative and Periodogram Analysis of Dependence of Continuous Gamma Spectrum in the Shallow Underground Laboratory on Cosmic Ray and Climate Variables”. у: с. 47—50.

M, Banjanac Radomir, Udovicic Vladimir I и др. (2015). “Background Spectrum Characteristics of the HPGE Detector Long-Term Measurement in the Belgrade Low-Background Laboratory”. у: с. 151—153.

Veselinović, N. и др. (2014). “Some peculiarities of digital gamma-ray spectroscopy with germanium detectors performed in presence of neutrons”. у: т. 59, с. 63—70.

Banjanac, R., V. Udovičić и др. (2014). “Relation between daily gamma-ray background and radon variability in the underground low-level laboratory in Belgrade”. у: с. 99—101.

Banjanac, R., A. Dragić и др. (2013). “Comparative study of gamma-ray background and radon concentration inside ground level and underground low-level laboratories”. у: с. 9—12.

M, Maletic Dimitrije, Dragic Aleksandar L и др. (2013). “Stopped cosmic-ray muons in plastic scintillators on the surface and at the depth of 25 m.w.e.” у: т. 409, с. -.

L, Dragic Aleksandar, Anicin Ivan V и др. (2013). “Neutrons produced by muons at 25 mwe”. у: т. 409, с. -.

Maletić, D, V Udovičić, R Banjanac, A Dragić, D Joković, M Savić и др. (2012). “Semi-empirical simulation of natural background in underground laboratory”. у: *Proceedings of the 3rd International Conference on Environmental Protection, Veszprém, Hungary*, с. 83—88.

M34

Udovičić, V. и др. (2015). “Merenje koncentracije radona i procena izloženosti u Bogovinskoj pećini”. у: *XXVIII Simpozijum DZZSCG, Vršac, Zbornik radova*, с. 207—211.

Filipović, J. и др. (2015). “Korelaciona i regresiona analiza varijabilnosti radona primenom multivarijantnih metoda”. у: *XXVIII Simpozijum DZZSCG, Vršac, Zbornik radova*, с. 254—259.

Maletić, D., N. Veselinović и др. (2015). “Monte Karlo simulacija kreiranja kosmogenih radionuklida u lesu”. у: *XXVIII Simpozijum DZZSCG, Vršac, Zbornik radova*, с. 481—486.

Banjanac, R., A. Dragić и др. (2015). “Gledanje u kuglu – 25 godina posle”. у: *XXVIII Simpozijum DZZSCG, Vršac, Zbornik radova*, с. 548—554.

Maletić, D., D. Joković, M. Savić и др. (2015a). “Određivanje temperaturskog profila atmosfere merenjem intenziteta kosmičkog zračenja na površini Zemlje”. у: *XXVIII Simpozijum DZZSCG, Vršac, Zbornik radova*, с. 577—583.

— (2015b). “Automatska obrada podataka kosmike i evaluacija koncentracije radona na internet (web) serveru”. у: *XXVIII Simpozijum DZZSCG, Vršac, Zbornik radova*, с. 584—588.

Maletić, D., D. Joković, R. Banjanac и др. (2015). “Korišćenje mobilnog telefona za testiranje i optimizaciju laboratorijskih merenja fotomultipliaktorima”. у: *XXVIII Simpozijum DZZSCG, Vršac, Zbornik radova*, с. 589—593.

Banjanac, R и др. (2013). “Varijacije radona i kosmičkog zračenja kao izvori vremenske varijacije fona gama zračenja u niskofonskoj gama spektrometriji”. у: *XII Kongres fizičara Srbije, Vrnjačka Banja, Zbornik radova*, с. 177—180.

Dragić, A и др. (2013a). “Indeks devijacije DTR i kosmički zraci”. у: *XII Kongres fizičara Srbije, Vrnjačka Banja, Zbornik radova*, с. 193—196.

— (2013b). “Produkcija neutrona mionima iz kosmičkog zračenja na dubini od 25 m.w.e”. у: *XII Kongres fizičara Srbije, Vrnjačka Banja, Zbornik radova*, с. 197—200.

Maletić, D, A Dragić и др. (2013a). “Paket programa za spektralnu i vremensku analizu podataka u digitalnoj nuklearnoj i spektroskopiji kosmičkog zračenja”. у: *XII Kongres fizičara Srbije, Vrnjačka Banja, Zbornik radova*, с. 220—223.

Maletić, D, A Dragić и др. (2013b). “Polarizacija miona kosmičkog zračenja na površini Zemlje i u podzemnoj laboratoriji”. у: *XII Kongres fizičara Srbije, Vrnjačka Banja, Zbornik radova*, с. 224—227.

Maletić, D, V Udovičić, R Banjanac, A Dragić, D Joković, N Veselinović и др. (2013). “Semi-empirijska simulacija prirodnog fona u podzemnoj laboratoriji”. у: *XII Kongres fizičara Srbije, Vrnjačka Banja, Zbornik radova*, с. 228—231.

Puzović, J. и др. (2013). “NA61/SHINE eksperiment i detektorski sistem”. у: *XII Kongres fizičara Srbije, Vrnjačka Banja, Zbornik radova*, с. 244—247.

M70

Савић, Михаило (2019). “Моделовање утицаја атмосфере на мионску компоненту секундарног космичког зрачења”. дис. ... док. Физички факултет Универзитета у Београду.

Scopus

Citation overview

The citation overview has been downloaded as a comma separated file (.csv).

Back to author details

Export Print

This is an overview of citations for this author.

Author *h*-index : 2 View *h*-graph

18 Cited Documents from"Savić, Mihailo R."

Save to list

Author ID:55499127000

Date range: 2015 to 2019 Exclude self citations of selected author Exclude self citations of all authors Exclude citations from books Update

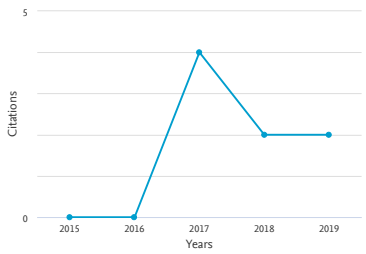

Sort on: Date (newest)

Page Remove

	Documents	Citations	<2015	2015	2016	2017	2018	2019	Subtotal	>2019	Total
		Total	8	0	0	4	2	2	8	0	16
1	A novel method for atmospheric correction of cosmic-ray data...	2019							0		0
2	First particle-by-particle measurement of emittance in the M...	2019							0		0
3	Rigidity dependence of Forbush decreases in the energy regio...	2019						1	1		1
4	Multiyear indoor radon variability in a family house – A cas...	2018							0		0
5	An underground laboratory as a facility for studies of cosmi...	2017							0		0
6	Lattice design and expected performance of the Muon Ionizati...	2017					1		1		1
7	The use of multivariate analysis of the radon variability in...	2016							0		0
8	Pressure and temperature effect corrections of atmospheric m...	2015							0		0
9	Cosmic rays muon flux measurements at Belgrade shallow under...	2015							0		0
10	Correlative and periodogram analysis of dependence of contin...	2015							0		0

	Documents	Citations	<2015	2015	2016	2017	2018	2019	Subtotal	>2019	Total
		Total	8	0	0	4	2	2	8	0	16
11	Background spectrum characteristics of the HPGE detector lon...	2015							0		0
12	Relation between daily gamma-ray background and radon variab...	2014							0		0
13	Some peculiarities of digital gamma-ray spectroscopy with ge...	2014				1			1		1
14	Variations of gamma-ray background in the Belgrade shallow u...	2014						1	1		1
15	Neutrons produced by muons at 25 mwe	2013	1						0		1
16	Stopped cosmic-ray muons in plastic scintillators on the sur...	2013							0		0
17	The New set-up in the Belgrade low-level and cosmic-ray labo...	2011	7			2			2		9
18	Yield from proton-induced reaction on light element isotopes...	2011				1	1		2		2

Универзитет у Београду ФИЗИЧКИ ФАКУЛТЕТ
Студентски трг 12, 11000 Београд
Поштански фах 44
Тел. 011 7158 151, 3281 375
ПИБ 100039173, Мат. бр. 07048190

University of Belgrade FACULTY OF PHYSICS
Studentski trg 12, 11000 Belgrade
Postal Box 44
Phone +381 11 7158 151, Fax +381 11 3282 619
www.ff.bg.ac.rs, dekanat@ff.bg.ac.rs

УНИВЕРЗИТЕТ У БЕОГРАДУ
ФИЗИЧКИ ФАКУЛТЕТ
Бр. 348/12
05.07. 2019 год.
БЕОГРАД, СТУДЕНТСКИ ТРГ 12-16
П. ФАХ 44

На основу члана 29 Закона о општем управном поступку («Службени гласник РС» број 18/2016 и 95/2018), и члана 149 Статута Универзитета у Београду - Физичког факултета, по захтеву МИХАИЛА САВИЋА, мастер физичара, издаје се следеће

У В Е Р Е Њ Е

МИХАИЛО САВИЋ, мастер физичар, дана 4. јула 2019. године , одбранио је докторску дисертацију под називом

„МОДЕЛОВАЊЕ УТИЦАЈА АТМОСФЕРЕ НА МИОНСКУ КОМПОНЕНТУ СЕКУНДАРНОГ КОСМИЧКОГ ЗРАЧЕЊА“

пред Комисијом Универзитета у Београду - Физичког факултета, и тиме испунио све услове за промоцију у ДОКТОРА НАУКА – ФИЗИЧКЕ НАУКЕ.

Уверење се издаје на лични захтев, а служи ради регулисања права из радног односа и важи до промоције, односно добијања докторске дипломе.

Уверење је ослобођено плаћања таксе.

Република Србија * Универзитет у Београду * Физички факултет * Београд

ДЕКАН ФИЗИЧКОГ ФАКУЛТЕТА

Проф. др Иван Белча

PHYSICAL REVIEW C **89**, 025205 (2014)

Measurements of production properties of K^0_S mesons and Λ hyperons in proton-carbon interactions at 31 GeV/c

N. Abgrall,[1] A. Aduszkiewicz,[2] Y. Ali,[3] T. Anticic,[4] N. Antoniou,[5] J. Argyriades,[1] B. Baatar,[6] A. Blondel,[1] J. Blumer,[7] M. Bogomilov,[8] A. Bravar,[1] W. Brooks,[9] J. Brzychczyk,[3] S. A. Bunyatov,[6] O. Busygina,[10] P. Christakoglou,[5] T. Czopowicz,[11] N. Davis,[5] S. Debieux,[1] H. Dembinski,[7] F. Diakonos,[5] S. Di Luise,[12] W. Dominik,[2] T. Drozhzhova,[13] J. Dumarchez,[14] K. Dynowski,[11] R. Engel,[7] A. Ereditato,[15] L. Esposito,[12] G. A. Feofilov,[13] Z. Fodor,[16] A. Fulop,[16] M. Gaździcki,[17,18] M. Golubeva,[10] K. Grebieszkow,[11] A. Grzeszczuk,[19] F. Guber,[10] H. Hakobyan,[9] A. Haesler,[1] T. Hasegawa,[20] M. Hierholzer,[15] R. Idczak,[21] S. Igolkin,[13] Y. Ivanov,[9] A. Ivashkin,[10] D. Jokovic,[22] K. Kadija,[4] A. Kapoyannis,[5] E. Kaptur,[19] D. Kielczewska,[2] D. Kikola,[11] M. Kirejczyk,[2] J. Kisiel,[19] T. Kiss,[16] S. Kleinfelder,[23] T. Kobayashi,[20] V. I. Kolesnikov,[6] D. Kolev,[8] V. P. Kondratiev,[13] A. Korzenev,[1] P. Kovesarki,[21] S. Kowalski,[19] A. Krasnoperov,[6] S. Kuleshov,[9] A. Kurepin,[10] D. Larsen,[24] A. Laszlo,[16] V. V. Lyubushkin,[6] M. Mackowiak-Pawlowska,[18,11] Z. Majka,[3] B. Maksiak,[11] A. I. Malakhov,[6] D. Maletic,[22] D. Manic,[22] A. Marchionni,[12] A. Marcinek,[3] V. Marin,[10] K. Marton,[16] H.-J. Mathes,[7] T. Matulewicz,[2] V. Matveev,[10,6] G. L. Melkumov,[6] St. Mrówczyński,[17] S. Murphy,[1] T. Nakadaira,[20] M. Nirkko,[15] K. Nishikawa,[20] T. Palczewski,[25] G. Palla,[16] A. D. Panagiotou,[5] T. Paul,[26] W. Peryt,[11] C. Pistillo,[15] A. Redij,[15] O. Petukhov,[10] R. Planeta,[3] J. Pluta,[11] B. A. Popov,[6,14] M. Posiadała,[2] S. Puławski,[19] J. Puzovic,[22] W. Rauch,[27] M. Ravonel,[1] R. Renfordt,[18] A. Robert,[14] D. Röhrich,[24] E. Rondio,[25] M. Roth,[7] A. Rubbia,[12] A. Rustamov,[18] M. Rybczynski,[17] A. Sadovsky,[10] K. Sakashita,[20] M. Savic,[22] K. Schmidt,[19] T. Sekiguchi,[20] P. Seyboth,[17] M. Shibata,[20] R. Sipos,[16] E. Skrzypczak,[2] M. Slodkowski,[11] P. Staszel,[3] G. Stefanek,[17] J. Stepaniak,[25] T. Susa,[4] M. Szuba,[7] M. Tada,[20] V. Tereshchenko,[6] T. Tolyhi,[16] R. Tsenov,[8] L. Turko,[21] R. Ulrich,[7] M. Unger,[7] M. Vassiliou,[5] D. Veberic,[26] V. V. Vechernin,[13] G. Vesztergombi,[16] L. Vinogradov,[13] A. Wilczek,[19] Z. Wlodarczyk,[17] A. Wojtaszek,[17] O. Wyszyński,[3] L. Zambelli,[14] and W. Zipper[19]
(NA61/SHINE Collaboration)

[1]*University of Geneva, Geneva, Switzerland*
[2]*Faculty of Physics, University of Warsaw, Warsaw, Poland*
[3]*Jagiellonian University, Cracow, Poland*
[4]*Rudjer Boskovic Institute, Zagreb, Croatia*
[5]*University of Athens, Athens, Greece*
[6]*Joint Institute for Nuclear Research, Dubna, Russia*
[7]*Karlsruhe Institute of Technology, Karlsruhe, Germany*
[8]*Faculty of Physics, University of Sofia, Sofia, Bulgaria*
[9]*The Universidad Tecnica Federico Santa Maria, Valparaiso, Chile*
[10]*Institute for Nuclear Research, Moscow, Russia*
[11]*Warsaw University of Technology, Warsaw, Poland*
[12]*ETH, Zurich, Switzerland*
[13]*St. Petersburg State University, St. Petersburg, Russia*
[14]*LPNHE, University of Paris VI and VII, Paris, France*
[15]*University of Bern, Bern, Switzerland*
[16]*Wigner Research Centre for Physics of the Hungarian Academy of Sciences, Budapest, Hungary*
[17]*Jan Kochanowski University in Kielce, Poland*
[18]*University of Frankfurt, Frankfurt, Germany*
[19]*University of Silesia, Katowice, Poland*
[20]*Institute for Particle and Nuclear Studies, KEK, Tsukuba, Japan*
[21]*University of Wrocław, Wrocław, Poland*
[22]*University of Belgrade, Belgrade, Serbia*
[23]*University of California, Irvine, USA*
[24]*University of Bergen, Bergen, Norway*
[25]*National Center for Nuclear Research, Warsaw, Poland*
[26]*Laboratory of Astroparticle Physics, University Nova Gorica, Nova Gorica, Slovenia*
[27]*Fachhochschule Frankfurt, Frankfurt, Germany*

(Received 14 September 2013; published 28 February 2014)

Spectra of K^0_S mesons and Λ hyperons were measured in p + C interactions at 31 GeV/c with the large acceptance NA61/SHINE spectrometer at the CERN SPS. The data were collected with an isotropic graphite target with a thickness of 4% of a nuclear interaction length. Interaction cross sections, charged pion spectra, and charged kaon spectra were previously measured using the same data set. Results on K^0_S and Λ production in p + C interactions serve as a reference for the understanding of the enhancement of strangeness production in nucleus-nucleus collisions. Moreover, they provide important input for the improvement of neutrino flux predictions for the T2K long baseline neutrino oscillation experiment in Japan. Inclusive production cross

sections for K^0_S and Λ are presented as a function of laboratory momentum in intervals of the laboratory polar angle covering the range from 0 up to 240 mrad. The results are compared with predictions of several hadron production models. The K^0_S mean multiplicity in production processes $\langle n_{K^0_S} \rangle$ and the inclusive cross section for K^0_S production $\sigma_{K^0_S}$ were measured and amount to 0.127 ± 0.005 (stat) $\pm$ 0.022 (sys) and 29.0 ± 1.6 (stat) $\pm$ 5.0 (sys) mb, respectively.

DOI: 10.1103/PhysRevC.89.025205 PACS number(s): 13.85.Lg, 13.85.Hd, 13.85.Ni, 25.40.Ve

I. INTRODUCTION

Experimental data on strange particle production in proton-proton and proton-carbon interactions in the region below few tens of GeV/c incident momentum are scarce [1–4]. There are at least two reasons why the knowledge of yields of strange mesons and baryons are of considerable interest at the beam momentum of 31 GeV/c. One is the need to include the tuned production of these particles in the precise neutrino flux calculation for accelerator neutrino experiments as an additional source of neutrinos and secondary pions. Production of neutral kaons is important for accurate calculation of the ν_e and $\bar{\nu}_e$ flux from $K^0_L \to \pi e \nu_e$ decays. The other is the understanding of the production of strangeness in nucleus-nucleus interactions in this energy region and its proposed interpretation as a signal of the onset of deconfinement. Hadron-nucleus interactions constitute an intermediate step between proton-proton and nucleus-nucleus interactions. Therefore their study permits one to understand better the influence of nuclear matter on strangeness production and can help one understand the role of the nucleus and nonexotic mechanisms of strangeness production. In addition to the primary goal of providing reference data for the T2K neutrino experiment in Japan, precise results on particle production in p + C interactions furnish important input to improve hadronic event generators which are required for the interpretation of air showers initiated by ultrahigh energy cosmic particles. The NA61/SHINE collaboration already published results on charged pion [5] and K^+ production [6]. In this paper we present results on K^0_S and Λ yields. These were obtained from the analysis of the same sample of p + C collisions at 31 GeV/c beam momentum collected with the NA61/SHINE large acceptance spectrometer at the CERN SPS in 2007. The statistics of this data sample is insufficient to obtain results on $\overline{\Lambda}$ yields, which are about 100 times smaller than Λ yields [7].

The paper is organized as follows. Section II provides information about the NA61/SHINE experimental apparatus. The main components of the detector and trigger system are presented. In addition, the target used is described and numbers of registered proton interactions are provided. The analysis technique is discussed in Sec. III. In this section, the procedure of the extraction of the K^0_S mesons and Λ hyperons is described in detail. The calculation of corrections and the normalization procedure are discussed. Section III A presents event and track selection criteria as well as the adopted phase space binning scheme. Information about extraction of the K^0_S mesons and Λ hyperons from the data and calculation of the correction factors used to correct raw yields for detector and other effects are described in Secs. III B and III C, respectively. The main sources of the systematic uncertainty are discussed in Sec. III D. The final results are shown in Sec. IV. They are compared to predictions of different hadron production models in Sec. V. Finally, Sec. VI summarizes the results of the paper.

II. THE NA61/SHINE EXPERIMENTAL SETUP

The NA61/SHINE experiment [8] is situated in the North Area H2 beam line of the CERN SPS. It is the successor of the NA49 experiment [9]. The NA61/SHINE detector is a large acceptance hadron spectrometer, which consists of a set of large volume time projection chambers (TPCs) and time-of-flight (ToF) scintillator walls. The schematic layout of the detector is shown in Fig. 1 together with the overall dimensions. Two of the TPCs (VTPC-1 and VTPC-2) are placed in the magnetic field produced by two superconducting dipole magnets with maximum combined bending power of 9 Tm. During the 2007 data-taking period the magnetic field was set to a bending power of 1.14 Tm to optimize the detector acceptance for the measurements needed for the T2K experiment. The TPCs were filled with Ar:CO_2 gas mixtures in proportions 90:10 for the VTPCs and 95:5 for the MTPCs. A set of scintillation and Cherenkov counters as well as beam position detectors (BPDs) upstream of the main detection system provided timing reference, identification, and position measurements of the incoming beam particles. The 31-GeV/c secondary hadron beam was produced from 400-GeV protons extracted from the SPS in slow extraction mode. The secondary beam was transported along the H2 beam line towards the experiment. Collimators in the beam line were adjusted to get an average beam particle rate of 15 kHz. Protons in the beam were identified by two Cherenkov counters, a CEDAR and a threshold counter, labeled C1 and C2, respectively. Two scintillation counters, S1 and S2, together with two veto counters, V0 and V1, were used to select beam particles. The S1 counter also provided the timing (start time for all counters). Beam protons were selected by the coincidence $S1 \cdot S2 \cdot \overline{V0} \cdot \overline{V1} \cdot C1 \cdot \overline{C2}$. The trajectory of individual beam particles is measured in the BPDs along the beam line. These counters are small (3×3 cm^2) proportional chambers with cathode strip readout (BPD-1/2/3 in Fig. 1). A special run was taken to measure the beam momentum by bending the incoming beam particles into the TPCs with the full magnetic field. From this measurement the mean momentum value of 30.75 GeV/c was obtained. Interactions in the target were selected by an anticoincidence of the incoming beam protons with a small, 2-cm diameter, scintillation counter (S4) placed on the beam trajectory between the two vertex magnets (see Fig. 1). This minimum bias trigger was based on the disappearance of the incident proton. The results presented here were obtained from 667×10^3 proton interactions recorded with an isotropic graphite target of dimensions 2.5(W) $\times$ 2.5(H) $\times$ 2(L) cm^3 and with a density of

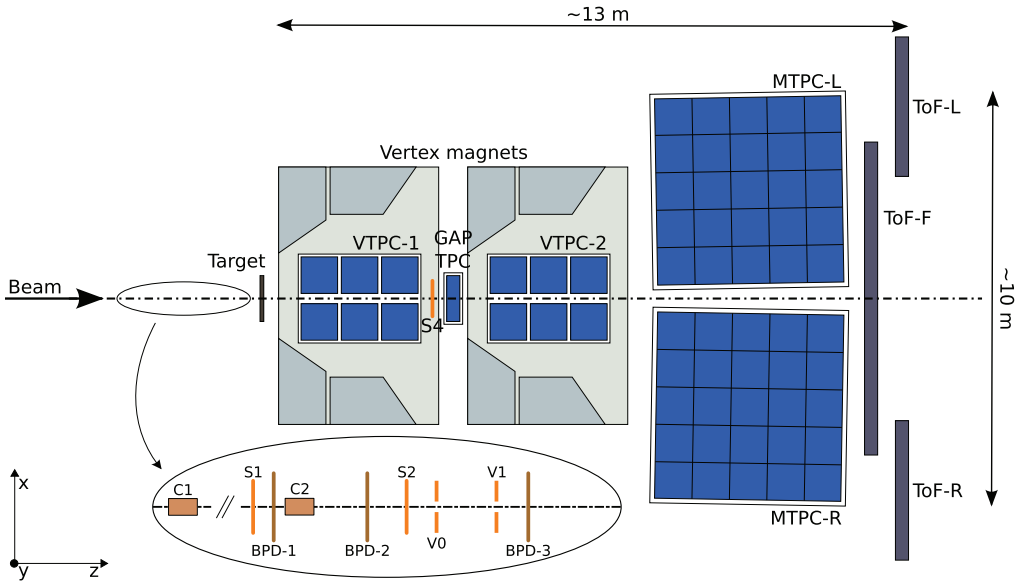

FIG. 1. (Color online) The NA61/SHINE experimental apparatus; see text for details.

$\rho = 1.84$ g/cm^3. For normalization purposes 46×10^3 proton interactions with the carbon target removed were also recorded. The carbon target was installed 80 cm in front of VTPC-1.

III. ANALYSIS TECHNIQUE

The most frequent decays of K^0_S mesons and Λ hyperons lead to the production of two oppositely charged particles. The measurement of particle tracks in the magnetic field allows one to determine their charges and momenta. This section presents the method of K^0_S and Λ analysis using invariant mass distributions. When the K^0_S hypothesis is studied, positively (negatively) charged tracks are assumed to be π^+ (π^-) mesons. For the Λ hypothesis the positively (negatively) charged particles are assumed to be protons (π^- mesons). The analysis was made in specific invariant mass windows. The selected window should cover the invariant mass peak of K^0_S (Λ) but also include regions below and above the peak for the background estimate. Fits of the background function depend somewhat on the selected side regions. This effect was checked and added to the systematic uncertainties (see Sec. III D). The number of K^0_S and Λ was determined from fitting a sum of Lorentzian function and polynomial function for the signal and the background, respectively. The Lorentzian function is described by

$$f(x) = A\frac{\frac{1}{2}F}{(x-x_0)^2 + \left(\frac{1}{2}F\right)^2}, \qquad (1)$$

where parameter A controls the height of the peak, F is the full width at half maximum (FWHM), and x_0 is the mean value (in this case, the fitted K^0_S or Λ mass). The low statistics data forced to constrain the width of the signal function according to the Monte Carlo predictions. Namely, the width from Monte Carlo was set as the initial value. Then, this parameter was allowed to vary for K^0_S up to $\pm 5 \cdot \Delta F_{\mathrm{MC}}$ and for Λ up to $\pm 7 \cdot \Delta F_{\mathrm{MC}}$, where ΔF_{MC} is the fit uncertainty of the fitted Monte Carlo width in a given $\{p, \theta\}$ bin. The fit results in the Lambda case were less stable and a lower value of the chi square was obtained for the larger range. The influence of these assumptions on the final result was checked and added to the systematic uncertainties (see Sec. III D). In the standard approach a fourth-order polynomial was used as the background function. The sensitivity to different shapes of the background function was studied and is included in the systematic uncertainties (see Sec. III D). The raw number of K^0_S and Λ was calculated as the integral of the fitted signal function Eq. (1). Corrections were applied to the raw numbers of K^0_S and Λ to obtain their yields produced in the primary p + C interactions after strong and electromagnetic decays. Correction factors were derived from a Monte Carlo procedure in which events were generated from the hadron production model VENUS 4.12 [10] and then sent through a full simulation of the detector. The procedure takes into account the trigger bias, the vertex fit requirement and cuts, the branching ratio for the studied type of decay, the geometrical acceptance, the reconstruction efficiency, feed-down from interactions with the target material, as well as Λ hyperons coming from Cascade hyperon decays. The inverse multiplicative Monte Carlo correction is calculated using the following formula,

$$E(p,\theta) = \left(\frac{n_x}{N}\right)^{\mathrm{MC}}_{\mathrm{acc}} \Big/ \left(\frac{n_x}{N}\right)^{\mathrm{MC}}_{\mathrm{gen}}, \qquad (2)$$

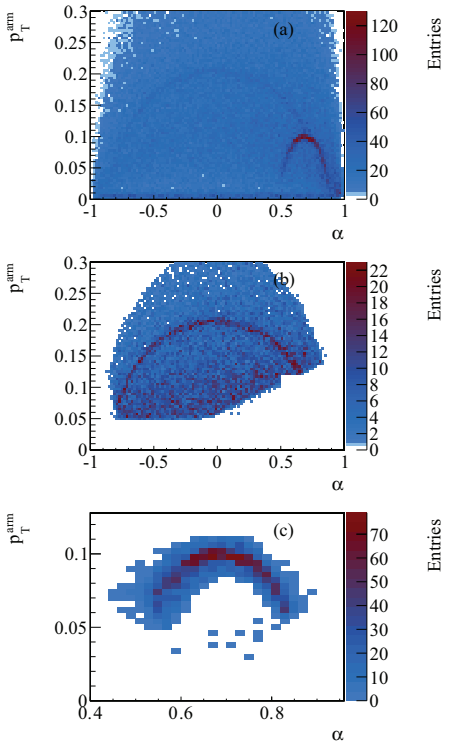

FIG. 2. (Color online) Armenteros-Podolanski plots before (a) and after all cuts for K_S^0 (b) and Λ candidates (c).

which compares the information on simulated particles at the primary hadron generator level (gen) with that on reconstructed identified particles (acc). The quantity n_x is the number of the identified particle of type x (K_S^0 or Λ) in a given bin of phase space, and N is the number of events. The correction can be split into two parts: the first one connected with the correction of numbers of a given particle of type x in a given bin ($n_x^{\rm acc}/n_x^{\rm gen}$ which will be denoted γ) and the second one connected with the correction of the number of events ($N^{\rm acc}/N^{\rm gen}$ which will be denoted η). Therefore, the correction can be rewritten as follows:

$$E(p,\theta) = \left(\frac{n_x^{\rm acc}}{n_x^{\rm gen}}\right)^{\rm MC} \Big/ \left(\frac{N^{\rm acc}}{N^{\rm gen}}\right)^{\rm MC} = \frac{\gamma}{\eta}. \tag{3}$$

The subtraction of nontarget interactions was performed using information from events recorded with the target removed. The normalization was obtained far away from the target where all reconstructed vertices originate from interactions with the detector material (neglecting the beam attenuation in the target). The number of particles per event in a given phase space bin, corrected for nontarget interactions, is calculated as

$$\frac{n}{N} = \frac{1}{E}\frac{n^I - Bn^R}{N^I - BN^R}, \tag{4}$$

where I and R superscripts indicate data with target inserted and removed, respectively. The factor B is calculated from the data:

$$B = \frac{N^I_{\rm beam}}{N^R_{\rm beam}} = \frac{N^I_{\rm far\,z}}{N^R_{\rm far\,z}}, \tag{5}$$

where $N^{R/I}_{\rm beam}$ is the number of beam particles in data with target removed and inserted, respectively, and $N^{R/I}_{\rm far\,z}$ is the corresponding number of events with fitted vertex longitudinal coordinate z, far away from the target. The differential spectrum is calculated as

$$\frac{dn}{dp} = \frac{n}{N}\frac{1}{\Delta p}. \tag{6}$$

Then the differential cross section is calculated as

$$\frac{d\sigma}{dp} = \sigma_{\rm prod}\frac{dn}{dp}, \tag{7}$$

where $\sigma_{\rm prod}$ is equal to $229.3 \pm 1.9 \pm 9.0$ mb. The uncertainties on $\sigma_{\rm prod}$ were not included in the uncertainties of the final results presented in this paper. The measurements of the inelastic and production cross sections are presented in Ref. [11].

A. Event and track selection, data binning

The analysis is based on 667 $\times 10^3$ event triggers with the graphite target inserted and 46 $\times 10^3$ triggers with the target removed. Only events with a properly reconstructed beam track (see Sec. II) were retained. First of all, the information from the beam position detectors, placed upstream of the target (see Fig. 1), was used to ensure a well-defined beam track (see Ref. [8] for details). Then, events with reconstructed primary

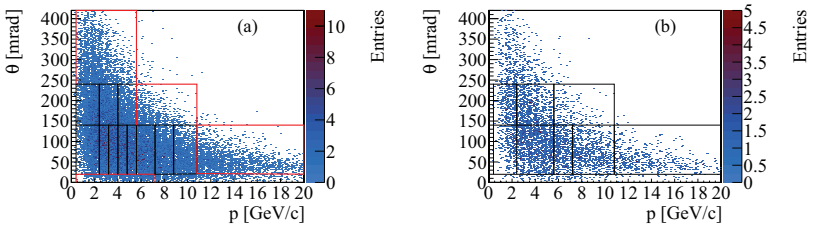

FIG. 3. (Color online) The momentum vs polar angle distributions for K_S^0 (a) and Λ (b) candidates with superimposed binning.

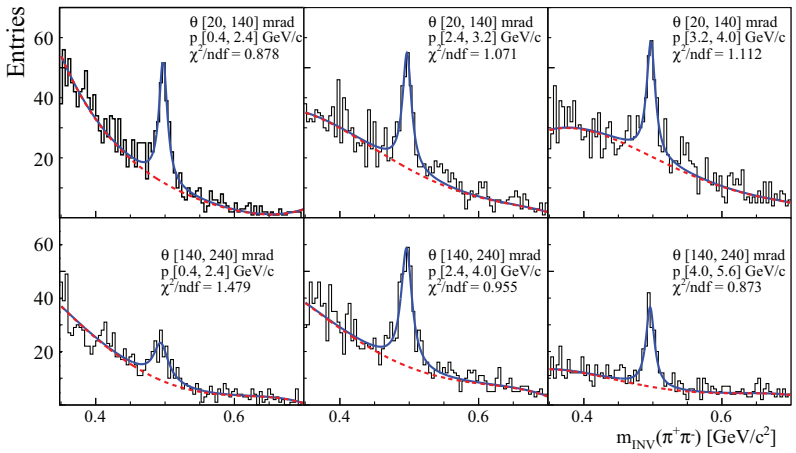

FIG. 4. (Color online) The invariant mass distributions for K^0_S candidates in selected $\{p, \theta\}$ bins. Data (black) with superimposed background function (red dashed) and global fit (blue solid) are shown.

vertex, within the target (vertex z position within the range $[-585.0, -575.0]$ cm), were selected to reject interactions that did not take place in the target but in the surrounding detector material. Any pair of tracks with opposite charges and distance of closest approach smaller than 1 cm was taken as a possible V^0 candidate. To purify the sample and select candidates which correspond to K^0_S or Λ with high probability additional cuts were applied:

(i) The distance along the beam direction between the primary vertex and the V^0 decay point had to be larger than 3 cm. This cut was used to reject cases in which primary vertex tracks were wrongly reconstructed as V^0 tracks. The same minimum distance cut was used for K^0_S and Λ. Although the decay lengths of the two particles are different, the signal to background ratio are very similar using the same cut.

(ii) The V^0 momentum vector had to point back to the primary vertex within a cut of d_x and $d_y < 3$ cm in the transverse $\{x, y\}$ plane for K^0_S and Λ candidates.

(iii) The analysis was performed in the invariant mass windows $[0.35, 0.7]$ GeV$/c^2$ and $[1.09, 1.16]$ GeV$/c^2$ for K^0_S and Λ, respectively.

(iv) A cut was applied on the angle between the momentum of the V^0 candidate and its decay products in the c.m. system. Because of the expected isotropy of the decay

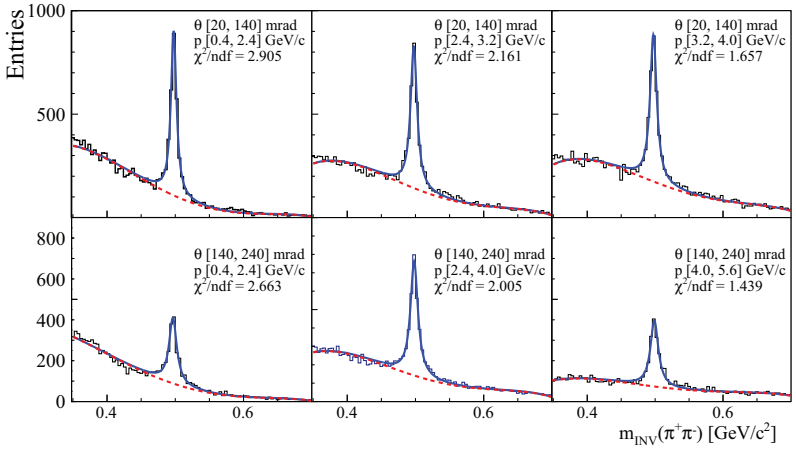

FIG. 5. (Color online) The invariant mass distributions for Λ candidates in selected $\{p, \theta\}$ bins. Data (black) with superimposed background function (red dashed) and global fit (blue solid) are shown.

TABLE I. The raw number of K^0_S and Λ extracted by the fitting procedure in selected momentum and polar angle intervals.

K^0_S						Λ			
θ_{low} (mrad)	θ_{up}	p_{low} (GeV/c)	p_{up}	n	Δn	p_{low} (GeV/c)	p_{up}	n	Δn
0	20	0.4	7.2	61	10				
20	140	0.4	2.4	178	23	0.4	2.4	53	8
		2.4	3.2	167	18	2.4	5.6	562	26
		3.2	4.0	165	18				
		4.0	4.8	126	18				
		4.8	5.6	132	16				
		5.6	7.2	130	16	5.6	7.2	248	16
		7.2	8.8	80	15	7.2	10.8	468	22
		8.8	10.8	115	15				
		10.8	20.0	102	17	10.8	20.0	362	19
140	240	0.4	2.4	93	15	0.4	2.4	60	12
		2.4	4.0	233	20	2.4	5.6	344	20
		4.0	5.6	135	20				
		5.6	10.8	88	12	5.6	10.8	72	17
240	420	0.4	5.6	135	26				

in the V^0 rest frame the distribution of the cosine of this angle ($\cos\epsilon$) should be flat. The cut was set to $-0.95 < \cos\epsilon < 0.8$ and $-0.8 < \cos\epsilon < 0.8$ for K^0_S and Λ, respectively.

(v) Cuts in the Armenteros-Podolanski plot were applied. The relation between Armenteros transverse momentum (p_T^{arm}) and longitudinal momentum asymmetry (α) can be used to separate K^0_S mesons from Λ hyperons with high probability. The separation of K^0_S and Λ candidates using the Armenteros-Podolanski plot is shown in Fig. 2. For the selection of K^0_S candidates, the regions p_T^{arm} and $\alpha < 0.05$ were excluded in addition to the diagonal cut implied by the the $\cos\epsilon$ (iv). In addition the region $\alpha > 0.5$ and $p_T^{arm} < 0.12$ is rejected to get rid of background originating from Λ particles. For the Λ selection, the region $p_T^{arm} < 0.03$ or >0.11 was excluded. Furthermore, the region $\alpha < 0.45$ was rejected.

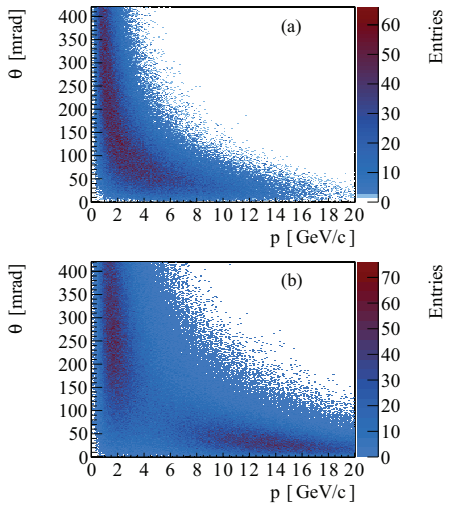

FIG. 6. (Color online) The momentum vs polar angle distribution for simulated K^0_S mesons (a) and Λ hyperons (b).

The K^0_S candidate momentum vs polar angle distribution after event, track, and V^0 selection cuts is shown in Fig. 3 with superimposed binning. The bins outlined in red were more sensitive to the model-dependent corrections because for them the uncertainty of the shape of the event generator distributions could significantly affect the final results.

B. Raw yields

The $(\pi^+\pi^-)$ invariant mass distributions in selected $\{p, \theta\}$ bins for K^0_S candidates are presented in Fig. 4. The invariant mass distributions for Λ candidates in selected $\{p, \theta\}$ bins are presented in Fig. 5. The raw number of K^0_S and Λ extracted in the selected momentum and polar angle intervals is presented in Table I.

C. Corrections

The simulation chain described in Ref. [5] was used to correct raw yields for detector effects (i.e., geometrical acceptance, reconstruction efficiency, resolution of p and θ measurements), contributions from nonprimary V^0 decays, and decay branching ratios. The correction factor was calculated according to Eq. (2). For this calculation information from the simulation about reconstructed and simulated particles of each type is needed. The number of reconstructed particles is obtained in the same way as for the real data as the result of the integration of the fitted signal function after background subtraction. The momentum versus polar angle distribution of simulated K^0_S and Λ from the employed VENUS 4.12 model [10] is presented in Fig. 6.

The invariant mass distributions for K^0_S and Λ candidates in selected $\{p, \theta\}$ bins are presented in Figs. 7 and 8, respectively.

The correction factors γ for K^0_S and Λ [see Eq. (3)] were evaluated in bins of momentum and polar angle variables and are presented in Tables II and III, respectively. The correction factor η is bin independent and was estimated to be equal to 0.8083 ± 0.0005.

The correction procedure was checked by evaluating the lifetime of K^0_S and Λ from the corrected distribution of distances between the production and decay vertices. The proper decay length ($c\tau$) distributions for K^0_S mesons and Λ hyperons are shown in Fig. 9.

The obtained average proper decay lengths of 2.68 ± 0.02 cm for K^0_S and 7.46 ± 0.33 cm for Λ are consistent with the world averages. The contribution of nontarget interactions has little impact on the final results. The ratio B was found to be equal to 2.198 ± 0.027. After all cuts there were no V^0 candidates found in the data recorded with the target removed. Therefore, the subtraction procedure for out of target interactions changes only the number of events used for the

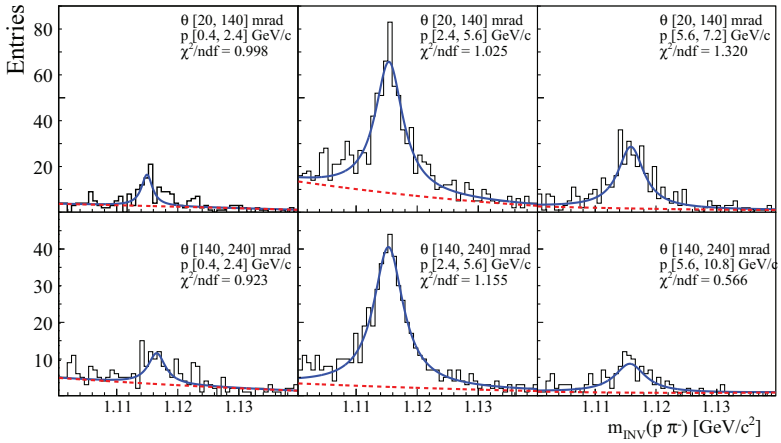

FIG. 7. (Color online) The invariant mass distributions for simulated K^0_S candidates in selected $\{p, \theta\}$ bins.

normalization of spectra. The values of N^I and N^I-BN^R were 276 481 and 276 421, respectively.

D. Systematic errors

The main sources of the systematic uncertainty are as follows.

(i) The uncertainty connected with the track cuts. The contribution of this source was studied by varying all standard track cuts (see Sec. III A). In particular the minimum distance between the primary vertex and the V^0 decay point was varied from 3 to 6 cm. The invariant mass window was changed to [0.4, 0.65] GeV/c^2 and to [1.09, 1.16] GeV/c^2 for K^0_S and Λ, respectively. The accepted region for the cos ϵ was reduced to $[-0.8, 0.6]$ for K^0_S and to $[-0.7,0.7]$ for Λ. The cuts in the Armenteros-Podolanski plots were varied by about 10%.

(ii) The uncertainty connected with the background function used in the fitting procedure. Apart from the standard fourth-order polynomial a set of different background functions was tried (third-order polynomial, sixth-order Chebyshev polynomial, Argus function).

(iii) The uncertainty connected with the fitting procedure. Because of the low statistics of the data, fit results depend on the fit strategy and the limits set for the parameters. The most prominent effect was observed when the width of the signal function was varied. The initial values of the position and the width of the signal

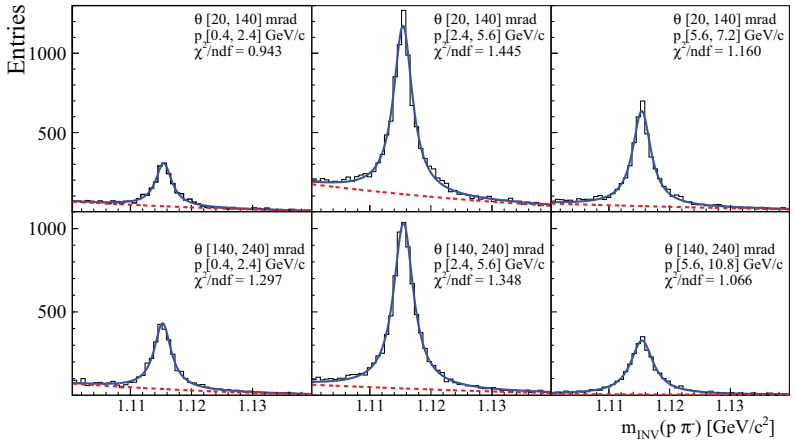

FIG. 8. (Color online) The invariant mass distributions for simulated Λ candidates in selected $\{p, \theta\}$ bins.

TABLE II. The number of simulated K^0_S ($n_{\rm sim}$), number of K^0_S found by the fitting procedure ($n_{\rm rec}$), the γ-correction factor, and their errors in selected momentum and polar angle intervals.

$\theta_{\rm low}$ (mrad)	$\theta_{\rm up}$	$p_{\rm low}$ (GeV/c)	$p_{\rm up}$	$n_{\rm sim}$	$\Delta n_{\rm sim}$	$n_{\rm rec}$	$\Delta n_{\rm rec}$	γ	$\Delta\gamma$
0	20	0.4	7.2	10908	104	1067	37	0.0979	0.0035
20	140	0.4	2.4	58087	241	2417	55	0.0416	0.001
		2.4	3.2	32905	181	2472	59	0.0751	0.0018
		3.2	4.0	31544	178	2624	62	0.0831	0.0020
		4.0	4.8	28274	168	2574	62	0.0910	0.0022
		4.8	5.6	24330	156	2241	57	0.0921	0.0024
		5.6	7.2	36936	192	3345	71	0.0905	0.0020
		7.2	8.8	24172	155	2325	60	0.0962	0.0025
		8.8	10.8	18054	134	1726	52	0.0956	0.0029
		10.8	20.0	16742	129	1521	54	0.0909	0.0033
140	240	0.4	2.4	69280	263	1359	45	0.0196	0.0006
		2.4	4.0	31443	177	2548	61	0.0810	0.0020
		4.0	5.6	10373	102	1417	46	0.1366	0.0046
		5.6	10.8	4250	65	661	34	0.1557	0.0083
240	420	0.4	5.6	119075	345	2209	61	0.0185	0.0005

were taken from the large statistic MC simulations and the variation within $\pm 10 \cdot \Delta F_{\rm MC}$ was used for the systematic error studies.

(iv) The uncertainty connected with the inaccurate description of the reconstructed primary vertex distribution in the Monte Carlo.

(v) The uncertainty connected with the inaccuracy of the geometrical acceptance obtained from Monte Carlo simulation, reconstruction efficiency, and different algorithms used for track merging.

(vi) The uncertainty connected with the $\{p, \theta\}$ bin size from imperfect modeling of K^0_S and Λ spectra in the Monte Carlo. This effect was only studied in the K^0_S case by looking at the distributions in different Monte Carlo generators.

(vii) The uncertainty from inaccuracy of the feed-down corrections was estimated to be smaller than 1%.

Moreover we compared the overall MC corrections obtained using VENUS and FLUKA generators. The differences were found to be within statistical errors. The systematic

TABLE III. The number of simulated Λ ($n_{\rm sim}$), number of Λ found by the fitting procedure ($n_{\rm rec}$), γ correction factor, and their errors in selected momentum and polar angle intervals.

$\theta_{\rm low}$ (mrad)	$\theta_{\rm up}$	$p_{\rm low}$ (GeV/c)	$p_{\rm up}$	$n_{\rm sim}$	$\Delta n_{\rm sim}$	$n_{\rm rec}$	$\Delta n_{\rm rec}$	γ	$\Delta\gamma$
20	140	0.4	2.4	38316	196	1557	43	0.041	0.001
		2.4	5.6	62777	250	7081	90	0.113	0.001
		5.6	7.2	30357	174	3896	64	0.128	0.002
		7.2	10.8	79015	281	9122	95	0.115	0.001
		10.8	20.0	121755	349	10883	102	0.089	0.001
140	240	0.4	2.4	61866	249	2377	52	0.038	0.001
		2.4	5.6	58957	243	6929	84	0.117	0.001
		5.6	10.8	15894	126	2595	51	0.163	0.003

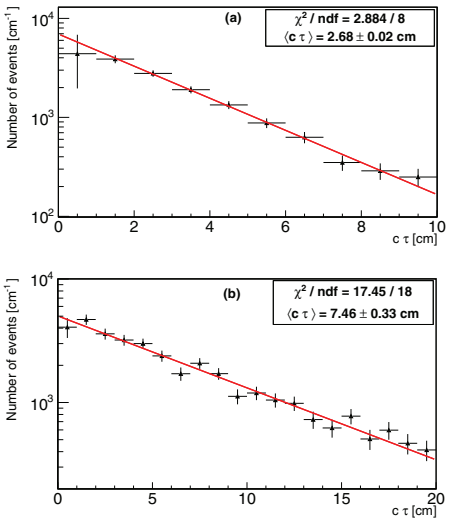

FIG. 9. (Color online) The proper decay length ($c\tau$) distributions for K^0_S mesons (a) and Λ hyperons (b).

errors connected with uncertainties discussed in points (i) and (iv) were found to be almost momentum independent. The uncertainties discussed in point (v) depend strongly on the selected $\{p, \theta\}$ bin. The systematic errors were estimated following the procedure presented in Refs. [5,6].

The final systematic errors, calculated as the sum in quadrature of errors connected with the uncertainties discussed above, were found to be about 13.5%–20.0% for K^0_S and Λ depending on the emission angle interval. The largest contributions always come from the uncertainty connected with the fitting

TABLE IV. The NA61/SHINE results for the differential K^0_S production cross section in the laboratory system for p + C interactions at 31 GeV/c. The overall cross-section normalization uncertainty of 2.5 % is not included in the systematic errors.

$\theta_{\rm low}$ (mrad)	$\theta_{\rm up}$	$p_{\rm low}$ (GeV/c)	$p_{\rm up}$	$d\sigma_{K^0_S}/dp$ (mb/GeV/c)	$\Delta_{\rm stat}$	$\Delta_{\rm stat}$ (%)	$\Delta_{\rm sys}$ (%)
0	20	0.4	7.2	0.061	0.010	16.8	18.4
20	140	0.4	2.4	1.434	0.188	13.1	17.8
		2.4	3.2	1.862	0.206	11.0	15.5
		3.2	4.0	1.662	0.186	11.2	14.4
		4.0	4.8	1.159	0.168	14.5	14.4
		4.8	5.6	1.200	0.158	13.1	14.4
		5.6	7.2	0.601	0.075	12.5	14.4
		7.2	8.8	0.348	0.066	18.9	14.4
		8.8	10.8	0.403	0.054	13.4	16.3
		10.8	20.0	0.082	0.014	17.0	18.6
140	240	0.4	2.4	1.589	0.26	16.5	19.5
		2.4	4.0	1.204	0.139	8.9	14.4
		4.0	5.6	0.414	0.063	15.2	14.4
		5.6	10.8	0.073	0.011	14.6	16.9
240	420	0.4	5.6	0.938	0.182	19.4	20.6

TABLE V. The NA61/SHINE results for differential Λ production cross section in the laboratory system for p + C interactions at 31 GeV/c. The overall cross-section normalization uncertainty of 2.5% is not included in the systematic errors.

θ_{low} (mrad)	θ_{up} (mrad)	p_{low} (GeV/c)	p_{up} (GeV/c)	$d\sigma_\Lambda/dp$ (mb/GeV/c)	Δ_{stat} (mb/GeV/c)	Δ_{stat} (%)	Δ_{sys} (%)
20	140	0.4	2.4	0.437	0.067	15.3	16.8
		2.4	5.6	1.193	0.057	4.8	16.1
		5.6	7.2	0.809	0.054	6.7	15.9
		7.2	10.8	0.755	0.036	4.8	16.6
		10.8	20.0	0.295	0.016	5.3	16.8
140	240	0.4	2.4	0.523	0.105	20.1	16.6
		2.4	5.6	0.701	0.042	5.9	15.9
		5.6	10.8	0.057	0.013	23.7	16.8

approach (iii) and the uncertainty connected with the fit of the background (ii). Typical systematic errors connected with these sources were about 8%–12% (iii) and about 7%–8% (ii). The second most important contribution is related to the track cuts (i) and it is typically 4%–5%. In addition an important contribution comes from an inaccurate agreement between the data and Monte Carlo distributions of the fitted z coordinate of the primary vertex (iv). The systematic error connected with this effect is about 5%. The contributions connected with geometrical acceptance, reconstruction efficiency, and different reconstruction algorithms (v) are 3%–4%, 2%, and 2%, respectively. The systematic error connected with bin size (vi) was found to be about 6% in highly populated bins and about 12% in low statistic bins.

In addition there is an overall cross-section normalization uncertainty of 2.5% mainly from the relation between trigger cross section and inelastic cross section [5]. This contribution is not included in the systematic errors listed in Tables IV and V.

IV. RESULTS

Differential inclusive cross sections were derived following the procedure described in Sec. III. They are tabulated in Tables IV and V as well as plotted in polar angle slices in Figs. 10 and 11 for K^0_S and Λ, respectively.

The mean multiplicity in production processes and the inclusive cross section for K^0_S production were evaluated from the results obtained in momentum and polar angle intervals. Regions outside the geometrical acceptance were corrected according to the VENUS 4.12 model [10] which predicts 23.91% of simulated K^0_S to be outside of our $\{p, \theta\}$ bins. In the URQMD [12] model this number is 20.27%.

The spread of model predictions was used to estimate the systematic error of the extrapolation to full phase space.

The final results with systematic errors are as follows.

The K^0_S mean multiplicity in production processes is

$$\langle n_{K^0_S} \rangle = 0.127 \pm 0.005 \text{ (stat)} \pm 0.022 \text{ (sys)}.$$

The inclusive cross section for K^0_S production is

$$\sigma_{K^0_S} = 29.0 \pm 1.6 \text{ (stat)} \pm 5.0 \text{ (sys) [mb]}.$$

Because of different phase-space distributions of Λ and K^0_S the model-dependent correction for the unmeasured yield of Λ hyperons is about two times larger than the one for K^0_S mesons. Therefore a reliable extrapolation of the Λ hyperon yield to the full phase was not possible.

V. COMPARISON WITH MODEL PREDICTIONS

The K^0_S mean multiplicity in production processes from p + C interactions was compared with a compilation [13] of total integrated K^0_S yields from p + p interaction experiments. For this purpose the NA61/SHINE result was scaled according to the wounded nucleon model (WNM) by a multiplicative scaling factor $2/(1 + \langle n_W \rangle)$ and according to the independent collisions model (ICM) by a multiplicative scaling factor $1/\langle n_W \rangle$, where $\langle n_W \rangle$ is the average number of wounded nucleons inside the carbon nucleus. The value of $\langle n_W \rangle$ was found to be 1.5240 ± 0.0011 using the Glauber initial-state simulation and more (GLISSANDO) model calculation [14]. The comparison of our result with the compilation of existing p + p results is shown in Fig. 12. Better agreement is observed between the scaled NA61/SHINE result and the measurement for p + p interactions when the ICM scaling is used. The larger value of the kaon multiplicity (0.127 ± 0.005) as compared to the WNM [(0.063 ± 0.002) × 1.26 = 0.0793 ± 0.0025] can be regarded as an indication of enhanced strange particle production in p + C collisions at 31 GeV/c. However, a

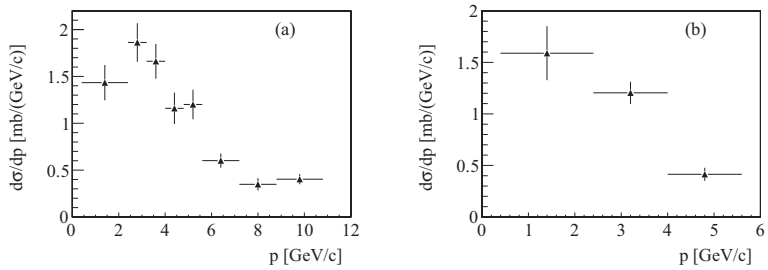

FIG. 10. K^0_S production cross sections in two polar angle intervals: [20, 140] mrad (a) and [140, 240] mrad (b). Only statistical errors are shown.

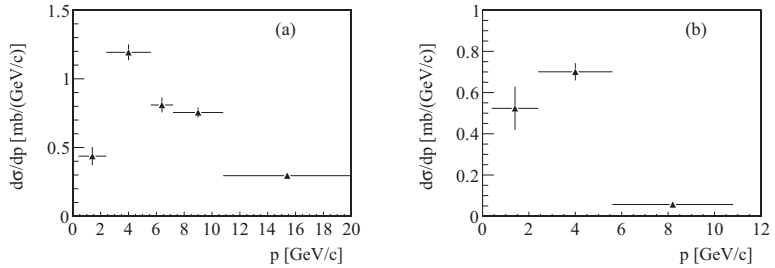

FIG. 11. Λ production cross sections in two polar angle intervals: [20, 140] mrad (a), [140, 240] mrad (b). Only statistical errors are shown.

definitive conclusion is not possible because of the systematic uncertainties of our results.

The K^0_S results in momentum and polar angle variables normalized to mean particle multiplicity in production processes are shown in Fig. 13 with predictions from the hadron production models VENUS and URQMD superimposed.

The K^0_S/π^- ratio is plotted versus momentum for selected polar angle intervals in Fig. 14. The π^- spectra were taken from Ref. [5]. The ratio of K^0_S/π^- is expected to be close to the ratio of the $\bar{s}$ to $\bar{u}$ quark production probabilities and it is therefore sensitive to the strangeness suppression factor λ_S. Furthermore, the ratio K^0_S/π^- was used in the calculation of the feed-down corrections when extracting primary pion multiplicities from the data in Ref. [5]. In that paper VENUS model predictions, not yet confronted with the NA61/SHINE measurements, were used and therefore large systematic errors were assigned. It is seen from Fig. 14 that the agreement between data and the model is rather satisfactory for the emission angle interval 20–140 mrad whereas there is a significant disagreement at larger angles. The measured average multiplicity of K^0_S differs by about 20% from the one predicted by VENUS and used in the NA61/SHINE correction procedure. This translates into a 1%–4% error for the pion multiplicity because of smaller feed-down corrections depending on the pion angle and momentum. The present statistical errors do not permit one to study changes of the bin-by-bin values of the corrections. We will make use of our measured V^0 multiplicities when extracting the pion cross sections from the new high statistics data currently being analyzed.

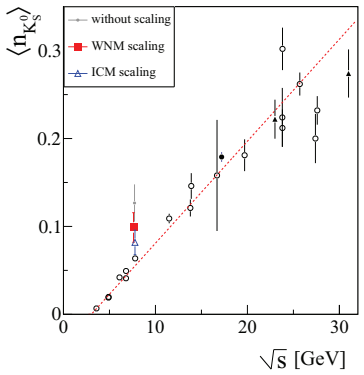

FIG. 12. (Color online) Mean multiplicity of K^0_S mesons as a function of $\sqrt{s}$. Open black points, p + p results from the compilation [13]. Solid circle, the NA49 result on $[(K^+ + K^-)/2]$ [13]. Triangles, the ISR measurements of $[(K^+ + K^-)/2]$ and the UA5 results [13]. Gray circle, the result from this paper for p + C interactions. Green solid star, the result from this paper after scaling according to the WNM model. Blue triangle, the result from this paper after scaling according to the ICM model. The dashed line is shown to guide the eye.

The K^0_S/K^+ ratio in the selected polar angle intervals is shown in Fig. 15. The K^+ spectra were measured in the same experiment [6] therefore some of the systematic errors cancel out. The d/u quark ratio in p + C interactions is 5:7. The smaller yield of K^0_S compared to that of K^+ is thus expected because it is more probable to find a u current quark to form a positively charged kaon ($u\bar{s}$) than a d quark to form a K^0 ($d\bar{s}$). The $\bar{K}$ ($\bar{d}$s) requires the production of two sea quarks and thus it is less frequent.

The Λ results in momentum and polar angle variables normalized to mean particle multiplicity in production processes are shown in Fig. 16 with the predictions from the hadron production models superimposed. None of the models provides a satisfactory description of our measurements.

VI. SUMMARY

We present the first measurement of the total cross section for K^0_S production in p + C interactions at 31 GeV/c in the experimentally sparsely covered region of a few tens of GeV/c beam momentum. The increase of the mean K^0_S multiplicity with respect to p + p collisions can be explained within errors by a factor equal to the average number of primary proton interactions in the carbon nucleus. Differential cross sections for K^0_S and Λ production were obtained in bins of laboratory momentum and emission angle and are compared with predictions of several hadron production models. Significant discrepancies between our experimental results and predictions of the VENUS 4.12 and URQMD models are observed. These new measurements will help to further refine the prediction of the neutrino beam flux in the T2K experiment.

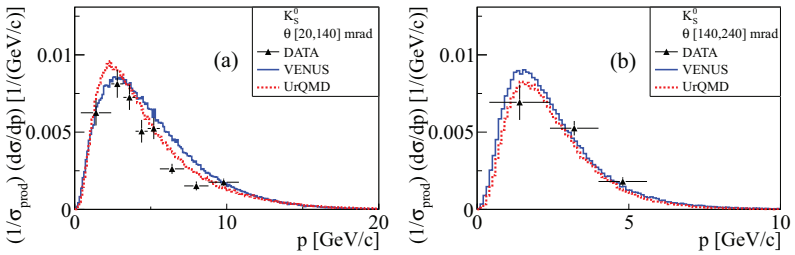

FIG. 13. (Color online) Mean multiplicity of K^0_S mesons in production processes in polar angle intervals: [20, 140] mrad (a), [140, 240] mrad (b). Two hadron production model predictions are superimposed. Only statistical errors are shown.

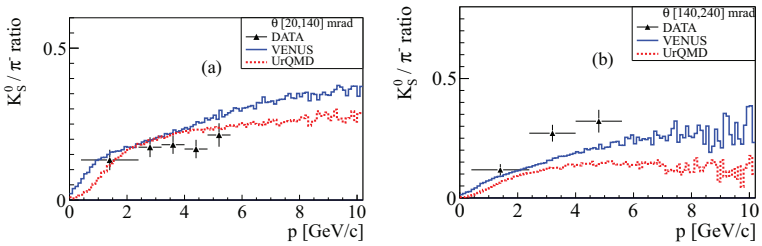

FIG. 14. (Color online) K^0_S/π^- ratios vs momentum in two polar angle intervals: [20, 140] mrad (a), [140, 240] mrad (b). The vertical error bars on the data points show the total (stat. and syst.) uncertainty. Predictions of two hadron production models are superimposed.

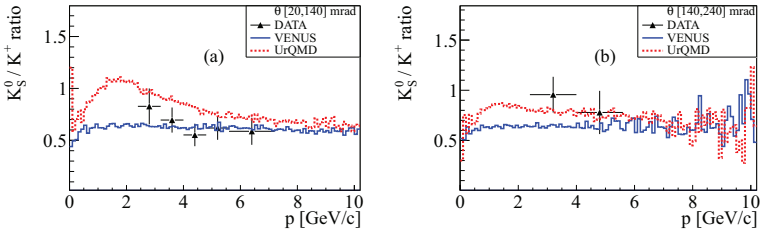

FIG. 15. (Color online) K^0_S/K^+ ratios in two polar angle intervals in two polar angle bins [20, 140] mrad (a) and [140, 240] mrad (b). The vertical error bars on the data points show the total (stat. and syst.) uncertainty. Predictions of hadron production models are superimposed.

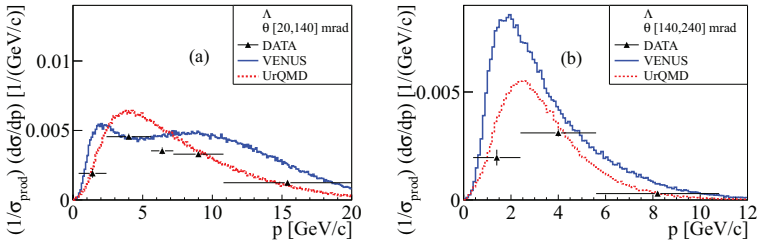

FIG. 16. (Color online) Mean multiplicity of Λ hyperons in production processes in polar angle intervals: [20, 140] mrad (a), [140, 240] mrad (b). Hadron production model predictions are superimposed. Only statistical errors are shown.

ACKNOWLEDGMENTS

This work was supported by the Hungarian Scientific Research Fund (OTKA Grants No. 68506 and No. 71989), the Polish Ministry of Science and Higher Education (Grants No. 667/N-CERN/2010/0, No. NN 202 48 4339, and No. NN 202 23 1837), the National Science Centre of Poland, Grant No. UMO-2012/04/M/ST2/00816, the Foundation for Polish Science–MPD program, co-financed by the European Union within the European Regional Development Fund, the Federal Agency of Education of the Ministry of Education, and Science of the Russian Federation (Grant No. RNP 2.2.2.2.1547), the Russian Academy of Science and the Russian Foundation for Basic Research (Grants No. 08-02-00018 and No. 09-02-00664 12-02-91503-CERN), the Ministry of Education, Culture, Sports, Science and Technology, Japan, Grant-in-Aid for Scientific Research (Grants No. 18071005, No. 19034011, No. 19740162, No. 20740160, and No. 20039012), the German Research Foundation (Grants No. GA 1480/2-1 and No. GA 1480/2-2), the Bulgarian National Scientific Foundation (Grant No. DDVU 02/19/2010), the Ministry of Education and Science of the Republic of Serbia (Grant No. OI171002), the Swiss National fonds Foundation (Grant No. 200020-117913/1), and ETH Research Grant No. TH-01 07-3. Finally, it is a pleasure to thank the European Organization for Nuclear Research for strong support and hospitality and, in particular, the operating crews of the CERN SPS accelerator and beam lines who made the measurements possible.

[1] P. Zh. Aslanyan *et al.*, Phys. Part. Nucl. Lett. **4**, 60 (2007).
[2] K. Jaeger *et al.*, Phys. Rev. D **11**, 1756 (1975).
[3] M. Yu. Bogolyubsky *et al.*, Yad. Fiz. **50**, 683 (1989) [Sov. J. Nucl. Phys. **50**, 424 (1989)].
[4] V. V. Ammosov *et al.*, Nucl. Phys. B **115**, 269 (1976).
[5] N. Abgrall *et al.* (NA61/SHINE Collaboration), Phys. Rev. C **84**, 034604 (2011); arXiv:1102.0983.
[6] N. Abgrall *et al.* (NA61/SHINE Collaboration), Phys. Rev. C **85**, 035210 (2012).
[7] I. Abt *et al.* (HERA-B.Collaboration), Eur. Phys. J. C **61**, 207 (2009); **64**, 167 (2009).
[8] N. Antoniou *et al.* (NA49-future Collaboration), CERN-SPSC-2006-034 (2006).
[9] S. Afanasev *et al.* (NA49 Collaboration), Nucl. Instrum. Meth. A **430**, 210 (1999).
[10] K. Werner, Nucl. Phys. A **525**, 501c (1991); Phys. Rep. **232**, 87 (1993).
[11] C. Strabel, Ph.D thesis, ETH Zurich, 2011, https://edms.cern.ch/document/1136130/1
[12] S. Bass *et al.*, Prog. Part. Nucl. Phys. **41**, 255 (1998); V. Uzhinsky, arXiv:1107.0374.
[13] T. Anticic *et al.* (NA49 Collaboration), Eur. Phys. J. C **68**, 1 (2010).
[14] W. Broniowski *et al.*, Comput. Phys. Commun. **180**, 69 (2009).

J Fusion Energ (2011) 30:487–489
DOI 10.1007/s10894-011-9418-z

ORIGINAL RESEARCH

Yield from Proton-Induced Reaction on Light Element Isotopes in the Hydrogen Plasma Focus

V. Udovičić · A. Dragić · R. Banjanac · D. Joković · N. Veselinović · I. Aničin · M. Savić · J. Puzović

Published online: 4 May 2011

Abstract The high Q-value of some (p,α) fusion reactions is very important in the investigation that can lead to power production with controlled fusion using advanced fuels (hydrogen-lithium-7, hydrogen-boron-11). For this reason, it is crucial to know the rates of these fusion reactions. Unfortunately, in the fusion machines such as plasma focus device, the interaction energy is usually far below the Coulomb barrier. Because of that, direct measurements of the relevant reaction cross sections are practically impossible. A few different indirect approaches have been proposed. In this work the Trojan Horse Method (THM) will be described. On the basis of the results obtained from the THM method and data, which are well-known from our previous work (Banjanac et al. in Radiat Meas 40:483–485, 2005), the reaction rate for proton-induced reaction ^{7}Li(p,α)α produced in the hydrogen plasma focus is calculated. This calculation will be compared with the measurements of α particles production rate using CR-39 detectors.

Keywords Plasma focus · Trojan horse method

Introduction

Proton-induced reaction on light element isotopes play a key role in nucleosynthesis of the elements in the earliest stages of the universe and in all the objects formed thereafter. In a few last years, these fusion reactions became the subject of the investigation because of their high Q-value [3]. Because of this it is very important to know the rates of these nuclear reactions. However, cross sections of reactions with charged particles become very small with decreasing energy and because of that cannot be directly measured. Therefore, the cross section $\sigma(E)$ at low energies is obtained by extrapolating experimental data at higher energies with the well-known astrophysical S factor. In the last ten years, several indirect methods have been developed to extract value for the astrophysical S factor at the low energy limit $S(0)$. One of these indirect methods is a Trojan Horse Method (THM). In this approach the relevant two-body nuclear reaction is replaced by a suitably chosen three-body reaction that is measured under special kinematical conditions [7].

In this work, the THM method will be explained on the example of the ^{7}Li(p,α)α fusion reaction. On the basis of the results obtained from the THM method and data, which are well-known from our previous work [3], the reaction rate for proton-induced reaction ^{7}Li(p,α)α produced in the hydrogen plasma focus can be calculated. This calculation is compared with the measurements of α particles production rate using CR-39 detectors.

Theory

The rates of the charged-particle-induced nuclear reactions for one par of the particles, $\langle \sigma v \rangle$ are well-known from the general theory of the nuclear reactions [6]:

$$\langle \sigma v \rangle = 7.20 \times 10^{-19} \frac{1}{\mu Z_1 Z_2} \tau^2 \exp(-\tau) S(E_0) \quad (1)$$

V. Udovičić (✉) · A. Dragić · R. Banjanac · D. Joković · N. Veselinović · I. Aničin
Institute of Physics, PO Box 57, 11080 Belgrade, Serbia
e-mail: udovicic@ipb.ac.rs

M. Savić · J. Puzović
Faculty of Physics, University of Belgrade, PO Box 368, 11000 Belgrade, Serbia

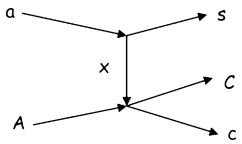

Fig. 1 Pseudo-Feynman diagram representing the quasi-free A + a → c + C +s reaction

where v is the relative velocity of the particles, μ is reduced mass, $\tau = \frac{3E_0}{kT}$ is undimensional parameter, Z_1, Z_2 are the charge numbers of the colliding nuclei and $S(E_0)$ is the astrophysical S factor for the Gamow energy E_0.

Direct measurements of the astrophysical S factor at the Gamow energies for the relevant fusion reactions, such as ^{7}Li(p,α)α are impossible. As it mentioned in the introduction, the powerful indirect method, called THM method has been developed.

The basic idea of the THM relies on the assumption that a three-body reaction a(A,cC)s can proceed via quasi free reaction mechanism that is dominant under particular kinematical conditions. In these conditions, the reaction a(A,cC)s is considered to be described by a polar diagram as it shown in Fig. 1 (pseudo-Feynman diagram). The target nucleus a is assumed to break-up into the clusters x and s, where s is then considered to be a spectator of the A + x → c + C reaction, where c and C are the outgoing particles. In this picture, the cross section of the three-body reaction can be factorized into two terms corresponding to the two vertices of the diagram (Fig. 1). It should be outlined that in order to apply the THM a suitable three-body and proper kinematical conditions should be found. The most relevant results obtained for the fusion reaction ^{7}Li(p,α)α using THM technique are reported [4].

The three-body reaction used in this case is ^{7}Li(d,αα)n, where deuteron is considered as a cluster of proton (interaction particle) and neutron (spectator). In the same work [4], important tests of the THM method have been done studying reaction, ^{11}B(p,α)2^{4}He which present a resonant behaviour. The high Q-value of this fusion reaction is very important in the investigation that can lead to power production with controlled fusion using advanced fuels [5].

All about THM method, including detailed calculations one can found in the review paper [7].

Experiment

In our previous works [2, 3], we have obtained the experimental data for the flux and energy of the accelerated protons (especially the axial protons) emitted from the hydrogen plasma focus. On the basis of these experimental data, we have performed experiment with the lithium target, which was thick wire (thicknesses of about 100 μm) placed on the CR-39 plate (2 × 2 cm). CR-39 nuclear track detectors manufactured by the Intercast were used for the detection of the α particles produced in the ^{7}Li(p,α)α fusion reaction. Both the lithium target and CR-39 plate were placed in one of the diagnostical windows positioned at the top of the plasma focus chamber along the central electrode axis. The fast protons were collimated with integrated collimators, so that the protons bombarded target at right angles.

All the experiments were performed on the Mather-type plasma focus device with hydrogen as a working gas. The gas discharges is produced by capacitator bank with stored energy of 5.76 kJ. After exposure the CR-39 detectors were etched by the similar procedure as in [1]. The CR-39 nuclear track detectors were chemically etched for an etching time of 2.5 h with a solution of 30% KOH at 70°C. The tracks were counted by the semi-automatic track-counting system consisting of a CCD camera and a high-resolution monitor.

Results and Conclusions

In all of the scanned CR-39 detectors, the alpha track density was on the background level (10^2 cm^{-2}). This result is in good agreement with the calculations based on (1) and the value for the astrophysical S factor obtained through THM method for the ^{7}Li(p,α)α fusion reaction [4]. The obtained experimental results and theoretical calculations show that it is not possible to realized ^{7}Li(p,α)α fusion reaction in a small plasma focus device (stored energy of 5.76 kJ).

Acknowledgments This work is supported by Ministry of Science and Environment Protection of Republic of Serbia by the contract number 141002.

References

1. M.I. Al-Jarallah, A.A. Naqvi, F.A. Abu-Jarad, S.M.A. Durrani, F.U. Rehman, S. Kidwai, Angular distribution measurements of 6Li(p, α)3He reaction at 140 keV proton energy using nuclear track detectors. Radiat. Meas. **34**, 331–335 (2001)
2. R. Antanasijević, Z. Marić, J. Vuković, B. Grabež, D. Đorđević, D. Joksimović, V. Udovičić, A. Dragić, J. Stanojević, R. Banjanac, D. Joković, Angular distribution of protons emitted from the hydrogen plasma focus. Radiat. Meas. **36**, 327–328 (2003)
3. R. Banjanac, V. Udovičić, B. Grabež, B. Panić, Z. Marić, A. Dragić, D. Joković, D. Joksimović, I. Aničin, Flux and energy distribution of axial protons emitted from the hydrogen plasma focus. Radiat. Meas. **40**, 483–485 (2005)

4. P. Corvisiero, LUNA Collaboration, Low energy cross sections and underground laboratories. Nuclear Physica A **752**, 491c–499c (2005)
5. E.J. Lerner, R.E. Terry, in *Advances Towards pB11 Fusion with the Dense Plasma Focus*, ed. by E. Panarella, R. Raman. Current Trends in International Fusion Research - Proceedings of the Sixth Symposium (NRC Research Press, Ottawa, ON, Canada, 2009)
6. C. Rolfs, W.S. Rodney, *Cauldrons in the Cosmos* (The University of Chicago Press, Chicago, USA, 1988)
7. S. Typel, G. Baur, Theory of the Trojan-Horse method. Ann. Phys. **305**, 228–265 (2003)

Eur. Phys. J. C (2019) 79:257
https://doi.org/10.1140/epjc/s10052-019-6674-y

THE EUROPEAN PHYSICAL JOURNAL C

Regular Article - Experimental Physics

First particle-by-particle measurement of emittance in the Muon Ionization Cooling Experiment

MICE Collaboration

D. Adams[15], D. Adey[25,34], R. Asfandiyarov[13], G. Barber[18], A. de Bari[6], R. Bayes[16], V. Bayliss[15], R. Bertoni[4], V. Blackmore[18,a], A. Blondel[13], J. Boehm[15], M. Bogomilov[1], M. Bonesini[4], C. N. Booth[20], D. Bowring[25], S. Boyd[22], T. W. Bradshaw[15], A. D. Bross[25], C. Brown[15,23], G. Charnley[14], G. T. Chatzitheodoridis[16,21], F. Chignoli[4], M. Chung[10], D. Cline[30], J. H. Cobb[19], D. Colling[18], N. Collomb[14], P. Cooke[17], M. Courthold[15], L. M. Cremaldi[28], A. DeMello[26], A. J. Dick[21], A. Dobbs[18], P. Dornan[18], F. Drielsma[13], K. Dumbell[14], M. Ellis[23], F. Filthaut[11,32], P. Franchini[22], B. Freemire[27], A. Gallagher[14], R. Gamet[17], R. B. S. Gardener[23], S. Gourlay[26], A. Grant[14], J. R. Greis[22], S. Griffiths[14], P. Hanlet[27], G. G. Hanson[29], T. Hartnett[14], C. Heidt[29], P. Hodgson[20], C. Hunt[18], S. Ishimoto[9], D. Jokovic[12], P. B. Jurj[18], D. M. Kaplan[27], Y. Karadzhov[13], A. Klier[29], Y. Kuno[8], A. Kurup[18], P. Kyberd[23], J-B. Lagrange[18], J. Langlands[20], W. Lau[19], D. Li[26], Z. Li[3], A. Liu[25], K. Long[18], T. Lord[22], C. Macwaters[15], D. Maletic[12], B. Martlew[14], J. Martyniak[18], R. Mazza[4], S. Middleton[18], T. A. Mohayai[27], A. Moss[14], A. Muir[14], I. Mullacrane[14], J. J. Nebrensky[23], D. Neuffer[25], A. Nichols[15], J. C. Nugent[16], A. Oates[14], D. Orestano[7], E. Overton[20], P. Owens[14], V. Palladino[5], M. Palmer[24], J. Pasternak[18], V. Pec[20], C. Pidcott[22,33], M. Popovic[25], R. Preece[15], S. Prestemon[26], D. Rajaram[27], S. Ricciardi[15], M. Robinson[20], C. Rogers[15], K. Ronald[21], P. Rubinov[25], H. Sakamoto[8,31], D. A. Sanders[28], A. Sato[8], M. Savic[12], P. Snopok[27], P. J. Smith[20], F. J. P. Soler[16], Y. Song[2], T. Stanley[15], G. Stokes[14], V. Suezaki[27], D. J. Summers[28], C. K. Sung[10], J. Tang[2], J. Tarrant[15], I. Taylor[22], L. Tortora[7], Y. Torun[27], R. Tsenov[1], M. Tucker[14], M. A. Uchida[18], S. Virostek[26], G. Vankova-Kirilova[1], P. Warburton[14], S. Wilbur[20], A. Wilson[15], H. Witte[24], C. White[14], C. G. Whyte[21], X. Yang[30], A. R. Young[21], M. Zisman[26]

[1] Department of Atomic Physics, St. Kliment Ohridski University of Sofia, Sofia, Bulgaria
[2] Institute of High Energy Physics, Chinese Academy of Sciences, Beijing, China
[3] Sichuan University, Chengdu, China
[4] Dipartimento di Fisica G. Occhialini, Sezione INFN Milano Bicocca, Milan, Italy
[5] Sezione INFN Napoli and Dipartimento di Fisica, Università Federico II, Complesso Universitario di Monte S. Angelo, Naples, Italy
[6] Sezione INFN Pavia and Dipartimento di Fisica, Pavia, Italy
[7] INFN Sezione di Roma Tre and Dipartimento di Matematica e Fisica, Università Roma Tre, Rome, Italy
[8] Department of Physics, Graduate School of Science, Osaka University, Toyonaka, Osaka, Japan
[9] High Energy Accelerator Research Organization (KEK), Institute of Particle and Nuclear Studies, Tsukuba, Ibaraki, Japan
[10] UNIST, Ulsan, Korea
[11] Nikhef, Amsterdam, The Netherlands
[12] Institute of Physics, University of Belgrade, Belgrade, Serbia
[13] DPNC, Section de Physique, Université de Genève, Geneva, Switzerland
[14] STFC Daresbury Laboratory, Daresbury, Cheshire, UK
[15] STFC Rutherford Appleton Laboratory, Harwell Oxford, Didcot, UK
[16] School of Physics and Astronomy, The University of Glasgow, Kelvin Building, Glasgow, UK
[17] Department of Physics, University of Liverpool, Liverpool, UK
[18] Blackett Laboratory, Department of Physics, Imperial College London, London, UK
[19] Department of Physics, University of Oxford, Denys Wilkinson Building, Oxford, UK
[20] Department of Physics and Astronomy, University of Sheffield, Sheffield, UK
[21] SUPA and the Department of Physics, University of Strathclyde, Glasgow, UK
[22] Department of Physics, University of Warwick, Coventry, UK
[23] Brunel University, Uxbridge, UK
[24] Brookhaven National Laboratory, Upton, NY, USA
[25] Fermilab, Batavia, IL, USA
[26] Lawrence Berkeley National Laboratory, Berkeley, CA, USA
[27] Illinois Institute of Technology, Chicago, IL, USA
[28] University of Mississippi, Oxford, MS, USA
[29] University of California, Riverside, CA, USA

Published online: 21 March 2019

[30] University of California, Los Angeles, CA, USA
[31] *Current address:* RIKEN, Wako, Japan
[32] *Also at* Radboud University, Nijmegen, The Netherlands
[33] *Current address:* Department of Physics and Astronomy, University of Sheffield, Sheffield, UK
[34] *Current address:* Institute of High Energy Physics, Chinese Academy of Sciences, Bejing, China

Received: 31 October 2018 / Accepted: 11 February 2019

Abstract The Muon Ionization Cooling Experiment (MICE) collaboration seeks to demonstrate the feasibility of ionization cooling, the technique by which it is proposed to cool the muon beam at a future neutrino factory or muon collider. The emittance is measured from an ensemble of muons assembled from those that pass through the experiment. A pure muon ensemble is selected using a particle-identification system that can reject efficiently both pions and electrons. The position and momentum of each muon are measured using a high-precision scintillating-fibre tracker in a 4 T solenoidal magnetic field. This paper presents the techniques used to reconstruct the phase-space distributions in the upstream tracking detector and reports the first particle-by-particle measurement of the emittance of the MICE Muon Beam as a function of muon-beam momentum.

1 Introduction

Stored muon beams have been proposed as the source of neutrinos at a neutrino factory [1,2] and as the means to deliver multi-TeV lepton-antilepton collisions at a muon collider [3,4]. In such facilities the muon beam is produced from the decay of pions generated by a high-power proton beam striking a target. The tertiary muon beam occupies a large volume in phase space. To optimise the muon yield for a neutrino factory, and luminosity for a muon collider, while maintaining a suitably small aperture in the muon-acceleration system requires that the muon beam be 'cooled' (i.e., its phase-space volume reduced) prior to acceleration. An alternative approach to the production of low-emittance muon beams through the capture of $\mu^+\mu^-$ pairs close to threshold in electron–positron annihilation has recently been proposed [5]. To realise the luminosity required for a muon collider using this scheme requires the substantial challenges presented by the accumulation and acceleration of the intense positron beam, the high-power muon-production target, and the muon-capture system to be addressed.

A muon is short-lived, with a lifetime of 2.2 μs in its rest frame. Beam manipulation at low energy ($\leq$ 1 GeV) must be carried out rapidly. Four cooling techniques are in use at particle accelerators: synchrotron-radiation cooling [6]; laser cooling [7–9]; stochastic cooling [10]; and electron cooling [11]. In each case, the time taken to cool the beam is long compared to the muon lifetime. In contrast, ionization cooling is a process that occurs on a short timescale. A muon beam passes through a material (the absorber), loses energy, and is then re-accelerated. This cools the beam efficiently with modest decay losses. Ionization cooling is therefore the technique by which it is proposed to increase the number of particles within the downstream acceptance for a neutrino factory, and the phase-space density for a muon collider [12–14]. This technique has never been demonstrated experimentally and such a demonstration is essential for the development of future high-brightness muon accelerators or intense muon facilities.

The international Muon Ionization Cooling Experiment (MICE) has been designed [15] to perform a full demonstration of transverse ionization cooling. Intensity effects are negligible for most of the cooling channels conceived for the neutrino factory or muon collider [16]. This allows the MICE experiment to record muon trajectories one particle at a time. The MICE collaboration has constructed two solenoidal spectrometers, one placed upstream, the other downstream, of the cooling cell. An ensemble of muon trajectories is assembled offline, selecting an initial distribution based on quantities measured in the upstream particle-identification detectors and upstream spectrometer. This paper describes the techniques used to reconstruct the phase-space distributions in the spectrometers. It presents the first measurement of the emittance of momentum-selected muon ensembles in the upstream spectrometer.

2 Calculation of emittance

Emittance is a key parameter in assessing the overall performance of an accelerator [17]. The luminosity achieved by a collider is inversely proportional to the emittance of the colliding beams, and therefore beams with small emittance are required.

D. Cline, M. Zisman: Deceased.

[a] e-mail: v.blackmore@imperial.ac.uk

A beam travelling through a portion of an accelerator may be described as an ensemble of particles. Consider a beam that propagates in the positive z direction of a right-handed Cartesian coordinate system, (x, y, z). The position of the i^{th} particle in the ensemble is $\mathbf{r}_i = (x_i, y_i)$ and its transverse momentum is $\mathbf{p}_{Ti} = (p_{xi}, p_{yi})$; $\mathbf{r}_i$ and $\mathbf{p}_{Ti}$ define the coordinates of the particle in transverse phase space. The normalised transverse emittance, ε_N, of the ensemble approximates the volume occupied by the particles in four-dimensional phase space and is given by

$$\varepsilon_N = \frac{1}{m_\mu}\sqrt[4]{\det \mathcal{C}}\,, \tag{1}$$

where m_μ is the rest mass of the muon, $\mathcal{C}$ is the four-dimensional covariance matrix,

$$\mathcal{C} = \begin{pmatrix} \sigma_{xx} & \sigma_{xp_x} & \sigma_{xy} & \sigma_{xp_y} \\ \sigma_{xp_x} & \sigma_{p_xp_x} & \sigma_{yp_x} & \sigma_{p_xp_y} \\ \sigma_{xy} & \sigma_{yp_x} & \sigma_{yy} & \sigma_{yp_y} \\ \sigma_{xp_y} & \sigma_{p_xp_y} & \sigma_{yp_y} & \sigma_{p_yp_y} \end{pmatrix}, \tag{2}$$

and $\sigma_{\alpha\beta}$, where $\alpha, \beta = x, y, p_x, p_y$, is given by

$$\sigma_{\alpha\beta} = \frac{1}{N-1}\left(\Sigma_i^N \alpha_i\beta_i - \frac{\left(\Sigma_i^N \alpha_i\right)\left(\Sigma_i^N \beta_i\right)}{N}\right), \tag{3}$$

and N is the number of muons in the ensemble.

The MICE experiment was operated such that muons passed through the experiment one at a time. The phase-space coordinates of each muon were measured. An ensemble of muons that was representative of the muon beam was assembled using the measured coordinates. The normalised transverse emittance of the ensemble was then calculated by evaluating the sums necessary to construct the covariance matrix, $\mathcal{C}$, and using Eq. 1.

3 The Muon Ionization Cooling Experiment

The muons for MICE came from the decay of pions produced by an internal target dipping directly into the circulating proton beam of the ISIS synchrotron at the Rutherford Appleton Laboratory (RAL) [18,19]. The burst of particles resulting from one target dip is referred to as a 'spill'. A transfer line of nine quadrupoles, two dipoles and a superconducting 'decay solenoid' selected a momentum bite and transported the beam into the experiment [20]. The small fraction of pions that remained in the beam were rejected during analysis using the time-of-flight hodoscopes, TOF0 and TOF1, and Cherenkov counters that were installed in the MICE Muon Beam line upstream of the cooling experiment [21,22]. A 'diffuser' was installed at the upstream end of the experiment to vary the initial emittance of the beam by introducing a changeable amount of tungsten and brass, which are high-Z materials, into the beam path [20].

A schematic diagram of the experiment is shown in Fig. 1. It contained an absorber/focus-coil module sandwiched between two spectrometer-solenoid modules that provided a uniform magnetic field for momentum measurement. The focus-coil module had two separate windings that were operated with the same, or opposed, polarities. A lithium-hydride or liquid-hydrogen absorber was placed at the centre of the focus-coil module. An iron Partial Return Yoke (PRY) was installed around the experiment to contain the field produced by the solenoidal spectrometers (not shown in Fig. 1). The PRY was installed at a distance from the beam axis such that its effect on the trajectories of particles travelling through the experiment was negligible.

The emittance was measured upstream and downstream of the absorber and focus-coil module using scintillating-fibre tracking detectors [26] immersed in the solenoidal field provided by three superconducting coils E1, C, and E2. The

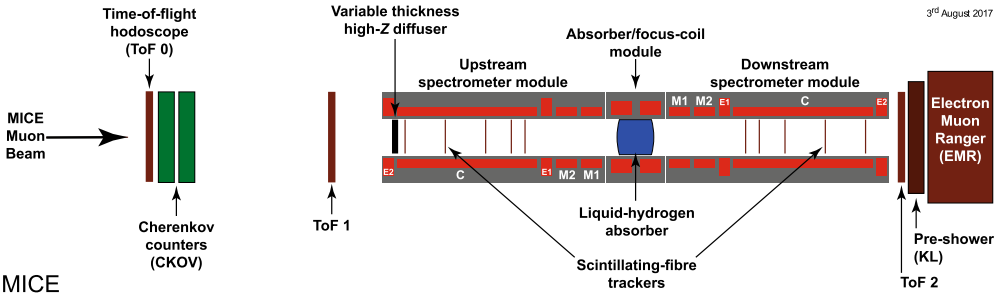

Fig. 1 Schematic diagram of the MICE experiment. The red rectangles represent the coils of the spectrometer solenoids and focus-coil module. The individual coils of the spectrometer solenoids are labelled E1, C, E2, M1 and M2. The various detectors (time-of-flight hodoscopes (TOF0, TOF1) [23,24], Cherenkov counters [25], scintillating-fibre trackers [26], KLOE-Light (KL) calorimeter [20,27], and Electron Muon Ranger (EMR) [28,29]) are also represented. The Partial Return Yoke (PRY) is not shown

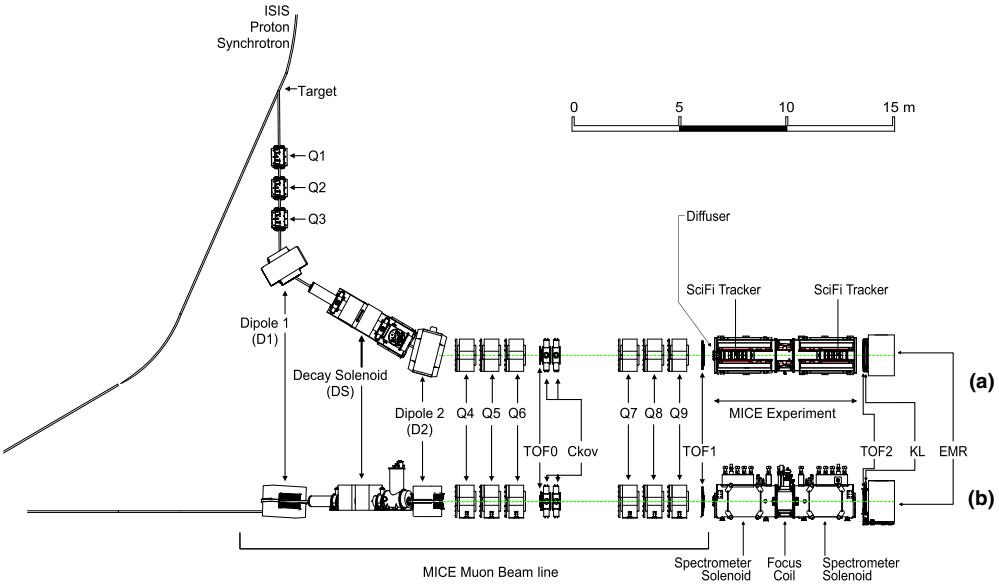

Fig. 2 **a** Top and **b** side views of the MICE Muon Beam line, its instrumentation, and the experimental configuration. A titanium target dipped into the ISIS proton synchrotron and the resultant spill of particles was captured with a quadrupole triplet (Q1–3) and transported through momentum-selecting dipoles (D1, D2). The quadrupole triplets (Q4–6, Q7–9) transported particles to the upstream spectrometer module. The time-of-flight of particles, measured between TOF0 and TOF1, was used for particle identification

trackers were used to reconstruct the trajectories of individual muons at the entrance and exit of the absorber. The trackers were each constructed from five planar stations of scintillating fibres, each with an active radius of 150 mm. The track parameters were reported at the nominal reference plane: the surface of the scintillating-fibre plane closest to the absorber [30]. Hall probes were installed on the tracker to measure the magnetic-field strength in situ. The instrumentation up- and downstream of the spectrometer modules was used to select a pure sample of muons. The reconstructed tracks of the selected muons were then used to measure the muon-beam emittance at the upstream and downstream tracker reference planes. The spectrometer-solenoid modules also contained two superconducting 'matching' coils (M1, M2) that were used to match the optics between the uniform-field region and the neighbouring focus-coil module. The MICE coordinate system is such that the z axis is coincident with the beam direction, the y axis points vertically upward, and the x axis completes a right-handed co-ordinate system. This paper discusses the measurement of emittance using only the tracker and beam-line instrumentation upstream of the absorber. The diffuser was fully retracted for the data presented here, i.e. no extra material was introduced into the centre of the beam line, so that the incident particle distribution could be assessed.

4 MICE Muon beam line

The MICE Muon Beam line is shown schematically in Fig. 2. It was capable of delivering beams with normalised transverse emittance in the range $3 \lesssim \varepsilon_N \lesssim 10$ mm and mean momentum in the range $140 \lesssim p_\mu \lesssim 240$ MeV/c with a root-mean-squared (RMS) momentum spread of ~ 20 MeV/c [20] after the diffuser (Fig. 1).

Pions produced by the momentary insertion of a titanium target [18,19] into the ISIS proton beam were captured using a quadrupole triplet (Q1–3) and transported to a first dipole magnet (D1), which selected particles of a desired momentum bite into the 5 T decay solenoid (DS). Muons produced in pion decay in the DS were momentum-selected using a second dipole magnet (D2) and focused onto the diffuser by a quadrupole channel (Q4–6 and Q7–9). In positive-beam running, a borated polyethylene absorber of variable thickness was inserted into the beam just downstream of the decay solenoid to suppress the high rate of protons that were produced at the target [31].

The composition and momentum spectra of the beams delivered to MICE were determined by the interplay between the two bending magnets D1 and D2. In 'muon mode', D2 was set to half the current of D1, selecting backward-going

muons in the pion rest frame. This produced an almost pure muon beam.

Data were taken in October 2015 in muon mode at a nominal momentum of 200 MeV/c, with ISIS in operation at 700 MeV. These data [32] are used here to characterise the properties of the beam accepted by the upstream solenoid with all diffuser irises withdrawn from the beam. The upstream E1-C-E2 coils in the spectrometer module were energised and produced a field of 4 T, effectively uniform across the tracking region, while all other coils were unpowered. Positively charged particles were selected due to their higher production rate in 700 MeV proton-nucleus collisions.

5 Simulation

Monte Carlo simulations were used to determine the accuracy of the kinematic reconstruction, to evaluate the efficiency of the response of the scintillating-fibre tracker, and to study systematic uncertainties. A sufficient number of events were generated to ensure that statistical uncertainties from the simulations were negligible in comparison to those of the data.

The beam impinging on TOF0 was modelled using G4beamline [33]. Particles were produced at the target using a parameterised particle-production model. These particles were tracked through the MICE Muon Beam line taking into account all material in and surrounding the beam line and using realistic models of the fields and apertures of the various magnets. The G4beamline simulation was tuned to reproduce the observed particle distributions at TOF0.

The MICE Analysis User Software (MAUS) [34] package was used to simulate the passage of particles from TOF0 through the remainder of the MICE Muon Beam line and through the solenoidal lattice. This simulation includes the response of the instrumentation and used the input distribution produced using G4beamline. MAUS was also used for offline reconstruction and to provide fast real-time detector reconstruction and data visualisation during MICE running. MAUS uses GEANT4 [35,36] for beam propagation and the simulation of detector response. ROOT [37] was used for data visualisation and for data storage. The particles generated were subjected to the same trigger requirements as the data and processed by the same reconstruction programs.

6 Beam selection

Data were buffered in the front-end electronics and read out at the end of each spill [20]. For the reconstructed data presented here, the digitisation of analogue signals received from the detectors was triggered by a coincidence of signals in the PMTs serving a single scintillator slab in TOF1. Any slab in TOF1 could generate a trigger.

The following cuts were used to select muons passing through the upstream tracker:

- *One reconstructed space-point in TOF0 and TOF1* Each TOF hodoscope was composed of two perpendicular planes of scintillator slabs arranged to measure the x and y coordinates. A space-point was formed from the intersection of hits in the x and y projections. Figure 3a, b show the hit multiplicity in TOF0 plotted against the hit multiplicity in TOF1 for reconstructed data and reconstructed Monte Carlo respectively. The sample is dominated by events with one space-point in both TOF0 and TOF1. This cut removes events in which two particles enter the experiment within the trigger window.
- *Relative time-of-flight between TOF0 and TOF1,* t_{rel}*, in the range* $1 \leq t_{\mathrm{rel}} \leq 6\,ns$ The time of flight between TOF0 and TOF1, t_{01}, was measured relative to the mean positron time of flight, t_e. Figure 3c shows the relative time-of-flight distribution in data (black, circles) and simulation (filled histogram). All cuts other than the relative time-of-flight cut have been applied in this figure. The time-of-flight of particles relative to the mean positron time-of-flight is calculated as

$$t_{\mathrm{rel}} = t_{01} - (t_e + \delta t_e)\ ,$$

  where δt_e accounts for the difference in transit time, or path length travelled, between electrons and muons in the field of the quadrupole triplets [21]. This cut removes electrons from the selected ensemble as well as a small number of pions. The data has a longer tail compared to the simulation, which is related to the imperfect simulation of the longitudinal momentum of particles in the beam (see Sect. 7.1).
- *A single track reconstructed in the upstream tracker with a track-fit* χ^2 *satisfying* $\frac{\chi^2}{N_{\mathrm{DOF}}} \leq 4$ N_{DOF} is the number of degrees of freedom. The distribution of $\frac{\chi^2}{N_{\mathrm{DOF}}}$ is shown in Fig. 3d. This cut removes events with poorly reconstructed tracks. Multi-track events, in which more than one particle passes through the same pixel in TOF0 and TOF1 during the trigger window, are rare and are also removed by this cut. The distribution of $\frac{\chi^2}{N_{\mathrm{DOF}}}$ is broader and peaked at slightly larger values in the data than in the simulation.
- *Track contained within the fiducial volume of the tracker* The radius of the track measured by the tracker, R_{track}, is required to satisfy $R_{\mathrm{track}} < 150$ mm to ensure the track does not leave and then re-enter the fiducial volume. The track radius is evaluated at 1 mm intervals between the stations. If the track radius exceeds 150 mm at any of these positions, the event is rejected.

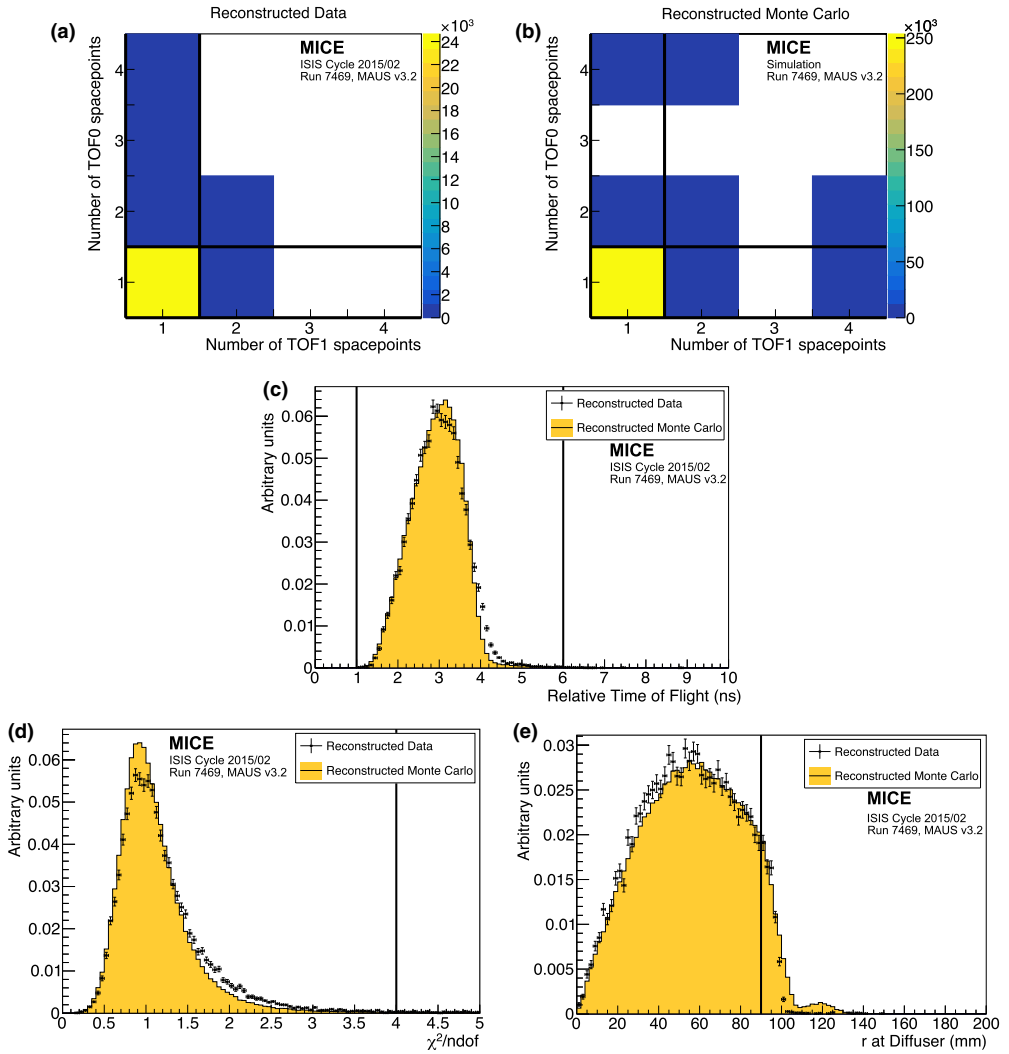

Fig. 3 Distribution of the quantities that were used to select the sample used to reconstruct the emittance of the beam: **a** the number of space-points in TOF0 plotted against the number of space-points in TOF1 for reconstructed data, and **b** reconstructed simulation; **c** distribution of the relative time-of-flight, t_{rel}; **d** distribution of $\frac{\chi^2}{N_{\mathrm{DOF}}}$; and **e** distribution of R_{diff}. The 1D distributions show reconstructed data as solid (black) circles and reconstructed MAUS simulation as the solid (yellow) histogram. The solid (black) lines indicate the position of the cuts made on these quantities. Events enter these plots if all cuts other than the cut under examination are passed

– *Extrapolated track radius at the diffuser,* $R_{\mathrm{diff}} \leq 90\,mm$
Muons that pass through the annulus of the diffuser, which includes the retracted irises, lose a substantial amount of energy. Such muons may re-enter the tracking volume and be reconstructed but have properties that are no longer characteristic of the incident muon beam. The aperture radius of the diffuser mechanism (100 mm) defines the transverse acceptance of the beam injected

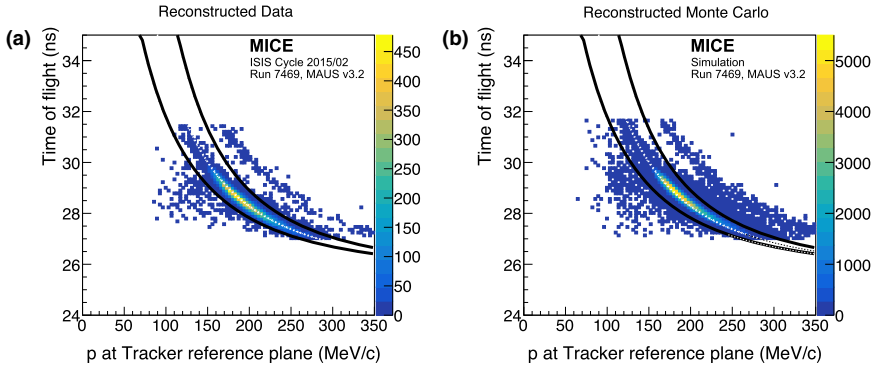

Fig. 4 Time of flight between TOF0 and TOF1 (t_{01}) plotted as a function of the muon momentum, p, measured in the upstream tracker. All cuts other than the muon hypothesis have been applied. Particles within the black lines are selected. The white dotted line is the trajectory of a muon that loses the most probable momentum (20 MeV/c) between TOF1 and the tracker in **a** reconstructed data, and **b** reconstructed Monte Carlo

Table 1 The number of particles that pass each selection criterion. A total of 24,660 particles pass all of the cuts

Cut	No. surviving particles	Cumulative surviving particles
None	53276	53276
One space-point in TOF0 and TOF1	37619	37619
Relative time of flight in range 1–6 ns	37093	36658
Single reconstructed track with $\frac{\chi^2}{N_{\mathrm{DOF}}} \leq 4$	40110	30132
Track within fiducial volume of tracker	52039	29714
Extrapolated track radius at diffuser $\leq$ 90 mm	42592	25310
Muon hypothesis	34121	24660
All	24660	24660

into the experiment. Back-extrapolation of tracks to the exit of the diffuser yields a measurement of R_{diff} with a resolution of $\sigma_{R_{\mathrm{diff}}} = 1.7$ mm. Figure 3e shows the distribution of R_{diff}, where the difference between data and simulation lies above the accepted radius. These differences are due to approximations in modelling the outer material of the diffuser. The cut on R_{diff} accepts particles that passed at least $5.9\sigma_{R_{\mathrm{diff}}}$ inside the aperture limit of the diffuser.

– *Particle consistent with muon hypothesis* Figure 4 shows t_{01}, the time-of-flight between TOF0 and TOF1, plotted as a function of p, the momentum reconstructed by the upstream tracking detector. Momentum is lost between TOF1 and the reference plane of the tracker in the material of the detectors. A muon that loses the most probable momentum, $\Delta p \simeq 20$ MeV/c, is shown as the dotted (white) line. Particles that are poorly reconstructed, or have passed through support material upstream of the tracker and have lost significant momentum, are excluded by the lower bound. The population of events above the upper bound are ascribed to the passage of pions, or misreconstructed muons, and are also removed from the analysis.

A total of 24,660 events pass the cuts listed above. Table 1 shows the number of particles that survive each individual cut. Data distributions are compared to the distributions obtained using the MAUS simulation in Figs. 3 and 4. Despite minor disagreements, the agreement between the simulation and data is sufficiently good to give confidence that a clean sample of muons has been selected.

The expected pion contamination of the unselected ensemble of particles has been measured to be $\leq 0.4\,\%$[22]. Table 2 shows the number of positrons, muons, and pions in the MAUS simulation that pass all selection criteria. The criteria used to select the muon sample for the analysis presented here efficiently reject electrons and pions from the Monte Carlo sample.

Table 2 The number of reconstructed electrons, muons, and pions at the upstream tracker that survive each cut in the Monte Carlo simulation. Application of all cuts removes almost all positrons and pions in the reconstructed Monte Carlo sample. In the Monte Carlo simulation, a total of 253,504 particles pass all of the cuts described in the text

Cut	e	μ	π	Total
None	14, 912	432,294	1610	463,451
One space-point in TOF0 and TOF1	11, 222	353,613	1213	376,528
Relative Time of flight in range 1–6 ns	757	369,337	1217	379,761
Single reconstructed track with $\frac{\chi^2}{N_{\mathrm{DOF}}} \leq 4$	10, 519	407,276	1380	419,208
Track within fiducial volume of tracker	14, 527	412,857	1427	443,431
Tracked radius at diffuser $\leq$ 90 mm	11, 753	311,076	856	334,216
Muon hypothesis (above lower limit)	3225	362,606	411	367,340
Muon hypothesis (below upper limit)	12, 464	411,283	379	424,203
Muon hypothesis (overall)	2724	358,427	371	361,576
All	22	253,475	5	253,504

7 Results

7.1 Phase-space projections

The distributions of x, y, p_x, p_y, p_z, and $p = \sqrt{p_x^2 + p_y^2 + p_z^2}$ are shown in Fig. 5. The total momentum of the muons that make up the beam lie within the range $140 \lesssim |p| \lesssim 260\,\mathrm{MeV}/c$. The results of the MAUS simulation, which are also shown in Fig. 5, give a reasonable description of the data. In the case of the longitudinal component of momentum, p_z, the data are peaked to slightly larger values than the simulation. The difference is small and is reflected in the distribution of the total momentum, p. As the simulation began with particle production from the titanium target, any difference between the simulated and observed particle distributions would be apparent in the measured longitudinal and total momentum distributions. The scale of the observed disagreement is small, and as such the simulation adequately describes the experiment. The distributions of the components of the transverse phase space (x, p_x, y, p_y) are well described by the simulation. Normalised transverse emittance is calculated with respect to the means of the distributions (Eq. 2), and so is unaffected by this discrepancy.

The phase space occupied by the selected beam is shown in Fig. 6. The distributions are plotted at the reference surface of the upstream tracker. The beam is moderately well centred in the (x, y) plane. Correlations are apparent that couple the position and momentum components in the transverse plane. The transverse position and momentum coordinates are also seen to be correlated with total momentum. The correlation in the (x, p_y) and (y, p_x) plane is due to the solenoidal field, and is of the expected order. The dispersion and chromaticity of the beam are discussed further in Sect. 7.2.

7.2 Effect of dispersion, chromaticity, and binning in longitudinal momentum

Momentum selection at D2 introduces a correlation, dispersion, between the position and momentum of particles. Figure 7 shows the transverse position and momentum with respect to the total momentum, p, as measured at the upstream-tracker reference plane. Correlations exist between all four transverse phase-space co-ordinates and the total momentum.

Emittance is calculated in $10\,\mathrm{MeV}/c$ bins of total momentum in the range $185 \leq p \leq 255\,\mathrm{MeV}/c$. This bin size was chosen as it is commensurate with the detector resolution. Calculating the emittance in momentum increments makes the effect of the optical mismatch, or chromaticity, small compared to the statistical uncertainty. The range of $185 \leq p \leq 255\,\mathrm{MeV}/c$ was chosen to maximise the number of particles in each bin that are not scraped by the aperture of the diffuser.

7.3 Uncertainties on emittance measurement

7.3.1 Statistical uncertainties

The statistical uncertainty on the emittance in each momentum bin is calculated as $\sigma_\varepsilon = \frac{\varepsilon}{\sqrt{2N}}$ [38–40], where ε is the emittance of the ensemble of muons in the specified momentum range and N is the number of muons in that ensemble. The number of events per bin varies from $\sim 4\,000$ for $p \sim 190\,\mathrm{MeV}/c$ to ~ 700 for $p \sim 250\,\mathrm{MeV}/c$.

7.4 Systematic uncertainties

7.4.1 Uncorrelated systematic uncertainties

Systematic uncertainties related to the beam selection were estimated by varying the cut values by an amount correspond-

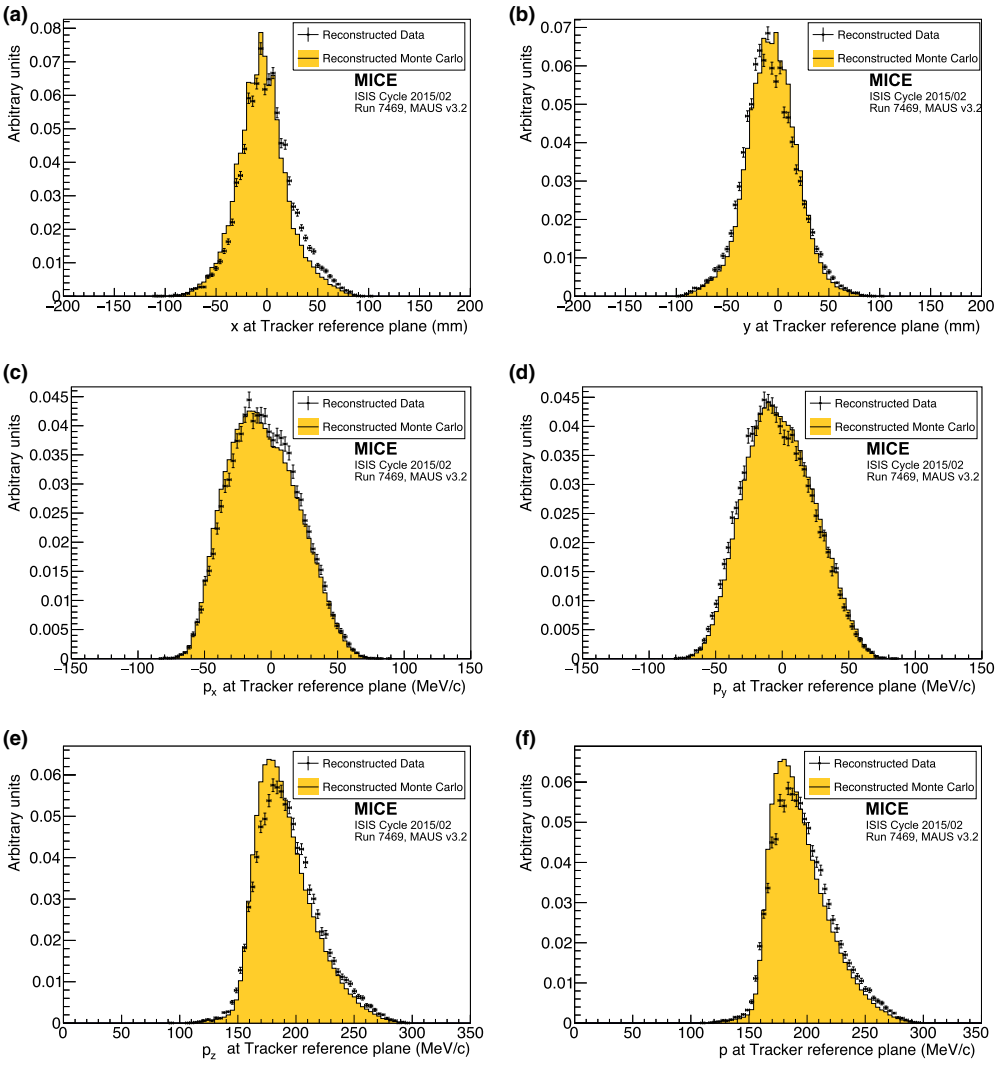

Fig. 5 Position and momentum distributions of muons reconstructed at the reference surface of the upstream tracker: **a** x, **b** y, **c** p_x, **d** p_y, **e** p_z, and **f** p, the total momentum. The data are shown as the solid circles while the results of the MAUS simulation are shown as the yellow histogram

ing to the RMS resolution of the quantity in question. The emittance of the ensembles selected with the changed cut values were calculated and compared to the emittance calculated using the nominal cut values and the difference taken as the uncertainty due to changing the cut boundaries. The overall uncertainty due to beam selection is summarised in Table 3. The dominant beam-selection uncertainty is in the selection of particles that successfully pass within the inner 90 mm of the diffuser aperture.

Systematic uncertainties related to possible biases in calibration constants were evaluated by varying each calibration constant by its resolution. Systematic uncertainties related to the reconstruction algorithms were evaluated using the MAUS simulation. The positive and negative deviations

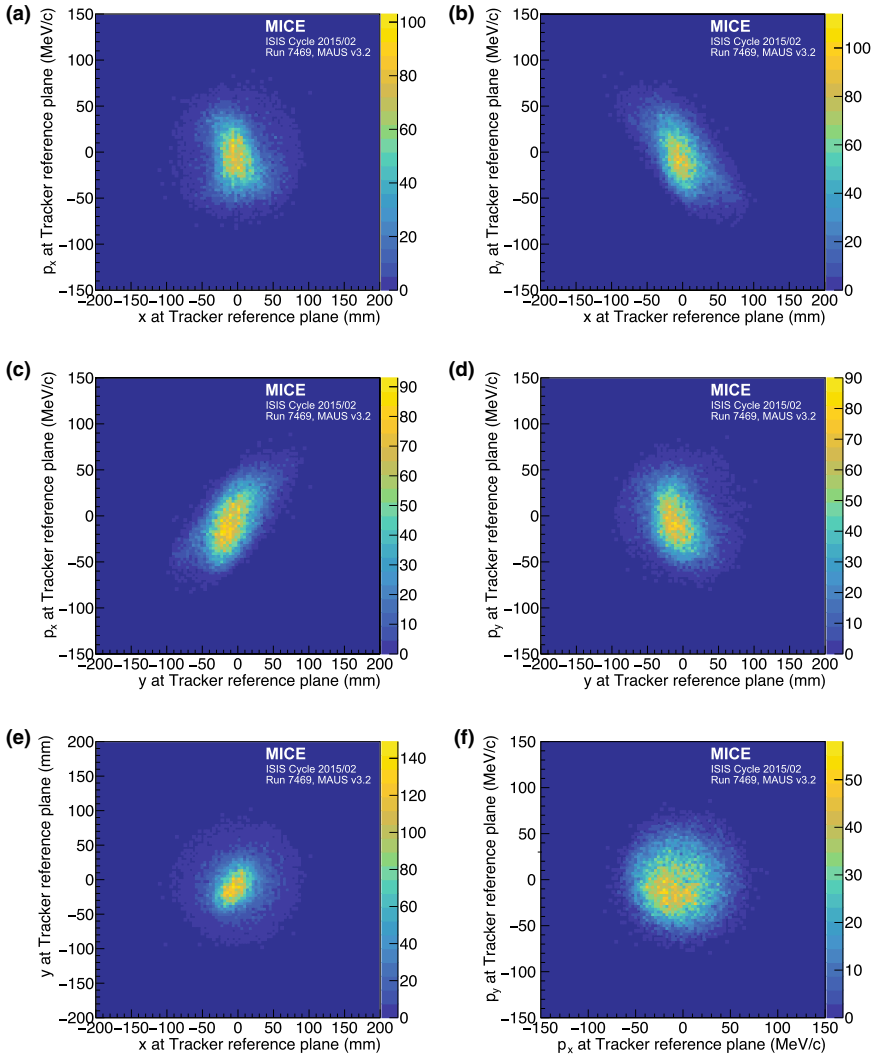

Fig. 6 Transverse phase space occupied by selected muons transported through the MICE Muon Beam line to the reference plane of the upstream tracker. **a** (x, p_x), **b** (x, p_y). **c** (y, p_x), **d** (y, p_y). **e** (x, y), and **f** (p_x, p_y)

from the nominal emittance were added in quadrature separately to obtain the total positive and negative systematic uncertainty. Sources of correlated uncertainties are discussed below.

7.4.2 Correlated systematic uncertainties

Some systematic uncertainties are correlated with the total momentum, p. For example, the measured value of p dictates the momentum bin to which a muon is assigned for the emittance calculation. The uncertainty on the emittance reconstructed in each bin has been evaluated by allowing the

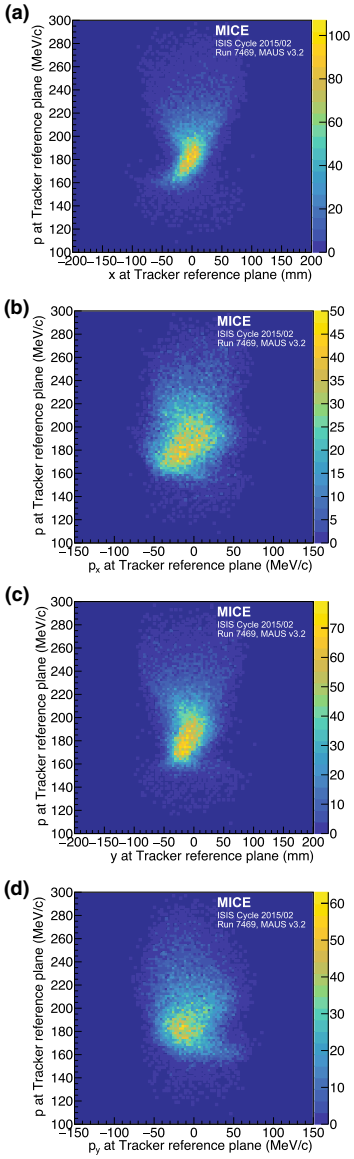

Fig. 7 The effect of dispersion, the dependence of the components of transverse phase space on the momentum, p, is shown at the reference surface of the upstream tracker: **a**) (x, p); **b** (p_x, p); **c** (y, p); **d** (p_y, p)

momentum of each muon to fluctuate around its measured value according to a Gaussian distribution of width equal to the measurement uncertainty on p. In Table 3 this uncertainty is listed as 'Binning in p'.

A second uncertainty that is correlated with total momentum is the uncertainty on the reconstructed x, p_x, y, and p_y. The effect on the emittance was evaluated with the same procedure used to evaluate the uncertainty due to binning in total momentum. This is listed as 'Tracker resolution' in Table 3.

Systematic uncertainties correlated with p are primarily due to the differences between the model of the apparatus used in the reconstruction and the hardware actually used in the experiment. The most significant contribution arises from the magnetic field within the tracking volume. Particle tracks are reconstructed assuming a uniform solenoidal field, with no fringe-field effects. Small non-uniformities in the magnetic field in the tracking volume will result in a disagreement between the true parameters and the reconstructed values. To quantify this effect, six field models (one optimal and five additional models) were used to estimate the deviation in reconstructed emittance from the true value under realistic conditions. Three families of field model were investigated, corresponding to the three key field descriptors: field scale, field alignment, and field uniformity. The values of these descriptors that best describe the Hall-probe measurements were used to define the optimal model and the uncertainty in the descriptor values were used to determine the 1σ variations.

7.4.3 Field scale

Hall-probes located on the tracker provided measurements of the magnetic field strength within the tracking volume at known positions. An optimal field model was produced with a scale factor of 0.49 % that reproduced the Hall-probe measurements. Two additional field models were produced which used scale factors that were one standard deviation, ± 0.03 %, above and below the nominal value.

7.4.4 Field alignment

A field-alignment algorithm was developed based on the determination of the orientation of the field with respect to the mechanical axis of the tracker using coaxial tracks with $p_T \approx 0$ [41]. The field was rotated with respect to the tracker by 1.4 ± 0.1 mrad about the x axis and 0.3 ± 0.1 mrad about the y axis. The optimal field model was created such that the simulated alignment is in agreement with the measurements. Two additional models that vary the alignment by one standard deviation were also produced.

7.4.5 Field uniformity

A COMSOL [42] model of the field was used to generate the optimal model which includes the field generated by each coil

Table 3 Emittance together with the statistical and systematic uncertainties and biases as a function of mean total momentum, $\langle p \rangle$

Source	$\langle p \rangle$ (MeV/c)						
	190	200	210	220	230	240	250
Measured emittance (mm rad)	3.40	3.65	3.69	3.65	3.69	3.62	3.31
Statistical uncertainty	$\pm 3.8 \times 10^{-2}$	$\pm 4.4 \times 10^{-2}$	$\pm 5.0 \times 10^{-2}$	$\pm 5.8 \times 10^{-2}$	$\pm 7.0 \times 10^{-2}$	$\pm 8.4 \times 10^{-2}$	$\pm 9.2 \times 10^{-2}$
Beam selection:							
Diffuser aperture	4.9×10^{-2}	5.3×10^{-2}	4.9×10^{-2}	4.7×10^{-2}	4.2×10^{-2}	11.0×10^{-2}	4.4×10^{-2}
	-3.5×10^{-2}	-5.1×10^{-2}	-5.7×10^{-2}	-5.0×10^{-2}	-3.5×10^{-2}	-5.0×10^{-2}	-9.6×10^{-2}
$\frac{\chi^2}{N_{\mathrm{DOF}}} \leq 4$	5.1×10^{-3}	2.0×10^{-3}	1.0×10^{-2}	4.1×10^{-3}	1.2×10^{-3}	5.5×10^{-3}	7.9×10^{-3}
	-4.8×10^{-3}	-1.3×10^{-3}	-1.8×10^{-3}	-3.3×10^{-3}	-2.8×10^{-4}	-6.5×10^{-3}	-4.7×10^{-4}
Muon hypothesis	4.5×10^{-3}	2.2×10^{-4}	6.4×10^{-3}	3.1×10^{-3}	1.4×10^{-3}	2.6×10^{-3}	1.3×10^{-3}
	-3.2×10^{-3}	-6.8×10^{-3}	-8.8×10^{-4}	-4.7×10^{-3}	-1.1×10^{-2}	-6.7×10^{-2}	-4.1×10^{-3}
Beam selection (Overall)	4.9×10^{-2}	5.3×10^{-2}	5.0×10^{-2}	4.7×10^{-2}	4.2×10^{-2}	1.1×10^{-1}	4.5×10^{-2}
	-3.6×10^{-2}	-5.2×10^{-2}	-5.8×10^{-2}	-5.0×10^{-2}	-3.9×10^{-2}	-8.4×10^{-2}	-9.6×10^{-2}
Binning in p	$\pm 1.8 \times 10^{-2}$	$\pm 2.1 \times 10^{-2}$	$\pm 2.3 \times 10^{-2}$	$\pm 2.9 \times 10^{-2}$	$\pm 3.5 \times 10^{-2}$	$\pm 4.3 \times 10^{-2}$	$\pm 5.2 \times 10^{-2}$
Magnetic field misalignment and scale:							
Bias	-1.3×10^{-2}	-1.4×10^{-2}	-1.5×10^{-2}	-1.6×10^{-2}	-1.6×10^{-2}	-1.7×10^{-2}	-1.6×10^{-2}
Uncertainty	$\pm 2.0 \times 10^{-4}$	$\pm 2.9 \times 10^{-4}$	$\pm 8.0 \times 10^{-4}$	$\pm 4.8 \times 10^{-4}$	$\pm 5.5 \times 10^{-4}$	$\pm 4.8 \times 10^{-4}$	$\pm 4.9 \times 10^{-4}$
Tracker resolution	$\pm 1.6 \times 10^{-3}$	$\pm 2.1 \times 10^{-3}$	$\pm 2.8 \times 10^{-3}$	$\pm 3.8 \times 10^{-3}$	$\pm 5.3 \times 10^{-3}$	$\pm 7.0 \times 10^{-3}$	$\pm 9.5 \times 10^{-3}$
Total systematic uncertainty	5.2×10^{-2}	5.7×10^{-2}	5.5×10^{-2}	5.6×10^{-2}	5.5×10^{-2}	11.7×10^{-2}	6.9×10^{-2}
	-4.0×10^{-2}	-5.6×10^{-2}	-6.2×10^{-2}	-5.8×10^{-2}	-5.2×10^{-2}	-9.5×10^{-2}	-11.0×10^{-2}
Corrected emittance (mm rad)	3.41	3.66	3.71	3.67	3.71	3.65	3.34
Total uncertainty	± 0.06	± 0.07	$+0.07$	± 0.08	± 0.09	$+0.14$	$+0.12$
			-0.08			-0.13	-0.14
Total uncertainty (%)	$+1.90$	$+1.96$	$+2.01$	$+2.19$	$+2.40$	$+3.97$	$+3.47$
	-1.63	-1.94	-2.15	-2.34	-2.37	-3.49	-4.30

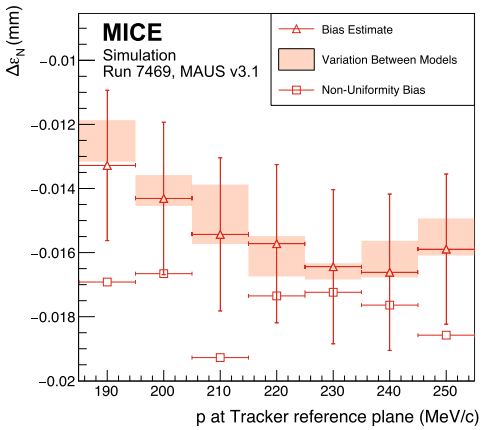

Fig. 8 The systematic bias and uncertainty on the reconstructed emittance under different magnetic field model assumptions. The bias estimate (open triangles) includes the non-uniformity bias (open squares). The variation between the models (see text) is indicated by the shaded bands

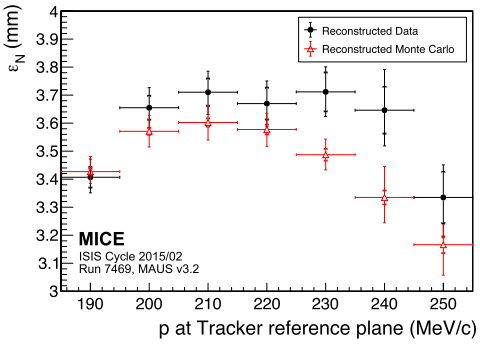

Fig. 9 Normalised transverse emittance as a function of total momentum, p, for data (black, filled circle) and reconstructed Monte Carlo (red, open triangle). The inner error bars show the statistical uncertainty. The outer error bars show the quadratic sum of the statistical and systematic uncertainties

using the 'as-built' parameters and the partial return yoke. A simple field model was created using only the individual coil geometries to provide additional information on the effect of field uniformity on the reconstruction. The values for the simple field model were normalised to the Hall-probe measurements as for the other field models. This represents a significant deviation from the COMSOL model, but demonstrates the stability of the reconstruction with respect to changes in field uniformity, as the variation in emittance between all field models is small (less than 0.002 mm).

For each of the 5 field models, multiple 2000-muon ensembles were generated for each momentum bin. The deviation of the calculated emittance from the true emittance was found for each ensemble. The distribution of the difference between the ensemble emittance and the true emittance was assumed to be Gaussian with mean ε and variance $s^2 = \sigma^2 + \theta^2$, where σ is the statistical uncertainty and θ is an additional systematic uncertainty. The systematic bias for each momentum bin was then calculated as [43]

$$\Delta\varepsilon_N = \langle\varepsilon\rangle - \varepsilon_{\text{true}}\,, \tag{4}$$

where $\varepsilon_{\text{true}}$ is the true beam emittance in that momentum bin and $\langle\varepsilon\rangle$ is the mean emittance from the N ensembles. The systematic uncertainty was calculated assuming that the distribution of residuals of ε_i from the mean, $\langle\varepsilon\rangle$, satisfies a χ^2 distribution with $N-1$ degrees of freedom,

$$\chi^2_{N-1} = \sum_i^N \frac{(\varepsilon_i - \langle\varepsilon\rangle)^2}{\sigma^2 + \theta^2}\,, \tag{5}$$

and θ was estimated by minimising the expression $(\chi^2_{N-1} - (N-1))^2$ [43].

The uncertainty, θ, was consistent with zero in all momentum bins, whereas the bias, $\Delta\varepsilon_N$, was found to be momentum dependent as shown in Fig. 8. The bias was estimated from the mean difference between the reconstructed and true emittance values using the optimal field model. The variation in the bias was calculated from the range of values reconstructed for each of the additional field models. The model representing the effects of non-uniformities in the field was considered separately due to the significance of the deviation from the optimal model.

The results show a consistent systematic bias in the reconstructed emittance of ≈ -0.015 mm that is a function of momentum (see Table 3). The absolute variation in the mean values between the models that were used was smaller than the expected statistical fluctuations, demonstrating the stability of the reconstruction across the expected variations in field alignment and scale. The effect of the non-uniformity model was larger but still demonstrates consistent reconstruction. The biases calculated from the optimal field model were used to correct the emittance values in the final calculation (Sect. 7.5).

7.5 Emittance

The normalised transverse emittance as a function of p is shown in Fig. 9. The emittance has been corrected for the systematic bias shown in Table 3. The uncertainties plotted are those summarised in Table 3, where the inner bars represent the statistical uncertainty and outer bars the total uncertainty. The emittance of the measured muon ensembles (black, filled circle) is approximately flat in the range

$195 \leq p \leq 245\,\text{MeV}/c$, corresponding to the design momentum of the experiment. The mean emittance in this region is $\approx 3.7\,\text{mm}$. The emittance of the reconstructed Monte Carlo is consistently lower than that of the data, and therefore gives only an approximate simulation of the beam.

8 Conclusions

A first particle-by-particle measurement of the emittance of the MICE Muon Beam was made using the upstream scintillating-fibre tracking detector in a 4 T solenoidal field. A total of 24,660 muons survive the selection criteria. The position and momentum of these muons were measured at the reference plane of the upstream tracking detector. The muon sample was divided into 10 MeV/c bins of total momentum, p, from 185–255 MeV/c to account for dispersion, chromaticity, and scraping in apertures upstream of the tracking detector. The emittance of the measured muon ensembles is approximately flat from $195 \leq p \leq 245\,\text{MeV}/c$ with a mean value of $\approx 3.7\,\text{mm}$ across this region.

The total uncertainty on this measurement ranged from $^{+1.9}_{-1.6}\%$ to $^{+3.5}_{-4.3}\%$, increasing with total momentum, p. As p increases, the number of muons in the reported ensemble decreases, increasing the statistical uncertainty. At the extremes of the momentum range, a larger proportion of the input beam distribution is scraped on the aperture of the diffuser. This contributes to an increase in systematic uncertainty at the limits of the reported momentum range. The systematic uncertainty introduced by the diffuser aperture highlights the need to study ensembles where the total momentum, p, is close to the design momentum of the beam line. The total systematic uncertainty on the measured emittance is larger than that on a future measurement of the ratio of emittance before and after an absorber. The measurement is sufficiently precise to demonstrate muon ionization cooling.

The technique presented here represents the first precise measurement of normalised transverse emittance on a particle-by-particle basis. This technique will be applied to muon ensembles up- and downstream of a low-Z absorber, such as liquid hydrogen or lithium hydride, to measure emittance change across the absorber and thereby to study ionization cooling.

Acknowledgements The work described here was made possible by grants from Department of Energy and National Science Foundation (USA), the Instituto Nazionale di Fisica Nucleare (Italy), the Science and Technology Facilities Council (UK), the European Community under the European Commission Framework Programme 7 (AIDA project, grant agreement no. 262025, TIARA project, grant agreement no. 261905, and EuCARD), the Japan Society for the Promotion of Science, the National Research Foundation of Korea (No. NRF-2016R1A5A1013277), and the Swiss National Science Foundation, in the framework of the SCOPES programme. We gratefully acknowledge all sources of support. We are grateful for the support given to us by the staff of the STFC Rutherford Appleton and Daresbury Laboratories. We acknowledge the use of Grid computing resources deployed and operated by GridPP in the UK, http://www.gridpp.ac.uk/.

Data Availability Statement This manuscript has associated data in a data repository. [Authors' comment: The data that support the findings of this study are publicly available on the GridPP computing Grid via the data DOIs (the MICE unprocessed data: 10.17633/rd.brunel.3179644; the MICE reconstructed data: 10.17633/rd.brunel.5955850). Publications using the MICE data must contain the following statement: "We gratefully acknowledge the MICE collaboration for allowing us access to their data. Third-party results are not endorsed by the MICE collaboration and the MICE collaboration does not accept responsibility for any errors in the third-party's understanding of the MICE data."]

Funded by SCOAP[3].

References

1. S. Geer, Phys. Rev. D **57**, 6989 (1998). https://doi.org/10.1103/PhysRevD.57.6989
2. M. Apollonio, et al., Oscillation physics with a neutrino factory (2002). arXiv:hep-ph/0210192
3. D.V. Neuffer, R.B. Palmer, Conf. Proc. C **940627**, 52 (1995)
4. R.B. Palmer, Rev. Accel. Sci. Tech. **7**, 137 (2014). https://doi.org/10.1142/S1793626814300072
5. M. Boscolo, M. Antonelli, O.R. Blanco-Garcia, S. Guiducci, S. Liuzzo, P. Raimondi, F. Collamati, Low emittance muon accelerator studies with production from positrons on target (2018). https://doi.org/10.1103/PhysRevAccelBeams.21.061005. arXiv:1803.06696 [physics.acc-ph]
6. S.Y. Lee, *Accelerator Physics*, 3rd edn. (World Scientific Publishing Co, Singapore, 2012). https://doi.org/10.1142/8335
7. S. Schröder, R. Klein, N. Boos, M. Gerhard, R. Grieser, G. Huber, A. Karafillidis, M. Krieg, N. Schmidt, T. Kühl, R. Neumann, V. Balykin, M. Grieser, D. Habs, E. Jaeschke, D. Krämer, M. Kristensen, M. Music, W. Petrich, D. Schwalm, P. Sigray, M. Steck, B. Wanner, A. Wolf, Phys. Rev. Lett. **64**, 2901 (1990). https://doi.org/10.1103/PhysRevLett.64.2901
8. J.S. Hangst, M. Kristensen, J.S. Nielsen, O. Poulsen, J.P. Schiffer, P. Shi, Phys. Rev. Lett. **67**, 1238 (1991). https://doi.org/10.1103/PhysRevLett.67.1238
9. P.J. Channell, J. Appl. Phys. **52**(6), 3791 (1981). https://doi.org/10.1063/1.329218
10. J. Marriner, Nucl. Instrum. Methods A **532**, 11 (2004). https://doi.org/10.1016/j.nima.2004.06.025
11. V.V. Parkhomchuk, A.N. Skrinsky, Physics-Uspekhi **43**(5), 433 (2000)
12. A.N. Skrinsky, V.V. Parkhomchuk, Sov. J. Part. Nucl. **12**, 223 (1981) [**Fiz. Elem. Chast. Atom. Yadra 12,557 (1981)**]
13. D. Neuffer, Conf. Proc. C **830811**, 481 (1983)
14. D. Neuffer, Part. Accel. **14**, 75 (1983)
15. The MICE collaboration, International MUON Ionization Cooling Experiment. http://mice.iit.edu. Accessed 4 Mar 2019
16. M. Apollonio et al., JINST **4**, P07001 (2009). https://doi.org/10.1088/1748-0221/4/07/P07001
17. J.B. Rosenzweig, *Fundamentals of Beam Physics* (Oxford University Press, Oxford, 2003)

18. C.N. Booth et al., JINST **8**, P03006 (2013). https://doi.org/10.1088/1748-0221/8/03/P03006
19. C.N. Booth et al., JINST **11**(05), P05006 (2016). https://doi.org/10.1088/1748-0221/11/05/P05006
20. M. Bogomilov et al., JINST **7**, P05009 (2012). https://doi.org/10.1088/1748-0221/7/05/P05009
21. D. Adams et al., Eur. Phys. J. C **73**(10), 2582 (2013). https://doi.org/10.1140/epjc/s10052-013-2582-8
22. M. Bogomilov et al., JINST **11**(03), P03001 (2016). https://doi.org/10.1088/1748-0221/11/03/P03001
23. R. Bertoni, Nucl. Instrum. Methods A **615**, 14 (2010). https://doi.org/10.1016/j.nima.2009.12.065
24. R. Bertoni, M. Bonesini, A. de Bari, G. Cecchet, Y. Karadzhov, R. Mazza, The construction of the MICE TOF2 detector (2010). http://mice.iit.edu/micenotes/public/pdf/MICE0286/MICE0286.pdf. Accessed 4 Mar 2019
25. L. Cremaldi, D.A. Sanders, P. Sonnek, D.J. Summers, J. Reidy Jr., I.E.E.E. Trans, Nucl. Sci. **56**, 1475 (2009). https://doi.org/10.1109/TNS.2009.2021266
26. M. Ellis, Nucl. Instrum. Methods A **659**, 136 (2011). https://doi.org/10.1016/j.nima.2011.04.041
27. F. Ambrosino, Nucl. Instrum. Methods A **598**, 239 (2009). https://doi.org/10.1016/j.nima.2008.08.097
28. R. Asfandiyarov et al., JINST **11**(10), T10007 (2016). https://doi.org/10.1088/1748-0221/11/10/T10007
29. D. Adams et al., JINST **10**(12), P12012 (2015). https://doi.org/10.1088/1748-0221/10/12/P12012
30. A. Dobbs, C. Hunt, K. Long, E. Santos, M.A. Uchida, P. Kyberd, C. Heidt, S. Blot, E. Overton, JINST **11**(12), T12001 (2016). https://doi.org/10.1088/1748-0221/11/12/T12001
31. S. Blot, *Proceedings 2nd International Particle Accelerator Conference (IPAC 11) 4–9 September 2011* (San Sebastian, 2011) https://accelconf.web.cern.ch/accelconf/IPAC2011/papers/mopz034.pdf. Accessed 4 Mar 2019
32. The MICE Collaboration, The MICE RAW Data. https://doi.org/10.17633/rd.brunel.3179644 (**MICE/Step4/07000/07469.tar**)
33. T. Roberts, et al., G4beamline; a "Swiss Army Knife" for Geant4, optimized for simulating beamlines. http://public.muonsinc.com/Projects/G4beamline.aspx. Accessed 17 Sept 2018
34. D. Rajaram, C. Rogers, The mice offline computing capabilities (2014). http://mice.iit.edu/micenotes/public/pdf/MICE0439/MICE0439.pdf (**MICE Note 439**)
35. S. Agostinelli, Nucl. Instrum. Methods Phys. Res. A **506**, 250 (2003)
36. J. Allison et al., IEEE Trans. Nucl. Sci. **53**, 270 (2006). https://doi.org/10.1109/TNS.2006.869826
37. R. Brun, F. Rademakers, Nucl. Instrum. Methods A **389**, 81 (1997). https://doi.org/10.1016/S0168-9002(97)00048-X
38. J. Cobb, Statistical errors on emittance measurements (2009). http://mice.iit.edu/micenotes/public/pdf/MICE341/MICE268.pdf. Accessed 4 Mar 2019
39. J. Cobb, Statistical errors on emittance and optical functions (2011). http://mice.iit.edu/micenotes/public/pdf/MICE341/MICE341.pdf. Accessed 4 Mar 2019
40. J.H. Cobb, Statistical Errors on Emittance (2015, Private communication)
41. C. Hunt, Private communication Publication-in-progress
42. COMSOL Multiphysics software Webpage: https://www.comsol.com. Accessed 4 Mar 2019
43. L. Lyons, J. Phys. A Math. Gen. **25**(7), 1967 (1992). http://stacks.iop.org/0305-4470/25/i=7/a=035

Astroparticle Physics 109 (2019) 1–11

Contents lists available at ScienceDirect

Astroparticle Physics

journal homepage: www.elsevier.com/locate/astropartphys

A novel method for atmospheric correction of cosmic-ray data based on principal component analysis

M. Savić, A. Dragić*, D. Maletić, N. Veselinović, R. Banjanac, D. Joković, V. Udovičić

Institute of Physics, University of Belgrade, Pregrevica 118, Zemun 11080, Serbia

ARTICLE INFO

Article history:
Received 23 August 2018
Revised 8 December 2018
Accepted 29 January 2019
Available online 29 January 2019

Keywords:
Cosmic rays
Muons
Atmospheric corrections
Principal component analysis

ABSTRACT

A new method for atmospheric correction of cosmic ray data is designed. It's fully empirical, based on the principal component analysis. The method requires knowledge of the pressure and the temperature profile of the atmosphere. It's applicable to all muon detectors. The method is tested on muon data from two detectors in Belgrade cosmic ray station, one located on the ground level and the other at the depth of 25 mwe. Correction reduces variance by 64.5% in ground level detector data and 38.1% in underground data. At the same time, the amplitude of the annual variation is reduced by 86.0% at ground level and 54.9% underground. With the same data sets the presented method performs better than the integral correction method.

1. Introduction

Count rates of ground based or underground cosmic-ray (CR) muon detectors are affected by atmospheric parameters (air pressure and temperature at different heights). The proper description of atmospheric effects is necessary for understanding primary CR variations, originating outside of the atmosphere.

Early studies in CR temporal variations [1,2] revealed the existence of a variation caused by the change of air pressure, the so called "barometric effect". With the increase in pressure the atmosphere represents thicker absorber, resulting in reduced number of muons reaching the ground level. Therefore, muon flux is expected to be anti-correlated with atmospheric pressure.

Observed negative correlation between muon flux and atmospheric temperature, the so called "negative temperature effect", has been explained by Blackett [3] to be a consequence of muon decay. During warm periods the atmosphere is expanded and the main layer of muon production (~100 mb) is higher, resulting in longer muon path and lower surviving probability to the ground level. Low energy muons are more affected, while the flux of high energy muons, capable of penetrating great depth, does not suffer. At deep underground experiments another type of temperature effect, "positive temperature effect" is pronounced [4]. Development of nuclear emulsions capable of detecting energetic charged particles lead to discovery of charged pions in CRs and $\pi - \mu$ decay [5–7]. The positive temperature effect is interpreted as a consequence of latter process [8,9]. Pions created in the interactions of primary CR particles with the atmospheric nuclei can decay into muons or interact with air nuclei. Higher temperature in the production layer means lower air density and consequently, lower interaction probability and higher muon production.

In most cases linear regression is sufficient to account for the barometric effect. The temperature effects are treated by empirical and theoretical methods. In addition to the barometric coefficient β, **the method of effective level of generation** [8] introduces two empirical parameters: α_H to encounter for muon intensity variations δI_μ correlated with the change of the height of generation level δH (negative effect) and α_T for the changes of the temperature of this level (positive temperature effect).

$$\delta I_\mu = \beta \delta p + \alpha_H \delta H + \alpha_T \delta T \tag{1}$$

Duperier method has been successfully used in many studies for the atmospheric corrections of muon data ([10–15] etc.).

It's been argued [16,17] that for correct temperature correction of muon detectors count rate the vertical temperature profile of the entire atmosphere needs to be known. In the so called **integral method** the muon intensity variations caused by the temperature are described by the equation:

$$\frac{\delta I_\mu}{I_\mu} = \int_0^{h_0} W_T(h)\delta T(h)dh \tag{2}$$

where $\delta T(h)$ is the variation of temperature at isobaric level h with respect to the referent value and $W_T(h)$ is the temperature coefficient density. The coefficients are calculated theoretically and the best known calculations are given in references [18,19].

* Corresponding author.
E-mail address: dragic@ipb.ac.rs (A. Dragić).

https://doi.org/10.1016/j.astropartphys.2019.01.006
0927-6505/

The **mass-average temperature method** [20] is a variant of the integral method, based on the assumption of small changes of the temperature coefficient density $W_T(h)$ with the atmospheric depth h allowing its average value $\overline{W}_T$ to be put in front of the integral in the Eq. (2) and on determination of the mass-averaged temperature T_m:

$$\frac{\delta I_\mu}{I_\mu} = \overline{W}_T(h) \int_0^{h_0} \delta T(h) dh = \overline{W}_T(h) \cdot \delta T_m \tag{3}$$

The method was used in numerous studies ([21–23] to name a few).

Another form of the integral method is **the effective temperature method** [24]. By introducing the temperature coefficient α_T:

$$\alpha_T = \int_0^{h_0} W_T(h) dh$$

the Eq. (2) can be normalized as:

$$\frac{\delta I_\mu}{I_\mu} = \int_0^{h_0} W_T(h) dh \cdot \frac{\int_0^{h_0} W_T(h) \delta T(h) dh}{\int_0^{h_0} W_T(h) dh} = \alpha_T \cdot \delta T_{eff} \tag{4}$$

where the effective temperature T_{eff} is defined as:

$$T_{eff} = \frac{\int_0^{h_0} W_T(h) T(h) dh}{\int_0^{h_0} W_T(h) dh}$$

The latter method is popular with the underground muon telescopes [25,26].

Different methods of atmospheric correction might be compared on the basis of several criteria. One is requirement of the lowest variance of corrected data. Since the most prominent temperature effect on CR time series is seasonal variation, another criterion is the smallest residual amplitude of seasonal variation after correction is applied. The latter does not take into account possible genuine seasonal variation of non-atmospheric origin.

Early studies comparing Dupierier's empirical and Dorman's theoretical methods ([27] and references therein) found similar accuracy of two methods, with essentially the same corrections at sea level, but with the integral method overestimating the temperature effect.

A more recent study [28] compared different methods of atmospheric correction for data from Nagoya and Tibet supertelescopes, as well as Yakutsk, Moscow and Novosibirsk telescopes. They found the mass-averaged temperature method to practically coincide with the integral method. On the other hand, the effective level of generation method for Nagoya shows discrepancy from the integral method in winter time, being able to eliminate only 50% of the temperature effect. Even with the integral method in the case of Tibet muon telescope the removal of temperature effect is achieved with the density of temperature coefficients 3 times higher than calculated ones. The precise origin of disagreement is unknown.

The method of the effective level of generation takes care of key physical causes of the temperature effect. However, it does not make optimal use of the temperature data. Also, the assumption of a single level of main muon production is a simplification. Detailed CORSIKA simulation of the shower development in the atmosphere reveals the actual distribution of the muon generation heights (see Fig. 1).

Different implementations of the integral method exist, employing different approximations, choice of parameters, models of the atmosphere, whether kaon contribution is taken into account, leading to differences in calculated density temperature coefficients (see for instance discussion in [29]). As already mentioned, on the case of Tibet telescope [28] theoretical calculations do not fully correspond to the local experimental conditions and the origin of disagreement is difficult to trace.

The effective temperature method lacks universality, since it works best with the data from deep underground detectors.

Here we propose a new method for atmospheric corrections. It's fully empirical, makes use of the available temperature data through entire atmosphere and it's applicable to arbitrary detector irrespective to energy sensitivity and is simple to implement. The method is based on the principal component analysis, thus reducing dimensionality of the problem, exploiting correlations between atmospheric variables and ensuring mutual independence of correction parameters. The price is loss of clear physical interpretation of these parameters, since the pressure and the temperature at different levels are treated on equal footing.

2. Method description

2.1. Meteorological data

Set of variables that enter principal component decomposition consists of atmospheric temperature profile for the given location as well as locally measured atmospheric pressure. Meteorological balloon soundings for Belgrade are not done frequently enough to be used for suggested analysis. As a consequence, modeled temperatures were used instead. However, there were enough balloon sounding data for testing consistency of the modeled temperatures.

There are several weather and global climate numerical models available today. Here, Global Forecast System [30] data was used. GFS is a weather forecast model, developed by National Centers for Environmental Prediction [31], which is able to predict large number of atmospheric and land-soil parameters. Apart from forecast data, GFS also provides retrospective data produced taking into account most recent measurements by a world wide array of meteorological stations. Retrospective data are produced four times a day at 00:00, 06:00, 12:00 and 18:00 UTC. Data with finer temporal resolution are obtained by cubic spline interpolation. Temperatures for the following 25 isobaric levels (in mb) were used for initial analysis: 10, 20, 30, 50, 70, 100, 150, 200, 250, 300, 350, 400, 450, 500, 550, 600, 650, 700, 750, 800, 850, 900, 925, 975, 1000. Horizontal spatial resolution for modeled data is 0.5 degrees, so coordinates closest to the experiment location (latitude 44.86, longitude 20.39), were selected with this precision. Before any further analysis was done, GFS modeled temperature profiles were compared to local meteorological balloon soundings for Belgrade, where balloon data was available. Fig. 2 shows profile of differences between modeled and measured values for different isobaric levels. Disagreement was found between measured and modeled temperature at the lowest level. As a result, it was decided not to use temperature data for isobaric level of 1000 mb in further analysis. Ground temperature data measured by local meteorological stations was used for lowest layer instead. Similar problem with the GFS data was reported before by [28] who found 5° C deviation in the summer time near ground level at Yakutsk location.

Atmospheric pressure and ground level temperature from the Republic Hydro-meteorological Service of Serbia was used to compose unique local pressure and temperature time series.

2.2. Cosmic-ray data

The analysis is performed on data from Belgrade muon detectors. The Belgrade cosmic-ray station, together with the present detector arrangement is described in details elsewhere [32]. Two muon detectors are located in the laboratory, one at the ground level and the other at the depth of 25 mwe. Data are recorded on the event-by event basis and can be integrated into the time series with the arbitrary time resolution. For most purposes hourly data are used. Muon detectors are sensitive to primary cosmic rays

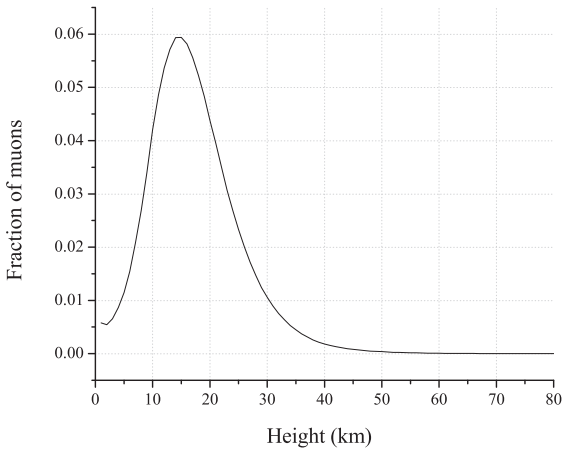

Fig. 1. Distribution of muon generation at different heights in the atmosphere, according to CORSIKA simulation.

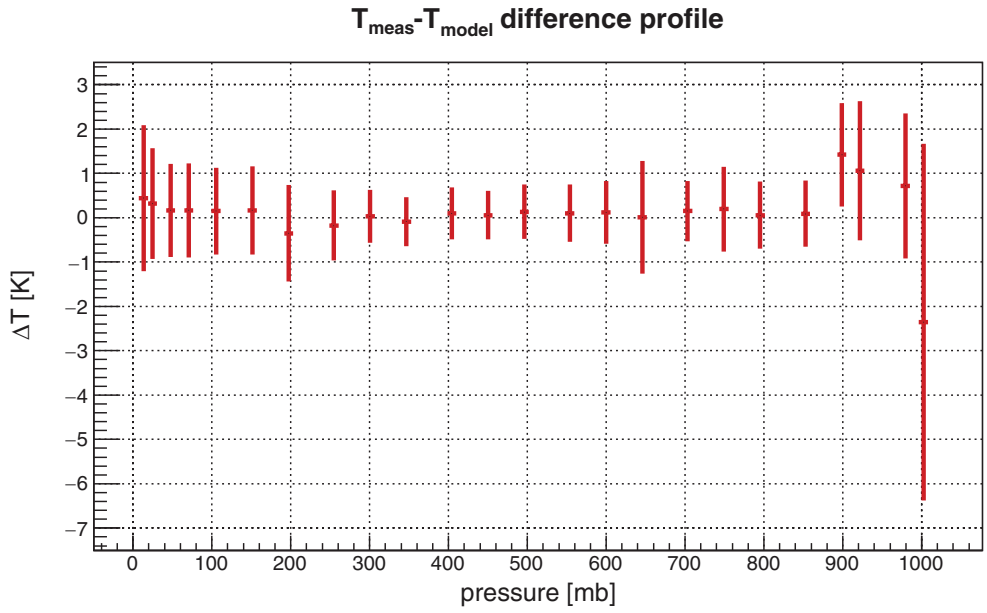

Fig. 2. Distribution of differences between measured temperatures and modeled by GFS.

of 59 GeV median energy in the case of ground level detector and 137 GeV for underground detector.

2.3. Principal component decomposition

Principal component analysis is a convenient and widely used data reduction method when dealing with strongly correlated data. It transforms the original set of variables into a set of uncorrelated variables (called principal components (PC)). The principal components are ordered according to decreasing variance. In our case, there are 26 input variables: 24 modeled temperatures (isobaric level 1000 mb temperature excluded), locally measured ground level temperature and local atmospheric pressure. Initial variables were centered and normalized before

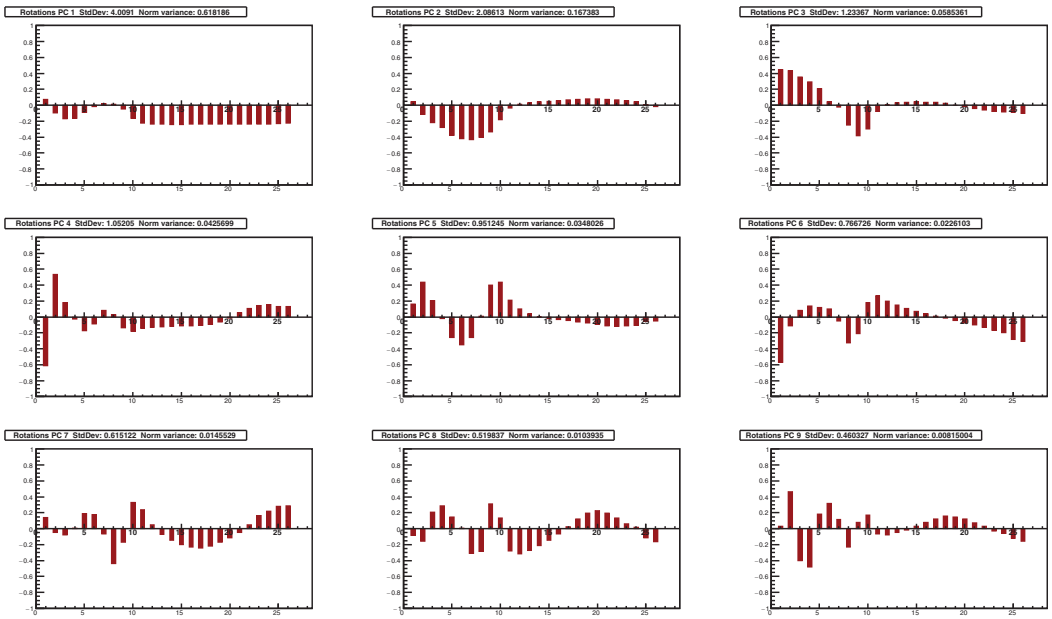

Fig. 3. Composition of nine principal components with largest variance (in decreasing order). Input variables are displayed on *X*-axis: 1 being pressure, 2 temperature of 10 mb isobaric level, 26 being local ground level temperature. *Y*-axis represents rotations.

decomposition. After decomposition, a new set of 26 principal components was obtained. Decomposition should not be regarded as universal, but it should be redone for every location and period under study.

One year was selected as a suitable time period for the analysis, in order to reduce possible seasonal bias, due to atmospheric temperature annual variation. Additional criteria were quality and consistency of muon data. Taking this into account, final time interval selected for analysis was from 01.06.2010 to 31.05. 2011.

Fig. 3 shows composition plots for the first nine principal components, that account for 98% of total variance. *X*-axis represents input atmospheric variables, first being atmospheric pressure, followed by 10 mb layer temperature, last being ground level local temperature. *Y*-axis represents decomposition rotations for a given principal component. Interesting features observed on these plots are that first two principal components depend almost exclusively on temperature. The first one is mostly combination of temperatures in the troposphere (isobaric levels 250–1000 mb) with almost equal weights. The second eigenvector accounts for significant variance of temperatures in higher atmospheric levels (10–250 mb), with the strongest contribution centered in the tropopause. Components 3 to 6 have mixed p-T composition. The correlation of atmospheric pressure and temperature at different heights is not surprising. The diurnal and semi-diurnal oscillations of pressure are attributed to the warming of the upper atmosphere by the Sun [33]. This correlation makes it impossible to define a single barometric parameter in PCA based method of atmospheric corrections. It's worth mentioning that Dorman [34] recognizes three different barometric effects: absorption, decay and generation effect. It also indicates that empirical methods with separated pressure and temperature corrections might lead to overcorrection.

The values of the eigenvectors for these first nine components are also given in Table 1.

Fig. 4 shows plot of proportion of variance as well as plot of cumulative variance for obtained principal components. Corresponding numerical values are given in Table 2.

Usually, only a first few principal components (containing high fraction of total variance) are of practical interest. There are various different methods and rules for choosing how many PCs to retain in the analysis, none completely free of subjectivity (see for example a thorough discussion in [35]). A rule based on cumulative percentage of total variation usually recommends to retain PCs responsible for 70–90% of total variation. When one or two components are dominant, higher value (95%) is appropriate. In our case it would mean keeping first 6 PCs. According to Kaisser's rule only PCs with the eigenvalue $\lambda > 1$ should be retained. Jolliffe [35] suggested 0.7 as correct level, exceeded by six of our PCs. Another rule proposes to retain components with the eigenvalue above mean, a condition satisfied by first seven of our PCs. Another popular model is broken stick, but in application to our problem is too restrictive, leading to only two relevant PCs. The scree graph or log-eigenvalue diagram don't provide clean cut with our set of PCs.

To test the meaningfulness of potentially relevant PCs, the time series from PC data are constructed and tested whether they are distinguishable from white noise. The procedure is often done when principal component analysis is applied to atmospheric physics problems [36]. The time series with hourly resolution for the first three PCs are plotted on Fig. 5.

Table 1
Definition of first nine principal components.

Variables	Principal components								
	PC1	PC2	PC3	PC4	PC5	PC6	PC7	PC8	PC9
p	0.07699	0.04117	0.44694	−0.61285	0.16301	−0.57121	0.14028	−0.08106	0.03443
T(10)	−0.0947	−0.11603	0.43488	0.5344	0.43741	−0.11036	−0.04499	−0.15825	0.46469
T(20)	−0.16947	−0.21766	0.35754	0.18029	0.20527	0.08546	−0.07719	0.20635	−0.40309
T(30)	−0.16476	−0.27825	0.29593	−0.02505	−0.02204	0.14134	0.00634	0.28574	−0.47812
T(50)	−0.09124	−0.37682	0.20969	−0.17322	−0.25798	0.12084	0.19349	0.14645	0.18493
T(70)	−0.01483	−0.42304	0.04507	−0.08651	−0.3472	0.09965	0.18155	0.01024	0.31886
T(100)	0.02192	−0.43132	−0.02451	0.08228	−0.25692	−0.04937	−0.06464	−0.3103	0.1183
T(150)	0.01487	−0.40127	−0.24673	0.03037	0.012	−0.32566	−0.43658	−0.28393	−0.23316
T(200)	−0.04737	−0.33404	−0.38636	−0.13563	0.40141	−0.2069	−0.16852	0.31181	0.07995
T(250)	−0.16218	−0.17984	−0.29739	−0.18123	0.43708	0.18013	0.32866	0.13662	0.17389
T(300)	−0.22473	−0.03266	−0.07561	−0.14073	0.21179	0.26504	0.23807	−0.27931	−0.06785
T(350)	−0.2369	0.01439	0.00488	−0.12991	0.0998	0.1988	0.05306	−0.31612	−0.0771
T(400)	−0.23956	0.03362	0.02958	−0.12159	0.04075	0.14932	−0.06959	−0.27189	−0.04852
T(450)	−0.24028	0.04271	0.0402	−0.11503	0.00384	0.10744	−0.14772	−0.21165	−0.01823
T(500)	−0.24005	0.04935	0.0428	−0.11304	−0.02187	0.07218	−0.19893	−0.14512	0.03068
T(550)	−0.23958	0.05695	0.03965	−0.11295	−0.03254	0.0388	−0.23263	−0.06843	0.08056
T(600)	−0.23881	0.06549	0.03681	−0.10649	−0.04369	0.01102	−0.24562	0.02401	0.12499
T(650)	−0.23854	0.07279	0.0236	−0.09184	−0.06132	−0.01542	−0.21788	0.12597	0.15977
T(700)	−0.23835	0.0801	0.00429	−0.06052	−0.07601	−0.04668	−0.16785	0.19559	0.14932
T(750)	−0.23842	0.08071	−0.01837	−0.01332	−0.09245	−0.07308	−0.11295	0.22563	0.12401
T(800)	−0.23814	0.07557	−0.03907	0.05036	−0.10989	−0.09943	−0.04696	0.19596	0.07735
T(850)	−0.23701	0.0675	−0.06202	0.1081	−0.11988	−0.12745	0.04989	0.13672	0.0304
T(900)	−0.23535	0.05462	−0.07977	0.14776	−0.11454	−0.16955	0.16551	0.06204	−0.02952
T(925)	−0.23414	0.04606	−0.08313	0.15641	−0.10257	−0.19925	0.21877	0.01715	−0.05804
T(975)	−0.23108	0.00789	−0.08827	0.13022	−0.05888	−0.28046	0.284	−0.11523	−0.12249
T(1000)	−0.22494	−0.01582	−0.10092	0.13401	−0.04977	−0.30749	0.28553	−0.16516	−0.15908

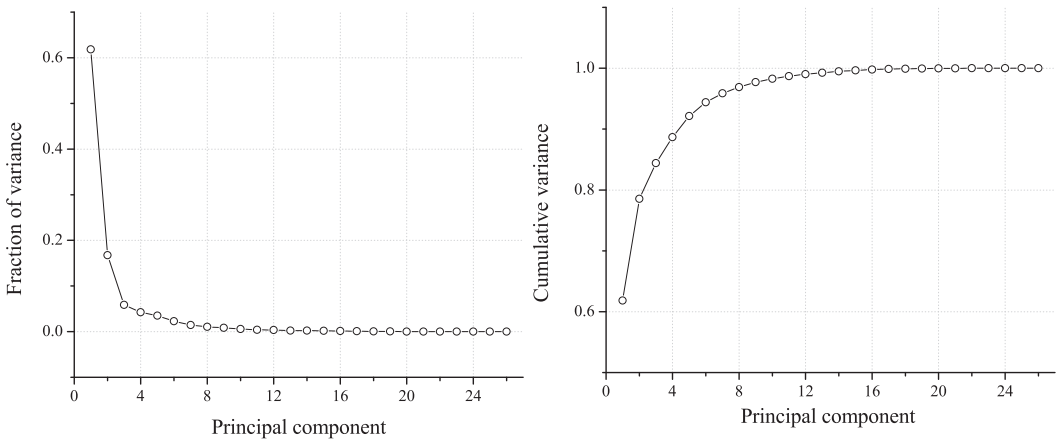

Fig. 4. Proportion of variance (left) and cumulative proportion of variance (right) for all 26 principal components.

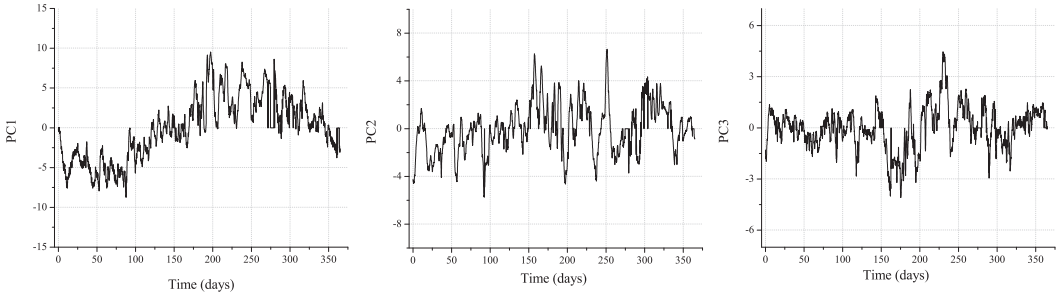

Fig. 5. Time series of the first 3 PCs.

Table 2
Variance (individual and cumulative) for all 26 PCs.

Principal component	Eigenvalue	Percentage of variance	Cumulative variance (%)
1	4.0091	0.618186	0.618186
2	2.08613	0.167383	0.785569
3	1.23367	0.0585361	0.844105
4	1.05205	0.0425699	0.886675
5	0.951245	0.0348026	0.921478
6	0.766726	0.0226103	0.944088
7	0.615122	0.0145529	0.958641
8	0.519837	0.0103935	0.969034
9	0.460327	0.00815004	0.977184
10	0.382006	0.00561263	0.982797
11	0.32832	0.00414592	0.986943
12	0.294489	0.00333553	0.990278
13	0.247876	0.00236317	0.992642
14	0.239462	0.00220546	0.994847
15	0.206157	0.00163465	0.996482
16	0.184453	0.00130857	0.99779
17	0.144657	8.04834E−4	0.998595
18	0.119676	5.5086E−4	0.999146
19	0.0938189	3.38538E−4	0.999485
20	0.0739496	2.10328E−4	0.999695
21	0.0586253	1.32189E−4	0.999827
22	0.0414996	6.62391E−5	0.999893
23	0.0338811	4.41511E−5	0.999937
24	0.0281359	3.04472E−5	0.999968
25	0.0219102	1.84637E−5	0.999986
26	0.0188263	1.36319E−5	1

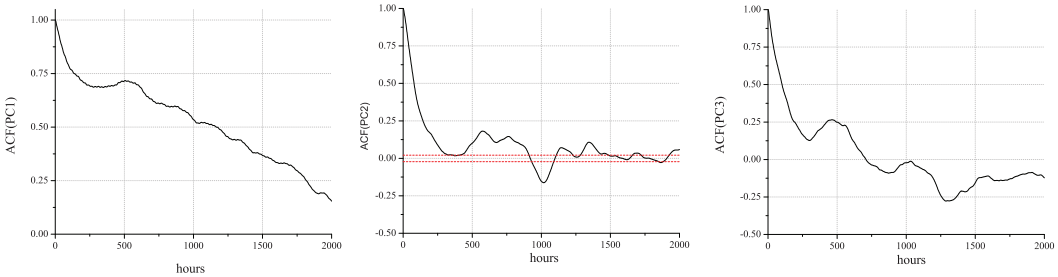

Fig. 6. Autocorrelation function of the first 3 PCs. Time lag is given in hours. In the case of PC2, 95% significance level is indicated by dashed red line. (For interpretation of the references to color in this figure legend, the reader is referred to the web version of this article.)

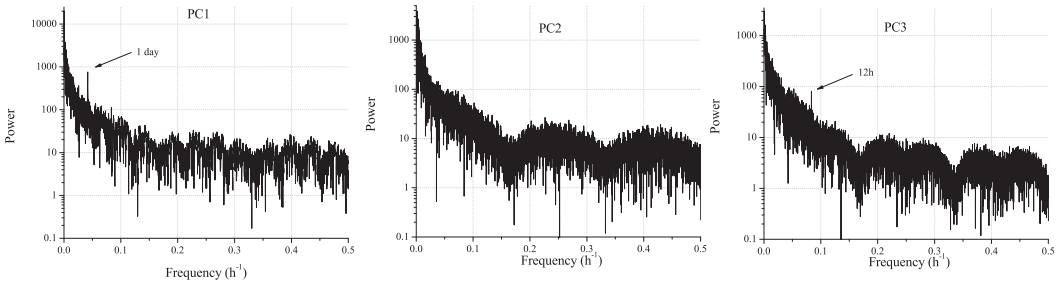

Fig. 7. Spectral analysis of time series of the first 3 PCs.

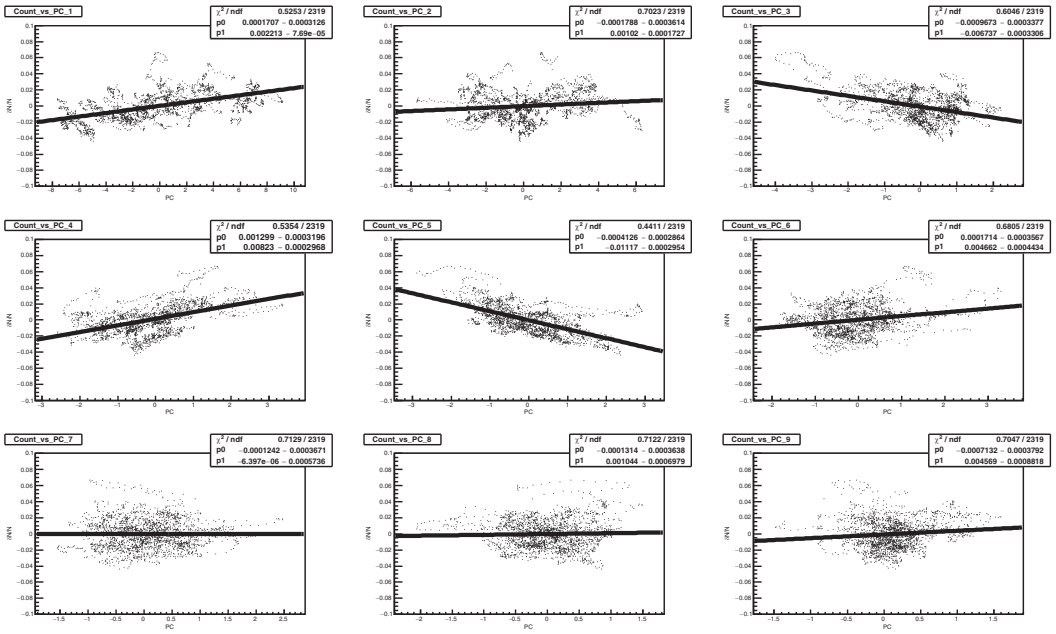

Fig. 8. Muon count dependence on principal components for the first nine principal components (GLL).

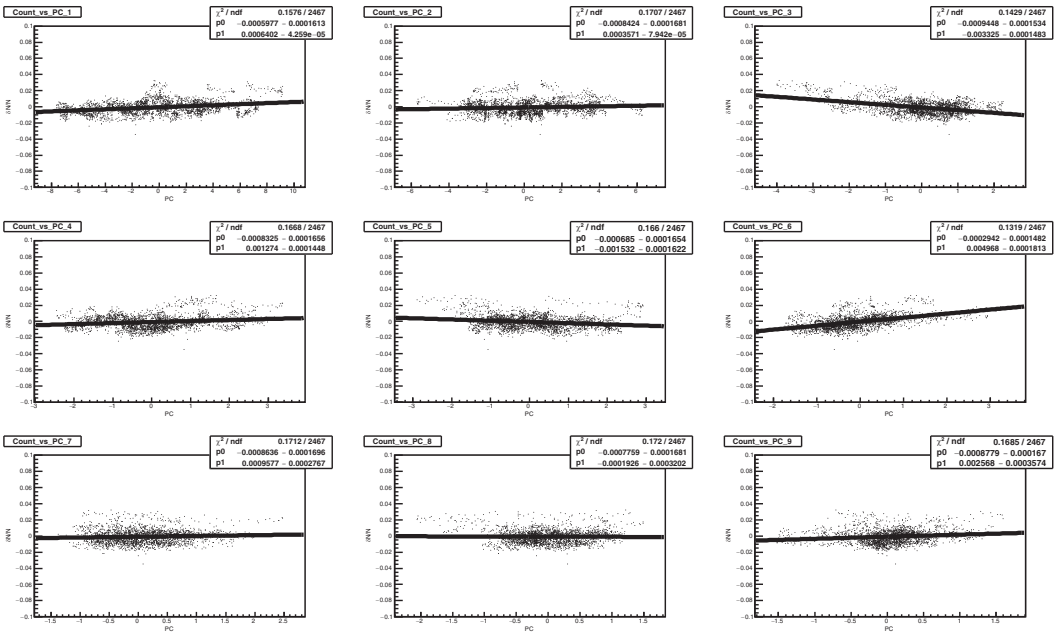

Fig. 9. Muon count dependence on principal components for the first nine principal components (UL).

The subsequent temperature and pressure measurements are highly correlated, as evident from autocorrelation function plot for selected PCs (Fig. 6).

The spectral analysis of the PC time series reveals, for PCs with the strong pressure component, semi-diurnal periodicity in addition to diurnal (Fig. 7).

Since our purpose is the regression of muon data with principal components, selecting the components with significantly high variance is not the main issue. It is more important to identify PCs with high correlation with CR data. Components with relatively low variance, can have high predictive power.

2.4. Correlation of principal components with CR muon count rate and correction of muon data

Scatter plot of muon count rate vs. PCs, together with the linear fit for the first nine principal components are shown on Fig. 8 (GLL) and Fig. 9 (UL). In the analysis hourly summed muon counts and principal component values for the respective hour were used. To minimize the effect of geomagnetic disturbances, only data for International Quiet Days were taken into account. The International Quiet Days are the days with minimum geomagnetic activity for each month. The selection of quiet days is deduced from K_p index. In our analysis 5 quietest days for each month are considered. The values of correlation coefficients are listed in Table 3.

Principal components PC1, PC3, PC4, PC5 and PC6 have been identified as ones with significant contribution to the muon flux variation. Interestingly enough, the PC2, responsible for 16.7% variance of the meteorological data has very little effect on muon flux, at neither ground nor underground level. Ground level muon flux variation is more affected by the first principal component, depending chiefly on the temperature in the troposphere. The finding agrees with usual negative temperature effect. The other PCs are difficult to compare with traditional correction parameters. Yet, the effect of PC3, that is composed more from upper atmosphere temperatures and hence could be loosely associated with positive temperature effect, is more pronounced for the underground muon flux. Fourth and fifth principal components with strong pressure contribution affect more ground level muon flux. On the other hand, PC6, also the one with high pressure component, has more pronounced influence on underground muon flux.

Gradients obtained from the fits for the significant principal components 1, 3, 4, 5 and 6 were then used to calculate the PCA corrected muon count according to the formula:

$$N_{\mu}^{(corr)} = N_{\mu} - < N_{\mu} > \sum_{i} k_i PC_i, \quad i = 1, 3, 4, 5, 6 \tag{5}$$

where $N_{\mu}^{(corr)}$ corr is the corrected muon count, N_{μ} is the raw muon count, $< N_{\mu} >$ is the mean count for the whole period, k_i are the gradients and PC_i are the corresponding principal components. Resulting corrected muon count time series are plotted on Figs. 10 (GLL) and 11 (UL) along with raw and pressure only corrected time series. Pressure corrected time series are produced for reference. Barometric coefficient was determined by applying linear regression to the same data set used for PCA. Data was previously corrected for temperature effect using integral method, as in Ref. [37]. Pressure corrected and PCA corrected time series are fitted with sine function with annual period in order to illustrate how PCA correction affects yearly variation induced by temperature effect.

PCA based atmospheric corrections remove 64.5% of total variance in GLL time series and 38.1% in UL time series. Pressure corrected CR time series exhibit annual variation, a consequence of

Table 3
Correlation coefficients between principal components and muon count rate in the ground level laboratory (GLL) and underground laboratory (UL).

PC	1	2	3	4	5	6	7	8	9	10	11	12	13	14	15	16	17	18	19	20	21	22	23	24	25	26
GLL	0.43	0.01	−0.37	0.48	−0.55	0.30	−0.01	0.03	−0.01	0.06	0.00	−0.04	0.00	0.01	0.02	−0.01	0.00	−0.01	−0.01	0.03	−0.03	0.00	0.02	−0.01	0.04	0.02
UL	0.26	0.02	−0.48	0.21	−0.19	0.52	0.02	0.04	0.07	0.04	0.01	−0.04	−0.07	0.06	−0.02	−0.05	0.04	0.04	−0.02	0.00	0.00	0.01	0.00	−0.03	0.01	0.01

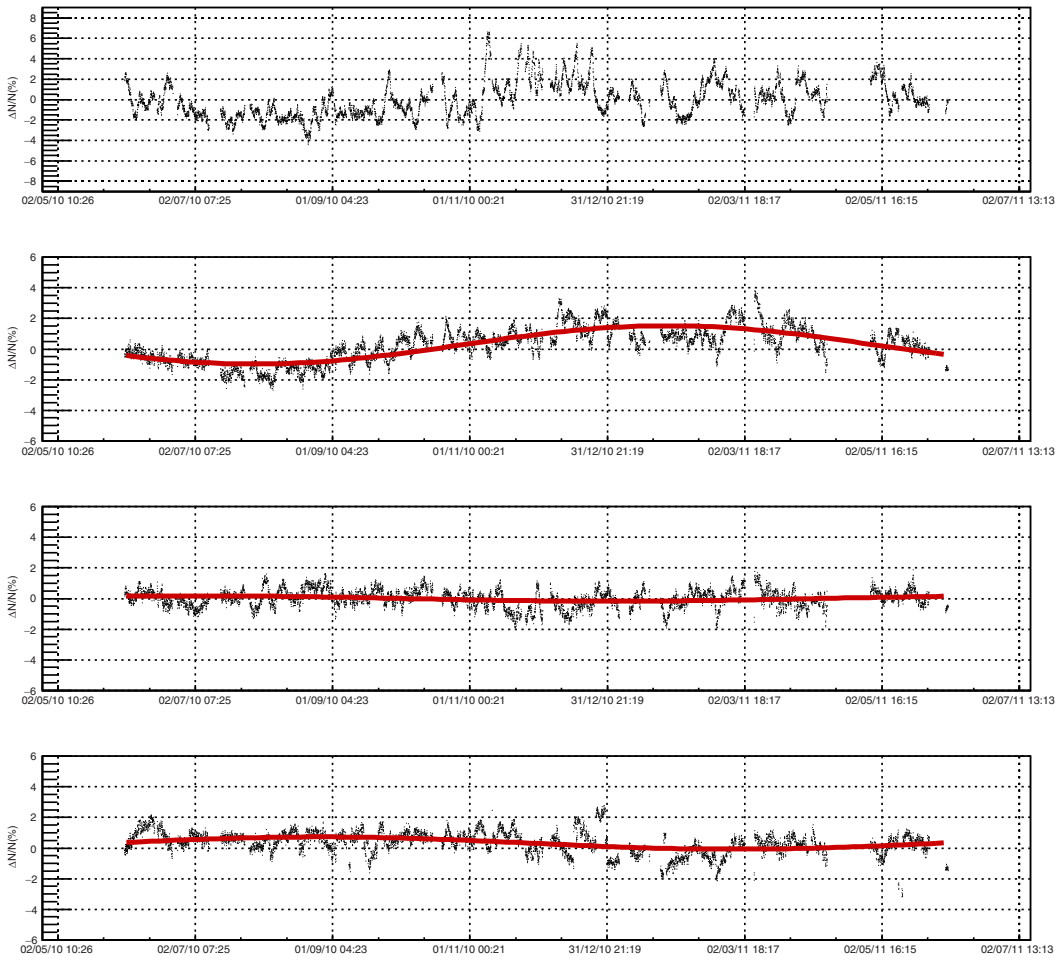

Fig. 10. Raw (upper panel), pressure corrected (middle panel), pressure+temperature corrected with PCA method (3rd panel from the top) and pressure+temperature corrected with integral method (lower panel) normalized muon count rate for GLL. The sine function with one year period is fitted to the data.

the temperature effect. The performance of the temperature correction may be tested by comparing the amplitude of the annual variation before and after correction. With presented method the amplitude of the annual variation is reduced by 86% (54.9%) in the case of GLL (UL) with respect to the pressure only corrected time series.

To further test the new method, the atmospheric correction of GLL data are performed by the integral method. The correction resulted in 56.25% of variance reduction and 68.1% of reduction of the amplitude of the annual wave. At least in the case of our CR data set the new method performs somewhat better than the integral method.

3. Conclusion

The principal component analysis is successfully used to construct a new empirical method for the atmospheric corrections of CR muon data. The method is equally applicable to all muon detectors, irrespective to location: ground level, shallow or deep underground. It requires knowledge of the atmospheric pressure and temperatures along the entire atmosphere, which is nowadays available in databases such as GFS. The method is suitable for the near real-time correction, with the delay defined by the availability of the atmospheric data (one day in the case of present GFS data). When applied to Belgrade muon data from two detectors

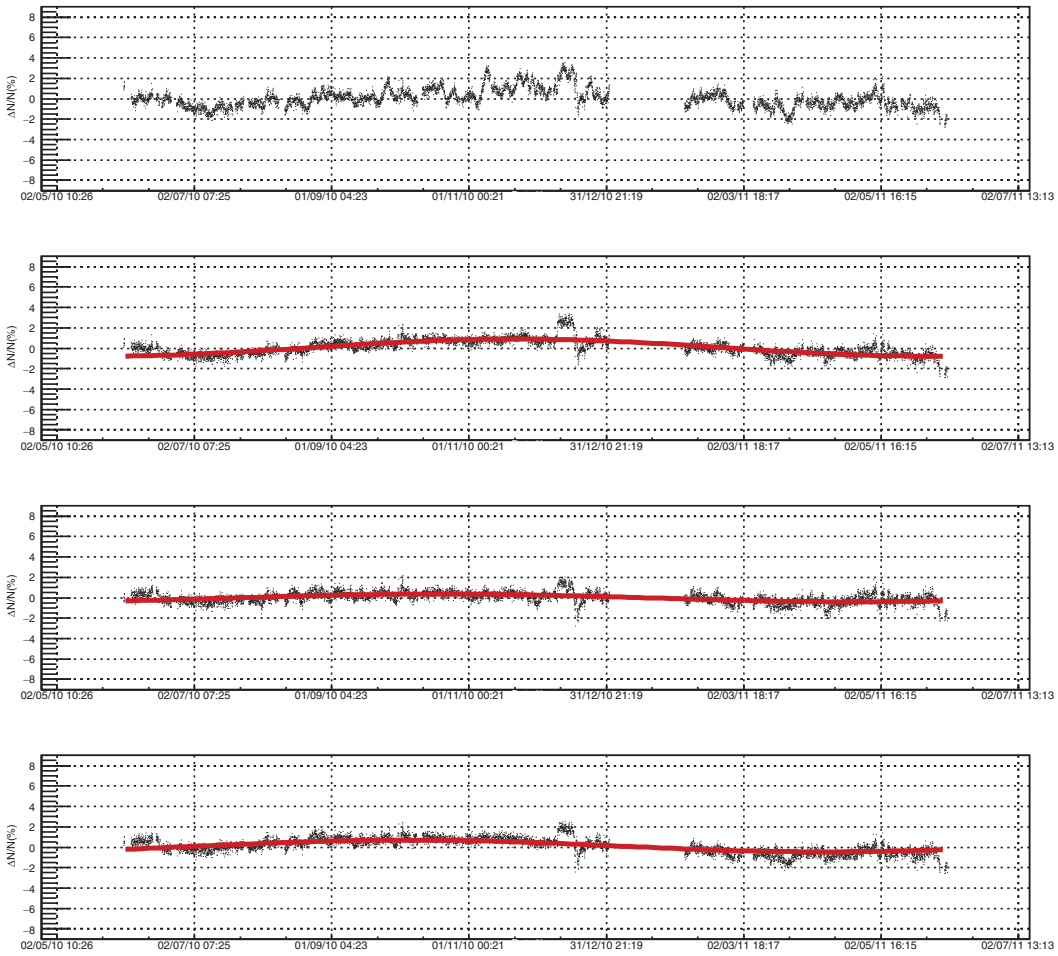

Fig. 11. Raw (upper panel), pressure corrected (middle panel), pressure+temperature corrected with PCA method (3rd panel from the top) and pressure+temperature corrected with integral method (lower panel) normalized muon count rate for UL. The sine function with one year period is fitted to the data.

(ground level and at 25 mwe), the method requires correction to five parameters, determined from linear regression. With the same CR dataset, the present method yields results superior to the integral method in terms of variance reduction and reduction of the annual variation. The new method is also suitable for temperature corrections of the neutron monitor data, which is seldom done in practice.

Acknowledgments

The authors are deeply grateful to Dr. Viktor Yanke for the encouragement and useful advice. The present work was funded by the Ministry of Education, Science and Technological Development of the Republic of Serbia, under the Project no. 171002.

References

[1] L. Myssowsky, L. Tuwim, Unregelmäßige intensitätsschwankungen der höhenstrahlung in geringer seehöhe, Zeitsch. Phys. 39 (2–3) (1926) 146–150.
[2] E. Steinke, Über schwankungen und barometereffekt der kosmischen ultrastrahlung im meeresniveau, Zeitsch. Phys. 64 (1–2) (1930) 48–63.
[3] P.M. Blackett, On the instability of the barytron and the temperature effect of cosmic rays, Phys. Rev. 54 (11) (1938) 973.
[4] M. Forro, Temperature effect of cosmic radiation at 1000-m water equivalent depth, Phys. Rev. 72 (9) (1947) 868.
[5] C.M.G. Lattes, G.P. Occhialini, C.F. Powell, Observations on the tracks of slow mesons in photographic emulsions, Nature 160 (4067) (1947) 486.
[6] C.M.G. Lattes, H. Muirhead, G.P. Occhialini, C.F. Powell, Processes involving charged mesons, Nature 159 (4047) (1947) 694.
[7] G. Occhialini, C. Powell, Nuclear disintegrations produced by slow charged particles of small mass, Nature 159 (4032) (1947) 186.
[8] A. Duperier, The meson intensity at the surface of the earth and the temperature at the production level, Proc. Phys. Soc. Lond. Sect. A 62 (11) (1949) 684.
[9] A. Duperier, Temperature of the upper atmosphere and meson production, Nature 167 (4243) (1951) 312.

[10] C. Baker, D. Hall, J. Humble, M. Duldig, Atmospheric correction analysis for the Mawson muon telescopes, in: International Cosmic Ray Conference, 3, 1993, p. 753.
[11] A. Maghrabi, M. Almutayri, Atmospheric effect on cosmic ray muons at high cut-off rigidity station, Adv. Astron. 2016 (2016).
[12] C.R. Braga, A. Dal Lago, T. Kuwabara, N.J. Schuch, K. Munakata, Temperature effect correction for the cosmic ray muon data observed at the Brazilian Southern Space Observatory in São Martinho da Serra, J. Phys. 409 (2013) 012138 IOP Publishing..
[13] G.C. Castagnoli, M. Dodero, Temperature effect of the muon component underground and pion attenuation length, Il Nuovo Cimento B (1965–1970) 51 (2) (1967) 525–534.
[14] A. Fenton, R. Jacklyn, R. Taylor, Cosmic ray observations at 42 m we underground at hobart, tasmania, Il Nuovo Cimento (1955–1965) 22 (2) (1961) 285–295.
[15] M. Zazyan, M. Ganeva, M. Berkova, V. Yanke, R. Hippler, Atmospheric effect corrections of mustang data, J. Space Weather Space Clim. 5 (2015) A6.
[16] L. Dorman, The temperature effect of the hard component of cosmic rays, Doklady Akad. Nauk SSSR 95 (1954).
[17] E. Feinberg, On the nature of cosmic ray barometric and temperature effects, DAN SSSR 53 (5) (1946) 421–424.
[18] L.I. Dorman, Cosmic ray variations, Technical Report, Foreign Technology Div Wright-Patterson AFB OHIO, 1957.
[19] K. Maeda, M. Wada, Atmospheric temperature effect upon the cosmic-ray intensity at sea level, J. Sci. Res. Inst. 48 (1954).
[20] V. Dvornikov, Y.Y. Krest'yannikov, A. Sergeev, Determination of the variation of average-mass temperature of the atmosphere by data of cosmic ray intensity, Geomag. Aeron. 16 (1976) 923–925.
[21] V. Yanchukovsky, G.Y. Filimonov, R. Hisamov, Atmospheric variations in muon intensity for different zenith angles, Bull. Russ. Acad. Sci. 71 (7) (2007) 1038–1040.
[22] R. De Mendonça, C. Braga, E. Echer, A. Dal Lago, K. Munakata, T. Kuwabara, M. Kozai, C. Kato, M. Rockenbach, N. Schuch, et al., The temperature effect in secondary cosmic rays (muons) observed at the ground: analysis of the Global MUON Detector Network data, Astrophys. J. 830 (2) (2016) 88.
[23] A. Dmitrieva, I. Astapov, A. Kovylyaeva, D. Pankova, Temperature effect correction for muon flux at the earth surface: estimation of the accuracy of different methods, J. Phys. 409 (2013) 012130. IOP Publishing.
[24] P.H. Barrett, L.M. Bollinger, G. Cocconi, Y. Eisenberg, K. Greisen, Interpretation of cosmic-ray measurements far underground, Rev. Mod. Phys. 24 (3) (1952) 133.
[25] S. Tilav, P. Desiati, T. Kuwabara, D. Rocco, F. Rothmaier, M. Simmons, H. Wissing, et al., Atmospheric variations as observed by IceCube, arXiv:1001.0776 (2010).
[26] P. Adamson, C. Andreopoulos, K. Arms, R. Armstrong, D. Auty, D. Ayres, C. Backhouse, J. Barnett, G. Barr, W. Barrett, et al., Observation of muon intensity variations by season with the Minos far detector, Phys. Rev. D 81 (1) (2010) 012001.
[27] H. Carmichael, M. Bercovitch, J.F. Steljes, Introduction of meteorological corrections into meson monitor data, Tellus 19 (1) (1967) 143–160, doi:10.1111/j.2153-3490.1967.tb01468.x.
[28] M.D. Berkova, A.V. Belov, E.A. Eroshenko, V.G. Yanke, Temperature effect of the muon component and practical questions for considering it in real time, Bull. Russ. Acad. Sci. 75 (6) (2011) 820–824, doi:10.3103/S1062873811060086.
[29] A. Dmitrieva, R. Kokoulin, A. Petrukhin, D. Timashkov, Corrections for temperature effect for ground-based muon hodoscopes, Astropart. Phys. 34 (6) (2011) 401–411, doi:10.1016/j.astropartphys.2010.10.013.
[30] Global forecast system (GFS), https://www.ncdc.noaa.gov/data-access/modeldata/model-datasets/global-forcast-system-gfs.
[31] National centers for environmental prediction (NCEP), http://www.ncep.noaa.gov/.
[32] A. Dragić, V. Udovičić, R. Banjanac, D. Joković, D. Maletić, N. Veselinović, M. Savić, J. Puzović, I.V. Aničin, The new setup in the Belgrade low-level and cosmic-ray laboratory, Nucl. Technol. Radiat. Protect. 26 (3) (2011) 181–192.
[33] B. Haurwitz, The diurnal surface-pressure oscillation, Arch. Meteorol. Geophys. Bioklimatol. Ser. A 14 (4) (1965) 361–379, doi:10.1007/BF02253483.
[34] L.I. Dorman, Cosmic Rays in the Earth's Atmosphere and Underground, Springer Netherlands, 2004, doi:10.1007/978-1-4020-2113-8.
[35] I. Jolliffe, Principal Component Analysis, Springer-Verlag, 2002, doi:10.1007/b98835.
[36] R.W. Preisendorfer, D.M. Curtis, Principal component analysis in meteorology and oceanography, Elsevier, Amsterdam, 1988.
[37] M. Savić, D. Maletić, D. Joković, N. Veselinović, R. Banjanac, V. Udovičić, A. Dragić, Pressure and temperature effect corrections of atmospheric muon data in the belgrade cosmic-ray station, J. Phys. Conf. Ser. 632 (1) (2015) 012059.

Nuclear Inst. and Methods in Physics Research, A 875 (2017) 10–15

Contents lists available at ScienceDirect

Nuclear Inst. and Methods in Physics Research, A

journal homepage: www.elsevier.com/locate/nima

An underground laboratory as a facility for studies of cosmic-ray solar modulation

N. Veselinović, A. Dragić *, M. Savić, D. Maletić, D. Joković, R. Banjanac, V. Udovičić

Institute of Physics, University of Belgrade, Pregrevica 118, 11080 Zemun, Serbia

ARTICLE INFO

Keywords:
Cosmic ray muons
Forbush decrease
Response function

ABSTRACT

The possibility of utilizing a shallow underground laboratory for the study of energy dependent solar modulation process is investigated. The laboratory is equipped with muon detectors at ground level and underground (25mwe), and with an underground asymmetric muon telescope to have a single site detection system sensitive to different median energies of primary cosmic-ray particles. The detector response functions to galactic cosmic rays are determined from Monte Carlo simulation of muon generation and propagation through the atmosphere and soil, based on CORSIKA and GEANT4 simulation packages. The present setup is suitable for studies of energy dependence of Forbush decreases and other transient or quasi-periodic cosmic-ray variations.

1. Introduction

Galactic cosmic rays (GCR) arriving at Earth after propagating through the heliosphere interact with nuclei in the atmosphere. These interactions of primary CRs lead to production of a cascade (shower) of secondary particles: hadrons, electrons, photons, muons, neutrinos. Ground based CR detectors are designed to detect some species of secondary cosmic radiation. Widely in use are neutron monitors [1,2], muon telescopes [3,4], various types of air shower arrays [5], γ-ray air Cherenkov detectors [6], air fluorescence detectors [7] etc.

The flux and energy spectra of GCR are modulated by the solar magnetic field, convected by the solar wind. Particularly affected are GCR at the low energy side of the spectrum (up to ~100 GeV). Therefore, secondary CRs generated in the atmosphere can be used for studying solar and heliospheric processes. Among the best known effects of the solar modulation are CR flux variations with 11 year period of the solar cycle, 22 year magnetic cycle, diurnal variation and Forbush decrease. The so called corotation with the solar magnetic field results in the flux variation with the 27-day period of solar rotation.

Modulation effects have been studied extensively by neutron monitors (NM) [8,9], sensitive up to several tens of GeV, depending on their geomagnetic location and atmospheric depth. Muon detectors at ground level are sensitive to primary particles of higher energies than NMs. Underground muon detectors correspond to even higher energy primaries. For this reason muon observations complement NM observations in studies of long-term CR variations, CR anisotropy and gradients or rigidity spectrum of Forbush decreases. However, muon observations suffer from difficulties to disentangle variations of atmospheric origin. While the effect of atmospheric pressure is similar to NMs and easy to account for, the temperature effect is more complicated. The entire temperature profile of the atmosphere is contributing, with different net temperature effect on muon flux at different atmospheric layers, as a result of interplay of positive and negative temperature effects. The positive temperature effect is a consequence of reduced atmospheric density with the temperature increase, resulting in less pion interactions and more decays into muons [10]. The negative temperature effect comes from the increased altitude of muon production at the periods of high temperature, with the longer muon path length and the higher decay probability before reaching the ground level [11]. Both effects are accounted for by the integral method of Dorman [12]. The negative temperature effect is dominant for low energy muons (detected at ground level) and the positive for high energy muons (detected deep underground). At shallow depth of several tens of meters of water equivalent both temperature effects contribute to the overall temperature effect. Several detector systems with different sensitivity to primaries at the same location have the advantage of sharing common atmospheric and geomagnetic conditions.

Belgrade CR station is equipped with muon detectors at ground level and at the depth of 25 m.w.e. Underground laboratory is reached only by muons exceeding energy threshold of 12 GeV. The existing detectors are recently amended by additional setup in an attempt to fully exploit laboratory's possibilities to study solar modulation at different

* Corresponding author.
E-mail address: dragic@ipb.ac.rs (A. Dragić).

http://dx.doi.org/10.1016/j.nima.2017.09.008
Received 31 May 2017; Received in revised form 30 August 2017; Accepted 3 September 2017
Available online 7 September 2017
0168-9002/

median rigidities. In the present paper the detector systems at the Belgrade CR station are described. Response functions of muon detectors to galactic cosmic rays are calculated. The detector system represents useful extension of modulation studies with neutron monitors to higher energies, as it is demonstrated in the case of a recent Forbush event.

2. Description of Belgrade CR station

The Belgrade cosmic-ray station, situated at the Low Background Laboratory for Nuclear Physics at Institute of Physics, is located at near-sea level at the altitude of 78 m a.s.l. Its geographic position is: latitude 44°51′N and longitude 20°23′E, with vertical cut-off rigidity 5.3 GV. It consists of the ground level lab (GLL) and the underground lab (UL) which has useful area of 45 m^2, dug at a depth of 12 m. The soil overburden consists of loess with an average density 2.0 ± 0.1 g/cm^3. Together with the 30 cm layer of reinforced concrete the laboratory depth is equivalent to 25 m.w.e. At this depth, practically only the muonic component of the atmospheric shower is present [13].

2.1. Old setup

The experimental setup [14] consists of two identical sets of detectors and read out electronics, one situated in the GLL and the other in the UL. Each setup utilizes a plastic scintillation detector with dimensions 100 cm × 100 cm × 5 cm equipped with 4 PMTs optically attached to beveled corners of a detector. Preamplifier output of two diagonally opposing PMTs are summed and fed to a digitizer input (CAEN FADC, type N1728B). FADC operates at 100 MHz frequency with 14 bit resolution. The events generating enough scintillation light to produce simultaneous signals in both inputs exceeding the given threshold are identified as muon events. The simulated total energy deposit spectrum is presented on the left panel of Fig. 1. After the appropriate threshold conditions are imposed on the signals from two diagonals, the spectrum is reduced to the one represented on the right panel of the same figure. Contribution from different CR components are indicated on both graphs and experimentally recorded spectrum is plotted as well.

Particle identification is verified by a two-step Monte Carlo simulation. In the first step development of CR showers in the atmosphere is traced, starting from the primary particles at the top of the atmosphere by CORSIKA simulation package. CORSIKA output contains information on generated particles (muons, electrons, photons, etc.) and their momenta at given observation level. More details on CORSIKA simulation will be given in Section 3. This output serves as an input for the second step in simulation, based on GEANT4. In the later step energy deposit by CR particles in the plastic scintillator detector are determined, together with the light collection at PMTs. Contributions from different CR components to recorded spectrum are also shown in Fig. 1.

According to the simulation, 87.5% of events in the coincident spectrum originate from muons. To account for the contribution from other particles to the experimental spectrum not all the events in the spectrum are counted when muon time series are constructed. Muon events are defined by setting the threshold corresponding to muon fraction of recorded spectrum. Threshold is set in terms of "constant fraction" of the spectrum maximum, which also reduces count rate fluctuations due to inevitable shifts of the spectrum during long-term measurements.

2.2. Upgrade of the detector system

Existing detectors enable monitoring of CR variations at two different median energies. An update is contemplated that would provide more differentiated response. Two ideas are considered. First one was to extend the sensitivity to higher energies with detection of multi-muon events underground. An array of horizontally oriented muon detectors ought to be placed in the UL. Simultaneous triggering of more than one detector is an indication of a multi-muon event. The idea was exploited in the EMMA underground array [15], located at the deeper underground laboratory in Pyhasalmi mine, Finland, with the intention to reach energies in the so called knee region. For a shallow underground laboratory, exceeding the energy region of solar modulation would open the possibility to study CR flux variations originating outside the heliosphere. Second idea is an asymmetric muon telescope separating muons with respect to zenith angle. Later idea is much less expensive to be put into practice.

Both ideas will be explained in detail and response function to GCR for existing and contemplated detectors calculated in the next section.

3. Calculation of response functions

Nature of variations of primary cosmic radiation can be deduced from the record of ground based cosmic ray detectors provided relation between the spectra of primary and secondary particles at surface level are known with sufficient accuracy. Relation can be expressed in terms of rigidity or kinetic energy.

Total detector count rate can be expressed as:

$$N(E_{th}, h, t) = \sum_i \int_{E_{th}}^{\infty} Y_i(E, h) \cdot J_i(E, t) dE \tag{1}$$

where E is primary particle energy, i is type of primary particle (we take into account protons and α particles), $J_i(E, t)$ is energy spectrum of primary particles, h is atmospheric depth and $Y_i(E, h)$ is the so called yield function. E_{th} is the threshold energy of primary particles. It depends on location (geomagnetic latitude and atmospheric altitude) and detector construction details. At a given location on Earth, only particles with rigidity above vertical rigidity cut-off contribute to the count rate. Also, detector construction often prevents detection of low energy particles. For instance, muon detectors are sometimes covered with a layer of lead. In present configuration our detectors are lead free.

Historically, yield functions were calculated empirically, often exploiting the latitude variations of neutron and muonic CR component [16–18]. With the advancement of computing power and modern transport simulation codes it became possible to calculate yield functions from the interaction processes in the atmosphere [19,20]. The yield function for muons is calculated as:

$$Y_i(E, h) = \int_{E_{th}}^{\infty} \int S_i(\theta, \phi) \cdot \boldsymbol{\Phi}_{i,\mu}(E_i, h, E, \theta, \phi) dE d\Omega \tag{2}$$

where $S(\theta, \phi)$ is the effective detector area and integration is performed over upper hemisphere. $\boldsymbol{\Phi}_{i,\mu}(E_i, h, E, \theta, \phi)$ is the differential muon flux per primary particle of the type i with the energy E_i.

Total differential response function:

$$W(E, h, t) = \sum_i Y_i(E, h) \cdot J_i(E, t) \tag{3}$$

when normalized to the total count rate gives the fraction of count rate originating from the primary particles with the energy in the infinitesimal interval around E. Integration of differential response function gives the cumulative response function.

The response functions of our CR detectors are calculated using Monte Carlo simulation of CR transport through the atmosphere with CORSIKA simulation package. Simulation was performed with protons and α-particles as primary particles. They make ~94% (79% + 14.7%) of all primaries [21]. Implemented hadron interaction models were FLUKA for energies below 80 GeV, and QGSJET II-04 for higher energies. If the old version of QGSJET is used, a small discontinuity in response function is noticed at the boundary energy between two models. Geomagnetic field corresponds to the location of Belgrade $B_x = 22.61$ μT, $B_z = 42.27$ μT. Power law form of differential energy spectrum of galactic cosmic rays $J_p(E) \sim E^{-2.7}$ is assumed. Energy range of primary particles is between 1 GeV and $2 \cdot 10^7$ GeV. Interval of zenith angles is $0° < \theta < 70°$. Low energy thresholds for secondary particles are: 150 MeV for hadrons and muons and 15 MeV for electrons

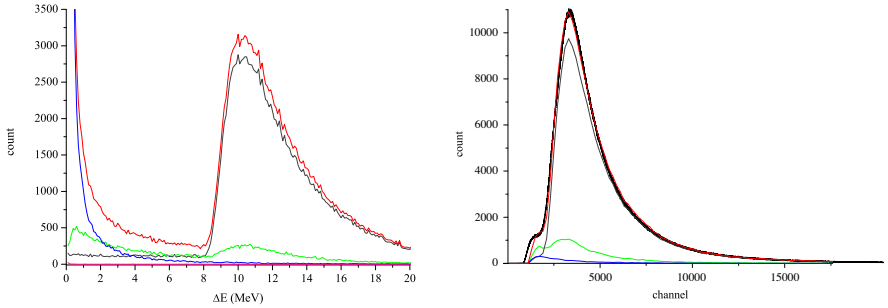

Fig. 1. Left — ΔE spectrum in the plastic scintillator detector, derived from GEANT simulation; right — the same, but for the events exceeding threshold on both diagonals. Contribution of different CR components to the total energy deposit in the detector: muons-gray line, photons-blue line, electrons-green line and sum of all contributions — red line. The black curve on the right panel is the experimental spectrum. (For interpretation of the references to color in this figure legend, the reader is referred to the web version of this article.)

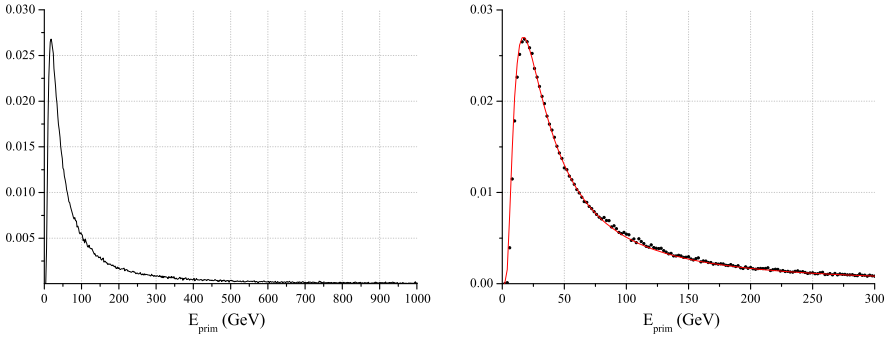

Fig. 2. Left: normalized total response function of ground level muon detector to galactic cosmic rays; right: same as left, fitted with Dorman function (red line). (For interpretation of the references to color in this figure legend, the reader is referred to the web version of this article.)

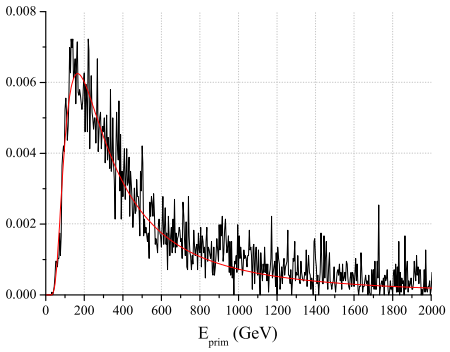

Fig. 3. Response function for multi-muon events in UL to galactic cosmic rays.

and photons. Selected atmospheric model is AT511 (Central European atmosphere for May 11 1993). Observational level is at 78m a.s.l.

For calculation of response functions for underground detectors, simulation of particle propagation through the soil overburden is performed using the code based on GEANT4 package. For precise calculation of energy loss, chemical composition of the soil needs to be known. The composition used in our work is taken from a geochemical study of neighboring loess sections of Batajnica and Stari Slankamen [22]. Most abundant constituents are quartz (SiO_2) 70%, alumina (Al_2O_3) 15% and quicklime (CaO) 10%, while others include Fe_2O_3, MgO, TiO_2, K_2O,... Inaccuracy of our knowledge of the soil chemical composition should not strongly affect our results since, at relevant energies, dominant energy loss mechanism for muons is ionization which, according to Bethe–Bloch formula depends mostly on $\langle Z\rangle/\langle A\rangle$. Soil density profile is probed during laboratory construction. It varies slowly with depth and average density is found to be (2.0 ± 0.1) g/cm^3.

In the simulation, the effective area and angular acceptance of different modes of asymmetric muon telescope (single, coincident and anticoincident) are taken into account.

According to Dorman [12], response function can be parametrized as:

$$W(E) = \begin{cases} 0, & \text{if } E < E_{th}; \\ \dfrac{a \cdot k \cdot \exp(-aE^{-k})}{E^{(k+1)}(1 - aE_{th}^{-k})}, & \text{otherwise;} \end{cases} \tag{4}$$

with the high energy asymptotics: $W(E) \approx a \cdot k \cdot E^{-(k+1)}$.

3.1. Ground level

Calculated response function for ground level muon detector is presented on Fig. 2, together with fitted Dorman function (4).

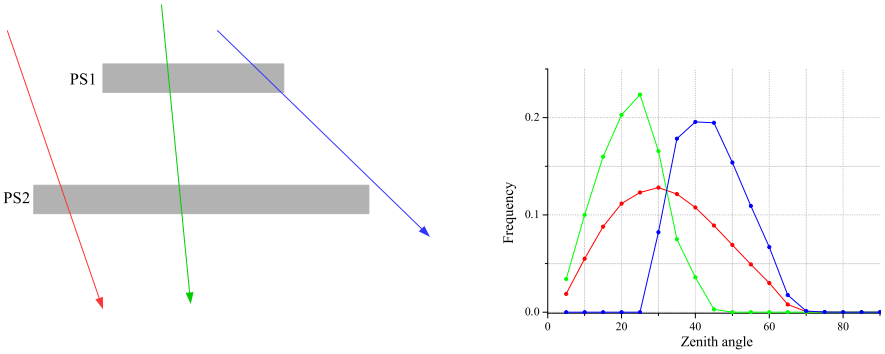

Fig. 4. Left: Schematic view of the asymmetric muon telescope; PS1 — plastic scintillator detector 1, PS2 — plastic scintillator detector 2. Right: angular distribution of detected muons in single mode (red), coincident mode (green) and anticoincident mode (blue), normalized to number of counts in each mode. (For interpretation of the references to color in this figure legend, the reader is referred to the web version of this article.)

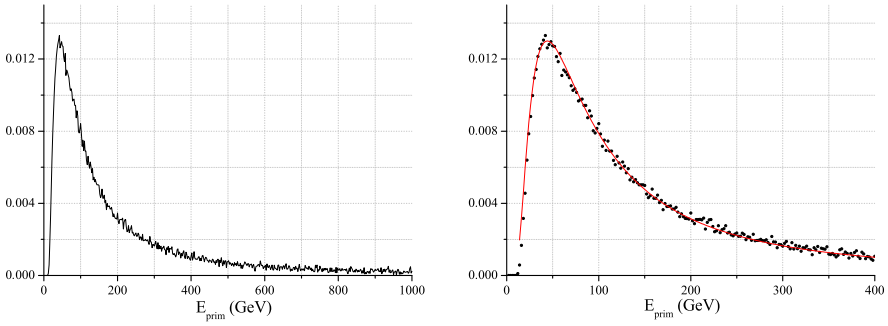

Fig. 5. Response function of single mode of ASYMUT in the UL to galactic cosmic rays. On the right panel the energy interval of interest is enlarged and Dorman function fit is plotted (red line). (For interpretation of the references to color in this figure legend, the reader is referred to the web version of this article.)

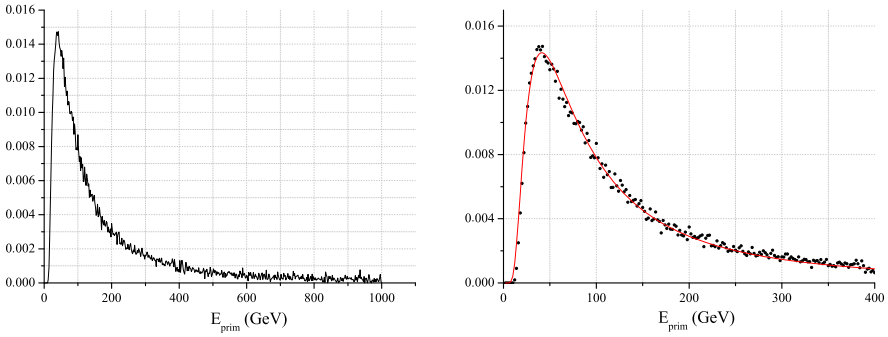

Fig. 6. Response function of coincident mode of asymmetric muon telescope in the UL to galactic cosmic rays. On the right panel the interesting energy interval is enlarged and Dorman function fit is plotted (red line). (For interpretation of the references to color in this figure legend, the reader is referred to the web version of this article.)

3.2. Underground

3.2.1. Multi-muon events

Count rate of multi-muon events underground turned out to be too low for the above mentioned array detector experiment to be feasible in our laboratory. To collect enough events for construction of the response function (Fig. 3), allowed muon separation is 200 m, fairly exceeding laboratory dimensions. Under these conditions calculated median energy is 270 GeV.

*3.2.2. **ASY**mmetric **MU**on **T**elescope (ASYMUT)*

Asymmetric muon telescope is an inexpensive detector, constructed from components already available in the laboratory. It consists of two plastic scintillators of unequal dimensions. The lower is identical to the

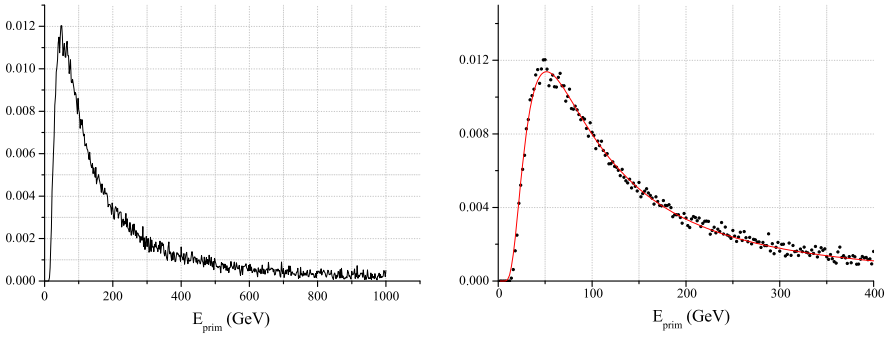

Fig. 7. Response function of anticoincident mode of asymmetric muon telescope in the UL to galactic cosmic rays. On the right panel the interesting energy interval is enlarged and Dorman function fit is plotted (red line). (For interpretation of the references to color in this figure legend, the reader is referred to the web version of this article.)

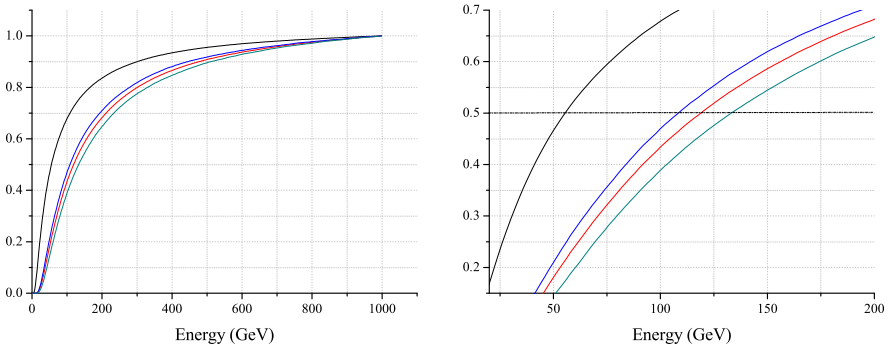

Fig. 8. Cumulative response function to galactic cosmic rays of different muon detectors in the Belgrade CR station: black curve — GLL; red curve — single UL; green curve — CC mode and blue curve — ANTI CC mode of asymmetric muon telescope. The 0.5 level corresponds to median energy. Cumulative response function with enlarged region around this level is shown in the right picture. (For interpretation of the references to color in this figure legend, the reader is referred to the web version of this article.)

one located in the GLL (100 ×100 ×5 cm) and upper one is 50 ×46 ×5 cm. Detectors are separated vertically by 78 cm, as depicted in Fig. 4, to have roughly the same count rate in the coincident and anticoincident mode. Lower detector in single mode operates in the same manner as the one in the GLL, with wide angular acceptance. The coincident mode is composed of the events registered in both upper and lower detector. In the anticoincident mode, muons passing through the upper but not the lower detector are counted. Therefore, the later mode favors inclined muon paths. Different angular distribution means different path length of muons registered in three modes of ASYMUT (right part of Fig. 4) and also different energy distribution of parental primary particles.

The response functions to GCR of three modes of ASYMUT are shown on Figs. 5–7 and respective cumulative response functions are shown on Fig. 8.

Important parameters describing shapes of response functions are summarized in Table 1. The most often used characteristics of a detector system is its median energy E_{med}. Primary particles with the energy below E_{med} give 50% contribution to detector count rate. The energy interval (($E_{0.05}$, $E_{0.95}$) is responsible for 90% of registered events. Fitted value of the parameter k from Dorman function (Eq. (4)) is also presented. The parameters $E_{0.05}$ and E_{med} are determined with 1 GeV accuracy, while the uncertainty of $E_{0.95}$ is much higher due to small number of very high energy events and is conservatively estimated as 10%.

Table 1
Sensitivity of Belgrade CR detectors (GLL — ground level; UL — underground based ASYMUT single mode; CC — ASYMUT coincident mode; ANTI — ASYMUT anticoincident mode) to GCR primary particles. Primaries with the energy below $E_{0.05}$ (and above $E_{0.95}$) contribute with 5% to the count rate of a corresponding detector. E_{med} is median energy, E_{th} threshold energy and k is Dorman parameter.

det	E_{th} (GeV)	$E_{0.05}$ (GeV)	E_{med} (GeV)	$E_{0.95}$ (GeV)	k
GLL	5	11	59	915	0.894(1)
UL	12	31	137	1811	0.971(4)
CC	12	27	121	1585	1.015(3)
ANTI	14	35	157	2031	0.992(4)

3.3. Conclusions

Usefulness of our setup for solar modulation studies is tested on the example of investigation of a Forbush decrease of 8 March 2012. In the first half of March 2012 several M and X class solar flares erupted from the active region 1429 on the Sun. The strongest were two X class flares that bursted on March 7. The first one is the X5.4 class flare (peaked at 00:24 UT) and the second one is the X1.3 class flare (peaked at 01:14 UT). The two flares were accompanied by two fast CMEs, one of which was Earth-directed [23]. Several magnetic storms were also registered on Earth, and a series of Forbush decreases is registered. The most pronounced one was registered on March 8. Characteristics of this event as recorded by various neutron monitors and our detectors are compared.

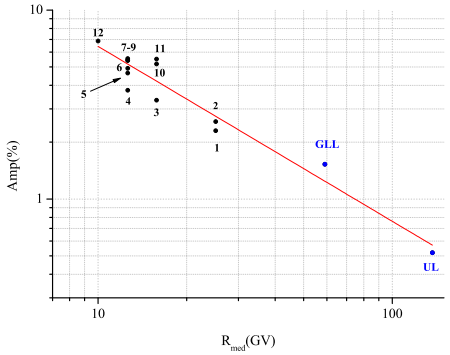

Fig. 9. Rigidity spectrum of FD from 12 March 2012. Black points represent the amplitude of the event as seen by twelve NMs: 1 — Athens, 2 — Mexico City; 3 — Almaty, 4 — Lomnicky stit; 5 — Moscow; 6 — Kiel; 7 — Yakutsk; 8 — Apatity; 9 — Inuvik; 10 — McMurdo; 11 — Thul; 12 — South Pole. Blue points are from Belgrade CR station: GLL — ground level and UL — underground. (For interpretation of the references to color in this figure legend, the reader is referred to the web version of this article.)

Amplitude of a Forbush decrease is one of its main characteristics. Dependence of FD amplitude on median rigidity (or energy) is expected to follow the power law: $\Delta N/N \sim R^{-\gamma}$ [12].

For investigation of rigidity spectrum of mentioned FD data from 12 NMs are combined with the data from our two detectors (GLL and UL) that were operational at the time of the event. Neutron monitor data in the period between 1 March 2012 and 1 April 2012 are taken from the NMDB database (www.nmdb.eu) [24]. The exponent of the rigidity spectrum of this FD γ is obtained by the least-square fitting of the data with the power function (Fig. 9) and found to be $\gamma = 0.92 \pm 0.18$. Presented analysis illustrates applicability of our setup for studies of consequences of CR solar modulation process in the energy region exceeding sensitivity of neutron monitors.

Acknowledgments

We are very grateful to late Prof. Ivan Aničin for his enthusiastic contributions, deep insights and valuable advice not just regarding work presented in this paper but also for being a real spiritus agens of our lab. We acknowledge the NMDB database (www.nmdb.eu), founded under the European Union's FP7 programme (contract no. 213007) for providing NM data. The present work was funded by the Ministry of Education, Science and Technological Development of the Republic of Serbia, under the Project No. 171002.

References

[1] J.A. Simpson, The cosmic ray nucleonic component: The invention and scientific uses of the neutron monitor, Cosmic Rays Earth (2000) 11–32.
[2] J.W. Bieber, Neutron monitoring: Past, present, future, in: Jonathan F.O. (Ed.) AIP Conference Proceedings, vol. 1516, No. 1, 2013.
[3] M.L. Duldig, Muon observations, in: Cosmic Rays and Earth, Springer, Netherlands, 2000, pp. 207–226.
[4] S. Cecchini, M. Spurio, Atmospheric muons: experimental aspects, Geosci. Instrum. Methods Data Syst. Discuss. 2 (2012) 603–641.
[5] K.-H. Kampert, A.A. Watson, Extensive air showers and ultra high-energy cosmic rays: a historical review, Eur. Phys. J. H 37 (3) (2012) 359–412.
[6] A. de Angelis, O. Mansutti, M. Persic, Very-high energy gamma astrophysics, Riv. Nuovo Cimento 31 (4) (2008) 187–246. http://dx.doi.org/10.1393/ncr/i2008-10032-2.
[7] F. Arqueros, J.R. Hörandel, B. Keilhauer, Air fluorescence relevant for cosmic-ray detection — review of pioneering measurements, Nucl. Instrum. Methods A 597 (2008) 23–31. http://dx.doi.org/10.1016/j.nima.2008.08.055.
[8] J.A. Lockwood, W.R. Webber, The 11 year solar modulation of cosmic rays as deduced from neutron monitor variations and direct measurements at low energies, J. Geophys. Res. 72 (23) (1967) 5977–5989.
[9] I.G. Usoskin, G.A. Bazilevskaya, G.A. Kovaltsov, Solar modulation parameter for cosmic rays since 1936 reconstructed from ground-based neutron monitors and ionization chambers, J. Geophys. Res. 116 (2011) A02104. http://dx.doi.org/10.1029/2010JA016105.
[10] A. Duperier, The meson intensity at the surface of the earth and the temperature at the production level, Proc. Phys. Soc. A 62 (11) (1949) 684.
[11] P.M. Blackett, On the instability of the barytron and the temperature effect of cosmic rays, Phys. Rev. 54 (11) (1938) 973.
[12] L. Dorman, Cosmic Rays in the Earth's Atmosphere and Underground, Springer Science + Business Media, LLC., New York, 2004.
[13] G. Hausser, Cosmic ray-induced background in ge-spectrometry, Nucl. Instrum. Methods B 83 (1–2) (1993) 223–228.
[14] A. Dragić, V. Udovičić, R. Banjanac, D. Joković, D. Maletić, N. Veselinović, M. Savić, J. Puzović, I.V. Aničin, The new setup in the Belgrade low-level and cosmic-ray laboratory, Nucl. Technol. Radiat. Prot. 26 (3) (2011) 181–192. http://dx.doi.org/10.2298/NTRP1101064N.
[15] T. Kalliokoski, L. Bezrukov, T. Enqvist, H. Fynbo, L. Inzhechik, P. Jones, J. Joutsenvaara, J. Karjalainen, P. Kuusiniemi, K. Loo, B. Lubsandorzhiev, V. Petkov, T. Rih, J. Sarkamo, M. Slupecki, W. Trzaska, A. Virkajrvi, Can EMMA solve the puzzle of the knee? Prog. Part. Nucl. Phys. 66 (2011) 468–472.
[16] W.H. Fonger, Cosmic radiation intensity-time variations and their origin. II. Energy dependence of 27-day variations, Phys. Rev. 91 (2) (1953) 351.
[17] E.E. Brown, Neutron yield functions for the nucleonic component of cosmic radiation, Il Nuovo Cimento (1955–1965) 6 (4) (1957) 956–962.
[18] L. Dorman, Cosmic Ray Variations, State Publishing House for Technical and Theoretical Literature, 1957.
[19] E.O. Fluckiger, et al., A parameterized neutron monitor yield function for space weather applications, in: Proceedings of the 30th International Cosmic Ray Conference, Mexico City, Mexico, vol. 1 (SH), 2008, pp. 289–292.
[20] M. Zazyan, A. Chilingarian, Calculations of the sensitivity of the particle detectors of ASEC and SEVAN networks to galactic and solar cosmic rays, Astropart. Phys. 32 (2009) 185–192.
[21] K. Nakamura, et al., 24. Cosmic rays, J. Phys. G 37 (2010) 075021.
[22] B. Buggle, B. Glaser, L. Zoller, U. Hambach, S. Markovic, I. Glaser, N. Gerasimenko, Geochemical characterization and origin of Southeastern and Eastern European loesses (Serbia, Romania, Ukraine), Quat. Sci. Rev. 27 (2008) 1058–1075.
[23] NASA Goddard Space Weather Research Center, Summary of the space weather event associated with the X5.4 and X1.3 flare on March 7.
[24] H. Mavromichalaki, et al., Applications and usage of the real-time Neutron Monitor Database, Adv. Space Res. 47 (12) (2011) 2210–2222.

NA61/SHINE facility at the CERN SPS: beams and detector system

2014 JINST 9 P06005

(http://iopscience.iop.org/1748-0221/9/06/P06005)

Jinst

PUBLISHED BY IOP PUBLISHING FOR SISSA MEDIALAB

RECEIVED: *January 23, 2014*
ACCEPTED: *April 14, 2014*
PUBLISHED: *June 5, 2014*

NA61/SHINE facility at the CERN SPS: beams and detector system

2014 JINST 9 P06005

The NA61/SHINE collaboration

N. Abgrall,[a] O. Andreeva,[b] A. Aduszkiewicz,[c] Y. Ali,[d] T. Anticic,[e] N. Antoniou,[f] B. Baatar,[g] F. Bay,[h] A. Blondel,[a] J. Blumer,[i] M. Bogomilov,[j] M. Bogusz,[k] A. Bravar,[a] J. Brzychczyk,[d] S.A. Bunyatov,[g] P. Christakoglou,[f] M. Cirkovic,[l] T. Czopowicz,[k] N. Davis,[f] S. Debieux,[a] H. Dembinski,[i] F. Diakonos,[f] S. Di Luise,[h] W. Dominik,[c] T. Drozhzhova,[m] J. Dumarchez,[n] K. Dynowski,[k] R. Engel,[i] I. Efthymiopoulos,[o] A. Ereditato,[p] A. Fabich,[o] G.A. Feofilov,[m] Z. Fodor,[q] A. Fulop,[q] M. Gaździcki,[r,s] M. Golubeva,[b] K. Grebieszkow,[k] A. Grzeszczuk,[t] F. Guber,[b] A. Haesler,[a] T. Hasegawa,[u] M. Hierholzer,[p] R. Idczak,[v] S. Igolkin,[m] A. Ivashkin,[b] D. Jokovic,[l] K. Kadija,[e] A. Kapoyannis,[f] E. Kaptur,[t] D. Kielczewska,[c] M. Kirejczyk,[c] J. Kisiel,[t] T. Kiss,[q] S. Kleinfelder,[w] T. Kobayashi,[u] V.I. Kolesnikov,[g] D. Kolev,[j] V.P. Kondratiev,[m] A. Korzenev,[a] P. Koversarski,[v] S. Kowalski,[t] A. Krasnoperov,[g] A. Kurepin,[b] D. Larsen,[d] A. Laszlo,[q] V.V. Lyubushkin,[g] M. Maćkowiak-Pawłowska,[r] Z. Majka,[d] B. Maksiak,[k] A.I. Malakhov,[g] D. Maletic,[l] D. Manglunki,[o] D. Manic,[l] A. Marchionni,[h] A. Marcinek,[d] V. Marin,[b] K. Marton,[q] H.-J. Mathes,[i] T. Matulewicz,[c] V. Matveev,[g,b] G.L. Melkumov,[g] M. Messina,[p] St. Mrówczyński,[s] S. Murphy,[a] T. Nakadaira,[u] M. Nirkko,[p] K. Nishikawa,[u] T. Palczewski,[x] G. Palla,[q] A.D. Panagiotou,[f] T. Paul,[i] W. Peryt,[k,1] O. Petukhov,[b] C. Pistillo,[p] R. Płaneta,[d,2] J. Pluta,[k] B.A. Popov,[g,n] M. Posiadala,[c] S. Puławski,[t] J. Puzovic,[l] W. Rauch,[y] M. Ravonel,[a] A. Redij,[p] R. Renfordt,[r] E. Richter-Wąs,[d] A. Robert,[n] D. Röhrich,[z] E. Rondio,[x] B. Rossi,[p] M. Roth,[i] A. Rubbia,[h] A. Rustamov,[r] M. Rybczyński,[s] A. Sadovsky,[b] K. Sakashita,[u] M. Savic,[l] K. Schmidt,[t] T. Sekiguchi,[u] P. Seyboth,[s] D. Sgalaberna,[h] M. Shibata,[u] R. Sipos,[q] E. Skrzypczak,[c] M. Słodkowski,[k] Z. Sosin,[d] P. Staszel,[d] G. Stefanek,[s]

[1]Deceased.
[2]Corresponding author.

doi:10.1088/1748-0221/9/06/P06005

J. Stepaniak,[x] **H. Stroebele,**[r] **T. Susa,**[e] **M. Szuba,**[i] **M. Tada,**[u] **V. Tereshchenko,**[g] **T. Tolyhi,**[q] **R. Tsenov,**[j] **L. Turko,**[v] **R. Ulrich,**[i] **M. Unger,**[i] **M. Vassiliou,**[f] **D. Veberic,**[i] **V.V. Vechernin,**[m] **G. Vesztergombi,**[q] **L. Vinogradov,**[m] **A. Wilczek,**[t] **Z. Włodarczyk,**[s] **A. Wojtaszek-Szwarz,**[s] **O. Wyszyński,**[d] **L. Zambelli**[n] **and W. Zipper**[t]

[a] *Departement de Physique Nucleaire et Corpusculaire, University of Geneva, 24 quai Ernest-Ansermet, CH-1211 Geneva 4, Switzerland*

[b] *Institute for Nuclear Research, 60-th October Anniversary prospect 7A, 117 312 Moscow, Russia*

[c] *Faculty of Physics, University of Warsaw, Hoża 69, PL-00-681 Warsaw, Poland*

[d] *Institute of Physics, Jagiellonian University, Reymonta 4, 30-059 Cracow, Poland*

[e] *Rudjer Boskovic Institute, Bijenička 54, HR-10000 Zagreb, Croatia*

[f] *Nuclear and Particle Physics Division, University of Athens, Panepistimiopolis, Ilisia GR 157 71 Athens, Greece*

[g] *Joint Institute for Nuclear Research, Joliot-Curie 6, 141980 Dubna, Moscow region, Russia*

[h] *Institut für Teilchenphysik (IPP), ETHZ Hoenggerberg, Swiss Federal Institute of Technology, Schafmattstr. 20, CH-8093 Zurich, Switzerland*

[i] *Karlsruhe Institute of Technology, Hermann-von-Helmholtz-Platz 1, D-76344 Karlsruhe, Germany*

[j] *Department of Atomic Physics, Faculty of Physics, Sofia University "St. Kliment Ohridski", 5 J. Bourchier Blvd, 1164 Sofia, Bulgaria*

[k] *Faculty of Physics, Warsaw University of Technology, Koszykowa 75, PL-00-662 Warsaw, Poland*

[l] *Faculty of Physics, University of Belgrade, Studentski trg 12-16, 11000 Belgrade, Serbia*

[m] *St. Petersburg State University, Ulyanovskaya str. 1, 198504 St. Petersburg, Russia*

[n] *LPNHE, Universites Paris VI and VII, Case 200, 4 Place Jussieu, 75005 Paris, France*

[o] *European Organization for Nuclear Research (CERN), CH-1211 Geneva 23, Switzerland*

[p] *Albert Einstein Center for Fundamental Physics, Laboratory for High Energy Physics, University of Bern, Sidlerstrasse 5, CH-3012 Bern, Switzerland*

[q] *Department of High Energy Physics, Wigner Research Centre for Physics of the Hungarian Academy of Sciences, Konkoly-Thege M. u. 29-33, 1121 Budapest, Hungary*

[r] *Institut für Kernphysik, Goethe-Universität, Max-von-Laue-Straße 1, D-60438 Frankfurt am Main, Germany*

[s] *Institute of Physics, Jan Kochanowski University, Swietokrzyska 15, 25-406 Kielce, Poland*

[t] *Institute of Physics, University of Silesia, Uniwersytecka 4, 40-007 Katowice, Poland*

2014 JINST 9 P06005

[u]*Institute of Particle and Nuclear Studies, High Energy Accelerator Research Organization (KEK), 1-1 Oho, Tsukuba, 305-0801, Japan*
[v]*Department of Physics and Astronomy, University of Wrocław, pl. M. Borna 9, 50-204 Wrocław, Poland*
[w]*Department of Electrical Engineering and Computer Science, University of California, 4416 Engineering Hall, Irvine, CA, 92697-2625, U.S.A.*
[x]*National Centre for Nuclear Research, Andrzeja Sołtana 7, 05-400 Otwock, Poland*
[y]*Fachhochschule Frankfurt am Main, Nibelungenplatz 1, D-60318 Frankfurt am Main, Germany*
[z]*Department of Physics and Technology, University of Bergen, Allegt. 55, 5007 Bergen, Norway*

E-mail: rplaneta@mail.cern.ch

ABSTRACT: NA61/SHINE (SPS Heavy Ion and Neutrino Experiment) is a multi-purpose experimental facility to study hadron production in hadron-proton, hadron-nucleus and nucleus-nucleus collisions at the CERN Super Proton Synchrotron. It recorded the first physics data with hadron beams in 2009 and with ion beams (secondary ^{7}Be beams) in 2011.

NA61/SHINE has greatly profited from the long development of the CERN proton and ion sources and the accelerator chain as well as the H2 beamline of the CERN North Area. The latter has recently been modified to also serve as a fragment separator as needed to produce the Be beams for NA61/SHINE. Numerous components of the NA61/SHINE set-up were inherited from its predecessors, in particular, the last one, the NA49 experiment. Important new detectors and upgrades of the legacy equipment were introduced by the NA61/SHINE Collaboration.

This paper describes the state of the NA61/SHINE facility — the beams and the detector system — before the CERN Long Shutdown I, which started in March 2013.

KEYWORDS: Particle identification methods; Time projection chambers; Instrumentation for radioactive beams (fragmentation devices; fragment and isotope, separators incl. ISOL; isobar separators; ion and atom traps; weak-beam diagnostics; radioactive-beam ion sources); Trigger detectors

ARXIV EPRINT: 1401.4699

2014 JINST 9 P06005

Contents

2014 JINST 9 P06005

1 Introduction

NA61/SHINE (SPS Heavy Ion and Neutrino Experiment) [1] is a multi-purpose facility to study hadron production in hadron-proton, hadron-nucleus and nucleus-nucleus collisions at the CERN Super Proton Synchrotron (SPS). The NA61/SHINE physics goals include:

(i) study the properties of the onset of deconfinement [2] and search for the critical point of strongly interacting matter which is pursued by investigating p+p, p+Pb and nucleus-nucleus collisions and

(ii) precise hadron production measurements for improving calculations of the initial neutrino beam flux in the long-baseline neutrino oscillation experiments [3, 4] as well as for more reliable simulations of cosmic-ray air showers [5, 6].

The experiment was proposed to CERN in November 2006 [1]. Based on this proposal pilot data taking took place in September 2007. The Memorandum of Understanding [7] between CERN and the collaborating institutions was signed in October 2008. The first physics data with hadron beams were recorded in 2009 and with ion beams (secondary ^{7}Be beams) in 2011. The first experimental results were published in [8, 9].

NA61/SHINE has greatly profited from the long development of the CERN proton and ion sources, the accelerator chain, as well as the H2 beamline of the CERN North Area. The latter has recently been modified to also serve as a fragment separator as needed to produce the Be beams for NA61/SHINE. Numerous components of the NA61/SHINE set-up were inherited from its predecessors, in particular, the last one, the NA49 experiment.

The layout of the NA61/SHINE detector is sketched in figure 1. It consists of a large acceptance hadron spectrometer with excellent capabilities in charged particle momentum measurements and identification by a set of six Time Projection Chambers as well as Time-of-Flight detectors. The high resolution forward calorimeter, the Projectile Spectator Detector, measures energy flow around the beam direction, which in nucleus-nucleus reactions is primarily a measure of the number of spectator (non-interacted) nucleons and thus related to the centrality of the collision. For hadron-nucleus interactions, the collision centrality is determined by counting low momentum particles emitted from the nuclear target with the LMPD detector (a small TPC) surrounding the target. An array of beam detectors identifies beam particles, secondary hadrons and ions as well as primary ions, and measures precisely their trajectories.

This paper describes the NA61/SHINE facility, the beams and the detector system. Special attention is paid to the presentation of the components which were constructed for NA61/SHINE. The components inherited from the past experiments and described elsewhere are presented only briefly here. The paper is organized as follows. In section 2 the proton and ion acceleration chains are introduced and the North Area H2 beamline is described. Moreover basic properties of the employed hadron and ion beams are given. The NA61/SHINE beam and trigger detectors as well as the trigger system are presented in section 3. Section 4 is devoted to the TPC tracking system which consists of the TPC detectors with front end electronics, two beam pipes filled with helium gas and two super-conducting magnets. The Time of Flight system is described in section 5 and the Projectile Spectator Detector in section 6. In section 7 the targets and the Low Momentum Particle

2014 JINST 9 P06005

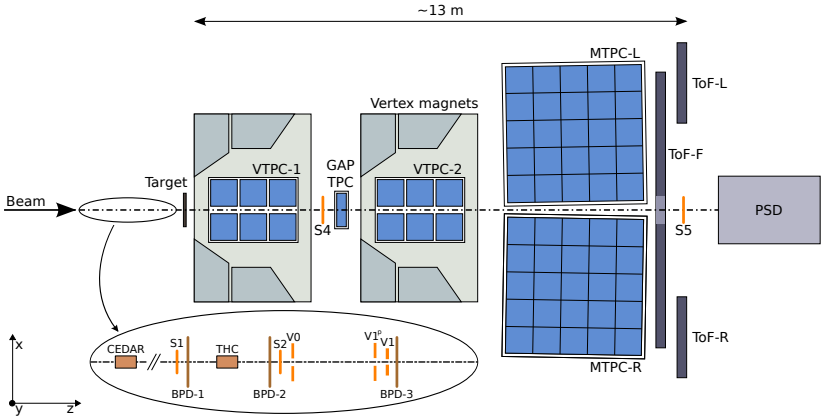

Figure 1. Schematic layout of the NA61/SHINE experiment at the CERN SPS (horizontal cut in the beam plane, not to scale). The beam and trigger counter configuration used for data taking on p+p interactions in 2009 is presented. The chosen right-handed coordinate system is shown on the plot. The incoming beam direction is along the z axis. The magnetic field bends charged particle trajectories in the *x*-*z* (horizontal) plane. The drift direction in the TPCs is along the y (vertical) axis.

Detector are presented. Finally, data acquisition and detector control systems are described in section 8. Section 9 closes the paper with summary and outlook.

2 Beams

This section starts from the presentation of the CERN proton and ion accelerator chains, and continues with a brief description of the H2 beamline and secondary hadron and ion beams for the experiment.

The CERN accelerator chain, with its components relevant for NA61/SHINE beams exposed, is shown in figure 2. From the source, the beams of ions and protons pass through a series of accelerators, before they reach the SPS for final acceleration and subsequent extraction to the North Area and the NA61/SHINE experiment. The protons and ions follow a different path in the pre-injector chain to the PS, required to match the beam parameters for their acceleration.

2.1 Proton acceleration chain

The proton beam is generated from hydrogen gas by a duo-plasmatron ion source, which can provide a beam current of up to 300 mA [10]. The Radio-Frequency Quadrupole RFQ2 [11] focuses and bunches the beam, and accelerates it to 750 keV for injection into LINAC2, a three-tank Alvarez drift tube linear accelerator. The three tanks have a total length of 33.3 m, and the energy of the beam at the exit of the tanks is respectively 10.3, 30.5, and 50 MeV. With a repetition rate of 0.8 Hz, LINAC2 delivers a current of up to 170 mA within a 90% transverse emittance of 15π mm mrad, during a 120 μs pulse length [12]. The 50 MeV proton beam from LINAC2 is then

2014 JINST 9 P06005

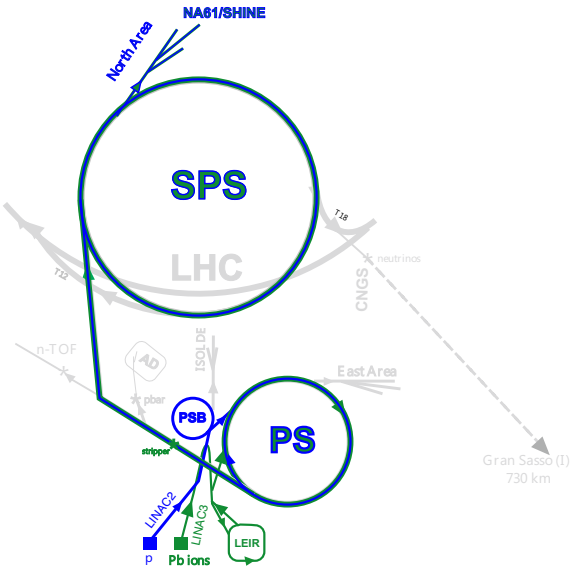

Figure 2. Schematic layout of the CERN accelerator complex relevant for the NA61/SHINE ion and proton beam operation. (Top view, not to scale).

distributed in the four rings of the PS booster (PSB) using a staircase-like kicker magnet in the transfer line. The multi-turn injection system of the PSB allows to accumulate for up to 13 turns, over 10^{13} protons per ring. After acceleration to 1.4 GeV, the beam from the four rings is extracted and recombined in the extraction line, to be sent to the Proton Synchrotron (PS), CERN's oldest accelerator [13]. The PS has a circumference of 628 m and accelerates the beams to 14 GeV/c for injection into the Super Proton Synchrotron (SPS). In a typical proton cycle for the fixed-target experiments, the PSB beam after recombination consists of a train of eight bunches (two per ring), which are injected into the eight consecutive buckets of the RF of the PS that operates at harmonic eight. During the acceleration to 14 GeV/c, the beam passes from an intermediate flat-top where the RF system splits the eight bunches into two and changes the operation to harmonic sixteen. At the top momentum, the beam is de-bunched and re-captured at harmonic 420 in order to easily match the RF structure of the receiving machine, the 6.8 km circumference SPS. The beam is extracted from the PS over five turns using a staircase-shaped kicker pulse. This "continuous transfer" multi-turn extraction is unique to the PS. As the SPS is 11 times larger than the PS in circumference, it takes two PS cycles to fill the SPS with the five-turn extraction. The remaining two half-turn gaps are used for the rising and falling edge of the SPS injection kicker. In the SPS, the 14 GeV/c beam is accelerated to 400 GeV/c, on fixed harmonic 4620 (200 MHz). At the top momentum, the beam is de-bunched and slowly extracted over several seconds using a third-integer resonance. The spill duration for the North Area experiments depends on the overall optimisation for the SPS machine and its users, and can be between 4.5 s and 10 s with a duty cycle of about 30%.

2014 JINST 9 P06005

2.2 Ion accelerator chain

The CERN ion production complex was first designed in the 1990s for the needs of the SPS fixed target programme [14, 15]. It was rejuvenated at the beginning of the 21st century [16] in order to cope with the LHC's stringent demands for high brightness ion beams [17]. The ions are generated in the ECR source. Here the case of the Pb beam production is considered as an example.

A sample of isotopically pure ^{208}Pb is inserted in a filament-heated crucible at the rear of the ECR source, whilst oxygen is injected as support gas. With a 10 Hz repetition rate, a 50 ms long pulse of 14.5 GHz microwaves accelerates electrons to form an oxygen plasma, which in turn ionizes the lead vapor at the surface of the crucible. The source operates in the so-called afterglow mode, i.e. the microwave pulse is switched off, when the intensity of the high charge state ions from the source increases dramatically. The ions are electrostatically extracted from the source with an energy of 2.5 keV/u. Out of the different ion species and charge states, a 135° spectrometer situated at the exit of the source selects those lead ions which were ionized 29 times (Pb29+) to enter the LINAC3 accelerator. The beam is first accelerated to 250 keV/u by the 2.66 m long RFQ which operates at 101.28 MHz. The RFQ is followed by a four-gap RF cavity which adapts the longitudinal bunch parameters to the rest of the linear accelerator which is a three-cavity interdigital H (IH) structure, that brings the beam energy up to 4.2 MeV/u requiring about 30 MV of accelerating voltage, for a total acceleration length of 8.13 m. The first cavity operates at the same frequency as the RFQ (101.28 MHz), while the second and third cavities operate at 202.56 MHz. Finally, a 250 kV "ramping cavity", also operating at 101.28 MHz, distributes the beam momentum over a range of $\pm 1\%$, according to the time along the 200 μs pulse. The LINAC3 currently operates at 5 Hz. A 0.3 μm thick carbon foil provides the first stripping stage at the exit of LINAC3, followed by a spectrometer which selects the Pb54+ charge state. A current of about 22 μA of Pb54+ from LINAC3 is injected over about 70 turns into the Low Energy Ion Ring (LEIR), whose unique injection system fills the 6-dimensional phase space. This is achieved by a regular multi-turn injection with a decreasing horizontal bump, supplemented by an electrostatic septum tilted at 45°, and the time dependence of the momentum distribution coupled with the large value (10 m) of the dispersion function in the injection region. The injection process is repeated up to six times, every 200 ms. The whole process is performed under electron cooling reducing the transverse and longitudinal emittances. At the end of the seven injections, the beam is bunched on harmonic 2, accelerated to 72 MeV/u by Finemet™ cavities, and fast-extracted towards the PS. At this point the total beam intensity is about 10^9 ions.

In the PS, the two ion bunches from LEIR are injected into two adjacent buckets of harmonic 16 and accelerated by the 3–10 MHz system to 5.9 GeV/u, with an intermediate flat-top for batch expansion. This process consists of a series of harmonic changes: $h = 16, 14, 12, 24, 21$, in order to finally reach a bunch spacing of 200 ns at the top energy. Before the fast extraction to the SPS, the bunches are finally rebucketed into $h = 169$, using one of the PS's three 80 MHz cavities. At the exit of the PS, the beam traverses a final stripping stage to produce Pb82+ ions, through a 1 mm thick aluminium foil.

The two bunches, now about 3×10^8 ions each, are injected into the SPS, with a bunch-to-bucket transfer into the 200 MHz system. This process can be repeated up to 12 times every 3.6 seconds; the repetition rate is limited by the duration of the LEIR cycle, while the total number of

2014 JINST 9 P06005

injections is currently limited by the SPS controls hardware. At a fixed harmonic, the heavy mass of the ions during acceleration would yield a too large frequency swing (198.51–200.39 MHz) for the range of the travelling wave cavities of the SPS (199.5–200.4 MHz). Hence, instead of using a fixed harmonic, the ions are accelerated using the "fixed frequency" method, in which a non-integer harmonic number is used, by turning the RF ON at the cavity centre frequency during the beam passage and switching it OFF during its absence, to correct the RF phase and be ready for its next beam passage through the cavities. The phase is adjusted by an appropriate modulation of the frequency. Aside from its complexity, one drawback of the method is that the beam has to be constrained in a relatively short portion (40%) of the circumference of the machine. In the SPS, the ion beam, after acceleration to the required energy, is left to de-bunch naturally and is then slowly extracted to the North Area using the third integer resonance like for protons. The acceleration range in SPS varies between the 13 GeV/u, which is the lowest possible operational range due to stability reasons, and 160 GeV/u due to the limits in the power supplies and energy in the magnets. The spill duration is preferred to be long at about 10 s, although as for the protons the overall structure depends on the number of users at the SPS.

2.3 H2 beamline

The extracted beam from the SPS is transported over about 1 km by bending and focusing magnets and then split into three parts each one directed towards a primary target where secondary particles are created. The H2 secondary beamline emerges from the T2 primary target and is able to transport momentum selected secondary particles to the Experimental Hall North 1 (EHN1). The NA61/SHINE experiment is located in the middle part of EHN1, the NA61/SHINE production target being at 535 m distance from the T2 target. The H2 beamline can transport charged particles in a wide range of momenta from $\sim 9\,\mathrm{GeV}/c$ up to the top SPS energy of $400\,\mathrm{GeV}/c$. Alternatively the beam can transport a primary beam of protons or ions, of low intensity to comply with the radiation safety conditions for the experimental hall.

The North Area target cavern (TCC2) where the T2 target is located, is about 11 m underground in order to contain the radiation produced from the impact of the high-intensity extracted beam from the SPS. In the proton mode the extracted intensity from the SPS is typically a few 10^{13} protons per cycle at $400\,\mathrm{GeV}/c$ from which only a fraction of about 40% interacts in the targets, and the rest is dumped in a controlled way in the TCC2 cavern. The surrounding earth acts as natural shielding for radiation and the height difference to the experimental hall is sufficient to reduce the muon background to the experiments. The T2 target station hosts several beryllium (Be) plates of different lengths. From these the target plate is chosen which best optimizes the yield of the requested secondary particle momentum and type. Beams for NA61/SHINE are usually produced using a target length of 100 or 180 mm. A further optimisation can be achieved using a set of upstream dipole magnets that can modify the incident angle of the primary proton beam on the target and thus the production angle of the secondary particles emitted into the H2 beamline.

The momentum selection in the beam is done in the vertical plane, as shown in figure 3, where the beamline basically consists of two large spectrometers able to select particles according to their rigidity, i.e. the momentum to charge ratio $B\rho \approx 3.33 p_b/Z$, where $B\rho$ in Tesla·meters is set by the beam optics, p_b is the momentum of the beam particles in GeV/c, and Z the charge of the particle (in proton charge units). For the energies discussed here the particle momentum can be

2014 JINST 9 P06005

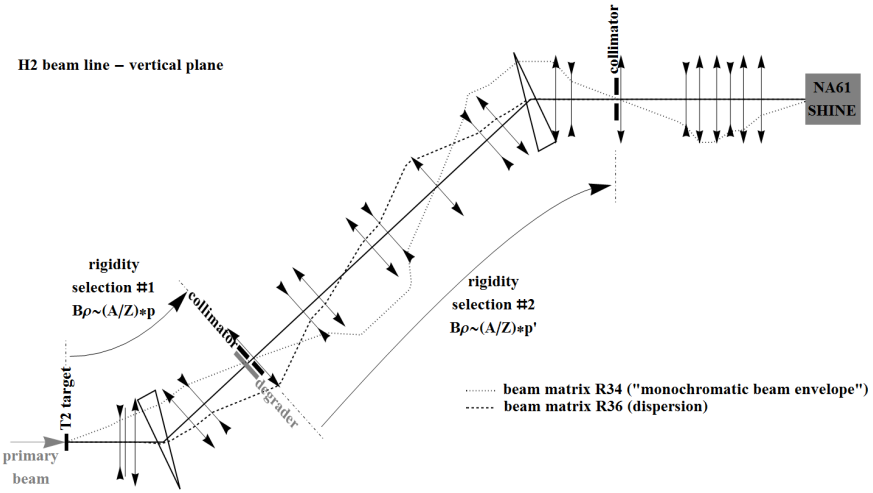

Figure 3. Schematic view of the vertical plane of the H2 beamline in the configuration used for the ion fragment separation. The dimensions are not to scale, e.g. the beamline is more than 600 m long, the height difference between T2 and the EHN1 is about 12 m, the aperture of the quadrupoles is ±45 mm.

written in the relativistic limit as $p_b = \gamma_b m$, where γ_b is the beam Lorentz factor and m the particle mass, which can be expressed in terms of the atomic mass number A times the atomic mass unit (1 amu = 0.931 GeV). So finally the rigidity relation for the beamline is $B\rho \approx 3.31\gamma_b(A/Z)$. Each spectrometer consists of six dipole magnets that deflect the beam by a total angle of 41 mrad and collimators defining the central trajectory. The beam spectrometer has an intrinsic resolution of about 0.13% and a maximum rigidity acceptance of ±1.7%. Besides the magnetic spectrometers, the beamline is equipped with dedicated devices which provide information on the beam position, profile and intensity at various locations, as well as particle identification detectors like Cherenkov or pulse height and spectrum analysis detectors to identify multiply charged particles like heavy ions.

For the NA61/SHINE experiment secondary hadron beams in the momentum range from 13 GeV/c to 350 GeV/c were used, as well as attenuated primary Pb82+ ion beams in the range from 13A GeV/c to 158A GeV/c. For the start of the ion physics program of the experiment secondary ^{7}Be ion beams in the same momentum range were used, as primary ions other than Pb82+ were not available before 2015. The secondary ^{7}Be ions were produced via fragmentation of the Pb82+ ions in the T2 target. Starting in 2015 attenuated primary ^{40}Ar and ^{131}Xe ion beams in the same momentum range will be delivered to NA61/SHINE. The next section presents further details of the hadron and ion beams employed by the experiment before Long Shutdown I.

2.4 Hadron beams

The H2 beamline can transport and deliver positively or negatively charged secondary hadrons (p, K^+, π^+ and $\bar{p}$, K^-, π^-) to the NA61/SHINE experiment, produced at the T2 target from the im-

2014 JINST 9 P06005

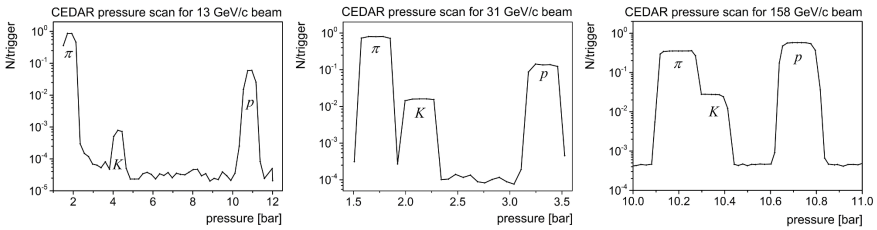

Figure 4. Counts of hadrons per incident beam particle from the CEDAR counter as a function of the gas pressure within the pressure range which covers maxima of pions, kaons and protons at 13 (*left*), 31 (*middle*) and 158 GeV/c (*right*).

pact of the primary proton beam from the SPS. For a given beam tune, i.e. rigidity selection, the momentum selected hadrons are mixed with muons, electrons and tertiary hadrons from interactions with the collimators or the beam aperture limits. In order to select the wanted hadrons, the beamline is equipped with a special differential Cherenkov counter, the Cherenkov Differential Counter with Achromatic Ring Focus (CEDAR) [18] counter. This counter uses a gas as radiator, Helium for beam momenta higher than 60 GeV/c and Nitrogen for lower momenta. The counter has a sophisticated optical system that collects and focuses the Cherenkov photons onto the plane of a diaphragm whose opening can be tuned, in relation to a given gas pressure, such as to allow only the photons from the wanted species to pass through and get detected by the 8 PMTs of the counter. By using a coincidence logic, 6-, 7- or 8- fold, a positive tagging of the wanted particles can be achieved. For the NA61/SHINE experiment the 6-fold coincidence signal is used for the beam trigger.

The pressure range at which counts of a wanted hadron (p ($\bar{p}$) or π^+ (π^-), or K^+ (K^-)) per incident particle are maximal is found by performing a pressure scan in the domain where the wanted hadron peak is expected. Results of the gas pressure scan performed in the full relevant pressure range for beams at 13 GeV/c, 31 GeV/c and 158 GeV/c are presented in figure 4. The final setting is the pressure corresponding to the centre of the wanted hadron peak. The actual value of the optimal pressure depends on possible admixtures in the gas, as well as on temperature, since the production angle of Cherenkov radiation is a function of the gas density. The width of the signal peaks and their separation can be modified by changing the aperture of the diaphragm. The counter is installed in a special location of the beamline where the beam has almost zero divergence. However to make sure the light is collected with high symmetry, an angular alignment of the CEDAR counter has to be performed each time the beam position at the detector changes. Under standard operational conditions the detection efficiency of the detectors is better than 95%. The number of misidentified particles is lower than 0.8%. For beam momenta lower than 40 GeV/c, the trigger definition also requires the signal from a carbon dioxide-filled Threshold Cherenkov [19, 20][1] detector in anti-coincidence.

[1] Ref. [19] discusses H_2 filled Cherenkov detectors, similar in construction to those used at present but operating up to 5 GeV/c.

2014 JINST 9 P06005

The H2 beam optics provides a smooth focus at the target of the NA61/SHINE experiment with an RMS width slightly larger than 2 mm at the lowest momenta and 1.2 mm at 158 GeV/c. The momentum spread is typically lower than 1%, defined by the collimator settings in the line.

2.5 Primary and secondary ion beams

The physics program of NA61/SHINE requires beams of Beryllium (Be), Argon (Ar) and Xenon (Xe) ions. For reasons of compatibility with the LHC program the Be beam is obtained from the fragmentation of Pb ions, whereas the Ar and Xe beams will be specifically produced for NA61/SHINE.

The transport of primary ions in the H2 beamline is straightforward. The beam tune, i.e. rigidity is set to match the ion momentum extracted from the SPS, and the detectors in the beamline are adapted to the non-standard (high) charge of the beam particles. To respect the radiation limits and classification in the Experimental Hall, the intensity in the SPS machine is kept to a minimum, typically using a single (or double) injection into the SPS resulting in a total of $\sim 6 \times 10^8$ ions. The intensity is further reduced in the H2 beamline by collimation, down to a rate of a few 10^5 ions at the experiment.

The selection and transport of a specific ion species from a fragmented heavy (Pb82+) ion beam for nuclear reaction experiments is not straightforward. The H2 beamline selects on rigidity, i.e. $\sim \gamma_b (A/Z)$, and the desired ions produced from the fragmentation of the primary Pb beam will be mixed with a variety of other nuclei with similar mass to charge ratios and slightly different rigidity values within the beam acceptance. Moreover, rigidity overlaps occur not only for ions with the same mass to charge ratio but also for neighbouring elements due to the nuclear Fermi motion which smears fragment momenta. Without Fermi motion the fragments would leave the interaction region almost undisturbed with the same momentum per nucleon as the incident Pb ions. The Fermi motion depends on the fragment and projectile mass, and can spread the longitudinal momenta for light nuclear fragments by up to 3–5%, much larger than the beam acceptance.

The ^{7}Be ion ("wanted ion") was selected for the NA61/SHINE beam, because it has no long-lived near neighbours and thus allows to make a light ion beam with a large ratio of wanted to all ions. The near neighbours to ^{7}Be are isotopes ^{6}Be and ^{8}Be and the nuclei with a charge difference of one and a similar mass to charge ratio (e.g. ^{5}Li, ^{9}B). Furthermore ^{7}Be has more protons ($Z = 4$) than neutrons ($N = 3$). Such nuclear configurations are disfavored with increasing nuclear mass, since a surplus of protons causes a Coulomb repulsion which cannot be balanced by the attractive potential of the fewer neutrons. As can be seen in figure 5, ^{7}Be fragments are accompanied mainly by ^{2}D and He ions whose rigidity overlaps with the one of the wanted ions due to Fermi motion. A problematic choice of wanted ion species would be a nucleus with mass to charge ratio of two, which would be accompanied by stable or long lived nuclei from ^{2}D up to ^{56}Ni.

At low energies, a better selectivity of the wanted ions is achieved with the "fragment separation" method [21], profiting from the double spectrometer of the H2 beamline (see figure 3). In the first spectrometer, ions are selected within a rigidity value that maximizes the wanted to all ratio for the fragments as produced by the primary fragmentation target. At the focal point of the first spectrometer, a piece of material (called degrader) is introduced, in which ions lose energy in dependence of their charge. Then in the second spectrometer the different ions will be spatially separated according to their charge state, which then can be selected using a thin slit (collimator).

2014 JINST 9 P06005

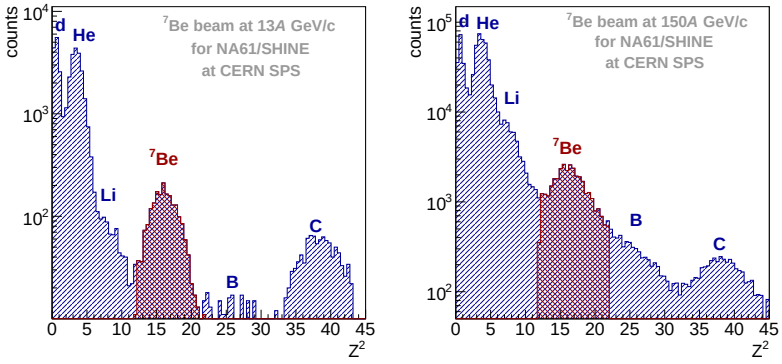

Figure 5. Charge spectrum measured with the Quartz Z-detector for 13A and 150A GeV/c ion beams.

The drawback of this method is a loss of beam intensity due to nuclear interactions and the beam blow-up due to multiple scattering in the material of the degrader which rises with increasing thickness. Thus a high separation power of the fragment separator spectrometer goes along with a high loss of intensity. Furthermore, for a given degrader thickness both the nuclear cross section and the energy loss are to a large extent energy independent. This means that the separation power ($\Delta E/E$) increases with decreasing energy.

Under typical running conditions a beam of several 10^8 Pb ions per spill from the SPS is focused onto the 180 mm long fragmentation target made of Be. During its passage through the target the Pb beam undergoes (mostly peripheral) collisions with the (light) target nuclei. Part of the resulting mix of nuclear fragments is captured by the H2 beamline, tuned to a rigidity such that the fraction of the created ^{7}Be to all ions is maximized (see figure 5). Ion fluxes at the NA61/SHINE apparatus were 5000 to 10 000 ^{7}Be particles with 10 to 20 times more unwanted ions.

The optional degrader (1 or 4 cm thick Cu plate) is located between the two spectrometer sections (see figure 3). The composition of the ion beam can be monitored by scintillator counters which measure the charge (Z^2) and time of flight (*tof*) of the ions. The latter allows mass (A) determination of the ions for momenta lower than 20A GeV/c and thus a check of the purity of the ^{7}Be beam. This is illustrated in figure 6 where the *tof* spectra of ions for the carbon (*left*) and beryllium (*right*) peaks resulting from fragmentation of the primary Pb beam at 13.9A GeV/c are shown. The carbon spectrum shows clear evidence for two isotopes, whereas only the single Be isotope (^{7}Be) is seen in the Be spectrum. We therefore decided to select ^{7}Be for data taking.

The fragment separation method was tested in 2010 with a 13.9A GeV/c Pb beam incident on the primary target of the H2 beamline with the 4 cm thick degrader in place. Figure 7 shows for a given rigidity setting the charge distributions resulting from two collimator settings which optimize either the ^{7}Be (filled purple histogram) or the ^{11}C (open blue histogram) content. Comparison with figure 5 demonstrates that by using the degrader the ratio of wanted to all ions is improved by nearly an order of magnitude.

During the 2011 running period the NA61/SHINE collaboration used the beamline configuration without degrader at beam momenta of 150A GeV/c, 75A GeV/c, and 40A GeV/c with settings

2014 JINST 9 P06005

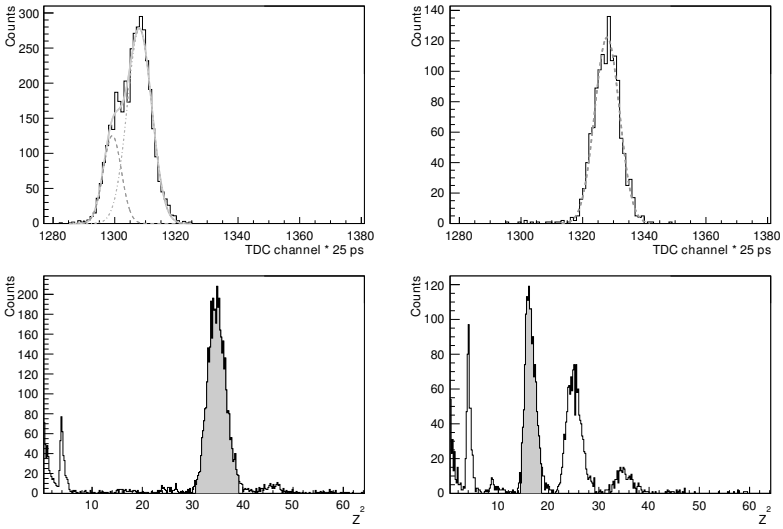

Figure 6. *Top*: the time of flight spectra of ions for the carbon (*left*) and beryllium (*right*) peaks resulting from fragmentation of the primary Pb beam at 13.9A GeV/c. The spectrum of carbon is fitted by a sum of two Gauss functions, whereas that of beryllium by a single Gaussian. *Bottom*: the Z^2 spectra with the selected (gray area) peaks of carbon (*left*) and beryllium (*right*). The spectra were measured by the A-detector.

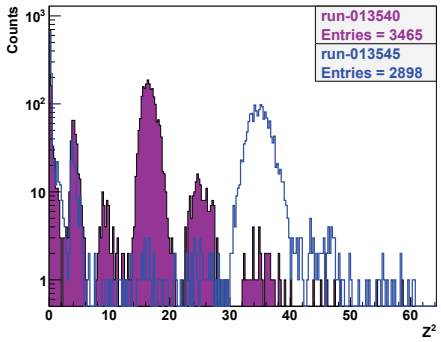

Figure 7. Fragment charge distributions obtained with the H2 beamline in fragment separator mode and collimator settings optimized for ^{7}Be (filled purple) and ^{11}C (open blue) fragments. The primary Pb beam momentum is 13.9A GeV/c.

optimised for ^{7}Be ions. This choice allowed tagging pure ^{7}Be ions without incurring the penalty on intensity from the degrader while still resulting in an acceptable ratio of wanted to all ions. In 2012 and early 2013 fragmented ion beams at 30A GeV/c, 19A GeV/c and at 13A GeV/c (the lower momentum limit of the accelerator capabilities) were provided to NA61/SHINE.

2014 JINST 9 P06005

Table 1. Summary of typical beam detector parameters: dimensions, positions along the beamline (z coordinates) and their material budget (in terms of the nuclear interaction length λ_I and radiation length X_0). Positions of most of these detectors varied in time by a few cm due to dismounting and remounting in subsequent runs. Exceptions are BPD-3, V1 and V1^p, for which positions varied up to 50 cm depending on the employed target. E.g. for the liquid hydrogen target the positions were: BPD-3 -6.93 m, V1 -7.20 m and V1^p -7.23 m. Positions of the A and V0^p detectors were not surveyed, therefore are known only approximately.

Detector	Dimensions [mm]	Hole [mm]	Position [m]	Material budget	
				[$\%\lambda_I$]	[$\%X_0$]
S1	$60\times60\times5$		-36.42	0.635	1.175
S2	$\phi = 28\times2$		-14.42	0.254	0.470
S3	$\phi = 26\times5$		-6.58	0.635	1.175
S4	$\phi = 20\times5$		-2.11	0.635	1.175
S5	$\phi = 20\times5$		9.80	0.635	1.175
V0	$\phi = 80\times10$	$\phi = 10$	-14.16		
V0^p	$300\times300\times10$	$\phi = 20$	≈ -14		
V1	$100\times100\times10$	$\phi = 8$	-6.72		
V1^p	$300\times300\times10$	$\phi = 20$	-6.74		
A	$150\times5\times15$		≈ -146	1.904	3.526
Z	$160\times40\times2.5$		-13.81	0.562	2.034
BPD-1	$48\times48\times32.6$		-36.20	0.025	0.070
BPD-2	$48\times48\times32.6$		-14.90	0.025	0.070
BPD-3	$48\times48\times32.6$		-6.70	0.025	0.070
Typical thin target position			-5.81		

3 Beam detectors and trigger system

A set of scintillation and Cherenkov counters as well as the beam position detectors located upstream of the target provide precise timing reference, along with charge and position measurement of the incoming beam particles. Interaction counters located downstream of the target allow to trigger on interactions in the target. Typical parameters of these detectors are summarized in table 1.

The locations of the beam detectors in four exemplary configurations of the beamline are indicated in figure 8. These were used for data taking on (from top to bottom):

(a) p+p interactions at 13 GeV/c and 158 GeV/c in 2011,

(b) p+(T2K replica target) interactions in 2009 and 2010 (the S3 detector was glued to the surface of the replica target),

(c) h$^-$+C interactions at 158 GeV/c and 350 GeV/c in 2009 (an additional interaction trigger was used with the S5 counter instead of S4 to estimate the trigger bias),

(d) ^{7}Be + ^{9}Be interactions at 13A GeV/c, 19A GeV/c and 30A GeV/c in 2013.

Colour indicates the detector function in the NA61/SHINE trigger. Namely signals of detectors in green are used in coincidence, in red in anti-coincidence and detectors in blue are not used in the trigger logic.

2014 JINST 9 P06005

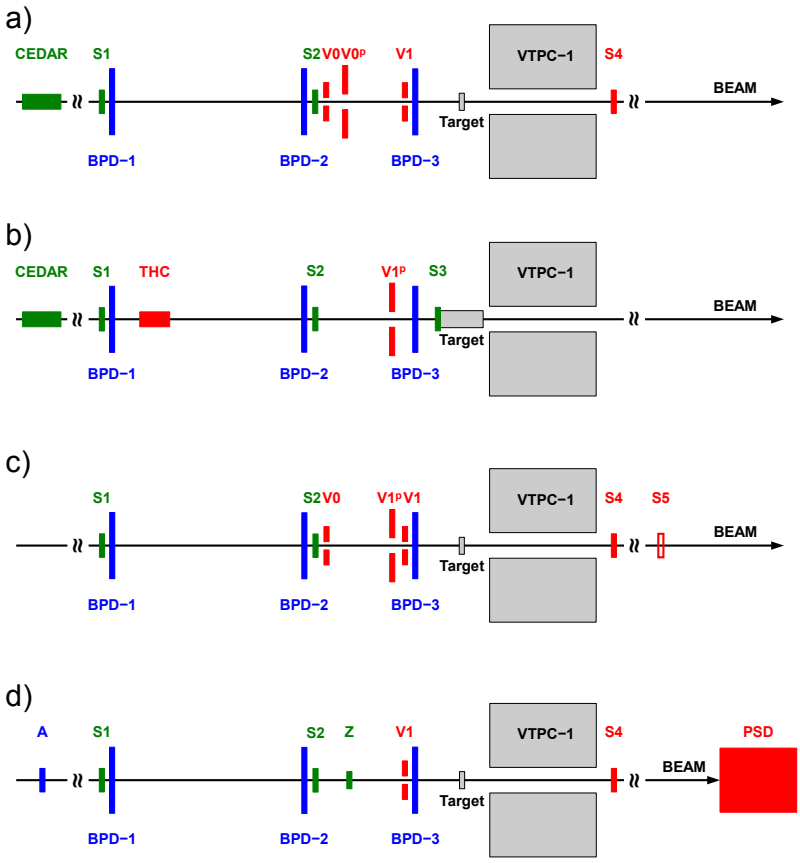

Figure 8. Schematic layout (horizontal cut in the beam plane, not to scale) of the beam detectors in four configurations of the beamline, see text for details.

3.1 Beam counters

Minimization of the total detector material in the beamline is a major concern, especially with ion beams. A minimal set of plastic scintillator (BC-408) beam counters (see figure 8) is therefore used. The first detector S1 is located upstream of the target at position $z = -36.42$ m. As the time of flight resolution in low-multiplicity events has to rely on a precise reference time, the S1 counter (0.5 cm thick) is equipped with four photomultipliers directly coupled to the scintillator. The second beam counter S2 (0.2 cm thick) is located just behind the BPD-2 detector at $z = -14.42$ m. In the case of primary heavy ion beams the S1 and S2 scintillator detectors will be replaced by quartz detectors of 200 μm thickness yielding sufficient timing and pulse height resolution from the Cherenkov effect. Downstream of the S2 detector two 1 cm thick veto scintillator detectors V0 and V1 are positioned

2014 JINST 9 P06005

at $z = -14.16$ m and $z = -6.72$ m, respectively. The round V0 detector has outer diameter of 8 cm and in the centre a hole of 1 cm diameter. The square ($10 \times 10\,\mathrm{cm}^2$) V1 detector also has a 1 cm central hole. Additionally two veto detectors V0′ and V1′ are installed for configurations of beam line a), b) and c), respectively. For configuration b) the Threshold Cherenkov, THC, detector is also positioned. The S4 and S5 detectors (2 cm diameter, 0.5 cm thickness) are located downstream of the target at $z = -2.11$ m and 9.80 m, respectively. They are used to select interactions of beam particles in the target. Interactions in the target are signaled by the absence of the beam particle signal in the counter. The beam counter parameters are summarized in table 1. In the plane transverse to the beam direction (the *x*-*y* plane) the detectors are centred at the maximum of the beam profile.

3.2 A-detector

The A-detector was constructed to verify whether the secondary Be beam consists only of the single isotope ^{7}Be. It was located about 140 m upstream of the target and measured the time of flight (*tof*) of beam ions between A- and S1 detectors. It consists of a plastic scintillator (BC-408) bar ($15 \times 0.5 \times 1.5\,\mathrm{cm}^3$) with light readout from both sides of the scintillator bar by the two fast PMTs, EMI 9133. The time resolution of the A-detector was measured to be about 80 ps during a test in the T10 beam of the CERN PS using pions.

The time of flight spectra measured by the A-detector at 13.6*A* GeV/*c* are shown in figure 6 (*top*) for carbon and beryllium ions selected by the Z^2 proportional signal amplitude simultaneously measured in the A-detector (*bottom*). The single isotope beryllium (^{7}Be) spectrum demonstrates a *tof* resolution of 60 ps. The expected difference of *tof* between ^{7}Be ions and its nearest isotopes is about 170 ps at the beam momentum of 13.6*A* GeV/*c* and distance of 140 m.

3.3 Beam Position Detectors

The positions of the incoming beam particles in the transverse plane are measured by a telescope of three Beam Position Detectors (BPDs) placed along the beamline upstream of the target. The NA61/SHINE BPDs (see figure 9 (*left*)) with active areas of $48 \times 48\,\mathrm{mm}^2$ were constructed in 2009. These detectors are proportional chambers operated with Ar/CO_2 85/15 gas mixture. Two orthogonal sense wire planes (15 μm tungsten wires with 2 mm pitch) are sandwiched between three cathode planes made of 25 μm aluminized Mylar. The outer cathode planes of these detectors are sliced into strips of 2 mm pitch which are connected to the readout electronics. In order to detect beam particles at high intensities (about 10^5 particles/second) shapers based on AD817 integrated amplifiers were constructed. The width of their output signal is about 350 ns. Negative undershoots of output signals observed with the NA49 shapers are practically eliminated (see figure 9 (*right*)).

Each BPD measures the position of the trigger-selected beam particle in two orthogonal directions independently using two planes of orthogonal strips. On each strip plane a charge distribution is induced with a width of about 5 strips on average. The reconstruction algorithm first searches for a cluster in each plane. The cluster is defined as a set of adjacent strips with signal amplitudes above a threshold value (to remove signals from pedestal fluctuations). Then, an average of the strip positions weighted with the signal amplitudes on the strips is calculated for the cluster to estimate the position of the beam particle (the so-called centroid method). A 3-dimensional point measured

2014 JINST 9 P06005

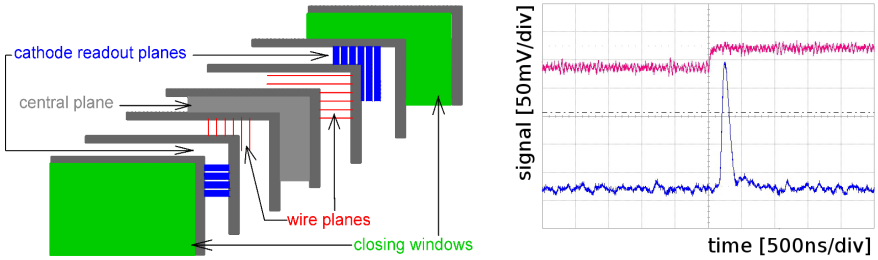

Figure 9. *Left*: the schematic layout of the BPD detector. *Right*: the signal generated by a BPD pre-amplifier (upper curve) and the corresponding signal at the output of a shaper (lower curve). The time scale of the x axis is 500 ns per division.

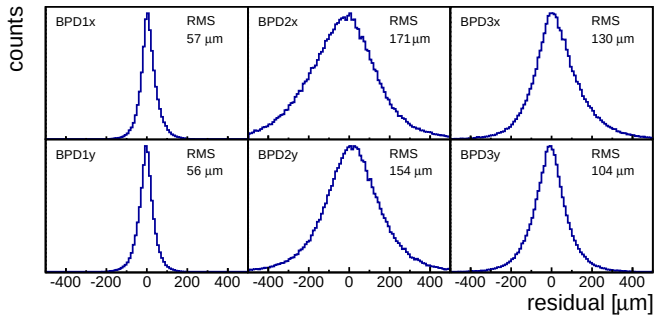

Figure 10. Distributions of residuals associated with beam track fits in each of the BPDs in the x-z (top row) and y-z (bottom row) planes. Differences in RMS widths are mainly due to non-equal distances between the detectors in the z direction. Plots are for the negatively charged hadron (mainly π^-) beam at 158 GeV/c.

by a given BPD is built from two transverse coordinates measured by the two strip planes and the position of the BPD along the beamline.

In order to reconstruct a beam particle track, least squares fits of straight lines are performed to the positions measured by the three BPDs in x-z and y-z planes independently. Distributions of residuals associated with those fits are shown in figure 10. The RMS widths of the distributions indicate the order of magnitude of the accuracy of the BPD measurements, which is in agreement with the design value of $\sim 100\,\mu$m. Differences of the RMS widths are mainly due to non-equal distances between the detectors in the z direction ($d(\mathrm{BPD}-1,\mathrm{BPD}-2) = 21$ m, $d(\mathrm{BPD}-2,\mathrm{BPD}-3) = 8$ m). This observation agrees qualitatively with predictions of Monte Carlo calculations.

3.4 Z-detectors

In order to select secondary ions by their charge at the trigger level, two Cherenkov counters (Z-detectors) were constructed and tested. These are:

(i) The Quartz Detector (QD) with a quartz (GE214P) plate $160 \times 40 \times 2.5\,\mathrm{mm}^3$ as the radiator is equipped with two photomultipliers (X2020Q) attached to both sides of the quartz plate. Optical grease (BC630) is applied between the PMTs and the quartz plate in order to achieve good light transmission.

(ii) The Gas Detector (GD) uses a 60 cm long C_4F_{10} gas radiator. The construction of this detector is based on the standard CERN threshold Cherenkov unit. Cherenkov photons are reflected by a 25 μm thick aluminized Mylar foil and focused by a parabolic mirror onto a single photomultiplier, Hamamatsu R2059.

Both Z-detectors were positioned between BPD-2 and BPD-3 (see figure 8). The large refraction index of the quartz radiator of about 1.458 leads to a low Cherenkov threshold momentum of $\approx 0.88\,\mathrm{GeV}/c$ per nucleon. Thus the detector performance is largely independent of the beam momentum in the momentum range relevant for the NA61/SHINE energy scan program. The refraction index of the C_4F_{10} gas at normal conditions is about 1.00142 leading to a Cherenkov threshold momentum of about $17.6\,\mathrm{GeV}/c$ per nucleon. For the momentum of $13A\,\mathrm{GeV}/c$ the lowest acceptable value of the refraction index is ≈ 1.0023 requiring a minimum gas pressure of 1.63 bar.

Both detectors were tested during the 2011 run using the secondary ion beam at $150A\,\mathrm{GeV}/c$. The ADC signals measured in the Quartz and Gas Detectors showed well separated peaks of proton and He beam particles. Both detectors performed well at this momentum, namely the measured width to mean value ratio for the ^{4}He peak was 18–19%. However, it was estimated that at the lowest beam momentum the performance of the GD will deteriorate both in terms of the charge resolution and the material budget (at the sufficiently high gas pressure it is about a factor of 2.5 larger than for the QD). Therefore the QD was used as the Z-detector for the physics data taking with secondary ^{7}Be beams in 2011–2013.

Figure 5 presents Z^2 distributions measured by the QD for secondary ion beams of $13A\,\mathrm{GeV}/c$, and $150A\,\mathrm{GeV}/c$ momentum used in the data taking on $^7\mathrm{Be} + {}^9\mathrm{Be}$ interactions.

3.5 Trigger system

In designing the NA61/SHINE trigger system, particular attention was paid to developing a flexible and robust system capable of handling and selecting different reactions using a variety of beams (pions, kaons, protons, ions) and targets as required by the NA61/SHINE physics programme [1].

The trigger is formed using several of the beam counters listed in table 1, the Cherenkov detectors for beam particle (hadrons or ions) identification, and the PSD calorimeter, as illustrated in figure 8.

The core of the trigger logic is an FPGA (Xilinx XC3s1500) running at 120 MHz embedded in a CAMAC Universal Logic Module, the CMC206 [22]. CAMAC is used for backward compatibility with the legacy NA49 electronics. The trigger logic is divided into three main blocks:

(i) beam logic

(ii) beam particle identification

(iii) interaction logic.

2014 JINST 9 P06005

Up to four different triggers can be run simultaneously with a selectable 12 bit pre-scaler for each trigger. Different trigger configurations are recorded in a pattern unit on an event-by-event basis for off-line selection.

Analog signals from the beam counters are first discriminated with constant fraction and leading edge discriminators before entering a second discriminator, whose role is to shape the logic signals (12 ns width) and convert them to ECL levels, as required by the FPGA trigger logic. These logic signals are also recorded in pattern units on an event-by-event basis for verifying the trigger logic in the analysis of trigger data. The combined use of two discriminators with different output widths prevents also the pile-up in the trigger logic (the length of the output of the first discriminator is around 100 ns, while the length of the second discriminator is 12 ns). Correspondingly, the dead time of the trigger system is around 100 ns, small compared to the dead time gated trigger rate of ≈ 10 Hz.

The simultaneous use of the beam (T_{BEAM}) and interaction triggers (T_{INT}) allows for the direct determination of the interaction probability, P_{INT}:

$$P_{\mathrm{INT}} = \frac{N(T_{\mathrm{BEAM}} \wedge T_{\mathrm{INT}})}{N(T_{\mathrm{BEAM}})},$$

where $N(T_{\mathrm{BEAM}})$ is the number of events which satisfy the beam trigger condition and $N(T_{\mathrm{BEAM}} \wedge T_{\mathrm{INT}})$ is the number of events which satisfy both the beam trigger and interaction trigger conditions.

4 TPC tracking system

The main tracking devices of the NA61/SHINE experiment are four large volume Time Projection Chambers (TPC). Two of them (*Vertex* TPCs: VTPC-1 and VTPC-2) are located in the magnetic field, two others (*Main* TPCs: MTPC-L and MTPC-R) are positioned downstream of the magnets symmetrically to the beamline. In addition a smaller TPC (GAP-TPC) is mounted between the two VTPCs. It is centred on the beamline for measuring particles with the smallest production angles. Also the Low Momentum Particle Detector presented in section 7.2 consist of two small TPC chambers. The TPCs allow reconstruction of over 1000 tracks in a single Pb+Pb interaction. Up to 234 clusters and samples of energy loss per particle trajectory provide high statistics for precise measurements.

The TPCs consist of a large gas volume in which particles leave a trail of ionization electrons. A uniform vertical electric field is established by a surrounding field cage made of aluminized Mylar strips that are kept at the appropriate electric potential by a voltage divider chain. The electrons drift with constant velocity under the influence of the field towards the top plate where their position, arrival time, and total number are measured with proportional wire chambers. In order to achieve high spatial resolution the chamber top plates are subdivided into pads of about one square centimeter area, a total of about 180 000 for all TPC's. From the recorded arrival times of the track signals and the known pixel positions one gets a sequence of 3-dimensional measured points along the particle trajectories.

An overview of the main parameters of the different TPCs is given in table 2.

2014 JINST 9 P06005

Table 2. Parameters of the VTPCs and MTPCs. The pad length in the VTPC-1 equals 16 mm only in the two upstream sectors. In the MTPCs the 5 sectors closest to the beam have narrower pads and correspondingly more pads per padrow.

	VTPC-1	VTPC-2	MTPC-L/R	GAP-TPC
size (L×W×H) [cm]	$250 \times 200 \times 98$	$250 \times 200 \times 98$	$390 \times 390 \times 180$	$30 \times 81.5 \times 70$
No. of pads/TPC	26 886	27 648	63 360	672
Pad size [mm]	$3.5 \times 28(16)$	3.5×28	3.6×40, 5.5×40	4×28
Drift length [cm]	66.60	66.60	111.74	58.97
Drift velocity [cm/μs]	1.4	1.4	2.3	1.3
Drift field [V/cm]	195	195	170	173
Drift voltage [kV]	13	13	19	10.2
Gas mixture	Ar/CO_2 (90/10)	Ar/CO_2 (90/10)	Ar/CO_2 (95/5)	Ar/CO_2 (90/10)
# of sectors	2×3	2×3	5×5	1
# of padrows	72	72	90	7
# of pads/padrow	192	192	192, 128	96

4.1 VTPC, MTPC and GAP-TPC

Each Main TPC has a readout surface at the top of $3.9 \times 3.9\,m^2$ and a height of the field cage of about 1.1 m. It is filled with a gas mixture of Ar/CO_2 in the proportion 95/5. The track signals are read out by 25 proportional chambers providing up to 90 measured points and ionization samples on each particle trajectory. The accuracy of the measurement of the average ionization energy loss for a particle is about 4%.

Each Vertex TPC consists of a gas box with $2.0 \times 2.5\,m^2$ top surface area and 0.67 m depth. The inserted field-cage structures exclude the region of 0.12 m on either side of the beamline in which the particle density in Pb+Pb reactions is so high that trajectories cannot be resolved. A gas mixture of Ar/CO_2 in the proportion 90/10 is employed. The readout is performed by 6 proportional chambers on the top which provide up to 72 measurements and ionization samples on the particle trajectories. More details about the Vertex and Main TPCs can be found in ref. [23].

Between VTPC-1 and VTPC-2 an additional tracking device, the GAP-TPC [24], is located directly on the beamline. It covers the gap left for the beam between the sensitive volumes of the VTPCs and MTPCs. High momentum tracks can be better extrapolated back to the primary vertex using the additional points measured in the GAP-TPC. Particles originating from the primary vertex but measured only in the MTPCs can be better distinguished from conversion electrons faking high momentum tracks outside the magnetic field. Since the beam passes through this detector its material budget was minimized to 0.15% of a radiation length and 0.05% of an interaction length. The design follows that of the other TPCs described above (the schematic layout is shown in figure 11). The electric field in the drift volume is generated by a field cage made from aluminized Mylar strips connected by a resistor chain. The electric field is 10.2 kV over 58.97 cm (173 V/cm) with a resulting drift time of about 50 μs. The support of the Mylar strips is provided by tubes of glass-epoxy with a wall thickness of 100 μm. The drift volume is enclosed by a gas box made of a single layer of 125 μm Mylar. The readout plane consists of 7 padrows with 96 pads each, the pad

2014 JINST 9 P06005

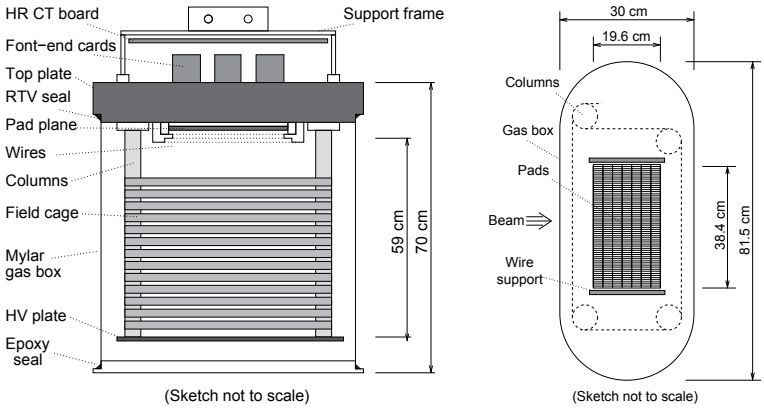

Figure 11. Schematic layout of the GAP TPC: front view (*left*) and bottom view (*right*).

dimensions are 28 mm by 4 mm. The gas composition is Ar/CO_2 (90/10) like in the VTPCs. For the readout three standard TPC front end cards are used together with one concentrator board.

4.2 He beam pipes

He filled beam pipes were installed in April 2011 in the gas volume of the VTPCs in order to reduce the number of δ-electrons by a factor of about 10. This is needed in order to decrease significantly event-by-event fluctuations of the track density in the TPCs and thus reduce systematic uncertainties of fluctuation measurements in nucleus-nucleus collisions. Installation of the pipes necessitated cutting openings in the double wall Mylar envelopes of VTPC-1 and VTPC-2. The openings were drilled using specially developed tools which prevented dust and debris of material from getting into the inner volume of the TPCs. These openings into the gas volume were precisely positioned around the beam axis and were used for gluing the lightweight interface units (200 μm wall thickness carbon fiber rings) providing support for the He beam pipes and ensuring hermetic VTPC volumes. The lightest possible He beam pipe structure was produced that is feasible with present technology. The close-to-normal gas pressure conditions allow to use thin (30 μm) gas-leakage-tight Tedlar polyvinyl fluoride (PVF) film [25] to produce 2.5 m length cylinder envelopes (pipes of 75 and 96 mm diameters), which form the He gas and protective gas volumes. The pipes were made by gluing the Tedlar film to special rigid, light-weight carbon fiber endcaps strengthened with Airex foam [26]. This provides low-mass beam pipe fixation, separation of gases and hermetic sealing. Use of light-weight low-Z materials minimizes the probability of secondary interaction processes. The used materials [25–27] include:

(i) Tedlar polyvinyl fluoride (PVF) film

(ii) Carbon Fiber M55J, $\rho = 1.92\,\mathrm{g/cm^3}$, $X_0 = 25\,\mathrm{cm}$

(iii) Toray and

(iv) Airex foam, $\rho = 0.03\,\mathrm{g/cm^3}$, $X_0 = 1390\,\mathrm{cm}$.

2014 JINST 9 P06005

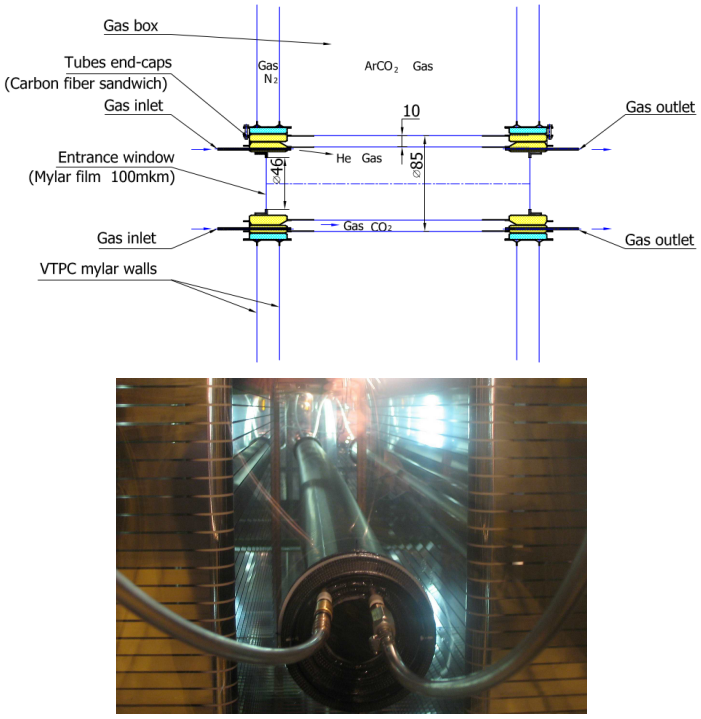

Figure 12. *Top*: schematic layout of the He beam pipe installed in the VTPC-1 gas volume between the two field cages. *Bottom*: the He beam pipe photo.

The construction is gas tight allowing separation of the working gas of the VTPCs from the helium used in the central pipe. In addition, during the operation an inert gas (CO_2) is flushed through the outer envelope of the pipe (the protective gas volume). The He beam pipe installed in the VTPC-1, with gas supply lines connected, is shown in figure 12. A special gas supply system was constructed to maintain the overpressure gradients in the two gas volumes of the pipes with respect to the pressure in the VTPCs. This is mandatory to ensure the mechanical stability of the pipes. The He pipes were tested under working conditions of the VTPCs. They showed good mechanical stability when operating different modes of gas circulation in the VTPCs. No leakage of helium from the central pipes to the outer envelope was observed. The surface of the pipes did not show any excessive charging-up which could distort the drift field in the active VTPC volume. Gas tightness of the fixations of the pipes to the Mylar foils closing the VTPC field cage was tested by monitoring of the oxygen content in the VTPC gas. The oxygen contamination of the working gas decreased to a few ppms during the first 48 hours of purge (see figure 13) and remained constant at this level. The measured level of oxygen impurity after gas stabilization in the VTPCs was the same as that observed during the operation before the installation of the He beam pipes.

2014 JINST 9 P06005

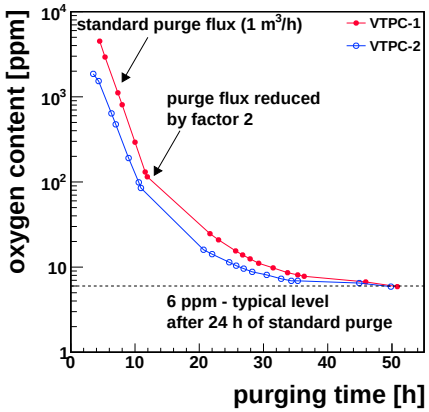

Figure 13. Oxygen level in the VTPC volumes during the gas purging period.

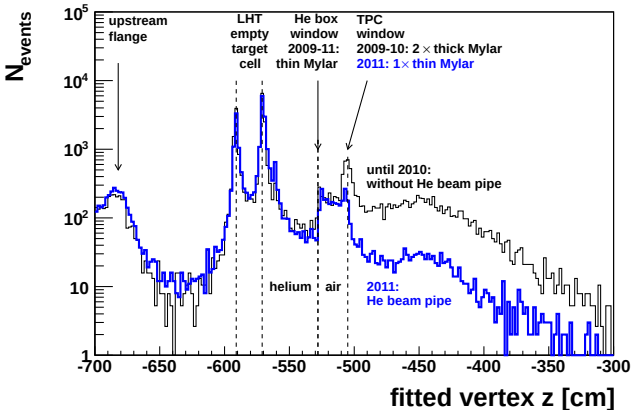

Figure 14. Interaction vertex distribution along the beam axis (data from p+p interactions at 158 GeV/c) before the He beam pipe installation (2009 and 2010 data) and with the He beam pipes installed and filled with helium gas (2011 data).

It is important to mention that the He beam pipe goes in between the two field cages and thus does not distort the drift field. Figure 14 shows the interaction vertex distribution along the beam axis (data for p+p interactions at 158 GeV/c) before the He beam pipe installation (2009 and 2010 data) and with the He beam pipes installed and filled with helium gas (2011 data). Clearly, the He beam pipes reduce the number of background interactions in the volume of the VTPCs by about a factor of 10.

2014 JINST 9 P06005

4.3 Magnets

The two identical super-conducting dipole magnets with a maximum total bending power of 9 Tm at currents of 5000 A have a width of 5700 mm and a length of 3600 mm. Their centres are approximately 2000 mm and 5800 mm downstream of the target. The shape of the magnet yokes is such that the opening in the bending plane is maximized at the downstream end. Inside the magnets a gap of 1000 mm between the upper and lower coils leaves room for the VTPCs. The coils have an iron-free central bore of 2 m diameter. This causes large field inhomogeneities where the minor components reach up to 60% of the central field at the extremities of the active TPC volumes. The magnetic field inside the sensitive volumes of the Vertex TPCs was precisely measured by Hall probes.

The standard configuration for data taking at beam momentum per nucleon of 150 GeV/c and higher is nominally 1.5 T, in the first and 1.1 T in the second magnet. At lower beam momenta the fields are reduced proportional to the beam momentum keeping the ratio of the two fields constant. More details about the magnets can found in ref. [23].

4.4 Gas system and monitoring

The gas in the VTPCs and MTPCs is supplied by four independent gas systems. A schematic drawing of one gas system is presented in figure 15.

Each system recirculates the gas with a compressor at a rate of about 20% of the detector volume per hour, i.e. 0.9 and 3 m^3/h for VTPCs and MTPCs, respectively. Fresh gas is mixed through mass flow controllers from pure Ar and CO_2. In normal operation, the fresh gas is supplied at only 3% detector volume per hour; in purge mode, the full recirculation rate is used. The recirculation flow is controlled by regulating the TPC overpressure to 0.50 ± 0.01 mbar via frequency modulation of the compressors.

Oxygen is cleaned from the detector gas by filter columns containing active Cu-granules chosen for use with the CO_2 gas mixtures. The filters are regenerated after typically 4–6 months operation periods, using Ar/H_2 (93/7) mixture at 200°C. Filters also absorb water contamination in the gas. Water content is reduced to 10–20 ppm during the first two weeks after regeneration, and several tens of ppm afterwards.

Two bypass lines allow to start recirculation with the TPC isolated, and to replace the oxygen filter without stopping the system. In case of compressor failure a safety bubbler protects the TPC from overpressure.

The VTPC and MTPC walls are made of two layers of 125 μm Mylar. Nitrogen is flushed between the layers, to prevent air from contaminating the TPC gas by diffusion through the walls, or a potential leak.

The monitoring of gas quality is one of the major tasks of the NA61/SHINE TPC gas system. Small amounts of gas can be directed to measuring units. Non-linearities and calibration drift of the flow controllers are followed by online measurements of drift velocity and gas amplification, as the required setting accuracy is beyond the specifications of the flow regulators. It is possible to measure the fresh gas mixture (point A in figure 15), and the gas from the TPC (point B). Each of the gas systems has a system of a drift velocity monitor and four gas amplitude monitors. Drift velocity is measured in a drift detector using the drift time difference from a pair of ^{241}Am

2014 JINST 9 P06005

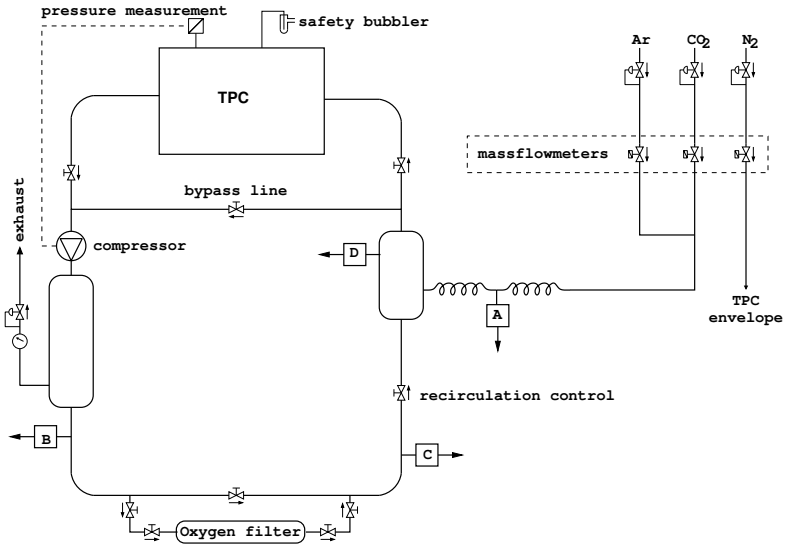

Figure 15. Schematic layout of one of the four TPC gas recirculation systems. The gas flow direction is marked by arrows next to the valves. The letters A, B, C and D mark points where small amounts of the gas can be directed to the measuring devices.

α sources at 10 cm distance. The gas amplification is checked in the amplitude monitors. The amplitude monitors measure the signal from ^{55}Fe photons in a proportional tube. The mixing and monitoring equipment is temperature stabilized to better than 0.1°C.

Oxygen and water contamination in the TPC gas (point B), filtered gas (point C), and the input gas mixture (point D) can be measured with two pairs of O_2/H_2O sensors. Gas purities of 2–5 ppm oxygen and about 20–100 ppm water are typically achieved.

The gas circulation is typically started 1–2 weeks before the beginning of detector operation. First, the detector is flushed with fresh gas for 2 days in the purge mode. Due to limited precision of the input flow meters the gas mixtures needs several days to stabilize after purge. The drift velocity approaches a stable value exponentially with a time constant of approximately 28 hours for the VTPCs and 35 hours for the MTPCs (see figure 16).

The drift velocity decreases by about 1% after purge which is attributed to out-gassing of the detector material. This is compensated by a slight increase of the argon content. Also, when the water contamination increases, the drift velocity decreases; the effect is on the order of 1% for the typical water content of several tens of ppm. The change is slow (about 0.0002 cm/μs per day) and is taken into account in the drift velocity calibration based on the online drift velocity measurements and more precise off-line drift velocity determinations.

The GAP-TPC with a volume of only about 150 l uses a much simpler gas system. About 20 l/h of fresh gas mixture is flushed through this detector. The gas coming out from the GAP-TPC is also passed through a drift velocity monitor.

2014 JINST 9 P06005

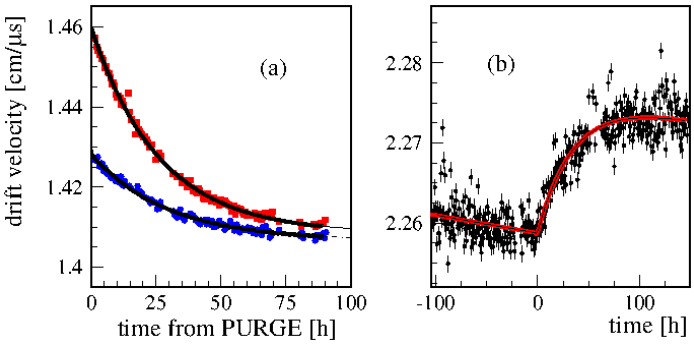

Figure 16. *Left*: drift velocity after purge measured for VTPC-1 (circles) and VTPC-2 (squares). The curves show the exponential dependence fitted to the data. *Right*: change of the drift velocity in the MTPCs after the reduction of CO_2 contents by 0.1% at time $t = 0$. Note that the vertical scale is expanded by a factor 2 with respect to the left plot.

The gas composition is Ar/CO_2 90/10 in the VTPCs and GAP-TPC, and 95/5 in the MTPCs. The higher argon content in the MTPCs is required to obtain higher drift velocity necessary to read out the longer drift length (the safety limit on the drift high voltage is about 20 kV). Typical drift velocities are 1.4 cm/μs in the VTPCs, 2.3 cm/μs in the MTPCs and 1.3 cm/μs in the GAP-TPC.

4.5 TPC Front End Electronics

The electron trace of the track ionization in the TPC gas drifts in the electric field to the amplification planes of the TPCs, which are operated in the proportional amplification range. After passing through the gating grid and the cathode grid, the drifted electrons get amplified by gas electron multiplication on the sense wires of the field and sense wire plane by about $\approx 5 \cdot 10^4$. The disappearance of this amplified electron signal on the sense wires capacitively induces an opposite-sign signal on the two-dimensionally segmented pad plane just behind the field and sense wire plane. Readout of the charge signal of the pads in consecutive short time intervals provides 3 dimensional information on the particle trajectories traversing the the TPCs. The electronic readout of the pads is performed by the TPC Front End Electronics (FEE).

One FEE channel is dedicated to each readout pad, pre-amplifies the signal and stores the analog charge of a given time sample in a capacitor array. 256 time slices with 200 ns time bins are used. It is also possible to use 512 time slices with 100 ns time bins. The time sampling is driven by a global clock for the full TPC system in order to eliminate relative phase shifts. 32 channels are handled by each FEE card, thus the full TPC system comprises about 6000 TPC FEE cards. After the analog charges are stored in the capacitor arrays their digitization is performed via a Wilkinson ADC on the card, and the digitized charge values are forwarded to the readout electronics.

The TPC FEE system [28, 29] was inherited from NA49 along with the TPC system.

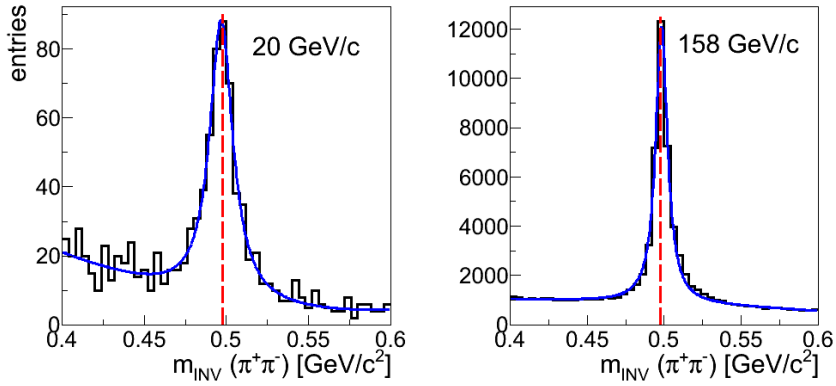

Figure 17. Invariant mass distribution of reconstructed K^0_S candidates in p+p interactions at 20 GeV/c (*left*) and 158 GeV/c (*right*). The curves show the result of a fit with the sum of a Lorentzian function for the signal and a second order polynomial for the background. The fitted peak positions are $496.8 \pm 0.6\,\mathrm{MeV}/c^2$ and $498.3 \pm 0.1\,\mathrm{MeV}/c^2$, respectively. The FWHM values are $17 \pm 2\,\mathrm{MeV}/c^2$ and $9.3 \pm 0.1\,\mathrm{MeV}/c^2$, respectively. The red dashed vertical line marks the PDG value of $497.6\,\mathrm{MeV}/c^2$. The magnetic fields were set for a total bending power of 1.1 Tm and 9 Tm at 20 GeV/c and 158 GeV/c, respectively.

4.6 Physics performance

Several examples of the physics performance of the TPC system are presented in this section, which were obtained from calibrated data. Details on the calibration procedure can be found in ref. [31].

The quality of measurements was studied by reconstructing masses of K^0_S particles from their V^0 decay topology. As an example the invariant mass distributions of K^0_S candidates found in p+p interactions at 20 GeV/c and 158 GeV/c are plotted in figure 17. The measured peak positions $496.8\,\mathrm{MeV}/ \pm 0.6\,\mathrm{MeV}/c^2$ and $498.3 \pm 0.1\,\mathrm{MeV}/c^2$ are in reasonable agreement with the PDG value $m_{K^0_S} = 497.6\,\mathrm{MeV}/c^2$.

The track reconstruction efficiency and resolution of kinematic quantities were studied using a GEANT3 simulation of the detector [30]. Estimates were obtained by matching of generated tracks to their reconstructed partners. As examples, the reconstruction efficiency as a function of rapidity y and transverse momentum p_T for negatively charged pions produced in p+p interactions at 20 GeV/c and 158 GeV/c is shown in figure 18. The measuring resolution of pion rapidity y and transverse momentum p_T is illustrated in figure 19. The resolution was calculated as the FWHM of the distribution of the difference between the generated and reconstructed y and p_T. Results presented in figures 18 and 19 were obtained for negatively charged pions passing the event and track selection criteria used in the data analysis [32], including rejection of the azimuthal angle regions where the reconstruction efficiency drops below 90%.

The specific energy loss in the TPCs for positively (*right*) and negatively (*left*) charged particles as a function of momentum measured for p+p interactions at 80 GeV/c is shown in figure 20. Curves show parametrizations of the mean dE/dx calculated for different particle species.

2014 JINST 9 P06005

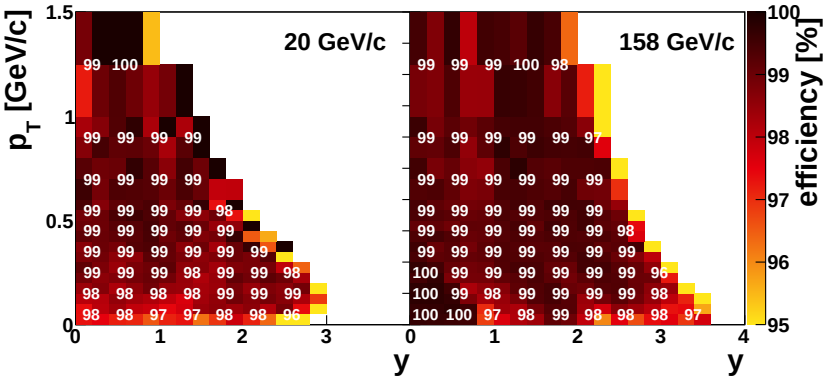

Figure 18. The reconstruction efficiency of negatively charged pions produced in p+p interactions at 20 GeV/c (*left*) and 158 GeV/c (*right*) as a function of pion rapidity and transverse momentum. The magnetic fields were set for a total bending power of 1.1 Tm and 9 Tm at 20 GeV/c and 158 GeV/c, respectively.

5 Time of Flight systems

Since particle identification based only on energy loss measurement can not be performed in the crossover region of the Bethe-Bloch curves, NA61/SHINE also uses additional and independent particle identification by Time of Flight (ToF) detectors. The ToF-L and ToF-R detectors were inherited from NA49. In order to extend the identification of NA61/SHINE to satisfy neutrino physics needs, a new forward detector (ToF-F) was constructed. It is placed between the ToF-L/R, just behind the MTPCs.

The particle's mass squared is obtained by combining the information from the particle's time of flight, *tof*, with the track length, l, and momentum, p, measured in the TPCs:

$$m^2 = p^2 \left[\frac{c^2 \, (tof)^2}{l^2} - 1 \right] . \tag{5.1}$$

5.1 ToF-L, ToF-R

Two walls, ToF-L(eft) and ToF-R(ight), of 4.4 m^2 total surface (see figure 21) are placed behind the MTPCs. The track length of particles produced in the target is about 14 meters. Each wall contains 891 individual scintillation detectors with rectangular dimensions, each having a single photomultiplier tube glued to the short side. The scintillators have a thickness of 23 mm matched to the photocathode diameter, a height of 34 mm and horizontal width of 60, 70 or 80 mm, with the shortest scintillators positioned closest to the beamline and the longest on the far end. The operating voltage for the PMTs in the ToF-L is about 1600 V and in the ToF-R is around 1300 V. For the ToF-L, photomultiplier signals enter constant-fraction discriminator modules (CFD, KFKI custom made), housed in VME crates (WIENER) where the analog signals are split before being passed through the actual discriminator units. One output signal is directly sent to FASTBUS analog-to-digital converters (96 channel ADC LeCroy 1885F) while the other signal passes first

2014 JINST 9 P06005

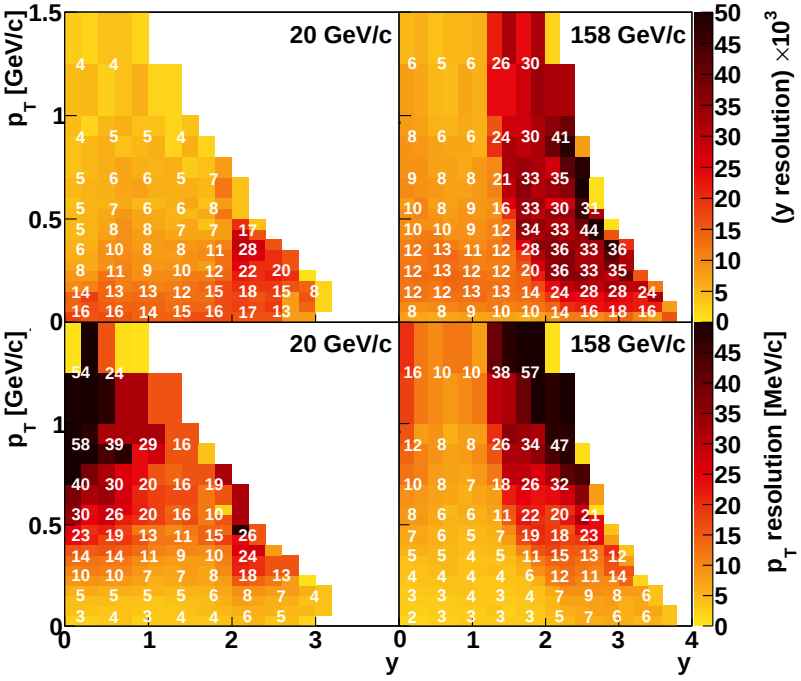

Figure 19. Resolution of rapidity (*top*, scaled by 10^3) and transverse momentum (*bottom*) measurements for negatively charged pions produced in p+p interactions at 20 GeV/c (*left*) and 158 GeV/c (*right*) as a function of pion rapidity and transverse momentum. Here resolution was calculated as the FWHM of the distribution of the differences betweee the generated and reconstructed y and p_T. The magnetic fields were set for a total bending power of 1.1 Tm and 9 Tm at 20 GeV/c and 158 GeV/c, respectively.

through the discriminator unit and is then sent to time-to-digital converters (64 channel FASTBUS TDC LeCroy 1775A). For ToF-R the PMT signals are first split, then one line is sent to an ADC (96 channel ADC LeCroy 1882F) while the other line goes into a FASTBUS CFD (Struck DIS Str138) followed by a TDC (64 channel FASTBUS TDC LeCroy 1772A). The start signal for the TDCs is provided by the S11 PMT of the upstream S1 beam counter (scintillator) while the stop signal comes from the CFDs if their input is above a threshold.

The calibration procedure is based on extrapolation of the tracks reconstructed in the MTPCs into the area of the ToF detectors, identifying scintillators they extrapolate to and checking for appropriate signals in the corresponding TDC and ADC channels. Afterwards detailed corrections are performed depending on charge deposition and relative position of the incident particle in each scintillator. Corrections for the position of the main interaction (in case of thick targets) and position of the beam particle in the S1 counter are also done.

The overall time resolution of the ToF-L/R system is estimated based on the distribution of the differences between the measured time of flight for particles identified as pions and that predicted

2014 JINST 9 P06005

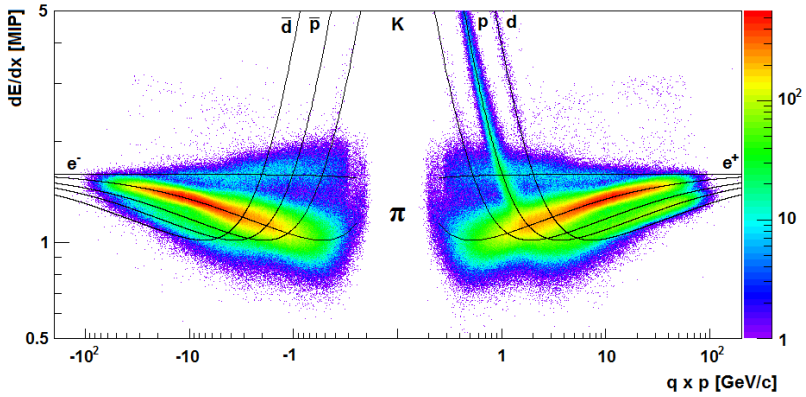

Figure 20. Specific energy loss in the TPCs for positively (*right*) and negatively (*left*) charged particles as a function of momentum measured for p+p interactions at 80 GeV/c. Curves show parametrizations of the mean dE/dx calculated for different particle species.

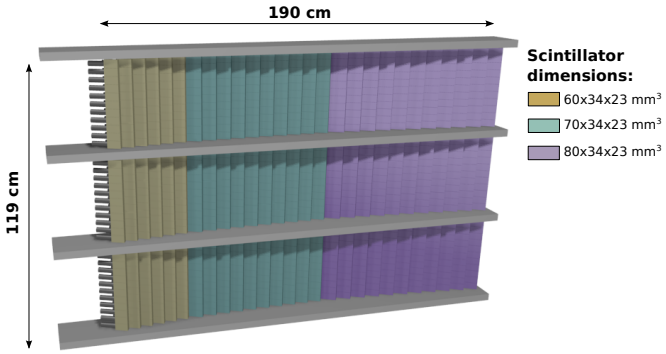

Figure 21. Schematic layout of scintillators in the ToF-R detector.

from the measured momentum and trajectory assuming the pion mass. The distribution can be described by a Gaussian where, in p+p and Be+Be collisions, a standard deviation of 95 ps was observed for ToF-L, while a standard deviation of 80 ps was observed for ToF-R. This value for the time resolution includes all contributions to the *tof* measurement (the intrinsic ToF detector resolution as well as the start detector resolution, uncertainties in tracking, etc.).

This resolution allows to separate pions and kaons for momenta up to 3 GeV/c (up to 5 GeV/c if *tof* information is used along with dE/dx information) and pions and protons for even higher momenta. Figure 22 (*top*, *left*) shows mass squared as a function of particle momentum for p+p interactions at 80 GeV/c. The standard deviation of the m^2 distribution is plotted as a function of momentum in figure 22 (*bottom*, *left*).

2014 JINST 9 P06005

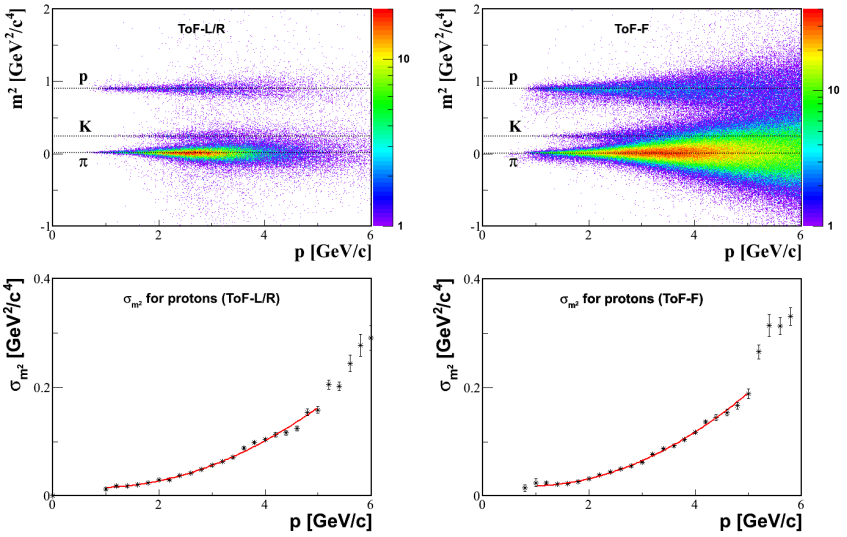

Figure 22. *Top*: mass squared versus momentum measured by ToF-L/R (*left*) and ToF-F (*right*) detectors for particles produced in p+p interactions at 80 GeV/c. The lines show the expected mass squared values for different hadrons. *Bottom*: the standard deviation of the m^2 distribution as a function of particle momentum for the ToF-L/R (*left*) and the ToF-F (*right*).

Due to aging of the electronics two upgrades are foreseen. The HV supply will be partially replaced and an upgrade of the readout electronics is planned. This should, modernize the whole system, ensure its long-term functioning, and also improve the quality of the obtained *tof* information, primarily the resolution.

5.2 ToF-F

The NA61/SHINE data taking for the T2K neutrino oscillation experiment requires particle identification in a phase space region which is not covered by the ToF-L/R. When operating at the T2K proton beam at 31 GeV/c, a large fraction of the tracks are produced by low-momentum particles which exit the spectrometer between the ToF-L and ToF-R. An additional time of flight detector, the forward ToF (ToF-F), was therefore constructed to provide full time of flight coverage of the downstream end of the MTPCs (see figure 1).

The ToF-F consists of 80 scintillator bars oriented vertically (see figure 23). The bars were tested and mounted in groups of 10 on independent frames (modules) out of which half were placed on the left side and half on the right side of the detector. The size of each scintillator is $120 \times 10 \times 2.5\,\mathrm{cm}^3$. They are staggered with 1 cm overlap to ensure full coverage in the ToF-F geometrical acceptance. This configuration provides a total active area of $720 \times 120\,\mathrm{cm}^2$. Each scintillator bar is read out on both sides with 2″ photomultipliers Fast-Hamamatsu R1828, for a total of 160 readout channels. The scintillators are plastic scintillator (*Bicron BC-408*) with

2014 JINST 9 P06005

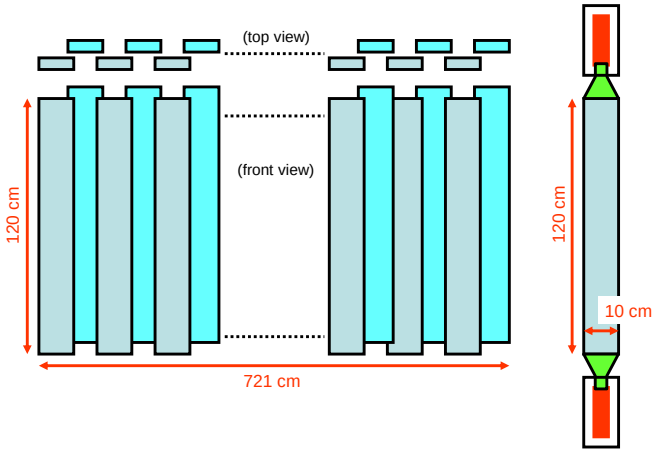

Figure 23. The schematic layout of scintillators in the ToF-F detector.

a scintillation rise time of 0.9 ns, a decay time of 2.1 ns and attenuation length of 210 cm. Their maximal emission wavelength is about 400 nm perfectly matching the PMT spectral response. Fish tail PMMA (Poly methyl methacrylate) light-guides were glued on both ends for the readout. The bars and light-guides were wrapped in aluminium foils to ensure light reflection towards the light-guide and covered with black plastic foils and tape. In order to ensure proper optical contact between the PMTs and the light-guides a 3 mm thick silicone cylinder matching the diameter of the PMT and light-guide is inserted at the interface.

Most of the electronics for the ToF-F were inherited from the two NA49 Grid ToFs [33] which were not used since their acceptance coverage is marginal. Each PMT channel is operated near 1700 V supplied by LeCroy1461 independent 12-channel high voltage (HV) cards. The analog signals are transported from the ToF to the counting house by 26 m RG58 50 Ω coaxial cables. In order to obtain fast logic signals and not be influenced by the variations in amplitude of the PMT response the cables are plugged into Constant Fraction Discriminators (16-channel KFKI CFD5.05 VME module). At the input these include an internal passive divider of 1:3 to provide the signals for the integrated charge and time measurements, respectively, and the necessary delay lines at their output. In order to minimize the crosstalk of the neighbouring channels an appropriate order is chosen between the PMT outputs and the CFD inputs. The output signals of the CFDs of the PMT-channels serve as "stop" signals for the time of flight measurements. The start signal is provided by the fast beam counter S1 of the central trigger system. The time measurement is carried out by LeCroy FASTBUS Time-to-Digital Converter (TDC) units digitizing the time in 12 bits dynamic range with a sampling time of 25 ps. The analog signals of the PMTs are converted by LeCroy Analog-to-Digital Converter (ADC) units into 12 bits. The time measurement, t, has an offset, t_0, which is specific to each channel as it depends on cable length, PMT gain or CFD response. t_0 was therefore carefully adjusted on a channel by channel basis by first assuming that all produced particles are pions and shifting the mean value of the $tof = t - t_\pi$ distribution accordingly. In a first

2014 JINST 9 P06005

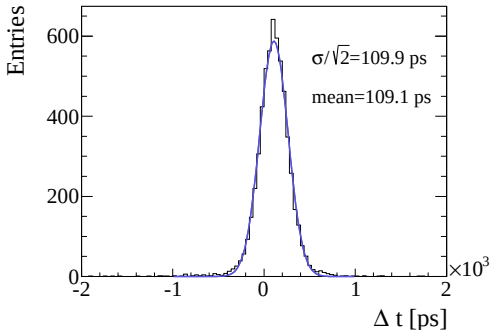

Figure 24. Distribution of the difference between a particle's time of flight measured independently by the overlapping scintillator bars of the ToF-F detector. The width of the distribution is about 155 ps, indicating a *tof* resolution of about 110 ps for a single measurement.

iteration, this method allows to discriminate pions from protons and was then repeated by selecting only pions.

The mass-squared distribution and its standard deviation as a function of momentum are presented in figure 22 (*right*). The intrinsic resolution of the ToF-F was also determined (see figure 24). This was achieved by selecting particles that hit the region where the scintillators overlap and plotting the time difference between the two signals. The Gaussian fit to the distribution gives a resolution $\sigma_{tof} = \frac{155}{\sqrt{2}}\,\text{ps} \approx 110\,\text{ps}$.

6 Projectile Spectator Detector

The development and construction of the forward hadron calorimeter was one of the most important upgrades of the NA61/SHINE experimental setup. This calorimeter is called the Projectile Spectator Detector (PSD). The purpose of the calorimeter is the measurement of projectile spectator energy in nucleus-nucleus collisions. The PSD is used to select central (with a small number of projectile spectators) collisions at the trigger level. Moreover, the precise event-by-event measurement of the energy carried by projectile spectators enables the extraction of the number of interacting nucleons from the projectile with the precision of one nucleon. The high energy resolution of the PSD is important for the study of fluctuations in nucleus-nucleus collisions which are expected to be sensitive to properties of the phase transition between the quark-gluon plasma and hadron-resonance matter. Namely, the PSD provides the precise control over fluctuations caused by the variation of the number of interacting nucleons and thus excludes the "trivial" fluctuations caused by variation of the collision geometry. Basic design requirements of the PSD are good energy resolution, $\sigma_E/E < 60\%/\sqrt{E(\text{GeV})}$, and good transverse uniformity of this resolution. The PSD is a fully compensating modular lead/scintillator hadron calorimeter [34, 35] and meets these requirements.

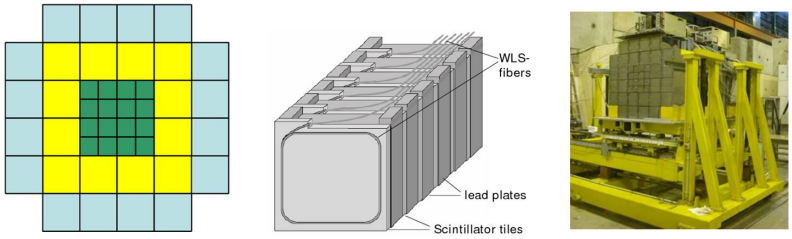

Figure 25. The PSD: schematic front view (*left*), schematic view of single module (*centre*) and the fully assembled detector (*right*).

6.1 Calorimeter design

The PSD calorimeter consists of 44 modules which cover a transverse area of $120 \times 120\,\mathrm{cm}^2$. A schematic front view of the PSD is shown in figure 25 (*left*). The central part of the PSD consists of 16 small modules with transverse dimension of $10 \times 10\,\mathrm{cm}^2$ and weight of 120 kg each. Such fine transverse segmentation decreases the spectator occupancy in one module and improves the reconstruction of the reaction plane. The outer part of the PSD consists of 28 large $20 \times 20\,\mathrm{cm}^2$ modules with a weight of 500 kg each.

Each module, schematically shown in figure 25 (*centre*), consists of 60 pairs of alternating lead plates and scintillator tiles with 16 mm and 4 mm thickness, respectively. The stack of plates is tied together with 0.5 mm thick steel tape and placed in a box made of 0.5 mm thick steel. Steel tape and box are spot-welded together providing appropriate mechanical rigidity. The full length of the modules corresponds to 5.7 nuclear interaction lengths.

Light readout is provided by Kuraray Y11 WLS-fibers embedded in round grooves in the scintillator plates. The WLS-fibers from each longitudinal section of 6 consecutive scintillator tiles are collected together in a single optical connector at the end of the module. Each of the 10 optical connectors at the downstream face of the module is read out by a single photodiode. The longitudinal segmentation into 10 sections ensures good uniformity of light collection along the module and delivers information on the type of particle which caused the observed particle shower. Ten photodetectors per module are placed at the rear side of the module together with the front end electronics. A photograph of the fully assembled calorimeter is shown in figure 25 (*right*). In order to fit the PSD transverse dimensions to the region populated by spectators the distance between the NA61/SHINE target and the calorimeter is increased from 17 m to 23 m with increasing collision energy. Interactions of spectators upstream of the PSD were minimized by the installation of a helium tube of length 5.5 m and diameter 125 cm between the upstream PSD face and the hut housing the MTPCs. The entrance and exit Mylar windows of the tube had a thickness of about 125 μm. This tube was inserted for data taking with ion beams of momenta larger than 40A GeV/c when the distance between the target and the PSD was 23 m.

6.2 PSD photodetectors

The longitudinal segmentation of the calorimeter modules requires 10 individual photodetectors per module for the signal readout. Silicon photomultipliers SiPMs or micro-pixel avalanche pho-

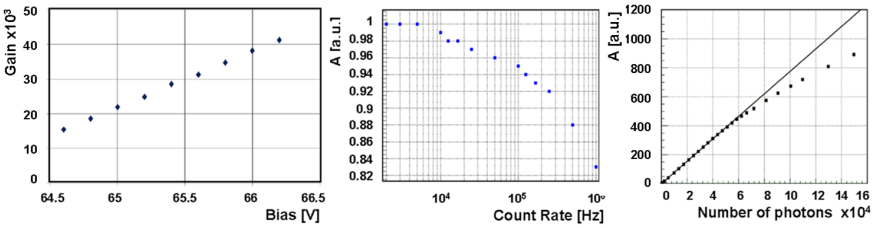

Figure 26. Performance of MAPD-3A photodiodes: dependence of gain on the bias voltage (*left*), dependence of signal amplitude (in arbitrary units) on the count rate capability (*centre*) and on the number of incident photons (*right*).

2014 JINST 9 P06005

todiodes, MAPDs [36, 37] are an optimum choice due to their remarkable properties such as high internal gain, compactness, low cost and immunity to the nuclear counter effect. Moreover, forward hadron calorimeter applications have some specific requirements such as large dynamic range and linearity of the photodetector response to intense light pulses. However, the dynamic range and linearity of MAPDs are limited by the finite number of pixels. Most of the existing types of MAPD with individual surface resistors have a pixel density of 10^3 pixels/mm^2. Such a limited number leads to serious restrictions of MAPD applications in calorimetry, where the number of detected photons is comparable and even larger than the pixel number. The effect of saturation, when a few photons hit the same pixel, leads to significant non-linear MAPD response to light pulses with high intensity. Evidently, the MAPD has linear response only if the number of pixels is much larger than the number of incident photons. This feature represents a disadvantage of MAPDs compared to the traditional PMTs. However, this drawback is essentially reduced for MAPDs with individual micro-well structure [36], for which a pixel density of $10^4/\text{mm}^2$ and higher is achievable. The above considerations motivated the choice of photodiodes of type MAPD-3A produced by Zecotek Photonics Inc. (Singapore) [37] for the readout of the PSD hadron calorimeter. These MAPDs have a pixel density of 15000/mm^2. Their 3×3 mm^2 active area fits well the size of the WLS-fiber bunch from one longitudinal section of the PSD modules and provides a total number of pixels of more than 10^5 in a single photodetector.

The MAPD-3A photon detection efficiency (PDE) for the Y11 WLS-fiber emission spectrum reaches 15% at 510 nm and is similar to the performance of PMTs. The operation voltage for different samples of MAPD-3A detectors ranges from 65 V to 68 V. The maximum achieved gain is 4×10^4, see figure 26 (*left*).

Since the PSD calorimeter has no beam hole to ensure maximum acceptance for the spectators, the central part of the PSD is exposed to ion beams with intensities up to 10^5 Hz. The average amplitude in one longitudinal section of a PSD module is expected to be about 1500 photoelectrons. Therefore, an important requirement for the calorimeter readout is a high count rate capability, at least in the central region. In particular, the recovery time of the selected MAPD-3A photodiode must be fast enough to deliver stable amplitudes at signal frequencies up to 10^5 Hz. To check the count rate capability of the MAPD-3A the dependence of its amplitude on the frequency of light pulses was measured. The stability of the amplitude of the pulses at different operation frequencies

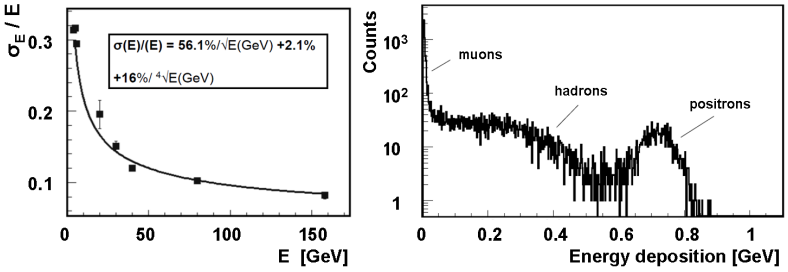

Figure 27. *Left*: energy resolution, σ_E/E, of the tested PSD prototype as a function of hadron beam energy. The solid line is a fit to the experimental data points by the function shown in the inset. *Right*: energy spectrum measured in the first section of the central module for a 30 GeV hadron beam containing a fraction of muons and positrons.

of the light emitting diode was checked by a normal PMT. The obtained behavior of the amplitude produced by the MAPD-3A is presented in figure 26 (*centre*). As seen, the MAPD-3A amplitude would drop about 5% for the maximum beam intensity foreseen.

In order to check the photodetector linearity, measurements of MAPD amplitudes were performed with light pulses of different intensity. The number of incident photons was determined by a reference photodiode with known quantum efficiency and gain equal to one. The dependence of the MAPD amplitude on the number of incident photons is shown in figure 26 (*right*). As seen, the MAPD linearity is preserved for light pulses with number of photons up to 6×10^4. Taking into account the different photon detection efficiencies of about 25% for the tested MAPD (with the same pixel density as the MAPD-3A type), the linear response is expected for amplitudes up to 15000 photoelectrons.

The reported comprehensive studies confirm that the selected MAPD-3A photodetectors satisfy the requirements of the NA61/SHINE experiment. At present, 440 MAPD-3A detectors are installed in the 44 PSD modules and show stable operation during data taking for calibration and physics with beryllium and proton beams.

6.3 Performance of the PSD calorimeter

In order to check the performance of the calorimeter, several tests were performed with hadron beams of various momenta. During the first stage of the R&D (in 2007) a PSD module array of nine small modules (3×3 array) was assembled and tested in the H2 beamline using hadron beams of 20–158 GeV/c momentum. The calibration of all readout channels was done with a muon beam. The energy resolution of the tested array was estimated from data taken with the hadron beams.

The dependence of the measured energy resolution, σ_E/E, on the pion energy is shown in figure 27 (*left*).

The tested prototype with $30 \times 30\,\mathrm{cm}^2$ transverse size is too small to contain the entire hadron shower. Therefore, a non-negligible lateral shower leakage is expected. Monte Carlo simulations confirm that about 16% of the hadron shower energy escapes from the tested array. The influence of shower leakage on the energy resolution was studied in refs. [38, 39], where a third term in

2014 JINST 9 P06005

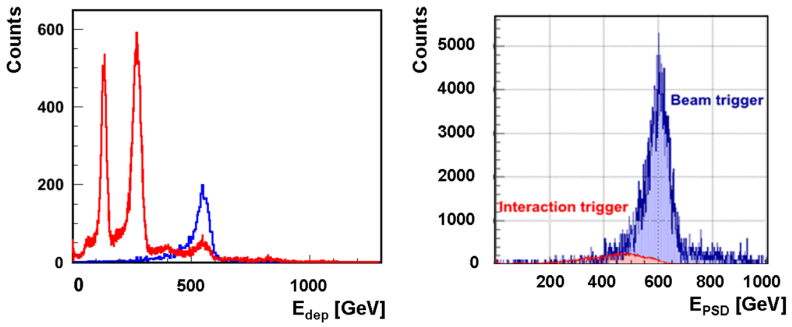

Figure 28. *Left*: PSD energy distributions for the secondary ion beam at 75*A* GeV/c with and without selection of the ^{7}Be ions by the Z-detector. *Right*: PSD energy distributions recorded during the data taking for ^{7}Be + ^{9}Be interactions at 75*A* GeV/c. Spectra are shown for the beam trigger (blue) and for the interaction trigger (red) events.

addition to the stochastic and constant terms was added in the parameterization of the resolution. The fit of the experimental data with the three-term formula, assuming a fixed leakage term of 16%, gives the coefficient of the stochastic term equal to 56.1% and of the constant term equal to 2.1%. The non-zero constant term might be an indication that the selected lead/scintillator sampling does not provide full compensation.

The spectrum of deposited energy in the first section of the central module exposed to the 30 GeV/c positively charged H2 beam is shown in figure 27 (*right*). The right-side peak in the spectrum corresponds to full positron energy absorption in the first longitudinal section which can be regarded as an electromagnetic calorimeter with coarse sampling. Due to the large thickness of lead absorber (96 mm) compared to the scintilator tiles (24 mm) most of the positron energy is absorbed in the lead and only about 0.7 GeV is deposited in the scintillator plates. As a consequence, the energy resolution for positrons at 30 GeV/c is about 6.5%.

During the 2011–2013 data taking for ^{7}Be + ^{9}Be collisions the PSD was also used in the trigger for online rejection of the most peripheral events. As a secondary ^{7}Be beam was used other ions were also present in the beam. The distribution of the energy deposited in the calorimeter by 75*A* GeV/c beam ions is shown in figure 28 (*left*) without cut (red) and with cut (blue) on the ^{7}Be peak in the amplitude distribution of the Z-detector. Clear identification of ^{7}Be ions in the fragmented beam is seen here as well as contamination of deuteron and helium ions. Figure 28 (*right*) shows the PSD energy spectra recorded during the data taking for ^{7}Be + ^{9}Be collisions at 75*A* GeV/c. Spectra are shown for the beam trigger (blue) and interaction trigger (red).

Figure 29 (*top*) shows the measured energy of 158 GeV/c protons as a function of the module number on which the beam was centred. Histograms and curves in figure 29 (*top*) distinguish different energy reconstruction methods by colour. Red corresponds to the energy sum of all PSD modules, while blue is for the sum of the corresponding clusters of modules around the beam spot. As seen, the mean values of reconstructed energies are close to the real beam energy in both cases.

2014 JINST 9 P06005

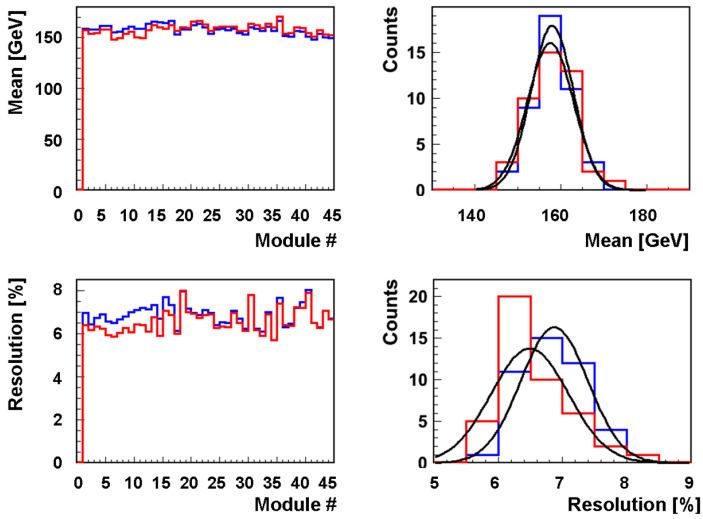

Figure 29. Mean values of reconstructed incident 158 GeV/c proton energy in the PSD modules (*top left*) and distributions of mean values for the 44 modules (*top right*). Energy resolution, σ_E/E, for 158 GeV/c protons (bottom left) and distributions of resolution for the 44 modules (*bottom right*).

Figure 29 (*bottom*) presents the energy resolution, σ_E/E, obtained for each of the 44 modules from the scan with 158 GeV/c protons. The small variations in the energy resolution can be explained by the precision of the energy calibration. These results are consistent with the prototype tests and with the MC simulations.

7 Targets and LMPD

The targets used by NA61/SHINE are positioned upstream of the VTPC-1 and centred at $z \approx -581$ cm. In data taking on p+Pb interactions the target was surrounded by the LMPD detector.

7.1 Targets

For data taking on p+p interactions the liquid hydrogen target (LHT) of 20.29 cm length (2.8% interaction length) and 3 cm diameter was placed 88.4 cm upstream of the VTPC-1. The target was filled with para-hydrogen obtained in a closed-loop liquefaction system which was operated at 75 mbar overpressure with respect to the atmosphere. At the atmospheric pressure of 965 mbar the liquid hydrogen density is $\rho_{\mathrm{LH}} = 0.07$ g/cm^3. The boiling rate in the liquid hydrogen was not monitored during the data taking and thus the liquid hydrogen density is known only approximately. Data taking with inserted and removed liquid hydrogen in the LHT was alternated in order to calculate a data-based correction for interactions with material surrounding the liquid hydrogen. The density of gaseous hydrogen ρ_{GH} present in the target after removal of liquid hydrogen was estimated from the ratio of high multiplicity events observed in a small fiducial volume around the

target centre for data taken with inserted and removed liquid hydrogen. The density ratio ρ_{GH}/ρ_{LH} varied within the range 0.4–0.6%. The typical absolute uncertainty of this ratio is 0.1 at 40 GeV/c, less at higher and more at lower beam momenta. This indicates that the operational conditions of the LHT varied during the data-taking period.

For data taking on ^{7}Be + ^{9}Be collisions in the period 2011–2013 two beryllium targets were used. Their density was $\rho = 1.85\,\mathrm{g/cm^3}$ at 20°C and dimensions were $2.5\,(\mathrm{W}) \times 2.5\,(\mathrm{H}) \times 1.2\,(\mathrm{L})\,\mathrm{cm^3}$ and $2.5\,(\mathrm{W}) \times 2.5\,(\mathrm{H}) \times 0.3\,(\mathrm{L})\,\mathrm{cm^3}$. The targets consisted of more than 99.4% ^{9}Be. The most abundant contaminant were oxygen nuclei (about 0.4%). The Be targets were placed in an aluminium container filled with atmospheric pressure helium gas.

For data taking on p+Pb collisions a special thin Pb target disc was used in order to reduce in-target absorption of slow protons which are measured by the LMPD and are used for event centrality tagging. Two different target thicknesses, 0.5 mm and 1 mm, were used to allow an experimental study of in-target absorption of slow protons. The transverse shape of the target was circular, with a diameter of 1 cm. The target material purity was 99.98% lead with natural isotope composition (52.4% ^{208}Pb, 22.1% ^{207}Pb, 24.1% ^{206}Pb, 1.4% ^{204}Pb). The target density was $11.34\,\mathrm{g/cm^3}$ at 20°C with a molar mass of 207.2 g/mol. The target disc was placed in a Tedlar [25] foil container filled with atmospheric pressure helium gas in order to reduce background of off-target collisions in the vicinity of the target. The target was removable from the beamline using a pneumatic piston for reference data taking with the target removed needed to estimate background due to off-target interactions.

For π+C measurements at 158 and 350 GeV/c a thin graphite target of dimensions $2.5\,(\mathrm{W}) \times 2.5\,(\mathrm{H}) \times 2\,(\mathrm{L})\,\mathrm{cm^3}$ and density $\rho = 1.84\,\mathrm{g/cm^3}$, placed in an aluminium container filled with helium gas, was employed by NA61/SHINE. The same target was used for hadro-production measurements of interest for the T2K neutrino oscillation experiment in Japan. In these measurements information about primary interactions of protons on carbon was extracted. The thickness of this target along the beam axis was equivalent to about 4% of a nuclear interaction length (λ_I).

For hadro-production measurements also a thick graphite target, a replica of the T2K target, was used. It consists of a 90 cm long rod with a radius of 1.3 cm and a density of $\rho = 1.83\,\mathrm{g/cm^3}$. The replica and the actual target of T2K are shown in figure 30. The upstream part of the graphite target is surrounded by aluminium flanges which are inserted into a target holder. Three screws in the target holder allow to align the target parallel to the beam axis. The target thickness along the beam axis is equivalent to about 1.9 interaction lengths. The downstream face of the replica target was placed at around 50 cm from VTPC-1. Hadro-production measurements taken with the T2K replica target allow to constrain the contributions from primary and secondary interactions within the target (for details see [40]).

7.2 Low Momentum Particle Detector

In hadron-nucleus interactions the collision centrality can be deduced from the number of emitted low momentum protons (the so-called grey protons). For this purpose a special detector, the Low Momentum Particle Detector (LMPD), was constructed [41]. The detector consists of two small size TPC chambers on the two sides of the target with a vertical drift field, and a sequence of detection layers picking up the ionization signal of radially emitted particles. Between the detection layers plastic absorber layers are inserted. Therefore the range of particles in the detector material

2014 JINST 9 P06005

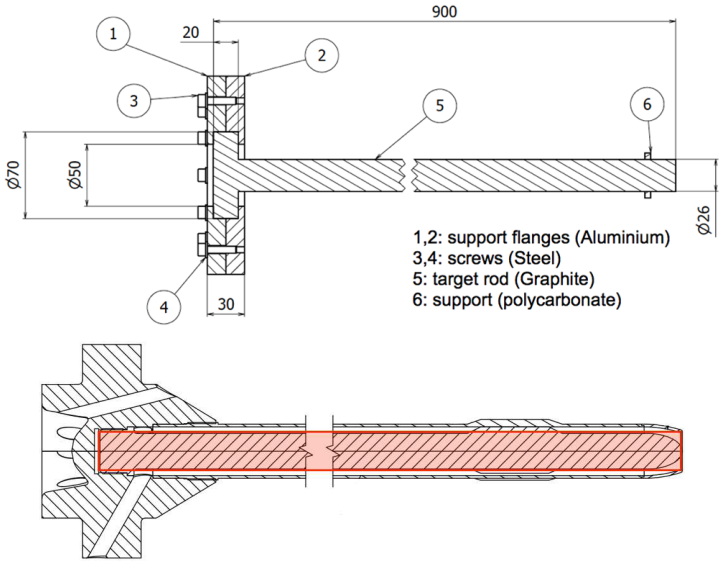

Figure 30. *Top*: technical drawing (side view) of the replica target used during the NA61/SHINE data taking consisting of a 90 cm long graphite rod and aluminium support flanges. *Bottom*: schematic layout of the complete geometry of the T2K target. The overlaid red rectangle represents the simplified geometry of the replica target.

can be determined. The range and energy loss by ionization of a particle depends on its energy and type, and therefore event-by-event counting of the number of emitted low energy protons becomes possible. Prototypes of the detector were tested in 2009 and 2010.

The final version of the LMPD, see figure 31 along with table 3, was manufactured in 2011, and was first tested in the NA61/SHINE experimental area, downstream of the NA61/SHINE detector, in parasitic mode. The tests showed the expected performance of the detector, namely its capability of proton identification and of counting the low energy (grey) protons. A typical raw event overlayed with the reconstructed clusters and tracks is seen in figure 32 (*left*). The ionization produced by particles with fixed range is shown in figure 32 (*right*). The signal of protons with a selected penetration range is clearly visible along with other fragment species such as helium nuclei. The cluster reconstruction uses a closest neighbour search algorithm, while the track reconstruction uses the Hough transform procedure combined with the maximum likelihood principle for pattern recognition. Figure 32 (*bottom*) shows the distributions of interaction vertex coordinates reconstructed from LMPD tracks for events recorded with inserted (red histograms) and removed target (blue histograms). The signal of events from interactions in the Pb target is clearly visible and the contribution from non-target interactions is small.

The operational parameters of the LMPD were optimized during the 2011 test. In particular, a gradual decrease of amplification in the layers close to the target was introduced. This is necessary

2014 JINST 9 P06005

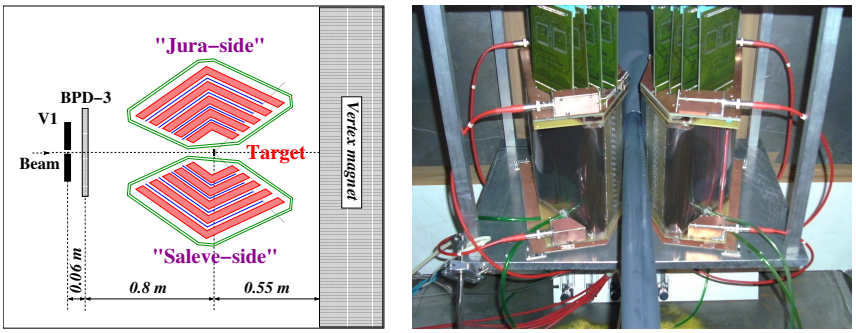

Figure 31. *Left*: schematic top view of the LMPD and the associated beamline. The internal structure of LMPD is also shown: thin absorber layers reside between sensitive layers depicted by coloured bands. The particular setting can be used to determine whether a given particle from the target crossed the absorber layer or stopped inside the absorber. *Right*: Front view photograph of the LMPD detector from the location upstream of the LMPD. The Pb target is located in the centre within the thin Tedlar foil He container tube surrounding the target disc. The field cage strips (copper strips on capton) of the LMPD are also visible. Standard NA61/SHINE TPC front end electronics were used for readout (on top).

Table 3. Parameters of the LMPD.

	LMPD
size (L×W×H) [cm]	$29 \times 15.5 \times 22.5$
No. of pads/sector	140
Pad size [mm]	$(4\text{–}9) \times 6$
Drift length [cm]	20.5
Drift velocity [cm/μs]	0.9
Drift field [V/cm]	195
Drift voltage [kV]	4
drift gas	Ar/CO_2 (85/15)
# of sectors	2×2
# of padrows	10
# of pads/padrow	8,8, 14,14, 16,16, 16,16, 16,16
Absorber thickness [mm]	0.5, 1.0, 2.0, 2.5

in order to adjust the dynamic range for the expected highly ionizing particles. After optimization large statistics physics-quality data were recorded in parasitic mode with the LMPD located downstream of MTPCs. They allow a systematic study of gray proton production and absorption in the target material. During the last 3 days of the 2011 data taking period with proton beams, the LMPD was mounted at the nominal position, and preliminary physics-quality p+Pb data were recorded for the final test of the operational parameters. Then, in 2012 large statistics 158 GeV/c p+Pb physics data were taken with the LMPD surrounding the target. This allows detection and tagging of grey protons and thus characterizing the centrality of the p+Pb collisions.

2014 JINST 9 P06005

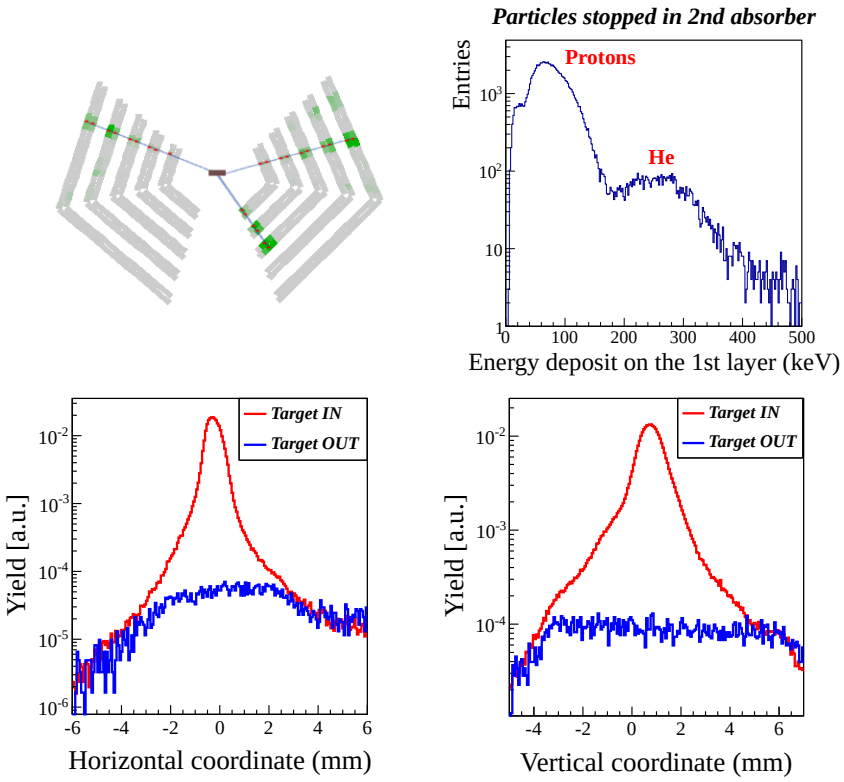

Figure 32. *Top left*: event display of the LMPD for a typical 158 GeV/c p+Pb collision, overlayed with the reconstructed clusters and tracks. Green colour indicates the energy deposit (ADC), red points indicate the position of the reconstructed clusters, blue lines depict the straight particle tracks fitted to the clusters. The particle tracks point to a common production vertex within the target. *Top right*: energy deposit of particles traversing the first absorber, but stopped within the second absorber layer. The proton energy deposit along with that of other nuclei are clearly seen. *Bottom*: distribution of reconstructed interaction coordinate for data taking with target inserted and removed. The off-target background is small.

8 Data acquisition and detector control systems

8.1 Readout electronics and DAQ

The readout electronics [42] consists of three main parts: the electronics responsible for reading out the TPC FEEs, the electronics for reading out the FASTBUS based ToF system, and the electronics for reading out the CAMAC based beam detectors (see figure 33).

In case of the TPC system, the FEE cards [28, 29] only host pre-amplifiers, shapers, and time-sampling capacitor arrays for 32 channels, along with ADCs. The necessary command logic is managed by the readout Mother Boards, which transmit the necessary clock signals to steer the

2014 JINST 9 P06005

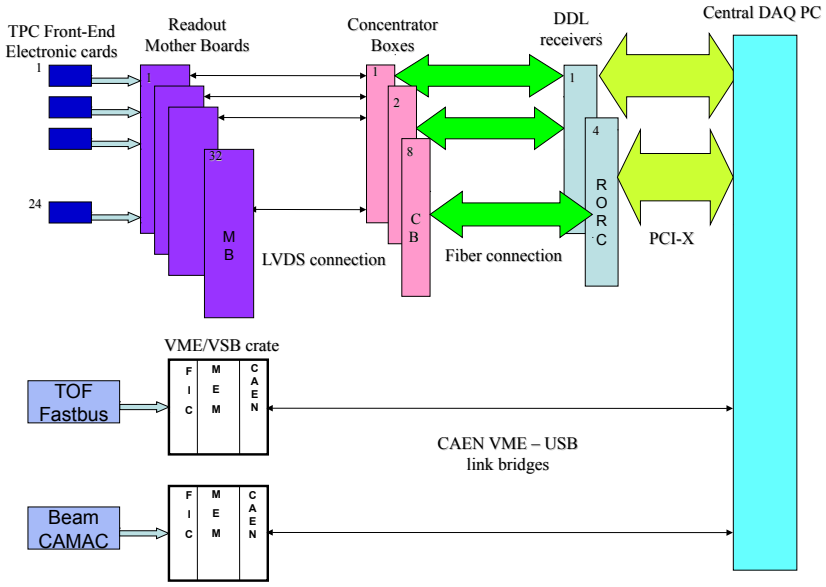

Figure 33. Block diagram of the three main parts of the NA61/SHINE readout system: TPC readout, ToF readout and CAMAC readout of beam detectors.

time sampling, ADC conversion and data transmission process. The FEE cards produce a 9 bit ADC value for each time slice of each TPC pad. These are pedestal subtracted, noise suppressed and zero compressed on the Mother Boards. The 250 Mother Boards, which are each capable of serving 24 FEE cards, were implemented using Cyclone II FPGA (EP2C35F672) arrays and SRAM units for pedestal table storage. Upon an event trigger, which is fanned out to all Mother Boards, the time sampling with subsequent digitization begins on the FEE cards, after which the ADC values are read out and processed on the fly by the Mother Boards with polling. The processed data stream is serialized onto a ground-independent LVDS connection line toward the Concentrator Boxes, which can receive data from 32 Mother Boards. These boxes act like further serializers and are implemented on Cyclone II FPGA (EP2C20F484) arrays. In order to ensure galvanic ground independence for the long-distance transfer, the DDL optical transfer line [43, 44] is used from this point to the Central DAQ PC. The data reaches the Central DAQ in push-data mode, i.e. the data stream is triggered by the lower level electronics and not via the Central DAQ. Upon the arrival of the first data headers at the Concentrator Box level, a Busy signal is issued as a feedback to the trigger electronics.

The ToF system uses legacy front end electronics based on FASTBUS technology. The readout of the beam-related detectors (Beam Position Detectors, beam counter pattern units, scalers, ADCs and TDCs) is based on traditional CAMAC units. A FASTBUS-to-VME bridge and a CAMAC-to-VME bridge, makes connection to VME crates dedicated to ToF and CAMAC readout, respectively. In each of these two VME crates a FIC8234 processor-based controller runs a low level OS9

based software as low level DAQ. As the processors are capable of receiving external signals as interrupt, the latter are used to initiate low level data taking. The measurement units are triggered by the experiment's accurate pre-trigger signal, but the measurement data are only read out if this is confirmed by the main-trigger signal within the time-out limit. In that case an interrupt is passed to the FIC8234 controllers to initiate readout. The data are transfered via the bridges to a MM6390 memory unit in the VME crate. The received data are stored in a ring buffer overwriting older data and a trigger counter is incremented. Meanwhile the Central DAQ polls for the incrementation of the trigger counter, and the new events are drained via a CAEN V1718 VME-to-USB bridge to the Central DAQ's ring buffer. Feedback to and control of the Busy logic is performed via RCB8047 CORBO register units in the pertinent VME crates.

The readout of the PSD, is designed along the principles of the TPC readout, and acts similarly to the Mother Boards in the TPC readout system.

Due to the push-data mode method, the event data in the different hardware channels arrive at the Central DAQ software asynchronously. The synchronization is performed via trigger counters in the sub-events on the final event-building level. For periodic checks the data stream is halted each minute, the data pipelines are drained and the trigger counter synchronicity is verified. In addition, the Busy signal of each hardware channel is monitored via a custom made galvanically isolated TTL to RS232 register in order to make sure that the event stream is never halted due to a stuck Busy signal caused by a hardware failure.

The Central DAQ software runs on a single Central DAQ PC (X7DB8-X motherboard, 64 bit, total 8 cores of Intel Xeon CPU @ 2 GHz, 8 GB memory, 10 PCI-X slots, 4 USB ports, and a serial port). The main components of the software and their functions are as follows:

(i) The core software of the Central DAQ written in C. Its user interface is a command line interpreter written using the GNU libreadline library.

(ii) The Central DAQ GUI script written in Tcl/Tk language.

(iii) The event server, created upon Central DAQ start for event monitoring. This is a fork-server serving up to 16 monitoring clients.

(iv) The following processes created upon run start:

  (i) The logger and monitoring/consistency checking process.

  (ii) The communication unit with the trigger system for summary information. This periodically gets scaler status information from the trigger server.

  (iii) The communication unit with the DCS system for summary information. This periodically gets information from the DCS server.

  (iv) The recorder process building the event, writing to disk and forwarding to the above event server upon request. This starts the following two processes for efficient parallelization of data receiving.

    (i) The receiver process for the DDL channels. This looks for data on any DDL channel on a first-come first-served basis.

    (ii) The receiver process for the VME channels. This looks for data on any VME channel on a first-come first-served basis.

2014 JINST 9 P06005

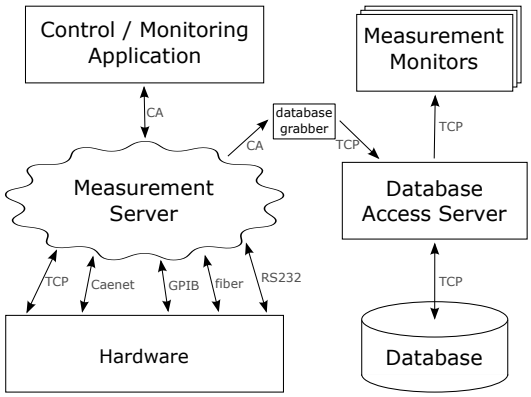

Figure 34. Block diagram of the NA61/SHINE Detector Control System.

The GUI and the command line interpreter communicate via standard Unix pipes and log files. The processes of the forked C program communicate via Linux shared memory. The data itself gets read into a special fast shared memory, called Physmem, outside the reach of the Linux kernel. Physmem is mapped by a special Linux kernel module shipped with the DDL libraries.

The central DAQ software is completed by a system of failure-tolerant scripts with checksum and size verification, which move the recorded data after consistency and Quality Assessment check onto the tape system of CASTOR. The typical trigger rate in our experiment was 60 Hz and the average event size was 2 Mbytes.

8.2 Detector Control System

The NA61/SHINE Detector Control System (DCS) is responsible for online monitoring and controlling of the working conditions of the detectors.

The system monitors parameters of the gas mixture in the TPCs (temperatures, pressure, flow, water and oxygen content, drift velocity, amplification, etc.). It also sets and monitors parameters of the high voltage in the sub-detectors: LMPD, TPCs, BPDs and the beam counters. The system also controls low voltage power supplies of the front end electronics and enables its cooling.

The block diagram of the DCS is shown in figure 34. Although the system logically consists of the following subsystems:

(i) Gas subsystem,

(ii) High Voltage subsystem,

(iii) Low Voltage subsystem,

(iv) PSD subsystem,

the main part of the system is a single EPICS-based [45] measurement server distributed over a few PCs. It communicates with various hardware (CAMAC, VME, PLC, etc.) via various interfaces

2014 JINST 9 P06005

(RS232, Caenet, TCP/IP, GPIB, etc.), performs all the measurements and makes the results accessible for the clients via the Channel Access protocol. The server runs constantly regardless of the presence of the clients or the database availability.

All measured data is stored in the relational database (PostgreSQL) by one of the EPICS clients. It can be accessed only via the Database Access Server by issuing ASCII commands.

There are two GUIs available. One of them, which controls the Measurement Server and monitors its performance, is an EPICS client and can be run only in the experimental area. The other one can be run anywhere and is graphically presenting results of measurements retrieved from the database.

9 Summary and outlook

NA61/SHINE (SPS Heavy Ion and Neutrino Experiment) is a multi-purpose facility for the study of hadron production in hadron-proton, hadron-nucleus and nucleus-nucleus collisions at the CERN Super Proton Synchrotron.

NA61/SHINE has greatly profited from the long development of the CERN proton and ion sources, the accelerator chain, as well as the H2 beamline of the CERN North Area. The latter has recently been modified to also serve as a fragment separator as needed to produce the Be beams for NA61/SHINE. Numerous components of the NA61/SHINE setup were inherited from its predecessors, in particular, the last one, the NA49 experiment.

This paper describes the facility — the beams and the detector system — as used up to March 2013, the start of the CERN Long Shutdown I. Special attention was paid to the presentation of the components which were constructed for NA61/SHINE. These are: the Projectile Spectator Detector, the Forward-ToF wall, the Low Momentum Particle Detector, the Z- and A-detectors, the Beam Position Detectors, the digital part of the TPC readout and the DAQ system, the Trigger System, the Detector Control System and the He-beam pipe. Moreover the upgraded CERN accelerator chain and the H2 beamline modified to serve as a fragment separator are described. The components inherited from the past experiments and described elsewhere are presented only briefly. These are the Time Projection Chambers and their gas system, the two super-conducting magnets, the ToF-L/R walls as well as the beam and trigger counters.

Upgrades of the facility are continuing and the physics goals are being expanded [4]. Among NA61/SHINE upgrades under preparation are: construction of Forward-TPCs and of a Silicon Vertex Detector, upgrade of the ToF and PSD readout systems, upgrade of the ToF HV system and extension of the gas system.

This paper will be followed by further publications presenting more details on the components which were newly constructed for the NA61/SHINE facility.

Acknowledgments

This work was supported by the Hungarian Scientific Research Fund (grants OTKA 68506 and 71989), the Polish Ministry of Science and Higher Education (grants 667/N-CERN/2010/0, NN 202 48 4339, NN 202 23 1837 and 7150/E-338/M/2013), the Foundation for Polish Science — MPD program, co-financed by the European Union within the European Regional Development

2014 JINST 9 P06005

Fund, the National Science Centre of Poland (grant UMO-2012/04/M/ST2/00816), the Federal Agency of Education of the Ministry of Education and Science of the Russian Federation (grant RNP 2.2.2.2.1547), the Russian Academy of Science and the Russian Foundation for Basic Research (grants 08-02-00018, 09-02-00664, and 12-02-91503-CERN), the Ministry of Education, Culture, Sports, Science and Technology, Japan, Grant-in-Aid for Scientific Research (grants 18071005, 19034011, 19740162, 20740160 and 20039012), the German Research Foundation (grants GA 1480/2-1, GA 1480/2-2), Bulgarian National Scientific Fondation (grant DDVU 02/19/2010), Ministry of Education and Science of the Republic of Serbia (grant OI171002), Swiss Nationalfonds Foundation (grant 200020-117913/1) and ETH Research Grant TH-01 07-3.

References

[1] NA49-FUTURE collaboration, N. Antoniou et al., *Study of hadron production in hadron-nucleus and nucleus-nucleus collisions at the CERN SPS*, CERN-SPSC-2006-034 (2006).

[2] M. Gazdzicki, M. Gorenstein and P. Seyboth, *Onset of deconfinement in nucleus-nucleus collisions: review for pedestrians and experts*, *Acta Phys. Polon.* **B 42** (2011) 307 [arXiv:1006.1765].

[3] T2K collaboration, Y. Itow et al., *The JHF-Kamioka neutrino project*, hep-ex/0106019.

[4] NA61/SHINE collaboration, N. Abgrall et al., *NA61/SHINE plans beyond the approved program*, CERN-SPSC-2012-022, SPSC-P-330-ADD-6 (2012).

[5] PIERRE AUGER collaboration, J. Abraham et al., *Properties and performance of the prototype instrument for the Pierre Auger Observatory*, *Nucl. Instrum. Meth.* **A 523** (2004) 50.

[6] KASCADE collaboration, T. Antoni et al., *The cosmic-ray experiment KASCADE*, *Nucl. Instrum. Meth.* **A 513** (2003) 490.

[7] *Memorandum of understanding for collaboration in the NA61/SHINE experiment for study of hadron production in hadron-nucleus and nucleus-nucleus collisions at the CERN SPS*, http://na61.web.cern.ch/na61/pages/downloads/mou_final_all.pdf.

[8] NA61/SHINE collaboration, N. Abgrall et al., *Measurements of cross sections and charged pion spectra in proton-carbon interactions at 31 GeV/c*, *Phys. Rev.* **C 84** (2011) 034604 [arXiv:1102.0983].

[9] NA61/SHINE collaboration, N. Abgrall et al., *Measurement of production properties of positively charged kaons in proton-carbon interactions at 31 GeV/c*, *Phys. Rev.* **C 85** (2012) 035210 [arXiv:1112.0150].

[10] R. Scrivens et al., *Overview of the status and developments on primary ion sources at CERN*, CERN-ATS-2011-172, in Proceedings of the *2nd International Particle Accelerator Conference*, San Sebastian Spain, 4–9 Sep 2011, pp. THPS025.

[11] M. Weiss, *The RFQ2 complex: the future injector to CERN Linac 2*, CERN-PS-92-34, in Proceedings of the *3rd European Particle Accelerator Conference*, Berlin Germany (1992).

[12] C.E. Hill, A.M. Lombardi, E. Tanke and M. Vretenar, *Present performance of the CERN proton Linac*, in Proceedings of the *XIX Linear Accelerator Conference Linac 98*, Chicago U.S.A. (1998).

[13] S. Gilardoni and D. Manglunki eds., *Fifty years of the CERN Proton Synchrotron*, CERN-2011-004 (2011).

[14] H. Haseroth ed., *Concept for a lead-ion accelerating facility at CERN*, CERN-90-01 (1990).

2014 JINST 9 P06005

[15] D.J. Warner ed., *CERN heavy-ion facility design report*, CERN-93-01 (1993).

[16] M. Benedikt et al. eds., *LHC design report. Vol. III: The LHC injector chain. Part 4: The LHC ion injector chain*, CERN-2004-003-V-3 (2004).

[17] O.S. Brüning et al. eds., *LHC design report. Vol. I: The LHC main ring. Chapter 21: The LHC as a lead ion collider*, CERN-2004-003-V-1 (2004).

[18] C. Bovet, S. Milner, A. Placci and M. Placidi, *The Cedar (Cherenkov differential counters with achromatic ring focus) project*, *IEEE Trans. Nucl. Sci.* **25** (1978) 572.

[19] M. Vivargent, G. Von Dardel, R. Mermod, G. Weber and K. Winter, *A threshold gas Čerenkov counter*, *Nucl. Instrum. Meth.* **22** (1963) 165.

[20] L. Gatignon, *Some information on threshold Cherenkovs*, http://web.archive.org/web/20070718185118/http://sl.web.cern.ch/SL/eagroup/XCETinfo.html.

[21] H. Geissel, G. Munzenberg and K. Riisager, *Secondary exotic nuclear beams*, *Ann. Rev. Nucl. Part. Sci.* **45** (1995) 163;
G. Münzenberg, *The separation techniques for secondary beams*, *Nucl. Instrum. Meth.* **B 70** (1992) 265.

[22] Cheesecote Mountain CAMAC, Pomona NY U.S.A., http://www.cmcamac.com/.

[23] NA49 collaboration, S. Afanasev et al., *The NA49 large acceptance hadron detector*, *Nucl. Instrum. Meth.* **A 430** (1999) 210.

[24] D. Varga, *Study of inclusive and correlated particle production in elementary hadronic interactions*, Ph.D. Thesis, Budapest Hungary (2003), http://edms.cern.ch/file/900941/1/phd_varga.pdf.

[25] Tedlar, http://www2.dupont.com/Tedlar_PVF_Film/en_US/.

[26] Airex foams, http://www.3acomposites.com/index.php?cmd=39.

[27] Carbon fiber Toray, http://www.toraycfa.com/pdfs/M55JDataSheet.pdf.

[28] S.A. Kleinfelder, *A 4096 cell switched capacitor analog waveform storage integrated circuit*, *IEEE Trans. Nucl. Sci.* **37** (1990) 1230.

[29] F. Bieser et al., *Design and performance of TPC readout electronics for the NA49 experiment*, *Nucl. Instrum. Meth.* **A 385** (1997) 535.

[30] R. Brun, R. Hagelberg, M. Hansroul and J.C. Lassalle, *Simulation program for particle physics experiments, GEANT: user guide and reference manual*, CERN-DD-78-2, CERN-DD-78-2-REV (1978).

[31] NA61/SHINE collaboration, N. Abgrall et al., *Calibration and analysis of the 2007 data*, CERN-SPSC-2008-018, SPSC-SR-033 (2008).

[32] NA61/SHINE collaboration, N. Abgrall et al., *Measurement of negatively charged pion spectra in inelastic p+p interactions at* $p_{\rm lab} = 20, 31, 40, 80$ *and* 158 *GeV/c*, *Eur. Phys. J.* **C 74** (2014) 2794 [arXiv:1310.2417] [CERN-PH-EP-2013-182].

[33] G. Palla et al., *The grid-geometry time-of-flight detector used in the NA49 experiment at the CERN SPS*, *Nucl. Instrum. Meth.* **A 451** (2000) 406.

[34] G.A. Alekseev et al., *Study of the compensated lead hadron calorimeter on hadron, electron and lead-ion beams*, *Nucl. Instrum. Meth.* **A 461** (2001) 381.

[35] JLC CALORIMETER GROUP collaboration, Y. Fujii, *Performance of compensated tile-fiber hadron calorimeter*, *Nucl. Instrum. Meth.* **A 453** (2000) 237.

2014 JINST 9 P06005

[36] Z. Sadygov, A. Olshevski, I. Chirikov, I. Zheleznykh and A. Novikov, *Three advanced designs of micro-pixel avalanche photodiodes: their present status, maximum possibilities and limitations*, *Nucl. Instrum. Meth.* **A 567** (2006) 70.

[37] Zecotek, http://zecotek.com.

[38] D. Acosta et al., *Electron, pion and multiparticle detection with a lead/scintillating-fiber calorimeter*, *Nucl. Instrum. Meth.* **A 308** (1991) 481.

[39] RD1 collaboration, J. Badier et al., *Test results of a fully projective lead/scintillating fiber calorimeter*, *Nucl. Instrum. Meth.* **A 337** (1994) 326.

[40] NA61/SHINE collaboration, N. Abgrall et al., *Pion emission from the T2K replica target: method, results and application*, *Nucl. Instrum. Meth.* **A 701** (2013) 99 [arXiv:1207.2114].

[41] K. Marton, G. Kiss, A. Laszlo and D. Varga, *Low momentum particle detector for the NA61 experiment at CERN*, submitted to *Nucl. Instrum. Meth. A* (2014) [arXiv:1401.4392].

[42] E. Denes et al., *Design and performance of the online system for the NA61/SHINE experiment*, in preparation.

[43] G. Rubin et al., *The ALICE detector data link*, in Proceedings of the *5th Workshop on Electronics for LHC Experiments*, Snowmass U.S.A. (1999), p. 493.

[44] W. Carena et al., *The ALICE data-acquisition read-out receiver card*, in Proceedings of the *10th Workshop on Electronics for LHC and Future Experiments*, Boston U.S.A. (2004), p. 273.

[45] EPICS, http://www.aps.anl.gov/epics.

2014 JINST 9 P06005

Eur. Phys. J. C (2014) 74:2794
DOI 10.1140/epjc/s10052-014-2794-6

THE EUROPEAN PHYSICAL JOURNAL C

Regular Article - Experimental Physics

Measurement of negatively charged pion spectra in inelastic p+p interactions at $p_{\mathrm{lab}} = 20, 31, 40, 80$ and 158 GeV/c

NA61/SHINE Collaboration

N. Abgrall[1], A. Aduszkiewicz[2,a], Y. Ali[3], T. Anticic[4], N. Antoniou[5], B. Baatar[6], F. Bay[7], A. Blondel[1], J. Blumer[8], M. Bogomilov[9], A. Bravar[1], J. Brzychczyk[3], S. A.Bunyatov[6], O. Busygina[10], P. Christakoglou[5], T. Czopowicz[11], N. Davis[5], S. Debieux[1], H. Dembinski[8], F. Diakonos[5], S. Di Luise[7], W. Dominik[2], T. Drozhzhova[12], J. Dumarchez[13], K. Dynowski[11], R. Engel[8], A. Ereditato[14], G. A. Feofilov[12], Z. Fodor[15], A. Fulop[15], M. Gaździcki[16,17], M. Golubeva[10], K. Grebieszkow[11], A. Grzeszczuk[18], F. Guber[10], A. Haesler[1], T. Hasegawa[19], M. Hierholzer[14], R. Idczak[20], S. Igolkin[12], A. Ivashkin[10], D. Joković[21], K. Kadija[4], A. Kapoyannis[5], E. Kaptur[18], D. Kiełczewska[2], M. Kirejczyk[2], J. Kisiel[18], T. Kiss[15], S. Kleinfelder[22], T. Kobayashi[19], V. I. Kolesnikov[6], D. Kolev[9], V. P. Kondratiev[12], A. Korzenev[1], P. Kovesarki[20], S. Kowalski[18], A. Krasnoperov[6], A. Kurepin[10], D. Larsen[18], A. László[15], V. V. Lyubushkin[6], M. Maćkowiak-Pawłowska[17], Z. Majka[3], B. Maksiak[11], A. I. Malakhov[6], D. Manić[21], A. Marcinek[3], V. Marin[10], K. Marton[15], H.-J. Mathes[8], T. Matulewicz[2], V. Matveev[6,10], G. L. Melkumov[6], St. Mrówczyński[16], S. Murphy[1], T. Nakadaira[19], M. Nirkko[14], K. Nishikawa[19], T. Palczewski[23], G. Palla[15], A. D. Panagiotou[5], T. Paul[24], C. Pistillo[14], W. Peryt[11,b], O. Petukhov[10], R. Płaneta[3], J. Pluta [11], B. A. Popov[6,13], M. Posiadała[2], S. Puławski[18], J. Puzović[21], W. Rauch[25], M. Ravonel[1], A. Redij[14], R. Renfordt[17], A. Robert[13], D. Röhrich[26], E. Rondio[23], M. Roth[8], A. Rubbia[7], A. Rustamov[17], M. Rybczyński[16], A. Sadovsky[10], K. Sakashita[19], M. Savić[21], K. Schmidt[18], T. Sekiguchi[19], P. Seyboth[16], D. Sgalaberna[7], M. Shibata[19], R. Sipos[15], E. Skrzypczak[2], M. Słodkowski[11], P. Staszel[3], G. Stefanek[16], J. Stepaniak[23], H. Ströbele[17], T. Šuša[4], M. Szuba[8], M. Tada[19], V. Tereshchenko[6], T. Tolyhi[15], R. Tsenov[9], L. Turko[20], R. Ulrich[8], M. Unger[8], M. Vassiliou[5], D. Veberič[24], V. V. Vechernin[12], G. Vesztergombi[15], L. Vinogradov[12], A. Wilczek[18], Z. Włodarczyk[16], A. Wojtaszek-Szwarc[16], O. Wyszyński[3], L. Zambelli[13], W. Zipper[18]

[1] University of Geneva, Geneva, Switzerland
[2] Faculty of Physics, University of Warsaw, Warsaw, Poland
[3] Jagiellonian University, Cracow, Poland
[4] Rudjer Bošković Institute, Zagreb, Croatia
[5] University of Athens, Athens, Greece
[6] Joint Institute for Nuclear Research, Dubna, Russia
[7] ETH, Zurich, Switzerland
[8] Karlsruhe Institute of Technology, Karlsruhe, Germany
[9] Faculty of Physics, University of Sofia, Sofia, Bulgaria
[10] Institute for Nuclear Research, Moscow, Russia
[11] Warsaw University of Technology, Warsaw, Poland
[12] St. Petersburg State University, St. Petersburg, Russia
[13] LPNHE, University of Paris VI and VII, Paris, France
[14] University of Bern, Bern, Switzerland
[15] KFKI Research Institute for Particle and Nuclear Physics, Budapest, Hungary
[16] Jan Kochanowski University in Kielce, Kielce, Poland
[17] University of Frankfurt, Frankfurt, Germany
[18] University of Silesia, Katowice, Poland
[19] High Energy Accelerator Research Organization (KEK), Tsukuba, Ibaraki 305-0801, Japan
[20] University of Wrocław, Wrocław, Poland
[21] University of Belgrade, Belgrade, Serbia
[22] University of California, Irvine, USA
[23] National Centre for Nuclear Research, Warsaw, Poland
[24] Laboratory of Astroparticle Physics, University Nova Gorica, Nova Gorica, Slovenia

[25] Fachhochschule Frankfurt, Frankfurt, Germany
[26] University of Bergen, Bergen, Norway

Received: 14 October 2013 / Accepted: 21 February 2014 / Published online: 15 March 2014

Abstract We present experimental results on inclusive spectra and mean multiplicities of negatively charged pions produced in inelastic p+p interactions at incident projectile momenta of 20, 31, 40, 80 and 158 GeV/c ($\sqrt{s}$ = 6.3, 7.7, 8.8, 12.3 and 17.3 GeV, respectively). The measurements were performed using the large acceptance NA61/SHINE hadron spectrometer at the CERN super proton synchrotron. Two-dimensional spectra are determined in terms of rapidity and transverse momentum. Their properties such as the width of rapidity distributions and the inverse slope parameter of transverse mass spectra are extracted and their collision energy dependences are presented. The results on inelastic p+p interactions are compared with the corresponding data on central Pb+Pb collisions measured by the NA49 experiment at the CERN SPS. The results presented in this paper are part of the NA61/SHINE ion program devoted to the study of the properties of the onset of deconfinement and search for the critical point of strongly interacting matter. They are required for interpretation of results on nucleus–nucleus and proton–nucleus collisions.

1 Introduction

This paper presents experimental results on inclusive spectra and mean multiplicities of negatively charged pions produced in inelastic p+p interactions at 20, 31, 40, 80 and 158 GeV/c. The measurements were performed by the multi-purpose NA61/SHINE—the SPS Heavy Ion and Neutrino Experiment [1]—at the CERN Super Proton Synchrotron (SPS). They are part of the NA61/SHINE ion program devoted to the study of the properties of the onset of deconfinement and search for the critical point of strongly interacting matter. Within this program data on p+p, Be+Be and p+Pb collisions were recorded and data on Ar+Ca and Xe+La collisions will be registered within the coming years. The started two dimensional scan in collision energy and size of colliding nuclei is mainly motivated by the observation of the onset of deconfinement [2,3] in central Pb+Pb collisions at about 30A GeV/c by the NA49 experiment at the CERN SPS. Recently the NA49 results were confirmed by the RHIC beam energy scan programme and their interpretation by the onset of deconfinement is supported by the LHC results (see Ref. [4] and references therein).

In addition to the ion programme, NA61/SHINE is conducting precise hadron production measurements for improving calculations of the initial neutrino flux in long-baseline neutrino oscillation experiments [5–8] as well as for more reliable simulations of cosmic-ray air showers [9,10].

An interpretation of the rich experimental results on nucleus–nucleus collisions relies to a large extent on a comparison to the corresponding data on p+p and p+A interactions. However, the available data concern mainly basic features of unidentified charged hadron production and they are sparse. Many needed results on hadron spectra, fluctuations and correlations are missing. Detailed measurements of hadron spectra in a large acceptance in the beam momentum range covered by the data presented in this paper exist only for inelastic p+p interactions at 158 GeV/c [11–13]. Thus the new high precision measurements of hadron production properties in p+p and p+A interactions are necessary and they are performed in parallel with the corresponding measurements in nucleus–nucleus collisions. Among the many different hadrons produced in high energy collisions pions are the lightest and by far the most abundant ones. Thus, data on pion production properties are crucial for constraining basic properties of models of strong interactions. In particular, the most significant signals of the onset of deconfinement (the "kink" and "horn") [14] require precise measurements of the mean pion multiplicity at the same beam momenta per nucleon as the corresponding A+A data. Moreover, the NA61/SHINE data are taken with the same detector and the same acceptance.

In the CERN SPS beam momentum range of 10–450 GeV/c the mean multiplicity of negatively charged pions in inelastic p+p interactions increases from about 0.7 at 10 GeV/c to about 3.5 at 450 GeV/c [15]. Among three charged states of pions the most reliable measurements in the largest phase–space are usually possible for π^- mesons. Neutral pions decay electromagnetically into two photons and thus measurements of their production properties require measurements of both photons and then extraction of the π^0 signal from the two-photon mass spectra. Charged pions are easy to detect by ionisation detectors as they decay weakly with a long lifetime ($c\tau$ = 7.8 m). A significant fraction of positively charged hadrons are protons (25 %) and kaons (5 %) [11–13]. Therefore measurements of π^+ mesons require their identification by measurements of the

[a] e-mail: Antoni.Aduszkiewicz@fuw.edu.pl
[b] Deceased

energy loss and/or time-of-flight (tof). This identification is not as important for π^- mesons because the contamination of negatively charged particles by K^- mesons and anti-protons is below 10 % [11–13] and can be subtracted reliably. The latter method is used in this paper and it allows to derive π^- spectra in the broadest phase–space region in a uniform way. Results obtained using explicit pion identification are planned in future NA61/SHINE publications.

The paper is organised as follows. In Sect. 2 the NA61/SHINE experimental set-up is described. Details on the beam, trigger and event selection are given in Sect. 3. Data reconstruction, simulation and detector performance are described in Sect. 4. Analysis techniques and final results are presented in Sects. 5 and 6, respectively. These results are compared with the corresponding data on central Pb+Pb collisions in Sect. 7. A summary in Sect. 8 closes the paper.

The pion rapidity is calculated in the collision centre of mass system: $y = \text{atanh}(\beta_L)$, where $\beta_L = p_L/E$ is the longitudinal component of the velocity, p_L and E are pion longitudinal momentum and energy given in the collision centre of mass system. The transverse component of the momentum is denoted as p_T and the transverse mass m_T is defined as $m_T = \sqrt{m_\pi^2 + p_T^2}$, where m_π is the charged pion mass. The nucleon mass and collision energy per nucleon pair in the centre of mass system are denoted as m_N and $\sqrt{s_{NN}}$, respectively.

2 The NA61/SHINE facility

The NA61/SHINE experimental facility [20] consists of a large acceptance hadron spectrometer located in the CERN North Area Hall 887 (EHN1) and the H2 beam-line to which beams accelerated in the CERN accelerator complex are delivered from the Super Proton Synchrotron. NA61/SHINE profits from the long development of the CERN proton and ion sources and the accelerator chain as well as the H2 beam line of the CERN North Area. The latter has recently been modified to also serve as a fragment separator as needed to produce the Be beams for NA61/SHINE. Numerous components of the NA61/SHINE set-up were inherited from its predecessor, the NA49 experiment [16].

The schematic layout of the NA61/SHINE detector is shown in Fig. 1.

A set of scintillation and Cherenkov counters as well as Beam Position Detectors (BPDs) upstream of the spectrometer provide timing reference, identification and position measurements of incoming beam particles. The trigger scintillator counter S4 placed downstream of the target is used to select events with collisions in the target area. Details on this system are presented in Sect. 3.

The main tracking devices of the spectrometer are large volume Time Projection Chambers (TPCs). Two of them, the vertex TPCs (VTPC-1 and VTPC-2 in Fig. 1), are located in the magnetic fields of two super-conducting dipole magnets with a maximum combined bending power of 9 Tm which corresponds to about 1.5 and 1.1 T fields in the upstream and downstream magnets, respectively. This field configuration was used for data taking on p+p interactions at 158 GeV/c. In order to optimise the acceptance of the detector at lower collision momenta, the field in both magnets was lowered in proportion to the beam momentum.

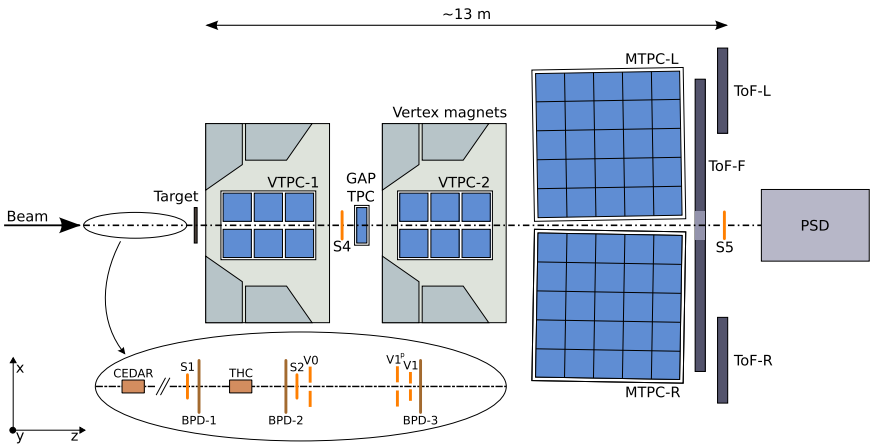

Fig. 1 The schematic layout of the NA61/SHINE experiment at the CERN SPS (horizontal cut, not to scale). The beam and trigger detector configuration used for data taking on p+p interactions in 2009 is shown. Alignment of the chosen coordinate system is shown in the figure; its origin lies in the middle of VTPC-2, on the beam axis. The nominal beam direction is along the z axis. The magnetic field bends charged particle trajectories in the x–z (*horizontal*) plane. The drift direction in the TPCs is along the y (*vertical*) axis

Two large TPCs (MTPC-L and MTPC-R) are positioned downstream of the magnets symmetrically to the beam line. The fifth small TPC (GAP-TPC) is placed between VTPC-1 and VTPC-2 directly on the beam line. It closes the gap between the beam axis and the sensitive volumes of the other TPCs.

The TPCs are filled with Ar:CO_2 gas mixtures in proportions 90:10 for the VTPCs and the GAP-TPC, and 95:5 for the MTPCs.

The particle identification capability of the TPCs based on measurements of the specific energy loss, $\mathrm{d}E/\mathrm{d}x$, is augmented by tof measurements using Time-of-Flight (ToF) detectors. The high resolution forward calorimeter, the Projectile Spectator Detector (PSD), measures energy flow around the beam direction, which in nucleus–nucleus collisions is primarily given by the projectile spectators.

NA61/SHINE uses various solid nuclear targets and a LHT (see Sect. 3 for details). The targets are positioned about 80 cm upstream of the sensitive volume of VTPC-1.

The results presented in this paper were obtained using information from the TPCs, the BPDs as well as from the beam and trigger counters.

3 Beams, target, triggers and data samples

This section summarises basic information on the beams, target, triggers and recorded data samples which is relevant for the results presented in this paper.

Secondary beams of positively charged hadrons at 20, 31, 40, 80 and 158 GeV/c are produced from 400 GeV protons extracted from the SPS in a slow extraction mode with a flat-top of 10 seconds. The secondary beam momentum and intensity is adjusted by proper setting of the H2 beam-line magnet currents and collimators. The beam is transported along the H2 beam-line towards the experiment. The precision of the setting of the beam magnet currents is approximately 0.5 %. This was verified by a direct measurement of the beam momentum at 31 GeV/c by bending the incoming beam particles into the TPCs with the maximum magnetic field [17]. The selected beam properties are given in Table 1.

The set-up of beam detectors is illustrated in the inset on Fig. 1. Protons from the secondary hadron beam are identified by two Cherenkov counters, a CEDAR [18] (either CEDAR-W or CEDAR-N) and a threshold counter (THC). The CEDAR counter, using a coincidence of six out of the eight photo-multipliers placed radially along the Cherenkov ring, provides positive identification of protons, while the THC, operated at pressure lower than the proton threshold, is used in anti-coincidence in the trigger logic. Due to their limited range of operation two different CEDAR counters were used, namely for beams at 20, 31, and 40 GeV/c the CEDAR-W counter and for beams at 80 and 158 GeV/c the CEDAR-N counter. The threshold counter was used for all beam energies. A selection based on signals from the Cherenkov counters allowed to identify beam protons with a purity of about 99 %. A consistent value for the purity was found by bending the beam into the TPCs with the full magnetic field and using the $\mathrm{d}E/\mathrm{d}x$ identification method [19]. The fraction of protons in the beams is given in Table 1.

Table 1 Basic beam properties and numbers of events recorded for p+p interactions at 20, 31, 40, 80 and 158 GeV/c. The first column gives the beam momentum. The second and third columns list typical numbers of beam particles at NA61/SHINE per spill (about 10 s) and the fraction of protons in the beam, respectively

p_{beam} (GeV/c)	Particles per spill (k)	Proton fraction (%)
20	1000	12
31	1000	14
40	1200	14
80	460	28
158	250	58

Two scintillation counters, S1 and S2, provide beam definition, together with the three veto counters V0, V1 and $\mathrm{V1^p}$ with a 1 cm diameter hole, which are defining the beam before the target. The S1 counter provides also the timing (start time for all counters). Beam protons are then selected by the coincidence $\mathrm{S1}\wedge\mathrm{S2}\wedge\overline{\mathrm{V0}}\wedge\overline{\mathrm{V1}}\wedge\overline{\mathrm{V1^p}}\wedge\mathrm{CEDAR}\wedge\overline{\mathrm{THC}}$. Trajectories of individual beam particles were measured in a telescope of BPDs placed along the beam line (BPD-1/2/3 in Fig. 1). These counters are small ($4.8\times4.8\ \mathrm{cm}^2$) proportional chambers with cathode strip readout, providing a resolution of about 100 μm in two orthogonal directions, see Ref. [20] for more details. The beam profile and divergence obtained from the BPD measurements are presented in Fig. 2. Due to properties of the H2 beam line both the beam width and divergence at the NA61/SHINE target increase with decreasing beam momentum.

For data taking on p+p interactions a LHT of 20.29 cm length (2.8 % interaction length) and 3 cm diameter placed 88.4 cm upstream of VTPC-1 was used. The Liquid Hydrogen Target facility (LHT) filled the target cell with para-hydrogen obtained in a closed-loop liquefaction system which was operated at 75 mbar overpressure with respect to the atmosphere. At the atmospheric pressure of 965 mbar the liquid hydrogen density is $\rho_{\mathrm{LH}} = 0.07\ \mathrm{g/cm}^3$. The boiling rate in the liquid hydrogen was not monitored during the data taking and thus the liquid hydrogen density is known only approximately. It has however no impact on the results presented in this paper as they are determined from particle yields per selected event and thus they are independent of the target density. Data taking with inserted and removed liquid hydrogen in the LHT was alternated in order to calculate a data-based correc-

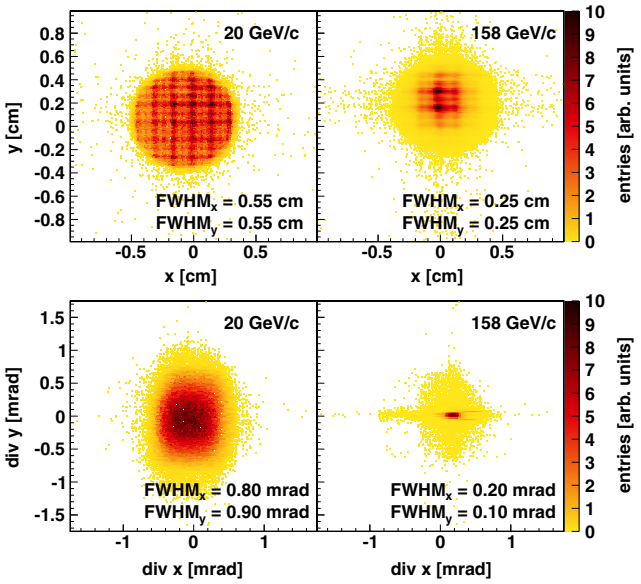

Fig. 2 *Top* The beam spot as measured by BPD-3 after the $\overline{\text{V1}}$ cut described in the text for 20 GeV/c (*left*) and 158 GeV/c (*right*) beams. *Bottom* The beam divergence in x and y for 20 GeV/c (*left*) and 158 GeV/c (*right*) beams. All distributions were arbitrarily scaled to the full colour scale. Widths of the distributions are given in the legend

tion for interactions with the material surrounding the liquid hydrogen.

Interactions in the target are selected by the trigger system by an anti-coincidence of the incoming beam protons with a small, 2 cm diameter, scintillation counter (S4) placed on the beam trajectory between the two vertex magnets (see Fig. 1). This minimum bias trigger is based on the disappearance of the incident proton. In addition, unbiased proton beam events were recorded with a frequency typically by a factor of 10 lower than the frequency of interaction events.

4 Data processing, simulation and detector performance

Detector parameters were optimised by a data-based calibration procedure which also took into account their time dependences. Small adjustments were determined in consecutive steps for:

(i) detector geometry, TPC drift velocities and distortions due to the magnetic field inhomogeneities in the corners of VTPCs,
(ii) magnetic field setting,
(iii) specific energy loss measurements,
(iv) tof measurements.

Each step involved reconstruction of the data required to optimise a given set of calibration constants and time dependent corrections followed by verification procedures. Details of the procedure and quality assessment are presented in Ref. [21]. The resulting performance in the measurements of quantities relevant for this paper is discussed below.

The main steps of the data reconstruction procedure are:

(i) cluster finding in the TPC raw data, calculation of the cluster centre-of-gravity and total charge,
(ii) reconstruction of local track segments in each TPC separately,
(iii) matching of track segments into global tracks,
(iv) track fitting through the magnetic field and determination of track parameters at the first measured TPC cluster,
(v) determination of the interaction vertex using the beam trajectory (x and y coordinates) fitted in the BPDs and the trajectories of tracks reconstructed in the TPCs (z coordinate),
(vi) refitting the particle trajectory using the interaction vertex as an additional point and determining the particle momentum at the interaction vertex,
(vii) matching of ToF hits with the TPC tracks.

An example of a reconstructed p+p interaction at 40 GeV/c is shown in Fig. 3. Long tracks of one negatively charged and two positively charged particles are seen. All particles leave signals in the ToF detectors.

A simulation of the NA61/SHINE detector response is used to correct the reconstructed data. Several MC models were compared with the NA61/SHINE results on p+p, p+C and π+C interactions: FLUKA2008, URQMD1.3.1,

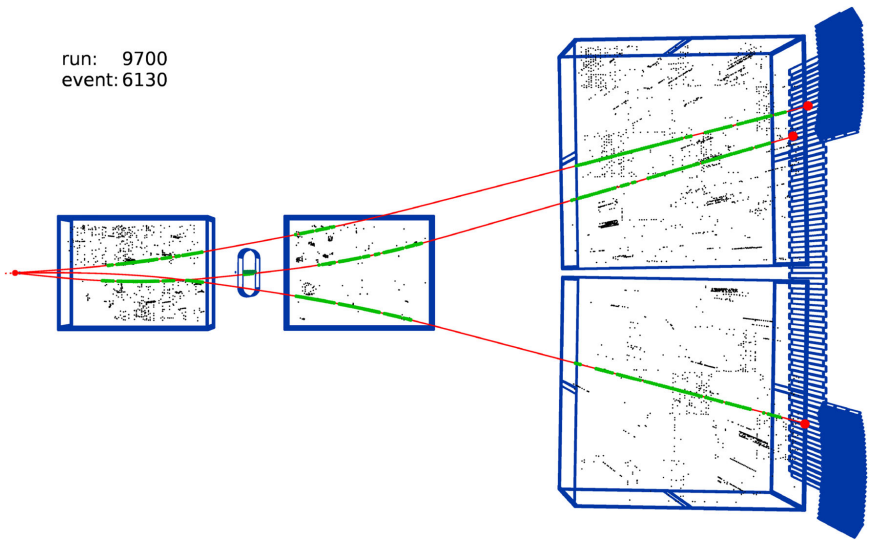

Fig. 3 An example of a p+p interaction at 40 GeV/c measured in the NA61/SHINE detector. The measured points (*green*) are used to fit tracks (*red lines*) to the interaction point. The *grey dots* show the noise clusters. Due to the central gap of the VTPCs only a small part of the trajectory of the negatively charged particle is seen in VTPC-1

VENUS4.12, EPOS1.99, GHEISHA2002, QGSJetII-3 and Sibyll2.1 [17,22–24]. Based on these comparisons and taking into account continuous support and documentation from the developers the EPOS model [25] was selected for the MC simulation. The simulation consists of the following steps (see Ref. [26] for more details):

(i) generation of inelastic p+p interactions using the EPOS model [25],
(ii) propagation of outgoing particles through the detector material using the GEANT 3.21 package [27] which takes into account the magnetic field as well as relevant physics processes, such as particle interactions and decays,
(iii) simulation of the detector response using dedicated NA61/SHINE packages which introduce distortions corresponding to all corrections applied to the real data,
(iv) simulation of the interaction trigger selection by checking whether a charged particle hits the S4 counter, see Sect. 3,
(v) storage of the simulated events in a file which has the same format as the raw data,
(vi) reconstruction of the simulated events with the same reconstruction chain as used for the real data and
(vii) matching of the reconstructed tracks to the simulated ones based on the cluster positions.

It should be underlined that only inelastic p+p interactions in the hydrogen in the target cell were simulated and reconstructed. Thus the Monte Carlo based corrections (see Sect. 5) can be applied only for inelastic events. The contribution of elastic events is removed by the event selection cuts (see Sect. 5.1), whereas the contribution of off-target interactions is subtracted based on the data (see Sect. 5.4).

Spectra of π^- mesons presented in this paper were derived from spectra of all negatively charged hadrons corrected for a small contamination of mostly K^- mesons and anti-protons. The typical acceptance in rapidity and transverse momentum is presented in Fig. 4 for p+p interactions at 20 and 158 GeV/c. This figure also shows acceptance regions for methods based on explicit pion identification using $\mathrm{d}E/\mathrm{d}x$ and tof measurements. They are limited due to the geometrical acceptance of the ToF detectors, the finite resolution of the $\mathrm{d}E/\mathrm{d}x$ measurements and limited data statistics.

The quality of measurements was studied by reconstructing masses of K^0_S particles from their V^0 decay topology. As an example the invariant mass distributions of K^0_S candidates found in p+p interactions at 20 and 158 GeV/c are plotted in Fig. 5. The differences between the measured peak positions and the literature value of the K^0_S mass [28] are smaller than 1 MeV/c^2. The width of the distributions, related to the detector resolution, is about 25 % smaller for the Monte Carlo than for the data. This implies that statistical and/or systematic uncertainties of track parameters reconstructed from the data are

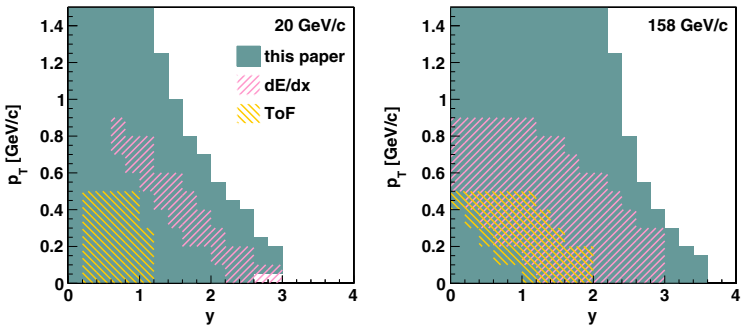

Fig. 4 Typical acceptance regions for π^- meson spectra in p+p interactions at 20 GeV/c (*left*) and 158 GeV/c (*right*) for different analysis methods: the method used in this paper which does not require an explicit pion identification, the method which identifies pions via their energy loss ($\mathrm{d}E/\mathrm{d}x$) and, in addition, their time-of-flight (tof)

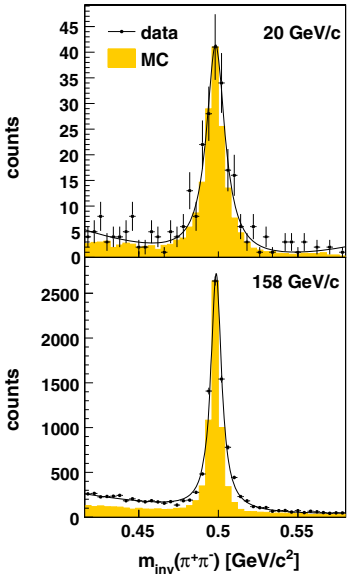

Fig. 5 Invariant mass distribution of reconstructed K^0_S candidates in p+p interactions at 20 (*top*) and 158 GeV/c (*bottom*) for the measured data and EPOS model based Monte Carlo simulations. The MC plot was normalised to the peak height of the data. The K^0_S candidates were selected within $0 < y < -1$ and $0 < p_T < 0.5$ GeV/c for 20 GeV/c and $-1 < y < 0$ and $0 < p_T < 0.5$ GeV/c for 158 GeV/c. The distribution was fitted with the sum of a Lorentzian function (signal) and a second order polynomial (background)

somewhat underestimated in the simulation. Systematic bias due to this imperfectness was estimated by varying the selection cuts and was found to be below 2 % (see Sect. 5.7.2).

The track reconstruction efficiency and the resolution of kinematic quantities were calculated by matching reconstructed tracks to their generated partners. In only 0.1–0.2 % of cases a single generated track is matched to more than one reconstructed partner, typically due to failure of matching reconstructed track segments. This effect is taken into account in the correction described in Sect. 5.6. As examples, the reconstruction efficiency as a function of rapidity and transverse momentum for negatively charged pions produced in p+p interactions at 20 and 158 GeV/c is shown in Fig. 6. The resolution of rapidity and transverse momentum measurements is illustrated in Fig. 7. The resolution was calculated as the FWHM of the distribution of the difference between the generated and reconstructed y and p_T. These results were obtained for negatively charged pions passing the track selection criteria described in Sect. 5.2. Resolution of the transverse momentum is worse at low beam momenta. This is caused by the lower magnetic field and by the fact that the same rapidity region in the centre of mass frame corresponds to lower momenta in the laboratory frame.

Figures 8 and 9 show further examples of the comparison between data and simulation. Distributions of the z coordinate of the fitted vertex are presented in Fig. 8. Distributions of the distance between the track trajectory extrapolated to the z coordinate of the vertex and the vertex in the x–y plane (b_x and b_y impact parameters) are given in Fig. 9. Differences visible in the tails of distributions are partially due to imperfect simulation of the detector response and, in case of the impact parameter, partially due to the contribution of background tracks from off-time beam particles which are not included in the simulation. The difference is smaller for events selected using more restrictive cuts on the off-time beam particles. A possible small bias due to these effects was estimated by varying the impact parameter cuts and was found to be below 1 %.

5 Analysis technique

This section presents the procedures used for data analysis consisting of the following steps:

(i) applying event and track selection criteria,

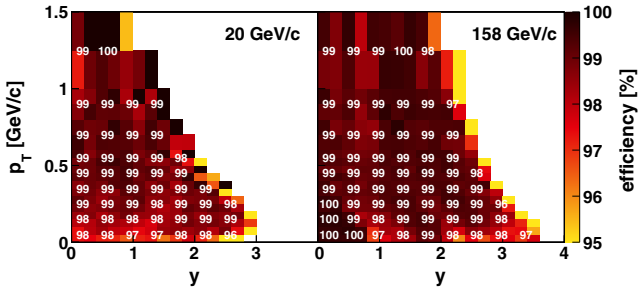

Fig. 6 Reconstruction efficiency of negatively charged pions produced in p+p interactions at 20 (*left*) and 158 GeV/*c* (*right*) as a function of rapidity and transverse momentum. It was calculated by dividing the number of tracks passing the track selection cuts specified in Sect. 5.2 by the number of the generated tracks. The selection criteria include the requirement of at least 90 % reconstruction efficiency

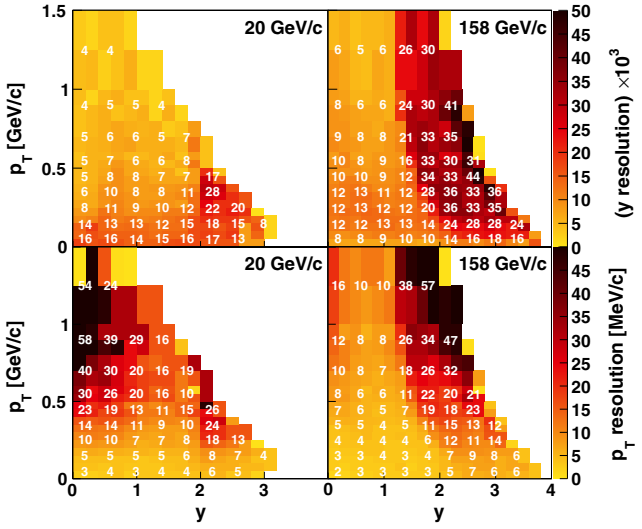

Fig. 7 Resolution of rapidity (*top*, scaled by 10^3) and transverse momentum (*bottom*) measurements for negatively charged pions produced in p+p interactions at 20 (*left*) and 158 GeV/*c* (*right*) as a function of pion rapidity and transverse momentum. The results are obtained using the track selection cuts specified in Sect. 5.2

(ii) determination of spectra of negatively charged hadrons using the selected events and tracks,
(iii) evaluation of corrections to the spectra based on experimental data and simulations,
(iv) calculation of the corrected spectra.

Corrections for the following biases were evaluated and applied:

(i) geometrical acceptance,
(ii) contribution of off-target interactions,
(iii) contribution of particles other than negatively charged pions produced in inelastic p+p interactions,
(iv) losses of inelastic p+p interactions as well as of negatively charged pions produced in accepted interactions due to the trigger and the event and track selection criteria employed in the analysis.

These steps are described in the successive subsections.

The final results refer to π^- mesons produced in inelastic p+p interactions by strong interaction processes and in electromagnetic decays of produced hadrons. Such pions are referred to as *primary* π^-. The term *primary* will be used in the above meaning also for other particles.

The analysis was performed independently in (y, p_T) and (y, m_T) bins. The bin sizes were selected taking into account

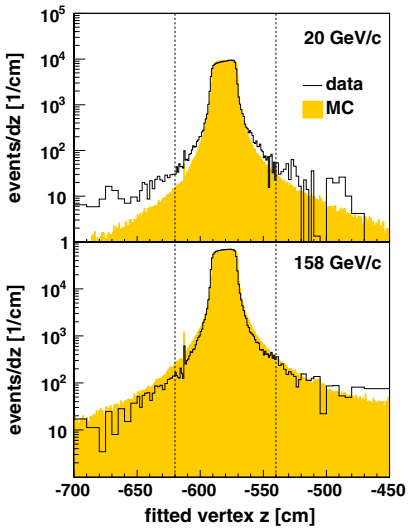

Fig. 8 Distribution of fitted vertex z coordinate for p+p interactions at 20 (*top*) and 158 GeV/c (*bottom*). The *black line* shows the data after target removed subtraction (see Sect. 5.4). The *filled area* shows the distribution for the reconstructed Monte Carlo simulation. This distribution was normalised to the total integral of the data plot. The *dashed vertical lines* show the z vertex selection range

Table 2 Number of events recorded with the interaction trigger (all) and selected for the analysis (selected)

p_{beam} (GeV/c)	Target inserted		Target removed	
	All (k)	Selected (k)	All (k)	Selected (k)
20	1324	233	123	4
31	3145	843	332	15
40	5239	1578	529	44
80	4038	1543	429	54
158	3502	1650	427	51

the statistical uncertainties as well as the resolution of the momentum reconstruction. Corrections as well as statistical and systematic uncertainties were calculated for each bin.

5.1 Event selection criteria

This section presents the event selection criteria. The number of events selected by the trigger (see Sect. 3) and used in the analysis is shown in Table 2. The fraction of events selected for the analysis increases with the interaction energy, mostly due to lower beam intensity (see Table 1) and resulting smaller off-time particle contamination, and smaller fraction of the low multiplicity events for which no tracks are found within the acceptance.

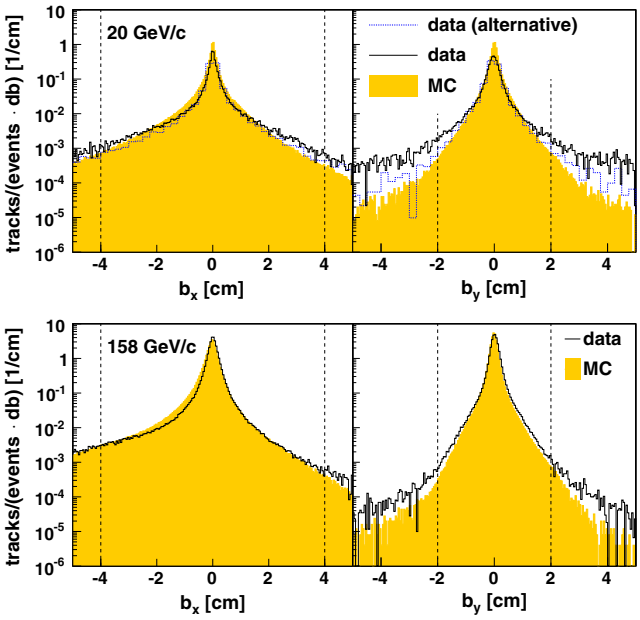

Fig. 9 Distribution of the impact parameter in the x (*left*) and y (*right*) coordinate for p+p interactions at 20 (*top*) and 158 GeV/c (*bottom*). The *black line* shows the data after target removed subtraction (see Sect. 5.4). The *filled area* shows the reconstructed Monte Carlo simulation. The *dashed vertical lines* show the accepted range (see Sect. 5.2). The *dotted blue line* in the 20 GeV/c plots show the distribution obtained using the alternative event selection. Namely only events with no off-time beam particles within the time window of ± 6 μs around the trigger particle time were accepted

Table 3 Momentum thresholds used to reject elastic interactions (cut (v))

Beam momentum (GeV/c)	20	31	40	80	158
Threshold momentum (GeV/c)	17	28	35	74	–

The following event selection criteria were applied to the events recorded with the interaction trigger:

(i) no off-time beam particle is detected within ± 2 μs around the trigger particle,
(ii) the beam particle trajectory is measured in at least one of BPD-1 or BPD-2 and in the BPD-3 detector positioned just in front of the LHT,
(iii) there is at least one track reconstructed in the TPCs and fitted to the interaction vertex,
(iv) the vertex z position (fitted using the beam and TPC tracks) is not farther away than 40 cm from the centre of the LHT,
(v) events with a single, well measured positively charged track with absolute momentum close to the beam momentum are rejected. The momentum thresholds are listed in Table 3.

The off-line (listed above) and on-line (the interaction trigger condition, see Sect. 3) event cuts select a large fraction of well measured (cuts (i) and (ii)) inelastic (cut (iii)) p+p interactions. The cut (iii) removes part of elastic interactions. However in some elastic events at beam momenta up to 80 GeV/c the beam particle is deflected enough to be measured in the detector. This is demonstrated in the momentum distributions shown in Fig. 10. Such events are removed by cut (v).

Moreover cut (iv) significantly suppresses interactions outside the hydrogen in the target cell. The corrections for the contribution of interactions outside the hydrogen in the target cell and the loss of inelastic events are presented in Sects. 5.4 and 5.6.

5.2 Track selection criteria

In order to select well-measured tracks of primary negatively charged hadrons as well as to reduce the contamination of tracks from secondary interactions, weak decays and off-time interactions the following track selection criteria were applied:

(i) the track momentum fit at the interaction vertex should have converged,
(ii) the fitted track charge is negative,
(iii) the fitted track momentum component p_x is negative. This selection minimises the angle between the track trajectory and the TPC pad direction for the chosen magnetic field direction. This reduces statistical and systematic uncertainties of the cluster position, energy deposit and track parameters,
(iv) the total number of reconstructed points on the track should be greater than 30,
(v) the sum of the number of reconstructed points in VTPC-1 and VTPC-2 should be greater than 15 or the number of reconstructed points in the GAP-TPC should be greater than 4,
(vi) the distance between the track extrapolated to the interaction plane and the interaction point (impact parameter) should be smaller than 4 cm in the horizontal (bending) plane and 2 cm in the vertical (drift) plane,
(vii) the track should be measured in a high ($\geq$90 %) TPC acceptance region (see Sect. 5.3),
(viii) tracks with $\mathrm{d}E/\mathrm{d}x$ and total momentum values characteristic for electrons are rejected. The electron contribution to particles with momenta above 20 GeV/c is corrected using the simulation. The electron selection procedure is visualised in Fig. 11.

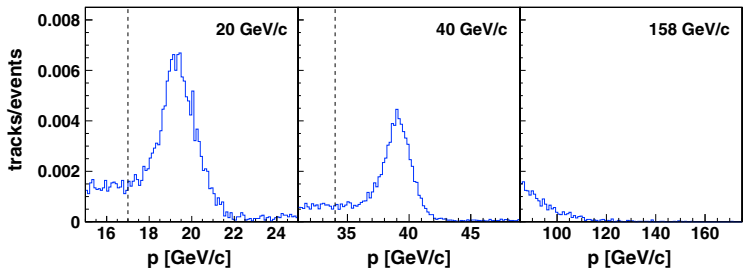

Fig. 10 Momentum distributions at 20 (*left*), 40 (*middle*) and 158 GeV/c (*right*) of the positively charged tracks in events passing selection cuts (*i*)–(*iv*), containing a single track, which is positively charged and measured in the GAP TPC and MTPC. The distributions were normalised to all events. The *vertical dashed lines* at 20 and 40 GeV/c show the momentum threshold used to remove elastic events (cut (*v*))

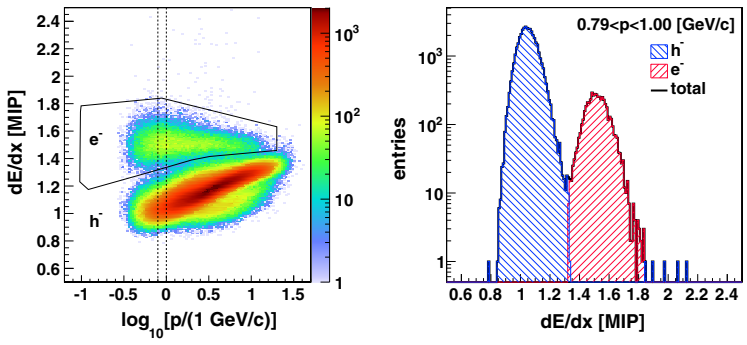

Fig. 11 *Left* Distribution of particle energy loss as a function of the logarithm of total momentum, for negatively charged particles produced in p+p interactions at 40 GeV/c. The *black contour* shows the electron selection region. *Right* $\mathrm{d}E/\mathrm{d}x$ distribution in the momentum range indicated in the figure and marked with *vertical dashed lines* in the *left panel*. Electrons and negatively charged hadrons show separated peaks

The spectra of negatively charged particles after track and event selections were obtained in 2-dimensional bins of (y, p_{T}) and (y, m_{T}). The spectra were evaluated in the centre-of-mass frame after rotation of the z axis into the proton beam direction measured event-by-event by the BPDs.

5.3 Correction for detector acceptance

The detection and reconstruction inefficiencies are corrected using the simulation described in Sect. 4. However, in order to limit the impact of possible inaccuracies of this simulation, only regions are accepted where the reconstruction efficiency (defined as the ratio of the number of reconstructed and matched MC π^- tracks passing the track selection criteria to the number of generated π^-) equals at least 90 %. These regions were identified using a separate, statistically independent simulation in three-dimensional bins of y, p_{T} or m_{T} and the azimuthal angle ϕ (5° bin width). The resulting acceptance maps are shown in Fig. 12. The acceptance calculated in the $y < 0$ region, not used for the final results, is shown also for comparison. We chose an upper limit of 1.5 GeV/c for the transverse momentum spectra, because beyond the admixture of background tracks reaches a level which cannot be handled by the correction procedures used in this paper. Future publications will be devoted to the high p_{T} region.

Since neither target nor beam are polarized, we can assume a uniform distribution of particles in ϕ. The data falling into the accepted bins is summed over ϕ bins and the (y, $p_{\mathrm{T}}/m_{\mathrm{T}}$) bin content is multiplied by a correction factor to compensate for the rejected ϕ ranges. The acceptance correction also compensates for the $p_x < 0$ selection (see Sect. 5.2, point (5.2)).

Even a small deviation of the beam direction from the nominal axis (z) results in a non-negligible bias in the reconstructed transverse momentum. The beam direction is measured in the BPDs, and the particle momenta are recalculated to the frame connected with the beam direction. However, the detector acceptance depends on the momentum in the detector frame. Therefore the acceptance selection is done in the detector frame, and the acceptance correction is applied as a weight to each track. The weights are used to obtain particle spectra corrected for the detector acceptance in the frame connected with the beam direction.

5.4 Correction for off-target interactions

The spectra were derived for events with liquid hydrogen in ($_{\mathrm{I}}$) and removed ($_{\mathrm{R}}$) from the LHT. The latter data set represents interactions outside the liquid hydrogen (interactions with materials downstream and upstream of the liquid hydrogen). The differential inclusive yield of negatively charged particles per event in interactions of beam protons with the liquid hydrogen inside the LHT ($n_{\mathrm{T}}[\mathrm{h}^-]$) is calculated as:

$$n_{\mathrm{T}}[\mathrm{h}^-] = \frac{1}{1-\varepsilon} \cdot \left(n_{\mathrm{I}}[\mathrm{h}^-] - \varepsilon \cdot n_{\mathrm{R}}[\mathrm{h}^-]\right), \tag{1}$$

where:

(i) $n_{\mathrm{I}}[\mathrm{h}^-]$ and $n_{\mathrm{R}}[\mathrm{h}^-]$ is the number of tracks in a given bin per event selected for the analysis (see Sect. 5.2) for the data with the liquid hydrogen inserted and removed, respectively,
(ii) ε is the ratio of the interaction probabilities for the removed and inserted target operation.

ε was derived based on the distribution of the fitted z coordinate of the interaction vertex. All vertices far away from the target originate from interactions with the beam-line and

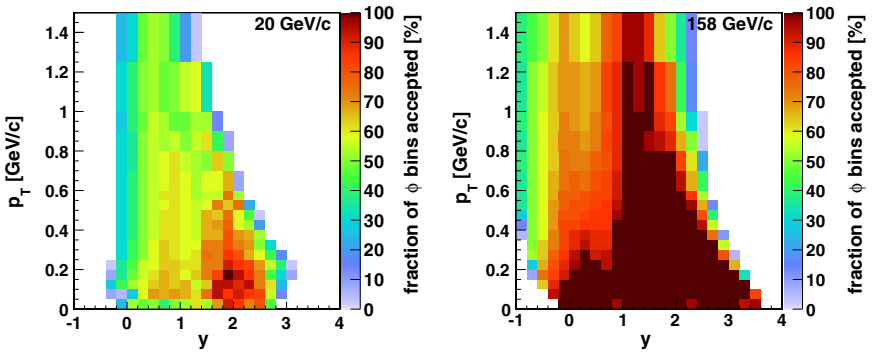

Fig. 12 Detector acceptance at 20 (*left*) and 158 GeV/*c* (*right*). The acceptance is calculated as fraction of (y, p_T, ϕ) bins accepted for given y and p_T for tracks with $p_x < 0$ selected for this analysis

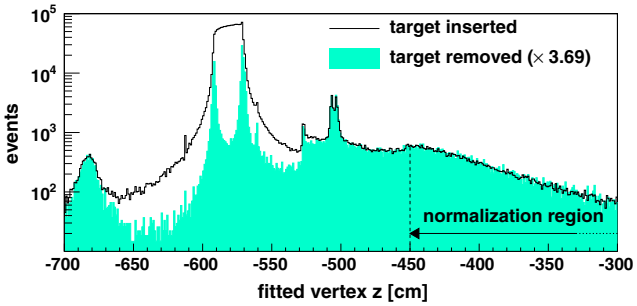

Fig. 13 Distribution of fitted vertex z coordinate for data on p+p interactions at 40 GeV/*c*. The distribution for the data recorded with the removed liquid hydrogen was multiplied by a factor of $N_I[z > -450\text{ cm}]/N_R[z > -450\text{ cm}]$

Table 4 The ratio of the interaction probabilities, ε, for the removed and inserted target operation for data taking on p+p interactions at 20, 31, 40, 80 and 158 GeV/*c*

p_{beam} (GeV/c)	ε (%)
20	8.0 ± 0.3
31	7.1 ± 0.1
40	10.4 ± 0.1
80	12.7 ± 0.1
158	12.6 ± 0.1

detector materials. Neglecting the beam attenuation in the target one gets:

$$\epsilon = \frac{N_R}{N_I} \cdot \frac{N_I[z > -450\text{ cm}]}{N_R[z > -450\text{ cm}]}, \quad (2)$$

where $N[z > -450\text{ cm}]$ is the number of events with fitted vertex $z > -450$ cm. Examples of distributions of z of the fitted vertex for events recorded with the liquid hydrogen inserted and removed are shown in Fig. 13. Values of ϵ are listed in Table 4.

The correction for the off-target interactions changes the yields obtained from the target inserted data by less than ± 5 %, except in the regions where the statistical uncertainty is high.

5.5 The correction for contamination of primary π^- mesons

More than 90 % of primary negatively charged particles produced in p+p interactions in the SPS energy range are π^- mesons [11–13]. Thus π^- meson spectra can be obtained by subtracting the estimated non-pion contribution from the spectra of negatively charged particles and additional particle identification is not required.

The simulation described in Sect. 4 was used to calculate corrections for the admixture of particles other than primary π^- mesons to the reconstructed negatively charged particles. The dominating contributions are primary K^- and $\bar{p}$, and secondary π^- from weak decays of Λ and K^0_S (feed-down) and from secondary interactions, incorrectly fitted to the primary vertex.

The EPOS spectra were adjusted based on the existing data [24,29]. Preliminary NA61/SHINE results were used to scale double differential spectra of K^-, and $\bar{p}$ [30]. EPOS spectra of π^- were replaced by the preliminary NA61/SHINE results [31] normalised to the multiplicity from the world data compilation [32]. Spectra of Λ and K^0_S were scaled by a constant factor derived at each energy using the world data compilation [33] of total multiplicities. The impact of the adjustments on the final spectra ranges from -2 % to $+5$ % in most regions, except of the low p_T region at the low beam momenta, where it reaches $+20$ %.

As it was found in [24] the yields of K^- and $\bar{p}$ are strongly correlated with the π^- yield. Thus the correction for the contribution of primary hadrons is performed via the multiplicative factor c_K. On the contrary the contribution due to weak decays and secondary interactions is mostly located in the low p_T region, and it is weakly correlated with the primary pion yield in this region. Thus this feed-down contribution is corrected for using the additive correction c_V. The total correction is applied in as:

$$n_{\text{prim}}[\pi^-] = \left(n_T[h^-] - c_V\right) \cdot c_K, \tag{3}$$

where

$$c_V = \left(n[\pi^-_\Lambda] + n[\pi^-_{K^0_S}] + n[\text{other}]\right)^{MC}_{sel}, \tag{4}$$

$$c_K = \left(\frac{n[\pi^-]}{n[K^-] + n[\bar{p}] + n[\pi^-]}\right)^{MC}_{sel}. \tag{5}$$

The spectrum of a particle x is denoted as $n[x]$ whereas n[other] stands for all primary and secondary particles other than K^-, $\bar{p}$, π^- and feed-down from Λ and K^0_S. The spectrum n[other] of all other particles originates mostly from secondary interactions with >90 % occurring in the hydrogen target. This contribution was taken from the simulations without an additional adjustment. The superscript ^{MC} marks adjusted EPOS spectra. The subscript $_{sel}$ indicates that the event and track selection criteria were applied and then the correction for the detector acceptance was performed; the reconstructed tracks were identified by matching.

5.6 Correction for event as well as track losses and migration

The multiplicative correction c_{loss} for losses of inelastic events as well as losses and bin-to-bin migration of primary π^- mesons emitted within the acceptance is calculated using the Monte Carlo simulation as:

$$c_{loss} = n[\pi^-]^{MC}_{gen} \,/\, n[\pi^-]^{MC}_{sel}, \tag{6}$$

where the subscript $_{gen}$ indicates the generated spectrum of primary π^- mesons binned according to the generated momentum vector. Then the final, corrected π^- meson spectrum in inelastic p+p interactions is calculated as

$$n[\pi^-] = c_{loss} \cdot n_{prim}[\pi^-]\,. \tag{7}$$

The dominating effects contributing to the c_{loss} correction are

- losses of inelastic events due to the trigger and off-line event selection,
- the pion migration between analysis bins,
- the pion reconstruction inefficiency.

5.7 Statistical and systematic uncertainties

5.7.1 Statistical uncertainties

Statistical errors receive contributions from the finite statistics of both the data as well as the simulated events used to obtain the correction factors. The dominating contribution is the uncertainty of the data which is calculated assuming a Poisson probability distribution for the number of entries in a bin. The Monte Carlo statistics was higher than the data statistics. Also the uncertainties of the Monte Carlo corrections are significantly smaller than the uncertainties of the number of entries in bins.

5.7.2 Systematic uncertainties

Systematic errors presented in this paper were calculated taking into account contributions from the following effects.

(i) Possible biases due to event and track cuts which are not corrected for. These are:

- a possible bias due to the dE/dx cut applied to remove electrons,
- a possible bias related to the removal of events with off-time beam particles close in time to the trigger particle.

The magnitude σ_i of possible biases was estimated by varying values of the corresponding cuts. The dE/dx cut was changed by ± 0.01 dE/dx units (where 1 corresponds to a minimum ionising particle, and 0.04 is a typical width of a single particle distribution), and the off-time interactions cut was varied from a ± 1 μs to a ± 3 μs time window. The assigned systematic uncertainty was calculated as the maximum of the absolute differences between the results obtained for both cut values. This contribution is drawn with a long-dashed red line in Fig. 14.

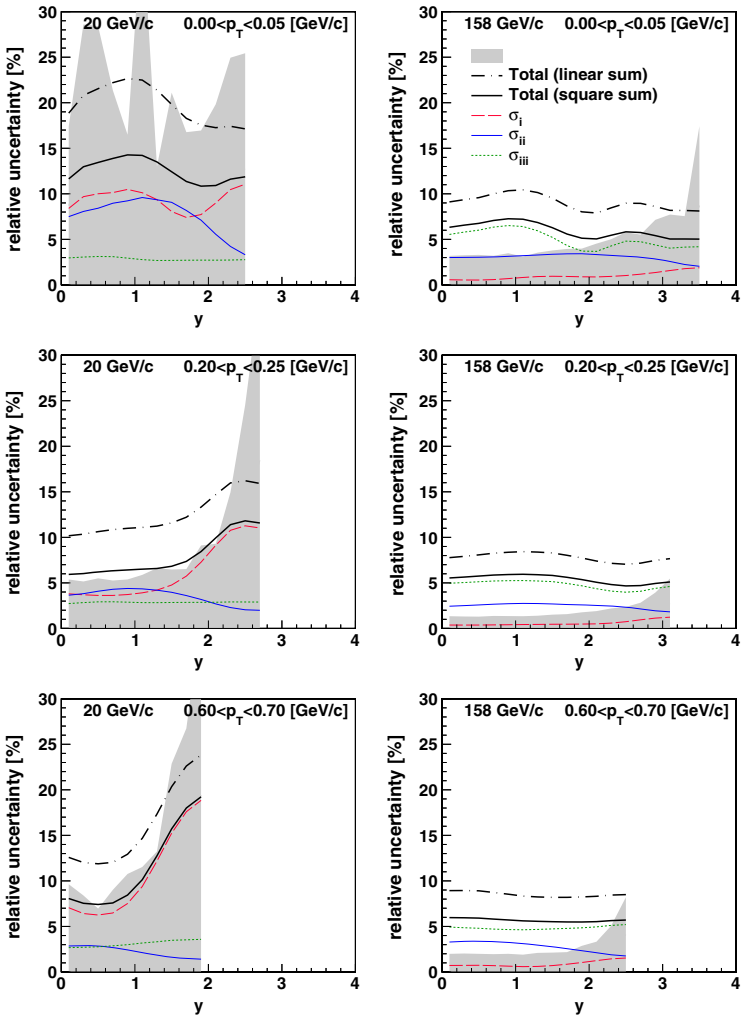

Fig. 14 Statistical and systematic uncertainties in selected bins of p_T for 20 (*left*) and 158 GeV/c (*right*) p+p data. The *shaded band* shows the statistical uncertainty. The *coloured thin lines* show the contributions to the systematic uncertainty listed in Sect. 5.7.2. The *thick black lines* show the total systematic uncertainty, which was calculated by adding the contributions in quadrature (*continuous line*) or linearly (*dashed/dotted line*, shown for comparison)

(ii) Uncertainty of the correction for contamination of the primary π^- mesons. The systematic uncertainty σ_{ii} of this correction was assumed as 20 % (for 40, 80 and 158 GeV/c) and 40 % (for 20 and 31 GeV/c) of the absolute value of the correction. At the low beam momenta there was less data available to adjust the simulated spectra, which was the reason to increase the uncertainty. This contribution is drawn with a dashed-dotted blue line in Fig. 14. The absolute correction is small thus the related systematic uncertainty is small also.

(iii) Uncertainty of the correction for the event losses. The uncertainty was estimated using 20 % of the correction magnitude and a comparison with the correction calculated using the VENUS [34,35] model:

$$\sigma_{\mathrm{iii}} = 0.2 \cdot \left|1 - c_{\mathrm{loss}}^{\mathrm{EPOS}}\right| + \left|c_{\mathrm{loss}}^{\mathrm{EPOS}} - c_{\mathrm{loss}}^{\mathrm{VENUS}}\right|. \quad (8)$$

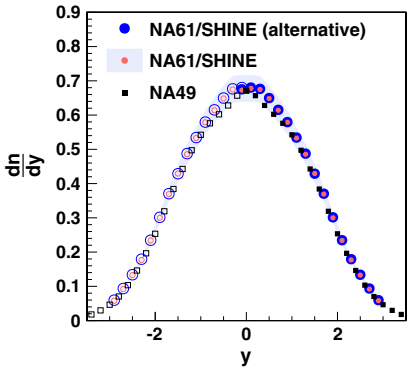

Fig. 15 Rapidity distribution of π^- mesons produced in inelastic p+p interactions at 158 GeV/c. The *big blue points* show the results obtained with an alternative method: without vertex fit requirement and rejection of events with a single very high momentum positively charged track. The results of NA61/SHINE (this paper, *red dots*) are compared with the NA49 measurements [11] (*black squares*). The *open symbols* show points reflected with respect to mid-rapidity. A single NA61/SHINE point measured at $y < 0$ is also shown for comparison. The *shaded band* shows the NA61/SHINE systematic uncertainty

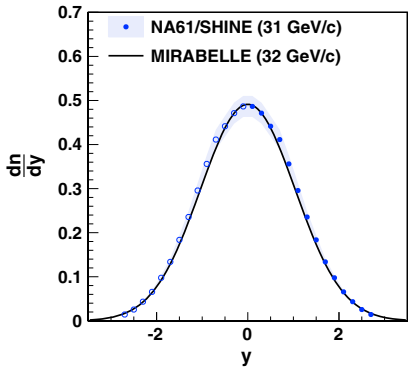

Fig. 16 Rapidity distribution of π^- mesons produced in inelastic p+p interactions. The NA61/SHINE results at 31 GeV/c (*blue points*) are compared with the MIRABELLE measurement (parametrised by the *black line*) at 32 GeV/c. The *shaded band* shows the NA61/SHINE systematic uncertainty

This contribution is drawn with a short-dashed green line in Fig. 14.

(iv) Uncertainty related to the track selection method. It was estimated by varying the track selection cuts: removing the impact parameter cut and decreasing the minimum number of required points to 25 (total) and 10 (in VTPCs) and by checking symmetries with respect to $y = 0$ and $p_T = 0$. The potential bias is below 2 % and the corresponding contribution was neglected.

The total systematic uncertainty was calculated by adding in quadrature the contributions $\sigma_{sys} = \sqrt{\sigma_i^2 + \sigma_{ii}^2 + \sigma_{iii}^2}$. This uncertainty is listed in the tables including numerical values and it is visualised by a shaded band around the data points in plots presenting the results. Statistical and systematic uncertainties in selected example regions are shown in Fig. 14. Systematic biases in different bins are correlated, whereas statistical fluctuations are almost independent.

Figure 15 presents a comparison of the rapidity spectrum of π^- mesons produced in inelastic p+p interactions at 158 GeV/c (for details see Sect. 6) from the present analysis with the corresponding spectrum measured by NA49 [11]. Statistical and systematic uncertainties of the NA49 spectrum are not explicitly given but the published information implies that the systematic uncertainty dominates and amounts to several %. The results agree within the systematic uncertainties of the NA61/SHINE spectra.

The analysis method of p+p interactions at 158 GeV/c performed by NA49 [11] differed from the one used in this paper. In particular, pions were identified by dE/dx measurement and the NA49 event selection criteria did not include the selection according to the fitted z coordinate of the interaction vertex and the rejection of elastic interactions. Namely, all events passing the trigger selection and off-line quality cuts were used for the analysis. For comparison, this event selection procedure was applied to the NA61/SHINE data. As a result 20 % more events were accepted. Approximately half of them were unwanted elastic and off-target interactions and half were wanted inelastic interactions. Then the corrections corresponding to the changed selection criteria were applied (the contribution of elastic events was subtracted using the estimate from Ref. [11]). The fully corrected rapidity spectrum obtained using this alternative analysis is also shown in Fig. 15. The differences between the results for the standard and alternative methods are below 0.5 % at $y < 2$ and below 2 % at higher y.

Figure 16 shows a comparison of the rapidity distribution at 31 GeV/c with the MIRABELLE results at 32 GeV/c [36, 37]. A parametrisation of the distribution and the total π^- multiplicity are provided. As the parametrisation appears to be incorrectly normalised, we normalised it to the total multiplicity. The results agree within the NA61/SHINE systematic uncertainties.

The spectra measured in p+p interactions should obey reflection symmetry with respect to mid-rapidity. As the NA61/SHINE acceptance extends somewhat below mid-rapidity a check of the reflection symmetry can be performed and used to validate the measurements. It was verified that the yields measured for $y < 0$ agree with those measured for $y > 0$ in the reflected acceptance within 1.5 %. A similar

agreement was also found at lower beam momenta. The measurements above mid-rapidity are taken as the final results. Nevertheless, for comparison the points at $y < 0$ were added in Figs. 15 and 20 in the regions where the p_T acceptance extends to zero.

6 Results

This section presents results on inclusive π^- meson spectra in inelastic p+p interactions at beam momenta of 20, 31, 40, 80 and 158 GeV/c. The spectra refer to pions produced by strong interaction processes and in electromagnetic decays of produced hadrons.

Numerical results corresponding to the plotted spectra as well as their statistical and systematic uncertainties are given in Ref. [38].

6.1 Double differential spectra

The double differential inclusive spectra of π^- mesons in rapidity and transverse momentum produced in inelastic p+p interactions at 20, 31, 40, 80 and 158 GeV/c are shown in Fig. 17. The transverse momentum distributions at 20 and 158 GeV/c are plotted in Fig. 18. Here $\frac{d^2n}{dy\,dp_T}$ or $\frac{d^2n}{dy\,dm_T}$ were calculated by dividing the fully corrected bin contents $n[\pi^-]$ (see Sect. 5) by the bin size. The spectra in (y, m_T) are not shown here but they are given in the compilation of the numerical values [38].

6.2 Transverse mass spectra

The transverse mass spectra at mid-rapidity ($0 < y < 0.2$) are shown in Fig. 19 (*left*). A function

$$\frac{dn}{dm_T} = A \cdot m_T \cdot \exp\left(-\frac{m_T}{T}\right) \tag{9}$$

was fitted in the range $0.2 < m_T - m_\pi < 0.7\,\mathrm{GeV}/c^2$ and is indicated by lines in Fig. 19 (*left*). The fitted parameters were the normalisation A and the inverse slope T. They minimise the χ^2 function which was calculated using statistical errors only. In the χ^2 calculation a measured bin content (dn/dm_T) was compared with the integral of the fitted function in a bin divided by the bin width.

Similar fits were performed to spectra in other rapidity bins containing data in the fit range. The rapidity dependence of the fitted inverse slope parameter T is presented in Fig. 19 (*right*). The T parameter decreases significantly when going from mid-rapidity to the projectile rapidity (y_{beam} = 1.877, 2.094, 2.223, 2.569 and 2.909 at 20, 31, 40, 80 and 158 GeV/c, respectively).

6.3 Rapidity spectra

The rapidity spectra are shown in Fig. 20 (*left*). They were obtained by summing the measured m_T spectra and using the exponential function Eq. (9). The function was fitted in the range ending at the maximum measured m_T, and starting 0.9 GeV/c^2 below (note this is a different fit from the one shown in Fig. 19). The correction is typically below 0.2 % and becomes significant (several %) only at $y > 2.4$. Half of the correction is added in quadrature to the systematic uncertainty in order to take into account a potential imperfectness of the exponential extrapolation. The pion yield increases with increasing collision energy at all measured rapidities.

The rapidity spectra are parametrised by the sum of two Gaussian functions symmetrically displaced with respect to mid-rapidity:

$$\frac{dn}{dy} = \frac{\langle\pi^-\rangle(y_0,\sigma_0)}{2\sigma_0\sqrt{2\pi}} \cdot \cdot \left[\exp\left(-\frac{(y-y_0)^2}{2\sigma_0^2}\right) + \exp\left(-\frac{(y+y_0)^2}{2\sigma_0^2}\right)\right], \tag{10}$$

where y_0 and σ_0 are fit parameters, and the total multiplicity $\langle\pi^-\rangle(y_0,\sigma_0)$ is calculated from the requirement that the integral over the measured spectrum equals the integral of the fitted function Eq. (10) in the range covered by the measurements. The χ^2 function was minimised in a similar way as in case of the m_T spectra, namely using the integral of the function in a given bin. The numerical values of the fitted parameters as well as the r.m.s. width $\sigma = \sqrt{y_0^2 + \sigma_0^2}$ are given in Table 5.

6.4 Mean multiplicities

Mean multiplicities of π^- mesons, $\langle\pi^-\rangle$, produced in inelastic p+p interactions at 20, 31, 40, 80 and 158 GeV/c were calculated as the integral of the fitted function Eq. (10). The extrapolation into the unmeasured region at large y contributes about 1 %. Half of it is added in quadrature to the systematic uncertainty.

The dependence of the produced average $\langle\pi^-\rangle$ multiplicity per inelastic p+p collision on the Fermi's energy measure [39],

$$F \equiv \left[\frac{(\sqrt{s_{NN}} - 2m_N)^3}{\sqrt{s_{NN}}}\right]^{1/4} \tag{11}$$

is plotted in Fig. 20 (*right*). The results of NA61/SHINE are in agreement with a compilation of the world data [11,32].

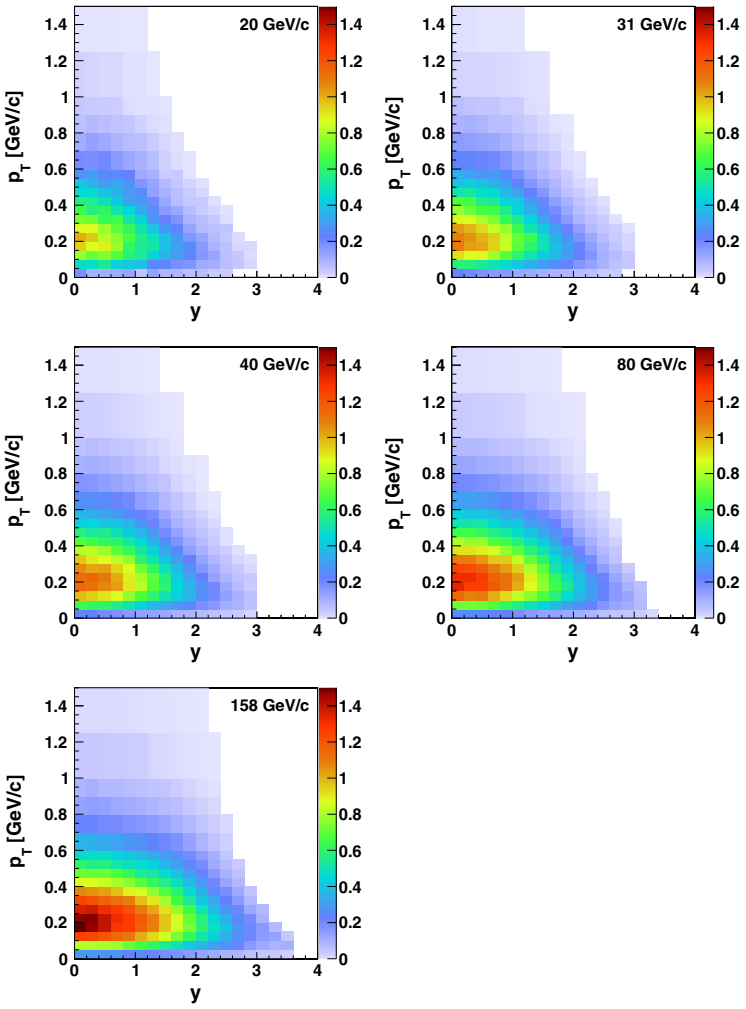

Fig. 17 Double differential spectra $d^2n/(dy\,dp_T)[(GeV/c)^{-1}]$ of π^- mesons produced in inelastic p+p interactions at 20, 31, 40, 80 and 158 GeV/c

7 Comparison with central Pb+Pb collisions

In this section the NA61/SHINE results on inelastic p+p interactions are compared with the corresponding data on central Pb+Pb collisions published previously by NA49 [2,3]. Pion production properties which are different and similar in p+p interactions and central Pb+Pb collisions are identified. For completeness selected plots include the compilation of the world data on inelastic p+p interactions [11,32], as well as results on central Au+Au collisions from AGS [40,41] and RHIC [42–46], as processed in Ref. [3].

Figure 21 shows the ratio of transverse mass spectra of π^- mesons produced at mid-rapidity ($0 < y < 0.2$) in central Pb+Pb collisions and p+p interactions at the same collision energy per nucleon. The spectra were normalised to unity before dividing. First, one observes that the ratio is not constant implying that the spectral shapes are different in p+p interactions and central Pb+Pb collisions. Second, it is seen that the ratio depends weakly, if at all, on collision energy. The ratio is higher than unity in the left ($m_T - m_\pi < 0.1\,GeV/c^2$) and right ($m_T - m_\pi > 0.5\,GeV/c^2$)

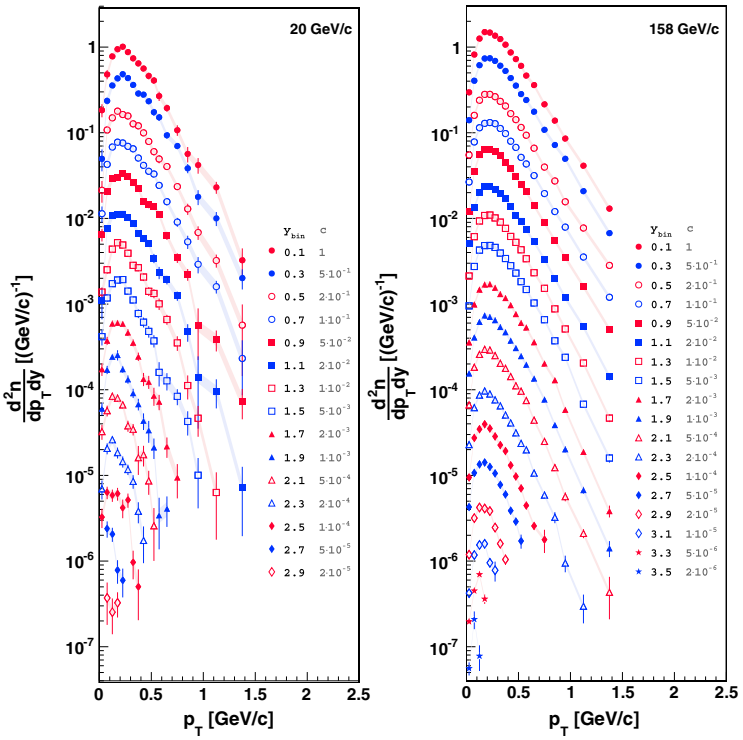

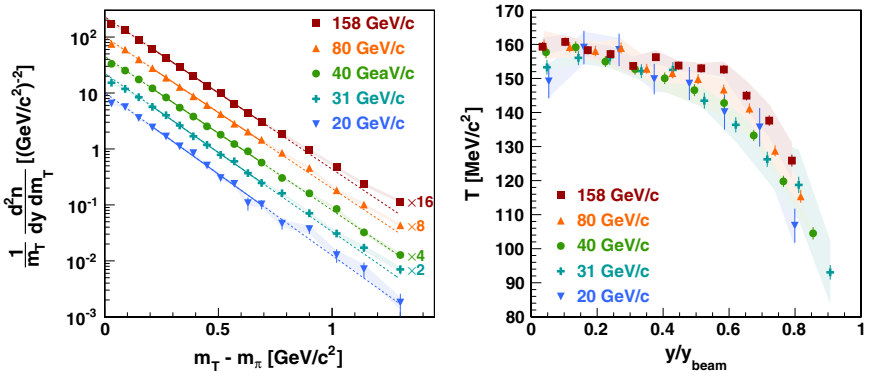

Fig. 18 Transverse momentum spectra of π^- mesons produced in inelastic p+p interactions at 20 (*left*) and 158 GeV/c (*right*) in various rapidity ranges. The legend provides the centres of the rapidity bins, y_{bin} and the scaling factor c used to separate the spectra visually

Fig. 19 *Left* Transverse mass spectra at mid-rapidity ($0 < y < 0.2$). The fitted exponential function Eq. (9) is indicated by solid lines in the fit range $0.2 < m_{\text{T}} - m_\pi < 0.7\,\text{GeV}/c^2$ and *dashed lines* outside the fit range. The data points for different beam momenta were scaled for better readability. *Right* The inverse slope parameter T of the transverse mass spectra as a function of rapidity divided by the projectile rapidity. The fit range is $0.2 < m_{\text{T}} - m_\pi < 0.7\,\text{GeV}/c^2$. The results refer to π^- mesons produced in inelastic p+p interactions at 20, 31, 40, 80 and 158 GeV/c

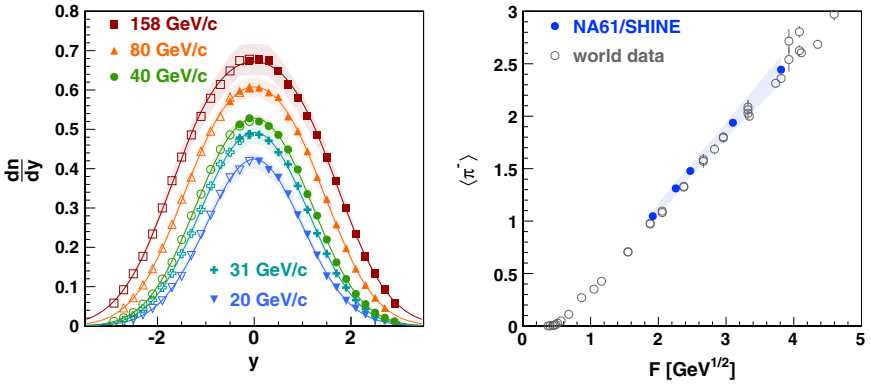

Fig. 20 *Left* Rapidity spectra obtained from sums of the measured and extrapolated m_T spectra. *Closed symbols* indicate measured points, open points are reflected with respect to mid-rapidity. The measured points at $y < 0$ are shown for systematic comparison only. The plotted statistical errors are smaller than the symbol size. The systematic uncertainties are indicated by the *coloured bands*. The *lines* indicate fits of the sum of two symmetrically displaced Gaussian functions (see Eq. (10)) to the spectra. The results refer to π^- mesons produced in inelastic p+p interactions at 20, 31, 40, 80 and 158 GeV/c. *Right* Dependence of the mean total multiplicity of π^- mesons produced in inelastic p+p interactions on Fermi's energy measure F (see Eq. (11)). The results of NA61/SHINE are indicated by *filled circles* and the compilation of the world data [32,11] by *open circles*. The plotted statistical errors are smaller than the symbol size. The systematic uncertainties are indicated by the *coloured band*

Table 5 Numerical values of the parameters fitted to rapidity (see Eq. (10)) and transverse mass (see Eq. (9)) spectra of π^- mesons produced in inelastic p+p interactions at 20, 31, 40, 80 and 158 GeV/c. In case of the rapidity fit parameters $\langle\pi^-\rangle$, σ, σ_0 and y_0, the systematic uncertainty dominates. The uncertainties written in the table are the quadrature sum of the statistical and systematic uncertainties. All uncertainties are given numerically in [38]. For T and $\langle m_T\rangle$ the statistical uncertainty is written first and the systematic one second

p_{beam} (GeV/c)	$\langle\pi^-\rangle$	σ	σ_0	y_0	$T\,(y=0)$ (MeV/c^2)	$\langle m_T\rangle(y=0) - m_\pi$ (MeV/c^2)
20	1.047 ± 0.051	0.981 ± 0.017	0.921 ± 0.118	0.337 ± 0.406	$149.1 \pm 5.0 \pm 4.8$	$237.8 \pm 6.4 \pm 2.3$
31	1.312 ± 0.069	1.031 ± 0.016	0.875 ± 0.050	0.545 ± 0.055	$153.3 \pm 2.2 \pm 1.2$	$246.1 \pm 2.7 \pm 0.9$
40	1.478 ± 0.051	1.069 ± 0.014	0.882 ± 0.045	0.604 ± 0.044	$157.7 \pm 1.7 \pm 2.1$	$247.3 \pm 2.0 \pm 0.9$
80	1.938 ± 0.080	1.189 ± 0.026	0.937 ± 0.019	0.733 ± 0.010	$159.9 \pm 1.5 \pm 4.1$	$253.5 \pm 1.9 \pm 1.1$
158	2.444 ± 0.130	1.325 ± 0.042	1.007 ± 0.051	0.860 ± 0.021	$159.3 \pm 1.3 \pm 2.6$	$253.6 \pm 1.6 \pm 1.4$

parts of the m_T range. It is below unity in the central region $0.1 < m_T - m_\pi < 0.5$ GeV/c^2.

The inverse slope parameter T of transverse mass spectra fitted in the range $0.2 < m_T - m_\pi < 0.7$ GeV/c^2 is plotted versus the collision energy in Fig. 22 (*left*). The T parameter is larger by about 10–20MeV/c^2 in central Pb+Pb collisions than in p+p interactions.

The transverse mass spectra measured by NA61/SHINE and NA49 allow a reliable calculation of mean transverse mass. A small correction to the measured value for the high m_T region not covered by the measurements was applied based on the exponential extrapolation of the tail of the distributions. Half of the correction was added to the systematic uncertainty on $\langle m_T\rangle$. In spite of the different shapes of the m_T spectra the mean transverse mass calculated for p+p interactions and central Pb+Pb collisions is similar, see Fig. 22 (*right*). This is because the differences shift the mean m_T in opposite directions for different regions of m_T and as a result leave it almost unchanged. Thus the mean transverse mass appears to be insensitive to the apparent changes of the pion production properties observed between p+p interactions and central Pb+Pb collisions.

Figure 23 (*left*) presents the ratio of the normalised π^- rapidity spectra produced in central Pb+Pb and inelastic p+p interactions at the same collision energy per nucleon. The spectra are plotted versus the rapidity scaled by the beam rapidity. Only weak, if any, energy dependence of the ratio is observed. Moreover, the ratio is close to unity in the central rapidity region ($y/y_{\text{beam}} < 0.6$), whereas it is higher closer to beam rapidity ($y/y_{\text{beam}} > 0.6$).

Consequently the r.m.s. width σ of rapidity distributions of π^- mesons produced in p+p interactions is smaller than

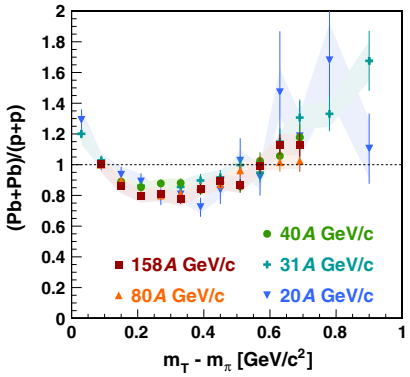

Fig. 21 The ratio of the normalised transverse mass spectra of π^- mesons at mid-rapidity produced in central Pb+Pb collisions and inelastic p+p interactions at the same collision energy per nucleon. The *coloured bands* represent the systematic uncertainty of the p+p data

the width in central Pb+Pb collisions. This is seen in Fig. 23 (*right*) where the energy dependence of σ is plotted. Additionally, p+p data from [11,36,37,47] are shown; they agree with the NA61/SHINE results.

Note, that when interpreting differences between results obtained for inelastic p+p interactions and central Pb+Pb collisions the isospin effects should be taken into account. This concerns both the spectra as well as the total multiplicities [11].

In order to reduce their influence the mean multiplicity of pions is obtained from a sum of mean multiplicities of negatively and positively charged pions using the phenomenological formula [15]:

$$\langle \pi \rangle = \frac{3}{2}\left(\langle \pi^+ \rangle + \langle \pi^- \rangle\right). \tag{12}$$

The results divided by the mean number of wounded nucleons ($N_W = 2$ for p+p) are shown in Fig. 24 as a function of the Fermi energy measure F. The value of $\langle \pi^+ \rangle$ for the NA61/SHINE results on inelastic p+p interactions was estimated from the measured $\langle \pi^- \rangle$ multiplicity assuming $\langle \pi^+ \rangle = \langle \pi^- \rangle + 2/3$. This assumption is based on the compilation of the world data presented in Ref. [15] and the model presented therein. At beam momenta lower than 40A GeV/c the $\langle \pi \rangle / \langle N_W \rangle$ ratio is higher in p+p interactions than in central Pb+Pb collisions. The opposite relation holds for beam momenta higher than 40A GeV/c. The energy dependence for inelastic p+p interactions crosses the one for central Pb+Pb (Au+Au) collisions at about 40A GeV/c.

8 Summary

We presented experimental results on inclusive spectra and mean multiplicities of negatively charged pions produced in inelastic p+p interactions at 20, 31, 40, 80 and 158 GeV/c. Two dimensional spectra in transverse momentum and rapidity and parameters characterizing them were given. The results agree with existing sparse measurements, extend their range, accuracy and depth of detail.

The results on inelastic p+p interactions were compared with the corresponding data on central Pb+Pb collisions obtained by NA49. The spectra in p+p interactions are narrower both in rapidity and in transverse mass, which might be

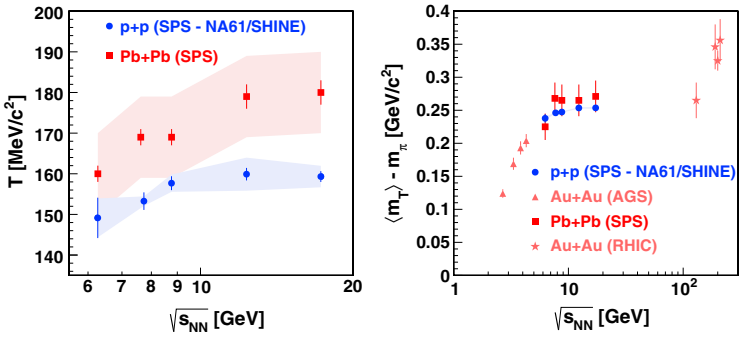

Fig. 22 *Left* Inverse slope parameter T of the transverse mass spectra at mid-rapidity ($0 < y < 0.2$) plotted against the collision energy per nucleon. The parameter T was fitted in the range $0.2 < m_T - m_\pi < 0.7$ GeV/c^2. The systematic uncertainty for the two lowest energy points for Pb+Pb, not given in [3] is assumed to be the same as for the higher energies [2]. *Right* Mean transverse mass $\langle m_T \rangle$ at mid-rapidity ($0 < y < 0.2$) versus the collision energy. The results on inelastic p+p interactions are compared with the corresponding data on central Pb+Pb (Au+Au) collisions

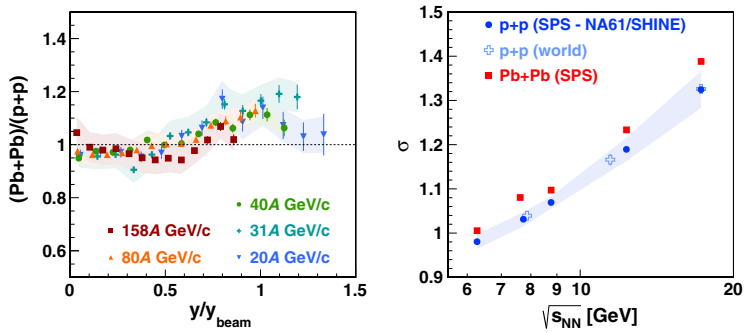

Fig. 23 *Left* The ratio of normalised rapidity spectra of π^- mesons produced in central Pb+Pb collisions and inelastic p+p interactions at the same collision energy per nucleon plotted versus the rapidity scaled by the beam rapidity. The *coloured bands* represent the NA61/SHINE systematic uncertainty. *Right* Energy dependence of the width of the rapidity distribution of π^- mesons produced in p+p interactions and central Pb+Pb collisions. The systematic uncertainty for the Pb+Pb points is not given

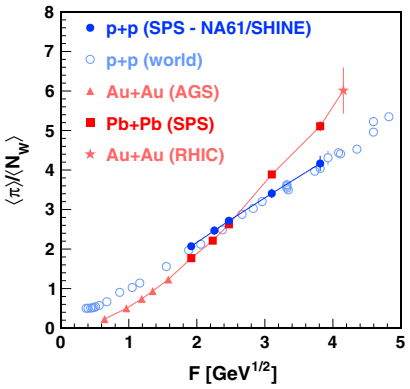

Fig. 24 Mean multiplicity of all pions per wounded nucleon produced in inelastic p+p interactions and central Pb+Pb (Au+Au) collisions. The *vertical lines* show the total uncertainty

attributed to isospin effects. The mean pion multiplicity per wounded nucleon in p+p interactions increases more slowly with energy in the SPS range and crosses the corresponding dependence measured in the Pb+Pb collisions at about 40*A* GeV/*c*.

Acknowledgments This work was supported by the Hungarian Scientific Research Fund (Grants OTKA 68506 and 71989), the Polish Ministry of Science and Higher Education (Grants 667/N-CERN/2010/0, NN 202 48 4339 and NN 202 23 1837), the National Science Center of Poland (Grant UMO-2012/04/M/ST2/00816), the Foundation for Polish Science—MPD program, co-financed by the European Union within the European Regional Development Fund, the Federal Agency of Education of the Ministry of Education and Science of the Russian Federation (Grant RNP 2.2.2.2.1547), the Russian Academy of Science and the Russian Foundation for Basic Research (Grants 08-02-00018, 09-02-00664, and 12-02-91503-CERN), the Ministry of Education, Culture, Sports, Science and Technology, Japan, Grant-in-Aid for Scientific Research (Grants 18071005, 19034011, 19740162, 20740160 and 20039012), the German Research Foundation (Grants GA 1480/2-1, GA 1480/2-2), Bulgarian National Scientific Foundation (Grant DDVU 02/19/2010), Ministry of Education and Science of the Republic of Serbia (Grant OI171002), Swiss Nationalfonds Foundation (Grant 200020-117913/1) and ETH Research Grant TH-01 07-3. Finally, it is a pleasure to thank the European Organization for Nuclear Research for a strong support and hospitality and, in particular, the operating crews of the CERN SPS accelerator and beam lines who made the measurements possible.

References

1. N. Antoniou et al. (NA49-future Collaboration), CERN-SPSC-2006-034 (2006)
2. S.V. Afanasiev et al., (NA49 Collaboration). Phys. Rev. C **66**, 054902 (2002). [arXiv:0205002 [nucl-ex]]
3. C. Alt et al., (NA49 Collaboration), Phys. Rev. C **77**, 024903 (2008). [arXiv:0710.0118 [nucl-ex]]
4. A. Rustamov, Central Eur. J. Phys. **10**, 1267 (2012). [arXiv:1201.4520 [nucl-ex]]
5. Y. Itow et al., (T2K Collaboration), arXiv:0106019 [hep-ex] (2001)
6. K. Abe et al., (T2K Collaboration), Nucl. Instrum. Meth. A **659**, 106–135 (2011)
7. N. Abgrall et al., (NA61/SHINE Collaboration), CERN-SPSC-2012-022; SPSC-P-330-ADD-6
8. K. Abe et al., (T2K Collaboration), Phys. Rev. D **87**, 012001 (2013)
9. J. Abraham et al., (Pierre Auger Collaboration), Nucl. Instrum. Meth. A **523**, 50 (2004)
10. T. Antoni et al., (KASCADE Collaboration), Nucl. Instrum. Meth. A **513**, 490 (2003)

11. C. Alt et al., (NA49 Collaboration), Eur. Phys. J. C **45**, 343–381 (2006). [arXiv:0510009 [hep-ex]]
12. T. Anticic et al., (NA49 Collaboration), Eur. Phys. J. C **65**, 9 (2010). [arXiv:0904.2708 [hep-ex]]
13. T. Anticic et al., (NA49 Collaboration), Eur. Phys. J. C **68**, 1 (2010). [arXiv:1004.1889 [hep-ex]]
14. M. Gazdzicki, M. Gorenstein, P. Seyboth, Acta Phys. Polon. B **42**, 307 (2011). [arXiv:1006.1765 [hep-ph]]
15. A.I. Golokhvastov, Phys. Atom. Nucl. **64**, 1841 (2001). [Yad. Fiz. 64, 1924 (2001)]
16. S. Afanasiev et al., (NA49 Collaboration), Nucl. Instrum. Meth. A **430**, 257 (1999)
17. N. Abgrall et al., (NA61/SHINE Collaboration), Phys. Rev. C **84**, 034604 (2011). [arXiv:1102.0983 [hep-ex]]
18. C. Bovet, R. Maleyran, L. Piemontese et al., CERN-YELLOW-82-13
19. C. Strabel, Ph.D. Thesis, ETH, Zurich, Switzerland (2011). https://edms.cern.ch/document/1136130/1
20. N. Abgrall et al., (NA61/SHINE Collaboration), J. Instrum. (submitted). [arXiv:1401.4699 [physics.ins-det]]
21. N. Abgrall et al., (NA61/SHINE Collaboration), Report No. CERN-SPSC-2008-018 (2008)
22. M. Unger, for the NA61/SHINE Collaboration, EPJ Web Conf. **52**, 01009 (2013). [arXiv:1305.5281 [nucl-ex]]
23. M. Unger et al., (NA61/SHINE Collaboration), PoS ICHEP **2010**, 449 (2010). arXiv:1012.2604 [nucl-ex]
24. A. Ilnicka, Master Thesis, University of Warsaw, Poland (2013) https://edms.cern.ch/document/1319366
25. K. Werner, Nucl. Phys. B **175**(Proc. Suppl.), 81 (2008)
26. N. Abgrall, Ph.D. Thesis, University of Geneva, Geneva, Switzerland (2011). https://edms.cern.ch/document/1172455/1
27. R. Brun, F. Carminati, GEANT Detector Description and Simulation Tool, CERN Program Library Long Writeup W5013 (1993). http://wwwasdoc.web.cern.ch/wwwasdoc/geant/geantall.html
28. J. Beringer, Particle Data Group, Phys. Rev. D **86**, 010001 (2012)
29. A. Aduszkiewicz, Ph.D. Thesis in preparation, University of Warsaw, Poland (2014)
30. S. Puławski, PoS, CPOD **2013**, 056 (2013). http://pos.sissa.it/archive/conferences/185/056/CPOD%202013_056.pdf
31. A. Aduszkiewicz, EuNPC 2012 (2012). http://www.nipne.ro/indico/contributionDisplay.py?contribId=268&sessionId=2&confId=0
32. M. Gazdzicki, D. Roehrich, Z.Phys.C **65**, 215 (1995)
33. M. Gaździcki, D. Röhrich, Z.Phys.C **71**, 55 (1996)
34. K. Werner, Nucl. Phys. A **525**, 501c (1991)
35. K. Werner, Phys. Rep. **232**, 87 (1993)
36. E.E. Zabrodin et al., Phys. Rev. D **52**, 1316 (1995)
37. E.E. Zabrodin, private communication.
38. https://edms.cern.ch/document/1314605
39. E. Fermi, Prog. Theor. Phys. **5**, 570 (1950)
40. J. Klay et al., (E895 Collaboration), Phys. Rev. C **68**, 054905 (2003)
41. L. Ahle et al., E802 Collaboration, Phys. Rev. C **57**, 466 (1998)
42. B.B. Back et al., (PHOBOS Collaboration). [arXiv:0301017 [nucl-ex]]
43. K. Adcox et al., (PHENIX Collaboration), Phys. Rev. C **69**, 024904 (2004)
44. S.S. Adler et al., (PHENIX Collaboration), Phys. Rev. C **69**, 034909 (2004)
45. J. Adams et al., (STAR Collaboration), Phys. Rev. Lett. **92**, 112301 (2004)
46. I.G. Bearden et al., (BRAHMS Collaboration), Phys. Rev. Lett. **94**, 162301 (2005)
47. V.V. Ammosov et al., Nuovo Cimento **40**, 237 (1977)

Applied Radiation and Isotopes 87 (2014) 70–72

Contents lists available at ScienceDirect

Applied Radiation and Isotopes

journal homepage: www.elsevier.com/locate/apradiso

Variations of gamma-ray background in the Belgrade shallow underground low-level laboratory

Radomir Banjanac [1,*], Aleksandar Dragić, Vladimir Udovičić, Dejan Joković, Dimitrije Maletić, Nikola Veselinović, Mihailo Savić

Institute of Physics, University of Belgrade, Belgrade 11080, Serbia

HIGHLIGHTS

- Time variability of Ge detector background was measured in two laboratories.
- Variations of cosmic ray intensity and radon concentration were tested.
- Advantage of an underground laboratory compared to a ground level one was proved.

ARTICLE INFO

Available online 1 December 2013

Keywords:
Underground low-level laboratory
Cosmic rays
Radon variability

ABSTRACT

During the last three years we investigated the variations of background simultaneously in two laboratories, the ground level (GLL) and the underground laboratory. The Forbush-like effect from March 2010 was observed in the GLL using a Ge detector and plastic veto scintillator. The underground plastic scintillator saw the same effect but the coincident veto spectrum did not detect the decrease of cosmic-ray intensity. Using a time series analysis of prominent post-radon lines, a significant radon daily variability was detected in the Ge detector background spectrum, but only in the GLL.

1. Introduction

Any long and even short-term gamma-ray background measurement is subject to certain temporal variations due to time variability of two prominent contributors to background—cosmic-ray intensity and radon concentration. The duration of background measurements may be anything from one day to several months, depending on the wanted final statistical accuracy of the envisaged measurements. These measurements, however, yield only average values of the background, what in principle may lead to systematic errors in later measurements, especially of NORM samples.

Radon concentrations are known to vary considerably, depending on many parameters that determine this concentration in every particular case. This includes the deposition of radon progenies on the walls of lead castles and detectors themselves, what makes even the traditional radon suppression method by flushing the interior of the sample chamber with nitrogen potentially ineffective.

On the other side, effective protection of Ge detectors from cosmic-rays is provided by active veto shielding using convenient large area detectors, although all significant periodic and aperiodic variations of cosmic ray intensity can usually be neglected since contributions to background, apart from the annihilation line, lie in the continuum.

2. Description of the laboratories and equipment

The Belgrade underground low-level laboratory (UL), located at a depth of 25 m. w. e (meter water equivalent) is equipped with ventilation system which provides low radon concentration of 13 (5) Bq/m^3, the mean value being obtained from more than two years long-term measurement. The UL is presented in more detail by Antanasijević et al. (1999), and the especially designed ventilation system for radon reduction in the laboratory has been described by Udovičić et al. (2009). This system consists of two "radon shields"—the passive and the active one. The passive shield consists of 1 mm thick aluminum foil which completely covers all the wall surfaces inside the laboratory, including floor and ceiling. It is hermetically sealed with a silicon sealant to prevent diffusion of radon from surrounding soil and concrete walls of the laboratory. As the active radon shield the laboratory is continuously ventilated with fresh air, filtered through one rough filter for dust elimination

* Corresponding author. Tel.: +381 11 3161274.
E-mail address: banjanac@ipb.ac.rs (R. Banjanac).
[1] Postal address: Pregrevica street, number 118, 11080 Belgrade, Serbia.

0969-8043/$ - see front matter © 2013 Elsevier Ltd. All rights reserved.
http://dx.doi.org/10.1016/j.apradiso.2013.11.091

followed by active charcoal filters (cross-section of 60 cm × 60 cm, weight of 40 kg) for radon adsorption.

The UL has an area of 45 m^2 and volume of 135 m^3 what required the rate of air inlet adjusted to 800 m^3/h. This huge amount of fresh air contributes to greater temperature variations and the long-term mean value of temperature inside the UL is 19 (4)°C. On the other side the rate of air outlet (700 m^3/h) was adjusted to get an overpressure of about 2 hPa over the atmospheric pressure, what prevents radon diffusion through eventual imperfections in the aluminum layer. The pressure buffer corridor to the laboratory (18 m^2) ensures almost constant value of this overpressure. Relative humidity is controlled by a dehumidifier device, what provides that the relative humidity in the underground laboratory does not exceed 60%.

All the measurements presented in this work which were performed in the underground laboratory were performed in the ground level laboratory (GLL) as well. The GLL is air-conditioned and represents a typical ground level laboratory. This laboratory is situated in two joined standard transportation containers with iron sheet walls, but furnished with quality thermal insulation. The GLL has an area of 30 m^2 and volume of 75 m^3. It is air-conditioned (average radon concentration of 50(30) Bq/m^3).

The low-level background detector system in the UL includes an intrinsically low-radioactivity level Ge detector (35% relative efficiency, named Ge1) and a plastic veto scintillator (1 m^2, named PS1) situated coaxially above the Ge1 detector. Comparative background study is performed in the GLL which is equipped with a Ge detector (18% relative efficiency and not intrinsically low-radioactivity level, named Ge2) and a small plastic scintillator (0.125 m^2, named PS2) in veto position.

Radon monitoring inside the laboratories was performed by radon monitor, model RM1029 manufactured by Sun Nuclear Corporation, NRSB approval-code 31822. The device consists of two diffused junction photodiodes as a radon detector, and is furnished with sensors for temperature, barometric pressure and relative humidity. The user can set the measurement intervals from half an hour to 24 h. The device has no online option (direct access to data) but the data are stored in the internal memory of the device and transferred to the personal computer after the measurement interval. The data obtained from the radon monitor (RM) for the temporal variations of the radon concentrations over a long period of time enable the study of the short-term periodical variations simultaneously with Ge detectors (Bossew, 2005).

Two flash analog to digital converters (FADC), made by C.A.E.N (type N1728B), which sample at 10 ns intervals into 2^{14} channels were used to analyze spectra from Ge detectors. User-friendly software was developed to analyze the C.A.E.N data with the possibility to choose the integration time for further time-series analysis that correspond to integration time of the radon monitor.

3. Results and discussion

For routine measurements of NORM samples the simplest arrangement of a Ge detector system is required due to frequent samples exchanges.

As the emphasis was on realistic conditions of radon and cosmic-ray influences on the Ge background neither any additional radon suppression method nor the full (2π coverage) veto arrangement were applied.

3.1. Cosmic-ray influence on the Ge detector background spectrum

The periodicities in cosmic-ray intensity variations (1-day and 27-days) are known to have small amplitudes. The Ge detectors can not see these variations neither in the annihilation line nor in the entire spectrum, mostly due to their small active area. Aperiodic variations of cosmic-ray intensity have greater amplitudes like a Forbush effect which typically lasts for several days. During simultaneously background measurements using two veto shielded Ge detectors the most intensive cosmic-ray variation occurred in March 2010. The decrease of cosmic-ray intensity, which lasted about four days, was very similar to characteristic decrease during a real Forbush effect, hence this event is appointed as a Forbush-like effect. Characteristic variation (decrease) of cosmic-ray intensity remains after cosmic-ray data correction on pressure variation (real Forbush effect) or vanishes after this correction (Forbush-like effect). A Ge detector does not recognize the cause of these cosmic-ray variations but it can detect them. The Forbush-like effect from March 2010 was registered in both single PS2 and single PS1 detectors inside the GLL and the UL, respectively. The cosmic-ray intensity decrease was relatively small, about 4% in the GLL and 2.5% as measured in the UL. Even small, it seems that a certain variation in number of coincidences between PS2 and Ge2 was registered, and both spectra followed each other during four days (Fig. 1). Integration time in the time series of the coincidence spectrum was chosen to be 6 h to emphasize the similarity between the two spectra. Strictly speaking it is only the time variation of the well-defined annihilation line, mostly caused by cosmic-ray pair-production, that can reflect the cosmic-ray changes, but its count rate is too low. Similarly, statistics is poor even for the high-energy continuous part of the Ge spectrum. The coincidence veto spectrum in Fig. 1 has no energy cuts and includes all gamma-ray lines what corresponds to the real condition of background measurement without a priori selected energy intervals. The single cosmic-ray spectrum was not corrected for atmospheric pressure and temperature because this represents the realistic situation in a typical ground level laboratory, which is probably without a veto shield.

The big plastic scintillator PS1 inside the UL registered the same Forbush-like effect, but the coincidence spectrum does not show any corresponding changes, Fig. 2. At a depth of 25 m.w.e, the mean energy of cosmic-ray muons is about 5 GeV higher than that of ground level muons, which is why they feel all solar modulation effects far less than the cosmic-rays particles on the ground level.

3.2. Radon influence on the Ge detector background spectrum

The significance of the other time variable background component was tested in simultaneous measurements of radon concentration by RM and gamma-ray background by the Ge detector. Inside the sample chamber (SC) of the Ge detector, in the space between the lead shield and the detector, radon concentration is influenced by the radon distribution outside the SC, when the SC is

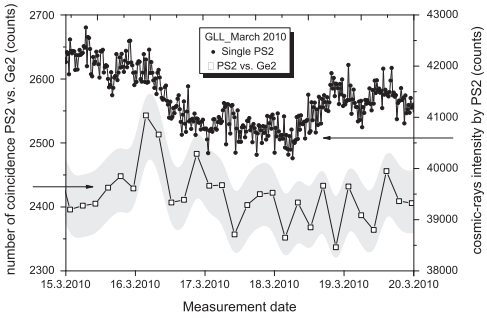

Fig. 1. Single cosmic-ray spectrum (circles) of PS2 and coincidence veto spectrum between PS2 and Ge2 (squares) inside the GLL during the Forbush-like effect in March 2010. The coincidence spectrum includes the error bars (1σ-B-spline).

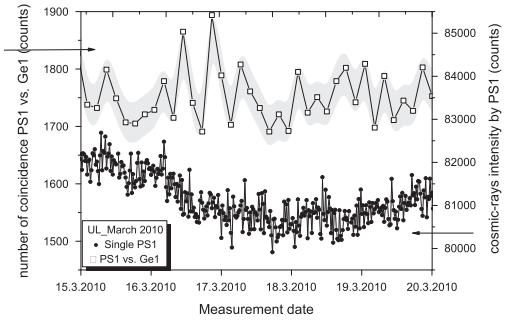

Fig. 2. Single cosmic-ray spectrum (circles) of PS1 and coincidence veto spectrum between PS1 and Ge1 (squares) inside the UL during the Forbush-like effect in March 2010. The coincidence spectrum includes the error bars (1σ-B-spline).

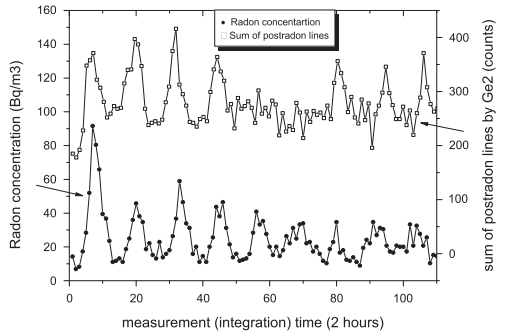

Fig. 3. Variability of radon concentration measured by RM inside the sampling chamber of the Ge2 detector (circles) and the sum of four post-radon lines (squares) measured by Ge2 inside the GLL.

not hermetically sealed. The Ge detector can see the radon daughters (^{214}Pb and ^{214}Bi) not only from the air inside SC but also from surface depositions on the detector and its passive shield.

Fig. 3 presents how the summed intensity of the four most prominent radon daughter lines (295.2 keV and 351.9 keV from ^{214}Pb, 609.3 keV and 1120.3 keV from ^{214}Bi) varies with time, as seen by the small shielded Ge detector (Ge2) inside the air-conditioned GLL. This follows closely the readings of the radon monitor positioned inside the SC (air volume of 1 dm^3). Here, we used the summed intensity of post-radon lines since the detector is small, but for high-efficiency detectors every single line should manifest the same behavior.

The radon monitor recorded radon and atmospheric parameters readings every 2 h and the integration in the time series of post-radon lines was chosen accordingly. This is sufficient to show clearly the one-day radon periodicity (Fig. 3).

Inside the UL, the radon concentration is kept at the low value under stable atmospheric parameters. The variability of radon concentration in the fresh air on the ground level is maximally suppressed in the UL by the ventilation system. The value of the summed post-radon lines inside the UL is almost constant as well as is the radon concentration.

The issue of stability of the gamma-ray background requires special attention when low-level ^{226}Ra measurements are performed by Ge detectors due to radon variability in ground level laboratories and sampling chambers of Ge detectors. Even a small Ge detector can see significant changes of background, if the mean radon concentration in ambient air is of the order or above 10 Bq/m^3 and some kind of radon suppression method inside a sample chamber must be applied (Neumaier et al., 2009).

Acknowledgements

The authors wish to thank Prof. Ivan Aničin for constant interest and support.

This work is supported by the Ministry of Education, Science and Technological Development of Republic of Serbia under project OI 171002.

References

Antanasijević, R., Aničin, I., Bikit, I., Banjanac, R., Dragić, A., Joksimović, D., Krmpotić, Đ., Udovičić, V., Vuković, J., 1999. Radon measurements during the building of a low-level laboratory. Radiat. Meas. 31, 371–374.

Bossew, P., 2005. A very long-term HPGe-background gamma spectrum. Appl. Radiat. Isot 62, 635–644.

Neumaier, S., Wojcik, M., Dombrowski, H., Arnold, D., 2009. Improvements of a low-level gamma-ray spectrometry system at the underground laboratory "UDO". Appl. Radiat. Isot 67, 726–730.

Udovičić, V., Grabež, B., Dragić, A., Banjanac, R., Joković, D., Panić, B., Joksimović, D., Puzović, J., Aničin, I., 2009. Radon problem in an underground low-level laboratory. Radiat. Meas. 44, 1009–1012.

Nuclear Instruments and Methods in Physics Research A 701 (2013) 99–114

Contents lists available at SciVerse ScienceDirect

Nuclear Instruments and Methods in Physics Research A

journal homepage: www.elsevier.com/locate/nima

Pion emission from the T2K replica target: Method, results and application

N. Abgrall [a,*], A. Aduszkiewicz [b], T. Anticic [c], N. Antoniou [d], J. Argyriades [a], B. Baatar [e], A. Blondel [a], J. Blumer [f], M. Bogomilov [x], A. Bravar [a], W. Brooks [i], J. Brzychczyk [j], A. Bubak [k], S.A. Bunyatov [e], O. Busygina [l], P. Christakoglou [d], P. Chung [m,n], T. Czopowicz [g], N. Davis [d], S. Debieux [a], S. Di Luise [o], W. Dominik [b], J. Dumarchez [p], K. Dynowski [g], R. Engel [f], A. Ereditato [q], L.S. Esposito [o], G.A. Feofilov [r], Z. Fodor [h], A. Ferrero [a], A. Fulop [h], M. Gaździcki [s], M. Golubeva [l], B. Grabez [aa], K. Grebieszkow [g], A. Grzeszczuk [k], F. Guber [l], A. Haesler [a], H. Hakobyan [i], T. Hasegawa [v], R. Idczak [w], S. Igolkin [r], Y. Ivanov [i], A. Ivashkin [l], K. Kadija [c], A. Kapoyannis [d], N. Katryńska [w], D. Kiełczewska [b], D. Kikola [g], M. Kirejczyk [b], J. Kisiel [k], T. Kiss [h], S. Kleinfelder [ab], T. Kobayashi [v], O. Kochebina [r], V.I. Kolesnikov [e], D. Kolev [x], V.P. Kondratiev [r], A. Korzenev [a], S. Kowalski [k], A. Krasnoperov [e], S. Kuleshov [i], A. Kurepin [l], R. Lacey [n], D. Larsen [z], A. Laszlo [h], V.V. Lyubushkin [e], M. Maćkowiak-Pawłowska [g], Z. Majka [j], B. Maksiak [g], A.I. Malakhov [e], D. Maletic [aa], A. Marchionni [o], A. Marcinek [j], I. Maris [f], V. Marin [l], K. Marton [h], T. Matulewicz [b], V. Matveev [l,e], G.L. Melkumov [e], M. Messina [q], St. Mrówczyński [s], S. Murphy [a], T. Nakadaira [v], K. Nishikawa [v], T. Palczewski [y], G. Palla [h], A.D. Panagiotou [d], T. Paul [f], W. Peryt [g], O. Petukhov [l], R. Płaneta [j], J. Pluta [g], B.A. Popov [e,p], M. Posiadała [b], S. Puławski [k], J. Puzovic [aa], W. Rauch [u], M. Ravonel [a], R. Renfordt [t], A. Robert [p], D. Röhrich [z], E. Rondio [y], B. Rossi [q], M. Roth [f], A. Rubbia [o], A. Rustamov [t], M. Rybczyński [s], A. Sadovsky [l], K. Sakashita [v], M. Savic [aa], T. Sekiguchi [v], P. Seyboth [s], M. Shibata [v], M. Sipos [h], E. Skrzypczak [b], M. Słodkowski [g], P. Staszel [j], G. Stefanek [s], J. Stepaniak [y], C. Strabel [o], H. Ströbele [t], T. Susa [c], M. Szuba [f], M. Tada [v], A. Taranenko [n], V. Tereshchenko [e], T. Tolyhi [h], R. Tsenov [x], L. Turko [w], R. Ulrich [f], M. Unger [f], M. Vassiliou [d], D. Veberič [f], V.V. Vechernin [r], G. Vesztergombi [h], A. Wilczek [k], Z. Włodarczyk [s], A. Wojtaszek-Szwarc [s], O. Wyszyński [j], L. Zambelli [p], W. Zipper [k], V. Galymov [ac], M. Hartz [ac,ad], A.K. Ichikawa [ae], H. Kubo [ae], A.D. Marino [af], K. Matsuoka [ae], A. Murakami [ae], T. Nakaya [ae], K. Suzuki [ae], T. Yuan [af], E.D. Zimmerman [af]

[a] University of Geneva, Geneva, Switzerland
[b] Faculty of Physics, University of Warsaw, Warsaw, Poland
[c] Rudjer Boskovic Institute, Zagreb, Croatia
[d] University of Athens, Athens, Greece
[e] Joint Institute for Nuclear Research, Dubna, Russia
[f] Karlsruhe Institute of Technology, Karlsruhe, Germany
[g] Warsaw University of Technology, Warsaw, Poland
[h] Wigner Research Centre for Physics, Budapest, Hungary
[i] Universidad Tecnica Federico Santa Maria, Valparaiso, Chile
[j] Jagiellonian University, Cracow, Poland
[k] University of Silesia, Katowice, Poland
[l] Institute for Nuclear Research, Moscow, Russia
[m] Pusan National University, Pusan, Republic of Korea
[n] State University of New York, Stony Brook, USA
[o] ETH, Zurich, Switzerland
[p] LPNHE, University of Paris VI and VII, Paris, France
[q] University of Bern, Bern, Switzerland
[r] St. Petersburg State University, St. Petersburg, Russia
[s] Jan Kochanowski University in Kielce, Poland
[t] University of Frankfurt, Frankfurt, Germany
[u] Fachhochschule Frankfurt, Frankfurt, Germany
[v] High Energy Accelerator Research Organization (KEK), Tsukuba, Ibaraki-ken, Japan
[w] University of Wrocław, Wrocław, Poland
[x] Faculty of Physics, University of Sofia, Sofia, Bulgaria
[y] National Centre for Nuclear Research, Warsaw, Poland
[z] University of Bergen, Bergen, Norway
[aa] University of Belgrade, Belgrade, Serbia
[ab] University of California, Irvine, USA

0168-9002/$ - see front matter Published by Elsevier B.V.
http://dx.doi.org/10.1016/j.nima.2012.10.079

[ac] York University, Toronto, Canada
[ad] University of Toronto, Toronto, Canada
[ae] Kyoto University, Kyoto, Japan
[af] University of Colorado, Boulder, USA

The NA61/SHINE Collaboration

ARTICLE INFO

Article history:
Received 23 August 2012
Received in revised form
24 October 2012
Accepted 24 October 2012
Available online 30 October 2012

Keywords:
Hadron production
Long target
Neutrino flux predictions

ABSTRACT

The T2K long-baseline neutrino oscillation experiment in Japan needs precise predictions of the initial neutrino flux. The highest precision can be reached based on detailed measurements of hadron emission from the same target as used by T2K exposed to a proton beam of the same kinetic energy of 30 GeV. The corresponding data were recorded in 2007–2010 by the NA61/SHINE experiment at the CERN SPS using a replica of the T2K graphite target. In this paper details of the experiment, data taking, data analysis method and results from the 2007 pilot run are presented. Furthermore, the application of the NA61/SHINE measurements to the predictions of the T2K initial neutrino flux is described and discussed.

Published by Elsevier B.V.

1. Introduction

Neutrino beams have become a major tool to perform studies of neutrino properties. At the T2K long-baseline neutrino oscillation experiment in Japan [1,2], a high-intensity neutrino beam is produced at J-PARC by a 30 GeV proton beam impinging on a 90 cm long graphite target. A schematic view of the neutrino beamline is shown in Fig. 1. Positively charged hadrons exiting the target (mainly π and K mesons) are focused by a set of three magnetic horns and decay along a 96 m long decay tunnel. The flavor content and energy spectrum of the beam are measured at the near detector complex located 280 m away from the target station, and by the Super-Kamiokande (SK) detector at a distance of 295 km. For the first time in the history of accelerator-based neutrino experiments, T2K adopted the off-axis technique [3] to generate a dedicated neutrino beam with the off-axis angle set to 2.5° for both the near and far detectors.

T2K was the first experiment to make a direct measurement of a non-zero value of the θ_{13} mixing angle via $\nu_\mu \rightarrow \nu_e$ appearance. The published 90% CL inclusion interval of $0.03(0.04) < \sin^2 2\theta_{13} < 0.28(0.34)$ for the normal (inverted) mass hierarchy, $\delta_{CP}=0$, $\sin^2 2\theta_{32}=1$ and $\Delta m^2_{32}=2.4\times10^{-3}$ eV^2 was obtained with only 2% of the final statistics [4]. Later, these results were confirmed with greater precision by measurements of electron anti-neutrino disappearance at reactors [5,6]. With the same set of data T2K also provided new measurements of the neutrino oscillation parameters $\sin^2 2\theta_{32}$ and Δm^2_{32} by studying ν_μ disappearance [7], and aims at a precision of 1% for $\sin^2 2\theta_{32}$ and 3% for Δm^2_{32} for the full statistics.

Although neutrino beams provide well defined and controlled sources of neutrinos, intrinsic uncertainties on the fluxes predicted with Monte Carlo (MC) simulations arise from models employed to simulate hadron emission from long nuclear targets used in accelerator based experiments. In these types of experiments, a non-negligible fraction of the neutrino flux actually arises from particles which are produced in hadronic re-interactions in the long target. Up to now, neutrino flux predictions have been (if ever) constrained using either parametrizations based on existing hadron production data available in the literature, e.g. Refs. [8–10], or dedicated hadron production measurements performed on thin nuclear targets, e.g. HARP p+Al data [11] for K2K [12], HARP p+Be data [13] for MiniBooNE [14] and SciBooNE, SPY p+Be data [15] for NOMAD [16]. T2K recently followed this approach using the NA61/SHINE results on p+C interactions at 30 GeV extracted from measurements of hadron production in a thin (2 cm) graphite target [17,18].

Although such measurements provide constraints on the production of secondary particles in the primary interaction of the beam protons in the target, the lack of direct measurements of the production of tertiary particles in re-interactions, and hence the use of sparse data sets to cover these contributions, limits the achievable precision of the flux prediction. The main motivation for measurements of hadron emission from a replica of the T2K target is therefore to reduce the systematic uncertainties on the prediction of the initial neutrino flux originating from products of interactions in the target.

The NA61/SHINE (SPS Heavy Ion and Neutrino Experiment) experiment at the CERN Super Proton Synchrotron (SPS) is pursuing a rich physics program in various fields [19–22] from precise hadron production measurements for T2K and more reliable simulations of cosmic-ray air showers for the Pierre Auger and KASCADE experiments [23,24], to the study of the properties of the onset of deconfinement with measurements of p+p, p+Pb and nucleus+nucleus collisions at the SPS energies.

In addition to recently published thin-target (0.04 λ_I) measurements of charged pion and kaon production [17,18] already used for the T2K neutrino flux predictions [4,7], the NA61/SHINE collaboration studies hadron emission from a replica of the T2K target (1.9 λ_I) exposed to a 30 GeV proton beam. A total of 0.2×10^6 events were recorded during a pilot data taking in 2007. High statistics data were recorded in 2009 (4×10^6 events) and 2010 (10×10^6 events). For the first time, the kinematical phase space of pions and kaons exiting the target and producing neutrinos in the direction of the near and far detectors is fully covered by a single hadron production experiment.

The long-target analysis presented in this paper uses the low-statistics data collected in 2007. It however sets the ground for the ongoing analysis of high-statistics NA61/SHINE data with the replica of the T2K target. It demonstrates that high-quality long-target data were successfully taken with the NA61/SHINE apparatus for T2K, and that such data can be used effectively to constrain the T2K neutrino flux predictions. A comparison of neutrino flux predictions based on thin-target hadron production measurements and long-target hadron emission measurements is performed as an illustration of the complete procedure.

* Corresponding author. Tel.: +1 510 599 9223.
E-mail address: nicolas.abgrall@cern.ch (N. Abgrall).

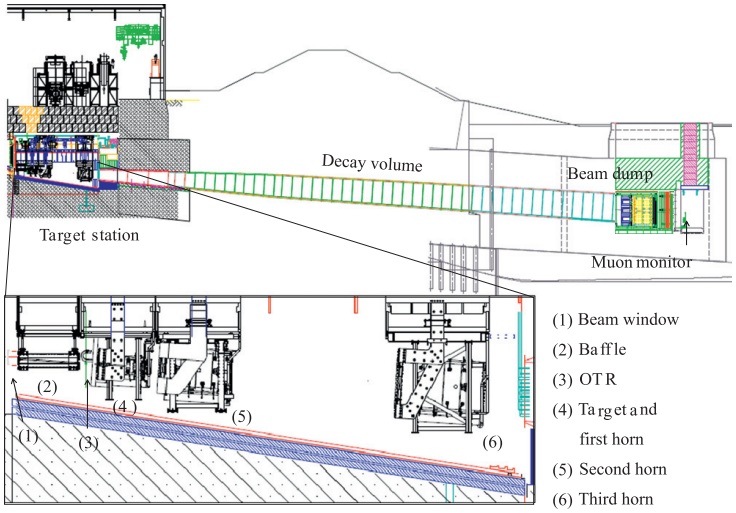

Fig. 1. A side view of the T2K neutrino beamline. See Ref. [2] for a detailed description and for notations used.

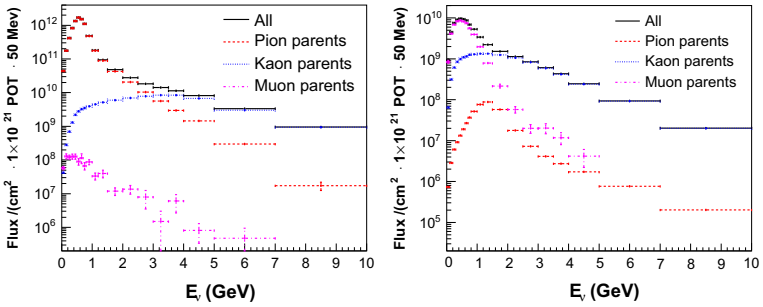

Fig. 2. Prediction (based on FLUKA2008.3b and re-weighted by the NA61 thin target data) of the ν_μ (left) and ν_e (right) fluxes at the near detector of T2K. The contribution of different parent particles to the total flux are shown.

This paper is organized as follows: Section 2 briefly reviews the current T2K flux predictions based on the NA61/SHINE thin-target data and points out the need for additional long-target measurements to improve the precision of the predictions. Section 3 describes the NA61/SHINE experimental setup, kinematical coverage of the data, event selection and data normalization, reconstruction method and particle identification. The NA61/SHINE simulation chain is presented in Section 4. Yields of positively charged pions measured at the surface of the replica of the T2K target are given in Section 5. Possible strategies to use long-target measurements in the T2K beam simulation are proposed in Section 6 which also provides an illustration of the complete procedure.

2. Requirements on hadron production data for the prediction of T2K neutrino fluxes

The T2K beam MC simulation [2] is used to predict the initial neutrino flux at the near and far detectors. It comprises a full description of the beam line, including the target, magnetic horns, decay tunnel and beam dump. Hadronic interactions in the target are simulated by the FLUKA2008.3b [25] model. The propagation of outgoing particles is then modeled by the GEANT3 [26] package with GCALOR [27] for hadronic interactions.

Measurements of particle emission from the replica of the T2K target are necessary to constrain the model calculations and to reach a 5% precision on the absolute flux prediction as required by the T2K physics goals (i.e. 3% precision on the ratio of the far to near fluxes for precision ν_μ disappearance and ν_e appearance analyses).

Predictions obtained for horn currents of 250 kA are shown in Fig. 2 for the ν_μ and ν_e fluxes at the near detector. The ν_μ flux below 2 GeV predominantly (95%) originates from the in-flight decay of positively charged pions focused by the magnetic horns of the beam line (see Ref. [2] for a detailed description of the T2K beam line). The ν_e flux is dominantly produced by the decay of positively charged kaons above 1.5 GeV, whereas at lower energy ν_e's originate mostly from the decay of pions via the subsequent muon decay, i.e. $\pi^+ \to \mu^+ \nu_\mu$ followed by $\mu^+ \to e^+ \nu_e \bar{\nu}_\mu$. Thus, pion production data can constrain most of the ν_μ flux and a significant fraction of the ν_e flux below 2 GeV neutrino energy.

In terms of hadron production measurements, neutrino fluxes can be decomposed into *secondary* and *tertiary* components. The *secondary* component originates from neutrino parents produced in the primary interaction of the beam protons in the target, e.g. secondary pions, $p+C\rightarrow\pi^{+}+X$. This *secondary* component can be constrained mainly by pion (and kaon) production cross-sections obtained from measurements on a thin target. The *tertiary* component refers to neutrino parents produced in interactions of secondary particles, whether such interactions occur in the target or out of the target in the elements of the beamline. The contribution to the neutrino flux from parents produced in the target is therefore defined as the sum of the *secondary* component and the *tertiary* component due to interactions in the target. This contribution can be obtained from measurements of pion (and kaon) emission from a replica target.

The dependence of the *secondary* and *tertiary* contributions on the neutrino energy is depicted in Fig. 3 for the ν_μ and ν_e fluxes at the far detector. The *secondary* component contributes 60% of the ν_μ (ν_e) flux at the peak of the beam energy spectrum (600 MeV). The remaining 40% constitutes the *tertiary* component due to interactions in the target and elements of the beam line. Thus, thin-target measurements for T2K (i.e. positively charged pion and kaon inclusive production cross-sections at 30 GeV [17,18]) can directly constrain up to 60% of the ν_μ (ν_e) flux prediction.

The lack of direct measurements of secondary interactions however requires in most cases scaling to energies and nuclei relevant for the T2K experimental setup, as well as extrapolating to uncovered regions of the kinematical phase space. Such procedures have been used in addition for the T2K flux prediction. This brings in new sources of systematic uncertainties on top of the uncertainty of the measurements.

As an example, the systematic errors of the ν_μ and ν_e flux predictions at the far detector for the first published T2K analysis are depicted in Fig. 4. Details about the procedure developed to re-weight the original predictions of the T2K beam simulation (based on FLUKA2008.3b) with the NA61 thin-target data are given elsewhere [28]. The total fractional error on the ν_μ and ν_e fluxes is about 15% at the peak of the beam energy spectrum. At this energy the fractional error attributed to the re-weighting of tertiary pions produced in interactions of secondary nucleons is about half the size of that associated with the re-weighting of secondary pions. However the error associated with the production of the related secondary nucleons is of the same order. The achievable precision on the flux prediction based on thin-target data alone is therefore limited due to the uncertainty on the *tertiary* component of the flux.

Measurements of particle emission from a full-size replica of the T2K target have the advantage to cover at once the production of secondary particles exiting the target, as well as the emission of particles originating from secondary interactions inside the target. Such measurements can be used in a single-step approach in which simulated yields of outgoing particles are directly re-weighted by yields measured at the surface of the target. In this case, uncertainties on the flux predictions are almost entirely limited to the uncertainties of the measurements. Actually, as depicted in Fig. 3, at the peak of the beam energy spectrum the *secondary* component and the *tertiary* component due to interactions in the target sum up to 90% of the ν_μ (ν_e) flux. Hadron emission measurements with the replica of the T2K target (i.e. yields of charged pions and kaons exiting the target) can thus constrain up to 90% of the flux prediction.

Note that both thin-target and replica-target based approaches are necessary as discrepancies observed in a comparison of a flux prediction based on thin-target data to one obtained when yields of outgoing particles are re-weighted with the replica-target data would point to an inappropriate re-weighting of the secondary interactions in the target. Such comparisons would allow further precise tuning of the employed hadron production model.

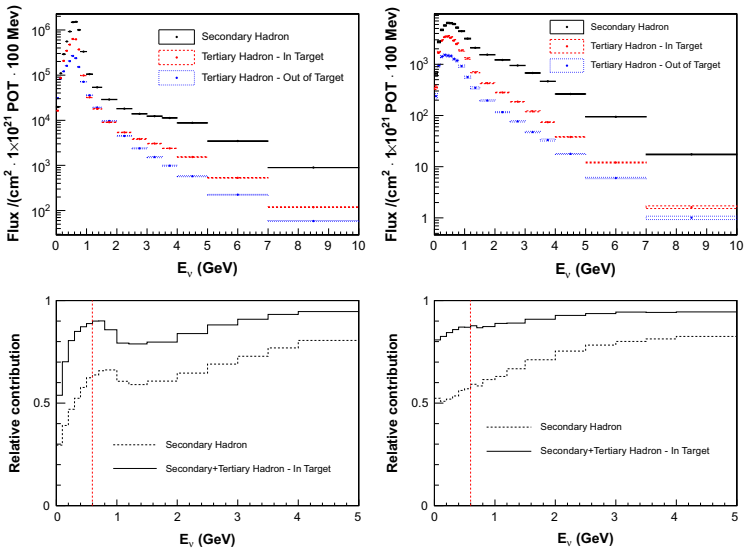

Fig. 3. *Secondary* and *tertiary* components of the ν_μ (top left) and ν_e (top right) fluxes at the far detector. The contribution of parents originating from the target sums up to 90%, among which 60% are due to the *secondary* component and 30% due to re-interactions in the target (the in-target component). The relative contributions of the secondary and total in-target (secondary+tertiary in-target) components are shown for ν_μ (bottom left) and ν_e[bottom right] as a function of energy. The dashed vertical line shows the location of the peak of the beam energy spectrum (600 MeV). Predictions are based on FLUKA2008.3b and re-weighted by the NA61 thin-target data.

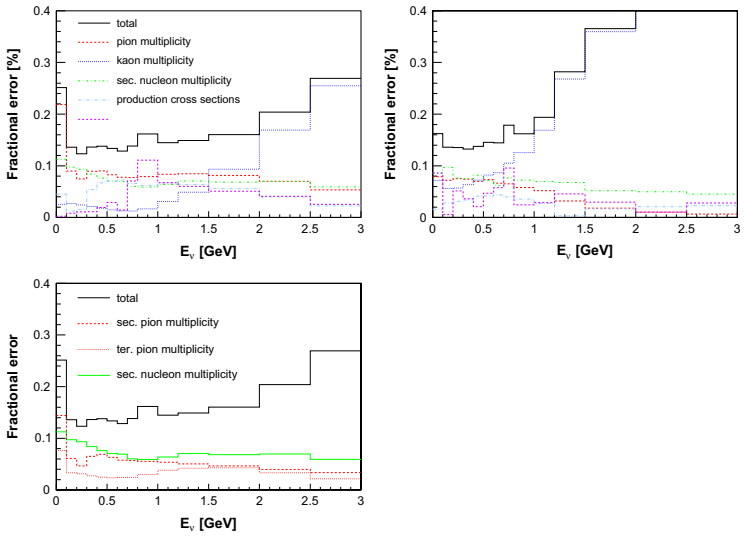

Fig. 4. Systematic errors of the ν_μ (top left) and ν_e (top right) fluxes at the far detector of T2K for the analysis described in Refs. [4,7]. The *beamline* uncertainty combines contributions from the proton beam, off-axis angle, target-horn alignment and horn current uncertainties. The bottom plot shows the breakdown of the uncertainty on the pion multiplicity in secondary and tertiary contributions for the ν_μ fractional error.

3. The NA61/SHINE replica-target measurements for T2K

3.1. Experimental setup

The NA61 detector is a large acceptance spectrometer located in the North Area H2 beam line of the CERN SPS. Most detector components were inherited from the NA49 experiment and are described in detail in Ref. [29]. The detector consists of a set of five time projection chambers (TPCs). Two of them, called Vertex TPCs (VTPC-1 and VTPC-2), are placed inside superconducting dipole magnets. The magnetic field was set to 1.14 Tm in order to optimize the geometrical acceptance for the T2K measurements. A small TPC is placed between VTPC-1 and VTPC-2 and is referred to as the GAP TPC. Two large TPCs, the Main TPCs (MTPC-L and MTPC-R), are positioned downstream of the VTPC-2, symmetrically with respect to the beamline. The set of TPCs is complemented by time-of-flight (ToF) detectors located downstream of the MTPCs. Before the 2007 run the experiment was upgraded with a new forward time-of-flight detector (ToF-F) in order to extend the acceptance. The ToF-F consists of 64 scintillator bars with photomultiplier (PMT) readout at both ends resulting in a time resolution of about 115 ps. An overview of the NA61 setup is shown in Fig. 5 together with the definition of the NA61 coordinate system.

The replica of the T2K target used in NA61 consists of a 90 cm ($1.9\lambda_I$) long graphite rod of density $\rho = 1.83\ \mathrm{g/cm^3}$. The downstream face of the target was located 52 cm upstream of the mylar entrance window of VTPC-1, and the target was held in position by aluminium support flanges fixed at its upstream end. The replica and the actual target of T2K in its complete environment are shown in the drawings in Fig. 6. There are small differences between the two targets. Systematic uncertainties related to these differences have been studied and are reported in Section 6.2.

A 15 kHz beam rate was used during the 2007 measurements. Due to the thickness of the replica target each beam proton is assumed to interact in the target and the trigger simply consists of selecting all beam protons using a coincidence of various counters and vetos along the beam line (see Ref. [17] for more details). In particular, the so-called S1 scintillation counter provides timing information and triggers the data acquisition from the TPCs and ToF detectors. The 100 ns dead time of S1 results in a 0.2% pile up probability. The trajectory of each beam proton is reconstructed in a telescope of three beam position detectors that allows the determination of the position of the beam at the upstream face of the target with a precision of better than 300 μm in both directions.

More details on the experimental setup, detector calibration and performance as well as a description of the proton identification in the beam are given elsewhere [17].

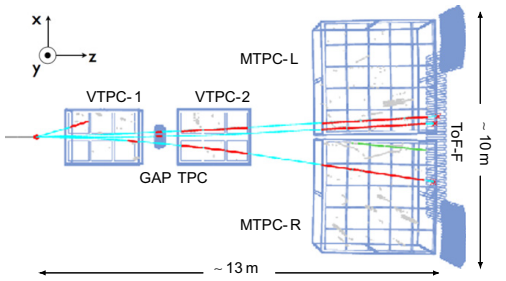

Fig. 5. An example of a reconstructed p+C interaction at 30 GeV beam energy in the replica of the T2K target showing tracks reconstructed in the TPCs and associated with hits in the ToF-F detector. The incoming beam direction is along the z-axis. The magnetic field bends the trajectory of outgoing charged particles in the x–z (horizontal) plane. The drift direction in the TPCs is along the y-axis.

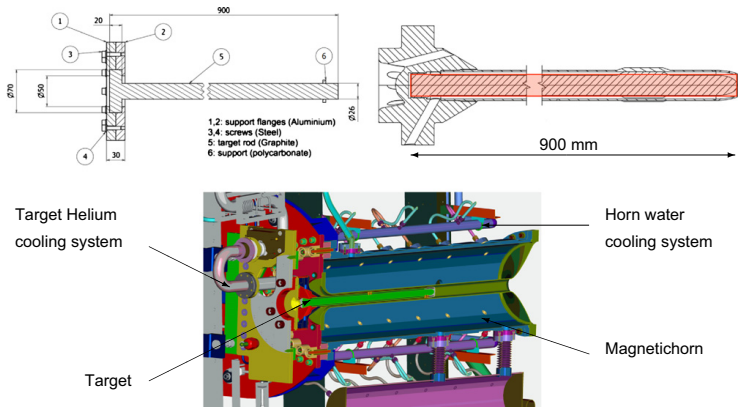

Fig. 6. Technical drawing with dimensions given in mm (side view) of the replica target used during the NA61 data taking (top left) consisting of a 90 cm long graphite rod and aluminium support flanges. Drawing of the complete geometry of the T2K target (top right). The overlaid red rectangle represents the simplified geometry of the replica target. View of the T2K target and its cooling envelope embedded in the first focusing horn of the T2K beamline (bottom). (For interpretation of the references to color in this figure caption, the reader is referred to the web version of this article.)

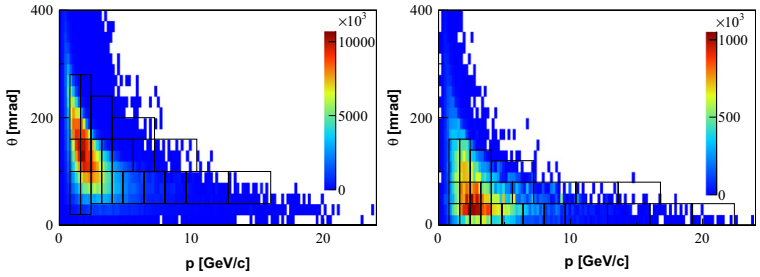

Fig. 7. Kinematical phase space of positively charged pions (for 10^{21} pot) exiting from the side of the target (summed over five longitudinal bins along the target, see text) (left) or from the downstream face (right), and producing neutrinos in the direction of the far detector of T2K. The respective analysis binning of the NA61 data with the replica of the T2K target is overlaid on top. Predictions obtained from the T2K beam simulation.

3.2. Coverage of the T2K kinematical phase space in NA61/SHINE

The phase space of interest for positively charged pions that exit the T2K target and produce neutrinos in the direction of the far detector is depicted in Fig. 7 as a function of (p,θ), where p is the laboratory momentum of the pion at the surface of the target, and θ is the angle of its direction calculated with respect to the beam axis. For comparison the binning used in the NA61 data analysis is overlaid.

The phase space of interest is divided into two kinematical regions: pions which exit from the side of the target with emission peaking at large angle and low momentum, and pions exiting from the downstream face which populate mainly the region of small angle and large momenta. In the T2K beam line the latter are not(or less) focused by the magnetic horns and are mainly the pions that decay to muons with momentum larger than 5 GeV/c. These muons are detected by the muon monitor (MUMON) located downstream of the beam dump and provide a spill-by-spill monitoring of the direction of the beam [2,30]. The comparison of the MUMON measurements to the beam simulation is thus an important step in the validation of the MC model. For that purpose, in NA61 a dedicated run was taken in 2010 with a replica of the T2K target to measure precisely the very forward region of particle production below 20 mrad polar angle. In this run, the spectrometer was operated with the highest magnetic field configuration (of about 9 Tm), which deflected forward going particles into the sensitive regions of the TPCs, thus avoiding the uninstrumented region along the beam axis.

The binning for the analysis in (p,θ) is driven by the acceptance of the NA61 apparatus. As shown in Fig. 7, it covers most of the region of interest for T2K. The relatively large size of the bins, ranging from 0.8 to 3.2 GeV/c in momentum and from 40 to 120 mrad in polar angle, is due to the low statistics of the 2007 data. In addition to (p,θ), data are further binned with respect to the longitudinal position of the outgoing particles at the surface of the target. As shown in Fig. 6, part of the T2K target is embedded in the first magnetic horn of the beam line. In this configuration and due to the extension of the target, the focusing properties of the horn depend on the longitudinal position of the outgoing particles. We investigated this effect with the T2K beam MC and determined that at least five longitudinal bins are required to obtain a prediction that does not differ significantly from a nominal non-binned prediction in terms of mean neutrino energy and overall normalization. Five bins of 18 cm each are therefore used along the beam direction. An additional bin is used for the downstream face of the target.

The acceptance of the NA61 detector in (p,θ) does not vary by more than 10% over the length of the target for pions exiting the

side of the target. An identical (p,θ) binning is therefore applied to all longitudinal bins along the target. For pions exiting the downstream face of the target, the coverage extends to higher momenta. The same binning in p is maintained while a finer binning is used for the polar angle θ. The azimuthal acceptance of the detector in the $x-y$ plane is however highly non-uniform due to the finite extent of the TPCs along the drift direction (y axis) and the uninstrumented region of the detector along the beam line. This is illustrated in Fig. 8 which depicts the distribution of azimuthal angle ϕ of the TPC tracks (in the flat regions the track reconstruction efficiency is very close to 100%). For this reason, the NA61 replica-target data cannot be used as a direct input on a track-by-track basis in the T2K beam simulation for the flux predictions. Other suitable methods are therefore considered in Section 6.1.

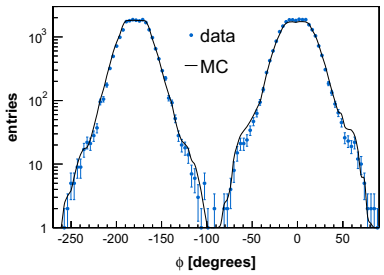

Fig. 8. Distribution of the azimuthal angle, ϕ, of all TPC tracks in data (markers) and MC (line).

3.3. Event selection and data normalization

As mentioned in Section 3.1, the NA61 beam is defined by a set of scintillation and veto counters along the beam line and the proton beam tracks are reconstructed in three beam position detectors. The beam tracks are further selected to assure that protons hit the upstream face of the target. The selection is based on two main cuts: the first one on the χ^2 of the fit of the beam tracks, the second on the extrapolated position on the upstream face of the target. The selection rejects 32% of the events.

The distribution of beam particles in time with respect to the trigger time is shown in Fig. 9 over a 40 μs time window. Due to the relatively high beam intensity, about 40% of the events include a second beam particle within ± 25 μs around the trigger time. The acquisition window of the TPCs extends over a maximum drift time of 50 μs for the gas composition and drift voltages applied in 2007. Multiple interactions can therefore occur in the target during a single acquisition window. Such interactions result in so-called *off-time* tracks, i.e. tracks reconstructed in the TPCs but not associated in time with the beam proton that triggered the acquisition system.

Since the measured yields are normalized to the number of protons on target, tracks reconstructed in the TPCs are associated to the triggering beam proton by requiring a signal in the appropriate ToF-F detector.

Actually, for the 2007 beam rate, tracks that leave a valid signal in the ToF-F can only have been produced in the interaction of the same beam proton in the target since the 100 ns acquisition window of the detector is much smaller than the mean distance in time between two beam particles. Hits associated with off-time tracks in the ToF-F detector result in overflows which are rejected at the analysis level. The effect of this cut on the track multiplicity in the TPCs is depicted in Fig. 10. Although many beam particles

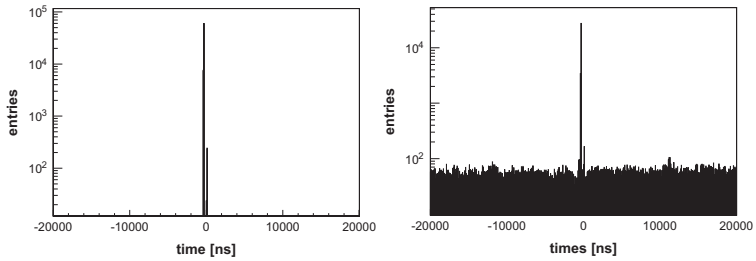

Fig. 9. Time distribution of beam particles in a 40 μs time window for single beam particle events (left) (~ 60% of all events), and events with two beam particles (right) (~ 40% of all events). The beam time is centered at −300 ns.

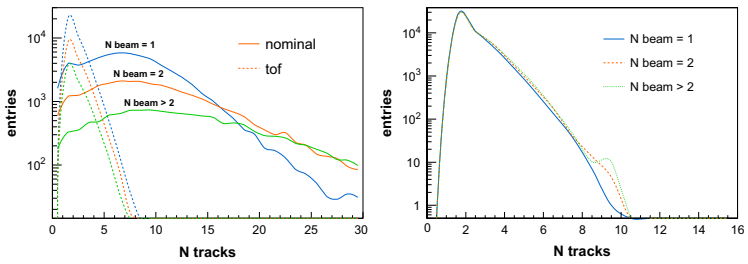

Fig. 10. Track multiplicity in the TPCs without (solid) and with (dashed) the ToF-F requirement for events with different numbers of beam particles (left). Multiplicity distributions normalized to the number of single beam particle events with the ToF-F requirement (right).

are present in a ± 25 μs window around the beam time, the track multiplicity in the TPCs is consistent with that of single-interaction events once the ToF-F requirement is applied.

The NA61 yields from the replica of the T2K target are thus normalized to the total number of protons on target which produced a valid trigger. After the quality cuts described above, a total of 114,885 events were selected for this analysis.

3.4. Reconstruction of track parameters at the surface of the target

Reconstruction algorithms applied for the analysis described here are based on those used to produce the NA61 thin-target results with the exception that the fitting procedure at the primary interaction vertex is replaced by a backward extrapolation procedure to the surface of the replica target. The main steps of the reconstruction are:

(i) cluster finding in the TPC raw data and calculation of the cluster weighted mean position and total charge,
(ii) reconstruction of local track segments in each TPC separately,
(iii) matching of track segments from different TPCs into global tracks,
(iv) track fitting through the magnetic field and determination of the track parameters at the first measured TPC cluster,
(v) matching of ToF-F hits with TPC tracks,
(vi) backward extrapolation of the global tracks from their first measured TPC cluster to the surface of the target.

The backward extrapolation procedure is depicted in Fig. 11. If the extrapolated trajectory crosses the surface of the target at a certain position, the track parameters and associated covariance matrix are determined at this point. Otherwise a minimization procedure is performed along the length of the target to find a point of closest approach between the track trajectory and the surface of the target. The track parameters are then determined at this point. Tracks are associated with the target if the point of closest approach is found within 0.6 cm from the surface of the target. This value actually corresponds to the mean radial uncertainty of the extrapolation over the full length of the target.

The resolution of the track parameters, p and θ, at the surface of the target is driven by that estimated at the first fitted TPC cluster. The latter strongly depends on the track topology. In order to improve the resolution, tracks are therefore grouped into four topologies and specific cuts on the minimum number of clusters on track are applied to each class. For all tracks a minimum number of 40 clusters is required in the MTPCs as well as a valid signal in the ToF-F detector. The following topologies are defined: the VTPC-1+VTPC-2 topology corresponds to tracks with segments in both VTPCs, while the VTPC-1 and VTPC-2 topologies correspond to tracks with a segment in one VTPC only. The GAP TPC topology corresponds to tracks which have measured points only in the small GAP TPC and a MTPC. Examples of such topologies (VTPC-2, GAP TPC and VTPC-1+VTPC-2 from top to bottom) are shown in Fig. 5. A minimum of 40 clusters in the VTPC-1 is required for the VTPC-1 topology, 45 clusters for the VTPC-2 topology, 50 clusters for the VTPC-1+VTPC-2 topology and six clusters for the GAP TPC topology. In addition, tracks are required to be reconstructed in a $\pm 30^\circ$ symmetrical wedge in the azimuthal angle with respect to the x-axis. The quality cuts mentioned above are used to define the detector acceptance for all related MC studies in what follows.

After a calibration procedure described in details in Ref. [17], the spatial resolution on TPC measurements (including the relative alignment between different TPCs) is better than 0.5 mm.

The resolution of p and θ at the first TPC cluster are shown in Fig. 12 as a function of momentum for the different toplogies. In particular, the GAP TPC tracks have their momentum measured with a maximum of seven clusters in the magnetic field in the very forward region of the spectrometer. Hence the larger error on the polar angle and a worse momentum resolution. The resolution obtained after the backward extrapolation to the surface of the target is estimated to be $\sigma_\theta/\theta = 6\%$ for the polar angle. The resolution on the longitudinal position depends on the track topology and its average value for the analyzed track sample is $\sigma_z = 5$ cm.

A precise knowledge of the relative alignment of the target and the beam is needed to reconstruct tracks at the surface of the target in bins of (p,θ,z). The position of the long target was first measured by surveyors. In addition, a procedure based on the backward extrapolation of the TPC tracks was developed to refine the measured position of the target with respect to the beam axis. For that purpose, the position of the upstream face of the target is used as a reference. It is actually precisely determined by the independent extrapolations of the TPC tracks from the downstream region, and that of the beam tracks from the upstream region.

Once the target position is known, the beam profile and radial distribution on the upstream face are determined by extrapolating the beam tracks reconstructed in the beam position detectors. These distributions for the 2007 run are shown in Fig. 13 together with the positions of the upstream and downstream faces of the target.

In 2007, the target was shifted upwards by 0.4 cm and tilted in the horizontal (vertical) plane by 5 (2.8) mrad. The hardware

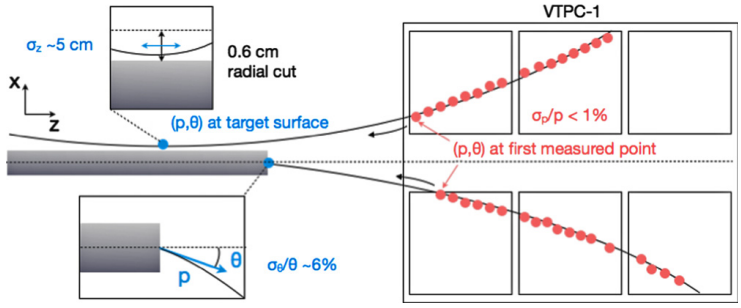

Fig. 11. Sketch depicting the backward extrapolation of TPC tracks onto the surface of the target. The point of the closest approach is determined and the track parameters p and θ are calculated at this point. Only tracks for which this point lies within a distance of 0.6 cm around the target surface are accepted. The resolution for the different track parameters are also given in the figure.

target alignment technique was improved before the 2009 data-taking period. For this data set, the target is well aligned along the direction of the beam (no tilt), but slightly shifted by 0.2 (0.1) cm in the vertical (horizontal) plane. As depicted in Fig. 14, the target transverse dimension is well reconstructed (with a precision of 0.6 cm) using the backward extrapolation procedure, which takes into account the transverse shifts and tilt of the target in the 2007 alignment configuration. Tracks are attached along the target with a precision of 5 cm. The longitudinal position of the target is however constrained to better than 1 cm by the geometrical survey and alignment procedure.

In order to measure yields of outgoing particles in a configuration as close as possible to that of T2K (i.e. with the target aligned along the beam axis), beam tracks were selected to hit the target over the overlap region of the upstream and downstream faces, thus retaining only beam protons that effectively pass through the full length of the target (see Fig. 13). The effect of the target tilt on the yields of outgoing particles was studied over the analysis binning with dedicated MC simulations, and finally treated as an additional systematic uncertainty.

The beam and target configurations in T2K and NA61 differ also by the beam profile on target. During the 2007 data-taking

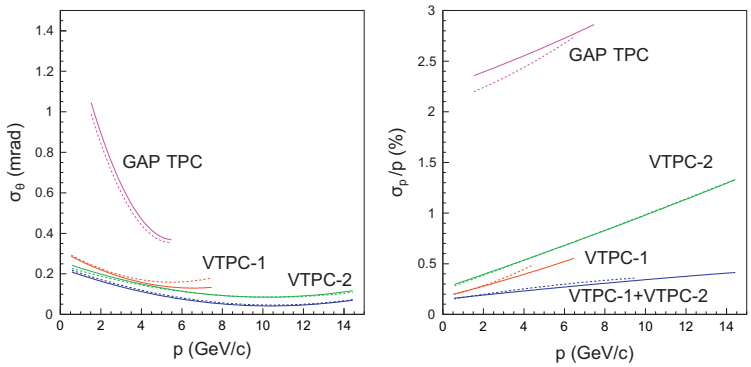

Fig. 12. Error on the polar angle (left) and momentum resolution (right) as a function of momentum of the TPC tracks for data (solid) and MC (dashed). Labels refer to track topologies defined in the text.

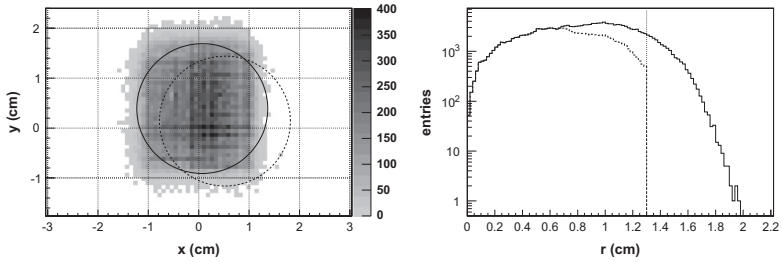

Fig. 13. Profile (left) and radial distribution (right) of the beam on the upstream face of the replica target. The radial distribution is shown before (solid) and after (dashed) applying a beam track selection defined in the text. The solid (dashed) circle shows the position of the upstream (downstream) face. The dotted vertical line shows the radius of the target.

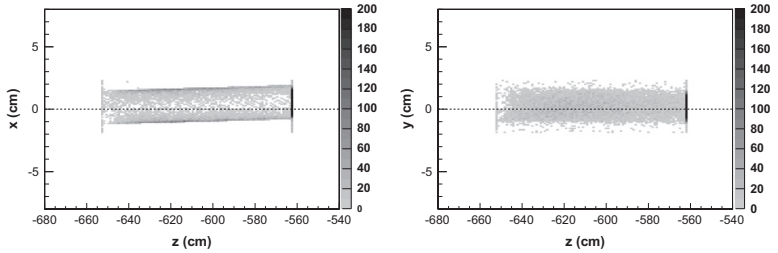

Fig. 14. Distribution of the point of closest approach of the TPC tracks in the $x-z$ (left) and $y-z$ (right) projections after backward extrapolation to the surface of the target. The fact that the side of the target appears fuzzy in the vertical projection (y) is a consequence of the azimuthal acceptance of the detector (see Fig. 8) which is further constrained by the $\pm$ 30° wedge cut defined in the text.

period with the replica target the beam was almost uniformly distributed on the target upstream face, while in T2K a narrow beam ($\sigma_{x,y} \approx 4.2$ mm) well-centered on the target is used. This difference could be taken into account by re-weighting the NA61 results with the T2K beam profile in the T2K beam MC. Due to the low statistics of the 2007 data such a re-weighting was not implemented. Dedicated MC studies (reported in Section 6.2) were performed to estimate the corresponding systematic uncertainty. However, re-weighting will be applied in the analysis of the 2009 and 2010 data. For that purpose, the trigger hardware and software were upgraded before the 2009 data taking. In particular, a multi-trigger acquisition system was introduced allowing pre-scaling of different trigger types. A certain fraction of the events was recorded in a configuration that defines a beam with uniform coverage of the upstream face of the target, and in a configuration that defines a narrow, centered beam.

3.5. Particle identification

The particle identification (PID) in NA61 relies on energy loss measurements, dE/dx, in the TPCs and the time-of-flight that is used to compute the particle mass squared, m^2. For each TPC track, the dE/dx is calculated by ordering the reconstructed clusters by increasing charge and averaging the distribution over the lower 50%. For the calculation of the mass squared, the momentum is taken without vertex constraint and the path length of the track is calculated from a plane located at the center of the target along the beam axis to the ToF-F detector. The dE/dx and mass squared distributions of the data are shown for all tracks in Fig. 15 (top panel) as a function of the track momentum.

The dE/dx can provide an efficient PID below 1 GeV/c momentum and along the relativistic rise region, but is limited in the momentum region between 1 and 3 GeV/c where the different Bethe-Bloch curves overlap. The time-of-flight provides a good discrimination between pions and protons up to 6 GeV/c. The analysis of the NA61 data with the T2K replica target is based on the combined PID method developed for the thin-target data analysis [17]. Actually, the combination of the dE/dx and time of flight provides a powerful PID over a wide momentum range. The method is illustrated in Fig. 15 (bottom panel) which depicts how the different particles (p, K, π and e) can be separated in the (m^2,dE/dx) plane.

A (m^2,dE/dx) distribution for positively charged tracks is obtained for each bin in (p,θ,z) determined at the surface of the replica target. The data distributions are then fit to joint probability density functions (pdf) for the mass squared and the energy loss. Due to the independence of the dE/dx and m^2 variables, the joint pdf reduces to the product of the corresponding marginal distributions which are described by Gaussian distributions. The complete pdf is a sum of two-dimensional Gaussian distributions over four particle species, p, K, π and e. For the initialization of the fit, the resolution on the mass squared and the expected energy loss for each particle species are obtained from parametrizations of the data distributions shown in Fig. 15 as a function of the track momentum. The resolution on the expected energy loss is a function of the number of reconstructed clusters on a track ($\sim 1/\sqrt{N}$). For the topology dependent cuts defined in this analysis, it is approximated by a constant value of 3% due to the sufficiently large number of clusters on each track. Independent normalization factors are introduced for each particle species. Since the individual pdfs are normalized to unity, particle yields are given by the normalization factors which are obtained from a two-dimensional log-likelihood minimization illustrated in Fig. 16.

The two-dimensional fitting procedure is applied over the full momentum range of the analysis, although at high momenta when the width of the mass squared distribution becomes too large, the time-of-flight information can no longer constrain the fit significantly.

Due to the low statistics of the 2007 data, a more sophisticated pdf than a sum of two-dimensional Gaussian distributions was not justified in this analysis. For example, using multi-Gaussian distributions (i.e. a first Gaussian to describe the peak and a second one with a larger width for the tails) did not improve the results in terms of goodness of fit. It should also be noted that fits are performed in two dimensions which significantly relaxes the requirements on the pdf used to describe the data. Actually, although the one-dimensional Gaussian pdf's used for the dE/dx

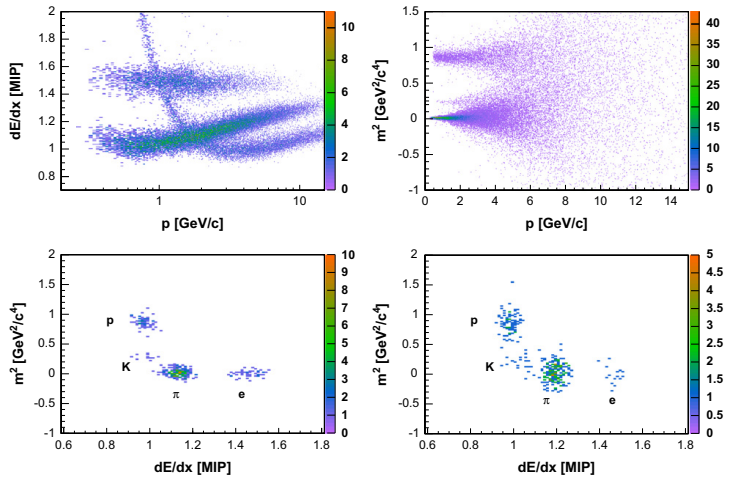

Fig. 15. Top panel: dE/dx (left) and mass squared (right) distributions for all TPC tracks as a function of the track momentum at the first fitted TPC cluster. Bottom panel: (m^2,dE/dx) distributions of positively charged tracks for $40 < \theta < 100$ mrad polar angle and $2.4 < p < 3.2$ GeV/c (left), $4 < p < 4.8$ GeV/c (right) momentum at the surface of the target.

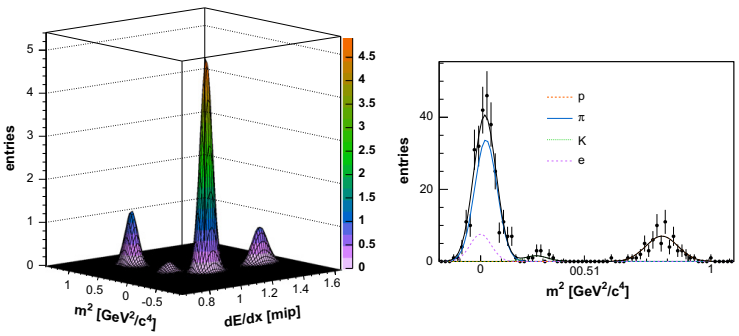

Fig. 16. Two-dimensional fit of the data in the $(m^2,dE/dx)$ plane (left) and respective mass squared projection [right], for $40<\theta<100$ mrad and $2.4<p<3.2$ GeV/c at the surface of the target. The different components of the fit are shown with different line styles.

and m^2 might not describe tails (contaminations) of the distributions exactly, the fact that particles are well separated in two dimensions does not require a precise description of the tails in the two-dimensional case.

4. The NA61/SHINE simulation chain

In NA61 interactions of the incident proton beam inside the replica target are generated, as in the T2K beam simulation, with the FLUKA transport code: the FLUKA2011.2 version was used for this analysis since the validity period for the FLUKA2008.3d version has already expired. The FLUKA2011 version reveals a much better agreement with the published NA61/SHINE charged pion data [17] compared to the older FLUKA2008 version. Thus, no additional re-weighting of secondary $\pi^{\pm}$ is needed when FLUKA2011 version is used for neutrino flux predictions in T2K. The beam input to the standalone FLUKA simulation is based on data distributions of the beam divergence as a function of the position measured in the beam detectors located upstream of the target. The trajectory of each simulated beam track thus takes into account correlations between the position and angle of the beam protons. Particles exiting the target are stored and passed on as input to the NA61 MC detector simulation chain starting at the surface of the target. The GEANT3 [26] package then propagates particles through the magnetic field and geometry of the detectors, and simulates physics processes such as particle decays. Interactions of the tracked particles in the detector material are simulated by the GCALOR [27] model which is also used for the same purpose in the T2K beam simulation. The simulated events are processed with the same reconstruction chain as used for the real data processing.

Fig. 17 shows that the employed model in the NA61 MC reasonably reproduces the kinematics of the tracks at the surface of the target for all the different topologies considered in this analysis. This is important to assure that the quality of the reconstruction of the track parameters is similar for data and MC. Actually, the latter strongly depends on the number of clusters on the track determined by the original kinematics at the surface of the target. As shown in Fig. 12, good agreement is obtained in terms of the resolution on the track parameters.

As a consequence, realistic dE/dx and m^2 values are generated for the reconstructed MC tracks using parametrizations of the data for the mean energy loss distribution and width of the m^2 distribution as a function of the track momentum (see Ref. [31] for details).

The backward extrapolation procedure shows similar performance for MC and real data. An additional analysis was performed to extract yields of outgoing negatively charged pions in the data and the simulation. As can be seen in Fig. 18, good agreement is obtained between MC and data for the momentum distribution of negatively charged pion-like tracks after backward extrapolation, requirement of a point of closest approach closer than 0.6 cm to the surface of the target and a simple dE/dx-based PID selection to reject electrons. In both analyses, the efficiency of the procedure was estimated to be at least 98% as a function of p, θ and z at the surface of the target.

The PID analysis applied to data described in the previous section is performed identically on the MC. Fig. 19 shows the result of the log-likelihood fit to the simulated $(m^2,dE/dx)$ distribution in the (p,θ) bin shown for data in Fig. 16.

5. Yields of positively charged pions at the surface of the replica target

Yields of positively charged pions were extracted in bins of (p,θ,z) at the surface of the target for real and simulated data, using a log-likelihood fit (see Section 3.5) in the $(m^2,dE/dx)$ plane. Spectra are presented differentially as a function of momentum for different angular intervals, and different longitudinal bins along the target. For simplicity, the notations dn_{NA61}/dp and dn_{FLUKA}/dp are used to refer to the data and simulated momentum spectra, respectively, in a given angular interval and longitudinal bin.

For data, the differential corrected spectra are defined as

$$\frac{dn_{\mathrm{NA61}}}{dp}=\frac{N_{\mathrm{NA61}}}{\Delta p}\frac{1}{N^{pot}_{\mathrm{NA61}}}\prod_i\frac{1}{C^i(p,\theta,z)}, \tag{1}$$

where N_{NA61} is the measured *raw* yield (i.e. after reconstruction and PID analysis) in a given angular interval and longitudinal bin for a momentum bin of width Δp, N^{pot}_{NA61} is the number of protons on target selected for the analysis, and the C^is are correction factors that depend on the track parameters (p,θ,z). It was checked that track migration between bins is well below 10% and thus the unfolding of the measured spectra is not necessary.

Similarly, the differential spectra obtained for FLUKA with the same PID analysis are defined as

$$\frac{dn_{\mathrm{FLUKA}}}{dp}=\frac{N_{\mathrm{MC}}}{\Delta p}\frac{1}{N^{pot}_{\mathrm{MC}}}\prod_i\frac{1}{C^i(p,\theta,z)} \tag{2}$$

where N_{MC} is the simulated *raw* yield in a given angular interval and longitudinal bin for a momentum bin of width Δp, and N^{pot}_{MC} is

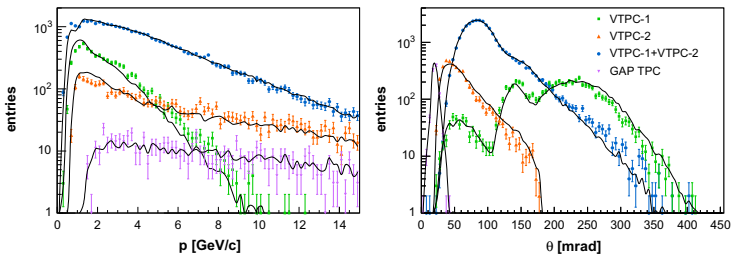

Fig. 17. Distributions of momentum (left) and polar angle (right) of TPC tracks at the surface of the target for data (markers) and MC (solid smoothed curves). The different track topologies are specified in the legend on the right plot and described in the text. Small data-MC differences at large angles (above $\sim$25 mrad) do not influence the results reported here.

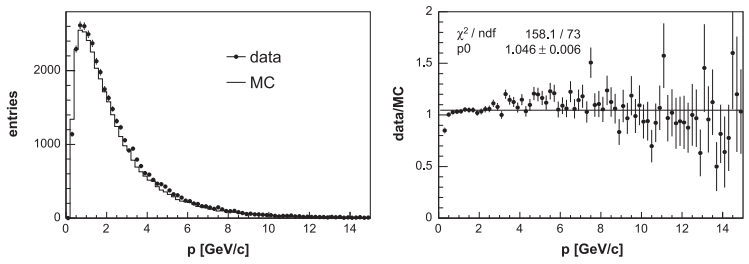

Fig. 18. Momentum distribution of negatively charged pion-like tracks (left) after backward extrapolation, requirement for a point of closest approach closer than 0.6 cm to the surface of the target and a simple dE/dx-based PID selection to reject electrons. Ratio of data to MC (right).

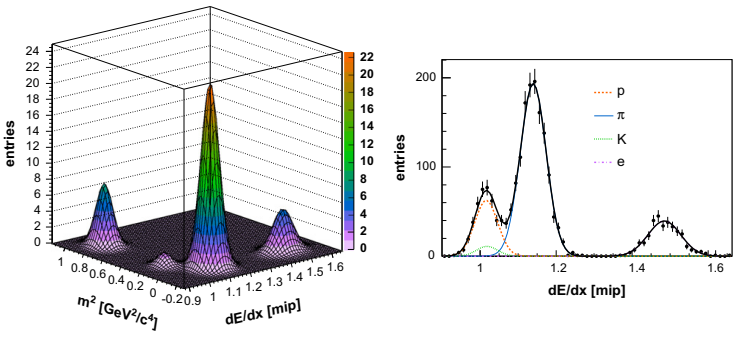

Fig. 19. Two-dimensional fit of the simulated data in the (m^2,dE/dx) plane (left) and respective dE/dx projection (right), for $40 < \theta < 100$ mrad and $2.4 < p < 3.2$ GeV/c at the surface of the target. The different components of the fit are shown with different line styles.

the number of protons on target generated for the simulation. The N_{MC} raw yield contains part of the original FLUKA information which is reconstructed within the acceptance of the detector, as well as contaminations from weak decays generated in GEANT3 and interactions in the detector material generated by the GCALOR model. Within the errors of the correction factors, dn_{FLUKA}/dp is equivalent to the original information generated at the surface of the target in the standalone FLUKA simulation.

The C^i factors in Eqs. (1) and (2) include efficiencies for the reconstruction, the backward extrapolation and the time-of-flight detector, as well as corrections for the detector geometrical acceptance, pion losses (decays and interactions in the detector material) and contamination from weak decays (feed-down). With the exception of the time-of-flight efficiency evaluated from the data, all the C^i factors are MC based corrections. These are applied identically to data and simulation and cancel in the ratio of the data and simulated yields evaluated according to Eqs. (1) and (2).

As will be further explained in Section 6.1, the use of the NA61 2007 replica-target data in T2K is based on the ratio of data and simulated yields. Thus, only *raw* yields are considered in what follows. The *raw* spectra of positively charged pions are defined following Eqs. (1) and (2) as

$$\frac{dN_{NA61}}{dp} = \frac{N_{NA61}}{\Delta p}\frac{1}{N^{pot}_{NA61}}\frac{1}{\epsilon^{ToF}_{NA61}} \tag{3}$$

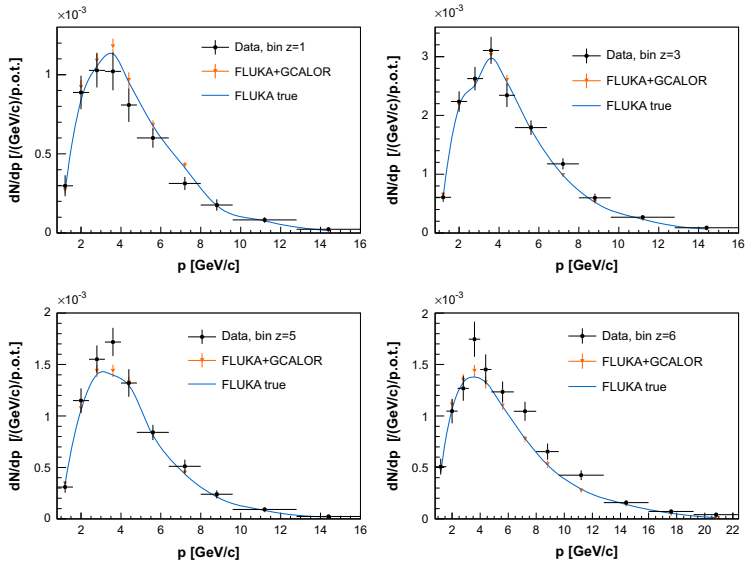

Fig. 20. Spectra of outgoing positively charged pions normalized to the momentum bin size and number of protons on target in the angular interval [40–100] mrad for the most upstream (top left), central (top right) and most downstream (bottom left) longitudinal bins, and in the angular interval [0–40] mrad for the downstream face of the target (bottom right). Error bars correspond to the sum in quadrature of statistical and systematic uncertainties. Smooth curves show the prediction of FLUKA2011.2 associated to tracks reconstructed within the acceptance of the NA61 detector (described in Section 3.4). FLUKA+GCALOR refers to the MC yields after reconstruction and PID analysis.

for the data, and

$$\frac{dN_{\mathrm{MC}}}{dp} = \frac{N_{\mathrm{MC}}}{\Delta p}\frac{1}{N_{\mathrm{MC}}^{pot}} \tag{4}$$

for the MC. For data, the ToF-F detector efficiency, $\epsilon_{\mathrm{NA61}}^{ToF}$, is evaluated as a function of p and θ. Due to the ToF response not being simulated in the NA61 MC, $\epsilon_{\mathrm{MC}}^{ToF}$ is set to 1. Thus, the time-of-flight detector efficiency is the only correction that does not cancel in the ratio of real data to simulation and consequently it is included in the definition of the *raw* spectra for data. As an example, *raw* spectra measured over the most upstream, central and most downstream longitudinal bins, as well as the spectra measured at the downstream face of the target are depicted in Fig. 20 in the angular interval [40–100] mrad for the real and simulated data.

Systematic uncertainties on the spectra computed via Eqs. (3) and (4) arise from the PID and normalization for both real data and simulation. A systematic uncertainty due to the time-of-flight detector efficiency is accounted for in the data. The systematic uncertainty associated with the PID procedure was evaluated with the MC by comparing the pion yields obtained from the log-likelihood fit to the generated number of pions in the sample as a function of the reconstructed track momentum. The full statistics of the MC sample was used to estimate the uncertainty in the simulation. For the data, an independent MC sample with statistics equivalent to that of data was used. The estimated systematic uncertainty varies from 1% to 3% for the MC and 1% to 5% for the data with increasing momentum. A systematic uncertainty of 1.4% was assigned to the normalization to the number of protons on target in data. It was estimated by varying the cuts used for the selection of the beam tracks on target. The same uncertainty is propagated to the MC since the simulation of the beam tracks impinging on the target is based on real data distributions for the beam position and divergence. The systematic uncertainty associated with the ToF-F efficiency comes from the eventual inclusion of off-time tracks in the calculation. In order to estimate this uncertainty a first calculation was made using the full 50 μs drift of the MTPCs. Additional calculations were performed over only the first and last 25 μs drift distances. By comparing these calculations the uncertainty on the time-of-flight efficiency was estimated below 1–3%.

Table 1
Main systematic uncertainties and their dependence on momentum, p, and polar angle, θ.

Systematic error	Dependence	Estimation	Value (%)
Particle identification	p	MC	1–5
Normalization	Uniform	data	1.4
ToF efficiency	(p, θ)	data	<3
Beam momentum	Uniform	MC	<3
Target density	Uniform	MC	<3
Target alignment	Uniform	MC	3

The total systematic uncertainties are typically 3–5% and contributions are summarized in Table 1. For data however, the overall uncertainty is dominated by the statistical uncertainty which is in the range of 10–15%.

6. Re-weighting of flux predictions with long-target data

6.1. Re-weighting methods

At least two different approaches based on the NA61 replica-target data can be followed to re-weight the predictions of the

model used in the T2K beam MC for the simulation of hadronic interactions in the target

1. Re-weighting factors are calculated in bins of (p,θ,z) within the T2K simulation. In this case weights are defined as

$$w(p,\theta,z) = N^{corr}_{\mathrm{NA61}}(p,\theta,z)/N^{sim}_{\mathrm{T2K}}(p,\theta,z), \quad (5)$$

where N^{corr}_{NA61} are the NA61 measured yields at the surface of the target corrected for various efficiencies, detector geometrical acceptance and particle losses (i.e. *absolute* yields), and N^{sim}_{T2K} are the yields of emitted particles *simulated* within the T2K beam MC;

2. Re-weighting factors are calculated in bins of (p,θ,z) within the NA61 simulation. In this case weights are defined as

$$w(p,\theta,z) = N^{data}_{\mathrm{NA61}}(p,\theta,z)/N^{MC}_{\mathrm{NA61}}(p,\theta,z), \quad (6)$$

where N^{data}_{NA61} are the NA61 measured yields at the surface of the target without any corrections (i.e. *raw* yields), and N^{MC}_{NA61} are the reconstructed yields obtained from the NA61 simulation based on the model used in T2K.

In the first approach, absolute yields are obtained by applying various corrections to the measured *raw* yields. This approach has the advantage that the corresponding re-weighting factors are almost model independent. Actually, dependencies on the model used in the NA61 MC occur only via several relatively small correction factors. This includes in particular losses due to secondary interactions in the detector material or contamination from weak decays that result in a maximum 5% correction in the NA61 2007 thin-target analysis for positively charged pions [17]. This approach does not necessarily require the use of the same hadroproduction model within NA61 and T2K.

In the second approach, which was chosen for the analysis presented in this paper, there are two prerequisites: the same MC model must be used in the T2K simulation and the NA61 analysis, and the simulated data in NA61 must go through the same reconstruction and PID analysis procedure as the real data. In this case, re-weighting factors can be calculated from *raw* yields in both data and MC since all common corrections used to obtain absolute yields in the first method will cancel in the ratio. Thus, we avoid introducing additional systematic errors on top of the large statistical uncertainties of the low-statistics 2007 data. However, the re-weighting factors obtained in this way are specific to the common version of the model used in both simulations (i.e. if the model were to be changed in the T2K simulation, a new set of re-weighting factors would have to be calculated within NA61).

Unlike thin-target based re-weighting factors which are calculated as ratios of production cross-sections, factors calculated with the replica-target data in both methods described above are based on yields of outgoing particles that depend upon the beam parameters of the NA61 measurements. Thus, a relative re-weighting of the NA61 and T2K beam distributions is necessary when beam distributions differ significantly in the two experiments. Eqs. (5) and (6) should then slightly be modified to account for that additional degree of freedom. The final NA61 results with the replica of the T2K target based on the high-statistics 2009 and 2010 data sets will be obtained using the first approach which provides absolute particle yields per proton on target. As explained at the end of Section 3.4, the high statistics data will allow for the accounting for the relative re-weighting of the NA61 and T2K beams on target.

Note that a total systematic error of typically 7% was estimated for pion spectra obtained from the 2007 thin-target data [17]. Some of the contributions to the total systematic uncertainty (e.g. feed-down correction) are expected to be significantly smaller for the T2K replica-target data. Thus, for absolute yields of particles measured at the surface of the target, we expect a precision of 5% or better.

6.2. Application to the T2K beam simulation

T2K beam MC predictions (based on FLUKA2011.2) can be re-weighted with the NA61 2007 replica-target data by calculating the re-weighting factors defined in Eq. (6). Using Eqs. (3) and (4), these are given for each (p,θ,z) bin by

$$w(p,\theta,z) = \frac{N_{\mathrm{NA61}}}{N_{\mathrm{MC}}}\frac{N^{pot}_{\mathrm{MC}}}{N^{pot}_{\mathrm{NA61}}}\frac{1}{\epsilon^{ToF}_{\mathrm{NA61}}} \quad (7)$$

Fig. 21 shows the re-weighting factors corresponding to the spectra depicted in Fig. 20, measured over the most upstream, central and most downstream longitudinal bins, as well as at the downstream face of the target.

In addition to the systematic uncertainties arising from the PID analysis, the normalization and the time-of-flight detector efficiency, sources related to differences between the T2K target and the NA61 replica are accounted for in the total systematic uncertainty of the re-weighting factors. Dedicated FLUKA2011.2 simulations were performed to estimate the systematic uncertainties on the yields of outgoing charged pions due to differences in the replica-target geometry (i.e. contribution of the aluminium support flanges), alignment and density (1.83 g/cm^3 for the replica, 1.804 g/cm^3 for the T2K target) for the respective beam profiles on target in NA61 and T2K. The estimated uncertainty (within the statistical precision of the simulations) was below 3% for the differences in target geometry and density, while an overall 3% uncertainty was assigned for the target misalignment. An additional systematic uncertainty ($<2\%$) was estimated to account for the measured width of the beam momentum distribution which is not simulated in the NA61 MC.

The overall systematic uncertainty on the re-weighting factors is typically about 6%, with main contributions from the PID analysis at large momentum and from the target misalignment. The total error is however dominated by the statistical uncertainty which varies between 10% and 15%.

In order to use the re-weighting factors calculated with the NA61 replica-target data in the T2K beam simulation, a new class was implemented in the existing re-weighting software based on the NA61 thin-target data (described in Ref. [28]). The class is implemented in such a way that either of two procedures can be followed to re-weight the production of positively charged pions: use of the thin-target data to re-weight the secondary and tertiary production in the target, or use of the replica-target data to re-weight outgoing pions at the surface of the target. A common re-weighting method is used for hadronic interactions that occur outside the target.

For illustration of the complete re-weighting procedure, the T2K beam simulation was run with default beam parameters in FLUKA2011.2 and horn currents set to 250 kA. The prediction of the ν_μ flux at the far detector re-weighted with the replica-target data is shown in Fig. 22 (left) together with the prediction re-weighted with the thin-target data.

For the replica-target re-weighted prediction, the maximum possible errors are shown and correspond to a fully correlated 1-sigma shift of the pion re-weighting factors only. In the case of the thin-target re-weighted prediction, two sets of errors are shown: the first one corresponds to the total error which is shown

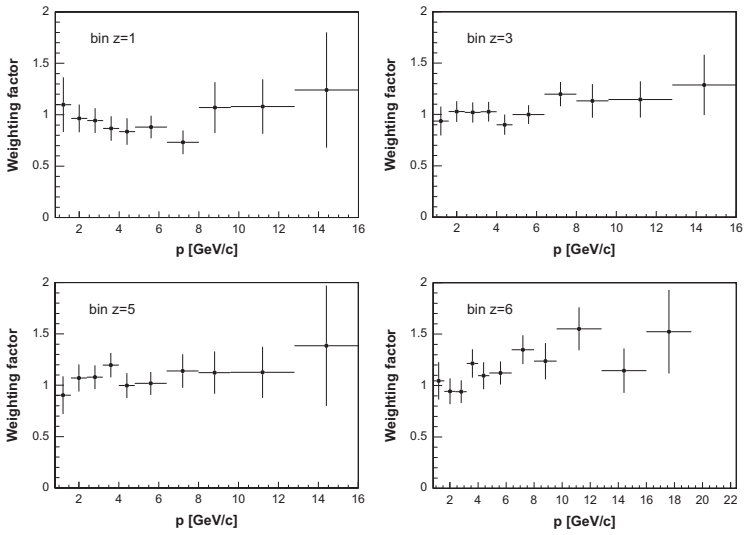

Fig. 21. Re-weighting factors for outgoing positively charged pions in the angular interval [40–100] mrad for the most upstream (top left), central (top right) and most downstream (bottom left) longitudinal bins, and in the angular interval [0–40] mrad for the downstream face of the target (bottom right). Error bars correspond to the sum in quadrature of statistical and systematic uncertainties.

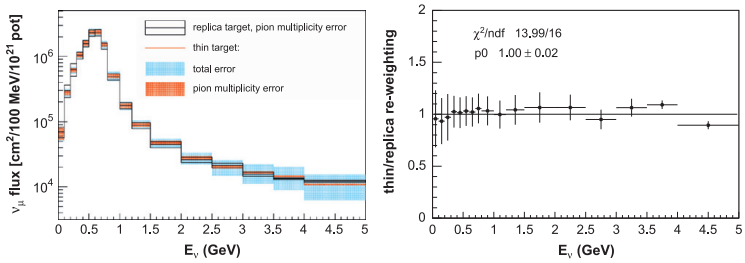

Fig. 22. Re-weighted ν_μ flux predictions at the far detector of T2K based on the NA61 thin-target and replica-target data (left) and ratio of the two predictions (right). Details about the associated errors are given in the text. A linear fit to the ratio (right) is shown by the solid line.

in fractional form in Fig. 4, the second one corresponds only to the error associated with the pion multiplicity (shown in Fig. 4 as well) and can be compared directly to the error shown for the replica-target re-weighted prediction. Large uncertainties above 2 GeV neutrino energy for the thin-target based prediction are dominated by the error propagation of the kaon re-weighting.

The ratio of the two predictions is shown in Fig. 22 (right) and indicates good agreement between the results of both methods. Errors on the ratio correspond to the error propagation in quadrature where only errors associated with the pion multiplicity are considered for the thin-target based prediction. Both re-weighting methods are consistent within the uncertainties considered in this study for the re-weighting of the pion multiplicity. Although uncertainties are of the same order for the two approaches, it should be noted that in the case of the long-target based re-weighting, results were obtained with half the statistics of the thin-target case. The analysis of the 2009 and 2010 long-target data will not only significantly decrease the dominant statistical uncertainty but also some of the currently large systematics (target misalignment).

The relative re-weighting of the NA61 and T2K beam distributions is not included at this stage of the analysis but is not expected to significantly alter the comparison presented here as a simple illustration of the re-weighting procedure.

7. Summary and conclusions

Precise predictions of the initial neutrino flux are needed by the T2K long-baseline neutrino oscillation experiment in Japan. This paper argues that the highest precision predictions can be reached by detailed measurements of hadron emission from the same target as used by T2K exposed to a proton beam of the same kinetic energy of 30 GeV. The corresponding data were recorded in 2007–2010 by the NA61/SHINE experiment at the CERN SPS using a replica of the T2K graphite target.

First, details of the experiment and data taking were described. Second, results from the pilot analysis of the NA61 data taken in 2007 with a replica of the T2K target were presented. Yields of positively charged pions were reconstructed at the surface of the

replica target in bins of the laboratory momentum and polar angle as a function of the longitudinal position along the target. Third, re-weighting factors for the model used to simulate hadronic interactions in the T2K target were calculated using these measurements. As an illustration of the complete procedure, the re-weighting factors were propagated to the neutrino flux prediction in T2K. The prediction obtained in this way for the ν_μ flux at the far detector of T2K was finally compared to that obtained with a re-weighting based on the NA61 thin-target measurements.

In the global framework of accelerator-based neutrino oscillation experiments, the paper demonstrates that high quality long-target measurements can be performed with the NA61 setup and that such measurements will lead to a significant reduction of systematic uncertainties on the neutrino flux predictions in long-baseline neutrino experiments.

Acknowledgments

This work was supported by the Hungarian Scientific Research Fund (grants OTKA 68506 and 71989), the Polish Ministry of Science and Higher Education (grants 667/N-CERN/2010/0 and N N202 484339), the Foundation for Polish Science—MPD program, co-financed by the European Union within the European Regional Development Fund, the Federal Agency of Education of the Ministry of Education and Science of the Russian Federation (grant RNP 2.2.2.2.1547), grant 12-02-91503-CERN_a of the RFBR-CERN Foundation, the Ministry of Education, Culture, Sports, Science and Technology, Japan, Grant-in-Aid for Scientific Research (grants 18071005, 19034011, 19740162, 20740160 and 20039012), the Toshiko Yuasa Laboratory (France-Japan Particle Physics Laboratory), the Institut National de Physique Nucléaire et Physique des Particules (IN2P3, France), the German Research Foundation (grant GA 1480/2-1), Bulgarian National Scientific Foundation (grant DDVU 02/19/2010), Swiss Nationalfonds Foundation (grant 200020-117913/1) and ETH Research grant TH-01 07-3.

References

[1] Y. Itow, et al., T2K Collaboration, 2001, arXiv:hep-ex/0106019.
[2] K. Abe, et al., T2K Collaboration, Nuclear Instruments and Methods in Physics Research Section A 659 (2011) 106, e-Print: arXiv:1106.1238.
[3] D. Beavis, et al., Long Baseline Neutrino Oscillation Experiment at the AGS (Proposal E889), Physics Design Report BNL 52459, 1995.
[4] K. Abe, et al., T2K Collaboration, Physical Review Letters 107 (2011) 041801.
[5] F.P. An, et al., DAYA-BAY Collaboration, Physical Review Letters 108 (2012) 171803.
[6] J.K. Ahn, et al., RENO Collaboration, Physical Review Letters 108 (2012) 191802.
[7] K. Abe, et al., T2K Collaboration, Physical Review D 85 (2012) 031103.
[8] J.R. Sanford, C.L. Wang, Empirical formulas for particle production in p-Be collisions between 10 and 35 BeV/c, BNL/AGS Internal Report JRS/CLW-1, 1967.
[9] A.J. Malensek, Empirical Formula for Thick Target Particle Production, FERMILAB Report FN-341, 1981.
[10] M. Bonesini, et al., The European Physical Journal C 20 (2001) 13.
[11] M.G. Catanesi, et al., HARP Collaboration, Nuclear Physics B 732 (2006) 1.
[12] M.H. Ahn, et al., K2K Collaboration, Physical Review D 74 (2006) 072003.
[13] M.G. Catanesi, et al., HARP Collaboration, The European Physical Journal C 52 (2007) 29.
[14] A.A. Aguilar-Arevalo, Physical Review D 79 (2009) 072002, e-Print: arXiv:0806.1449.
[15] G. Ambrosini, et al., NA56/SPY Collaboration, The European Physical Journal C 10 (1999) 605.
[16] P. Astier, et al., NOMAD Collaboration, Nuclear Instruments and Methods in Physics Research Section A 515 (2003) 800.
[17] N. Abgrall, et al., NA61/SHINE Collaboration, Physical Review C 84 (2011) 034604.
[18] N. Abgrall, et al., NA61/SHINE Collaboration, Physical Review C 85 (2012) 035210.
[19] N. Antoniou, et al., NA49-future Collaboration, Report No. CERN-SPSC-2006-034, 2006.
[20] N. Antoniou, et al., NA61/SHINE Collaboration, Report No. CERN-SPSC-2007-004, 2007.
[21] N. Antoniou, et al., NA61/SHINE Collaboration, Report No. CERN-SPSC-2007-019, 2007.
[22] N. Abgrall, et al., NA61/SHINE Collaboration, Report No. CERN-SPSC-2008-018, 2008.
[23] J. Abraham, et al., Pierre Auger Collaboration, Nuclear Instruments and Methods in Physics Research Section A 523 (2004) 50.
[24] T. Antoni, et al., KASCADE Collaboration, Nuclear Instruments and Methods in Physics Research Section A 513 (2003) 490.
[25] A. Fasso, A. Ferrari, J. Ranft, P.R. Sala, CERN-2005-10, INFN/TC_05/11, SLAC-R-773.
[26] R. Brun, F. Bruyant, M. Maire, A.C. McPherson, P. Zanarini, GEANT3, CERN-DD-EE-84-1.
[27] 〈http://www.atlas.uni-wuppertal.de/zeitnitz/gcalor〉.
[28] V. Galymov, Contribution to NUFACT11, in: XIIIth International Workshop on Neutrino Factories, Super Beams and Beta Beams, IOP Conference Series, 1–6 August 2011, CERN and University of Geneva, submitted for publication.
[29] S. Afanasiev, et al., NA49 Collaboration, Nuclear Instruments and Methods in Physics Research Section A 430 (1999) 257.
[30] K. Matsuoka, et al., Nuclear Instruments and Methods in Physics Research Section A 624 (2010) 591.
[31] N. Abgrall, PhD Thesis, CERN-THESIS-2011-165, available on 〈http://weblib.cern.ch〉.

Journal of Instrumentation

MAUS: the MICE analysis user software

Published by IOP Publishing for Sissa Medialab

Received: *February 1, 2019*
Revised: *March 26, 2019*
Accepted: *April 15, 2019*
Published: *April 30, 2019*

Muon Accelerators for Particle Physics — MUON

MAUS: the MICE analysis user software

R. Asfandiyarov,[a] R. Bayes,[b] V. Blackmore,[c] M. Bogomilov,[d] D. Colling,[c] A.J. Dobbs,[c] F. Drielsma,[a] M. Drews,[h] M. Ellis,[c] M. Fedorov,[e] P. Franchini,[f] R. Gardener,[g] J.R. Greis,[f] P.M. Hanlet,[h] C. Heidt,[i] C. Hunt,[c] G. Kafka,[h] Y. Karadzhov,[a] A. Kurup,[c] P. Kyberd,[g] M. Littlefield,[g] A. Liu,[j] K. Long,[c,n] D. Maletic,[k] J. Martyniak,[c] S. Middleton,[c] T. Mohayai,[h,j] J.J. Nebrensky,[g] J.C. Nugent,[b] E. Overton,[l] V. Pec,[l] C.E. Pidcott,[f] D. Rajaram,[h,1] M. Rayner,[m] I.D. Reid,[g] C.T. Rogers,[n] E. Santos,[c] M. Savic,[k] I. Taylor,[f] Y. Torun,[h] C.D. Tunnell,[m] M.A. Uchida,[c] V. Verguilov,[a] K. Walaron,[b] M. Winter[h] and S. Wilbur[l]

[a] *DPNC, section de Physique, Université de Genève, Geneva, Switzerland*
[b] *School of Physics and Astronomy, Kelvin Building, The University of Glasgow, Glasgow, U.K.*
[c] *Department of Physics, Blackett Laboratory, Imperial College London, London, U.K.*
[d] *Department of Atomic Physics, St. Kliment Ohridski University of Sofia, Sofia, Bulgaria*
[e] *Radboud University of Nijmegen, Netherlands*
[f] *Department of Physics, University of Warwick, Coventry, U.K.*
[g] *Brunel University, Uxbridge, U.K.*
[h] *Physics Department, Illinois Institute of Technology, Chicago, IL, U.S.A.*
[i] *University of California, Riverside, CA, U.S.A.*
[j] *Fermilab, Batavia, IL, U.S.A.*
[k] *Institute of Physics, University of Belgrade, Serbia*
[l] *Department of Physics and Astronomy, University of Sheffield, Sheffield, U.K.*
[m] *Department of Physics, University of Oxford, Denys Wilkinson Building, Oxford, U.K.*
[n] *STFC Rutherford Appleton Laboratory, Harwell Oxford, Didcot, U.K.*

E-mail: durga@fnal.gov

Abstract: The Muon Ionization Cooling Experiment (MICE) collaboration has developed the MICE Analysis User Software (MAUS) to simulate and analyze experimental data. It serves as the primary codebase for the experiment, providing for offline batch simulation and reconstruction as well as online data quality checks. The software provides both traditional particle-physics functionalities such as track reconstruction and particle identification, and accelerator physics functions, such as calculating transfer matrices and emittances. The code design is object orientated, but has a top-level structure based on the Map-Reduce model. This allows for parallelization to support live data reconstruction during data-taking operations. MAUS allows users to develop in

[1] Corresponding author.

https://doi.org/10.1088/1748-0221/14/04/T04005

2019 JINST 14 T04005

either Python or C++ and provides APIs for both. Various software engineering practices from industry are also used to ensure correct and maintainable code, including style, unit and integration tests, continuous integration and load testing, code reviews, and distributed version control. The software framework and the simulation and reconstruction capabilities are described.

KEYWORDS: Data reduction methods; Simulation methods and programs; Software architectures (event data models, frameworks and databases); Accelerator modelling and simulations (multi-particle dynamics; single-particle dynamics)

ARXIV EPRINT: 1812.02674

2019 JINST 14 T04005

Contents

2019 JINST 14 T04005

1 Introduction

1.1 The MICE experiment

The Muon Ionization Cooling Experiment (MICE) sited at the STFC Rutherford Appleton Laboratory (RAL) has delivered the first demonstration of muon ionization cooling [1] — the reduction of the phase-space of muon beams. Muon-beam cooling is essential for future facilities based on

muon acceleration, such as the Neutrino Factory or Muon Collider [2, 3]. The experiment was designed to be built and operated in a staged manner. In the first stage, the muon beamline was commissioned [4] and characterized [5]. A schematic diagram of the configuration used to study the factors that determine the performance of an ionization-cooling channel is shown in figure 1. The MICE experiment was operated such that muons passed through the experiment one at a time. The experiment included instrumentation to identify particle species (the particle-identification detectors, PID) [6–11] and to measure the phase-space coordinates of each muon. An ensemble of muons that was representative of the muon beam was then assembled using the measured coordinates. The techniques used to reconstruct the ensemble properties of the beam are described in [12] and the first observation of the ionization-cooling of a muon beam is presented in [1].

The configuration shown in figure 1 was used to study the factors that determine the performance of an ionization-cooling channel and to observe for the first time the reduction in transverse emittance of a muon beam.

The MICE Muon Beam line is described in detail in [4]. There are 5 different detector systems present on the beamline: time-of-flight (TOF) scintillators [6], threshold Cherenkov (Ckov) counters [13], scintillating-fiber trackers [14], a sampling calorimeter (KL) [8, 9], and the Electron Muon Ranger (EMR) — a totally active scintillating calorimeter [10, 11]. The TOF, Ckov, KL and EMR detectors are used for particle identification (PID), and the scintillating-fiber trackers are used to measure position and momentum. The TOF detector system consists of three detector stations, TOF0, TOF1 and TOF2, each composed of two orthogonal layers of scintillator bars. The TOF system determines PID via the time-of-flight between the stations. Each station also provides a low-resolution image of the beam profile. The Ckov system consists of two aerogel threshold Cherenkov stations, CkovA and CkovB. The KL and EMR detectors, the former using scintillating fibers embedded in lead sheets, and the latter scintillating bars, form the downstream calorimeter system.

The tracker system consists of two scintillating-fiber detectors, one upstream of the MICE cooling cell, the other downstream, in order to measure the change in emittance across the cooling cell. Each detector consists of 5 stations, each station having 3 fiber planes, allowing precision measurement of momentum and position to be made on a particle-by-particle basis.

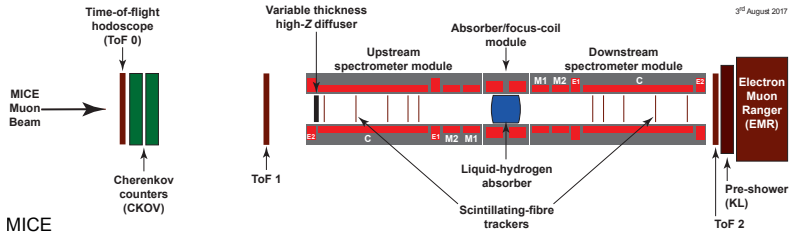

Figure 1. Schematic diagram of the MICE experiment.The red rectangles represent the coils of the spectrometer solenoids and focus-coil module. The individual coils of the spectrometer solenoids are labelled E1, C, E2, M1 and M2. The various detectors (time-of-flight hodoscopes (TOF0, TOF1) [6], Cherenkov counters [13], scintillating-fiber trackers [14], KLOE-Light (KL) calorimeter [7, 8], and Electron Muon Ranger (EMR) [10, 11]) are also represented.

2019 JINST 14 T04005

1.2 Software requirements

The MICE software must serve both the accelerator-physics and the particle-physics needs of the experiment. Traditional particle-physics functionality includes reconstructing particle tracks, identifying them, and simulating the response from various detectors, while the accelerator-physics aspect includes the calculation of transfer matrices and Twiss parameters and propagating the beam envelopes. All of these items require a detailed description of the beamline, the geometries of the detectors, and the magnetic fields, as well as functionality to simulate the various detectors and reconstruct the detector outputs. MICE aims to measure the change in emittance to 1%, which imposes requirements on the performance of the track reconstruction, particle identification and measurements of scattering widths. In addition, the computational performance of the software was also important in order to ensure that the software can reconstruct data with sufficient speed to support live online monitoring of the experiment.

2 MAUS

The MICE Analysis User Software (MAUS) is the collaboration's simulation, reconstruction, and analysis software framework. MAUS provides a Monte Carlo (MC) simulation of the experiment, reconstruction of tracks and identification of particles from simulations and real data, and provides monitoring and diagnostics while running the experiment.

Installation is performed via a set of shell scripts with SCons [15] as the tool for constructing and building the software libraries and executables. The codebase is maintained with GNU Bazaar [16], a distributed version control system, and is hosted on Launchpad [17], a website that provides functionalities to host and maintain the software repository. MAUS has a number of dependencies on standard packages such as Python, ROOT [18] and Geant4 [19] which are built as "third party" external libraries during the installation process. The officially supported platform is Scientific Linux 6 [20] though developers have successfully built on CentOS [21], Fedora [22], and Ubuntu [23] distributions.

Each of the MICE detector systems, described in section 1.1, is represented within MAUS. Their data structures are described in section 2.2 and their simulation and reconstruction algorithms in sections 3 and 4. MAUS also provides "global" reconstruction routines, which combine data from individual detector systems to identify particle species by the likelihood method and perform a global track fit. These algorithms are also described in section 4.

2.1 Code design

MAUS is written in a mixture of Python and C++. C++ is used for complex or low-level algorithms where processing time is important, while Python is used for simple or high-level algorithms where development time is a more stringent requirement. Developers are allowed to write in either Python or C++ and Python bindings to C++ are handled through internal abstractions. In practice, all the reconstruction modules are written in C++ but support is provided for legacy modules written in Python.

MAUS has an Application Programming Interface (API) that provides a framework on which developers can hang individual routines. The MAUS API provides MAUS developers with a well-defined environment for developing reconstruction code, while allowing independent development of the back-end and code-sharing of common elements, such as error handling.

2019 JINST 14 T04005

The MAUS data processing model is inspired by the Map-Reduce framework [24], which forms the core of the API design. Map-Reduce, illustrated in figure 2 is a useful model for parallelizing data processing on a large scale. A *map* process takes a single object as an input, transforms it, and returns a new object as the output (in the case of MAUS this input object is the *spill* class, see section 2.2).

A module is the basic building block of the MAUS API framework. Four types of module exist within MAUS:

1. ***Inputters*** generate input data either by reading data from files or over a network, or by generating an input beam;
2. ***Mappers*** modify the input data, for example by reconstructing signals from detectors, or tracking particles to generate MC hits;
3. ***Reducers*** collate the mapped data and provide functionality that requires access to the entire data set; and
4. ***Outputters*** save the data either by streaming over a network or writing to disk.

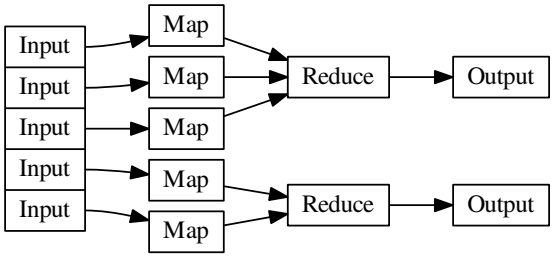

Figure 2. A Map-Reduce framework.

Each module type follows a common, extensible, object-orientated class hierarchy, shown for the case of the *map* and *reduce* modules in figure 3.

There are some objects that sit outside the scope of this modular framework but are nevertheless required by several of the modules. For instance, the detector geometries, magnetic fields, and calibrations are required by the reconstruction and simulation modules, and objects such as the electronics-cabling maps are required in order to unpack data from the data acquisition (DAQ) source, and error handling functionality is required by all of the modules. All these objects are accessed through a static singleton *globals* class.

MAUS has two execution concepts. A *job* refers to a single execution of the code, while a *run* refers to the processing of data for a DAQ run or MC run. A job may contain many runs. Since data are typically accessed from a single source and written to a single destination, *inputters* and *outputters* are initialized and destroyed at the beginning and end of a job. On the other hand, *mappers*

2019 JINST 14 T04005

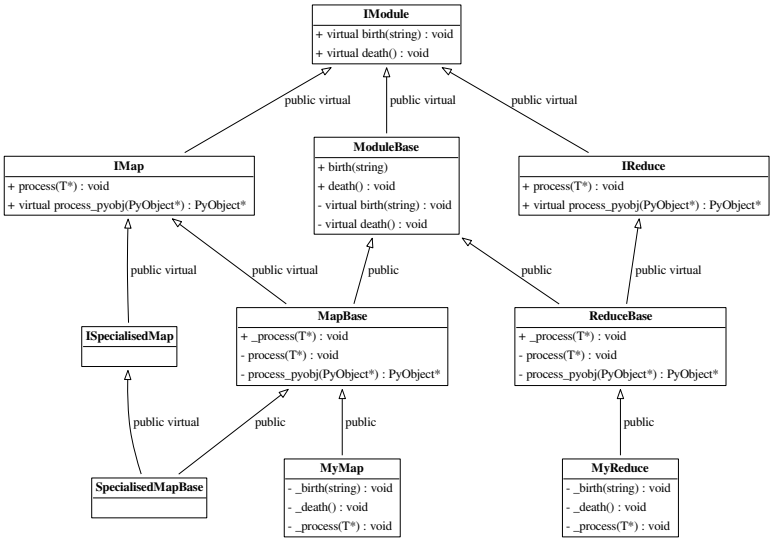

Figure 3. The MAUS API class hierarchy for Map and Reduce modules. The input and output modules follow related designs. *T* represents a templated argument. "+" indicates the introduction of a virtual void method, defining an interface, while "-" indicates that a class implements that method, fulfilling that aspect of the interface. The *process_pyobj* functions are the main entry points for Python applications, and *process* the entry points for C++ applications. The framework can be extended as many times as necessary, as exemplified by the "SpecialisedMap" classes.

and *reducers* are initialized at the beginning of a run in order to allow run-specific information such as electronics cabling maps, fields, calibrations and geometries to be loaded.

The principal data type in MAUS, which is passed from module to module, is the *spill*. A single spill corresponds to data from the particle burst associated with a dip of the MICE target [4]. A spill lasts up to $\sim$ 3 ms and contains several DAQ triggers. Data from a given trigger define a single MICE *event*. In the language of the Input-Map-Reduce-Output framework, an *Input* module creates an instance of spill data, a *Map* module processes the spill (simulating, reconstructing, etc.), a *Reduce* module acts on a collection of spills when all the *mappers* finish, and finally an *Output* module records the data to a given file format.

Modules can exchange spill data either as C++ pointers or JSON [25] objects. In Python, the data format can be changed by using a converter module, and in C++ *mappers* are templated to a MAUS data type and an API handles any necessary conversion to that type (see figure 3).

Data contained within the MAUS data structure (see section 2.2) can be saved to permanent storage in one of two formats. The default data format is a ROOT [18] binary and the secondary format is JSON. ROOT is a standard high-energy physics analysis package, distributed with MAUS, through which many of the analyses on MICE are performed. Each spill is stored as a single entry in a ROOT TTree object. JSON is an ASCII data-tree format. Specific JSON parsers are available — for example, the Python *json* library, and the C++ *JsonCpp* [26] parser come prepackaged with MAUS.

2019 JINST 14 T04005

In addition to storing the output from the *map* modules, MAUS is also capable of storing the data produced by *reducer* modules using a special *Image* class. This class is used by *reducers* to store images of monitoring histograms, efficiency plots, etc. *Image* data may only be saved in JSON format.

2.2 Data structure

2.2.1 Physics data

At the top of the MAUS data structure is the spill class which contains all the data from the simulation, raw real data and the reconstructed data. The spill is passed between modules and written to permanent storage. The data within a spill is organized into arrays of three possible event types: an *MCEvent* contains data representing the simulation of a single particle traversing the experiment and the simulated detector responses; a *DAQEvent* corresponds to the real data for a single trigger; and a *ReconEvent* corresponds to the data reconstructed for a single particle event (arising either from a Monte Carlo(MC) particle or a real data trigger). These different branches of the MAUS data structure are shown diagrammatically in figures 4–9.

The sub-structure of the MC event class is shown in figure 5. The class is subdivided into events containing detector hits (energy deposited, position, momentum) for each of the MICE detectors (see section 1.1). The event also contains information about the primary particle that created the hits in the detectors.

The sub-structure of the reconstruction event class is shown in figure 6. The class is subdivided into events representing each of the MICE detectors, together with the data from the trigger, and data for the global event reconstruction. Each detector class and the global-reconstruction class has several further layers of reconstruction data. This is shown in figures 7–9.

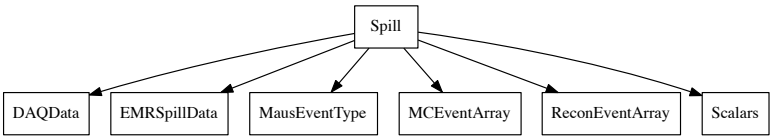

Figure 4. The MAUS output structure for a spill event. The label in each box is the name of the C++ class.

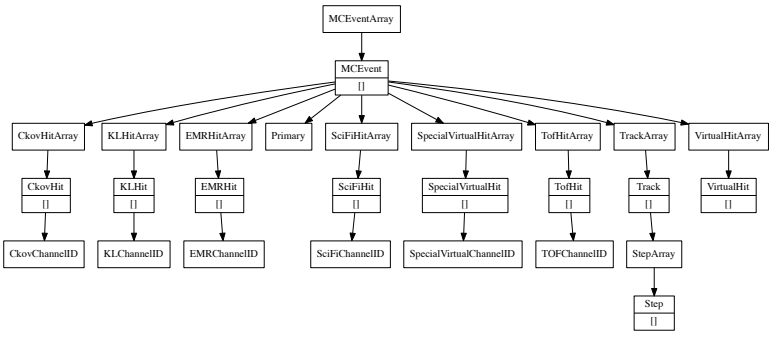

Figure 5. The MAUS data structure for MC events. The label in each box is the name of the C++ class and [] indicates that child objects are array items.

2019 JINST 14 T04005

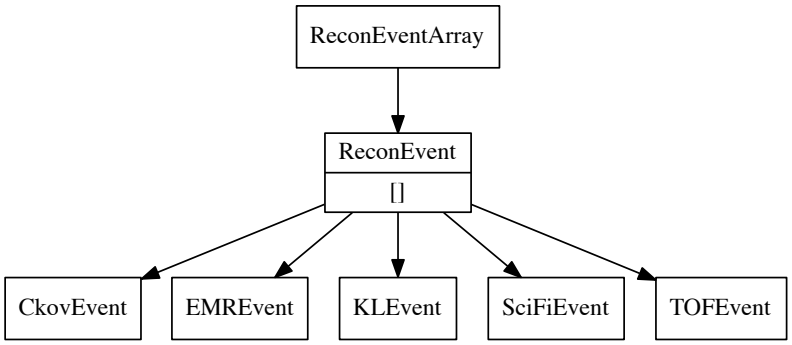

Figure 6. The MAUS data structure for reconstructed events. The label in each box is the name of the C++ class.

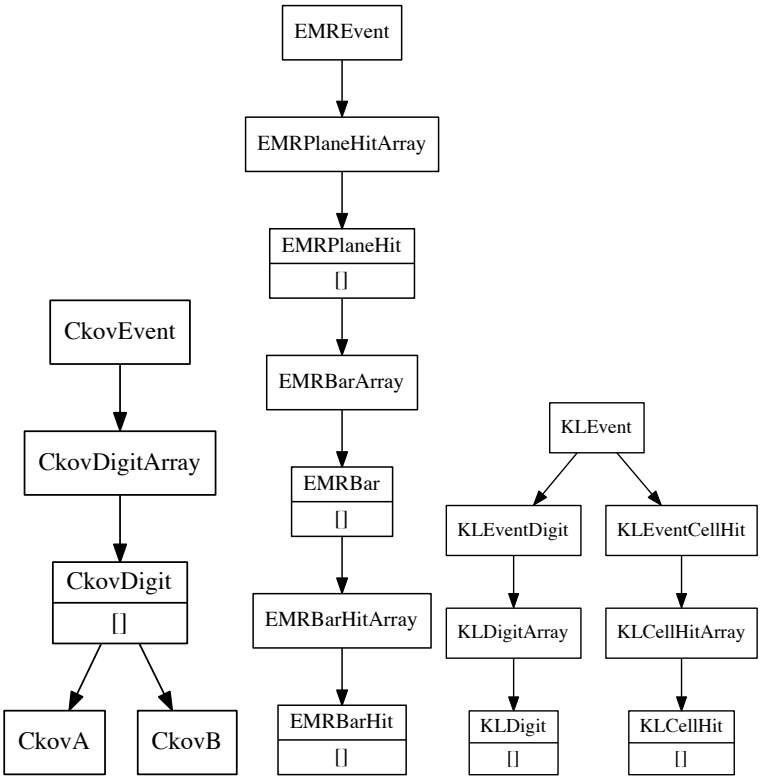

Figure 7. The MAUS data structure for CKOV (left), EMR (middle) and KL (right) reconstructed events. The label in each box is the name of the C++ class [] indicates that child objects are array items.

2019 JINST 14 T04005

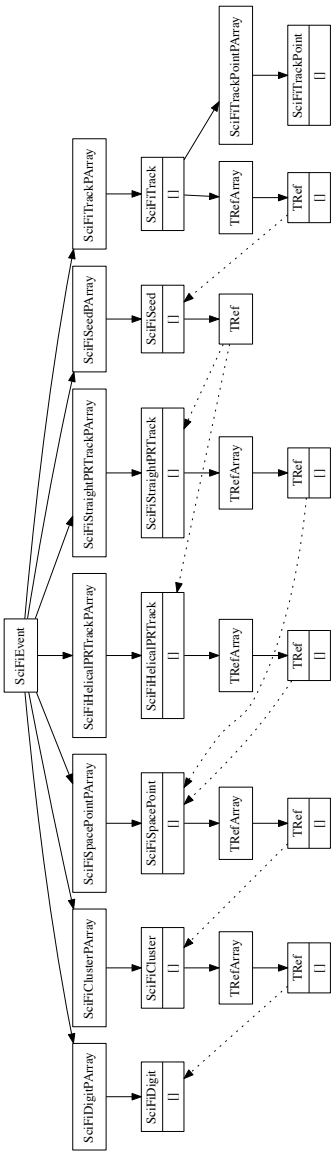

Figure 8. The MAUS data structure for the tracker. The label in each box is the name of the C++ class and [] indicates that child objects are array items.

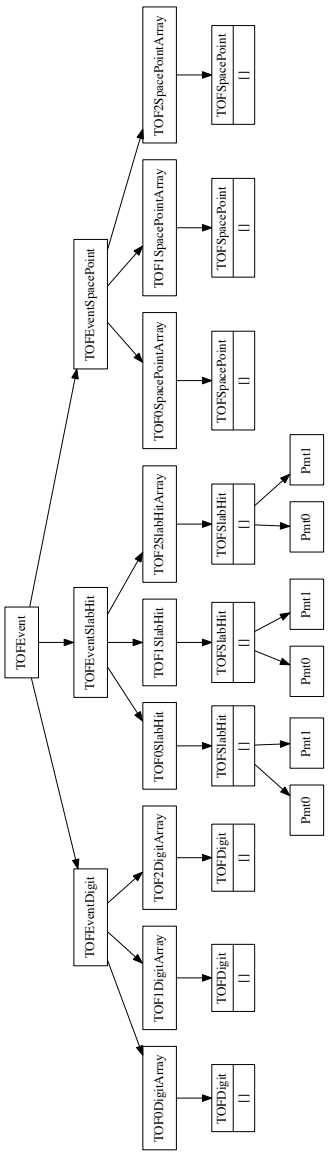

Figure 9. The MAUS data structure for the TOFs. The label in each box is the name of the C++ class and [] indicates that child objects are array items.

2.2.2 Top level data organization

In addition to the spill data, MAUS also contains structures for storing supplementary information for each run and job. These are referred to as *JobHeader* and *JobFooter*, and *RunHeader* and *RunFooter*. The *JobHeader* and *JobFooter* represent data, such as the MAUS release version, associated with the start and end of a job, and the *RunHeader* and *RunFooter* represent data, such as the geometry and calibrations associated with a run, associated with the start and end of a run. These are saved to the output along with the spill.

In order to interface with ROOT, particularly in order to save data in the ROOT format, thin wrappers for each of the top level classes, and a templated base class, were introduced. This allows the ROOT TTree, in which the output data is stored (see section 2.2.1), to be given a single memory address to read from. The wrapper for Spill is called *Data*, while for each of RunHeader, RunFooter, JobHeader and JobFooter, the respective wrapper class is just given the original class name with "Data" appended, e.g., *RunHeaderData*. The base class for each of the wrappers is called *MAUSEvent*. The class hierarchy is illustrated in figure 10.

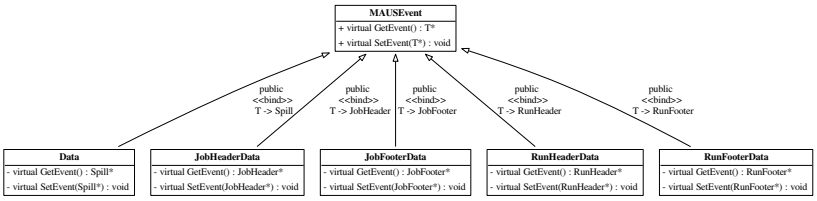

Figure 10. Class hierarchy for the wrappers and base class of the top-level classes of the MAUS data structure.

2.3 Data flow

The MAUS data-flow, showing the reconstruction chain for data originating from MC or real data, is depicted in figure 11. Each item in the diagram is implemented as an individual module. The data flow is grouped into three principal areas: the simulation data flow used to generate digits (electronics signals) from particle tracking; the real data flow used to generate digits from real detector data; and the reconstruction data flow which illustrates how digits are built into higher level objects and converted to parameters of interest. The reconstruction data flow is the same for digits from real data and simulation. In the case of real data, separate input modules are provided to read either directly from the DAQ, or from archived data stored on disk. A *reducer* module for each detector provides functionality to create summary histograms.

2.4 Testing

MAUS has a set of tests at the unit level and the integration level, together with code-style tests for both Python and C++. Unit tests are implemented to test a single function, while integration tests operate on a complete workflow. Unit tests check that each function operates as intended

2019 JINST 14 T04005

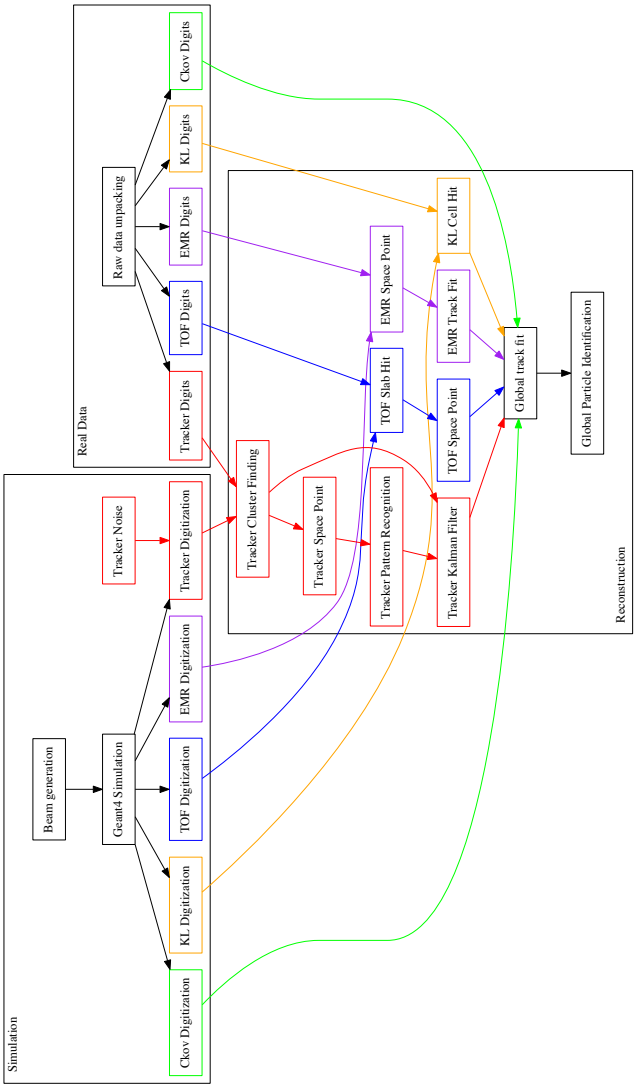

Figure 11. Data flow for the MAUS project. The data flow is color-coded by detector: Ckov — green, EMR — purple, KL — orange, TOF — blue, Tracker — red.

2019 JINST 14 T04005

by the developer. Tests are run automatically for every version committed to the repository and results show that a high level of code coverage has been achieved. Integration tests allow the overall performance of the code to be checked against specifications. The MAUS team provides unit test coverage that executes 70–80 % of the total code base. This level of coverage typically results in a code that performs the major workflows without any problems.

The MAUS codebase is built and tested using a Jenkins [27] continuous integration environment deployed on a cluster of servers. Builds and tests of the development branch are automatically triggered when there is a change to the codebase. Developers are asked to perform a build and test on a personal branch of the codebase using the test server before requesting a merge with the development trunk. This enables the MAUS team to make frequent clean releases. Typically MAUS works on a 4–8 week major-release cycle.

3 Monte Carlo

The Monte Carlo simulation of MICE encompasses beam generation, geometrical description of detectors and fields, tracking of particles through detectors and digitization of the detectors' response to particle interactions.

3.1 Beam generation

Several options are provided to generate an incident beam. Routines are provided to sample particles from a multivariate Gaussian distribution or generate ensembles of identical particles (pencil beams). In addition, it is possible to produce time distributions that are either rectangular or triangular in time to give a simplistic representation of the MICE time distribution. Parameters, controlled by data-cards, are available to control random seed generation, relative weighting of particle species and the transverse-to-longitudinal coupling in the beam. MAUS also allows the generation of a polarized beam.

Beam particles can also be read in from an external file created by G4Beamline [28] — a particle-tracking simulation program based on Geant4, or ICOOL [29] — a simulation program that was developed to study the ionization cooling of muon beams, as well as files in user-defined formats. In order to generate beams which are more realistic taking into account the geometry and fields of the actual MICE beamline, we use G4Beamline to model the MICE beamline from the target to a point upstream of the second quad triplet (upstream of Q4). The beamline settings, e.g., magnetic field strengths and number of particles to generate, are controlled through data-cards. The magnetic field strengths have been tuned to produce beams that are reasonably accurate descriptions of the real beam. Scripts to install G4beamline are shipped with MAUS.

Once the beam is generated, the tracking and interactions of particles as they traverse the rest of the beamline and the MICE detectors are performed using Geant4.

3.2 Geant4

A drawing of the MICE Muon Beam line [4] is shown in figure 12. It consists of a quadrupole triplet (Q123) that captures pions produced when the MICE target intersects the ISIS proton beam, a pion-momentum-selection dipole (D1), a superconducting solenoid (DS) to focus and transport the particles to a second dipole (D2) that is used to select the muon-beam momentum, and a transport

2019 JINST 14 T04005

channel composed of a further two quadrupole triplets (Q456 and Q789). As described in the next section, the positions and apertures of the beamline magnets were surveyed and are reproduced in the geometry along with windows and materials in the path of the muon beams. The Geant4 simulation within MAUS starts 1 m downstream of the second beamline dipole magnet D2. Geant4 bindings are encoded in the Simulation module. Geant4 groups particles by run, event and track. A Geant4 run maps to a MICE spill; a Geant4 event maps to a single inbound particle from the beamline; and a Geant4 track corresponds to a single particle in the experiment.

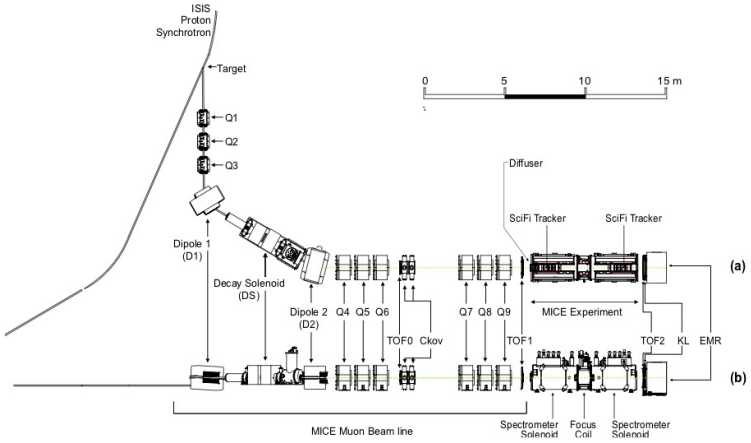

Figure 12. (a) Top and (b) side views of the MICE Muon Beamline, its instrumentation, and the experimental configuration. A titanium target dipped into the ISIS proton synchrotron and the resultant spill of particles was captured with a quadrupole triplet (Q1–3) and transported through momentum-selecting dipoles (D1, D2). The quadrupole triplets (Q4–6, Q7–9) transported particles to the upstream spectrometer module. The time-of-flight of particles, measured between TOF0 and TOF1, was used for particle identification.

Geant4 provides a variety of reference physics processes to model the interactions of particles with matter. The default process in MAUS is "*QGSP_BERT*" which causes Geant4 to model hadron interactions using a Bertini cascade model up to 10 GeV/*c* [30]. MAUS provides methods to set up the Geant4 physical processes through user-controlled data-cards. Finally, MAUS provides routines to extract particle data from the Geant4 tracks at user-defined locations.

3.3 Geometry

MAUS uses an online Configuration Database to store all of its geometries. These geometries have been extracted from CAD drawings which are updated based on the most recent surveys and technical drawings available. The CAD drawings are translated to a geometry-specific subset of XML, the Geometry Description Markup Language (GDML) [31] prior to being recorded in the configuration database through the use of the FastRAD [32] commercial software package.

The GDML formatted description contains the beamline elements and the positions of the detector survey points. Beam-line elements are described using tessellated solids to define the

2019 JINST 14 T04005

shapes of the physical volumes. The detectors themselves are described using an independently generated set of GDML files using Geant4 standard volumes. An additional XML file is appended to the geometry description that assigns magnetic fields and associates the detectors to their locations in the GDML files. This file is initially written by the geometry maintainers and formatted to contain run-specific information during download.

The GDML files can be read via a number of libraries in Geant4 and ROOT for the purpose of independent validation. The files are in turn translated into the MAUS-readable geometry files either by accessing directly the data using a python extension or through the use of EXtensible Stylesheet Language Transformations (XSLT) [33].

3.4 Tracking, field maps and beam optics

MAUS tracking is performed using Geant4. By default, MAUS uses 4$^{\text{th}}$ order Runge-Kutta (RK4) for tracking, although other routines are available. RK4 has been shown to have very good precision relative to the MICE detector resolutions, even for step sizes of several cm.

In a solenoid focussing lattice a cylindrically symmetric beam can be described by the 4D RMS beam emittance ε_N and optical parameters $\beta_\perp$ and $\beta'_\perp$, its derivative with respect to z. $\beta_\perp$ is related to the variance of the position of particles x by [34]:

$$\beta_\perp = \frac{p_z \mathrm{Var}(x)}{\varepsilon_N mc}; \tag{3.1}$$

where m is the particle mass, c is the speed of light, and p_z is the beam longitudinal momentum. In the approximation that particles travel near to the solenoid axis, transport of the beam envelope can be performed by integration of the differential equation:

$$2\beta_\perp\beta''_\perp - (\beta'_\perp)^2 + 4\beta_\perp^2\kappa^2 - 4(1+\mathcal{L})^2 = 0. \tag{3.2}$$

Transport of individual particles can be performed using numerical integration of the Lorentz force law. Alternately transport can be performed by calculating a transfer map $\mathbf{M}$ defined by:

$$\vec{u}_{ds} = \mathbf{M}\vec{u}_{us}; \tag{3.3}$$

where $\vec{u}_{us}$ and $\vec{u}_{ds}$ are the upstream and downstream transverse phase space vectors $\vec{u} = (x, p_x, y, p_y)$. MAUS can calculate the transfer map at arbitrary order by transporting a handful of particles and fitting to a multidimensional polynomial in $\vec{u}$.

Electromagnetic field maps are implemented in a series of overlapping regions. The world volume is divided into a number of voxels, and the field maps that impinge on each voxel is stored in a list. At each tracking step, MAUS iterates over the list of fields that impinge on the voxels within which the particle is stepping. For each field map, MAUS transforms to the local coordinate system of the field map, and calculates the field. The field values are transformed back into the global coordinate system, summed, and passed to Geant4. The voxelization enables the simulation of long accelerators without a performance penalty.

Numerous field types have been implemented within the MAUS framework. Solenoid fields can be calculated numerically from cylindrically symmetric 2D field maps, by taking derivatives of an on-axis solenoidal field or by using the sum of fields from a set of cylindrical current sheets.

2019 JINST 14 T04005

The use of field maps enables the realistic reproduction of the MICE apparatus, while a derivatives-based approach enables the exclusion of different terms in the higher order parts of the transfer map [35]. Multipole fields can be calculated from a 3D field map, or by taking derivatives from the usual multipole expansion formulae. Linear, quadratic and cubic interpolation routines have been implemented for field maps. Pillbox fields can be calculated by using the Bessel functions appropriate for a TM010 cavity or by reading a cylindrically symmetric field map.

The transport algorithms have been compared with each other and experimental data and show agreement at linear order [36] in $\vec{u}$. Work is ongoing to study the effect of aberrations in the optics, indicated by non-linear terms in the transfer map relationship. These aberrations can cause distortion of the beam leading to emittance growth, which has been observed in the tails of the MICE beam. The tracking in MAUS has been benchmarked against ICOOL, G4Beamline, and MaryLie [37], demonstrating good agreement. The routines have been used to model a number of beamlines and rings, including a neutrino factory front-end [38].

3.5 Detector response and digitization

The modeling of the detector response and electronics enables MAUS to provide data used to test reconstruction algorithms and estimate the uncertainties introduced by detectors and their readout.

The interaction of particles in materials is modeled using Geant4. For each detector, a "sensitive detector" class processes Geant4 hits in active detector volumes and stores hit information such as the volume that was hit, the energy deposited and the time of the hit. Each detector's digitization routine then simulates the response of the electronics to these hits, modeling processes such as the photo-electron yield from a scintillator bar, attenuation in light guides and the pulse shape in the electronics. The data structure of the outputs from the digitizers are designed to match the output from the unpacking of real data from the DAQ.

4 Reconstruction

The reconstruction chain takes as its input either digitized hits from the MC or DAQ digits from real data. Regardless, the detector reconstruction algorithms, by requirement and design, operate the same way on both MC and real data.

4.1 Time of flight

There are three time-of-flight detectors in MICE which serve to distinguish particle type. The detectors are made of plastic scintillator and in each station there are orthogonal x and y planes with 7 or 10 slabs in each plane.

Each Geant4 hit in the TOF is associated with a physical scintillator slab. The energy deposited by a hit is first converted to units of photo-electrons. The photo-electron yield from a hit accounts for the light attenuation corresponding to the distance of the hit from the photomultiplier tube (PMT) and is then smeared by the photo-electron resolution. The yields from all hits in a given slab are then summed and the resultant yield is converted to ADC counts.

The time of the hit in the slab is propagated to the PMTs at either end of the slab. The propagated time is then smeared by the PMT's time resolution and converted to TDC counts. Calibration

2019 JINST 14 T04005

corrections based on real data are then added to the TDC values so that, at the reconstruction stage, they can be corrected just as is done with real data.

The reconstruction proceeds in two main steps. First, the slab-hit-reconstruction takes individual PMT digits and associates them to reconstruct the hit in the slab. If there are multiple hits associated with a PMT, the hit which is earliest in time is taken to be the real hit. Then, if both PMTs on a slab have fired, the slab is considered to have a valid hit. The TDC values are converted to time and the hit time and charge associated with the slab hit are taken to be the average of the two PMT times and charges respectively. In addition, the product of the PMT charges is also calculated and stored. Secondly, individual slab hits are used to form space-points. A space-point in the TOF is a combination of x and y slab hits. All combinations of x and y slab hits in a given station are treated as space-point candidates. Calibration corrections, stored in the Configurations Database, are applied to these hit times and if the reconstructed space-point is consistent with the resolution of the detector, the combination is said to be a valid space-point. The TOF has been shown to provide good time resolutions at the 60 ps level [6].

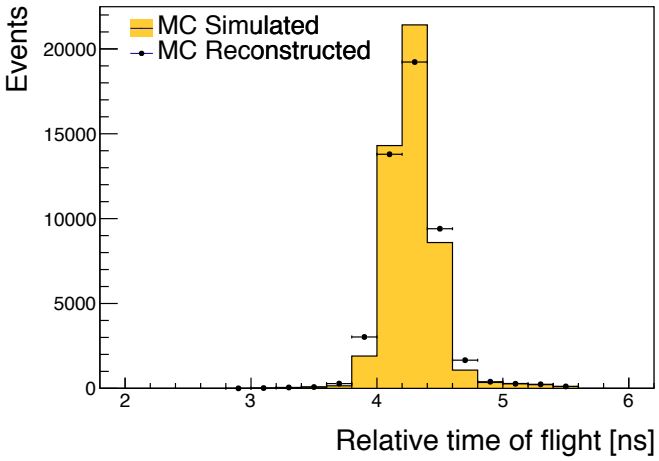

Figure 13. Relative time of flight between TOF0 and TOF1. The yellow histogram represents true MC events and the solid markers represent the same sample reconstructed with MAUS.

4.2 Scintillating-fiber trackers

The scintillating-fiber trackers are the central piece of the reconstruction. As mentioned in section 1.1, there are two trackers, one upsteam and the other downstream of an absorber, situated within solenoidal magnetic fields. The trackers measure the emittance before and after particles pass through the absorber.

The tracker software algorithms and performance are described in detail in [39]. Digits are the most basic unit fed into the main reconstruction module, each digit representing a signal from one channel. Digits from adjacent channels are assumed to come from the same particle and are grouped to form clusters. Clusters from channels which intersect each other, in at least two planes from the

2019 JINST 14 T04005

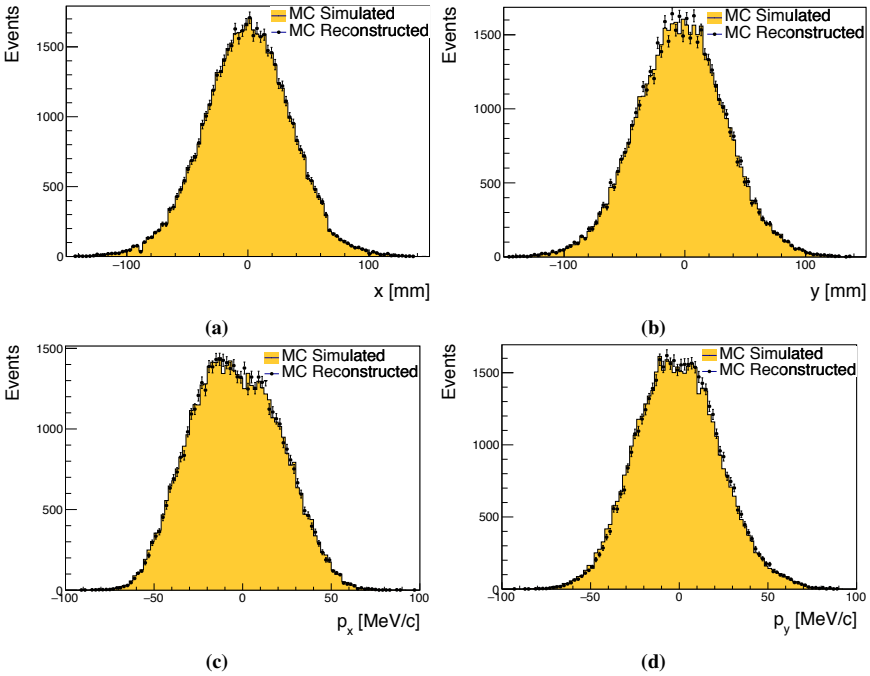

Figure 14. Position and momentum distributions of muons reconstructed at upstream tracker station nearest to the absorber: a) x, b) y, c) p_x, d) p_y. The yellow histograms represent true MC simulations, and the markers represent the MC sample reconstructed using MAUS.

same station, are used to form space-points, giving x and y positions where a particle intersected a station. Once space-points have been found, they are associated with individual tracks through pattern recognition (PR), giving straight or helical PR tracks. These tracks, and the space-points associated with them, are then sent to the final track fit. To avoid biases that may come from space-point reconstruction, the Kalman filter uses only reconstructed clusters as input.

4.3 KL calorimeter

Hit-level reconstruction of the KL is implemented in MAUS. Individual PMT hits are unpacked from the DAQ or simulated from MC and the reconstruction associates them to identify the slabs that were hit and calculates the charge and charge-product corresponding to each slab hit. The KL has been used successfully to estimate the pion contamination in the MICE muon beamline [9].

4.4 Electron-muon ranger

Hit-level reconstruction of the EMR is implemented in MAUS. The integrated ADC count and time over threshold are calculated for each bar that was hit. The EMR reconstructs a wide range of

2019 JINST 14 T04005

variables that can be used for particle identification and momentum reconstruction. The software and performance of the EMR are described in detail in [10].

4.5 Cherenkov

The CKOV reconstruction takes the raw flash-ADC data, subtracts pedestals, calculates the charge and applies calibrations to determine the photo-electron yield.

4.6 Global reconstruction

The aim of the Global Reconstruction is to take the reconstructed outputs from individual detectors and tie them together to form a global track. A likelihood for each particle hypothesis is also calculated.

4.6.1 Global track matching

Global track matching is performed by collating particle hits (TOFs 0, 1 and 2, KL, Ckovs) and tracks (Trackers and EMR) from each detector using their individual reconstruction and combining them using a RK4 method to propagate particles between these detectors.The tracking is performed outwards from the cooling channel — i.e., from the upstream tracker to the TOF0 detector, and from the downstream tracker to the EMR detector. Track points are matched to form tracks using an RK4 method. Initially this is done independently for the upstream and downstream sections (i.e., either side of the absorber). As the trackers provide the most accurate position reconstruction, they are used as starting points for track matching, propagating hits outwards into the other detectors and then comparing the propagated position to the measured hit in the detector. The acceptance criterion for a hit belonging to a track is an agreement within the detector's resolution with an additional allowance for multiple scattering. Track matching is currently performed for all TOFs, KL and EMR.

The RK4 propagation requires the mass and charge of the particle to be known. Hence, it is necessary to perform track matching using a hypothesis for each particle type (muons, pions, and electrons). Tracks for all possible PID hypotheses are then passed to the Global PID algorithms.

4.6.2 Global PID

Global particle identification in MICE typically requires the combination of several detectors. The time-of-flight between TOF detectors can be used to calculate velocity, which is compared with the momentum measured in the trackers to identify the particle type. For all events but those with very low transverse momentum (p_t), charge can be determined from the direction of helical motion in the trackers. Additional information can be obtained from the CKOV, KL and EMR detectors. The global particle identification framework is designed to tie this disparate information into a set of hypotheses of particle types, with an estimate of the likelihood of each hypothesis.

The Global PID in MAUS uses a log-likelihood method to identify the particle species of a global track. It is based upon a framework of PID variables. Simulated tracks are used to produce probability density functions (PDFs) of the PID variables. These are then compared with the PID variables for tracks in real data to obtain a set of likelihoods for the PIDs of the track.

The input to the Global PID is several potential tracks from global track matching. During the track matching stage, each of these tracks was matched for a specific particle hypothesis. The Global PID then takes each track and determines the most likely PID following a series of steps:

2019 JINST 14 T04005

1. Each track is copied into an intermediate track;
2. For each potential PID hypothesis p, the log-likelihood is calculated using the PID variables;
3. The track is assigned an object containing the log-likelihood for each hypothesis; and
4. From the log-likelihoods, the confidence level, C.L., for a track having a PID p is calculated and the PID is set to the hypothesis with the best C.L.

4.7 Online reconstruction

During data taking, it is essential to visualize a detector's performance and have diagnostic tools to identify and debug unexpected behavior. This is accomplished through summary histograms of high and low-level quantities from detectors. The implementation is through a custom multi-threaded application based on a producer-consumer pattern with thread-safe FIFO buffers. Raw data produced by the DAQ are streamed through a network and consumed by individual detector *mappers* described in section 3. The reconstructed outputs produced by the *mappers*, are in turn consumed by the *reducers*. The *mappers* and *reducers* are distributed among the threads to balance the load. Finally, outputs from the *reducers* are written as histogram images. Though the framework for the online reconstruction is based on parallelized processing of spills, the reconstruction modules are the same as those used for offline processing. A lightweight tool based on Django [40] provides live web-based visualization of the histogram images as and when they are created. Typical data rates during experimental operations were ~ 300 MB/s. The average event rate varied, depending on the configuration of the beamline, with the maximum instantaneous rate being ~ 150 kHz. MAUS performance matched the data rates and online reconstruction happened virtually "live" with the reconstructed outputs available instantly allowing collaborators to monitor the quality of the data being acquired.

5 Summary

The MICE collaboration has developed the MAUS software suite to simulate the muon beamline, simulate the MICE detectors, and reconstruct both simulated and real data. The software also provides global track-matching and particle-identification capabilities. Simplified programming interfaces and testing environments enable productive development. MAUS has been successfully used to reconstruct data online during data collection. In addition, MAUS is routinely used to perform reconstruction of the entire MICE data volume on batch production systems. MICE has collected ~ 15 TB of raw data and a full reconstruction of the data is performed with each released version of MAUS. The batch systems are also used to perform compute-intensive simulations with various configurations of the beamline and the cooling channel.

Acknowledgments

The work described here was made possible by grants from Department of Energy and National Science Foundation (U.S.A.), the Instituto Nazionale di Fisica Nucleare (Italy), the Science and Technology Facilities Council (U.K.), the European Community under the European Commission Framework Programme 7 (AIDA project, grant agreement no. 262025, TIARA project, grant

2019 JINST 14 T04005

agreement no. 261905, and EuCARD), the Japan Society for the Promotion of Science and the Swiss National Science Foundation, in the framework of the SCOPES programme. We gratefully acknowledge all sources of support. We are grateful to the support given to us by the staff of the STFC Rutherford Appleton and Daresbury Laboratories. We acknowledge the use of Grid computing resources deployed and operated by GridPP [41] in the U.K.

References

[1] MICE collaboration, *First Demonstration of Ionization Cooling in MICE*, in *Proceedings of the International Particle Accelerator Conference*, Vancouver, Canada, 29 April–May 4 2018, pp. 5035–5040.

[2] IDS-NF collaboration, *International design study for the neutrino factory: Interim design report*, 2011.

[3] S. Geer, *Muon Colliders and Neutrino Factories*, *Annu. Rev. Nucl. Part. Sci.* **59** (2009) 345.

[4] MICE collaboration, *The MICE Muon Beam on ISIS and the beam-line instrumentation of the Muon Ionization Cooling Experiment*, 2012 *JINST* **7** P05009 [arXiv:1203.4089].

[5] MICE collaboration, *Characterisation of the muon beams for the Muon Ionisation Cooling Experiment*, *Eur. Phys. J.* **C 73** (2013) 2582 [arXiv:1306.1509].

[6] MICE collaboration, *The design and commissioning of the MICE upstream time-of-flight system*, *Nucl. Instrum. Meth.* **A 615** (2010) 14 [arXiv:1001.4426].

[7] KLOE collaboration, *The KLOE electromagnetic calorimeter*, *Nucl. Instrum. Meth.* **A 494** (2002) 326.

[8] F. Ambrosino et al., *Calibration and performances of the KLOE calorimeter*, *Nucl. Instrum. Meth.* **A 598** (2009) 239.

[9] MICE collaboration, *Pion Contamination in the MICE Muon Beam*, 2016 *JINST* **11** P03001 [arXiv:1511.00556].

[10] MICE collaboration, *Electron-Muon Ranger: performance in the MICE Muon Beam*, 2015 *JINST* **10** P12012 [arXiv:1510.08306].

[11] R. Asfandiyarov et al., *The design and construction of the MICE Electron-Muon Ranger*, 2016 *JINST* **11** T10007 [arXiv:1607.04955].

[12] MICE collaboration, *First particle-by-particle measurement of emittance in the Muon Ionization Cooling Experiment*, *Eur. Phys. J.* **C 79** (2019) 257 [arXiv:1810.13224].

[13] L. Cremaldi, D.A. Sanders, P. Sonnek, D.J. Summers and J. Reidy, Jr, *A Cherenkov Radiation Detector with High Density Aerogels*, *IEEE Trans. Nucl. Sci.* **56** (2009) 1475 [arXiv:0905.3411].

[14] M. Ellis et al., *The Design, construction and performance of the MICE scintillating fibre trackers*, *Nucl. Instrum. Meth.* **A 659** (2011) 136 [arXiv:1005.3491].

[15] https://scons.org.

[16] https://bazaar.canonical.com.

[17] https://launchpad.net.

[18] R. Brun and F. Rademakers, *ROOT: An object oriented data analysis framework*, *Nucl. Instrum. Meth.* **A 389** (1997) 81.

[19] GEANT4 collaboration, *GEANT4: A Simulation toolkit*, *Nucl. Instrum. Meth.* **A 506** (2003) 250.

2019 JINST 14 T04005

[20] https://scientificlinux.org.

[21] https://centos.org.

[22] https://getfedora.org.

[23] https://ubuntu.com.

[24] J. Dean and S. Ghemawat, *MapReduce: Simplified data processing on large clusters*, in *Proceedings of OSDI04*, San Francisco, CA, U.S.A., 2004, pp. 137–150.

[25] https://json.org.

[26] https://github.com/open-source-parsers/jsoncpp.

[27] https://jenkins-ci.org.

[28] T.J. Roberts and D.M. Kaplan, *G4BeamLine programme for matter dominated beamlines*, in *Proceddings of the Particle Accelerator Conference*, Albuquerque, NM, U.S.A., 25–29 June 2007, pp. 3468–3470.

[29] R.C. Fernow, *Icool: A simulation code for ionization cooling of muon beams*, in *Proceedings of the Particle Accelerator Conference*, New York, NY, U.S.A., 27 March–2 April 1999, pp. 3020–3022.

[30] J. Apostolakis et al., *Geometry and physics of the geant4 toolkit for high and medium energy applications*, *Radiat. Phys. Chem.* **78** (2009) 859.

[31] R. Chytracek, J. McCormick, W. Pokorski and G. Santin, *Geometry description markup language for physics simulation and analysis applications.*, *IEEE Trans. Nucl. Sci.* **53** (2006) 2892.

[32] https://fastrad.net.

[33] https://www.w3.org/standards/xml/transformation.

[34] G. Penn and J.S. Wurtele, *Beam envelope equations for cooling of muons in solenoid fields*, *Phys. Rev. Lett.* **85** (2000) 764.

[35] R. Ryne and C. Rogers, *Nonlinear effects in the MICE step iv lattice*, MICE-NOTE-461, 2015.

[36] S.C. Middleton, *Characterisation of the MICE experiment*, Ph.D. Thesis, Imperial College London (2018).

[37] R.D. Ryne et al., *Recent progress on the MARYLIE/IMPACT beam dynamics code*, in *Proceedings of the 9th International Computational Accelerator Physics Conference*, Chamonix, France, 2–6 October 2006, pp. 157–159.

[38] C.T. Rogers, D. Stratakis, G. Prior, S. Gilardoni, D. Neuffer, P. Snopok et al., *Muon front end for the neutrino factory*, *Phys. Rev. ST Accel. Beams* **16** (2013) 040104.

[39] A. Dobbs, C. Hunt, K. Long, E. Santos, M.A. Uchida, P. Kyberd et al., *The reconstruction software for the MICE scintillating fibre trackers*, 2016 *JINST* **11** T12001 [arXiv:1610.05161].

[40] https://www.djangoproject.com.

[41] https://www.gridpp.ac.uk.

2019 JINST 14 T04005

Available online at www.sciencedirect.com

ScienceDirect

Advances in Space Research 63 (2019) 1483–1489

ADVANCES IN SPACE RESEARCH (a COSPAR publication)

www.elsevier.com/locate/asr

Rigidity dependence of Forbush decreases in the energy region exceeding the sensitivity of neutron monitors

M. Savić, N. Veselinović *, A. Dragić, D. Maletić, D. Joković, R. Banjanac, V. Udovičić

Institute of Physics, University of Belgrade, Pregrevica 118, 11080 Zemun, Serbia

Received 2 May 2018; received in revised form 14 September 2018; accepted 24 September 2018
Available online 28 September 2018

Abstract

Applicability of our present setup for solar modulation studies in a shallow underground laboratory is tested on four prominent examples of Forbush decrease during solar cycle 24. Forbush decreases are of interest in space weather application and study of energy-dependent solar modulation, and they have been studied extensively. The characteristics of these events, as recorded by various neutron monitors and our detectors, were compared, and rigidity spectrum was found. Linear regression was performed to find power indices that correspond to each event. As expected, a steeper spectrum during more intense extreme solar events with strong X-flares shows a greater modulation of galactic cosmic rays. Presented comparative analysis illustrates the applicability of our setup for studies of solar modulation in the energy region exceeding the sensitivity of neutron monitors.

Keywords: Forbush decrease; Muon CR station; Median rigidity

1. Introduction

Galactic cosmic rays (GCRs) traverse the heliosphere; this leads to variation in the cosmic ray (CR) flux due to solar activity. The influence of solar and heliospheric modulation is pronounced for primary CR particles with low rigidity or momentum over unit charge. CRs interact, upon arrival, with Earth's atmosphere causing electromagnetic and hadronic showers. A network of ground-based CR detectors, neutron monitors (NMs), and muon detectors, located at various locations around the globe, as well as airborne balloons and satellites, provide valuable data to study the effect of these modulations on the integrated CR flux with time. Energies of the primary particles in NMs are sensitive to the state of solar activity and reach up to 40 GeV. Muon detectors have a significant response from 10 GeV up to several hundred GeV for surface, and one order of magnitude greater for underground detectors, depending on the depth (Duldig, 2000). This energy interval allows muon detectors to monitor not only modulation effects on lower-energy CRs but also galactic effects on primary CRs with high energies where solar modulation is negligible. Because of the sensitivity to different energies of the primary particle flux, observations of muon detectors complement those of NMs in studies of long-term CR variations, CR anisotropy, and gradients or rigidity spectrum of Forbush decreases (FDs).

FDs (Forbush, 1954) represent decreases of the observed GCR intensity under the influence of coronal mass ejections (CMEs) and interplanetary counterparts of coronal mass ejections (ICMEs) and/or high-speed streams of solar wind (HSS) from the coronal holes (Belov, 2008). FDs belong to two types depending on the drivers: non-recurrent and recurrent decreases. This work addresses several non-recurrent FDs.

These sporadic FDs are caused by ICMEs. As the matter with its magnetic field moves through the solar system,

* Corresponding author.
E-mail address: veselinovic@ipb.ac.rs (N. Veselinović).

https://doi.org/10.1016/j.asr.2018.09.034
0273-1177/

it suppresses the CR intensity. FDs of this kind have an asymmetric profile, and the intensity of GCRs has a sudden onset and recovers gradually. Sometimes an early phase of FD prior to the dip (precursor of FD) shows an increase in CR intensity. These precursors of FDs are caused by GCR acceleration at the front of the advancing disturbance on the outer boundary of the ICME, as the primary CR particles are being reflected from the approaching shock (Papailiou et al., 2013). The FD profile depends on the area, velocity, and intensity of CME magnetic field produced in extreme events that originate at the Sun (Chauhan et al., 2008).

Data from observed modulation of GCR intensity contain information regarding the transport of GCRs through the interplanetary environment. GCR transport parameters are connected with the interplanetary magnetic field (IMF) in the heliosphere. It is empirically established that the radial diffusion coefficient is proportional to the rigidity of CR (Ahluwalia, 2005). In this article, we present an analysis of the amplitude of FD during four events, which were recorded by plastic scintillator muon detectors, located at the Belgrade muon station, as well as by a network of NMs.

2. Belgrade CR station

The Low-Background Laboratory for Nuclear Physics (LBLNP) is a part of the Institute of Physics, University of Belgrade. It is composed of two separate laboratory facilities, ground-level laboratory (GLL) and underground laboratory (UL), dug into a cliff. The overburden of the UL is approximately 12 m of loess soil, which is equivalent to 25 m of water (m.w.e). Laboratory is dedicated to measurements of low radiation activities and studies of muon and electromagnetic components of CRs at ground and shallow underground levels. The geographic position of the laboratory is at 75 m a.s.l., at 44°51′N latitude and 20°23′E longitude; geomagnetic vertical rigidity cutoff is 5.3 GV at the surface. The equipment was upgraded in 2008, and now, it consists of two identical sets of detectors and accompanying data processing electronics: one is situated in GLL and the other in UL. Detectors are a pair of plastic scintillator detectors, with dimensions of 100 cm × 100 cm × 5 cm and four PMTs that are directly coupled to the corners. Signals from two opposite PMTs on a single detector are summed, and the coincidence of the two diagonals is found. Fig. 1 presents the coincident sum spectra of two diagonals of large scintillator detectors.

Summing over diagonals suppresses the acquisition of electromagnetic component of the secondary CR shower and collects mainly the muon component of secondary CRs. A well-defined peak in the energy spectra corresponds to a muon energy loss of ~11 MeV. The average muon flux measured in the laboratory is 137(6) muons/m^{2}s for GLL and 45(2) muons/m^{2}s for UL. For more detailed description, see Dragić et al. (2011). Integral of this distribution, without low energy part, is used to form time series of this

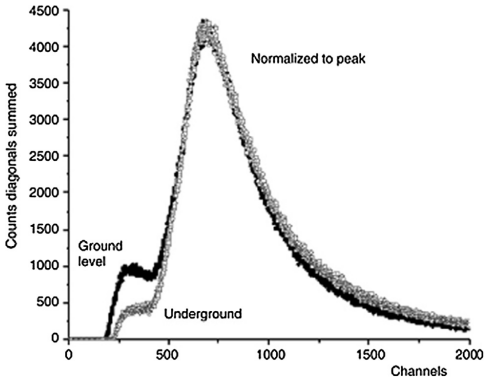

Fig. 1. The coincident spectra of two diagonals of large plastic detectors in UL and GLL normalized for comparison.

CR muons spectrum integrated over different time intervals. This time series is then corrected for efficiency, atmospheric pressure, and temperature (Savić et al., 2015).

The CR flux measured at the ground level varies because of changes in atmospheric conditions. Effects of the atmospheric pressure can be easily accounted for, similar like for NMs, but the temperature effect is somewhat more difficult to treat. The difficulties arise from the interplay of positive and negative temperature effects. With temperature increase, the atmospheric density decreases; hence, less pions interact and more muons are created from decay. The result is a positive effect of more muons at the ground level. On the other hand, the altitude of muon production level is high due to the expansion of the atmosphere when the temperature is high, muon path length is long, and decay probability of muons is high before they reach the ground level. Negative effect is dominant for low-energy muons (mostly detected in GLL) and positive for high-energy muons. A proper treatment of the temperature effect requires knowledge of the entire temperature profile of the atmosphere. This meteorological variation must be corrected to study CR variations originating outside the atmosphere.

For ground (and underground)-based CR detectors, the response function, i.e., the relation between particles of GCR spectra at the top of the atmosphere and recorded secondary particles at the surface level, should be accurately known. The total detector count rate can be expressed as follows (Caballero-Lopez and Moraal, 2012):

$$N(R_0,h,t) = \sum_i \int_{R_0}^{\infty} (S_i|(R,h) j_i(R,t))dR = \int_{R_0}^{\infty} W(R,h,t)dR \quad (1)$$

where $N(R_0,h,t)$ is the detector counting rate, R_0 is the geomagnetic cutoff rigidity, h is the atmospheric depth, and t represents time. $S_i(R,h)$ represents the detector yield

function for primary particles of type i and $j_i(R,t)$ represents the primary particle rigidity spectrum of type i at time t. The total response function $W(R,h,t)$ is the sum of $S_i(R,h)$ and $j_i(R,t)$. The maximum value of this function is in the range of 4–7 GV at sea level, depending on the solar modulation epoch at time t (Clem and Dorman, 2000). One of the methods to find this response function is to use the numerical simulation of propagation of CRs through the atmosphere. CORSIKA simulation package (Heck et al., 1998) was to simulate CR transport through the atmosphere and GEANT4 (Agostinelli et al., 2003) to simulate the propagation of secondary CRs through overburden and response of the detectors to find the relationship between the count rate at our site and the flux of primary particles on top of the atmosphere.

The excellent agreement of the simulated and measured flux (Fig. 2) allows us to establish that the cutoff energy for primary CR protons for showers detected in GLL is caused by its geomagnetic rigidity, and the median energy is ~60 GeV. For UL, the cutoff energy due to earth overburden is 12 GeV, and the median energy is ~120 GeV. These values give us opportunity to study solar modulation at energies exceeding energies detected with a NM. Observation of the solar activity and related magnetic disturbances in the heliosphere that create transient CR intensity variation at several different energies can provide an energy-dependent description of these phenomena.

3. Data analysis

The new setup in the LBLNP, presented by Dragić et al. (2011) coincides with the start of the 24th solar cycle, thus allowing us to observe the increase and decrease in solar activity and the effect of solar modulation at energies higher than ones studied using NMs.

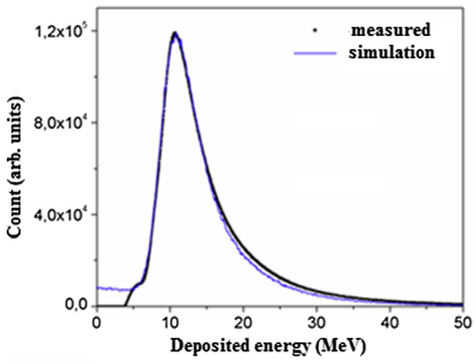

Fig. 2. Simulated (blue line) and measured spectra (black line) for muon detectors in UL. (For interpretation of the references to colour in this figure legend, the reader is referred to the web version of this article.)

Muon time series was searched for days where the average muon flux was significantly lower than the background level. The background level is determined from the moving averages of hourly count rates 10 days before the event. These decreases in the count rate, in GLL and UL, are then compared with space weather events of solar cycle 24. Data collected in UG and GLL are compared with four NM stations from the neutron monitor database [http://www.nmdb.eu/]. Three of these NMs (Athens, Rome, and Jungfraujoch) have cutoff rigidity and geographic proximity similar to the Belgrade CR station.

A high correlation is found between the count rates measured by the NMs in the LBLNP in March 2012 (Table 1), but for GLL and UL, as the cutoff energy of the primary flux increases, the correlation slightly decreases.

3.1. Selected Forbush decreases

The Belgrade CR station has detected, both in GLL and UL, several significant structures connected to some extreme solar effects. Several, more prominent, Forbush decreases occurred in March 2012, September 2014, June 2015, and most recently in September 2017.

The FD that occurred on March 8, 2012 was recorded at the Belgrade CR station as well as at other stations (Fig. 3). This FD was separated into two following two CMEs. These CMEs produced an intense disturbance in the interplanetary space and caused a severe geomagnetic storm when the shockwave reached Earth on March 8, 2012. During this event, a very complex combination of modulation occurs (Lingri et al., 2016). Two CMEs from the same active region as the September 10 (X1.6) flare produced FD on September 12, 2014. There was a relatively fast partial halo CME and a larger and rapidly moving halo CME trailing behind the first one on September 10. These two gave rise to the FD that was first detected by NMs on September 12, 2014. This FD was not a classical two-step FD as expected, probably due to the interaction of slower and faster CMEs. The FD profile (Fig. 3) showed a small second step several hours after the first, similar to the FD that occurred in February 2011 (Papaioannou et al., 2013). In June 2015, a large activity occurred in the Sun from powerful AR 2371 that produced several CMEs from the Sun. These CMEs induced a complex modulation of GCRs that led to an FD occurrence on June 22, 2015 with an unusual structure (Samara et al., 2018).

A sudden burst of activity from the Sun early in September 2017, after a prolonged period of low solar activity, produced several flares, including the largest solar flare seen from Earth since 2006, an X9.3 flare. This activity produced several Earth-directed CMEs. Throughout this time, Earth experienced a series of geomagnetic storms, which started promptly after the first CME. This unusual activity produced an FD, which was recorded with detectors in terms of ground level enhancement (GLE) on Earth and Mars (Guo et al., 2018).

Table 1
Correlation matrix of the linear correlation coefficient (in%) for recorded hourly flux at the Belgrade CR station with its temperature- and pressure-corrected underground and ground-level detectors (UL_tpc and GLL_tpc), only pressure-corrected detectors (UL_pc, GLL_pc), and raw data detectors (UL_raw and GLL_raw) and recordings at Rome, Oulu, Jungfraujoch (Jung.) and Athens NMs for March 2012.

UL_tpc	75	81	80	81	76	73	78	86	97	100
UL_pc	77	83	83	83	73	78	72	84	100	97
UL_raw	57	71	70	74	94	49	51	100	84	86
GLL_tpc	86	86	84	83	59	90	100	51	72	78
GLL_pc	90	92	90	89	56	100	90	49	78	73
GLL_raw	63	79	78	81	100	56	59	94	73	76
Oulu	90	98	98	100	81	89	83	74	83	81
Jung.	91	98	100	98	78	92	84	70	83	80
Rome	91	100	98	98	79	92	86	71	83	81
Athens	100	91	91	90	63	90	86	57	77	75
	Athens	Rome	Jung.	Oulu	GLL_raw	GLL_pc	GLL_tpc	UL_raw	UL_pc	UL_tpc

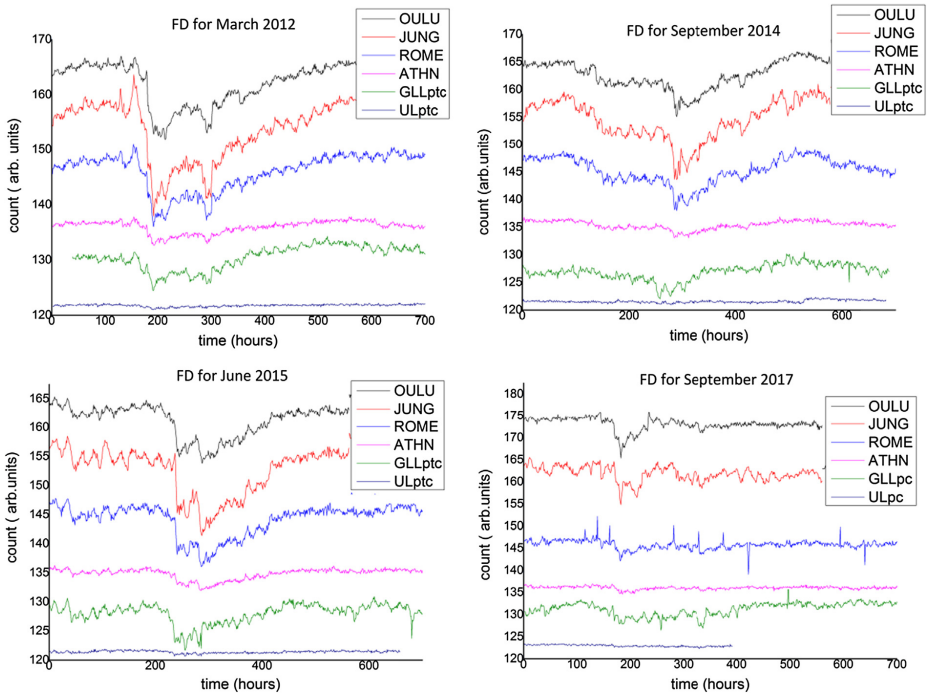

Fig. 3. Comparison of hourly time series over a one month period for pressure- and temperature-corrected count rates of the Belgrade muon monitor station (GLL_{ptc} and UL_{ptc}) and NMs at Athens (ATHN), Rome (ROME), Jungfraujoch (JUNG), and Oulu (OULU) for extreme solar events in March 2012, September 2014, and June 2015. Count rates are shifted for comparison. For extreme solar event in September 2017, for GLL and UL, the count rate is pressure-corrected only.

4. FD and median rigidity

For each event, we study the energy dependence of FD amplitude. The energy dependence of FD amplitude is expected to follow the power law: $\Delta N/N \sim R^{-\gamma}$ (Cane, 2000). To obtain reliable values of amplitudes, we defined amplitude as a relative decrease in the hourly count rate of the minimum compared with the average of seven days'

Table 2
Median and cutoff rigidity for several stations.

Stations	Median rigidity R_m (GV)	Min. rigidity R_0 (GV)
Athens	25.1	8.53
Mexico	25.1	8.28
Almaty	15.8	6.69
Lomnicky stit	12.6	3.84
Moscow	15.8	2.43
Kiel	15.8	2.36
Yakutsk	12.6	1.65
Apatity	12.6	0.65
Inuvik	12.6	0.3
Mc Murdo	12.6	0.3
Thule	12.6	0,3
South Pole	10	0.1
UL	122	12.3
GLL	63	5.3

count rate before FDs (not including possible precursory increases). Such a long base period was used because of the higher activity of the Sun prior to registrated FDs and sensitivity of the muon detectors.

Amplitudes are determined for two of our detectors and for 12 NMs. To investigate the rigidity spectrum of

Table 3
Power indices of the median rigidity dependence of the dip of the FD. Power indices are obtained for NMs only, NMs and the Belgrade muon station, and Belgrade station only.

γ	NM only	NM + Belgrade	Belgrade station only
March 2012	0.82 ± 0.08	0.78 ± 0.03	0.715
Sept. 2014	0.79 ± 0.16	0.67 ± 0.06	0.744
June 2015	0.57 ± 0.05	0.58 ± 0.02	0.764
Sept. 2017	1.27 ± 0.16	0.86 ± 0.07	0.739

mentioned FDs, the median rigidity R_m is defined. R_m is the rigidity of the response of the detector to GCR spectrum where 50% of the detector counting rate lies below R_m (Ahluwalia and Fikani, 2007). For this study, we used a list of R_m for 12 NM stations given by Minamino et al. (2014). For an NM, the median rigidity can be computed from the detector response function derived from surveys for particulate station, usually around the minima of solar activity; this is because the intensity of lowest rigidity GCRs is maximum at that time.

For the Belgrade muon station, R_m was found using the response function acquired by the Monte Carlo method of

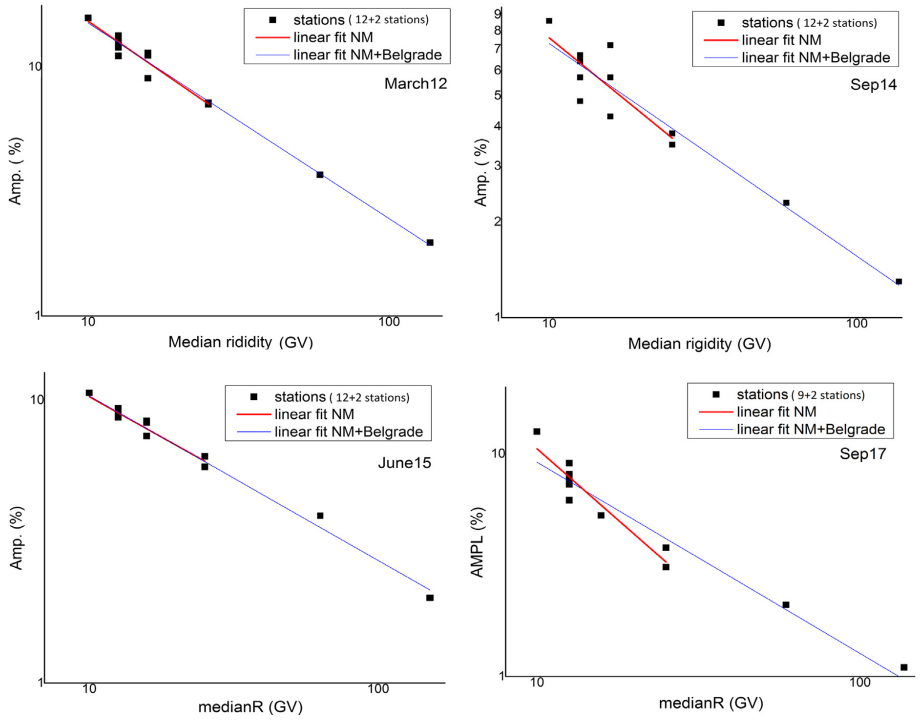

Fig. 4. Rigidity spectrum of FD from March 8, 2012, September 12, 2014, June 22, 2015, and September 8, 2017. Points represent the amplitude of the event as seen by NMs and the Belgrade CR station.

CR transport. Approximate values of R_m for the detectors used in this study are provided in Table 2.

For every selected event, a scatter plot is drawn (Fig. 4). All plots show, plotted in log-log scale, a clear median rigidity dependence of the amplitude of FD decrease.

Linear regression was performed to find power indices corresponding to each event. Power indices are given in Table 3.

Higher power indices can be due to more complex variations in GCRs. This more complex variation is a result of a series of CMEs during this event that leads to large compound ICME structure with multiple shocks and transient flow (Zhao and Zhang, 2016). Results obtained from the power law are generally consistent with those obtained in previous studies (Ahluwalia and Fikani, 2007, Lingri et al., 2016, Klyueva et al., 2017) conducted for NMs only.

A more significant difference observed for indices during the 2017 event was because we used only pressure-corrected data for the muon flux recorded at the Belgrade station. For all other events and data, we performed both pressure and temperature correction. Without temperature corrections, variation in the count rate in muon detectors is higher and it can affect the results.

We expect that when the newly improved, internally developed technique for temperature correction of the CR flux is implemented, the amplitude of the FD measured at the Belgrade muon station will be more consistent with other events and measurements. More data points on the graphs are needed to understand indices better, particularly in an energy region between NM and our laboratory. Similar work (Braun et al., 2009) discussed the extension up to 15 and 33 GeV, but there are no data available for FDs during cycle 24 and cannot be incorporated into this work. As for other operating muon telescopes, there is an agreement between the data obtained at our stations data and the URAGAN data for FD in June 2015 (Barbashina et al., 2016), but we have no data on other FDs and/or median energies of other stations. Our new experimental setup described elsewhere (Veselinović et al. 2017) will provide two additional median energies (121 and 157 GeV) to monitor variations in the CR flux.

5. Conclusion

The Belgrade CR station, with both ground level and underground setups, monitors the effect of solar modulation on the CR flux since 2008. Extreme solar events, like Forbush decreases, were detected during solar cycle 24 at the site, suggesting that these phenomena can be studied at energies higher than typical ones detected with NMs. GLL and UL data, as well as data from several NM stations, were used to analyze four intense FDs. The magnitude of FDs is energy (rigidity) dependent and follows the power law. Data used to find the rigidity dependence of these transient solar modulation of GCR were obtained over much higher range of rigidities than region NMs are sensitive in, thus allowing more extensive studies of CR solar modulation processes.

Acknowledgements

We acknowledge the NMDB (www.nmdb.eu), founded under the European Union's FP7 programme (contract no. 213007), for providing data. We acknowledge individual monitors for following the information given on the respective station information page. *Athens NM data were kindly provided by the Physics Department of the National and Kapodistrian University of Athens. Jungfraujoch NM data were kindly provided by the Physikalisches Institut, University of Bern, Switzerland.* Oulu NM *data were kindly provided by* http://cosmicrays.oulu.fi and Sodankyla Geophysical Observatory. Rome NM data were kindly provided by SVIRCO NM, supported by INAF/IAPS-UNIRoma3 COLLABORATION. We thank the anonymous referees for useful advices.

The present work was funded by the Ministry of Education, Science and Technological Development of the Republic of Serbia, under Project No. 171002.

References

Agostinelli, S., et al., GEANT4—A Simulation Toolkit, 2003. Nuclear Instruments and Methods in Physics Research Section A 506, pp. 250–303. https://doi.org/10.1016/S0168-9002(03)01368-8.

Ahluwalia, H.S., 2005. Cycle 20 solar wind modulation of galactic cosmic rays: understanding the challenge. J. Geophys. Res. 110, A10106. https://doi.org/10.1029/2005JA011106.

Ahluwalia, H.S., Fikani, M.M., 2007. Cosmic ray detector response to transient solar modulation: Forbush decreases. J. Geophys. Res. 112 (A8), A08105. https://doi.org/10.1029/2006JA011958.

Barbashina, N.S., Ampilogov, N.V., Astapov, I.I., Borog, V.V., Dmitrieva, A.N., Petrukhin, A.A., Sitko, O.A., Shutenko, V.V., Yakovleva, E.I., 2016. Characteristics of the Forbush decrease of 22 June 2015 measured by means of the muon hodoscope URAGAN. J. Phys.: Conf. Ser. 675 (3). https://doi.org/10.1088/1742-6596/675/3/032038, article id. 032038.

Belov, A.V., 2008. Forbush effects and their connection with solar, interplanetary and geomagnetic phenomena. In: Proceedings of the International Astronomical Union 4.S257, pp. 439–450. https://doi.org/10.1017/S1743921309029676.

Braun, I., Engler, J., Hörandela, J.R., Milke, J., 2009. Forbush decreases and solar events seen in the 10–20 GeV energy range by the Karlsruhe Muon Telescope. Adv. Space Res. 43 (4), 480–488. https://doi.org/10.1016/j.asr.2008.07.012.

Caballero-Lopez, R.A., Moraal, H., 2012. Cosmic-ray yield and response functions in the atmosphere. J. Geophys. Res. Space Phys. 117 (A12), 7461–7469. https://doi.org/10.1029/2012JA017794.

Cane, H.V., 2000. Coronal mass ejections and Forbush decreases. Space Sci. Rev. 93 (1–2), 55–77. https://doi.org/10.1023/1026532125747.

Chauhan, M.L., Jain Manjula, S.K., Shrivastava, S.K., 2008. Study of two major Forbush decrease events of 2005. In: Proceedings of the 30th International Cosmic Ray Conference, Mexico City, vol. 1 (SH), pp. 307–310. https://doi.org/10.7529/ICRC2011/V10/0097.

Clem, J.M., Dorman, L.I., 2000. Neutron monitor response functions, cosmic rays and earth. Space Sci. Rev. 93 (1/2), 335–359. https://doi.org/10.1023/A:1026515722112.

Dragić, A., Udovičić, V., Banjanac, R., Joković, D., Maletić, D., Veselinović, N., Savić, M., Puzović, J., Aničin, I.V., 2011. The new setup in the Belgrade low-level and cosmic-ray laboratory. Nucl.

Technol. Radiat. Protect. 26 (3), 181–192. https://doi.org/10.2298/NTRP1101064N.

Duldig, M.L., 2000. Muon observations. In: Bieber, J.W., Eroshenko, E., Evenson, P., Flückiger, E.O., Kallenbach, R. (Eds.), Cosmic Rays and Earth. Space Sciences Series of ISSI. Springer, Dordrecht, pp. 207–226. https://doi.org/10.1007/978-94-017-1187-6_1.

Forbush, S.E., 1954. World-wide cosmic ray variations, 1937–1952. J. Geophys. Res. 59 (4), 525–542. https://doi.org/10.1029/JZ059i004p00525.

Guo, J., Dumbović, M., Wimmer-Schweingruber, R.F., Temmer, M., Lohf, H., Wang, Y., Veronig, A., Hassler, D.M., Leila, M., Mays, L. M., Zeitlin, C., Ehresmann, B., Witasse, O., Freiherr von Forstner, J. L., Heber, B., Holmström, M., Posner, A., 2018. Modeling the evolution and propagation of the 2017 September 9th and 10th CMEs and SEPs arriving at Mars constrained by remote-sensing and in-situ measurement. Also Available at: arXiv preprint arXiv:1803.00461.

Heck, D., Knapp, J., Capdevielle, J.N., Schatz, G., Thouw, T., 1998. CORSIKA: a Monte Carlo code to simulate extensive air showers. Forschungszentrum Karlsruhe GmbH, p. V +90, TIB Hannover, D-30167 Hannover.

Klyueva, A.I., Belov, A.V., Eroshenko, E.A., 2017. Specific features of the rigidity spectrum of Forbush effects. Geomag. Aeron. 57 (2), 177–189. https://doi.org/10.1134/S0016793217020050.

Lingri, D., Mavromichalaki, H., Belov, A., Eroshenko, E., Yanke, V., Abunin, A., Abunina, M., 2016. Solar activity parameters and associated Forbush decreases during the minimum between cycles 23 and 24 and the ascending phase of cycle 24. Sol. Phys. 291 (3), 1025–1041. https://doi.org/10.1007/s11207-016-0863-8.

Minamino, Mohanty, Morishita, et al. for the GRAPES-3 Collaboration, 2014. Rigidity Dependence of Forbush Decreases, Poster #654. In: Proceedings of the 33rd International Cosmic Ray Conference, Rio de Janeiro, Brazil, pp. 3612–3615.

Papailiou, M., Mavromichalaki, H., Abunina, M., Belov, A., Eroshenko, E., Yanke, V., Kryakunova, O., 2013. Forbush decreases associated with western solar sources and geomagnetic storms: a study on precursors. Sol. Phys. 283 (2), 557–563. https://doi.org/10.1007/s11207-013-0231-x.

Papaioannou, A., Belov, A.A., Mavromichalaki, H., Eroshenko, E., Yanke, V., Asvestari, E., Abunin, A., Abunina, M., 2013. The first Forbush decrease of solar cycle 24. J. Phys. Conf. Ser. 409 (1). https://doi.org/10.1088/1742-6596/409/1/012202.

Samara, E., Smponias, I.A., Lytrosyngounis, I., Lingri, D., Mavromichalaki, H., Sgouropoulos, C., 2018. Unusual cosmic ray variations during the Forbush decreases of June 2015. Sol. Phys. 293 (67). https://doi.org/10.1007/S11207-018-1290-9.

Savić, M., Maletić, D., Joković, D., Veselinović, N., Banjanac, R., Udovičić, V., Dragić, V., 2015. Pressure and temperature effect corrections of atmospheric muon data in the Belgrade cosmic-ray station. J. Phys. Conf. Ser. 632 (1). https://doi.org/10.1088/1742-6596/632/1/012059, article id. 012059.

Veselinović, N., Dragić, A., Savić, M., Maletić, D., Joković, D., Banjanac, R., Udovičić, V., 2017. An underground laboratory as a facility for studies of cosmic-ray solar modulation. Nucl. Instrum. Meth. A875, 10–15. https://doi.org/10.1016/j.nima.2017.09.008.

Zhao, L.-L., Zhang, H., 2016. Transient galactic cosmic-ray modulation during solar cycle 24: a comparative study of two prominent forbush decrease events. Astrophys. J. 827 (1). https://doi.org/10.3847/0004-637X.

THE NEW SET-UP IN THE BELGRADE LOW-LEVEL AND COSMIC-RAY LABORATORY

by

***Aleksandar DRAGIĆ*[1*], *Vladimir I. UDOVIČIĆ*[1], *Radomir BANJANAC*[1], *Dejan JOKOVIĆ*[1], *Dimitrije MALETIĆ*[1], *Nikola VESELINOVIĆ*[1], *Mihailo SAVIĆ*[2], *Jovan PUZOVIĆ*[2], *and Ivan V. ANIČIN*[1]**

[1]Institute of Physics, Belgrade, Serbia
[2]Faculty of Physics, University of Belgrade, Belgrade, Serbia

Scientific paper
UDC: 543.428/.429:551.521.6:539.166
DOI: 10.2298/NTRP1103181D

The Belgrade underground laboratory consists of two interconnected spaces, a ground level laboratory and a shallow underground one, at 25 meters of water equivalent. The laboratory hosts a low-background gamma spectroscopy system and cosmic-ray muon detectors. With the recently adopted digital data acquisition system it is possible to simultaneously study independent operations of the two detector systems, as well as processes induced by cosmic-ray muons in germanium spectrometers. Characteristics and potentials of the present experimental setup, together with some preliminary results for the flux of fast neutrons and stopped muons, are reported here.

Key words: underground laboratory, gamma-ray spectroscopy, low-level measurements, cosmic rays

INTRODUCTION

The low-level and cosmic-ray laboratory in Belgrade is dedicated to the measurement of low activities and cosmic-ray (CR) muon components. At the intersection of the two research subjects, the study of muon-induced background in gamma spectroscopy is of particular interest. The laboratory adds to the list of relatively shallow underground laboratories worldwide (see the recent review [1]). It is located on the right bank of the river Danube in the Belgrade borough of Zemun, on the grounds of the Institute of Physics. The ground level portion of the laboratory (GLL), at 75 meters above sea level (m.a.s.l), is situated at the foot of a vertical loess cliff, about 10 meters high. The underground part of the laboratory (UL), useful area 45 m^2, is dug into the foot of the cliff and is accessible from the GLL via a 10 meters long horizontal corridor which also serves as a pressure buffer for a slight overpressure that is constantly maintained in the UL (fig. 1). The overburden of the UL is about 12 meters of loess soil, equivalent to 25 meters of water. The container, which is to accommodate the top laboratory (TL), is situated at the top of the cliff, just above the UL. The GLL and UL have been in some use for a number of years now, while the TL is still not functional.

Continuous measurements of the cosmic-ray muon flux by means of a pair of small plastic scintillators 50 cm 23 cm 5 cm started in the GLL and UL back in 2002 and lasted for about 5 years. These measurements yielded the precise values of the integral CR muon flux at ground level and at the depth of 25 m.w.e. [2]. Different analyses of the time series of these measurements have also been performed [3, 4].

Significant efforts are being made to contain the low radon concentration within the laboratory. The UL is completely lined with a hermetically sealed, 1 mm thick aluminum foil. The ventilation system maintains the overpressure of 2 mbar, so as to prevent radon diffusion from the soil. Fresh air entering the laboratory is passed through a two-stage filtering system. The first stage is a mechanical filter for dust removal. The second one is a battery of coarse and fine charcoal active filters. The concentration of radon is kept at an average value of about 10 Bq/m^3. Throughout the years, certain interesting behaviors of the said concentration have also been reported [5, 6].

The two laboratory spaces have recently been furnished with a new experimental set-up which is now ready for routine measurements. Here presented are some preliminary results of wider interest, ob-

* Corresponding author; e-mail: dragic@ipb.ac.rs

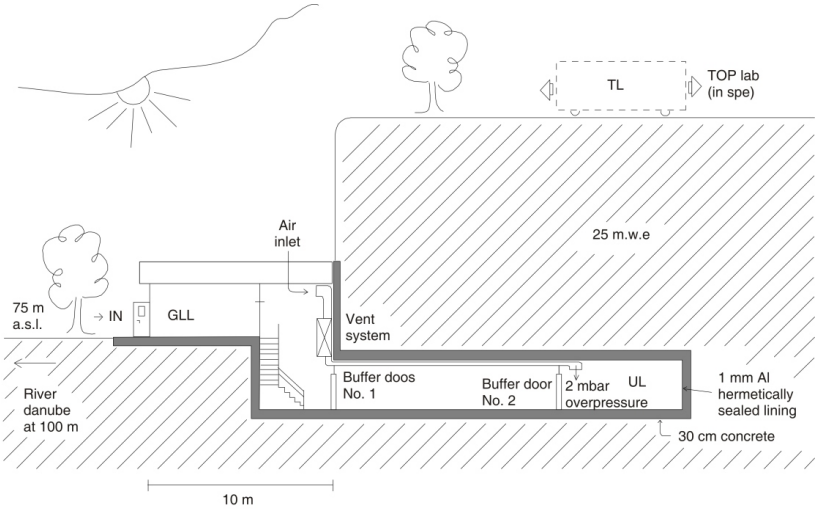

Figure 1. Cross-section of the low-level and CR laboratory at IOP, Belgrade, 44°49'N, 20°28'E, vertical rigidity cutoff 5.3 GV

tained during the testing period of the new equipment and the development of the needed software.

EXPERIMENTAL SET-UP

The equipment now consists of two almost identical sets of detectors and analyzing electronics, one set situated in the GLL, the other in the UL. Each set is composed of muon detectors and a gamma spectrometer.

A pair of plastic scintillator detectors is used for CR muon measurements. One of them is a larger 100 cm 100 cm 5 cm detector, equipped with four PMT directly coupled to the corners beveled at 45°, made by Amcrys-H, Kharkov, Ukraine. The other, a small 50 cm 23 cm 5 cm plastic scintillator detector, with a single PMT looking at its longest side via a Perspex light guide tapering to the diameter of a PMT, made by JINR, Dubna, Russia, and assembled locally. The smaller detector may serve as a check of stability of the muon time series obtained from the larger detector, which is important for long term measurements. It can also be used (in coincidence with the larger detector) for measurements of the lateral spread of particles in CR showers. Plastic scintillation detectors are also employed for active shielding of gamma spectrometers.

In the UL, a 35% efficiency radio-pure p-type HPGe detector, made by ORTEC, in its 12 cm thick cylindrical lead castle, is deployed. Another HPGe detector, of 10% efficiency, is put to use in the GLL. It is shielded with lead of the same origin, parts of a plumbing system collected at a demolition site of an old housing estate. The exact history of this lead is not known, but all the components are known to be older than two half-lives of Pb-210.

At the heart of the data acquisition system are two flash: analog to digital converter (ADC), flash analog to digital converter (FADC), one in each laboratory, made by CAEN (type N1728B). These are versatile instruments, capable of working in the so-called energy histogram mode when performing as digital spectrometers or, in the oscillogram mode, when they perform as digital storage oscilloscopes. In both modes, they sample at 10 ns intervals into 2^{14} channels in four independent inputs. The full voltage range is 1.1 V.

They are capable of operating in the list mode, when every analyzed event is fully recorded by the time of its occurrence and its amplitude. This enables the correlation of events, both prompt and arbitrarily delayed, at all four inputs with the time resolution of 10 ns. Single and coincident data can be organized into time series within any integration period from 10 ns up. The two N1728B units are synchronized, enabling coincidence/correlation of the events recorded in both of them. The flexible software encompassing all above said off-line analyses is user-friendly and entirely homemade.

The usual disposition of FADC inputs is described next. The preamplifier outputs of the PMT of

the larger detectors are paired diagonally, the entire detector thus engaging these two inputs of the FADC. Signals from these inputs are later coincided off-line and their amplitudes added to produce the single spectra of these detectors. This procedure results in a practically complete suppression of the uninteresting low-energy portion of the background spectrum (up to some 3 MeV), mostly due to environmental radiation, leaving only high-energy loss events due to CR muons and EM showers that peak at about 10 MeV. The output of the PMT of the smaller detector is fed to the third input. The fourth input is reserved for the HPGe detectors.

In some instances, auxiliary measurements are performed with a different definition of the inputs of the data acquisition system. For example, a (3 3)" NaI detector is used in the GLL to scan the response of the larger detector to CR as a function of the position of the interaction point.

In the UL, the HPGe detector is positioned beneath the center of the larger detector (fig. 2). For the purpose of measuring low activities, the large plastic detector is used in anticoincidence, as a cosmic-ray muon veto detector. In order to study the effects of cosmic rays on the spectra in low-level high-resolution gamma-ray spectroscopy, it is used in coincidence as the trigger for the CR-induced processes. These two functions of the system are performed simultaneously and do not interfere, as they are realized by different off-line analyses of the same set of data.

Figure 2. Detectors in the underground laboratory (UL). The big plastic scintillator is positioned over the HPGe detector, seen in its lead shielding. The small plastic scintillator is in the front upper right corner. A hermetically sealed, 1 mm Al lining covering the entire UL, which enables the doubly filtrated ventilation system to sustain an overpressure of 2 mbar and keeps the radon concentration at an average level of some 10 Bq/m^3, is also shown

TESTING THE SYSTEM AND DEVELOPING THE SOFTWARE

In order to test the performance of the digital spectroscopy system, a series of test measurements with different count rates and different types of radiation detectors at the input of the FADC are performed.

One of the tests is designed to correspond to the real situations where neutrons created by CR muons in the lead shield produce certain effects in HPGe detectors. Neutrons produced by muons in the vicinity of the detector or the surrounding rock mass represent a significant source of background in ultra-low background experiments carried out deep underground, such as those searching for dark matter or double beta decay. In the test, done at the GLL, Cf-252 was used as a neutron source and the small plastic scintillator as a trigger for neutrons. To distinguish between the effects of fast and slow neutrons, some materials common in neutron work, such as rubberized B_4C, Cd sheets, paraffin, lead and iron slabs, were placed around and in between the source and the detectors. In addition to the environmental background, the HPGe spectra consists of different features induced by slow and fast neutrons in the HPGe detector and surrounding materials.

Results of measurements are stored as a list of events represented with their amplitudes, time tags, designation of input channels and some additional information (pile-up event or not, *etc*.). The time tag for every event is determined by the moment of crossing the set-triggering level. In order to minimize the amplitude walk, there is a possibility to choose between different types of triggers, termed here as simple, digital or CFD. We have stuck to the digital trigger which was found to work reliably and, if necessary, to the off-line correction of the amplitude walk [7].

The distribution of time intervals between events in the trigger detector and the HPGe is deduced from the recorded data in off-line analysis. There is no need to implement the hardware tome-to-amplitude converter (TAC). For convenience, in what follows we will refer to this distribution as the TAC spectrum.

As an illustration, the TAC spectrum between events in the plastic scintillator and HPGe is presented here (fig. 3).The prompt-time distribution is seen to be about 90 ns wide, while the tail of delayed coincidences is discernable beyond approx. 100 ns upon the prompt peak. The same time spectrum, off-line corrected for the amplitude walk, according to the procedure described in [7], is presented in fig. 3(b). The full

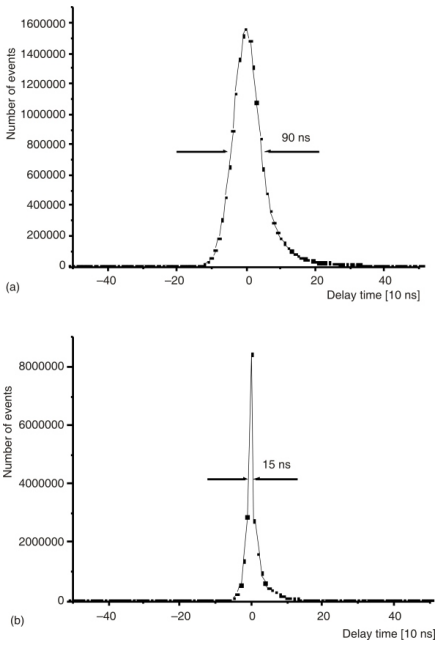

Figure 3. (a) The time spectrum between events in the plastic scintillator and the HPGe; (b) the same time spectrum, but with off-line time corrected for the amplitude walk

with at half maximum (FWHM) is now only 15 ns and delayed coincidences, perhaps, start as early as at approximately 20 ns after the prompt peak. Minding the geometry of our set-up, we expect the effects induced by fast neutrons, both in the environment and the HPGe detector itself, to be within the prompt peak, while those induced by thermalized neutrons should be found in the tail of delayed coincidences.

To illustrate the complete separation of the effects due to fast and slow neutrons, here presented (fig. 4) are the portions of the coincident HPGe spectrum around the spectral lines originating from different processes induced by neutrons in different materials, gated with different portions of the time spectrum – with the prompt peak, tail of delayed events up to one microsecond and the flat portion of random coincidences. Short comments can be found in the caption under fig. 4.

We will now briefly comment on the two well-known structures induced by neutrons in the HPGe detector itself, the structures at 596 keV and 692 keV. Their appearance in the coincidence spectra is depicted in fig. 5. The triangular distributions result from the summing of the radiations depopulating the state ex-

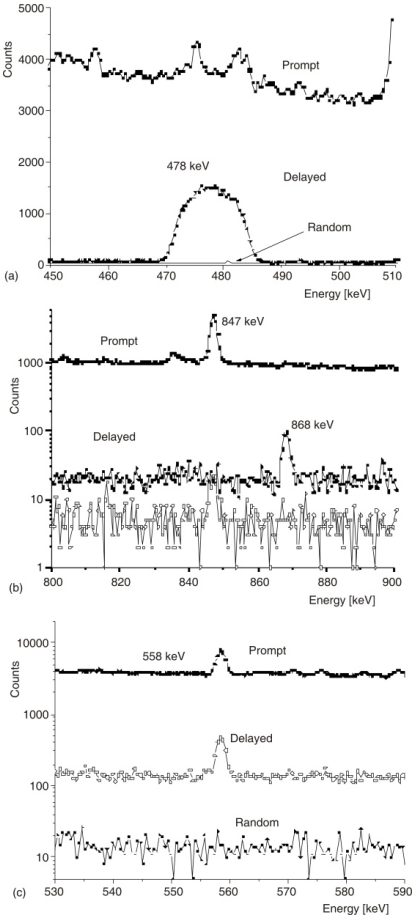

Figure 4. The prompt, delayed (up to 1 μs), and random coincidence spectra of: (a) the 478 keV Doppler-widened line from the (n, α) reaction on ^{10}B which appears only in the delayed spectrum; (b) the 847 keV line from the (n, n') inelastic scattering on ^{56}Fe which appears only in the prompt spectrum; (c) the 558 keV line which appears in both the prompt and delayed spectra, proving that this line originates partly from the usually assumed thermal neutron capture by ^{113}Cd and, depending on the hardness of the neutron spectrum, in part, from the fast neutron (n, n') reaction on ^{114}Cd

cited in inelastic neutron scattering with the energy of the recoiling nucleus. The one at 596 keV appears in the prompt spectrum, since the state at 596 keV in Ge-74 is short-lived. The regular peak of this energy in the delayed spectrum results from the thermal neutron capture by Ge-7, as is the case with the neighboring 609 keV line stemming from the same capture reaction. If the neutron flux at the detector is high, some of the intensity of the ubiquitous background line of 609 keV, usually entirely attributed to ^{214}Bi, is due to this process.

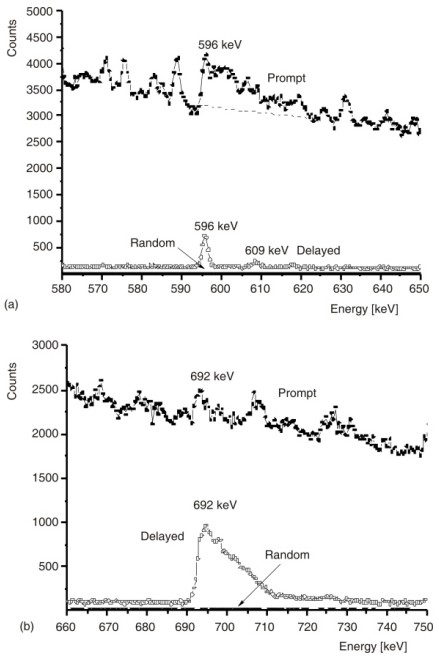

Figure 5. The spectrum of prompt, delayed, and random coincidences (practically negligible) containing: (a) the structure at 596 keV from inelastic fast neutron scattering on Ge-74 in the prompt spectrum, and the line of the same energy from slow neutron capture on Ge-73, in the delayed spectrum; (b) the structure at 692 keV from the inelastic scattering of fast neutrons on Ge-72, this time in the delayed spectrum, due to the finite lifetime of 444 ns at the excited state of 692 keV

The structure at 692 keV, however, appears in the delayed spectrum since the excited state of this energy in Ge-72 is comparatively long-lived, with a half-life of 444 ns, which is long in comparison to the time resolution of our system. As a demonstration of the capabilities of the system, we determined this half-life by setting the software gate to encompass the whole triangular structure in the coincident Ge spectrum, thus producing a time spectrum corresponding to this condition, thanks to which the fit produced a satisfactory value of 447(25) ns for the said half-life.

This particular structure has been studied in detail many times in the past, since 692 keV radiation is pure E0, detectable with 100% efficiency, which is why the integral of the triangular structure is a reliable measure of the fast neutron flux at the position of the detector [8-12]. These studies were performed with analog spectroscopy systems where the integration constants are long and the recoils invariably sum up with the 692 keV pulses. In digital spectroscopy systems, however, there is one important caveat to keep in mind when using the integral of this structure for fast neutron flux determination. It appears that here the shape and the intensity of the distribution strongly depend on the height of the triggering level. The recoil pulse is prompt, while the corresponding 692 keV pulse follows the recoil with delay distributed according to the decay law with the half-life of 444 ns. When the trigger is higher than the height of the recoil pulse, 692 keV pulse sums practically completely with the recoil. When the trigger is lower than the recoil, it will trigger the ADC, and this pulse, together with the following 692 keV pulse, will be rejected by the pile-up rejecting algorithm. This is illustrated in fig. 6 where the same portion of the direct HPGe spectrum is presented, with two different triggering levels. The width of the triangular structure appears proportional to the height of the triggering level. If this structure is to be used for quantitative purposes, the safe height of the triggering level that may be recommended is, thus,

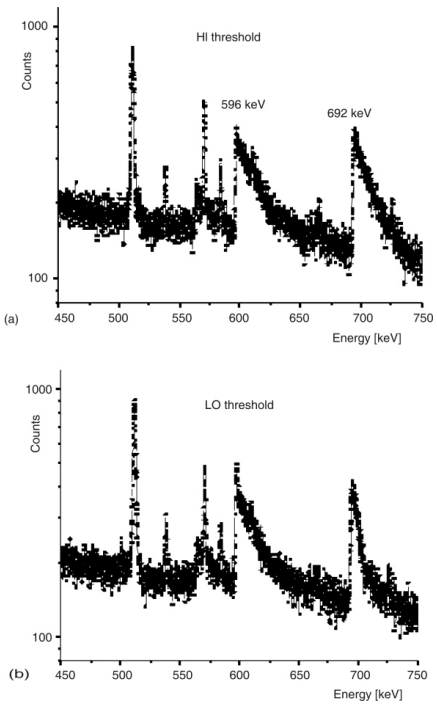

Figure 6. The 692 keV distribution in the direct spectrum with the triggering level set at 50 keV (a) and at 20 keV (b)

perhaps about 50 keV, when the loss of the counts within the structure is expected to be negligible.

After the system satisfactorily passed all the tests, we started some preliminary measurements of

the type that we plan to perform in the long run in the future, and it is of these results that we report in what follows.

PLANNED MEASUREMENTS

We plan to continuously collect the background spectra of all detectors in both laboratories, eventually changing only their mutual spatial arrangements. The spectra of the large scintillators will stretch up to a couple of hundreds of MeV, so as to include all multiple CR and shower events, while the one corresponding to the HPGe detector will go up to about 30 MeV, in order to include all possible nuclear radiations induced by CR radiations. Each event is to be recorded in a separate list, in accordance with the time of the occurrence of its trigger (with the resolution of 10 ns) and by its amplitude (in 32 k channels). By off-line analyses of this data we expect to directly obtain:

– the continuous time series of cosmic-ray intensity (muon plus electromagnetic – EM, components) in large and small plastic scintillators at ground level, as well as those generated underground,
– decoherence curves of cosmic-ray coincidence counts and coincidence spectra at different separations of the said detectors, be it at ground level or the underground one, the idea being to first define and, afterwards, separate muon from EM components,
– the spectrum of the HPGe detector in coincidence and anticoincidence with the large plastic scintillator positioned right above it, in the underground, and
– as well as the signatures of the soft component of EM showers in the spectrum of the unshielded NaI detector, taken in coincidence with the plastic detectors.

Since all above mentioned measurements are spectral, we hope to exploit this feature to some advantage, even in the case of rather featureless spectra of plastic scintillators. With the help of MC simulation programs (mainly CORSIKA and GEANT4), we expect to discriminate the signatures of CR muons from those of electromagnetic showers to some degree.

If all the measurements are performed continuously, we estimate that, together, both set-ups will produce about 1 TB of data per year, all of which would be kept permanently for later analyses.

To illustrate the potential of these measurements, we will now briefly report on some preliminary results obtained during a testing period, approximately yearlong. We will first briefly discuss the performance of low-level measurements and then those pertaining to CR measurements.

LOW-LEVEL MEASUREMENTS

Future applications of the low-background gamma spectroscopic system include the study of rare nuclear processes, measurements of environmental radioactivity and radiopurity of materials.

The cylindrical lead shielding of the 35% efficiency radio-pure HPGe ORTEC detector, with a wall thickness of 12 cm and an overall weight of 900 kg, was cast locally out of scratch plumbing retrieved after the demolition of some old housing. The integral background rate in the region from 50 keV to 3 MeV is about 0.5 cps. The lines of Co-60 are absent in the background spectrum, while the line of Cs-137 with the rate of $1\ 10^{-4}$ cps starts to appear significantly only if the measurement time approaches one month. Fukushima activities, though strongly present in our inlet air filter samples, did not enter the background at observable levels, in spite of the great quantities of air that we pump into the UL to maintain the overpressure, and it seems that the double air filtering and double buffer door system, along with stringent radiation hygiene measures, is capable of keeping the UL clean in cases of global accidental contaminations (see *e. g.* [13]).

No signatures of environmental neutrons, neither slow nor fast, are present in direct background spectra. The rates of some characteristic background

Table 1. Count rates in some background lines. Rotes are given in counts per second (cps)

Energy [keV]	Count rate [cps]
186.2 (Ra-226)	$2.4\ 10^{-4}$
351.9 (Pb-214	$1.1\ 10^{-3}$
583.1 (Tl-208)	$6.6\ 10^{-4}$
609.3 (Bi-214)	$1.1\ 10^{-3}$
911.1 (Ac-228)	$4.5\ 10^{-4}$
1460.8 (K-40)	$3.5\ 10^{-3}$
2614.5 (Tl-208)	$1.1\ 10^{-3}$

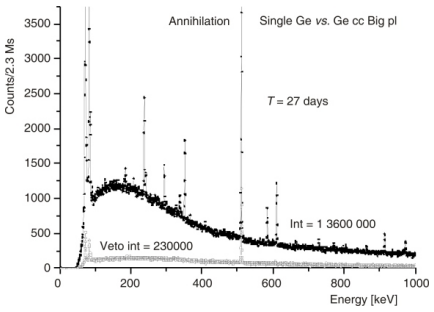

Figure 7. The background spectrum of the HPGe detector in its lead castle in the UL and the part of the spectrum coincident with the large scintillator positioned right above it

lines are listed in tab. 1. With the large plastic scintillator currently positioned rather high over the detector top, at a vertical distance of 60 cm from the top of the lead castle, in order to allow for the placing of voluminous sources in front of the vertically oriented detector, the off-line reduction of this integral count by the CR veto condition is about 18% (see fig. 7). Up to a factor of two might be gained if the veto detector were to be positioned at the closest possible distance over the HPGe detector. This agrees well with simple estimates of the rate of events susceptible to the veto condition [14]. The veto spectrum contains all events, prompt as well as those with delays of up to 10 s, which is why besides the continuum it contains only the lead X-rays and the annihilation line. As we shall see, the selection of delayed events only reveals some other details in this spectrum. Since for the time being we are not able to improve on the intrinsic background of our detector, when analyzing the analytical powers of our system, at present, we do not insist on the lowering of statistical errors which depend on background levels solely and are difficult to reduce further with available means, but rather emphasize its stability due to the low and controlled radon concentration in the laboratory. This is essential, especially in NORM measurements, and makes our system virtually free of systematic errors as compared to systems which operate in environments where radon is not controlled and where the reduction of post-radon background activities is achieved by flushing the detector cavity with liquid nitrogen vapor, where the transient regimes during sample changes and possible deposition of radon progenies [15] may introduce systematic uncertainties which are difficult to estimate.

COSMIC-RAY MEASUREMENTS

Muon spectra and the time series

During the commissioning of the large plastic detectors, we tested the response of these detectors to CR muons and their stability over a prolonged period of time. Certain results of these preliminary studies are presented here.

In fig. 8, we present the spectra of the two diagonals of the large plastic scintillator in the UL. Contrary to the situation in the GLL, the peak of charged particle energy losses situated at about 10 MeV (due to both muons and electrons from EM showers), is not fully separated from the low-energy tail of Compton electrons in the UL, because of gamma-ray interactions (both environmental and from EM showers).

Figure 9 presents the coincident sum spectra of the two diagonals. Energy spectra now contain only the well-defined peak of charged particles energy losses. The offsets are not imposed and occur simply

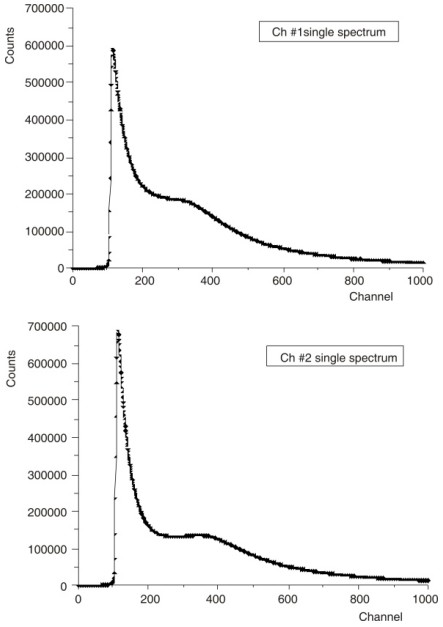

Figure 8. The spectra of two diagonals of the large plastic detector in the UL. Note that the peak of charged particle energy losses of 10 MeV, which corresponds to channel 320, is not separated from the low-energy tail of Compton scattered environmental gamma radiations. When summed, in coincidence they produce the spectrum from fig. 9

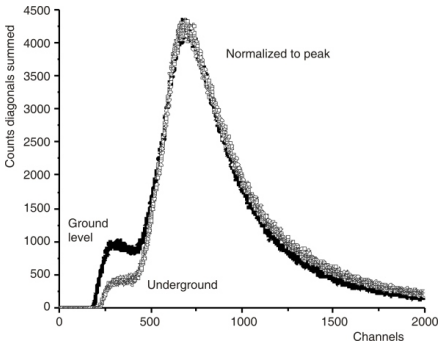

Figure 9. The sum spectra of two diagonals of the large plastic detectors in the UL and GLL. For comparison, the spectra are normalized for the peaks to coincide. Channel 650 now corresponds to the muon energy loss of 10 MeV. The integral of this peaked distribution is taken as the first approximation to the CR muon count by the large detectors

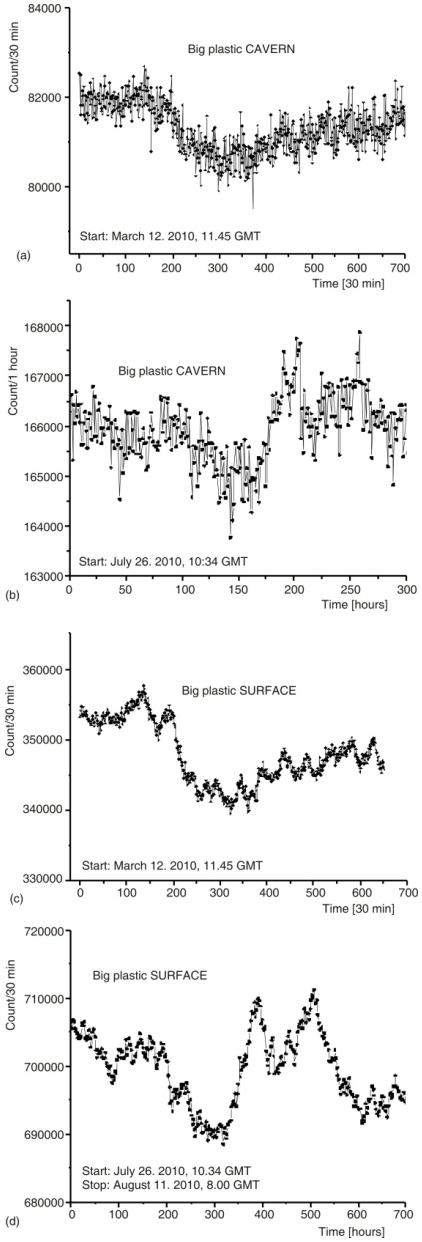

Figure 10. The time series of the CR muon count of the large plastic detector in the UL – (a) and (b) graphs – and GLL (c) and (d) graphs for the period starting with March 12, 2010, averaged to half hour intervals, as opposed to the period starting with July 26, 2010, averaging to one hour intervals. It is evident that the modulation in the two laboratories is correlated and that the amplitude of the modulation in the UL is roughly half

because at low energies there are no coincident events. As the simulations demonstrate, this is so because single Compton electrons do not produce enough light to trigger both diagonals.

The majority of events that produce this peaked distribution are due to CR muons that pass through the detector. We thus form the time series of this spectrum integrated over different time intervals. As an example, in fig. 10 we present the time series of this count in 30-minute intervals, both in the UL and in the GLL, for a period of 16 days in March 2010, and in one-hour intervals for the period starting with July 26, 2010. The data are not corrected either for atmospheric pressure or temperature.

The two series appear highly correlated, the amplitude of the modulation of this count in the UL is about 1.8%, while the corresponding one in the GLL is about 3.5%. At these integrating times, this is already sufficiently statistically significant, even in the UL.

Previous measurements at the same location with the small detectors yielded results for the muon flux of $1.37(6)\ 10^{-2}$ per cm^2s in the GLL, and of $4.5(2)\ 10^{-3}$ per cm^2s in the UL [2].

NEUTRONS AND STOPPED POSITIVE MUONS IN THE UNDERGROUND LABORATORY

During the testing period, we have accumulated some six months of data-taking in the underground laboratory. The background spectrum of the HPGe de-

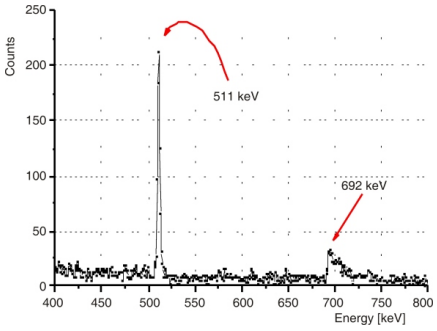

Figure 11. The portion of the background of the HPGe spectrum coincident with the large plastic detector with delays in the range of 1 to 5 μs, after 187 days of measurement time. It shows the annihilation line which is due to the decays of positive muons stopped in the lead castle, and the triangular structure at 692 keV, which is due to inelastic scattering of fast neutrons on 72-Ge, the neutrons originating mostly from direct fast muon interactions with nuclei and certainly less from captures of stopped negative muons. The threshold in this spectrum is sufficiently high to leave this last structure unscathed

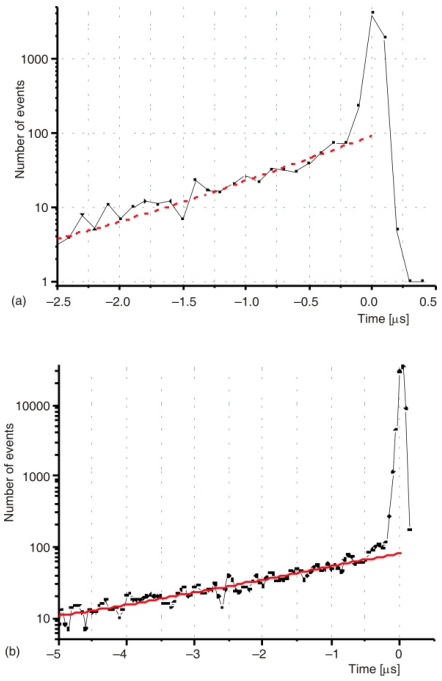

Figure 12. Time distributions of events that belong (a) to the structure of 692 keV, the slope of which yields 500(50) ns for the half-life of the state of this energy in 72-Ge and, (b) that of the annihilation line, which yields 2.24(9) s for the mean life of the muon

tector containing the coincidences with the large plastic scintillator from the delayed tail of the corresponding TAC distribution in the region of 1 to 5 s, shows at this statistics only two interesting features (fig. 11), though some more seem to emerge, but still insufficiently significant. The first is the already discussed triangular structure at 692 keV already discussed, which originates from the inelastic (n, n') scattering exciting the first excited state of the stable Ge-72 within the Ge detector itself. In this case the trigger was sufficiently high, and according to our finding, the intensity of the 692 keV distribution can be reliably used for the estimate of the fast CR-induced neutron flux at the position of the detector. To verify this, we applied the software gate to this structure and obtained the TAC distribution presented in fig. 12(a). Although the statistics is poor, the fit through the tail of delayed coincidences yields the half-life of 500(50) ns, which compares well with the known value of 444 ns. Using the expression from ref. [8], we obtain the value of 4(1) 10^{-7} $cm^{-2}s^{-1}$ for the flux of neutrons of CR origin with energies over 1 MeV. This refers to the flux at the depth of 25 m.w.e., (see *e. g.* [16]) within roughly a ton of lead, a common environment in most measurements of low activities.

The second feature of this spectrum is the annihilation line. The gate put on this line gives the TAC distribution presented in fig. 12(b), where the fit through the tail of delayed coincidences yields the mean life of 2.24(9) s. This justifies the assumption that these events are due to the decays of stopped positive muons. We further assume that the source of these delayed annihilations is homogeneously distributed throughout the volume of the lead castle and use GEANT4 to find the overall detection efficiency. From the intensity of these delayed annihilations, we then obtain that the number of stopped positive muons per kg of lead per second equals 3.0(5) 10^{-4} μ_{stop}/kgs.

We have also been able to estimate the number of stopped muons in the large plastic scintillators themselves, both in the GLL and the UL (*e. g.* [16]). For this

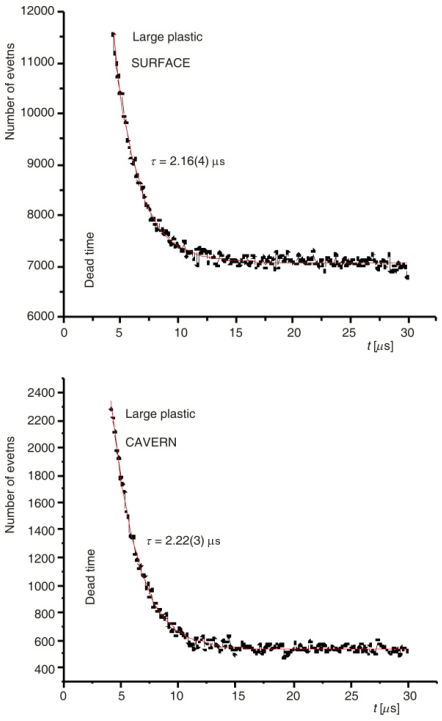

Figure 13. The distributions of short time intervals between successive counts in large plastic scintillators which sit on the distribution of time intervals between successive counts with a long exponential constant that corresponds to the total counting rate and appears flat on this scale. The decay constant of short time interval distributions, however, equals that of a muon mean life. Note that the first two lifetimes are missing, due to the dead time of the system, which in this particular case equals 4 s

purpose, we looked into the distribution of time intervals between the successive counts of these detectors. The gross structure of this distribution is nicely exponential, corresponding to the average CR counting rate and to an average time interval between the counts, reciprocal to the said rate. At short time intervals, however, the distribution strongly departs from this shape (fig. 13).

It is again exponential, now with the time constant of 2.16(4) and 2.22(3) μs in the GLL and UL, respectively, reproducing satisfactorily the muon mean life. This suggests that these events originate from muons that both stop and decay within the detector. Minding that the fiducial volume for this kind of signature has not been estimated, the intensity of this exponential distribution, taking in account the missing events due to the 4 s long dead time, now gives the estimate for the lower limit of the number of muons that stop in 5 cm of plastic per square meter per second, at ground level as 6 10^{-2} $_{\text{stop}}$ per m^{2}s, and at a depth of 25 m.w.e. as 1.52 10^{-2} μ_{stop} per m^{2}s. It is interesting to compare those figures with the results obtained recently at Gran Sasso [18, 19].

DECOHERENCE CURVES AND SPECTRA

In test measurements, coincidence spectra between large and small detectors at different separations between the two were recovered in off-line analyses, both in the GLL and the UL. These are predominantly the spectra of EM showers, as seen by respective detectors. The comparison with their direct spectra, which at lower energies are composed mostly of the signatures of environmental gamma radiations and at higher energies of the signatures of CR muons,

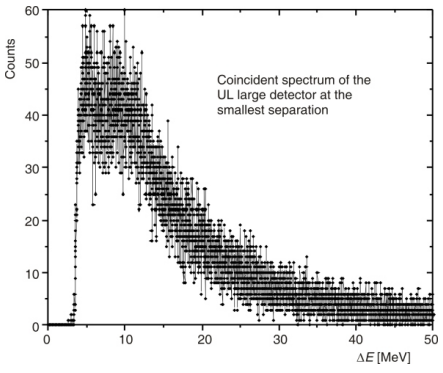

Figure 14. The coincident spectrum of the large plastic detector in the UL, with the small detector at the smallest separation between them. Compare this with the direct spectrum presented in fig. 9

enables the disentanglement of the signatures of these radiations. As an illustration, fig. 14 presents the spectrum of the large plastic detector in the UL, in coincidence with the small detector, at their smallest possible separation. This is to be compared with the direct spectrum of the large detector, as presented in fig. 9. Reflecting the structure of the EM component at the given location, not only the intensity, but also the

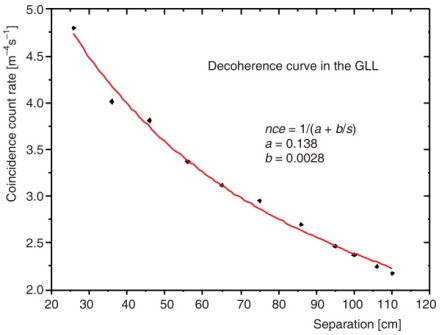

Figure 15. The decoherence curve in the GLL, reflecting the lateral profile of EM showers on the surface; the nce denotes number of coincident events

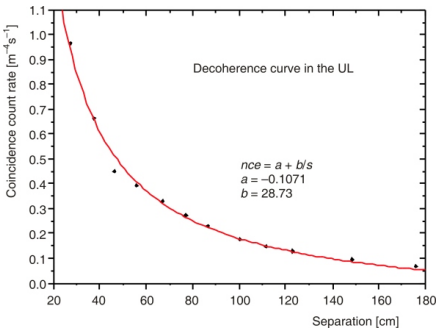

Figure 16. The decoherence curve in the UL, reflecting the lateral profile of EM showers at the equivalent depth of 25 m.w.e; the nce denotes number of coincident events

shape of the spectrum changes with detector separation, and the differences between these coincidence spectra in the GLL and the UL reflect the difference in the composition of showers on the surface and underground. The simplest integral characteristic of the shower profile is presented by the integral of this coincidence spectrum as a function of detector separation, sometimes referred to as the decoherence curve. Figure 15 shows the decoherence curve at the GLL, fig. 16 the same in the UL.

Note that the two curves cannot be satisfactorily fitted with quite the same type of functional dependence, so that the width of the distributions on the surface and underground cannot be directly compared. The much narrower distribution underground is a result of the harder CR muon spectrum and of the different radiation and attenuation lengths, as well as of the geometry of the shower-producing medium. The ratio of the intensities of the distributions on the surface and underground is roughly twice the ratio of CR muon intensities at two locations. Full interpretation awaits better statistics.

CONCLUSION

We have presented some preliminary results for muon and neutron fluxes at ground level and underground spaces of the Belgrade low-level and CR laboratory, obtained during the commissioning of the new equipment consisting of two scintillation detectors, a HPGe detector, and a digital spectroscopy system based on two CAEN N1728B units. The main advantage of the present set-up is that it enables complex measurements involving routine low activity measurements with modest means, along with some interesting research work related to cosmic-ray physics. We find that the results obtained in this testing phase justify the planned program of measurements and that the future improvement on statistics will contribute not only to the quality of the results already obtained, but furthemore with increased sensitivity new results are also expected to emerge.

ACKNOWLEDGEMENT

The present work was funded by the Ministry of Education and Science of the Republic of Serbia, under the Project No. 171002. The Belgrade Laboratory bears the name of "Dr. Radovan Antanasijević", in honor of its early deceased founder and first director.

REFERENCES

[1] Niese, S., Underground Laboratories for Low-Level Radioactivity Measurements, in: Analysis of Environmental Radionuclides (Ed. P. Povinec), Elsevier, Amsterdam, 2008, pp. 209-239
[2] Dragić, A., *et al*., Measurement of Cosmic Ray Muon Flux in the Belgrade Ground Level and Underground Laboratories, *Nucl. Instr. and Meth. in Phys. Res. A591* (2008), pp. 470-475
[3] Dragić, A., *et al*., Comparative Study of Power Spectra of Ground and Shallow Underground Muon Data, *Int. Journal of Modern Physics A, 20* (2005), pp. 6953-6955
[4] Dragić, A., *et al*., Periodic Variations of CR Muon Intensity in the Period 2002-2004, *Proceedings*, 21st European Cosmic Ray Symposium, Košice, Slovakia, 2008, pp. 368-373
[5] Udovičić, V., *et al*., Radon Problem in an Underground Low-Level Laboratory, *Radiation Measurements 44* (2009), 9-10, pp. 1009-1012
[6] Udovičić, V., *et al*., Radon Time-Series Analysis in the Underground Low-Level Laboratory in Belgrade, Serbia, *Radiation Protection Dosimetry, 145* (2011), 2-3, pp. 155-158
[7] Puzović, J., Aničin, I., An Off-Line Method for the Correction of Amplitude Walk in Leading-Edge Timing, *Nucl. Instr. and Meth. in Phys. Res., A57*2 (2007), 2, pp. 926-928
[8] Škoro, G., *et al*., Environmental Neutrons as Seen by a Germanium Gamma-Ray Spectrometer, *Nucl. Instr. and Meth. in Phys. Res., A316* (1992), 2-3, pp. 333-336
[9] Fehrehbacher, G., Meckbach, R., Paretzke, H. G., Fast Neutron Detection with Germanium Detectors: Computation of Response Functions for the 692 keV Inelastic Scattering Peak, *Nucl. Instr. and Meth. in Phys. Res., A372* (1996), 1-2, pp. 239-245
[10] Fehrehbacher, G., Meckbach, R., Paretzke, H. G., Fast Neutron Detection with Germanium Detectors: Unfolding the 692 keV Peak Response dor Fission Neutron Spectra, *Nucl. Instr. and Meth. in Phys. Res., A377* (1997), 2-3, pp. 391-398
[11] Ataç, A., *et al*., Discrimination of Gamma Rays Due to Inelastic Neutron Scattering in AGATA, *Nucl. Instr. and Meth. in Phys. Res., A607* (2009), 3, pp. 554-563
[12] Jovančević, N., *et al*., Neutron Induced Background Gamma Activity in Low-Level Ge Spectroscopy Systems, *Nucl. Instr. and Meth. in Phys. Res., A612* (2010), 2, pp. 303-308
[13] Adžić, P., *et al*., The Background Gamma-Ray Study before and after the Chernobyl Accident, *Environment International, 14* (1988), 4, pp. 295-297
[14] Bikit, I., *et al*., Vetoing Techniques in Radioactive Contamination Research, in Radioactive Contamination Research Developments (Eds. N. K. Henshaw, C. S. Alleyne), Nova Science Publishers, Hauppauge, N. Y., USA, 2010, pp. 67-99
[15] Guiseppe, V. E., *et al*., A Radon Progeny Deposition Model, arXiv 1101.0126v1 [nucl-ex] 30 Dec, 2010
[16] Ryazhskaya, O., Neutrons from Cosmic-Ray Muons Underground, 20th European Cosmic Ray Symposium, Lisbon, 2006
[17] Coan, T., Liu, T., Ye, J., A Compact Apparatus for Muon Lifetime Measurement and Time Dilation Demonstration in the Undergraduate Laboratory, *Am. J. Phys., 74* (2006), 2, pp. 161-164
[18] Bonardi, A., *et al*., On a Measurement of Atmospheric Stopping Muons and Neutron Fluxes, 31st ICRC, Lodz, Poland, 2009
[19] Bonardi, A., Study of Cosmic Ray Neutrons, Ph. D. thesis, University of Torino, Torino, Italy, 2010

Received on September 27, 2011
Accepted on December 6, 2011

Александар ДРАГИЋ, Владимир И. УДОВИЧИЋ, Радомир БАЊАНАЦ, Дејан ЈОКОВИЋ, Димитрије МАЛЕТИЋ, Никола ВЕСЕЛИНОВИЋ, Михаило САВИЋ, Јован ПУЗОВИЋ, Иван В. АНИЧИН

НОВА ОПРЕМА У БЕОГРАДСКОЈ ЛАБОРАТОРИЈИ ЗА МЕРЕЊЕ НИСКИХ АКТИВНОСТИ И КОСМИЧКОГ ЗРАЧЕЊА

Београдска лабораторија састоји се од два лабораторијска простора, једног на површини и једног подземног, на дубини од 25 метара воденог еквивалента. Детаљно су описани и илустровани потенцијали ових лабораторија за мерење ниских активности и за континуирано мерење мионске и електромагнетне компоненте космичког зрачења, као и за студије процеса које ова зрачења индукују у германијумским спектрометрима смештеним у нискофонским подземним лабораторијама. Сва ова мерења се изводе симултано, новим системом за дигиталну спектроскопију, а подаци се записују догађај по догађај, и анализирају после завршених мерења. Такође су приказани прелиминарни резултати који су у фази тестирања опреме добијени за флукс брзих неутрона и заустављених миона у површинској и у подземној лабораторији.

Кључне речи: подземна лабораторија, гама спектроскопија, мерења ниских активности, космичко зрачење

MULTIYEAR INDOOR RADON VARIABILITY IN A FAMILY HOUSE – A CASE STUDY IN SERBIA

by

Vladimir I. UDOVIČIĆ [1*], ***Dimitrije M. MALETIĆ*** [1], ***Radomir M. BANJANAC*** [1], ***Dejan R. JOKOVIĆ*** [1], ***Aleksandar L. DRAGIĆ*** [1], ***Nikola B. VESELINOVIĆ*** [1], ***Jelena Z. ŽIVANOVIĆ*** [1], ***Mihailo R. SAVIĆ*** [1], ***and Sofija M. FORKAPIĆ*** [2]

[1] Institute of Physics, University of Belgrade, Belgrade, Serbia
[2] Department of Physics, Faculty of Science, University of Novi Sad, Novi Sad, Serbia

Scientific paper
http://doi.org/10.2298/NTRP1802174U

The indoor radon behavior has complex dynamics due to the influence of the large number of different parameters: the state of indoor atmosphere (temperature, pressure, and relative humidity), aerosol concentration, the exchange rate between indoor and outdoor air, construction materials, and living habits. As a result, indoor radon concentration shows variation, with the usual periodicity of one day and one year. It is well-known that seasonal variation of the radon concentration exists. It is particularly interesting to investigate indoor radon variation at the same measuring location and time period, each year, due to estimation of individual annual dose from radon exposure. The long-term indoor radon measurements, in a typical family house in Serbia, were performed. Measurements were taken during 2014, 2015, and 2016, in February and July, each year. The following measuring techniques were used: active and charcoal canisters methods. Analysis of the obtained results, using multivariate analysis methods, is presented.

Key words: radon variability, multivariate regression analysis, multi-seasonal radon measurements, indoor radon

INTRODUCTION

The research of the dynamics of radon in various environments, especially indoors, is of great importance in terms of protection against ionizing radiation and in designing of measures for its reduction. Published results and development of many models to describe the behavior of indoor radon, indicates the complexity of this research, especially with models for prediction of the variability of radon [1-3]. This is because the variability of radon depends on a large number of variables such as local geology, permeability of soil, building materials used for the buildings, the state of the indoor atmosphere (temperature, pressure and relative humidity), aerosol concentration, the exchange rate between indoor and outdoor air, construction materials, as well as the living habits of people. It is known that the indoor radon concentration variation has periodicity of one day and one year. It is also well-known that the seasonal variation of the radon concentration exists. This is why it is particularly interesting to investigate indoor radon variation at the same measuring location and time period, year after year, in order to estimate the individual annual dose from radon exposure. In that sense, we performed long-term indoor radon measurements in a typical family house in Serbia. Measurements were taken during the 2014, 2015, and 2016, in February and July, each year. We used the following measuring techniques: active and charcoal canisters methods. The detailed analysis of the obtained results using multivariate analysis (MVA) methods is presented in this paper.

First, MVA methods were tested on the radon variability studies in the Underground Low Background Laboratory in the Institute of Physics, Belgrade [4, 5]. Several climate variables: air temperature, pressure, and humidity were considered. Further advance was made by using all the publicly available climate variables monitored by nearby automatic meteorological station. In order to analyze the dependence of radon variation on multiple variables, multivariate analysis needs to be used. The goal was to find an appropriate method, out of the wide spectrum of multivariate analysis methods that are developed for the analysis of data from high-energy physics experiments, to analyze the measurements of variations of radon concentrations in indoor spaces. Previous

* Corresponding author; e-mail: udovicic@ipb.ac.rs

analysis were done using the maximum of 18 climate parameters and use and comparison of 8 different multivariate methods. In this paper the number of variables is reduced to the most important ones and new derived variables, like vapor pressure, simple modeled solar irradiance and simple modeled precipitation, which were introduced in the multivariate analysis.

INDOOR RADON MEASUREMENTS METHODS

Depending on the integrated measurement time, methods of measurement of the indoor radon concentrations may be divided into long-term and short-term ones. The device for the performed short-term radon measurements is SN1029 radon monitor (manufactured by the Sun Nuclear Corporation, NRSB approval-code 31822) with the following characteristics: the measurement range from 1 Bqm^{-3} to 99.99 $kBqm^{-3}$, accuracy equal to +25 %, sensitivity of 0.16 counts hour per Bqm^{-3}. The device consists of two diffused junction photodiodes as the radon detector which is furnished with sensors for temperature, barometric pressure, and relative humidity. The sampling time was set to 2 h. The method for Charcoal Canister used is: EERF Standard Operating Procedures for Radon-222 Measurement Using Charcoal Canisters [6], also used by major laboratories which conduct radon measurements in Serbia [7]. Exposure time of the charcoal canisters was 48 h. The connection between short term and long term measurements has attracted some interest previously [8].

The family house, selected for the measurements and analysis of variations of radon concentrations, is a typical house in Belgrade residential areas, with requirement of existence of cellar. House is built on limestone soil. Radon measurements were carried out in the living room of the family house, which is built of standard materials (brick, concrete, mortar) and isolated with styrofoam. During the period of measurements (winter-summer 2014, 2015, and 2016), the house was naturally ventilated and air conditioning was used in heating mode at the beginning of the measurement period. During the winter period measurements, the electrical heating was used in addition to air conditioning. Measured radon concentrations, room temperature (T_id), atmospheric pressure (P_id) and relative humidity (H_id) inside the house, were obtained using radon monitor. Values of meteorological variables, in the measurement period, were obtained from an automatic meteorological station, located near the house in which the measurement was performed. We used the following meteorological variables: external air temperature (T), also at height of 5cm, pressure (P) and humidity (H), solar irradiation, wind speed, precipitation, temperature of the soil at depths of 10 cm, 20 cm and 50 cm. The natural ventilation routine was not monitored. Since the ventilation is of crucial importance for the level of radon indoors [9], Multivariate regression analysis was used mainly for winter periods.

MULTIVARIATE REGRESSION ANALYSIS

In many fields of physics, especially in high-energy physics, there is the demand for detailed analyses of a large amount of data. For this purpose, the data analysis environment ROOT [10], is developed. ROOT is modular scientific software framework, which provides all the functionalities needed to deal with big data processing, statistical analysis, visualization and storage. A specific functionality gives the developed Toolkit for Multivariate Analysis (TMVA) [11]. The TMVA provides an environment for the processing, parallel evaluation and application of multivariate regression techniques.

TMVA is used to create, test and apply all available regression multivariate methods, implemented in ROOT, in order to find methods which are the most appropriate and yield maximum information on the dependence of indoor radon concentrations on the multitude of meteorological variables. Regression methods are used to find out which regression method can, if any, on the basis of input meteorological variables only, give an output that would satisfactorily close match the observed variations of radon concentrations. The output of usage of multivariate regression analysis methods has mapped functional behavior, which can be used to evaluate the measurements of radon concentrations using input meteorological variables only. All the methods make use of training events, for which the desired output is known and is used for training of Multivariate regression methods, and test events, which are used to test the MVA methods outputs.

RESULTS

Measurements were performed during February and July in 2014, 2015, and 2016 using radon monitor and charcoal canister measurements. The descriptive results are summarized in tab. 1. The measurements using radon monitor and charcoal canisters are in good agreement.

Previous work done by researchers from the Low Background Laboratory, Institute of Physics, Belgrade, using the MVA analysis in search of connections between radon concentration and meteorological variables, included only one period of measurement, February or July 2014 [4]. Now the MVA analysis is using all the measured data February/July 2014-2016. New variables introduced in MVA analysis are modeled solar irradiance, modeled precipitation and vapor

Table 1. Descriptive results of February and July 2014, 2015, and 2016 measurements, using radon monitor and charcoal canisters (only in February)

Results of measurements	2014		2015		2016	
	Feb.	July	Feb.	July	Feb.	July
Minimal radon activity using radon monitor [Bqm^{-3}]	15	0	28	0	12	3
Maximal radon activity using radon monitor [Bqm^{-3}]	1000	286	915	88	1013	262
Median radon activity using radon monitor [Bqm^{-3}]	418	25	524	22	412	28
Arithmetic mean of radon activity using radon monitor (standard deviation) [Bqm^{-3}]	402 (216)	40 (41)	508 (207)	27 (18)	423 (214)	39 (32)
Room temperature using radon monitor (standard deviation) [°C]	20.4 (0.8)	24.7 (0.9)	21.2 (0.6)	24.9 (0.8)	22.3 (0.6)	24.6 (0.8)
Relative humidity using radon monitor (standard deviation) [%]	67.4 (5.7)	67.8 (4.8)	68.2 (4.8)	51.5 (4.7)	64.0 (6.4)	58.9 (7.5)
Radon activity using charcoal canister (standard deviation) [Bqm^{-3}]	432 (10)	/	518 (6)	/	407 (5)	/

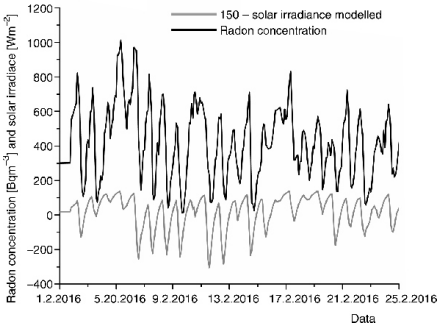

Figure 1. Modeled solar irradiance in comparison with measured radon concentration during February 2016

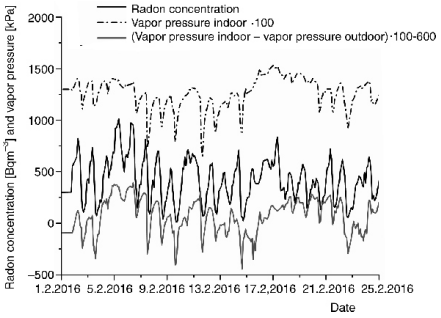

Figure 2. Vapor pressure in comparison with measured radon concentration during February 2016

pressure. In order to make use of intensity of solar irradiance during the whole day and night, the solar irradiance is modeled so that it includes 80 % of solar irradiance value from the previous measurement (previous hour) with addition of solar irradiance value for the actual hour of measurement (fig. 1). The value of 80 % is chosen so that the modeled solar irradiation has the best correlation with the radon measurements. Similar model of precipitation was used in this analysis. The next new variable is vapor pressure. The vapor pressure variable is calculated using the slope s(T), of the relationship between saturation vapor pressure and air temperature and is given by [12, 13], so that the vapor pressure equals relative humidity times saturation vapor pressure, fig. 2.

Before the start of training of Multivariate regression methods using TMVA toolkit in ROOT, the description of input meteorological variables is performed, mainly by looking into inter-correlations of input variables and their connections with the measured radon concentrations. The MVA is using all the measured data. Table 2 presents the meteorological variables and their module value of correlation with the measured radon concentrations (target), which is indicative in finding linear dependence of radon measurements and input variables. The second column in tab. 2 presents us with correlation ration values which indicate if there are some functional dependence (not only linear) between input variables and radon concentration, and the last column presents the mutual information which indicates if there is a non-functional dependence of input variables and radon measurements [11].

From tab. 2 it can be noticed that linear correlated values are not the only ones which can be used in MVA analysis, for example variable solar irradiance has high mutual information with the radon measurements.

In the data preparation for MVA training the whole dataset is consisting of many events. An event includes time of measurement, radon measurement and meteorological variables. The dataset is randomly split in two halves, one half of the events will be used for training of multivariate regression methods, and the other half of events for testing of methods, mainly to compare the measured and MVA evaluated values for radon concentration.

It turns out that the methods best suited for our purpose is the Boosted Decision Trees (BDT) method. This means that BDT gives the smallest difference be-

Table 2. Input variable rank and values for correlation, correlation ratio and mutual information, all with the measured radon concentrations (target) for February and July 2014-2016 measurements

Variable	Correlation with target		Correlation ratio		Mutual information	
	Rank	Value	Rank	Value	Rank	Value
Soil temperature depth 20 cm [°C]	1	0.87	1	0.60	13	1.48
Soil temperature depth 50 cm [°C]	2	0.86	2	0.57	14	1.31
Soil temperature depth 10 cm [°C]	3	0.82	3	0.54	9	1.84
Temperature outdoor [°C]	4	0.82	5	0.53	8	1.85
Vapor indoor – vapor od [mbar]	5	0.81	9	0.41	11	1.73
Temperature od – temperature id [°C]	6	0.80	4	0.53	6	1.92
Temperature height 5 cm [°C]	7	0.77	8	0.48	7	1.91
Vapor od [mbar]	8	0.76	10	0.41	5	1.92
Temperature id [°C]	9	0.75	7	0.49	17	1.16
Solar irradiance [Wm^{-2}]	10	0.61	6	0.50	2	2.23
Humidity indoor [%]	11	0.45	11	0.26	1	2.26
Humidity outdoor [%]	12	0.31	13	0.20	10	1.76
Air pressure outdoor [mbar]	13	0.27	17	0.07	12	1.55
Wind speed [ms^{-1}]	14	0.22	16	0.01	16	1.28
Air pressure indoor [mbar]	15	0.17	18	0.04	15	1.31
Humidity od – Humidity id [%]	16	0.10	14	0.19	4	2.11
Precipitation [Lm^{-2}]	17	0.01	15	0.19	18	1.13
Vapor indoor [mbar]	18	0.002	12	0.02	3	2.17

tween the measured radon concentration from test sample and the evaluation of value of radon concentration using input variables only. This can be seen in fig. 3, which shows the distribution of BDT and BDTG regression method outputs (evaluated values) in comparison with the measured radon concentration during February 2016.

Since TMVA has 12 different regression methods implemented, only some of those will give useful results when evaluating the radon concentration measurements. Table 4 summaries the results of MVA analysis. It shows the MVA methods RMS of difference of evaluated and measured radon concentration. Also, tab. 4 shows the mutual information of measured and MVA evaluated radon concentration. Besides

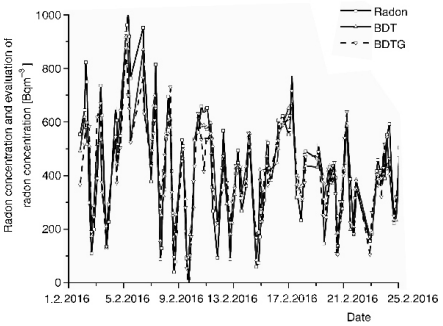

Figure 3. Comparison of MVA evaluated radon concentration and measured one from the test sample of events during February 2016

BDT, the Multi-Layer Perceptron (MLP) [10], an implementation of Artificial Neural Network multi variate method, also gives good results.

The MVA regression analysis results in mapped functional behavior and, as opposed to possible existence of theoretical modeling, which is independent of the number of measurements, MVA depends on the number of events. More events, the better mapped function we get as a result. In this sense, if the number of measurements is not great, multivariate analysis can be used only as help, to indicate which variables are more important to be used in theoretical modeling, for comparison of mapped and modeled functions, and modeled function test.

CONCLUSION

Indoor radon variation at one location in the same periods (February and July), was investigated for three years. Long-term indoor radon measurements show intense seasonal variation. The results obtained with different measuring methods are in good agreement. The radon behavior in the house is almost the same and shows good reproducibility year by year. The small variations in the year by year dynamics are originated mostly from the variations in meteorological variables during winter seasons and mostly due to ventilation habits during summer season. Ventilation habits were not monitored nor taken into account in MVA regression analysis. The preliminary results using multivariate analysis methods in TMVA are shown. Main output of Multivariate regression analy-

Table 3. Input variable correlation with the measured radon concentrations for February and July 2016

Correlation with target			
February 2016		July 2016	
Variable	Value	Variable	Value
Vapor id-vapor od [mbar]	0.58	Soil temperature depth 20 cm [°C]	0.46
Humidity id [%]	0.54	Soil temperature depth 50 cm [°C]	0.42
Vapor id [mbar]	0.52	Solar irradiance	0.32
Solar irradiance [Wm^{-2}]	0.48	Temperature id [°C]	0.30
Temperature od – temperature id [°C]	0.46	Soil temperature depth 10 cm [°C]	0.24
Temperature [°C]	0.44	Temperature od [°C]	0.21
Soil temperature depth 10 cm [°C]	0.43	Humidity od [%]	0.20
Soil temperature depth 20 cm [°C]	0.42	Humidity id [%]	0.19
Humidity [%]	0.38	Air pressure [mbar]	0.17
Temperature height 5 cm [°C]	0.32	Precipitation [Lm^{-2}]	0.17
Temperature id [°C]	0.29	Temperature od – temperature id [°C]	0.16
Air pressure od [mbar]	0.23	Air pressure_id [mbar]	0.16
Air pressure id [mbar]	0.21	Humidity od – humidity id [%]	0.14
Soil temperature depth 50 cm [°C]	0.20	Wind speed [ms^{-2}]	0.13
Precipitation [Lm^{-2}]	0.19	Temperature height 5 cm [°C]	0.12
Humidity od – humidity id [%]	0.15	Vapor id [mbar]	0.06
Vapor od [mbar]	0.08	Vapor od [mbar]	0.03
Wind speed [ms^{-1}]	0.05	Vapor id – vapor od [mbar]	0.02

Table 4. RMS of MVA method's evaluation error and mutual information; February/July 2014-2016

MVA method	RMS [Bqm^{-3}]	Mutual information
BDT	85.5	1.477
BDTG	92.1	1.614
MLP	101	1.401

sis is the initial version of *mapped* function of radon concentration dependence on multitude of meteorological variables. Simplification of MVA methods can be made by choosing only the most important input variables and exclude the other variables.

ACKNOWLEDGEMENTS

The authors acknowledge the financial support of the Ministry of Science, Technology and Development of Serbia within the projects: Nuclear Methods Investigations of Rare Processes and Cosmic Rays (grant number 171002) and Biosensing Technologies and Global System for Continuous Research and Integrated Management (grant number 43002).

AUTHORS' CONTRIBUTIONS

The idea for this paper came as a result of discussions of V. I. Udovičić, R. M. Banjanac, D. R. Joković, A. L. Dragić, and D. M. Maletić. Gathering climate data and MVA analysis was done by D. M. Maletić and V. I. Udovičić. Performed indoor radon measurements were done by V. I. Udovičić and S. M. Forkapić. Writing of the paper was done by D. M. Maletić and V. I. Udovičić. A. L. Dragić gave idea about using MVA methods in cosmic and radon measurements. N. B. Veselinović and M. R. Savić analyzed and validated climate data. J. Z. Živanović helped with MVA analysis. D. R. Joković helped with data analysis and paper technical preparation.

REFERENCES

[1] Collignan, B., *et al*., Development of a Methodology to Characterize Radon Entry in Dwellings, *Building and Environment, 57* (2012), Nov., pp. 176-183
[2] Li, F., Baixeras, C., The RAGENA Dynamic Model of Radon Generation, Entry and Accumulation Indoors, *Science of the Total Environment, 307* (2003), 1-3, pp. 55-69
[3] Jelle, B. P., *et al*., Development of a Model for Radon Concentration in Indoor Air, *Science of the Total Environment, 416* (2012), Jan., pp. 343-350
[4] Maletić, D., *et al*., Comparison of Multivariate Classification and Regression Methods for Indoor Radon Measurements, *Nucl Technol Radiat, 29* (2014), 1, pp. 17-23
[5] Udovičić, V., *et al*., Radon Problem in an Underground Low-Level Laboratory, *Radiation Measurements, 44* (2009), 9-10, pp. 1009-1012
[6] ***, EPA 520/5-87-005, Gray D.J, Windham S.T, United States Environmental Protection Agency, Montgomery, 1987
[7] Živanović, M. Z., *et al*., Radon Measurements with Charcoal Canisters, *Nucl Technol Radiat, 31* (2016), 1, pp. 65-72
[8] Stojanovska, Z., *et al*., Prediction of Long-Term Indoor Radon Concentrations Based on Short-Term Measurements, *Nucl Technol Radiat, 32* (2017), 1, pp. 77-84
[9] Nikolić, M. D., *et al*., Modelling Radiation Exposure in Homes from Siporex Blocks by Using Exhalation Rates of Radon, *Nucl Technol Radiat, 30* (2015), 4, pp. 301-305
[10] Brun, R., Rademakers, F., ROOT – An Object Oriented Data Analysis Framework, *Nucl. Inst. Meth. in Phys. Res., A 389* (1997), 1-2, pp. 81-86

[11] Hoecker, A., *et al*., TMVA – Toolkit for Multivariate Data Analysis, PoS ACAT 040, arXiv:physics/070 303, 2007
[12] Murray, F. W., On the Computation of Saturation Vapor Pressure, *J. Applied Meteorology, 6* (1967), 1, pp. 203-204
[13] Tetens, O., About Some Meteorological Aspects (in German), *Z. Geophys, 6* (1930), pp. 207-309

Received on October 6, 2018
Accepted on June 8, 2018

Владимир И. УДОВИЧИЋ, Димитрије М. МАЛЕТИЋ, Радомир М. БАЊАНАЦ, Дејан Р. ЈОКОВИЋ, Александар Л. ДРАГИЋ, Никола Б. ВЕСЕЛИНОВИЋ, Јелена З. ЖИВАНОВИЋ, Михаило Р. САВИЋ, Софија М. ФОРКАПИЋ

СТУДИЈА СЛУЧАЈА ВИШЕГОДИШЊЕ ВАРИЈАБИЛНОСТИ РАДОНА У ПОРОДИЧНОЈ КУЋИ У СРБИЈИ

Понашање радона у затвореном простору има сложену динамику због утицаја великог броја различитих параметара који утичу на његову варијабилност: метеоролошких (температура, притисак и релативна влажност), концентрације аеросола, брзине размене између унутрашњег и спољашњег ваздуха, грађевинских материјала и животних навика. Као резултат, концентрација радона у затвореним просторијама показује варијацију, уз стандардну периодичност од једног дана и једне године. Годишња варијабилност је добро позната сезонска варијација концентрације радона. Посебно је интересантно пратити вишегодишње варијације концентрације радона на истој мерној локацији и временском периоду, пре свега због процене индивидуалних годишњих доза од изложености радону. У типичној породичној кући у Србији извршена су дуготрајна мерења радона у дневном боравку. Мерења су рађена током 2014, 2015, и 2016. године, у фебруару и јулу, сваке године. Коришћене су следеће мерне технике: активна и метода коришћења угљених канистера. Добијени резултати анализирани су коришћењем мултиваријантне регресионе анализе.

Кључне речи: варијабилност радона, мултиваријантна регресиона анализа, радон у затвореним просторијама, вишегодишње мерење радона

Lattice design and expected performance of the Muon Ionization Cooling Experiment demonstration of ionization cooling

M. Bogomilov,[1] R. Tsenov,[1] G. Vankova-Kirilova,[1] Y. Song,[2] J. Tang,[2] Z. Li,[3] R. Bertoni,[4] M. Bonesini,[4] F. Chignoli,[4] R. Mazza,[4] V. Palladino,[5] A. de Bari,[6] G. Cecchet,[6] D. Orestano,[7] L. Tortora,[7] Y. Kuno,[8] S. Ishimoto,[9] F. Filthaut,[10] D. Jokovic,[11] D. Maletic,[11] M. Savic,[11] O. M. Hansen,[12] S. Ramberger,[12] M. Vretenar,[12] R. Asfandiyarov,[13] A. Blondel,[13] F. Drielsma,[13] Y. Karadzhov,[13] G. Charnley,[14] N. Collomb,[14] K. Dumbell,[14] A. Gallagher,[14] A. Grant,[14] S. Griffiths,[14] T. Hartnett,[14] B. Martlew,[14] A. Moss,[14] A. Muir,[14] I. Mullacrane,[14] A. Oates,[14] P. Owens,[14] G. Stokes,[14] P. Warburton,[14] C. White,[14] D. Adams,[15] R. J. Anderson,[15] P. Barclay,[15] V. Bayliss,[15] J. Boehm,[15] T. W. Bradshaw,[15] M. Courthold,[15] V. Francis,[15] L. Fry,[15] T. Hayler,[15] M. Hills,[15] A. Lintern,[15] C. Macwaters,[15] A. Nichols,[15] R. Preece,[15] S. Ricciardi,[15] C. Rogers,[15] T. Stanley,[15] J. Tarrant,[15] M. Tucker,[15] A. Wilson,[15] S. Watson,[16] R. Bayes,[17] J. C. Nugent,[17] F. J. P. Soler,[17] R. Gamet,[18] G. Barber,[19] V. J. Blackmore,[19] D. Colling,[19] A. Dobbs,[19] P. Dornan,[19] C. Hunt,[19] A. Kurup,[19] J.-B. Lagrange,[19,*] K. Long,[19] J. Martyniak,[19] S. Middleton,[19] J. Pasternak,[19] M. A. Uchida,[19] J. H. Cobb,[20] W. Lau,[20] C. N. Booth,[21] P. Hodgson,[21] J. Langlands,[21] E. Overton,[21] M. Robinson,[21] P. J. Smith,[21] S. Wilbur,[21] A. J. Dick,[22] K. Ronald,[22] C. G. Whyte,[22] A. R. Young,[22] S. Boyd,[23] P. Franchini,[23] J. R. Greis,[23] C. Pidcott,[23] I. Taylor,[23] R. B. S. Gardener,[24] P. Kyberd,[24] J. J. Nebrensky,[24] M. Palmer,[25] H. Witte,[25] A. D. Bross,[26] D. Bowring,[26] A. Liu,[26] D. Neuffer,[26] M. Popovic,[26] P. Rubinov,[26] A. DeMello,[27] S. Gourlay,[27] D. Li,[27] S. Prestemon,[27] S. Virostek,[27] B. Freemire,[28] P. Hanlet,[28] D. M. Kaplan,[28] T. A. Mohayai,[28] D. Rajaram,[28] P. Snopok,[28] V. Suezaki,[28] Y. Torun,[28] Y. Onel,[29] L. M. Cremaldi,[30] D. A. Sanders,[30] D. J. Summers,[30] G. G. Hanson,[31] and C. Heidt[31]

(The MICE collaboration)

[1]*Department of Atomic Physics, St. Kliment Ohridski University of Sofia, Sofia 1164, Bulgaria*
[2]*Institute of High Energy Physics, Chinese Academy of Sciences, Beijing 100039, China*
[3]*Sichuan University, Sichuan Sheng 610000, China*
[4]*Sezione INFN Milano Bicocca, Dipartimento di Fisica G. Occhialini, Milano 20126, Italy*
[5]*Sezione INFN Napoli and Dipartimento di Fisica, Università Federico II, Complesso Universitario di Monte S. Angelo, Napoli 80126, Italy*
[6]*Sezione INFN Pavia and Dipartimento di Fisica, Pavia 27100, Italy*
[7]*INFN Sezione di Roma Tre and Dipartimento di Matematica e Fisica, Università Roma Tre, 00146 Roma, Italy*
[8]*Osaka University, Graduate School of Science, Department of Physics, Toyonaka, Osaka 565-0871, Japan*
[9]*High Energy Accelerator Research Organization (KEK), Institute of Particle and Nuclear Studies, Tsukuba 305-0801, Ibaraki, Japan*
[10]*Nikhef, Amsterdam, The Netherlands and Radboud University, Nijmegen 1098, The Netherlands*
[11]*Institute of Physics, University of Belgrade, Belgrade 11080, Serbia*
[12]*CERN, Geneva 1217, Switzerland*
[13]*DPNC, Section de Physique, Université de Genève, Geneva 1205, Switzerland*
[14]*STFC Daresbury Laboratory, Daresbury, Cheshire WA4 4AD, United Kingdom*
[15]*STFC Rutherford Appleton Laboratory, Harwell Oxford, Didcot OX11 0QX, United Kingdom*
[16]*STFC Rutherford UK Astronomy Technology Centre, Royal Observatory, Edinburgh, Blackford Hill, Edinburgh EH9 3HJ, United Kingdom*
[17]*School of Physics and Astronomy, Kelvin Building, The University of Glasgow, Glasgow G12 8SU, United Kingdom*
[18]*Department of Physics, University of Liverpool, Liverpool L69 7ZE, United Kingdom*
[19]*Department of Physics, Blackett Laboratory, Imperial College London, London SW7 2BB, United Kingdom*
[20]*Department of Physics, University of Oxford, Denys Wilkinson Building, Oxford OX1 3PJ, United Kingdom*
[21]*Department of Physics and Astronomy, University of Sheffield, Sheffield S10 2TN, United Kingdom*
[22]*SUPA and the Department of Physics, University of Strathclyde, Glasgow G1 1XQ, United Kingdom and Cockroft Institute, United Kingdom*
[23]*Department of Physics, University of Warwick, Coventry CV4 7AL, United Kingdom*
[24]*Brunel University, Uxbridge UB8 3PH, United Kingdom*
[25]*Brookhaven National Laboratory, New York NY 11967, USA*
[26]*Fermilab, Batavia, Illinois 60510, USA*

[27]*Lawrence Berkeley National Laboratory, Berkeley, California 94720, USA*
[28]*Illinois Institute of Technology, Chicago, Illinois 60616, USA*
[29]*Department of Physics and Astronomy, University of Iowa, Iowa City, Iowa 52242, USA*
[30]*University of Mississippi, Oxford, Mississippi 38677, USA*
[31]*University of California, Riverside, California 92521, USA*
(Received 30 January 2017; published 19 June 2017)

Muon beams of low emittance provide the basis for the intense, well-characterized neutrino beams necessary to elucidate the physics of flavor at a neutrino factory and to provide lepton-antilepton collisions at energies of up to several TeV at a muon collider. The international Muon Ionization Cooling Experiment (MICE) aims to demonstrate ionization cooling, the technique by which it is proposed to reduce the phase-space volume occupied by the muon beam at such facilities. In an ionization-cooling channel, the muon beam passes through a material in which it loses energy. The energy lost is then replaced using rf cavities. The combined effect of energy loss and reacceleration is to reduce the transverse emittance of the beam (transverse cooling). A major revision of the scope of the project was carried out over the summer of 2014. The revised experiment can deliver a demonstration of ionization cooling. The design of the cooling demonstration experiment will be described together with its predicted cooling performance.

DOI: 10.1103/PhysRevAccelBeams.20.063501

I. INTRODUCTION

Stored muon beams have been proposed as the source of neutrinos at a neutrino factory [1,2] and as the means to deliver multi-TeV lepton-antilepton collisions at a muon collider [3,4]. In such facilities the muon beam is produced from the decay of pions generated by a high-power proton beam striking a target. The tertiary muon beam occupies a large volume in phase space. To optimize the muon yield while maintaining a suitably small aperture in the muon-acceleration system requires that the muon beam be "cooled" (i.e., its phase-space volume reduced) prior to acceleration. A muon is short-lived, decaying with a lifetime of 2.2 μs in its rest frame. Therefore, beam manipulation at low energy ($\lesssim$1 GeV) must be carried out rapidly. Four cooling techniques are in use at particle accelerators: synchrotron-radiation cooling [5]; laser cooling [6–8]; stochastic cooling [9]; and electron cooling [10]. Synchrotron-radiation cooling is observed only in electron or positron beams, owing to the relatively low mass of the electron. Laser cooling is limited to certain ions and atomic beams. Stochastic cooling times are dependent on the bandwidth of the stochastic-cooling system relative to the frequency spread of the particle beam. The electron-cooling time is limited by the available electron density and the electron-beam energy and emittance. Typical cooling times are between seconds and hours, long compared with the muon lifetime. Ionization cooling proceeds by passing a muon beam through a material, the absorber, in which it loses energy through ionization, and subsequently restoring the lost energy in accelerating cavities. Transverse and longitudinal momentum are lost in equal proportions in the absorber, while the cavities restore only the momentum component parallel to the beam axis. The net effect of the energy-loss/reacceleration process is to decrease the ratio of transverse to longitudinal momentum, thereby decreasing the transverse emittance of the beam. In an ionization-cooling channel the cooling time is short enough to allow the muon beam to be cooled efficiently with modest decay losses. Ionization cooling is therefore the technique by which it is proposed to cool muon beams [11–13]. This technique has never been demonstrated experimentally and such a demonstration is essential for the development of future high-brightness muon accelerators.

The international Muon Ionization Cooling Experiment (MICE) collaboration proposes a two-part process to perform a full demonstration of transverse ionization cooling. First, the "Step IV" configuration [14] will be used to study the material and beam properties that determine the performance of an ionization-cooling lattice. Second, a study of transverse-emittance reduction in a cooling cell that includes accelerating cavities will be performed.

The cooling performance of an ionization-cooling cell depends on the emittance and momentum of the initial beam, on the properties of the absorber material and on the transverse betatron function ($\beta_\perp$) at the absorber. These factors will be studied using the Step IV configuration. Once this has been done, "sustainable" ionization cooling must be demonstrated. This requires restoring energy lost by the muons as they pass through the absorber using rf cavities. The experimental configuration with which the MICE collaboration originally proposed to study ionization cooling was presented in [15]. This configuration was revised to accelerate the timetable on which a demonstration of ionization cooling could be delivered and to reduce

*j.lagrange@imperial.ac.uk

cost. This paper describes the revised lattice proposed by the MICE collaboration for the demonstration of ionization cooling and presents its performance.

II. COOLING IN NEUTRINO FACTORIES AND MUON COLLIDERS

At production, muons occupy a large volume of phase space. The emittance of the initial muon beam must be reduced before the beam is accelerated. A neutrino factory [16] requires the transverse emittance to be reduced from 15–20 mm to 2–5 mm. A muon collider [17] requires the muon beam to be cooled in all six phase-space dimensions; to achieve the desired luminosity requires an emittance of ∼0.025 mm in the transverse plane and ∼70 mm in the longitudinal direction [18,19].

Ionization cooling is achieved by passing a muon beam through a material with low atomic number (Z), in which it loses energy by ionization, and subsequently accelerating the beam. The rate of change of the normalized transverse emittance, $\varepsilon_\perp$, is given approximately by [12,20,21]:

$$\frac{\mathrm{d}\varepsilon_\perp}{\mathrm{d}z} \simeq -\frac{\varepsilon_\perp}{\beta^2 E_\mu}\left\langle\frac{\mathrm{d}E}{\mathrm{d}z}\right\rangle + \frac{\beta_\perp (13.6\ \mathrm{MeV}/c)^2}{2\beta^3 E_\mu m_\mu X_0}; \qquad (1)$$

where z is the longitudinal coordinate, βc is the muon velocity, E_μ the energy, $\langle\frac{\mathrm{d}E}{\mathrm{d}z}\rangle$ the mean rate of energy loss per unit path-length, m_μ the mass of the muon, X_0 the radiation length of the absorber and $\beta_\perp$ the transverse betatron function at the absorber. The first term of this equation describes "cooling" by ionization energy loss and the second describes "heating" by multiple Coulomb scattering. Equation (1) implies that the equilibrium emittance, for which $\frac{\mathrm{d}\varepsilon_\perp}{\mathrm{d}z} = 0$, and the asymptotic value of $\frac{\mathrm{d}\varepsilon_\perp}{\mathrm{d}z}$ for large emittance are functions of muon-beam energy.

In order to have good performance in an ionization-cooling channel, $\beta_\perp$ needs to be minimized and $X_0\langle\frac{\mathrm{d}E}{\mathrm{d}z}\rangle$ maximised. The betatron function at the absorber is minimized using a suitable magnetic focusing channel (typically solenoidal) [22,23] and $X_0\langle\frac{\mathrm{d}E}{\mathrm{d}z}\rangle$ is maximized using a low-Z absorber such as liquid hydrogen (LH_2) or lithium hydride (LiH) [24].

III. THE MUON IONIZATION COOLING EXPERIMENT

The muons for MICE come from the decay of pions produced at an internal target dipping directly into the circulating proton beam in the ISIS synchrotron at the Rutherford Appleton Laboratory (RAL) [25,26]. A beam line of 9 quadrupoles, 2 dipoles and a superconducting "decay solenoid" collects and transports the momentum-selected beam into the experiment [27]. The small fraction of pions that remain in the beam may be rejected during analysis using the time-of-flight hodoscopes and Cherenkov counters that are installed in the beam line upstream of the experiment [28]. A diffuser is installed at the upstream end of the experiment to vary the initial emittance of the beam. Ionization cooling depends on momentum through β, E_μ and $\langle\frac{\mathrm{d}E}{\mathrm{d}z}\rangle$ as shown in Eq. (1). It is therefore proposed that the performance of the cell be measured for momenta in the range 140 MeV/c to 240 MeV/c [15].

A. The configuration of the ionization-cooling experiment

The configuration proposed for the demonstration of ionization cooling is shown in Fig. 1. It contains a cooling cell sandwiched between two spectrometer-solenoid modules. The cooling cell is composed of two 201 MHz cavities, one primary (65 mm) and two secondary (32.5 mm) LiH absorbers placed between two superconducting "focus-coil" (FC) modules. Each FC has two separate windings that can be operated either with the same or in opposed polarity.

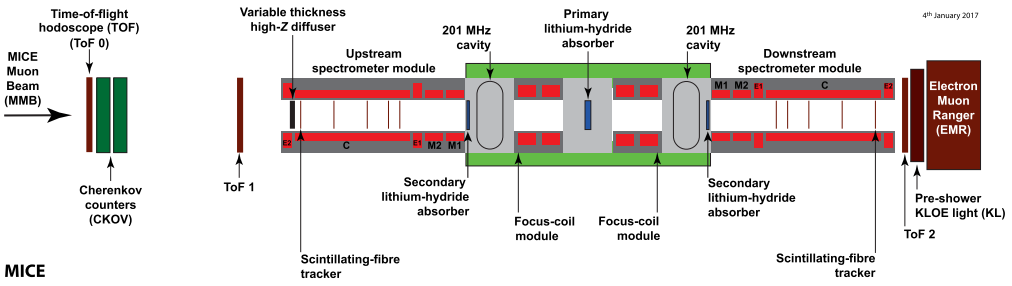

FIG. 1. Layout of the lattice configuration for the cooling demonstration. The red rectangles represent the solenoids. The individual coils in the spectrometer solenoids are labeled E1, C, E2, M1 and M2. The ovals represent the rf cavities and the blue rectangles the absorbers. The various detectors (time-of-flight hodoscopes [29,30], Cerenkov counters [31], scintillating-fibre trackers [32], KLOE Light (KL) calorimeter [27,33], electron muon ranger [34]) used to characterize the beam are also represented. The green-shaded box indicates the cooling cell.

The emittance is measured upstream and downstream of the cooling cell using scintillating-fiber tracking detectors [32] immersed in the uniform 4 T magnetic field provided by three superconducting coils (E1, C, E2). The trackers are used to reconstruct the trajectories of individual muons at the entrance and exit of the cooling cell. The reconstructed tracks are combined with information from instrumentation upstream and downstream of the spectrometer modules to measure the muon-beam emittance at the upstream and downstream tracker reference planes. The instrumentation upstream and downstream of the spectrometer modules serves to select a pure sample of muons. Time-of-flight hodoscopes are used to determine the time at which the muon crosses the rf cavities. The spectrometer-solenoid magnets also contain two superconducting "matching" coils (M1, M2) that are used to match the optics between the uniform field region and the neighboring FC.

The secondary LiH absorbers (SAs) are introduced between the cavities and the trackers to minimize the exposure of the trackers to "dark-current" electrons originating from the rf cavities. Experiments at the MuCool Test Area (MTA) at Fermilab [35] have observed that the rate of direct x-ray production from the rf cavities can be managed to ensure it does not damage the trackers [36]. The SAs are introduced to minimize the exposure of the trackers to energetic dark-current electrons that could produce background hits. The SAs are positioned between the trackers and the cavities such that they can be removed to study the empty channel. The SAs increase the net transverse-cooling effect since the betatron functions at these locations are small.

Retractable lead radiation shutters will be installed on rails between the spectrometer solenoids and the rf modules to protect the trackers against dark-current induced radiation during cavity conditioning. The SAs will be mounted on a rail system similar to that which will be used for the lead shutters and will be located between the cavities and the lead shutters. Both mechanisms will be moved using linear piezoelectric motors that operate in vacuum and magnetic field. The design of both the radiation shutter and the movable SA inside the vacuum chamber is shown in Fig. 2.

The rf cavities are 201 MHz "pillbox" resonators, 430 mm in length, operating in the TM_{010} mode with large diameter apertures to accommodate the high emittance beam. The apertures are covered by thin (0.38 mm) beryllium windows to define the limits for the accelerating rf fields whilst minimizing the scattering of muons. The cavity is excited by two magnetic-loop couplers on opposite sides of the cavity. At the particle rate expected in MICE there is no beam-loading of the rf fields. An effective peak field of 10.3 MV/m is expected for a drive power of 1.6 MW to each cavity. This estimate was used to define the gradient in the simulations described below.

The original configuration of the MICE cooling cell described in [15] was composed of three focus-coil modules, each of which housed a liquid-hydrogen absorber, and two, four-cavity, linac modules. Each linac module incorporated a large, superconducting "coupling coil" to transport the beam. The configuration described in this paper was developed to simplify the lattice described in [15] such that the coupling coils are not required and acceleration is provided by two single-cavity modules. The revision of the magnetic lattice substantially reduces the technical risks associated with the implementation of the experiment since all of the superconducting solenoids required to transport and focus the beam have been commissioned on the beam line. Further, by reducing the number of cavities from eight to two and reconfiguring the rf-power-distribution system the cost of implementing the experiment has been reduced and the timetable on which the experiment can be mounted has been advanced. The present configuration was optimized to maximize its cooling performance as described in Sec. IV. The performance of the optimized lattice, though reduced compared to that described in [15], is sufficient for the principle of ionization-cooling to be demonstrated (see Sec. VI).

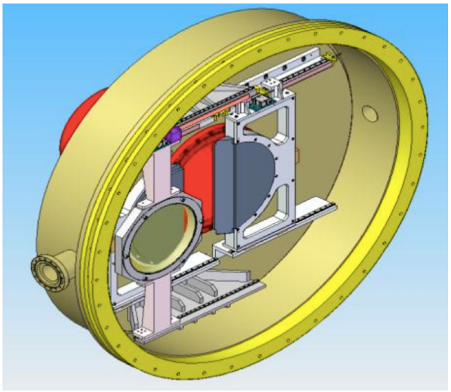

FIG. 2. Design of the movable frame for the secondary absorber (front) and the lead radiation shutter (back). The half discs of the lead shutter (grey) can be seen together with the rails (white) inside the vacuum chamber (yellow).

IV. LATTICE DESIGN

A. Design parameters

The lattice has been optimized to maximize the reduction in transverse emittance. The optimum is obtained by matching the betatron function to a small value in the central absorber while minimizing its maximum values in the FC modules; limiting the size of the betatron function in the FCs helps to reduce the influence of nonlinear terms in the magnetic-field expansion. The matching accounts for the change in energy of the muons as they pass through the cooling cell by adjusting currents in the upstream and

downstream FCs and in the matching coils in the spectrometer solenoids independently while maintaining the field in the tracking volumes at 4 T. In this configuration, it is also possible to keep the betatron function relatively small at the position of the secondary absorbers whilst maintaining an acceptable beam size at the position of the cavities.

Chromatic aberrations caused by the large momentum spread of the beam (∼5% rms) lead to a chromatic mismatch of the beam in the downstream solenoid unless the phase advance across the cooling cell (i.e., the rate of rotation of the phase-space ellipse) is chosen appropriately. The phase advance of the cell is obtained by integrating the inverse of the beta-function along the beam axis from the reference plane in the upstream spectrometer-solenoid to the reference plane in the downstream spectrometer-solenoid. Such a mismatch reduces the effective transverse-emittance reduction through the chromatic decoherence that results from the superposition of beam evolutions for the different betatron frequencies that result from the range of momenta in the beam. For beams with a large input emittance, spherical aberrations may lead to phase-space filamentation. The chromatic and spherical aberrations were studied by tracking samples of muons through the lattice using the "MICE Analysis User Software" (MAUS, see Sec. V). The betatron-function and emittance evolution of a 200 MeV/c beam with the initial parameters given in Table I are shown, for different phase advances, in Figs. 3 and 4, respectively. The phase advance of $2\pi \times 1.81$ showed the largest transverse-emittance reduction and was therefore chosen. The lattice parameters for this phase advance are presented in Table II.

TABLE I. General parameters of the initial beam conditions used in the simulations.

Parameter	Value
Particle	muon μ^+
Number of particles	10000
Longitudinal position [mm]	−4612.1
Central energy (140 MeV/c settings) [MeV]	175.4
Central energy (200 MeV/c settings) [MeV]	228.0
Central energy (240 MeV/c settings) [MeV]	262.2
Transverse Gaussian distribution:	
$\alpha_\perp$	0
$\beta_\perp$ (140 MeV/c settings) [mm]	233.5
$\varepsilon_\perp$ (140 MeV/c settings) [mm]	4.2
$\beta_\perp$ (200 MeV/c settings) [mm]	339.0
$\varepsilon_\perp$ (200 MeV/c settings) [mm]	6.0
$\beta_\perp$ (240 MeV/c settings) [mm]	400.3
$\varepsilon_\perp$ (240 MeV/c settings) [mm]	7.2
Longitudinal Gaussian distribution:	
Longitudinal emittance [mm]	20
Longitudinal β [ns]	11
Longitudinal α	−0.7
rms momentum spread (140 MeV/c settings)	4.8%
rms time spread (140 MeV/c settings) [ns]	0.40
rms momentum spread (200 MeV/c settings)	4.0%
rms time spread (200 MeV/c settings) [ns]	0.34
rms momentum spread (240 MeV/c settings)	3.6%
rms time spread (240 MeV/c settings) [ns]	0.31

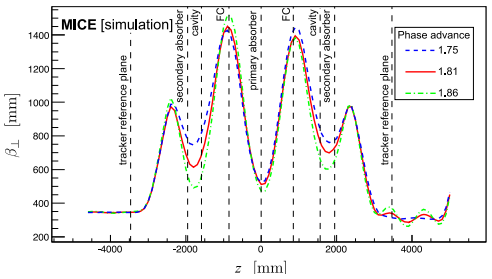

FIG. 3. Transverse 4D beta-function versus longitudinal coordinate z in the cooling-demonstration lattice for 200 MeV/c settings with a phase advance of $2\pi \times 1.75$ (dashed blue line), $2\pi \times 1.81$ (solid red line) and $2\pi \times 1.86$ (dot-dashed green line). The vertical dashed lines with labels show the positions of the tracker reference planes and the centers of the absorbers, rf cavities, and focus coil modules.

The currents that produce the optimum magnetic lattice were obtained using the procedure described above for three momentum settings: 140 MeV/c, 200 MeV/c, and 240 MeV/c. The magnetic field on axis for each of these settings is shown in Fig. 5. The fields in the downstream FC and spectrometer are opposite to those in the upstream FC and spectrometer, the field changing sign at the primary absorber. Such a field flip is required in an ionization cooling channel to reduce the build-up of canonical angular momentum [37]. The currents required to produce the magnetic fields shown in Fig. 5 are listed in Table III. All currents are within the proven limits of operation for the

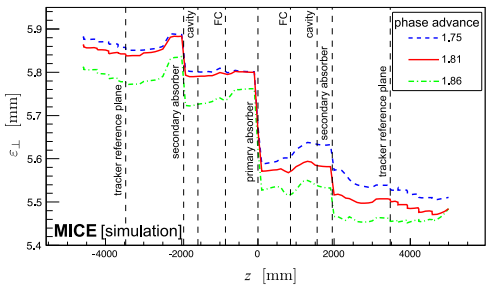

FIG. 4. 4D emittance evolution in the cooling-demonstration lattice for 200 MeV/c settings with a phase advance of $2\pi \times 1.75$ (dashed blue line), $2\pi \times 1.81$ (solid red line) and $2\pi \times 1.86$ (dot-dashed green line). The vertical dashed lines with labels show the positions of the tracker reference planes and the centers of the absorbers, rf cavities, and focus coil modules.

TABLE II. Parameters of the cooling-demonstration lattice. $L_{SS\to FC}$ is the distance between the center of the spectrometer solenoid and the center of the neighboring FC, $L_{FC\to FC}$ the distance between the centers of the FCs, and $L_{RF\ module\to FC}$ the distance between the rf module and the neighboring FC.

Parameter	Value
Length $L_{SS\to FC}$ [mm]	2607.5
Length $L_{FC\to FC}$ [mm]	1678.8
Length $L_{rf\ module\to FC}$ [mm]	784.0
rf Gradient [MV/m]	10.3
Number of rf cavities	2
Number of primary absorbers	1
Number of secondary absorbers	2

individual coil windings. The magnetic forces acting on the coils have been analyzed and were found to be acceptable. Configurations in which there is no field flip can also be considered.

Figure 6 shows matched betatron functions versus longitudinal position for beams of different initial momentum. These betatron functions are constrained, within the fiducial-volume of the trackers, by the requirements on the Courant-Snyder parameters $\alpha_\perp = 0$ and $\beta_\perp = \frac{2p_z}{eB_z}$ (where p_z is the mean longitudinal momentum of the beam, e the elementary charge and B_z the longitudinal component of the magnetic field). A small betatron-function "waist" in the central absorber is achieved. Betatron-function values at relevant positions in the different configurations are summarized in Table IV.

V. SIMULATION

Simulations to evaluate the performance of the lattice have been performed using the official MICE simulation and reconstruction software MAUS (MICE Analysis User Software) [38]. In addition to simulation, MAUS also provides a framework for data analysis. MAUS is used for offline analysis and to provide fast real-time detector reconstruction and data visualisation during MICE running. MAUS uses GEANT4 [39,40] for beam propagation and the simulation of detector response. ROOT [41] is used for data visualisation and for data storage.

Particle tracking has been performed for several configurations. The parameters of the initial beam configurations used for the simulations are summarized in Table I.

TABLE III. Coil currents used for 140 MeV/c, 200 MeV/c, and 240 MeV/c lattice settings.

Coil	140 MeV/c Lattice [A]	200 MeV/c Lattice [A]	240 MeV/c Lattice [A]
Upstream E2	+253.00	+253.00	+253.00
Upstream C	+274.00	+274.00	+274.00
Upstream E1	+234.00	+234.00	+234.00
Upstream M2	+126.48	+155.37	+163.50
Upstream M1	+175.89	+258.42	+280.72
Upstream FC-coil 1	+54.14	+79.35	+89.77
Upstream FC-coil 2	+54.14	+79.35	+89.77
Downstream FC-coil 1	−47.32	−74.10	−85.35
Downstream FC-coil 2	−47.32	−74.10	−85.35
Downstream M1	−140.43	−231.60	−261.71
Downstream M2	−100.12	−149.15	−159.21
Downstream E1	−234.00	−234.00	−234.00
Downstream C	−274.00	−274.00	−274.00
Downstream E2	−253.00	−253.00	−253.00

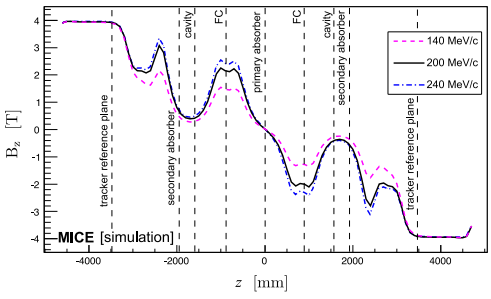

FIG. 5. Magnetic field B_z on-axis versus the longitudinal coordinate z for the cooling-demonstration lattice design for 200 MeV/c (solid black line), 140 MeV/c (dashed purple line), and 240 MeV/c (dot-dashed blue line) settings. The vertical dashed lines with labels show the positions of the tracker reference planes and the centres of the absorbers, rf cavities, and focus coil modules.

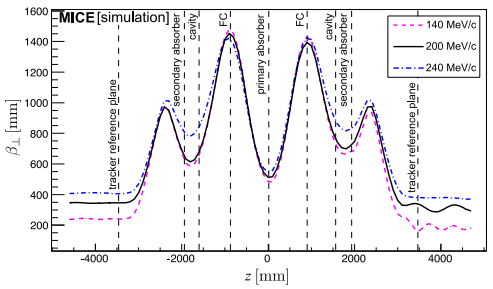

FIG. 6. $\beta_\perp$ versus the longitudinal coordinate z for 200 MeV/c (solid black line), 140 MeV/c (dashed purple line) and 240 MeV/c (dot-dashed blue line) in the cooling-demonstration lattice. The vertical dashed lines with labels show the positions of the tracker reference planes and the centers of the absorbers, rf cavities, and focus coil modules.

TABLE IV. Beta-function values at relevant positions for an initial beam at 140 MeV/c, 200 MeV/c, and 240 MeV/c in the cooling-demonstration lattice design.

Parameter	Value for 140 MeV/c	Value for 200 MeV/c	Value for 240 MeV/c
$\beta_\perp$ at primary absorber [mm]	480	512	545
$\beta_\perp$ at upstream secondary absorber [mm]	660	710	840
$\beta_\perp$ at downstream secondary absorber [mm]	680	740	850
$\beta_{\perp\,\mathrm{max}}$ at FC [mm]	1480	1450	1430

The simulation of the beam starts at a point between the diffuser and the first plane of the tracker. The beam is generated by a randomizing algorithm with a fixed seed. The number of particles launched for each simulation is a compromise between the statistical uncertainty required (≈1%) and computing time. Each cavity is simulated by a TM_{010} ideal cylindrical pillbox with a peak effective gradient matched to that expected for the real cavities. The reference particle is used to set the phase of the cavities so that it is accelerated "on crest." The initial distributions defined in Table I are centred on the reference particle in both time and momentum. Table V lists the acceptance criteria applied to all analyses presented here. Trajectories that fail to meet the acceptance criteria are removed from the analysis.

The normalized transverse emittance is calculated by taking the fourth root of the determinant of the four-dimensional phase-space covariance matrix [20,21]. The MICE collaboration plans to take data such that the statistical uncertainty on the relative change in emittance for a particular setting is 1%. The MICE instrumentation was designed such that the systematic uncertainty related to the reconstruction of particle trajectories would contribute at the ∼0.3% level to the overall systematic uncertainty [15]; such uncertainties would thus be negligible.

VI. PERFORMANCE

Figure 7 shows the evolution of the mean energy of a muon beam as it traverses the lattice. Beams with initial normalised transverse emittance $\varepsilon_\perp = 4.2$ mm, $\varepsilon_\perp = 6$ mm, and $\varepsilon_\perp = 7.2$ mm for initial muon beam momenta of 140 MeV/c, 200 MeV/c, and 240 MeV/c respectively are shown. The initial normalized transverse emittance is chosen such that the geometrical emittance of the three beams is the same. A 200 MeV/c muon passing through two 32.5 mm thick secondary LiH absorbers and one 65 mm thick primary LiH absorber loses an energy of 18.9 MeV. Including losses in the scintillating-fiber

TABLE V. Acceptance criteria for analysis.

Parameter	Acceptance condition
Particle	muon μ^+
Transmission: pass through two planes	$z = -4600$ mm and $z = 5000$ mm
Radius at $z = -4600$ mm	≤150.0 mm
Radius at $z = 5000$ mm	≤150.0 mm

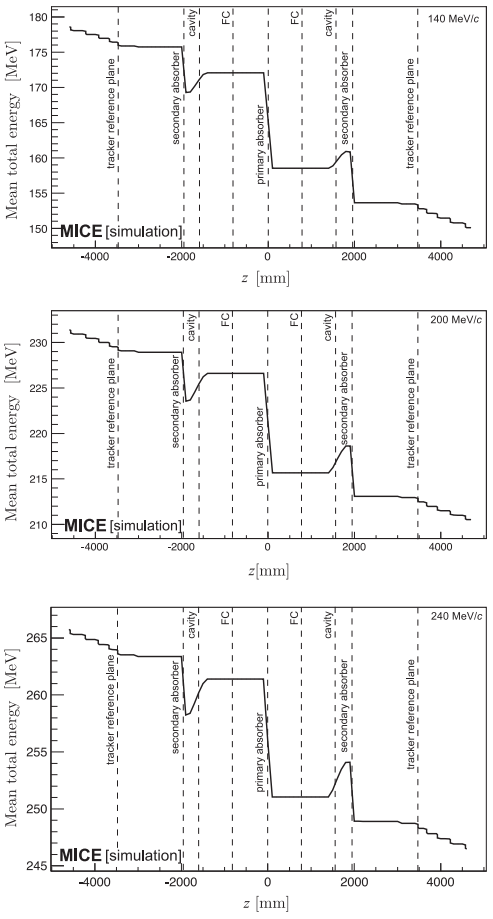

FIG. 7. Mean energy of the beam versus longitudinal coordinate (z) in the cooling-demonstration lattice. Top: the 140 MeV/c configuration for initial emittance $\varepsilon_\perp = 4.2$ mm. Middle: the 200 MeV/c configuration for initial emittance $\varepsilon_\perp = 6$ mm. Bottom: the 240 MeV/c configuration for initial emittance $\varepsilon_\perp = 7.2$ mm. The vertical dashed lines with labels show the positions of the tracker reference planes, and the centers of the absorbers, rf cavities, and focus coil modules.

trackers and windows, this increases to 24.3 MeV. The accelerating gradient that can be achieved in each of the two cavities is constrained by the available rf power and is insufficient to replace all the lost energy. Therefore, a comparison of beam energy with and without acceleration is required. With acceleration an energy deficit of $\langle \Delta E \rangle = 19$ MeV will be observed. This measurable difference will be used to extrapolate the measured cooling effect to that which would pertain if all the lost energy were restored.

The evolution of normalized transverse emittance across the lattice is shown in Fig. 8. The beam is subject to nonlinear effects in regions of high $\beta_\perp$, which cause the normalized transverse emittance to grow, especially in the 140 MeV/c configuration. This phenomenon can be seen in three different regions of the lattice: a moderate increase in emittance is observed at $z \approx -2500$ mm and $z \approx 1000$ mm while a larger increase is observed at $z \approx 3000$ mm. The nonlinear effects are mainly chromatic in origin, since they are greatly lessened when the initial momentum spread is reduced. This is illustrated for the 140 MeV/c case for which the evolution of normalized emittance for beams with an rms momentum spread of 6.7 MeV/c and 2.5 MeV/c are shown. Nonetheless, in all cases a reduction in emittance is observed between the upstream and downstream trackers ($z = \pm 3473$ mm). The lattice is predicted to achieve an emittance reduction between the tracker reference planes of ≈8.1%, ≈5.8% and ≈4.0% in the 140 MeV/c, 200 MeV/c, and 240 MeV/c cases, respectively. A reduction as large as ≈10% can be reached in the 140 MeV/c configuration with an rms momentum spread of 1.4%.

The transmission of the cooling-demonstration lattice for beams of mean momentum 140 MeV/c, 200 MeV/c, and 240 MeV/c is shown in Fig. 9. Transmission is computed as the ratio of the number of particles that satisfy the acceptance criteria observed downstream of the cooling cell divided by the number that enter the cell. This accounts

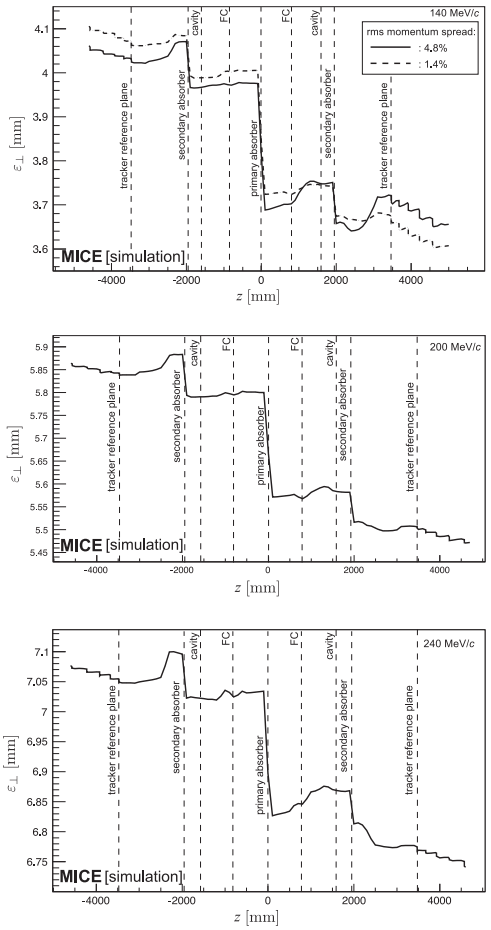

FIG. 8. Emittance variation versus the longitudinal coordinate (z) for the cooling-demonstration lattice design. Top: 140 MeV/c beam with initial $\varepsilon_\perp = 4.2$ mm with an rms momentum spread of 6.7 MeV/c (rms spread 4.8%, solid line) and 2.5 MeV/c (rms spread 1.8%, dashed line). Middle: 200 MeV/c beam with initial $\varepsilon_\perp = 6$ mm (rms spread 4.0%). Bottom: 240 MeV/c beam with initial $\varepsilon_\perp = 7.2$ mm (rms spread 3.6%). The vertical dashed lines with labels show the positions of the tracker reference planes, and the centers of the absorbers, rf cavities, and focus coil modules.

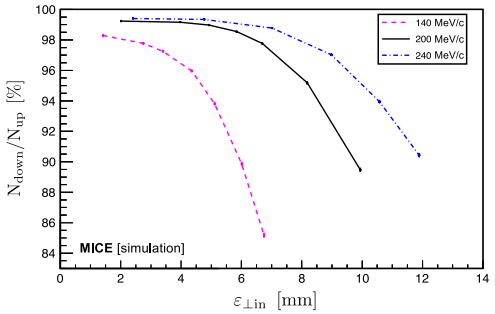

FIG. 9. Transmission (defined as the ratio of good muons observed downstream of the cooling cell, N_{down}, to those observed upstream, N_{up}) in percent versus initial emittance ($\varepsilon_{\perp in}$) for the cooling-demonstration lattice. The transmission of the 140 MeV/c, 200 MeV/c, and 240 MeV/c lattices are shown as the purple-dashed, solid black, and dot-dashed blue lines respectively. The error bars indicate the statistical precision that would be achieved using a sample of 100,000 muons.

for decay losses and implies that, in the absence of scraping or acceptance losses, the maximum transmission for beams of mean momentum 140 MeV/c, 200 MeV/c, and 240 MeV/c is 98.9%, 99.2%, and 99.5%, respectively. The lattice delivers transmission close to the maximum for 200 MeV/c and 240 MeV/c beams with input emittance below ≈5 mm and ≈7 mm, respectively. For beams of larger input emittance, the transmission gradually decreases with increasing initial emittance due to the scraping of high amplitude muons. The beam is subject to chromatic effects in regions of high $\beta_\perp$, which causes nonlinear emittance growth and limits the transmission. The behavior of the transmission for the various beam energies results from the different geometrical emittance values of the beam for the same initial normalised emittance and the energy dependence of the energy loss and scattering in the material through which the beam passes.

The fractional change in normalized transverse emittance with respect to the input emittance for beams of mean momentum 140 MeV/c, 200 MeV/c, and 240 MeV/c is shown in Fig. 10. The different values of the equilibrium emittance and the asymptote at large emittance for each momentum are clearly visible in Fig. 10. A maximum cooling effect of 15%, 8%, and 6% can be observed for beams with 140 MeV/c, 200 MeV/c, and 240 MeV/c, respectively.

The performance of the configuration proposed here is comparable to that described in [15]. In the "Step V" configuration, that incorporated two liquid-hydrogen absorbers each placed within a focus-coil module capable of providing a value $\beta_\perp$ smaller than that which can be achieved with the present lattice, the maximum cooling effect with an input momentum and emittance of 200 MeV/c and 10 mm respectively, was ∼10%. Figures 9 and 10 show the statistical uncertainties that will result from the reconstruction of a sample of 100,000 muons [42] with the configuration proposed in this paper. The instrumentation was specified to ensure that no single source of systematic uncertainty would contribute more than one third of the statistical uncertainty on the fractional change in emittance [15]. All of the instrumentation has been commissioned on the beam-line and performs to specification. The emittance-change evolution presented in Fig. 10 can therefore be measured with high significance.

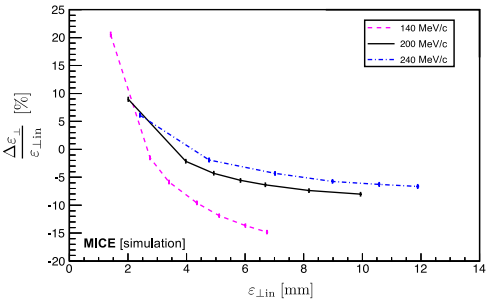

FIG. 10. Fractional change in emittance versus initial emittance ($\varepsilon_{\perp\mathrm{in}}$) for the cooling-demonstration lattice design measured at the tracker reference planes. The fractional change in emittance of the 140 MeV/c, 200 MeV/c, and 240 MeV/c lattices are shown as the purple-dashed, solid black, and dot-dashed blue lines, respectively. The error bars indicate the statistical precision that would be achieved using a sample of 100,000 muons.

VII. CONCLUSION

An experiment by which to demonstrate ionization cooling has been described that is predicted by simulations to exhibit cooling over a range of momentum. The demonstration is performed using lithium-hydride absorbers and with acceleration provided by two 201 MHz cavities. The equipment necessary to mount the experiment is either in hand (the superconducting magnets and instrumentation), or at an advanced stage of preparation. The configuration of the demonstration of ionization cooling has been shown to deliver the performance required for the detailed study of the ionization-cooling technique.

The demonstration of ionization cooling is essential to the future development of muon-based facilities that would provide the intense, well characterized low-emittance muon beams required to elucidate the physics of flavor at a neutrino factory or to deliver multi-TeV lepton-antilepton collisions at a muon collider. The successful completion of the MICE programme would therefore herald the establishment of a new technique for particle physics.

ACKNOWLEDGMENTS

The work described here was made possible by grants from the Science and Technology Facilities Council (UK), the Department of Energy and National Science Foundation (USA), the Instituto Nazionale di Fisica Nucleare (Italy), the Bulgarian Academy of Sciences, the Chinese Academy of Sciences, the Dutch National Science Foundation, the Ministry of Education, Science and Technological Development of the Republic of Serbia, the European Community under the European Commission Framework Programme 7 (AIDA project, Grant Agreement No. 262025, TIARA project, Grant Agreement No. 261905, and EuCARD), the Japan Society for the Promotion of Science and the Swiss National Science Foundation in the framework of the SCOPES programme. We gratefully acknowledge all sources of support. We are grateful to the support given to us by the staff of the STFC Rutherford Appleton and Daresbury Laboratories. We acknowledge the use of Grid computing resources deployed and operated by GridPP in the UK, http://www.gridpp.ac.uk/.

[1] S. Geer, Neutrino beams from muon storage rings: Characteristics and physics potential, Phys. Rev. D **57**, 6989 (1998).

[2] M. Apollonio *et al.*, Oscillation Physics with a Neutrino Factory, arXiv:hep-ph/0210192.

[3] D. V. Neuffer and R. B. Palmer, A high-energy high-luminosity μ^+-μ^- collider in *Proceedings of the Fourth European Particle Accelerator Conference EPAC 94, London, England* (World Scientific, River Edge, NJ, 1994), p. 52.

[4] R. B. Palmer, Muon colliders, Rev. Accel. Sci. Techol. **07**, 137 (2014).

[5] S. Y. Lee, *Accelerator Physics*, 3rd ed., edited by S. Y. Lee (World Scientific, Singapore, 2012).

[6] S. Schröder *et al.*, First laser cooling of relativistic ions in a storage ring, Phys. Rev. Lett. **64**, 2901 (1990).

[7] J. S. Hangst, M. Kristensen, J. S. Nielsen, O. Poulsen, J. P. Schiffer, and P. Shi, Laser cooling of a stored ion beam to 1 mK, Phys. Rev. Lett. **67**, 1238 (1991).

[8] P. J. Channell, Laser cooling of heavy ion beams, J. Appl. Phys. **52**, 3791 (1981).

[9] J. Marriner, Stochastic cooling overview, Nucl. Instrum. Methods Phys. Res., Sect. A **532**, 11 (2004).

[10] V. V. Parkhomchuk and A. N. Skrinsky, Electron cooling: 35 years of development, Phys. Usp. **43**, 433 (2000).

[11] A. N. Skrinsky and V. V. Parkhomchuk, Cooling methods for beams of charged particles, Fiz. Elem. Chastits At. Yadra **12**, 557 (1981) [Sov. J. Part. Nucl. **12**, 223 (1981)].

[12] D. Neuffer, Principles and applications of muon cooling, in *Proceedings, 12th International Conference on High-Energy Accelerators, HEACC 1983: Fermilab, Batavia, 1983*, Vol. C830811 (Fermi National Accelerator Laboratory, Batavia, 1983), p. 481–484.

[13] D. Neuffer, Principles and applications of muon cooling, Part. Accel. **14**, 75 (1983).

[14] D. Rajaram and V. C. Palladino, The status of MICE Step IV, in *Proceedings, 6th International Particle Accelerator Conference (IPAC 2015): Richmond, Virginia, USA, 2015* (JACoW, Geneva, 2015), p. 4000.

[15] MICE Collaboration, MICE: An International Muon Ionization Cooling Experiment, http://mice.iit.edu/micenotes/public/pdf/MICE0021/MICE0021.pdf (2003), MICE Note 21.

[16] M. Apollonio *et al.* (ISS Accelerator Working Group Collaboration), Accelerator design concept for future neutrino facilities, J. Instrum. **4**, P07001 (2009).

[17] C. M. Ankenbrandt *et al.*, Status of muon collider research and development and future plans, Phys. Rev. ST Accel. Beams **2**, 081001 (1999).

[18] M. M. Alsharoa *et al.* (Neutrino Factory and Muon Collider Collaboration), Recent progress in neutrino factory and muon collider research within the Muon collaboration, Phys. Rev. ST Accel. Beams **6**, 081001 (2003).

[19] R. B. Palmer, J. S. Berg, R. C. Fernow, J. C. Gallardo, H. G. Kirk, Y. Alexahin, D. Neuffer, S. A. Kahn, and D. Summers, A complete scheme of ionization cooling for a muon collider, in *Proceedings of the 22nd Particle Accelerator Conference, PAC-2007, Albuquerque, NM* (IEEE, New York, 2007), p. 3193.

[20] G. Penn and J. S. Wurtele, Beam Envelope Equations for Cooling of Muons in Solenoid Fields, Phys. Rev. Lett. **85**, 764 (2000).

[21] C. Rogers, Ph.D. dissertation, Imperial College of London, 2008.

[22] D. Stratakis and R. B. Palmer, Rectilinear six-dimensional ionization cooling channel for a muon collider: A theoretical and numerical study, Phys. Rev. ST Accel. Beams **18**, 031003 (2015).

[23] D. Neuffer, H. Sayed, T. Hart, and D. Summers, Final Cooling for a High-Energy High-Luminosity Lepton Collider, arXiv:1612.08960.

[24] A. V. Tollestrup and J. Monroe, Fermi National Accelerator Laboratory Technical Report No. FERMILAB-MUCOOL-176, 2000.

[25] C. N. Booth *et al.*, The design, construction and performance of the MICE target, J. Instrum. **8**, P03006 (2013).

[26] C. N. Booth *et al.*, The design and performance of an improved target for MICE, J. Instrum. **11**, P05006 (2016).

[27] M. Bogomilov *et al.* (MICE Collaboration), The MICE Muon Beam on ISIS and the beam-line instrumentation of the Muon Ionization Cooling Experiment, J. Instrum. **7**, P05009 (2012).

[28] D. Adams *et al.* (MICE Collaboration), Characterisation of the muon beams for the Muon Ionisation Cooling Experiment, Eur. Phys. J. C **73**, 2582 (2013).

[29] R. Bertoni *et al.*, The design and commissioning of the MICE upstream time-of-flight system, Nucl. Instrum. Methods Phys. Res., Sect. A **615**, 14 (2010).

[30] R. Bertoni, M. Bonesini, A. de Bari, G. Cecchet, Y. Karadzhov, and R. Mazza, The construction of the MICE TOF2 detector, http://mice.iit.edu/micenotes/public/pdf/MICE0286/MICE0286.pdf (2010).

[31] L. Cremaldi, D. A. Sanders, P. Sonnek, D. J. Summers, and J. Reidy, Jr., A Cherenkov radiation detector with high density aerogels, IEEE Trans. Nucl. Sci. **56**, 1475 (2009).

[32] M. Ellis *et al.*, The design, construction and performance of the MICE scintillating fibre trackers, Nucl. Instrum. Methods Phys. Res., Sect. A **659**, 136 (2011).

[33] F. Ambrosino *et al.*, Calibration and performances of the KLOE calorimeter, Nucl. Instrum. Methods Phys. Res., Sect. A **598**, 239 (2009).

[34] R. Asfandiyarov *et al.*, The design and construction of the MICE Electron-Muon Ranger, J. Instrum. **11**, T10007 (2016).

[35] M. Leonova *et al.*, MICE cavity installation and commissioning/operation at MTA, in *Proceedings, 6th International Particle Accelerator Conference (IPAC 2015): Richmond, Virginia, USA, 2015* (JACoW, Geneva, 2015), p. 3342–3344.

[36] Y. Torun *et al.*, Final commissioning of the MICE RF module prototype with production couplers, in *Proceedings, 7th International Particle Accelerator Conference (IPAC 2016): Busan, Korea, 2016* (JACoW, Geneva, 2016), p. 474.

[37] R. C. Fernow and R. B. Palmer, Solenoidal ionization cooling lattices, Phys. Rev. ST Accel. Beams **10**, 064001 (2007).

[38] C. D. Tunnell and C. T. Rogers, MAUS: MICE Analysis User Software, in *Proceedings of the 2nd International Particle Accelerator Conference, San Sebastiáán, Spain* (EPS-AG, Spain, 2011), p. 850.

[39] S. Agostinelli *et al.* (GEANT4 Collaboration), GEANT4: A simulation toolkit, Nucl. Instrum. Methods Phys. Res., Sect. A **506**, 250 (2003).

[40] J. Allison *et al.*, Geant4 developments and applications, IEEE Trans. Nucl. Sci. **53**, 270 (2006).

[41] R. Brun and F. Rademakers, ROOT: An object oriented data analysis framework, Nucl. Instrum. Methods Phys. Res., Sect. A **389**, 81 (1997).

[42] C. Hunt, Ph.D. dissertation, Imperial College of London, 2017.

NUKLEONIKA 2016;61(3):357–360
doi: 10.1515/nuka-2016-0059

ORIGINAL PAPER

DE GRUYTER
OPEN

The use of multivariate analysis of the radon variability in the underground laboratory and indoor environment

**Jelena Filipović,
Dimitrije Maletić,
Vladimir Udovičić,
Radomir Banjanac,
Dejan Joković,
Mihailo Savić,
Nikola Veselinović**

Abstract. The paper presents results of multivariate analysis of variations of radon concentrations in the shallow underground laboratory and a family house, depending on meteorological variables only. All available multivariate classification and regression methods, developed for data analysis in high-energy physics and implemented in the toolkit for multivariate analysis (TMVA) software package in ROOT, are used in the analysis. The result of multivariate regression analysis is a mapped functional behaviour of variations of radon concentration depending on meteorological variables only, which can be used for the evaluation of radon concentration, as well as to help with modelling of variation of radon concentration. The results of analysis of the radon concentration variations in the underground laboratory and real indoor environment, using multivariate methods, demonstrated the potential usefulness of these methods. Multivariate analysis showed that there is a potentially considerable prediction power of variations of indoor radon concentrations based on the knowledge of meteorological variables only. In addition, the online system using the resulting mapped functional behaviour for underground laboratory in the Institute of Physics Belgrade is implemented, and the resulting evaluation of radon concentrations are presented in this paper.

Key words: multivariate analysis • radon variability

J. Filipović, D. Maletić, V. Udovičić✉, R. Banjanac, D. Joković, M. Savić, N. Veselinović
Institute of Physics Belgrade,
University of Belgrade,
118 Pregrevica Str., 11080 Belgrade, Serbia,
E-mail: udovicic@ipb.ac.rs

Received: 4 January 2016
Accepted: 24 March 2016

Introduction

The research of the dynamics of radon in various environments, especially indoors, is of great importance in terms of protection against ionizing radiation and in designing of measures for its reduction. Research of radioactive emanations (of radon (^{222}Rn) and thoron (^{220}Rn)) are in the domain of radiation physics, but since a few decades ago, subject of radioactive emanation involves many other scientific disciplines, thus giving a multidisciplinary character to this research. Published results and development of many models to describe the behaviour of indoor radon indicate the complexity of this research, especially with models for the prediction of the variability of radon, simply because the variability depends on large number of variables. Large number of factors (such as local geology, permeability of soil, building materials used to build the buildings as well as the habits of people) impact the variation of radon, and therefore, it is important to study their correlation. In this paper, the results of correlative analysis of indoor radon and meteorological variables are presented. Furthermore, the results of multivariate classification and regression analysis is presented. More details of this study can be found in [1].

Indoor radon variation depends significantly on large number of factors, which include the local ge-

ology, soil permeability, building materials, lifestyle characteristics and meteorological variables. In order to analyse the dependence of radon variation on multiple variables, multivariate analysis needs to be used.

The demand for detailed analyses of large amount of data in high-energy physics resulted in wide and intense development and usage of multivariate methods. Many of multivariate methods and algorithms for classification and regression are already integrated into the analysis framework ROOT [2], more specifically, into the toolkit for multivariate analysis (TMVA [3]). Multivariate analysis toolkit is used to create, test and apply all available classifiers and regression multivariate methods implemented in the TMVA in order to find methods that are the most appropriate and yield maximum information on the dependence of indoor radon concentrations on the multitude of meteorological variables. Classification methods are used to find out if it is possible to classify radon concentrations into low and high concentrations, using arbitrary cut value for radon concentrations. Regression methods are used as a next step with a goal to find out which regression method can, if any, on the basis of input meteorological variables only, give an output that would satisfactorily close match the observed variations of radon concentrations. The output of usage of multivariate regression analysis methods is mapped functional behaviour, which can be used to evaluate the measurements of radon concentrations using input meteorological variables only. The prediction of radon concentrations can be an output of mapped function when the prediction of input meteorological variables exists.

Short-term radon measurements in laboratory and real environment

Depending on the integrated measurement time, methods of measurement of radon concentrations in air may be divided into long-term and short-term ones. For the measurements of radon concentration presented in this paper, the SN1029 radon monitor (manufactured by the Sun Nuclear Corporation, NRSB approval-code 31822) has been used as active, short-term measurement device. The device consists of two diffused junction photodiodes as a radon detector and is furnished with sensors for temperature, barometric pressure and relative humidity. The user can set the measurement intervals from 30 min to 24 h. It was set to record simultaneously the radon concentration, temperature, atmospheric pressure and relative humidity.

For the purposes of determining the best multivariate methods to use in the analysis, the results are obtained using radon monitor are from measurements in two locations, the Low-Background Laboratory for Nuclear Physics in the Institute of Physics in Belgrade and in a family house.

The underground Low-Background Laboratory for Nuclear Physics is selected for measurement and analysis because routine measurements in this laboratory require low levels of radon concentration with minimum temporal variations. Low-background laboratory is located on the right bank of the river Danube in the Belgrade borough of Zemun, on the grounds of the Institute of Physics. The ground level portion of the laboratory, at 75 m above sea level, is situated at the foot of a vertical loess cliff, about 10 m high. The underground part of the laboratory, useful area of 45 m^2, is dug into the foot of the cliff. Underground laboratory is surrounded with 30-cm thick concrete wall. The overburden of the underground laboratory is thus about 12 m of loess soil. Significant efforts are being made to contain the low radon concentration within the laboratory. The underground laboratory is completely lined with a hermetically sealed, 1-mm thick aluminium foil. The ventilation system maintains the overpressure of 2 mbar, so as to prevent radon diffusion from the soil. Fresh air entering the laboratory is passed through a two-stage filtering system. The first stage is a mechanical filter for dust removal. The second one is a battery of coarse and fine charcoal active filters. The concentration of radon is kept at an average value of about 10 Bq/m^3.

In the Low-Background Laboratory for Nuclear Physics, radon concentrations were measured in period from 2008 to 2011 and continued later on periodically about a couple of months each year. Measurements of meteorological variables used in the analysis were recorded since 2008 and are taken from the meteorological station located 4 km from the laboratory. Measurements of radon concentrations, room temperature, atmospheric pressure and relative humidity inside the laboratory were obtained using radon monitor. The results obtained from the measurements of radon concentrations and their influence on gamma and cosmic ray measurements in the laboratory were published in several articles in international scientific journals [4–6].

The family house selected for the measurements and analysis of variations of radon concentrations is a typical house in Belgrade residential areas, with requirement of existence of cellar. House is built on limestone soil. Radon measurements were carried out in the living room of the family house, which is built of standard materials (brick, concrete, mortar) and isolated with styrofoam. During the period of measurements (spring–summer), the house was naturally ventilated and air conditioning was used in heating mode at the beginning of the measurement period. During the winter period measurements, the electrical heating was used in addition to air conditioning. Measured radon concentrations, room temperature, atmospheric pressure and relative humidity inside the house were obtained using radon monitor. Values of meteorological variables in measurement period were obtained from an automatic meteorological station located 400 m from the house in which the measurement was performed. We used the following meteorological variables: external air temperature, pressure and humidity, solar radiation, wind speed at a height of 10 m above ground, precipitation, evaporation and temperature and humidity of the soil at a depth of 10, 20, 30 and 50 cm.

Correlation and regression analysis of the results

All multivariate methods implemented in the TMVA are used in our search. All multivariate methods in TMVA belong to the family of 'supervised learning' algorithms [1]. All methods make use of training events, for which the desired output is known, to determine the mapping function that either describes a decision boundary (classification) or an approximation of the underlying functional behaviour defining the target value (regression). Every MVA methods see the same training and test data. The two best performing multivariate methods for our purposes are boosted decision trees (BDT) and artificial neural networks (ANN).

The determination of correlation coefficients between measured radon concentration and meteorological variables serves as a good tool for identifying the variables with strongest correlation, which are not excluded from the analysis later on. Also, correlation coefficient tables gives a good overview of input data and their intercorrelations. In Fig. 1, the correlation matrix of linear correlation coefficients as an overview of intercorrelations of measured radon concentration and all input meteorological variables are shown for underground laboratory. The input variables in case of analysis of underground laboratory are atmospheric pressure, temperature and humidity in laboratory (P_{rm}, T_{rm}, H_{rm}) and outdoor (P, T, H) and differences in measured values of pressure ($P - P_{rm}$), temperature ($T - T_{rm}$) and humidity ($H - H_{rm}$) in laboratory and outdoor. Input meteorological variables in case of family house are the same as the list of measured meteorological variables from nearby meteorological station, with the addition of differences in temperature ($T - T_{rm}$) and humidity ($H - H_{rm}$) from indoor and outdoor values, where indoor measurements results were obtained using radon monitor.

Multivariate methods within the package TMVA in ROOT can search for best multivariate approximation of functional behaviour for the classification function of radon concentration depending on meteorological variables. In the analysis, several multivariate methods were tested, and best performed method was BDT. This can be seen by presenting the receiver operating characteristics (ROC) curve for all tested multivariate methods in case of house measurements (Fig. 2). The BDT method has the highest value of integrated ROC function.

Linear correlation coefficients in %

	T_rmn	P_rmn	H_rmn	T	P	H	T-T_rmn	P-P_rmn	H-H_rn	Radon
Radon	17	4	25	14	5	1	13	5	-14	100
H-H_rmn	-81	13	-73	-94	10	79	-94	-8	100	-14
P-P_rmn	9	-15	13	1	15			100	-8	5
T-T_rmn	80	-14	77	99	-14	-68	100		-94	13
H	-43	3	-18	-65	3	100	-68		79	1
P	-4	95	-12	-13	100	3	-14	15	10	5
T	86	-13	80	100	-13	-65	99	1	-94	14
H_rmn	84	-17	100	80	-12	-18	77	13	-73	25
P_rmn	-7	100	-17	-13	95	3	-14	-15	13	4
T_rmn	100	-7	84	86	-4	-43	80	9	-81	17

Fig. 1. Correlation matrix with linear correlation coefficients as an overview of radon and meteorological variables intercorrelations in case of the Low-Background Laboratory for Nuclear Physics.

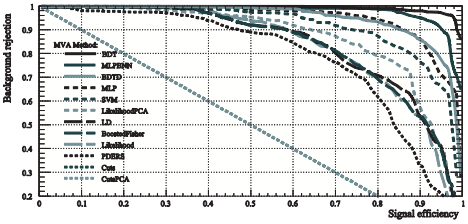

Fig. 2. ROC curve for all multivariate methods in case of house measurements.

BDT has proven to be the most effective method for the classification of radon concentrations in case of data obtained from the house as well as those obtained from measurements in the Low-Background Laboratory for Nuclear Physics.

The next step in the analysis is the regression analysis, which is the way of finding a mapped function behaviour of dependence of radon concentrations and meteorological input variables. The regression analysis was done using the TMVA packages, already used in classification analysis, and for the same set of measured radon concentration and meteorological variables in underground laboratory and a family house in Serbia. Multivariate method BDT was found to be the best suited for regression analysis also, as was the case in classification analysis.

The data of measured radon concentration in house and BDT evaluated values, using only the values of meteorological variables, without the knowledge of measured values (i.e. in the testing set of multivariate analysis), is presented for comparison in Fig. 3.

One of the possible application of having resulting mapped function, given by multivariate regression analysis, is to have prediction of radon concentration values (evaluated) based on meteorological variables alone. The online application of the regression multivariate analysis can be imple-

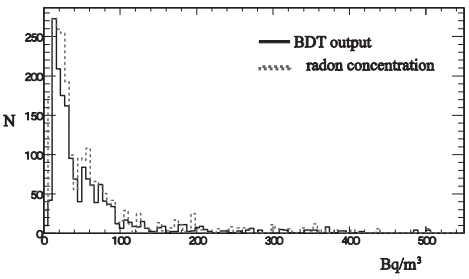

Fig. 3. BDT evaluated (predicted) values of radon concentrations based on meteorological variables using regression analysis within TMVA packages in house (left) and measured values (right).

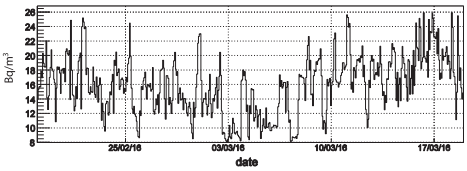

Fig. 4. BDT evaluated (predicted) values of radon concentration, based on meteorological variables alone of underground laboratory posted online and updated daily.

mented, as the one posted online for evaluation (and prediction) based on meteorological variables alone (Fig. 4).

Limitation of multivariate methods

As the multivariate methods used in the analysis are 'supervised learning' algorithms, the performance of the main result of multivariate analysis, the resulting mapped functional behaviour, depends on learning process. Limitation of multivariate analysis in the analysis of radon dependence on meteorological variables are coming from small number of measurements used in learning process, unlike the great number of measurements in high--energy physics experiments. As the next logical step in multivariate analysis presented in this paper should be inclusion of variables such as local geology, permeability of soil, building materials used to build the buildings as well as the habits of people, the requirement for efficient multivariate analysis is to have many measurements in many different houses. Many measurements would help to get good mapped functional behaviour, as opposed to possible existence of theoretical modelling that is independent on number of measurements. In this sense, if the number of measurements is not great, multivariate analysis can be used only as hell to indicate which variables are more important to be used in theoretical modelling, for comparison of mapped and modelled functions, and modelled function test. Another important limitation of multivariate analysis is that no 'straightforward' interpretation of mapped functional behaviour is possible, or simply, the mapped function is a 'black box'. This comes from the fact that the error minimization in learning algorithms, while mapping the functional behaviour, is an important part in learning process.

Conclusions

The paper presents the results of multivariate analysis of variations of radon concentrations in the shallow underground laboratory and a family house, depending on meteorological variables only. This test of multivariate methods, implemented in the TMVA software package, applied to the analysis of the radon concentration variations connection with meteorological variables in underground laboratory (with ventilation system turned on and off) and typical house in Serbia, demonstrated the potential usefulness of these methods. It appears that the method can be used for the prediction of the radon concentrations, on the basis of predicted meteorological variables. The next step in multivariate analysis presented in this paper should be inclusion of variables such as local geology, permeability of soil, building materials used to build the buildings as well as the habits of people. The requirement for efficient multivariate analysis is to have many measurements in many different houses, which makes multivariate method very useful only when having many measurement, for instance, during radon mapping campaigns. Many measurements would help to get good mapped functional behaviour, as opposed to possible existence of theoretical modelling that is independent on number of measurements. Generally, multivariate analysis can be used to help indicate which variables are more important to be used in theoretical modelling, furthermore, for comparison of mapped and modelled functions, and modelled function test.

Another usage of the results of classification multivariate analysis presented in this paper is the implementation of online warning system for possible increased radon concentration in family houses based on meteorological variables only.

References

1. Maletić, D., Udovičić, V., Banjanac, R., Joković, D., Dragić, A., Veselinović, N., & Filipović, J. (2014). Comparison of multivariate classification and regression methods for indoor radon measurements. *Nucl. Technol. Radiat. Prot*., *29*, 17–23.
2. Hoecker, A., Speckmayer, P., Stelzer, J., Therhaag, J., Von Toerne, E., & Voss, H. (2007). TMVA – Toolkit for Multivariate Data Analysis. *PoS ACAT 040*. arXiv:physics/070303.
3. Brun, R., & Rademakers, F. (1997). ROOT – An Object Oriented Data Analysis Framework. *Nucl. Instrum. Methods Phys. Res. Sect. A-Accel. Spectrom. Dect. Assoc. Equip*. *389*(1/2), 81–86.
4. Udovičić, V., Grabež, B., Dragić, A., Banjanac, R., Joković, D., Panić, B., Joksimović, D., Puzović, J., & Aničin, I. (2009). Radon problem in an underground low-level laboratory. *Radiat. Meas*., *44*, 1009–1012.
5. Udovičić, V., Aničin, I., Joković, D., Dragić, A., Banjanac, R., Grabež, B., & Veselinović, N. (2011). Radon time-series analysis in the Underground Low-Level Laboratory in Belgrade, Serbia. *Radiat. Prot. Dosim*., *145*(2/3), 155–158.
6. Banjanac, R., Udovičić, V., Dragić, A., Joković, D., Maletić, D., Veselinović, N., & Grabež, B. (2013). Daily variations of gamma-ray background and radon concentration. *Rom. J. Phys*., *58*(Suppl.), S14–S21.

Neutrons produced by muons at 25 mwe

2013 J. Phys.: Conf. Ser. 409 012054

(http://iopscience.iop.org/1742-6596/409/1/012054)

Journal of Physics: Conference Series **409** (2013) 012054 doi:10.1088/1742-6596/409/1/012054

Neutrons produced by muons at 25 mwe

A Dragić[1], I Aničin[1], R Banjanac[1], V Udovičić[1], D Joković[1], D Maletić[1], M Savić[1], N Veselinović[1] and J Puzović[2]

1 Institute of Physics, University of Belgrade, Belgrade, Serbia
2 Faculty of Physics, University of Belgrade, Belgrade, Serbia

E-mail: dragic@ipb.ac.rs

Abstract. The flux of fast neutrons produced by CR muons in lead at the depth of 25 mwe is measured. Lead is a common shielding material and neutrons produced in it in muon interactions are unavoidable background component, even in sensitive deep underground experiments. A low background gamma spectrometer, equipped with high purity Ge detector in coincidence with muon detector is used for this purpose. Neutrons are identified by the structure at 692 KeV in the spectrum of delayed coincidences, caused by the neutron inelastic scattering on Ge-72 isotope. Preliminary result for the fast neutron rate is $3.1(5) \times 10^{-4} n/cm^2 \cdot s$.

1. Introduction

Muons are very penetrating particles, present even in deep underground laboratories. Muons themselves and secondary radiation they produce are important source of background in sensitive experiments hosted in these laboratories. Neutrons produced in muon interactions in rock or detector surroundings are particularly troublesome. In dark matter experiments neutrons can produce recoil signal in detectors, similar to expected signal from WIMPs.

Another example of dangerous background arising from neutrons is in double beta experiments. In $(n, n'\gamma)$ reaction on lead, gamma rays of 2041 KeV energy can be produced, close to Q value for neutrinoless double beta decay in Ge-76[1].

Our measurements are performed in a shallow underground site, but even these measurements are of relevance for deeply underground located experiments [2].

2. Description of the experiment

The Belgrade underground laboratory is located on the right bank of river Danube in the Belgrade borough of Zemun, on the grounds of the Institute of Physics. The ground level part of the laboratory, at altitude 78 m above sea level, is situated at the foot of the vertical loess cliff, which is about 10 meters high. The underground part of the laboratory, of the useful area of 45 m^2, is dug into the foot of the cliff and is accessible from the ground level lab via the 10 meters long horizontal corridor, which serves also as a pressure buffer for a slight overpressure in the laboratory. More detailed description of the laboratory could be find in the ref. [3].

Experimental setup consist of a plastic scintillator detector and HPGe detector operating in coincidence. Scintillator detector with dimensions $100 \times 100 \times 5$cm, equipped with four PMTs directly coupled to the corners bevelled at 45°, is made by Amcrys-H of Kharkov, Ukraine. A radiopure HPGe detector of 35% efficiency and 149 cm^3 volume, made by ORTEC, in its 12 cm thick cylindrical lead castle is positioned beneath the center of the scintillator detector.

The core of digital data acquisition system is a FADC unit with four independent inputs each, made by CAEN, of the type N1728B. It samples signal at 10 ns intervals, into 2^{14} channels.

The preamplifier outputs of the PMTs of plastic scintillator detector are paired diagonally, the whole detector thus engaging the two inputs of the FADC. The third FADC input is reserved for HPGe, and fourth is used by auxiliary detector, unrelated to the present purpose.

Every event in each input channel is fully recorded by the time of its occurrence over the set triggering level, and its amplitude. This enables to off-line coincide the events at all four inputs, prompt as well as arbitrarily delayed.

Plastic scintillator detector serves as a muon flux monitor when its data are organized into time series. In independent operation HPGe detector is a typical low background gamma spectrometer. In anticoincident regime the plastic detector serves as a muon veto for gamma detector.

The coincident mode enables one to study cosmic-ray induced effects in gamma spectrometer. We are particularly interested in the signature of neutrons produced by CR muons in the lead shield.

All the operating modes of the system are performed simultaneously and do not interfere, as they are realized by performing different off-line analyses of the same set of data.

3. Results

After over 35 million seconds (400+ days) of measurements enough data are accumulated to present first results on neutron production from CR muons. Neutron identification is based on the process of inelastic scattering on Ge-72 isotope, within the HPGe detector itself, leading to the excited state at 692 KeV of energy. The abundance of Ge-72 isotope is 27.7% in natural Ge. The 692 keV state is an isomer state, with the half-life of 444 ns, and the depopulating radiation is pure E0, meaning that detection efficiency for the 692 keV radiation is practically 100%.

The spectrum of the HPGe detector containing the coincidences with the plastic scintillator delayed with respect to prompt between 500 ns and 2 μs, shows at this statistics only two interesting features (Fig.1).

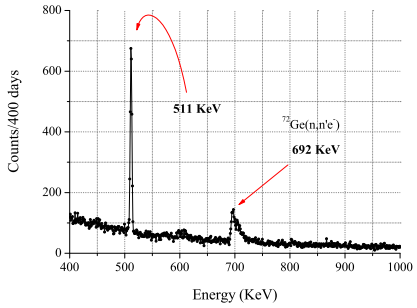

Figure 1. Portion of the background HPGe spectrum coincident with the plastic scintillator with the delays in the range from 100 ns to 2 μs, after 400 days of measurement time. It shows the annihilation line, which is due to the decays of positive muons stopped in the lead castle, and the triangular structure at 692 keV, which is due to inelastic scattering of fast neutrons on Ge-72.

The first is the quasi-triangular structure at 692 keV, whose shape is a result of summing of the energy of transition radiation with the energy of the recoil of Ge nucleus. This structure has been studied many times [4, 5, 6, 7]. The second is annihilation line originating mainly from the decay of stopped positive muons.

The time spectra, or distribution of time intervals between start and stop signal, with the software gate on these two structures confirms previous statement.

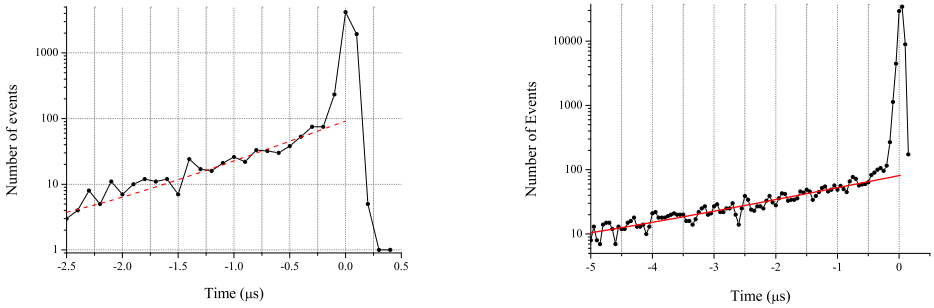

Figure 2. Time distributions of the events from Fig.1 that belong to the structure of 692 keV (left), the slope of which yields 500(50) ns for the half-life, and that of the annihilation line (right), which yields 2.24(9) μs for the mean life of the muon. Note logarithmic scale and interchange of start and stop signals.

With the gate on 692 KeV structure, though the statistics is poor, the fit through the tail of delayed coincidences yields the half-life of 500(50) ns (left panel of Fig2). The gate on 511 KeV line yields the mean life of 2.24(9)μs (right panel of Fig2). It is our intention to use the intensity of 692 KeV structure to estimate the flux of fast neutrons, produced in lead by CR muons, with the energy above the threshold. The empirical relation:

$$\Phi_F = k\frac{I_{692}}{V} \tag{1}$$

introduced by Škoro et al. [8] has been reasonably verified in the past. Here, I_{692} is the count rate in 692 KeV structure in counts per second, V is detector volume in cm^3 and k is parameter found to be (900 ± 150)cm.

This relation has been used before with analog spectroscopy systems, where the integration constants are long and the recoils invariably sum up with the 692 keV pulses. In digital spectroscopy systems, however, one important caveat is in place when using the integral of this structure for fast neutron flux determination. It appears that the shape, and the intensity of the distribution, here strongly depends on the height of the triggering level. When the trigger is higher then the height of the recoil pulse, the corresponding 692 keV pulse sums practically completely with its recoil. When the trigger is lower than the recoil it will trigger the ADC, and this pulse, together with the following 692 keV pulse, will be rejected by the pile-up rejecting algorithm. In our case the trigger was sufficiently high and according to our finding the intensity of the 692 keV distribution can be reliably used for the estimate of the fast CR induced neutron flux at the position of the detector. For the flux of neutrons of CR origin with energies over 1

MeV the value of $3.1(5) \times 10^{-4} n/cm^2 \cdot s$ is obtained. This refers to the flux at the depth of 25 m.w.e., within roughly one ton of lead, which is a common environment in most measurements of low activities.

This work is supported by the Ministry of Education and Science of the Republic of Serbia, under project ON171002.

References

[1] Mei D-M, Elliott S R, Hime A, Gehman V and Kazkaz K 2008 *Phys.Rev.C* **77** 054614
[2] Ryazhskaya O 2006 *Proc. 20th ECRS (Lisabon)*
[3] Dragić A, Udovičić V, Banjanac R, Joković D, Maletić D, Veselinović N, Savić M, Puzović J and Anicin I 2011 *NT & RP* **XXVI** 181-192
[4] Wordel R, Mouchel D, Altzitzoglou T, Heusser G, Quintana Arnes B and Meynendonckx P 1996 *Nucl. Instrum. Meth. A* **369** 557-562
[5] Fehrenbacher G, Meckbach R and Paretzke H G 1996 *Nucl. Instrum. Meth. A* **372** 239-245
[6] Fehrenbacher G, Meckbach R and Paretzke H G 1997 *Nucl. Instrum. Meth. A* **397** 391-398
[7] Gete E, Measday D F, Moftah B A, Saliba M A and Stocki T J 1997 *Nucl. Instrum. Meth. A* **388** 212-219
[8] Škoro G, Aničin I, Kukoč A, Krmpotić Dj, Adžić P, Vukanović R and Župančić M 1992 *Nucl. Instrum. Meth.* **A316** 333-336

SEMI-EMPIRICAL SIMULATION OF NATURAL BACKGROUND IN UNDERGROUND LABORATORY

Dimitrije Maletić[1], Vladimir Udovičić[1], Radomir Banjanac[1], Aleksandar Dragić[1], Dejan Joković[1], Mihailo Savić[1], Nikola Veselinović[1], Jovan Puzović[2]

[1]*Institute of Physics, University of Belgrade, Belgrade, Serbia*
[2]*Faculty of Physics, University of Belgrade, Belgrade, Serbia*

Abstract

This paper describes a method of preparing simulation data which can be used as an input for any given Monte Carlo simulation. An assumed natural spectrum is composed of an ambient gamma radiation spectrum and a cosmic (induced) ray spectrum. The ambient gamma spectrum is obtained semi-empirically, based on the analysis of HPGe measurements of natural background. The cosmic ray spectrum is obtained using CORSIKA simulation package. The cosmic induced spectrum for an underground location is produced in an additional step of MC simulations (using Geant4) which uses surface cosmic ray spectrum and simulates its modification due to the passage of the particles through soil, under which the underground laboratory is placed. The data sample obtained this way is used for MC simulation of plastic scintillators and HPGe detectors with different absorber shieldings.

Introduction

The method which is presented in the following was developed while constructed a Sandwich detector (scintillator-lead-scintillator) in order to have a detector capable to separate contributions to the observed radiation spectrum stemming from cosmic radiation and from ambient radionuclides, respectively.

With MC simulation and data sample prepared for this MC simulation we were able to optimize the detector performance for its task. Also we saw it as a convenient tool for other studies in our surface and underground laboratories.

To generate a spectral sample of natural radioactivity, we use a semi-empirical method. This method is based on the analysis of background spectrum of a HPGe detector, without any shielding, on the ground surface in the Low background laboratory of the Institute of Physics, Belgrade. With known gamma efficiency of the HPGe detector, we get ratios of intensities of spectrum lines. Further, we assumed that the natural radioactivity does not reach the detector from depths greater then 30 cm form soil and concrete around the HPGe detector. Finally, the intensity of radon and its progenies originates in surrounding air. All information we get is then used to simulate in detail natural radiation spectra using Geant4 [(1)] simulation of propagation of particles originating from all mentioned natural radioactivity radiation sources. This adds mostly events resulting from Compton scattering in the environmental materials which surround the detectors.

For Cosmic ray simulation the CORSIKA (COsmic Ray Simulation for KAskade) [2] Monte Carlo package was used. This program simulates the propagation of primary cosmic rays and showers, induced by these particles, through the Earth's atmosphere.

Natural radioactivity semi-empirical simulation

The method is semi-empirical because we use experimental data to find out the composition of the natural radioactivity spectrum. The spectrum lines of the HPGe experimental data are indentified and its area determined. From this we can compare the relative intensities of radiation form various radionuclides. To be able to do this, the gamma efficiency curve has to be known.

We treated differently the radionuclides from radon and its progenies in the creation of final MC data sample, since we assumed that the radon is contained predominantly form the air surrounding the detector, while its precursors sit in the solid material around, such as walls and floors. As consequence the gamma lines of Rn progenies are produced by photons originating in the walls and in the air.

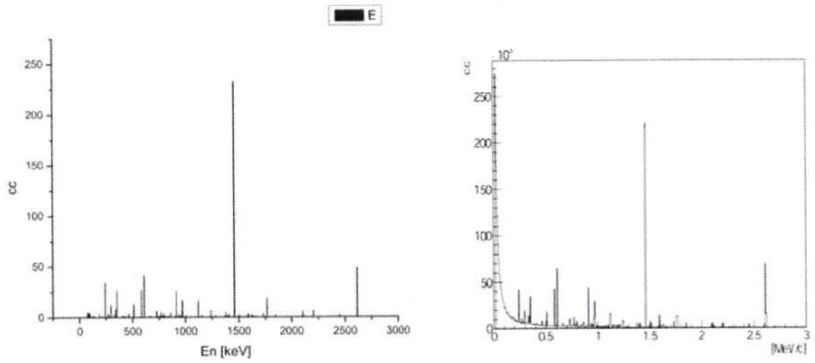

Figure 1: Indentified gamma lines in initial HPGe spectrum, and resulting environmental spectrum

To obtain final data sample, the MC simulation using Geant4 package is used which is intended to simulate propagation of particles through matter. For that program we defined geometries and compositions of the matter within and around our laboratory [3], assuming a surrounding soil thickness of 30 cm and the concrete liner.

The radionuclide sources are assumed placed homogenously in soil and concrete and we simulated the propagation of emitted gamma rays towards the location of the detector in our laboratory. When any primary or secondary particle reaches the detector it is recorded. The record contains particle type, energy and direction.

These particle records are the first part of our objective, namely a background data sample which can be used for any given MC simulation. The second part is the cosmic ray data sample.

Cosmic ray simulation

MC simulation of the flux of cosmic rays has been done using the CORSIKA package which simulates the interaction of showers of incumbent cosmic rays with the atmosphere. These showers are induced in the upper layers of the atmosphere by high energy hadrons which constitute the primary cosmic rays. The simulation includes modelling of electromagnetic, hadron and muon components. As an output we get events on observation level (altitude above sea level) with defined particle types, their positions and momentum vectors.

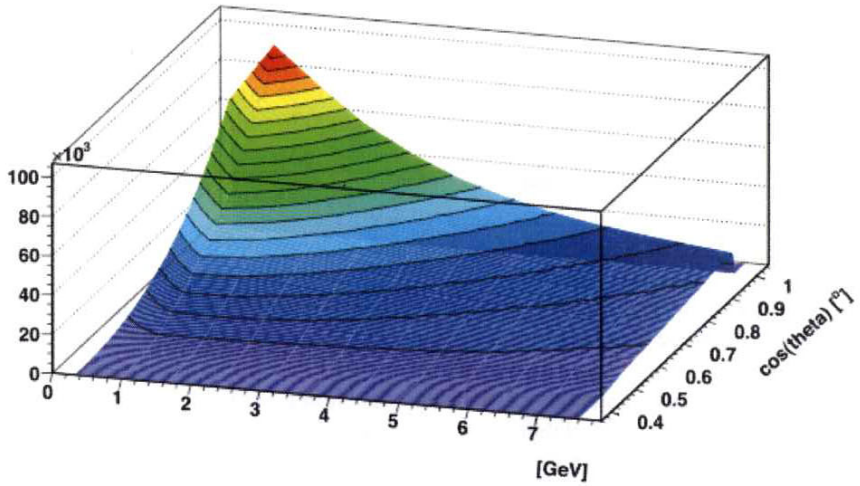

Figure 2: CORSIKA output for muon intensities
in dependence of cosine of incident angle and energy on the surface

For this simulation we developed the Geant4 interface for CORSIKA output. This interface included adding to the standard G4 HEPEvt interface the ability to have multi primary vertex events in Geant4 and particle's arrival times at observation level. Multi vertex events are important in order to include multiple particles that may fall into your detector, originating from a single primary cosmic ray particle. Also, we developed the web interface to run these simulations in order to unify simulation efforts in our group.

For modelling the response of the detector located in the underground laboratory we added an additional step. The CORSIKA output was used as input to simulate the history of particles which are passing through and are being produced in soil by interaction with incumbent secondary cosmic particles, between surface and underground laboratory.

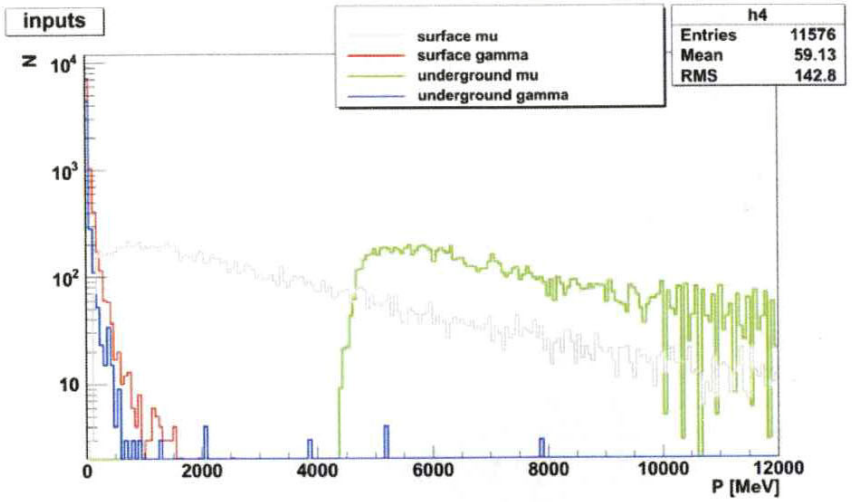

Figure 3: Spectrums of surface and underground laboratories

In order to have well described primary particles generator in G4 simulation that we aimed to produce a parameterized spectrums of Cosmic ray component on surface and background. In our case, having parameterized spectrums means that you could have distributions of intensities of particles depending on their energy and incident angles for every type of simulated particles *(Figure 2)*.

Also, since we made separate simulation for surface and underground laboratories, we are able to compare the respective spectrums *(Figure 3)*. The simulations show expected difference in muon spectrums on the surface and in the 12m underground laboratory (lower muon energy spectrum cut-off in the underground)[3].

Usage and tests of prepared data sample

We tested and used the obtained resulting MC data samples (Figure 3), on various detectors, most importantly, for the optimisation of design of sandwich detector, which is planed to be built in our laboratory and Faculty of physics, and for which this method was developed *(Figure 4)*. Furthermore, the method was applied on the plastic scintillators on the surface and in the underground, and on the HPGe within lateral lead shielding, located in the underground laboratory. Also, simulated spectrum of plastic scintillators is in good agreement with the experimental data *(Figure 5)*.

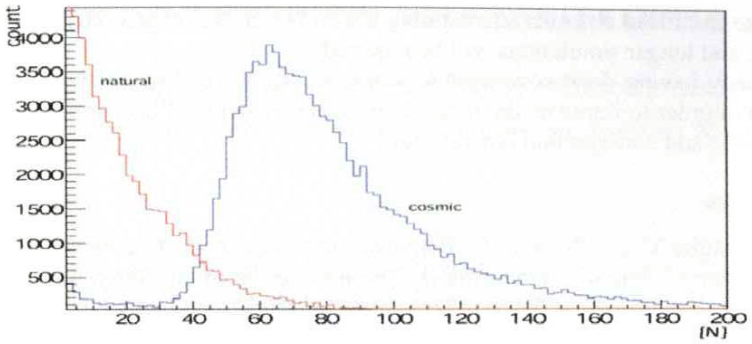

Figure 4: Ambiental and cosmic induced spectrum in Sandwich detector. X axis shows the number of optical photons which reach photomultipliers

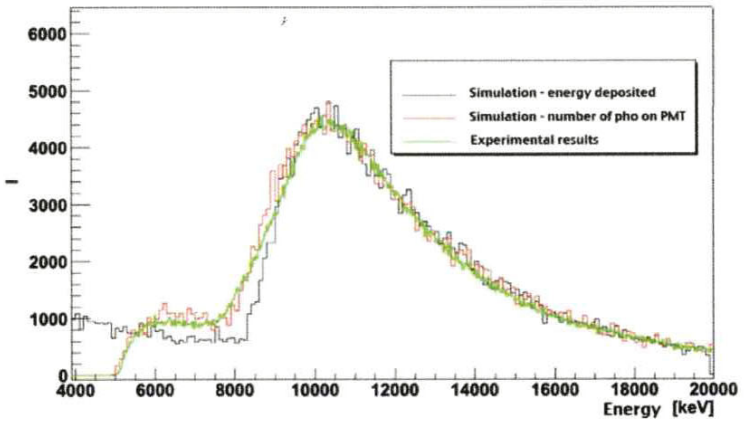

Figure 5: The comparison of MC and experimental spectra of plastic scintillator is in good agreement. Black-simulation – energy deposited in the plastic, red – number of photons which reach the photomultipliers with a threshold, and green – experimental data

Conclusion

The simulations and analysis done so far look promising, especially regarding our planes for building the sandwich detector. Besides our primary goal, we now have more and better tools do perform various analyses and simulations in order to better understand all detectors in our ground and underground laboratories.

For certain purposes the data sample created for MC simulation is sufficient, for example for showing that optimal design of sandwich detector could give us the operational detector for our purposes, but for others, like simulation of X rays which

originate from lead absorber surrounding the HPGe, higher precision, bigger MC data sample, and longer simulations will be required.

Already having done considerable work, we still intend to continue refining the method in order to improve simulations and measurements of background radiation in our surface and underground laboratories.

References

1. A. Dragić, V. I. Udovičić, R. Banjanac, D. Joković, D. Maletić, N. Veselinović, M. Savić, J. Puzović, I. V. Aničin: The new set-up in the Belgrade low-level and cosmic-ray laboratory. Nuclear Technology & Radiation Protection, 26(3), 181–192, (2011)
2. D. Heck, J. Knapp, J. N. Capdevielle, G. Schatz, T. Thouw: CORSIKA: A Monte Carlo Code to Simulate Extensive Air Showers, Forschungszentrum Karlsruhe GmbH, Karlsruhe, 1–90, (1998)
3. S. Agostinelli et. al.: Geánt4 – a simulation toolkit. Nuclear Instruments and Methods in Physics, Research Section A, 506(3), 250–303, (2003)

Effect of pressure and temperature corrections on muon flux variability at ground level and underground

M. Savic, A. Dragic, N. Veselinovic, V. Udovicic, R. Banjanac, D. Jokovic, D. Maletic
Institute of Physics, Belgrade, Pregrevica 118, Serbia

In Low Background Laboratory at Institute of Physics Belgrade, plastic scintillators are used to continuously monitor flux of the muon component of secondary cosmic rays. Measurements are performed on the surface as well as underground (25 m.w.e depth). Temperature effect on muon component of secondary cosmic rays is well known and several methods to correct for it are already developed and widely used. Here, we apply integral method to calculate correction coefficients and use GFS (Global Forecast System) model to obtain atmospheric temperature profiles. Atmospheric corrections reduce variance of muon flux and lead to improved sensitivity to transient cosmic ray variations. Influence of corrections on correlation with neutron monitor data is discussed.

Belgrade Low Background Laboratory (LBL) is located at Institute of Physics, Belgrade and consists of two interconnected spaces, a ground level laboratory (GLL) and a shallow underground one (UL) [Fig. 1]. GLL is at 75 meters above sea level while UL is dug under a 10 meter cliff and has a 12 meters of loess soil overburden (25 meters of water equivalent) [1]. Geographic latitude for the site is 44.86 and longitude is 20.39 while geomagnetic rigidity cutoff is 5.3 GV.

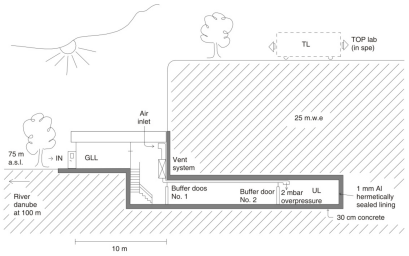

FIG. 1: Layout of the Low Background Laboratory.

Experimental setup consists of two identical sets of detectors and read out electronics, one situated in GLL and the other in UL. Each setup utilizes a plastic scintillator detector with dimensions 100cm x 100cm x 5cm (Amcrys-H, Kharkov, Ukraine) equipped with 4 PMTs (Hammamatsu R1306) directly coupled to the corners [Fig. 2]. Flash ADC (CAEN type N1728B) with 10ns sampling are used for read out [1].

Preamplifier outputs of two diagonally opposing PMTs are summed and fed to a single FADC input thus engaging two inputs of the FADC for two such diagonal pairings. Signals recorded by the two inputs are coincided in offline analysis, resulting in coincidence spectrum which is then used to determine the integral count [Fig. 3]. This procedure almost completely eliminates low-energy environmental background leaving only events induced by cosmic ray muons and muon related EM showers [1].

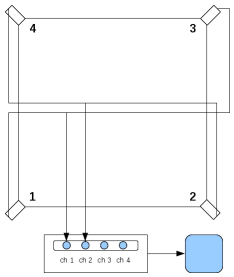

FIG. 2: Experimental setup scheme.

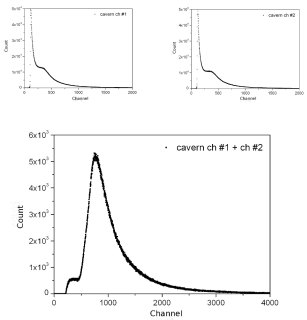

FIG. 3: Single summed diagonal and coincidence spectra.

I. SIGNIFICANCE OF METEOROLOGICAL EFFECTS

Meteorological effects on muon component of secondary cosmic rays are well known, with pressure and temperature effect being most dominant [2]. Correcting for these effects noticeably increases data usefulness, especially increasing sensitivity to periodic and aperiodic variations of non-atmospheric origin (vari-

ations of primary cosmic rays, different heliospheric processes, etc.)

In Belgrade Low Background Laboratory continual measurements utilizing described setup started in April of 2008 for the GLL and in November of 2008 for the UL, and with some interruptions are still ongoing. Base time resolution for integrated count is 5 minutes but time resolution of 1 hour is also often used in analysis. Link to Belgrade cosmic ray station can be found on the following address: http://www.cosmic.ipb.ac.rs/.

A. Pressure effect

Barometric effect is defined by the following equation:

$$\left(\frac{\delta I}{I}\right)_P = \beta \cdot \delta P \tag{1}$$

where $\frac{\delta I}{I}$ is the normalized variation of muon flux intensity, β is barometric coefficient and δP is pressure variation. Pressure variation is calculated as $\delta P = P - P_B$, where P is current pressure and P_B is base pressure value [4].

Since no in situ pressure measurement was performed prior to 2015, current pressure values have mostly been acquired from official meteorological measurements performed by Republic Hydrometeorological Service of Serbia as well as from Belgrade airport meteorological measurements. In all, data from 5 different stations were used. All pressure data was normalized to Belgrade main meteorological station. Stations were sorted according to geographical proximity and consistence of data. Unique pressure time series was composed by using data from the first station with available pressure entries for a given hour. Linear interpolation was then performed and pressure values were sampled with 5 minute step. Normalized variation of muon flux intensity vs. pressure variation was plotted for each year. Only data for the 5 geomagnetically most quiet days of each month were taken into account (selected from International Quiet Days list). Barometric coefficient for each year was determined from linear fits of these plots [Fig. 4].

B. Temperature effect

Temperature effect on hard muons is well known [2] and there are several methods developed to describe and correct for it. Method we used was integral method, where normalized variation of muon flux dependence on temperature variation is described as:

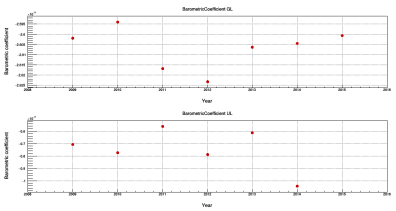

FIG. 4: Yearly values for barometric coefficient for GLL and UL.

$$\left(\frac{\delta I}{I}\right)_T = \int_0^{h_0} \alpha(h) \cdot \delta T(h) \cdot dh \tag{2}$$

$\alpha(h)$ being temperature coefficient density and temperature variation calculated as $\delta T = T - T_B$, where T is current temperature and T_B is base temperature value [3].

To correct for temperature effect using formula above it is necessary to have most complete information about atmospheric temperature profile for a given geographical location as well as to know temperature coefficient density function. Temperature profile measurements performed by local meteorological service are not done on consistent basis but more detailed information is available from meteorological models. One such model is GFS (Global Forecast System) that, among other data, provides temperatures for 25 isobaric levels for a given geographical location with latitude/longitude precision of 0.5 degrees [3].

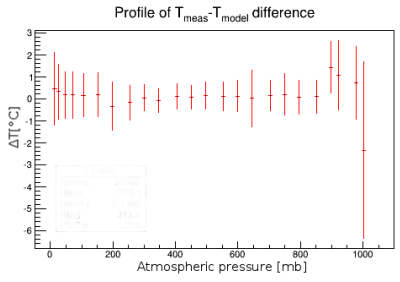

FIG. 5: Distribution of difference between modelled temperatures and temperatures measured by meteorological balloons above Belgrade (where such data was available).

Measured and modelled values seem to be in fairly good agreement [Fig. 5] except for the lowest isobaric level. That is why for this level temperature from local meteorological stations was used, treated in the same manner as described for local pressure data . Time

resolution for modelled temperatures is 6 hours so interpolation was performed using cubic spline [3] and temperature values were sampled in 5 minute steps.

Temperature density functions [Fig. 6] are calculated according to procedure described in [2].

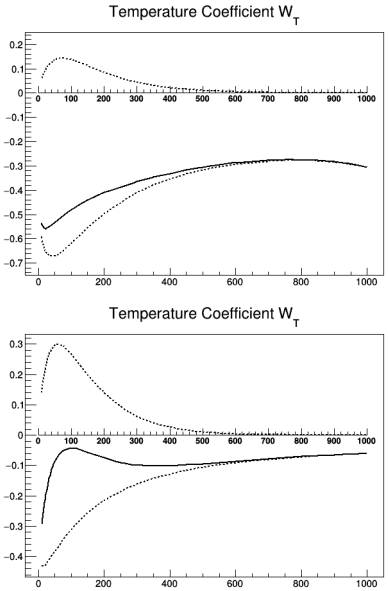

FIG. 6: Temperature coefficient density functions for ground level (above) and depth 25 m.w.e. (below).

II. RESULTS

A. PT corrected time series

It would seem that pressure correction successfully removes aperiodic pressure induced fluctuations while temperature correction most significantly affects annual variation induced by atmospheric temperature variations [Fig. 7].

B. Spectral analysis

Spectral analysis can give us more insight into effect of temperature correction on annual variation of muon count (presented for GLL data in [Fig. 8])

After temperature correction, peak related to annual periodicity in power spectrum appears to be significantly reduced relative to nearby peaks.

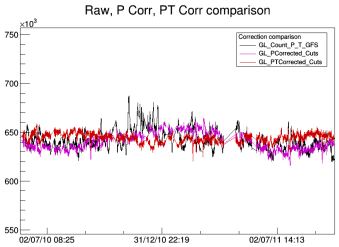

FIG. 7: GLL raw (black), pressure corrected (magenta) and PT corrected (red) muon count time series for a selected period.

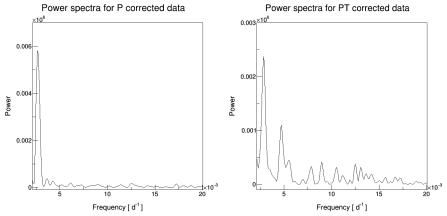

FIG. 8: Power spectra for pressure corrected and temperature and pressure corrected data.

C. Neutron monitor correlation

Possible validation for correction procedure would be agreement of pressure/temperature corrected muon count time series with neutron monitor data. BAKSAN neutron monitor was selected as a possible reference [Fig. 9].

III. CONCLUSIONS

Corrections for temperature and pressure effect are essential for muon data gathered at Belgrade LBL. Atmospheric temperature profile for Belgrade seems to be adequately modeled by GFS. Temperature correction utilizing integral method seems to give acceptable results (while quality can still be further improved). Also, other methods could be applied and results compared. Muon flux data after pressure and temperature corrections has increased sensitivity to periodic and aperiodic effects of non-atmospheric origin. Preliminary comparison with neutron monitor data supports this claim with more detailed correlation analysis to follow in the future.

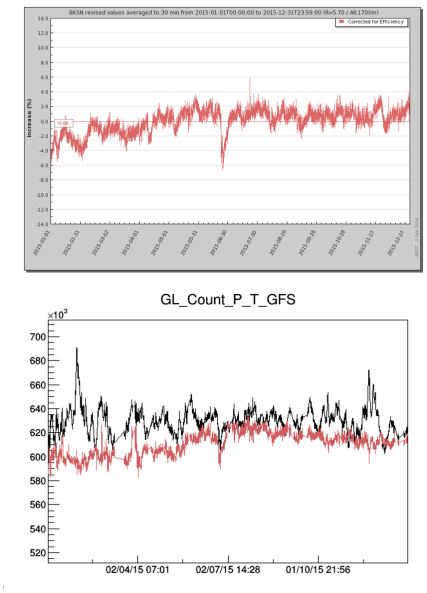

FIG. 9: BAKSAN neutron monitor (above) and GLL raw and pressure/temperature corrected data (below in red) comparison for year 2015.

IV. ACKNOWLEDGEMENTS

The present work was funded by the Ministry of Education and Science of the Republic of Serbia, under the Project No. 171002. The Belgrade Laboratory bears the name of Dr. Radovan Antanasijevic, in honour of its early deceased founder and first director.

V. REFERENCES

[1] The new set-up in the Belgrade low-level and cosmic-ray laboratory Nucl. Technol. Radiat. 26 (2011) 181-192. A.Dragic at all

[2] Dorman, Cosmic Rays in the Earths Atmosphere and Underground

[3] M. Berkova , A. Belov, E. Eroshenko, and V. Yanke, Temperature effect of muon component and practical questions of how to take into account in real time, Astrophys. Space Sci. Trans., 8, 41-44, 2012

[4] R. R. S. De Mendona, J. -P. Raulin, E. Echer, V. S. Makhmutov, and G. Fernandez, Analysis of atmospheric pressure and temperature effects on cosmic ray measurements. JOURNAL OF GEOPHYSICAL RESEARCH: SPACE PHYSICS, VOL. 118, 14031409, doi:10.1029/2012JA018026, 2013

Pressure and temperature effect corrections of atmospheric muon data in the Belgrade cosmic-ray station

2015 J. Phys.: Conf. Ser. 632 012059

(http://iopscience.iop.org/1742-6596/632/1/012059)

Pressure and temperature effect corrections of atmospheric muon data in the Belgrade cosmic-ray station

M Savić, D Maletić, D Joković, N Veselinović, R Banjanac, V Udovičić, A Dragić
Institute of Physics, University of Belgrade
Pregrevica 118, 11080 Belgrade, Serbia

E-mail: yokovic@ipb.ac.rs

Abstract. We present results of continuous monitoring of the cosmic-ray muon intensity at the ground and shallow underground level at the Belgrade cosmic-ray station. The cosmic-ray muon measurements have been performed since 2002, by means of plastic scintillation detectors. The scintillator counts are corrected for atmospheric pressure for the whole period of measurements and, as well, for vertical temperature profile for the period of the last six years. The results are compared with other correction methods available. One-hour time series of the cosmic-ray muon intensity at the ground level are checked for correlation with European neutron monitors, with emphasis on occasional extreme solar events, e.g. Forbush decreases.

1. Introduction

The Belgrade cosmic-ray station, situated in the Low-level Laboratory for Nuclear Physics at Institute of Physics, Belgrade, have been continuously measuring the cosmic-ray intensity since 2002. The station is at near-sea level at the altitude of 78 m a.s.l.; its geomagnetic latitude is 39° 32' N and geomagnetic vertical cut-off rigidity is 5.3 GV. It consists of two parts: the ground level lab (GLL) and the underground lab (UL); the UL is located at a depth of 12 metres below the surface, i.e. 25 metre water equivalent. At this depth practically only the muonic component is present. The cosmic-ray muon measurements are performed by means of plastic scintillation detectors, a pair of which is, along with instrumentation modules for data acquisition, placed in both the GLL and the UL. The set-up is quiet flexible, as the scintillators could be arranged in different ways, which allows conducting different experiments. The analyses of the measurements yielded some results on variations of the cosmic-ray muon intensity and on precise values of the integral muon flux at the ground level and at the depth of 25 m.w.e. [1,2,3,4].

2. Experimental set-up

The experimental set-up in both the GLL and the UL consists of a large plastic scintillation detector (rectangular shape, 100cm x 100cm x 5cm) and a data acquisition system (DAQ). The scintillator is polystyrene based UPS-89, with four 2-inch photomultiplier tubes attached to its corners, so that each PM tube looks at the rectangle diagonal. Preamplifier signals from two PM tubes looking at the same diagonal are summed in one output signal, thus two output signals are led to the DAQ from each scintillator.

The summed signals from the PM tubes on the same diagonal of the detectors are stored and digitized by the DAQ, which is based on 4-channel flash analog-to-digital converters (FADC), made by CAEN (type N1728B), with 100 MHz sampling frequency. The FADCs are capable of operating in

the event-list mode, when every analyzed event is fully recorded by the time of its occurrence and its amplitude. This enables the correlation of events, both prompt and arbitrarily delayed, at all four inputs with the time resolution of 10 ns. Single and coincident data can be organized into time series within any desired integration period. The FADCs can also be synchronized with each other for the additional coinciding of the events in the GLL and the UL.

For both the GLL and the UL detector, two input channels on the corresponding FADC are reserved for events recorded by each of detector's diagonals. The cosmic-ray events recorded by a single diagonal are drown in the background. Coinciding of the prompt events from two diagonals within a narrow time window gives the resulting experimental spectrum of the plastic scintillator, which is the energy deposit (ΔE) spectrum of the cosmic-ray particles (figure 1). Interpretation of the experimental spectra and their features as well as their calibration have been done using Geant4 based Monte Carlo simulation [4,5]. The spectra peak at ~11 MeV and have the instrumental thresholds at ~4 MeV. Comparing the spectra of the GLL detector and the UL detector one can notice the obvious difference in their shape, especially in the low-energy part below ~6 MeV. This difference points to the contribution of the cosmic-ray electrons and gammas (electromagnetic component) to the ΔE spectra at the ground level, which is absent in case of the underground detector.

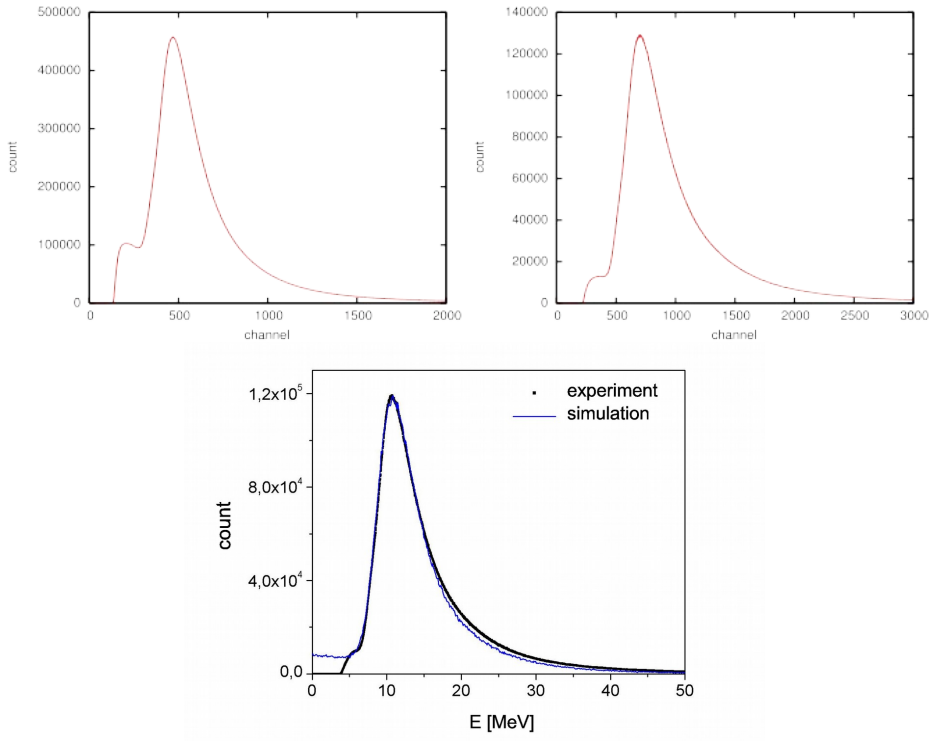

Figure 1. The cosmic-ray ΔE spectra of the GLL detector (top left) and the UL detector (top right). Experimental and simulated ΔE spectra of the UL detector (bottom).

3. Results and discussion

The cosmic-ray intensity data are automatically processed, using a web-based "robot" developed for this purpose, and published online at www.cosmic.ipb.ac.rs/muon_station. The online available data are raw scintillator counts in time series with resolution of 5 min or 1 h. Time series of the raw data are corrected for pressure and temperature effect; pressure corrections have been done for the whole data taking period and temperature effect corrections have been done for the the time period of the last six years.

3.1. Efficiency corrections

The first data corrections are related to detector assembly efficiency. As mentioned, the instrumental thresholds cut the spectra at ~3 MeV. However, the thresholds may vary, thus changing the initial spectrum and resulting in fluctuations of the integral spectrum count. Related to this, the necessary correction has been done by means of constant fraction discriminator (CFD) function (figure 2); with use of the CFD cut the spectrum fluctuations decreased significantly. The CFD is based on cut on chosen height as a percentage of peak height where the spectrum is cut. The simulation tells us that, for the underground detector, ~6% of muon events is also cut (figure 1).

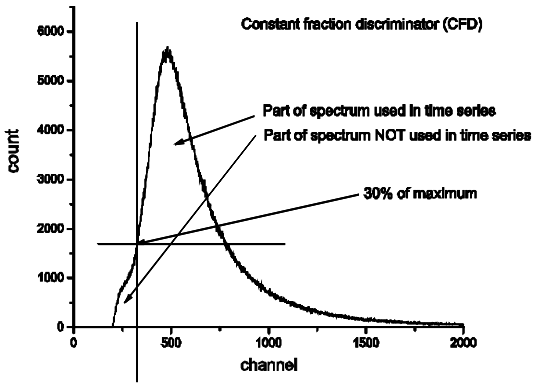

Figure 2. Constant fraction discriminator (CFD) applied in efficiency corrections. The obtained truncated spectrum is used for calculating time series.

The next step in the efficiency corrections is a correction of 5-min count values that are clearly lower than a mean 5-min count in surrounding time intervals. This undershoot comes at the beginning/end of runs, where events are not collected for all 5 min of measurement. The last and smallest correction is a correction of fluctuations of spectrum due to fluctuation in amplification which influence the cut on diagonals and efficiency of coincidence of two diagonals. We found that the CFD cut is proportional to efficiency of coincidence.

3.2. Corrections for atmospheric pressure and for temperature

Significant part of variation of cosmic ray muon component intensity can be attributed to meteorological effects. Here, two main contributors are barometric and temperature effect [6].

Barometric effect is caused by variation of the atmospheric mass above the detector. These pressure corrections are done by finding the linear regression coefficient, using only International Quiet Days, i.e. time series data from periods with more or less constant intensity of galactic cosmic rays, for creation of the distribution of scintillator counts vs. atmospheric pressure. Atmospheric pressure data are available due to on-site continuous measurement.

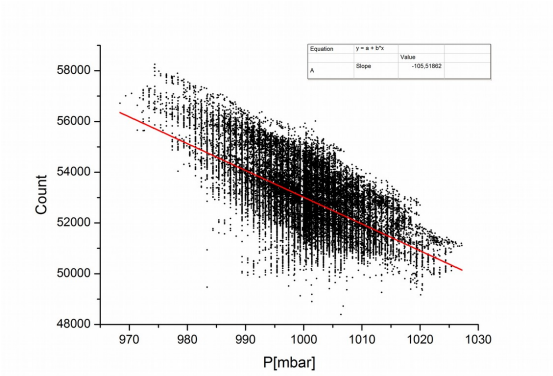

Figure 3. Dependence of 5-min counts on atmospheric pressure.

The temperature effect is related to the variation of the atmospheric temperature profile. The effect is two-fold, as it affects pion decay (positive contribution) as well as muon ionization losses and possible decay (negative contribution). To correct for these effects, integral correction method was applied [6,7]. The variation of the muon intensity due to temperature variations is calculated by using the formula:

$$\delta I_T = \int_0^{h_0} \alpha(h) \cdot \delta T(h) \cdot dh$$

where δI_T is the variation of the muon intensity due to the temperature effect, $\delta T(h)$ is the variation of the atmospheric temperature, which is calculated in reference to the mean temperature value for a given time period (denoted by index M): $\delta T(h) = T_M(h) - T(h)$, where h is atmospheric depth. Temperature coefficient densities $\alpha(h)$ are calculated according to [6].

Available meteorological models make it possible to have hourly atmospheric temperature profiles for 17 standard isobaric levels at the geographic position of the Belgrade muon station, necessary for application of formula shown above. The procedure used here is as described in [7]. Temperature profiles have been obtained from ftp://cr0.izmiran.rssi.ru/COSRAY!/FTP_METEO/blgd_Th/, courtesy of IZMIRAN laboratory.

3.3. Time series of the cosmic-ray intensity

In Figure 4 the count rate time series is shown for all corrections. First, the corrected count rate for efficiency corrected data is shown. Also, the atmospheric pressure and combined atmospheric pressure and temperature corrections time series of count rates are shown.

One-hour time series of the cosmic-ray muon intensity at the ground level are checked for correlation with European neutron monitors (NM), with emphasis on occasional extreme solar events, e.g. Forbush decreases.

In Figure 5 the comparison of time series of pressure corrected and pressure and temperature corrected count rates for the Belgrade muon station and Jungfraujoch, Rome, Baksan and Oulu neutron monitors is presented for Forbush candidate in March 2012. The count rates of neutron monitors are shifted to be close to each-other for visibility. The count rate for the Belgrade station is shown in percentages with additional shift down for visibility. The count rate drop for the neutron monitors is clearly more pronounced than for Belgrade muon monitor.

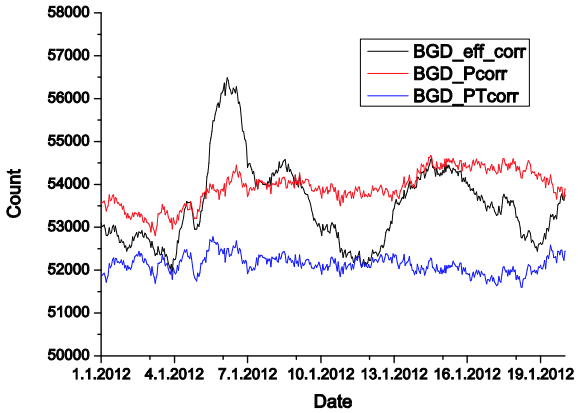

Figure 4. Time series of efficiency corrected, pressure corrected and pressure and temperature corrected counts.

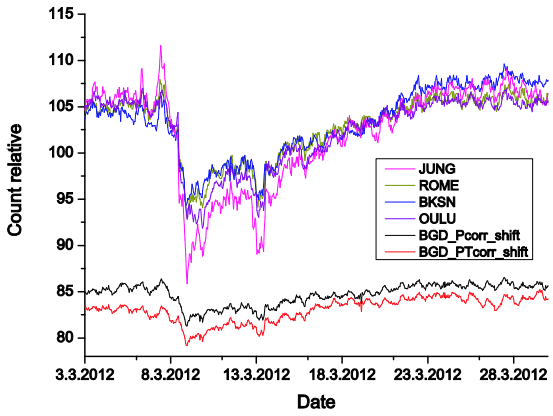

Figure 5. Comparison of time series of pressure corrected and pressure and temperature corrected count rates for the Belgrade muon monitor station and neutron monitors. Count rates are shifted for comparison.

In Figure 6 the comparison of time series of pressure corrected count rates for the Belgrade muon station Jungfraujoch, Rome, Baksan and Oulu neutron monitors is presented. The count rates of neutron monitors are shifted to be close to each-other for visibility. The count rate for Belgrade station is scaled in the way that the drop in count rate is similar to most of the stations (except Jungfraujoch, which is at high altitude). The visual comparison shows the good correlation of the count rates of Belgrade muon monitor and neutron monitors, previously noticed using correlative analyses of count rates. The pressure corrected count rates from Belgrade muon monitor is only dataset used for visual comparison, since neutron monitor data are also only pressure corrected. This was also observed previously using correlative analyses of count rates.

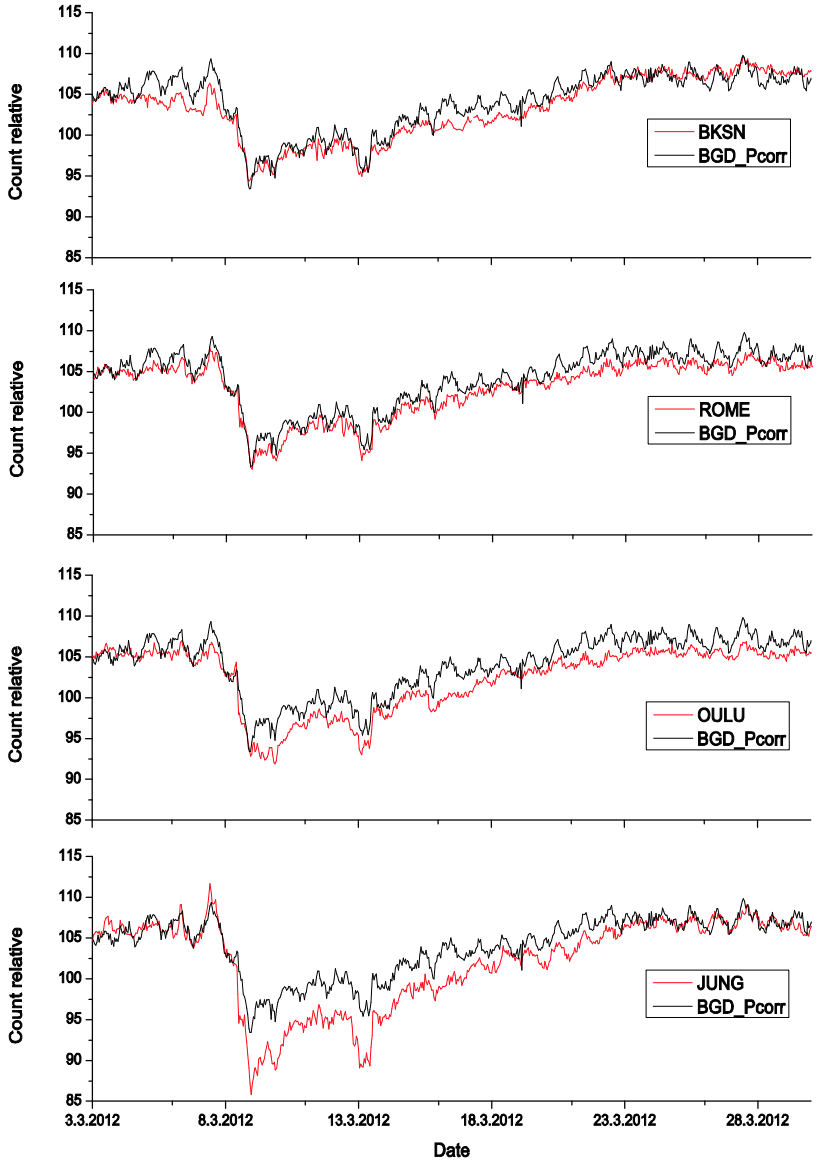

Figure 6. Comparison of time series of pressure corrected count rates for the Belgrade muon monitor station and neutron monitors. Count rates are shifted and scaled for comparison.

4. Conclusions

The results of continuous monitoring of the cosmic-ray muon intensity at the ground and shallow underground level at the Belgrade cosmic-ray station are presented. The scintillator counts are corrected for atmospheric pressure for the whole period of measurements and, as well, for vertical temperature profile for the period of the last six years. The results are compared with other correction methods available and showed excellent agreement. One-hour time series of the cosmic-ray muon intensity at the ground level are checked for correlation with European neutron monitors, with emphasis on occasional extreme solar events, e.g. Forbush decreases. As a result of correlative analysis, the Forbush candidate in March 2012 is the best choice to be used for visual comparison presented in this work. The comparison showed high correlation of the Belgrade muon monitor with neutron monitors, especially geographically closer neutron monitors such as Rome NM. In some specific time periods, like during the Forbush candidate in March 2012, we showed that our muon measurement system has sensitivity comparable to European neutron monitors in this period, but still not as efficient as NM with better geographical position (at high altitude), e.g. Jungfraujoch in the Swiss Alps.

5. Acknowledgements

This work is supported by the Ministry of Education, Science and Technological Development of Republic of Serbia, project no. OI171002. We acknowledge the NMDB database (www.nmdb.eu), founded under the European Union's FP7 programme (contract no. 213007) for providing data. We acknowledge the Department of Physical Sciences, University of Oulu, Finland, as the source of data used in publications. Jungfraujoch neutron monitor data were kindly provided by the Cosmic Ray Group, Physikalisches Institut, University of Bern, Switzerland. We acknowledge the ROME neutron monitor data. SVIRCO NM is supported by IFSI/INAF-UNIRoma3 collaboration. We acknowledge the Baksan Neutrino Observatory of Institute for Nuclear Research of Russian Academy of Science, Moscow, for providing data.

6. References

[1] Dragić A, Banjanac R, Udovičić V, Joković D, Aničin I and Puzović J 2005 *Int. J. Mod. Phys.* A **20** 6953
[2] Dragić A, Banjanac R, Udovičić V, Joković D, Puzović J and Aničin I 2008 *Proc. 21st European Cosmic Ray Symposium (Košice, Slovakia)* p 368
[3] Dragić A, Banjanac R, Udovičić V, Joković D, Aničin I and Puzović J 2009 *Proc. 31st Int. Cosmic Ray Conf. (Lodz, Poland)*
[4] Dragić A, Joković D, Banjanac R, Udovičić V, Panić B, Puzović J and Aničin I 2008 *Nucl. Instrum. Meth.* A **591** 470
[5] Joković D, Dragić A, Udovičić V, Banjanac R, Puzović J and Aničin I 2009 *Appl. Radiat. Isot.* **67** 719
[6] Dorman L.I. 2004 *Cosmic Rays in the Earth's Atmosphere and Underground* (Berlin: Springer)
[7] Berkova M, Belov A, Eroshenko E and Yanke V 2012 *Astrophys. Space Sci. Trans.* **8** 41

Cosmic rays muon flux measurements at Belgrade shallow underground laboratory

N. Veselinović, veselinovic@ipb.ac.rsA. Dragić, D. Maletić, D. Joković, M. Savić, R. Banjanac, V. Udovičić, and I. Aničin

Citation: AIP Conference Proceedings **1645**, 421 (2015); doi: 10.1063/1.4909614
View online: http://dx.doi.org/10.1063/1.4909614
View Table of Contents: http://aip.scitation.org/toc/apc/1645/1
Published by the American Institute of Physics

Cosmic Rays Muon Flux Measurements at Belgrade Shallow Underground Laboratory

N. Veselinović [a)], A. Dragić, D. Maletić, D. Joković, M. Savić, R. Banjanac, V. Udovičić, I. Aničin

Institute of Physics, University of Belgrade, Pregrevica 118, Belgrade, Serbia

[a)] Corresponding author: veselinovic@ipb.ac.rs

Abstract. The Belgrade underground laboratory is a shallow underground one, at 25 meters of water equivalent. It is dedicated to low-background spectroscopy and cosmic rays measurement. Its uniqueness is that it is composed of two parts, one above ground, the other bellow with identical sets of detectors and analyzing electronics thus creating opportunity to monitor simultaneously muon flux and ambient radiation. We investigate the possibility of utilizing measurements at the shallow depth for the study of muons, processes to which these muons are sensitive and processes induced by cosmic rays muons. For this purpose a series of simulations of muon generation and propagation is done, based on the CORSIKA air shower simulation package and GEANT4. Results show good agreement with other laboratories and cosmic rays stations.

Belgrade Cosmic Rays Station

Cosmic rays are energetic particles from outer space that continuously bombard Earth atmosphere, causing creation of secondary showers made of elementary particles. For last hundred years, after Hess' discoveries, cosmic rays (CR) has been studied at almost every location accessible to research, from deep underground to above atmosphere [1]. Low-level and cosmic-ray lab in Belgrade is dedicated to the measurement of low activities and CR muon component. One of the objectives is also intersection of these two fields, namely, muon–induced background in gamma spectroscopy. Belgrade lab is relatively shallow underground laboratory [2] located at the right bank of river Danube on the ground of Institute of Physics in Belgrade. It is located at near-sea level at the altitude of 78 m a.s.l. and its geographic position is 44° 51' N and longitude 20° 23' E with geomagnetic latitude 39° 32' N and geomagnetic vertical cut-off rigidity 5.3 GV. The lab has two portions, ground level portion (GL) is situated at the foot of the vertical loess cliff. Other portion, the underground level (UL) is dug into the foot of the cliff and is accessible from the GL via horizontal corridor as can be seen at Fig.1. Working area of UL has three niches for independent experiments.

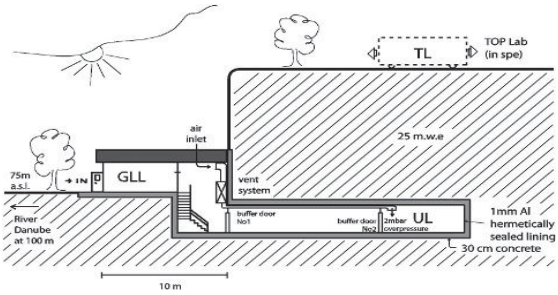

FIGURE 1. Scheme of low-level and CR laboratory at Institute of Physics, Belgrade

The overburden of the UL is about 12 meters of loess soil, which is equivalent to 25 meters of water. The walls are made of 30 cm thick reinforced concrete and covered with the hermetically sealed Al lining 1 mm thick, to

Exotic Nuclei and Nuclear/Particle Astrophysics (V). From Nuclei to Stars
AIP Conf. Proc. 1645, 421-425 (2015); doi: 10.1063/1.4909614

prevent the radon from the soil to diffuse into the laboratory. The low-level laboratory is equipped with an air ventilation system which keeps 2 mbar overpressure in the UL, in order to minimize radon diffusion through eventual imperfections in the Al lining.

Experimental Set-up

The equipment of the lab consists of two identical set of detectors and analyzing electronics. One set is situated in the GL and other in the UL. Each set is composed of gamma spectrometer and muon detectors. For muon measurements a pair of plastic scintillator detectors is used. One of the detectors is small, 50 cm x 23 cm x 5 cm plastic scintillator detector, with a single PMT looking at its longest side via a Perspex light guide tapering to the diameter of a PMT, made by JINR, Dubna, Russia, and assembled locally. The other, larger one has dimensions of 100 cm x 100 cm x 5 cm, equipped with four PMT directly coupled to the corners beveled at 45°,made by Amcrys-H, Kharkov, Ukraine. The smaller detector may serve as a check of stability of the muon time series obtained from the larger detector, which is important for long term measurements. It can also be used (in coincidence with the larger detector) for measurements of the lateral spread of particles in CR showers and decoherence. Plastic scintillation detectors are also employed for active shielding of gamma spectrometers. In the UL, a 35% efficiency radio-pure p-type HPGe detector, made by ORTEC, 12 cm thick cylindrical lead castle is deployed around the detector. One of the set-ups is presented at Fig.2. Another HPGe detector, of 10% efficiency, is placed in GL.

FIGURE 2. Detectors in the underground laboratory. Large scintillator detector is placed above HPGe and small scintillator can change position.

Data acquisition system is identical both in UL and GL and it has two flash analog to digital converter (FADC), one in each laboratory, made by CAEN (type N1728B). These are versatile instruments, capable of working in two modes, energy histogram mode when performing as digital spectrometers or, in the oscillogram mode, when they perform as digital storage oscilloscopes. In both modes, they sample at 10 ns intervals into 2^{14} channels in four independent inputs. The full voltage range is ±1.1 V. They are capable of operating in the list mode, when every analyzed event is fully recorded by the time of its occurrence and its amplitude. This enables the correlation of events, both prompt and arbitrarily delayed, at all four in puts with the time resolution of 10 ns. Single and coincident data can be organized into time series within any integration period from 10 ns up. The two N1728B units are synchronized, enabling coincidence/correlation of the events recorded in both of them. The flexible software encompassing all above said off-line analyses is user-friendly and entirely homemade. The preamplifier outputs of the PMT of the larger detectors are paired diagonally. Signals from these paired inputs are later coincided off-line and their amplitudes added to produce the single spectra. This procedure suppress low-energy portion of the background spectrum (up to some 3 MeV), mostly environmental radiation, leaving only high-energy loss events due to CR muons and EM showers that peak at about 10 MeV, shown at Fig 3. The output of the PMT of the smaller detector is fed to the third input of FADC. [3]

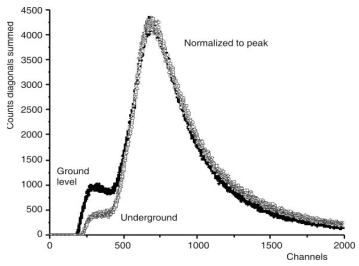

FIGURE 3. The sum spectra of two diagonals of the large plastic detectors in the UL and GLL. For comparison, the spectra are normalized for the peaks to coincide. Channel 650 corresponds to the muon energy loss of 10 MeV.

Simulation and Results

The experimental set-up is rather flexible, thus allowing different studies of the muon and electromagnetic components of cosmic rays at the ground level and at the shallow depth underground. The cosmic-ray muon flux in the underground laboratory has been determined from data taken from November 2008 till June 2013 (there were some small gaps in recording data during this period). These measurements yielded the precise values of the integral cosmic ray muon flux at the location of Belgrade. Measured muon flux is: 137(6) $m^{-2}s^{-1}$ at the ground level and 45(2) $m^{-2}s^{-1}$ at the underground level [4]. Different analyses of time series of these measurements have also been performed. Interpretation and calibration of the experimental spectra has been done using Monte Carlo simulation packages CORSIKA and Geant4 [5, 6]. CORSIKA simulates extensive air showers generated by the primary cosmic-rays in interactions with air nuclei at the top of the atmosphere. It gives spectra of the secondary cosmic-rays at the preferred observation level. These secondary particles, their energy and momentum direction distribution, obtained by CORSIKA, are then used as an input for the Geant4 based simulation of the detectors. In this simulation, particles first traverse through soil and infrastructure of the UL lab before hitting the detector. Then the response of the plastic scintillation detectors is simulated. For the UL scintillators, the simulated spectra are shown in Fig. 4.[7]

They agree very well with the experimental ones, except in the low-energy part where the ambiental gamma radiation is mostly present and where the cuts are applied. We also used these simulation packages to simulate different experimental set-ups and to obtain information about lower cut-of energy of primary cosmic rays at our site and for single muons and muons in coincidence. Energy of the primary particles from which detected muons originate increases for UL compared to GL but also for muons in coincidence compared with single detected muons.

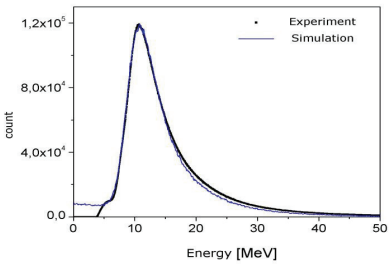

FIGURE 4. Experimental vs simulated spectrum of large plastic scintillator detector at UL

These measurements allow us to study fluctuations in muon flux intensity during the rising phase of Solar Cycle 24 and to make five-minutes or one-hour time series of the flux. The scintillator counts are corrected for atmospheric pressure for the whole period of measurements and, as well, for vertical temperature profile for the period of last six years. The results are compared with other correction methods available. One-hour time series of the cosmic ray muon intensity at the ground level are checked for correlation with European neutron monitors (NM), with emphasis on occasional extreme solar events, e.g. Forbush decreases (FD) in order to investigate claims of influence of cosmic-rays on cloud formation and climate [8,9] In some specific time periods, like during the FD in March 2012, we showed that our muon measurement system has sensitivity comparable to European neutron monitors in this period, but still not as efficient as NM with better geographical position (at high altitude), e.g. Jungfraujoch in the Swiss Alps.These results are presented at Fig. 5. Due to fact that muons detected underground originate from primary particles with energy around and above the limit for solar modulation time series from UL are less sensitive to these Solar events.

FIGURE 5. Time series for March 2012 recorded at NM at Jungfraujoch compared to time series obtained at Belgrade cosmic-rays station

Acknowledgement

The present work was funded by the Ministry of Education and Science of the Republic of Serbia, under the Project No. 171002.

References

[1] L.I. Dorman, *Cosmic-rays in the Earth's Atmosphere and Underground*, Kluwer, Dordrecht, 2004.

[2] S. Niese, *Underground laboratories for low-level radioactivity measurements*. Analysis of Environmental Radionuclides, 209-240, (2008) P.P. Povinec, ed.,Elsevier, Amsterdam.

[3] A.Dragić, V.Udovičić, R.Banjanac, D.Joković, D.Maletić, N.Veselinović, M.Savić, J.Puzović, I.Aničin, *The new set-up in the Belgrade low-level and cosmic-ray laboratory*, Nucl. Technol. Radiat. 26 (2011) 181-192

[4] A. Dragić, D. Joković, R. Banjanac, V. Udovičić, B. Panić, J. Puzović, I. Aničin, *Measurement of cosmic ray muon flux in the Belgrade ground level and underground laboratories*, Nuclear Instruments and Methods in Physics Research A 591 (2008) 470-475.

[5] D. Heck, *CORSIKA: a Monte Carlo code to simulate extensive air showers*, Report FZKA 6019, Forschungszentrum Karlsruhe, 1998.

[6] S. Agostinelli et al., *the Geant4 collaboration*, Nucl. Instrum. and Meth. A 506 (2003) 250-303

[7] A.Dragić, R. Banjanac, V. Udovičić, D. Joković, J.Puzović, I Aničin, I., *Periodic Variations of CR Muon Intensity in the Period 2002-2004* Proceedings of the 21st European cosmic-ray Symposium, Košice, Slovakia (2008) 368-373.

[8] A.Dragić, I.Aničin, R.Banjanac, V.Udovičić, D.Joković, D.Maletić, J.Puzović, *Forbush decreases - clouds relation in the neutron monitor era,* Astrophys. Space Sci. Trans. 7 (2011) 315-318.

[9] H. Svensmark, *Cosmoclimatology: a new theory emerges*, Astron. Geophys. 48 (2007) 1.18-1.24.

CORRELATIVE AND PERIODOGRAM ANALYSIS OF DEPENDENCE OF CONTINUOUS GAMMA SPECTRUM IN THE SHALLOW UNDERGROUND LABORATORY ON COSMIC RAY AND CLIMATE VARIABLES

Dimitrije Maletić, Radomir Banjanac, Dejan Joković, Vladimir Udovičić, Aleksandar Dragić, Mihailo Savić, Nikola Veselinović

Institute of Physics University of Belgrade, Serbia

***Abstract**. The continuous gamma spectrum, Cosmic ray intensity and climate variables; atmospheric pressure, air temperature and humidity were continually measured in the Underground laboratory of Low Background Laboratory in the Institute of Physics Belgrade. Same three climate variables for outside air were obtained from nearby meteorological station. The obtained gamma spectrum, measured using HPGe detector, is split into three energy ranges, low, intermediate and high ending with energy of 4.4 MeV. For each of the energy intervals periodogram and correlative analysis of dependence of continuous gamma spectrum on cosmic ray intensity and climate variables is performed. Periodogram analysis is done using Lomb-Scargle periodograms. The difference of linear correlation coefficients are shown and discussed, as well as the differences in resulting periodograms.*

Key words: *gamma spectroscopy, surface air, underground laboratory, correlative analysis, periodogram analysis.*

1. INTRODUCTION

The low-level and cosmic-ray laboratory in the Low-Background laboratory for Nuclear Physics in the Institute of Physics Belgrade is dedicated to the measurements of low activities and to the studies of the muon and electromagnetic components of cosmic rays at the ground level and at the shallow depth under-ground, and in particular to the detailed studies of the signatures of these radiations in HPGe spectrometers situated shallow underground. The ground level part of the laboratory (GLL), at 75 m above sea level, is situated at the foot of the vertical loess cliff, which is about 10 meters high. The underground part of the laboratory (UL), of the useful area of 45 m², is dug into the foot of the cliff and is accessible from the GLL via the 10 meters long horizontal corridor, which serves also as a pressure buffer for a slight overpressure in the UL (Fig.1). The overburden of the UL is about 12m of loess soil, equivalent to 25 meters of water. [1]

In the UL laboratory the gamma spectrum is recorded using HPGe detector and fast ADC unit made by CAEN, and analysed using software developed in our laboratory. Besides HPGe measurements the air pressure, temperature and humidity were recorded in UL also. Values for temperature, pressure and humidity of outside air was taken from publicly available web site. The time period from which the measurements were used in this analysis is from beginning of December 2009 till end of April 2010.

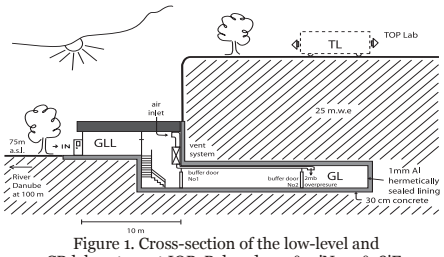

Figure 1. Cross-section of the low-level and CR laboratory at IOP, Belgrade, 44°49'N, 20°28'E, vertical rigidity cut off 5.3 GV.

Continuous Cosmic rays' (CR) spectrum measure-ments by means of a pair of small plastic scintillators [(50x25x5)cm] started in the GLL and UL back in 2002 and lasted for about 5 years. It agrees to the spectrum of relatively shallow underground laboratories worldwide [2]. These measurements yielded the precise values of the integral CR muon flux at the ground level and underground level laboratory, at the location of Belgrade [3]. Different analyses of the time series of these measurements have also been performed [4, 5]. Since the UL is completely lined with the hermetically sealed 1 mm thick aluminum lining, and the ventilation system keeps the overpressure of 2 mbars of doubly filtered air, the concentration of radon is kept at the low average value of about 10 Bq/m³.

Measurements and analysis of periodicy of gamma-rays in underground laboratory had been reported [6-7], and also for Radon measurements and periodicity [8-9] including advanced Multivariate Analysis tecniques [10-11].

Most recent research done in our laboratory [12] addresses the question of determination of origin of low energy gamma-rays detected by HPGe detector, which are coming either from environmental radiation or from CR. In this paper the correlative analysis is used to address the same question of composition of low-energy gamma-rays spectrum, thus giving us the new approach to the research done in [12].

The correlative analysis in this paper was done using Toolkit for Multivariate Analysis TMVA[13] package as part of the ROOT[14] software, widely used in analysis, especially for High Energy Physics experiments. The TMVA was used for analysis extensively in our laboratory, and it was the natural choice to use the software for correlative analysis also. Lomb-Scargle periodograms were produced using software developed in Low-Background laboratory.

2. EXPERIMENTAL SETUP

In the UL 35% efficiency radiopure HPGe detector, made by ORTEC, is used. The HPGe is sourounded by 12 cm thick cylindrical lead castle. Cosmic ray setup consists of a single [(100x100x5)cm] plastic scintillator detector equipped with four PMTs directly coupled to the corners beveled at 45^0, made by Amcrys-H of Kharkov, Ukraine. The signals from HPGe detector and plastic scintillators give output to fast ADC unit with four independent inputs each, made by CAEN, of the type N1728B. CAEN units are versatile instruments capable of working in the so-called energy histogram mode, when they perform like digital spectrometers, or/and in the oscillogram mode, when they perform like digital storage oscilloscopes. In both modes they sample at 10 ns intervals, into 2^{14} channels. The full voltage range is ±1.1V.

CAEN units are capable of operating in the list mode, when every analyzed event is fully recorded by the time of its occurrence over the set triggering level, and its amplitude, in the same PC, which controls their workings. This enables to off-line coincide the events at all four inputs, prompt as well as arbitrarily delayed, with the time resolution of 10 ns, as well as to analyze the time series not only of all single inputs, but also of arbitrary coincidences, with any integration period from 10 ns up. The flexible software that performs all these off-line analyses is user-friendly and is entirely homemade.

The preamplifier outputs of the PMTs of detectors are paired diagonally, the whole detector thus engaging the two inputs of the CAEN unit. The signals from these inputs are later off-line coincided and their amplitudes added, to produce the singles spectra of these detectors. Offline coincidence allows that the high intensity but uninteresting low energy portion of the background spectrum of this detector (up to some 3 MeV), which is mostly due to environmental radiations, is practically completely suppressed, leaving only the high energy-loss events due to CR muons and EM showers that peak at about 10 MeV, as shown in Figure 2.

Since event of HPGe gamma spectrum and Cosmic rays consists of time-stamp and the amplitude, off-line analysis is used to create time series of arbitrary time window with selection of specific part of gamma spectrum as well as the time series of Cosmic ray flux in UL (Figure 3.). This enables that whole gamma spectrum can be divided into energy ranges, and analyze each energy range separately. The spectrum separation is done on channel numbers, and after the energy calibration, the energy ranges used in our analysis are 180-440 keV, 620-1330 keV and 1800-4440 keV. The full gamma spectrum is recorded in range of 180-6670 keV. The part of gamma spectrum of the HPGe is shown in Figure 4.

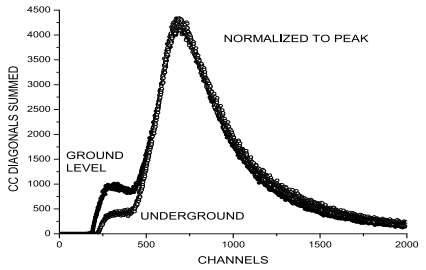

Fig. 2. The sum spectra of two diagonals of big plastic detectors in the UL and GLL .

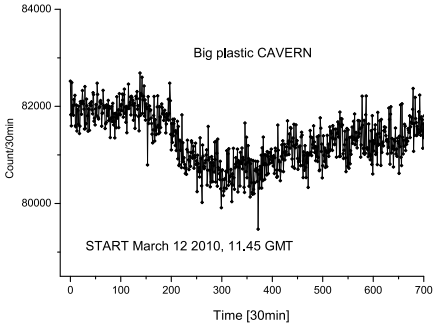

Fig. 3. The time series of the CR muon count of the big plastic detector in the UL.

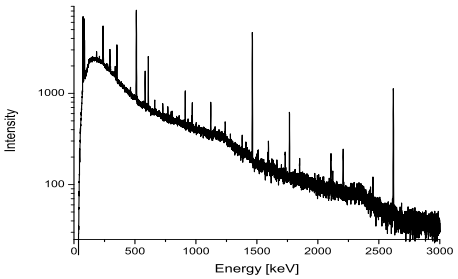

Figure 4. Gamma spectrum of the HPGe detector in 12cm lead castle in the Underground laboratory.

3. RESULTS AND DISCUSSIONS

The analysis starts with correlation analysis. The software for correlative analysis is a part of TMVA package. Hourly time series of variables, atmospheric pressure P, temperature T, and humidity H for UL (P_R, T_R, H_R), and outside (P,T,H) are used, Cosmic ray time series (CR) as well as T (DT) and H (DH) difference of UL and outside values make the number of nine input variables. The table summarizing the linear correlation coefficients is shown in Table 1. We can see correlation between each input variable and HPGe gamma spectrum for full energy range in Table 1 also.

DH	-10	69	-9	-86	57	-22	51	-25	-64	100
DT	7	-98	7	60	-30	10	-24	42	100	-64
CR	-14	-42	-65	36	-14	-52	13	100	42	-25
H_R	-2	30	-44	-1	42	-59	100	13	-24	51
P_R	14	-13	80	-8	-22	100	-59	-52	10	-22
T_R	1	43	-16	-41	100	-22	42	-14	-30	57
H	10	-63	-15	100	-41	-8	-1	36	60	-86
P	11	-9	100	-15	-16	80	-44	-65	7	-9
T	-6	100	-9	-63	43	-13	30	-42	-98	69
HPGe	100	-6	11	10	1	14	-2	-14	7	-10
	HPGe	T	P	H	T_R	P_R	H_R	CR	DT	DH

Table 1. Summary table of linear correlation coefficient for all 9 input variables' 1 hour time series and 1 hour time series of HPGe gamma spectrum for full energy range.

Correlation analysis was done also for three mentioned energy ranges, the Table 2. summarizes the results.

	180-6670 keV	180-440 keV	620-1330 keV	1780-4440 keV
T	-0.070	-0.045	-0.041	-0.096
P	**+0.111**	**+0.124**	**+0.033**	**+0.010**
H	+0.106	+0.056	+0.047	+0.101
T_{UG}	+0.013	-0.029	+0.014	-0.012
P_{UG}	+0.149	+0.111	+0.091	+0.061
H_{UG}	-0.029	-0.068	-0.030	+0.028
CR	**-0.140**	**-0.179**	**-0.030**	**+0.036**
T_{UG}-T	+0.076	+0.043	+0.046	+0.100
H_{UG}-H	-0.105	-0.083	-0.055	-0.072

Table 2. Linear correlation coefficients in % for full and three narrower energy ranges.

All the correlation of HPGe gamma spectrum hourly time series and input variables are not significant. The biggest correlation coefficient with HPGe time series is pressure time series measured underground followed by Cosmic ray time series. It is interesting to notice the change of correlation coefficients with HPGe for atmospheric pressure and Cosmic rays time series. While pressure correlation coefficients tend to drop going towards higher gamma energies, Cosmic rays' correlation coefficients are increasing from negative sign to positive one. This observation is in agreement with the fact that the Cosmic rays are contributing more to the the gamma spectrum of higher energies, as it was shown in [12]. Since Cosmic rays and pressure are anti-correlated with correlation coefficient of -65%, as can be seen in Table 1, increase in atmospheric pressure will give negative correlation coefficient of HPGe and Cosmic rays' time series. This can be explained by having in mind that Cosmic rays are contributing insignificantly to gamma spectrum on lower energies [12] behaving like constant in low energy range, while increase in pressure increases the air density, thus more gamma scattering events are contributing to low energy gamma spectrum.

In the periodogram analysis the Lomb-Scargle periodograms were produced for atmospheric variables P, T, H and HPGe gamma spectrum. The periodograms show only daily periodicity of T, H time series as shown on figures 5 and 6. The P periodogram on Figure 7. Shows expected daily and mid-daily periodicity. It is noticeable that the periodogram for P has lowest spectral powers, which means that periodicity of P is less noticeable. Also, the unexpected 1/3 day periodicity is with low spectral power. The periodogram analysis showed that there is no significant periodicity in HPGe gamma spectrum time series, as shown on Figure 8.

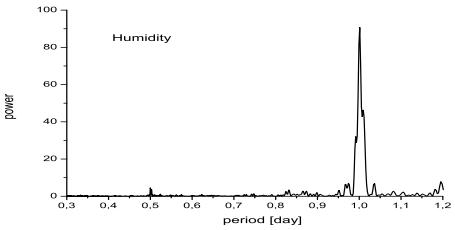

Figure 5. Lomb-Scargle periodogram of air humidity.

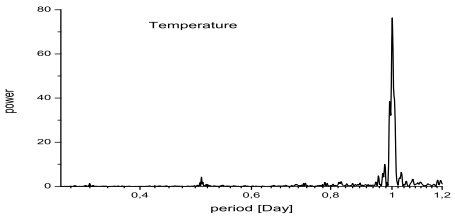

Figure 6. Lomb-Scargle periodogram of air temperature.

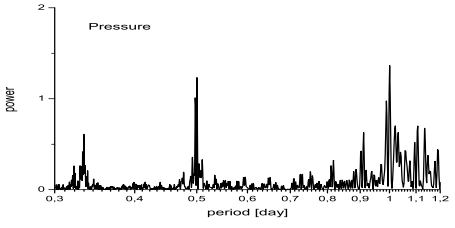

Figure 7. Lomb-Scargle periodogram of air pressure.

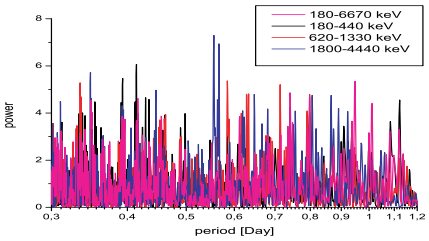

Figure 8. Lomb-Scargle periodogram of full and three different energy range HPGe gamma spectrum time series.

CONCLUSION

In the Underground laboratory of Low Background Laboratory in the Institute of Physics Belgrade the continuous HPGe gamma spectrum, Cosmic ray intensity and climate variables were continually measured in the period from beginning of December 2009 till the end of April 2010. The HPGe gamma spectrum is split into three energy ranges, low, intermediate and high. For each of the energy intervals periodogram and correlative analysis of dependence of continuous gamma spectrum on cosmic ray intensity time series and climate variables time series is performed. Periodogram analysis is done using Lomb-Scargle periodograms. The correlation coefficient between air pressure and Cosmic rays is -65%. The correlation coefficients between HPGe gamma spectrum and input variables are not significant. The decrease of values of correlation coefficients of gamma spectrum and air pressure is present. The increase of values of correlation coefficients of gamma spectrum and Cosmic rays is present also. Increase in atmospheric pressure is resulting in negative correlation coefficient between HPGe and Cosmic rays' time series for low energy gamma spectrum. The more significant contribution of Cosmic rays in high energy gamma spectrum, as opposite to insignificant contribution of Cosmic rays to low energy gamma spectrum is evident. Lomb-Scargle periodograms showed daily periodicity for air temperature and humidity, and additional mid-daily periodicity for air pressure. There is no noticeable periodicity for each of energy ranges of gamma spectrum.

Acknowledgement: *The paper is a part of the research done within the project "Nuclear research methods of rare events and cosmic radiation" (No. 171002) financed by the Ministry of Education, Science and Technological Development of the Republic of Serbia (2011-2015).*

REFERENCES

1. Dragic Aleksandar, Udovicic Vladimir I, Banjanac Radomir M, Jokovic Dejan R, Maletic Dimitrije M, Veselinovic Nikola B, Savic Mihailo, Puzovic Jovan M, Anicin Ivan V "The New Set-Up in the Belgrade Low-Level and Cosmic-Ray Laboratory", NUCLEAR TECHNOLOGY & RADIATION PROTECTION, vol. 26, br. 3, pp. 181-192, 2011
2. S. Niese, "Underground laboratories for low-level radioactivity measurements", Analysis of Environmental Radionuclides, Ed. P.Povinec, Elsevier, Amsterdam, pp.209-239, 2008
3. A.Dragić, D.Joković, R.Banjanac, V.Udovičić, B.Panić, J.Puzović and I.Aničin, "Measurement of cosmic ray muon flux in the Belgrade ground level and underground laboratories", Nucl. Instr. and Meth. in Phys. Res. A591 , pp. 470 – 475, 2008
4. A. Dragić, R. Banjanac, V. Udovičić, D. Joković, I. Aničin and J. Puzović, "Comparative study of power spectra of ground and shallow underground muon data", Int. Journal of Modern Physics A, Vol. 20 pp. 6953-6955, 2005
5. A. Dragić, R. Banjanac, V. Udovičić, D. Joković, J. Puzović, I. Aničin, "Periodic Variations of CR Muon Intensity in the Period 2002-2004", Proc. 21st European Cosmic Ray Symposium, Košice, Slovakia, pp.368-373, 2008.
6. Banjanac Radomir M, Udovicic Vladimir I, Dragic Aleksandar, Jokovic Dejan R, Maletic Dimitrije M, Veselinovic Nikola B, Grabez Bojana S "Daily Variations of Gamma-Ray Background and Radon Concentration", ROMANIAN JOURNAL OF PHYSICS, vol. 58, br. , pp. S14-S21, 2013
7. Banjanac Radomir M, Dragic Aleksandar, Udovicic Vladimir I, Jokovic Dejan R, Maletic Dimitrije M, Veselinovic Nikola B, Savic Mihailo "Variations of gamma-ray background in the Belgrade shallow underground low-level laboratory", APPLIED RADIATION AND ISOTOPES, vol. 87, br. , pp. 70-72, 2014
8. V. Udovičić, B. Grabež, A. Dragić, R. Banjanac, D. Joković, B. Panić, D. Joksimović, J. Puzović, I. Aničin, "Radon problem in an underground low-level laboratory", Radiation Measurements 44 pp. 1009-1012. 2009
9. V. Udovičić, I. Aničin, D. Joković, A. Dragić, R. Banjanac, B. Grabež, N. Veselinović, "Radon Time-series Analysis in the Underground Low-level Laboratory in Belgrade, Serbia", Radiation Protection Dosimetry 145 (2-3) pp. 155-158, 2011
10. Maletic Dimitrije M, Udovicic Vladimir I, Banjanac Radomir M, Jokovic Dejan R, Dragic Aleksandar L, Veselinovic Nikola B, Filipovic Jelena Z "Comparison of Multivariate Classification and Regression Methods for the Indoor Radon Measurements", NUCLEAR TECHNOLOGY & RADIATION PROTECTION, vol. 29, br. 1, pp. 17-23 (2014)
11. Maletic Dimitrije M, Udovicic Vladimir I, Banjanac Radomir M, Jokovic Dejan R, Dragic Aleksandar L, Veselinovic Nikola B, Filipovic Jelena Z "Correlative and Multivariate Analysis of Increased Radon Concentration in Underground Laboratory", RADIATION PROTECTION DOSIMETRY, vol. 162, br. 1-2, pp. 148-151, 2014
12. Banjanac Radomir M, Maletic Dimitrije M, Jokovic Dejan R, Veselinovic Nikola B, Dragic Aleksandar, Udovicic Vladimir I, Anicin Ivan V "On the omnipresent background gamma radiation of the continuous spectrum", NUCLEAR INSTRUMENTS & METHODS IN PHYSICS RESEARCH SECTION A, vol. 745, br. , str. 7-11, 2014.
13. R. Brun and F. Rademakers, "ROOT - An Object Oriented Data Analysis Framework", Nucl. Inst. Meth. in Phys. Res. A 389, 81, 1997
14. A. Hoecker, P. Speckmayer, J. Stelzer, J. Therhaag, E. von Toerne, and H. Voss, "TMVA - Toolkit for Multivariate Data Analysis", PoS ACAT 040 (2007), arXiv:physics/070303

BACKGROUND SPECTRUM CHARACTERISTICS OF THE HPGE DETECTOR LONG-TERM MEASUREMENT IN THE BELGRADE LOW-BACKGROUND LABORATORY

Radomir Banjanac, Vladimir Udovičić, Dejan Joković, Dimitrije Maletić, Nikola Veselinović, Mihailo Savić, Aleksandar Dragić, Ivan Aničin

Institute of Physics, Belgrade, Serbia

Abstract. *The Belgrade low-level background laboratory, built in 1997, is shallow (25 m.w.e) underground space (45m²) which is constantly ventilated with fresh air against radon. The muon intensity (about 3.5 times less than at ground level), radon concentration (suppressed to averaged value of 15 Bqm⁻³), as well as gamma-ray background are monitoring for more than eight years. After long-term measurement using the radiopure HPGe detector with 35% relative efficiency, the measured data includes radionuclide concentration of detector surroundings, estimation of background time variation due to radon and cosmic-rays as well as MDA values for typical samples of water matrix. The detailed characteristics of gamma-ray background spectra are here presented.*

Key words : *Underground laboratory, Low-level background, long-term gamma-ray measurement*

1. INTRODUCTION

Various experiments which strive for the detection of very rare events require the lowest possible background radiation which can be achieved only in a deep underground laboratory. Some of recent the most interesting are double beta-decay experiments, [1] and dark matter searches, [2]. In any applied measurements of low activities, a goal that is pursued by all gamma spectroscopist is to lower the minimum detectable activity (MDA) of their detection system obtaining more statistical evidence in less time.

But, any long and even short-term gamma-ray background measurement is subject to certain temporal variations due to time variability of two prominent contributors to background, cosmic-rays and radon. The most of the low background laboratories that deal with low activity measurements have developed routine measurements of background. The duration of these measurements may be from one day to even a month and they are designed to produce results with sufficiently low statistical errors for the envisaged measurements. These measurements yield only average values of the background, what in principle may lead to systematic errors in later measurements, especially of NORM samples.

The averaged values of the background, gamma lines and continuum, nuclide concentrations or MDA presenting a “personal card” of used detector system for certain samples in any low-level background laboratory, [3]. Here is attempt to present our low-level background laboratory in a similar way. First of all, the detailed description of the laboratories and used detector system are described.

2. DESCRIPTION OF THE LABORATORIES AND EQUIPMENT

The Belgrade underground low-level laboratory (UL), built in 1997 and located on the right bank of the river Danube in the Belgrade borough of Zemun, on the grounds of the Institute of Physics. The overburden of the UL is about 12 meters of loess soil, equivalent to 25 meters of water. It is equipped with ventilation system which provides low radon concentration of 15(5) Bq/m³. The “passive” shield consists of 1 mm thick aluminum foil which completely covers all the wall surfaces inside the laboratory, including floor and ceiling. As the active radon shield the laboratory is continuously ventilated with fresh air, filtered through one rough filter for dust elimination followed by active charcoal filters for radon adsorption. The UL has an area of 45m² and volume of 135m³ what required the rate of air inlet adjusted to 800m³/h. This huge amount of fresh air contributes to greater temperature variations and the long-term mean value of temperature inside the UL is 19(4)°C. The rate of air outlet (700m³/h) was adjusted to get an overpressure of about 200 Pa over the atmospheric pressure, what prevents radon diffusion through eventual imperfections in the aluminum layer. Relative humidity is controlled by a dehumidifier device, what provides that the relative humidity in the underground laboratory does not exceed 60%. The muon intensity (which is about 3.5 times less than at ground level), radon concentration and gamma-ray background are monitoring for more than eight years. Comparative background study is performing in the GLL (at ground level) which is equipped with a Ge detector (13% relative efficiency and not intrinsically low-radioactivity level, named SGe) and a big plastic scintillator (1m², named BPS) in veto position. The GLL is air-conditioned (average radon concentration of

50(30) Bq/m^3) has an area of 30m^2 and volume of 75m^3. The Fig. 1 presents veto arrangement of the HPGe detector (BGe, in 12cm lead shield) and big plastic scintillator, inside the UL.

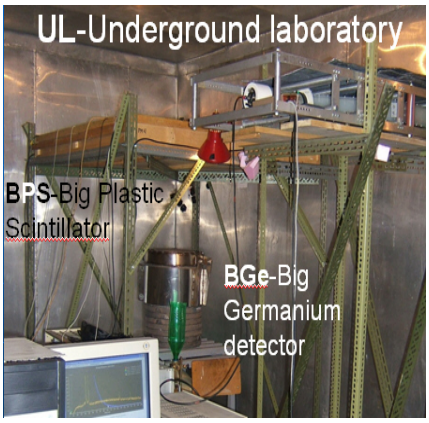

Fig. 1 Veto arrangement of the HPGe detector (BGe) and big plastic scintillator inside the UL

3. DESCRIPTION OF DETECTOR SYSTEMS IN THE UL

The low-level background detector system in the UL includes an intrinsically low-radioactivity level p-type Ge detector (35% relative efficiency, named BGe) and another plastic veto scintillator (1m^2, named BPS) situated coaxially above the BGe detector. The BGe is a GEM30 model (made by ORTEC) in LB-GEM-SV cryostat configuration with magnesium end cap. The energy resolution at 1332.5keV, measured by analog data acquisition system, is 1.72keV, 0.65keV at 122keV as well as the Peak to Compton ratio at 1332.5keV has value of 68. The cylindrical lead shielding of the BGe, with a wall thickness of 120 mm and an overall weight of about 900kg, was cast locally out of scratch plumbing retrieved after the demolition of some old housing. Radon monitoring inside the laboratories was performed by radon monitor, model RM1029 manufactured by Sun Nuclear Corporation. The device consists of two diffused junction photodiodes as a radon detector, and is furnished with sensors for temperature, pressure and relative humidity. A pair of plastic scintillator detectors is used for CR muon measurements at both laboratories. One of them is a larger (100cmx100cmx5cm) detector (BPS), equipped with four PMT directly coupled to the corners beveled at 45°, made by Amcrys-H, Kharkov, Ukraine. The other, a smaller 50cmx23cmx5cm plastic scintillator detector, with a single PMT looking at its longest side via a Perspex light guide tapering to the diameter of a PMT, made by JINR, Dubna, Russia, and assembled locally. The smaller detector may serve as a check of stability of the muon time series obtained from the larger detector, which is important for long term measurements. Two flash analog to digital converters (FADC), made by C.A.E.N (type N1728B), which sample at 10 ns intervals into 214 channels were used to analyze spectra from Ge detectors as well as corresponding BPS. User-friendly software was developed to analyze the C.A.E.N data with the possibility to choose the integration time for further time-series analysis that corresponds to integration time of the radon monitor. The performances of digital acquisition system as well as software developed for analysis were described in detail, [4].

4. THE RESULTS OF BACKGROUND MEASUREMENTS IN THE UL

Additional to intrinsically low-radioactivity level of the BGe itself, environmental radioactivity is low, too. The UL was built from low activity concrete about 12 Bq/kg of U-238 and Th-232, and of 23 Bq/kg and 30 Bq/kq of surrounding soil, respectively. Radioactivity of aluminum wall-lining is negligible. Pb-210 activity of used lead shield of 30Bq/kg is measured. After long-term cosmic-ray, [5], radon concentration, [6] and gamma-ray background measurements, no significant long-term time variations of gamma background was found, [7]. After several years of almost continuously background measurements, the integral background rate in the region from 40keV to 2700keV has mean value of about 0.5 cps. The lines of Co-60 are absent in the background spectrum, while the line of Cs-137 with the rate of 1×10^{-4} cps starts to appear significantly only if the measurement time approaches one month. Fukushima activities, though strongly presented in our inlet air filters samples, did not enter the background at observable levels, in spite of the great quantities of air that we pump into the UL to maintain the overpressure, and it seems that the double air filtering and double buffer door system, along with stringent radiation hygiene measures, is capable of keeping the UL clean in cases of global accidental contaminations. No signatures of environmental neutrons, neither slow nor fast, are present in direct background spectra.

The Fig. 2 shows a characteristic shape of background spectrum obtained in the UL after about 6 months of measuring, with distinctive Pb X-ray lines at the beginning of the spectrum, annihilation line, and lines from ^{40}K and ^{208}Tl (2614.5keV) at the end of the spectrum with a lot of post-radon lines between them.

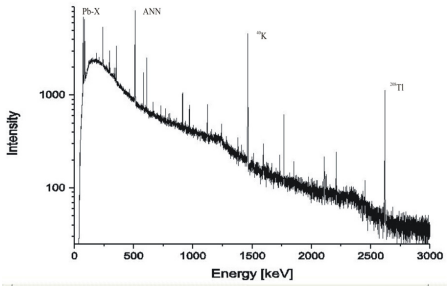

Fig. 2 Background spectrum of the HPGe detector (BGe) inside the UL after about 6 months of measuring

The table 1 in the third column presents gamma-ray background values of typical spectrum measured in

the UL using the BGe in direct (no veto) mode. The measurement time was about 6 months.

Table 1 The background characteristics of the BGe inside the UL

Line/ region (keV)	Radionuclide/ series/ nuclear reaction	Intensity (10^{-3} s^{-1})	MDA (mBq) for 100ks Water matrix
40-2700	-	500	-
46.5	Pb-210/U-238	0.38(11)	1500
53.2	U-234	-	9400
63.3	Th-234	-	700
72.8	Pb-X-$K_{\alpha 2}$	3.1(1)	-
75	Pb-X-$K_{\alpha 1}$	6.2(1)	-
84.9	Pb-X-$K_{\beta 1}$	4.2(1)	-
87.3	Pb-X-$K_{\beta 2}$	1.49(6)	-
92.5	Th-234	-	100
143.8	U-235	-	20
163.4	U-235	-	110
200.3	U-235	-	100
238.6	Pb-212/Th-232	0.83(4)	40
242	Pb-214/U-238	0.20(2)	-
295.2	Pb-214/U-238	0.71(4)	40
338.3	Ac-228/Th-232	0.15(2)	-
351.9	Pb-214/U-238	1.26(5)	30
477.6	Be-7	-	40
510.8+511	Tl-208/Th-232/ANN	7.0(1)	-
583.2	Tl-208/Th-232	0.30(3)	56
609.2	Bi-214/U-238	1.08(5)	60
661.7	Cs-137	0.10(5)	9
727.3	Bi-212	-	200
803.3	Pb-206 (n,n^{l}) Pb-206	0.11(2)	-
911.2	Ac-228/Th-232	0.25(2)	110
969	Ac-228/Th-232	0.11(2)	80
1001	Pa-234m	-	1300
1120.4	Bi-214/U-238	0.28(3)	-
1173.2	Co-60	-	19
1332.5	Co-60	-	11
1238.1	Bi-214/U-238	0.09(2)	-
1460.8	K-40	3.27(9)	850
1764.6	Bi-214/U-238	0.49(3)	230
2103.7	2614.5SE/Tl-208	0.13(2)	-
2204.2	Bi-214/U-238	0.15(2)	-
2614.5	Tl-208/Th-232	1.05(5)	-

The fourth column of the same table presents minimum detectable activity (MDA) calculated for predicted measurement time of 100000 seconds (approximately one day) for cylindrical sample (volume of 120cm^3) situated on the top of the detector. Efficiency calibration was obtained by GEANT4 simulation toolkit as well as experimentally using appropriate standard. The difference between the two efficiency calibration curves is less than 5% for sample of water matrix, which MDA is here presented. MDA values are calculated as MDA=L_D/(t x Eff x p), where the L_D=2.71+4.65$B^{1/2}$ is detection limit. B is background at the energy of gamma-ray line with absolute detection efficiency Eff and emission probability p. If the predicted measurement time t is valued in seconds then MDA values have Bq unit. The obtained MDA values are presented for water matrix cylindrical samples in bottles with volume of 120cm^3.

With the BPS currently positioned rather high over the detector top, at a vertical distance of 60cm from the top of the lead castle, in order to allow for the placing of voluminous sources in front of the vertically oriented detector, the off-line reduction of this integral count by the CR veto condition is only about 18%. Up to a factor of two might be gained if the veto detector were to be positioned at the closest possible distance over the BGe detector. This configuration requires some changes of the lead shield including introducing a sliding lead lid. Such a new shielding and veto configuration would be additionally reduce gamma-ray background up to the same factor that corresponds to factor of reduction expected for cosmic rays.

We do not insist on the lowering of statistical errors which depend on background levels solely and are difficult to reduce further with available means, but rather emphasize its stability due to the low and controlled radon concentration in the laboratory. This is essential, especially in NORM measurements, and makes our system virtually free of systematic errors as compared to systems which operate in environments where radon is not controlled. In that systems the reduction of post-radon background activities is achieved by flushing the detector cavity with liquid nitrogen vapor, where the transient regimes during sample changes and possible deposition of radon progenies may introduce systematic uncertainties which are difficult to estimate.

***Acknowledgement**: The paper is a part of the research done within the projects OI171002 and III43002.*

REFERENCES

1. W.G. Kang, *et al.*, "Ultra-low gamma-ray measurement system for neutrinoless double beta decay", Appl. Radiat. Isot. (2013), vol. 81, pp. 290–293.
2. G. Angloher, *et al.*, "Results from 730 kg days of the CRESST-II Dark Matter search", Eur. Phys. J. (2012), vol. C72, pp. 1971
3. L. Dragounová and P. Rulík, "Low level activity determination by means of gamma spectrometry with respect to the natural background fluctuation", Appl. Radiat. Isot. (2013), vol. 81, pp. 123–127
4. A. Dragić *et al.*, "The new set-up in the Belgrade low-level and cosmic-ray laboratory", Nucl. Techn. Radiat. Prot. (2011), vol. 26/3, pp. 181-192
5. A. Dragić *et al.*, "Variations of CR-muon intensity in the declining phase of the 23rd solar cycle in ground and shallow underground data", 29th International Cosmic Ray Conference, Pune (2005), vol. 1, pp. 249-252
6. V. Udovičić *et al.*, "Daily and seasonal radon variability in the underground low-background laboratory in Belgrade, Serbia", Radiation Protection Dosimetry (2014), vol. 160, Issue 1-3, pp. 62-64
7. R. Banjanac *et al.*, "Variations of gamma-ray background in the Belgrade shallow underground low-level laboratory", Applied Radiation and Isotopes, (2014), vol. 87, pp. 70-72

Available online at www.sciencedirect.com

ScienceDirect

Physics Procedia 59 (2014) 63 – 70

Physics Procedia

GAMMA-2 Scientific Workshop on the Emission of Prompt Gamma Rays in Fission and Related Topics

Some peculiarities of digital gamma-ray spectroscopy with germanium detectors performed in presence of neutrons

N. Veselinović[a*], D. Maletić[a], D. Joković, R. Banjanac[a], V. Udovičić[a], M. Savić[a], , J. Puzović[b], I.V. Aničin[a] and A.Dragić[a+]

[a]*Institute of Physics, Pregrevica 118, 11080 Belgrade,Serbia*
[b]*Faculty of Physics, Studentski trg 12, 11000 Belgrade, Serbia*
[+]*on leave at Joint Research Centre, Geel, Belgium*

Abstract

We measured the time-differentiated spectrum of the ^{252}Cf source as seen by an high-purity germanium detector triggered by the NE213 liquid scintillator detector. The detectors are off-line coincided from the event-by-event list formed with 10 ns resolution by the quad FADC unit of the CAEN N1728B type. The signatures of the processes induced by fast and slow neutrons, both within the detector itself and in its environment, appear completely separated. The processes induced by fast neutrons are found in the prompt part of the time spectrum and those induced by thermal neutrons in the long tail of delayed coincidences. We analyse the time behaviour of spectral structures at 692 keV, which are the signatures of inelastic neutron scattering on Ge-72, and comment on its suitability for determination of the fast neutron flux in general, and in the digital gamma-ray spectroscopy in particular.

Selection and peer-review under responsibility of Guest Editor: Mr. Stephan Oberstedt - stephan.oberstedt@ec.europa.eu

Keywords: background spectra; neutrons; germanium; Cf-252

* Corresponding author: Tel.: +381 113713000
Email-address: veselinovic@ipb.ac.rs

Selection and peer-review under responsibility of Guest Editor: Mr. Stephan Oberstedt - stephan.oberstedt@ec.europa.eu
doi:10.1016/j.phpro.2014.10.010

1. Introduction

Neutrons induce a number of nuclear reactions on stable isotopes of germanium, which produce characteristic signatures in the spectra of germanium detectors. These have been studied in great detail with the aim to either improve on the knowledge of background spectra of germanium detectors, or for determination of neutron fluxes at the position of the detector (Stelson et al., 1972; Škoro et al., 1992; Wordel et al., 1996; Fehrenbacher et al., 1996, 1997; Gete et al., 1997; Siiskonen and Toivonen, 2005; Ljungvall and Nyberg, 2005; Abt et al., 2007; Ataç et al., 2009; Jovančević et al., 2010). Some of the studies dealt with environmental neutrons of cosmic-ray origin while some used different neutron sources, mostly with the fission spectrum. The findings were quite similar, irrespective of the origin of the neutrons. We undertook the time-differentiated study of some of these processes induced by ^{252}Cf fission neutrons in order to gain some insight into the dynamics of neutron-induced background in the detectors themselves, as well as in their usual environments.

2. The experiment

Our experimental setup consists of a small volume (2 litres) liquid scintillator (NE213) detector placed in a steel container and a 15% efficiency coaxial high-purity germanium (HPGe) detector, positioned as schematically presented in Fig. 1.

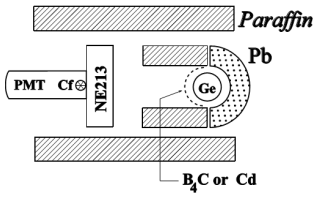

Fig. 1. The layout of the experiment (view from above)

The materials, which surround the detectors in the experiments, include lead, paraffin (hydrogen), boron, cadmium, aluminium and iron. The encapsulated ^{252}Cf source had a strength of about 2000 neutrons in 4π sr/s. On their way towards the HPGe detector the neutrons traverse the 7 cm thick layer of NE213. The distance between the end-cap of the NE213, which faces the HPGe detector, and the closest point of the HPGe detector is 10 cm. Fast neutrons with energies higher than 1 MeV, which leave the NE213 detector towards the HPGe detector, take less than 10 ns to reach this detector, while the neutrons which start as thermal take about 50 μs. Majority of neutrons, which slow down on their way towards the detector, take something in between these two values, but certainly closer to the lower one. The preamplifier outputs of both detectors are fed to the two out of four identical inputs of the flash ADC unit of the CAEN N1728B type. It can perform like a digital spectrometer capable to operate in the list, or the event-by-event mode. For every analysed event the time of its appearance over the triggering level is recorded with 10 ns resolution, while its amplitude is digitized and recorded in one of the available 32 k channels. This enables to off-line coincide the events of given amplitudes with 10 ns resolution. The software that produces and analyses the time spectra, which are equivalent to hardware TAC spectra, is entirely homemade.

3. The results

The singles spectrum of NE213 serves practically only as a trigger for the HPGe spectrum. The singles spectrum of the in this case lightly shielded germanium detector consists of the correspondingly rich environmental background spectrum, of the gamma rays given off by the californium source, and of the different features induced by fission neutrons of californium in the HPGe detector and in the surrounding materials. It stretches up to some 8 MeV. We shall here deal only with some interesting portions of this spectrum that are coincident with different delay times with the NE213 spectrum.

3.1. Effects in the environment

The time structure of the signatures of the effects, which neutrons induce in surrounding materials in our HPGe spectra, is particularly simple and illustrative. All the effects induced by fast neutrons which we see (mostly the inelastic scattering) tend to fall into the prompt peak of our time spectrum, while the effects induced by slow neutrons (mostly capture reactions) fall into the (very long) tail of delayed coincidences. The completeness of this separation is perhaps best illustrated by the cases of boron and iron. Fig.2a presents the portion of the HPGe spectrum that contains the 478 keV Doppler–widened line from the (n,α) reaction on ^{10}B, while Fig.2b depicts the part of the spectrum with the 847 keV line from (n, n') reaction on ^{56}Fe (found mostly in the NE213 casing). The first reaction has the high cross section for thermal neutrons, while the second is induced by neutron energies higher than about 1 MeV. The difference between the two cases is striking; the 478 keV structure is present only in the spectrum of delayed coincidences and on its place in the prompt spectrum the weak lines from the decay of californium appear, while the strong line of 847 keV exists only in the prompt spectrum and is completely absent in the delayed spectrum.

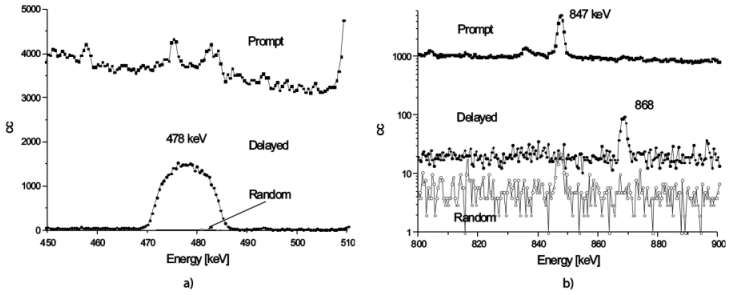

Fig. 2. The prompt, delayed (up to 1 μs) and random coincidence spectra of the 478 keV line from the reaction on boron (**a**), and of the 847 keV line from the reaction on iron (**b**). The line at 868 keV is from neutron capture on ^{73}Ge. Note that the first scale is linear while the second one is logarithmic.

Now the case of cadmium becomes instructive. Figure 3 is same as Fig. 2, but for the portion of the spectrum containing the most prominent line of 558 keV from the assumed thermal neutron capture on ^{113}Cd.

The prompt line is much more intense than the delayed one, implying that for the somewhat harder neutron spectrum, which we have in this case as compared to the one in the case when the boron absorber is present, the (n, n') reaction on ^{114}Cd contributes much more to the intensity of the 558 keV line, than the commonly assumed neutron capture by ^{113}Cd.The ratio of the prompt and delayed intensities could thus in principle serve as a simple estimate of the relative hardness of the neutron spectrum.

3.2. The structure at E_γ = 692 keV

The quasi-triangular structure starting at 692 keV, which is due to inelastic neutron scattering on the first excited state of ^{72}Ge, has been studied many times and in greatest detail [3-6]. The 692 keV state is an isomeric state, with a half-life of 444 ns, and the depopulating radiation is pure E0, meaning that detection efficiency for the 692 keV radiation is practically always 100%. This transition energy sums with the recoil energy from neutron scattering, which depends on the incident neutron energy and the scattering angle, and is reduced by the pulse-height defect. The shape of the resulting spectral distribution has been studied in detail, mostly because the intensity of this distribution has been frequently used to estimate the fast neutron flux at the position of the detector (Škoro et al., 1972; Wordel et al., 1996; Fehrenbacher et al., 1996; Jovančević et al., 2010).

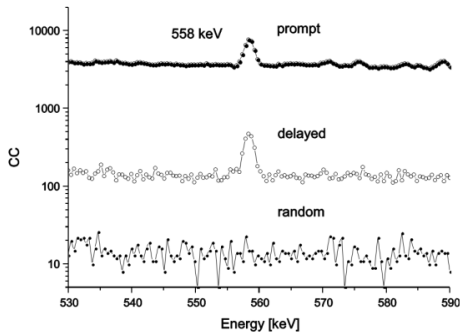

Fig. 3. Same as Fig. 2, but for the 558 keV line induced by neutrons on ^{113}Cd

The time structure of the 692 keV distribution can be seen in Fig. 4. It is seen that in the prompt spectrum, where the spectral background is quite high, the time interval narrow and the intensity of the 692 keV radiation consecutively low, the structure is barely discernible. On the other hand, in the delayed spectrum (here up to 1 μs), where the spectral background is virtually absent, the structure has the pronounced and typical triangular form.

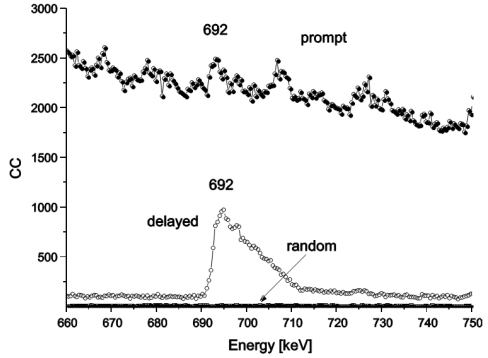

Fig. 4. Spectra of prompt, delayed, and random coincidences (practically negligible) containing the structure of 692 keV from inelastic neutron scattering on ^{72}Ge

Now, if we take the 30 keV-wide software gate, so as to fully embrace this structure (cf. Fig. 5), and find the corresponding time spectrum of coincidences with the entire NE213 spectrum, we obtain the time spectrum presented in Fig. 6a.The time spectrum is corrected for amplitude walk according to the procedure described in (Puzović and Aničin, 2007). The fit through the nicely exponential tail of delayed coincidences (Fig. 6b) yields at the 68% CL the half-life of 459(11) ns, which compares satisfactorily with the established value of 444 ns. This justifies the use of the intensity of this distribution for fast-neutron flux estimation in the case of digital spectroscopy as well. The treatment of the below-the-triggering-level pulses in a given digital spectroscopy system is essential in this respect. The condition is that the threshold is high enough, to let all the recoil pulses sum with the 692 keV pulses.

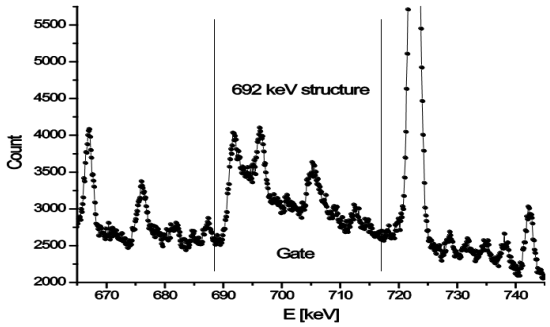

Fig. 5. The "triangular" structure at E_γ = 692 keV in the non-gated HPGe spectrum from the inelastic neutron scattering on ^{72}Ge. The position of the 30 keV-wide software gate, which is used to produce the time spectrum, shown in Fig. 6, is also shown.

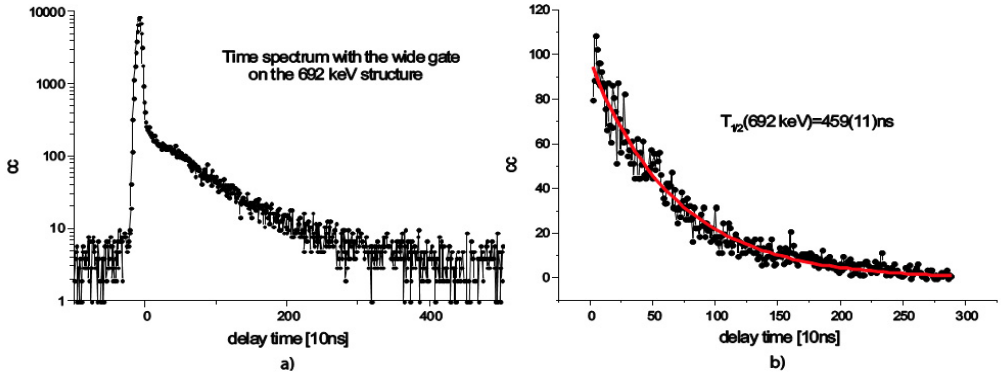

Fig. 6. Time spectrum of delayed coincidences of the 692 keV structure within the gate shown in Fig. 5 with the entire NE213 spectrum (a), which yields the half-life of the 692 keV state of 459(11) ns as shown in (b).

Finally, we took and analysed the direct HPGe californium spectrum in the so-called oscillogramme mode, when the pulses are sampled at 10 ns intervals, starting at the given number of points before the defined trigger level. To illustrate, we present in Fig. 7 the pulse with the amplitude that corresponds to 692 keV, preceded by its corresponding recoil pulse. Firstly, we produced the distribution of time intervals between the appearance of the recoil and 692 keV pulses.

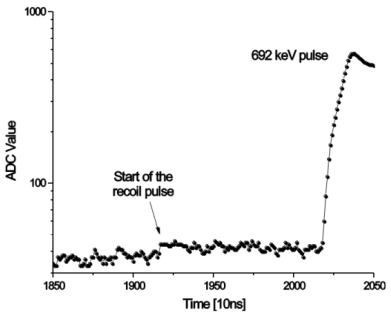

Fig.7. The joint pulses due to the recoil of the excited ^{72}Ge and the de-exciting 692 keV radiation, separated on the average for the mean lifetime of the 692 keV state. The distribution of these time intervals yields 442 to 446 ns for the half-life of this state, in excellent agreement with the accepted value.

We produce the spectrum in the 692 keV region, by the algorithm that defines the baseline after subtracting the corresponding recoil pulse. This, for the first time, produces the normal line at 692 keV, instead of the common summing structure (Fig.8, to be compared with Fig.5). The integral of the line equals the integral of the structure, This additional analysis validates our earlier conclusions concerning the suitability of the 692

keV structure for the determination of the fast neutron flux at the position of the detector.

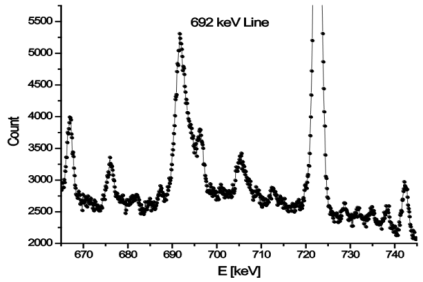

Fig. 8. The spectral line at 692 keV, from the de-excitation of the first excited state of ^{72}Ge, obtained by subtraction of the adjoined recoil pulses. This compares with the structure in Fig. 5, which results from the standard digital spectroscopy algorithm for baseline correction. In both cases the integral of the distributions contains all the events induced by fast neutrons on ^{72}Ge.

4. Conclusion

We measured the time-differentiated spectrum of the ^{252}Cf source as seen by an HPGe detector triggered by the NE213 liquid scintillator detector. The detectors were off-line coincided from the event-by-event list formed with 10 ns resolution by the quad FADC unit of the CAEN N1728B type. We tested the workings of the system on a number of effects generated by neutrons and found the time resolution satisfactory for the purpose. The signatures of the processes induced by fast and slow neutrons, both within the detector itself and in its environment, appear completely separated. The processes induced by fast neutrons are found in the prompt part of the time spectrum and those induced by thermal neutrons in the long tail of delayed coincidences. We find the intensity of the structure at 692 keV structure remains suitable for this purpose even in digital spectroscopy, if the threshold is higher than some 25 to 30 keV, and the germanium recoil pulses are let to sum with the 692 keV pulses.

Acknowledgments

The work is supported by the Ministry of “Education, Science and Technological Development” of the Republic of Serbia, under the Project No. 171002.

References

Abt, I. et al., arXiv:0711.2255v1 [nucl-ex] 14 Nov 2007
Ataç, A. et al., Nucl. Instr. Meth. A607 (2009) 554.
Fehrenbacher, G., Meckbach, R. and Paretzke, H.G., Nucl. Instr. Meth. A372 (1996) 239.
Fehrenbacher, G., Meckbach, R. and Paretzke, H.G., Nucl. Instr. Meth. A377 (1997) 391.
Gete, E. et. al., Nucl. Instr. Meth. A388 (1997) 212.
Jovančević, N. et al., Nucl. Instr. Meth. A612 (2010) 303.
Ljungvall, J. and Nyberg, J., Nucl. Instr. Meth. A550 (2005) 379.
Puzović, J. and Aničin, I., Nucl. Instr. Meth. A572 (2007) 926.
Siiskonen, T. and Toivonen, H., Nucl. Instr. Meth. A540 (2005) 403.
Škoro, G. et al., Nucl. Instr. Meth. A316 (1992) 333.

Stelson, P.H. et al., Nucl. Instr. Meth. 98 (1972) 481.
Wordel, R. et al., Nucl. Instr. Meth. A369 (1996) 557.

RELATION BETWEEN DAILY GAMMA-RAY BACKGROUND AND RADON VARIABILITY IN THE UNDERGROUND LOW-LEVEL LABORATORY IN BELGRADE

R. Banjanac, V. Udovičić, J. Filipović, D. Joković, D. Maletić, M. Savić, N. Veselinović, P. Kolarž, A. Dragić

Institute of Physics, Belgrade, Serbia

Abstract. *The most important background source in low-level gamma-ray spectrometry is radon which additionally causes background variability. Intensive daily radon variation at the same time with daily variation of gamma-ray background was already measured in our ground level laboratory. The new simultaneously measurements of radon concentration and gamma-ray background performed in the underground laboratory and correlation between them in a wide range of radon concentration was analyzed.*

Key words: *gamma-ray background, radon variability, underground laboratory*

1. INTRODUCTION

Correlation between diurnal variation of radon concentration and intensities of postradon background lines measured simultaneously in a surface laboratory was already analyzed, [1]. Daily variation of postradon gamma-ray lines intensity is important as a source of systematic error in low-level NORM-sample measuring, containing Ra-226. Background measurement in the underground laboratory, as well radon monitoring, [1], did not show obvious neither radon progenies nor radon daily periodicity but the new measurements inside the underground laboratory were done.

Description of laboratories, measuring techniques and used detectors is shown in detail in [1,2].

Radon concentration is known to vary considerably, depending on many parameters, but one of the most important is ventilation rate. For indoor spaces is known that depending of ventilation rate, equilibrium factor between radon concentration and its progenies is expecting to vary from 0.3 to 0.7. The UL is equipped with ventilation system which provide a low value of radon concentration due to, among other factors, constant exchange rate of fresh air thus radon monitoring should be preferably performed together with atmospheric parameters.

2. PRELIMINARY MEASUREMENTS

In order to prepare a new setup of „radon vs. postradon“ measurement inside the UL, the results from several different radon measurements proved useful.

Radon measurement using track detectors at several positions within the UL was done, during ventilation was switched on. Preliminary results show significant inhomogeneity in spatial distribution of radon concentration after 6 months of track detectors exposition. For this long time period a single value of radon concentration obtained by each track detector can not see diurnal radon variability inside the UL (air volume of 135 m^3).

For the last six years, radon concentration inside the UL was measured several times during transition ventilation regime. From the low avereged value (about 10 Bqm^{-3}) with ventilation on mode, radon concentartion rised lineary after ventilation was switched off up to saturated value. Rising time lasted for several days (3 to 4) while mean saturated value of radon concentartion varied from 300 Bqm^{-3} up to 900 Bqm^{-3}, which strongly depends on ambiental parameters and eventually on season. Obviously, diffusion rate of radon from 4pi surrounding soil and concrete must be measured precisely. For radon progenies spatial distribution is very important deposition rate of radon progenies on the walls of lead shielding as well on the detector itself. Relationship between deposition and attachment rates in Jacobi room model, [3], can be tested in order to explain spatial radon progenies distribution in the UL.

Additional preliminary result obtained using radon monitor (RM) positioned in front of one fresh-air inlet inside the UL, for ten days. The measured values of radon concentration have been often below detection level of the instrument, detecting a zero value, which confirms that radon-free air enters to the lab.

Finally, radon was simultaneously measured using a Rad7 detector for inside and RM for outside positions of lead shielding of the germanium detector (VGe). That measurements were conducted in ventilation „on“

regime, as well when ventilation was switched off. After a month of measurement there was no difference in radon concentration measured between two radon detectors, figure 1. The sampling time of both detectors was set to 12 hours during ventilation on mode in order to minimize statistical errors, and only 2 hours after ventilation was switched off.

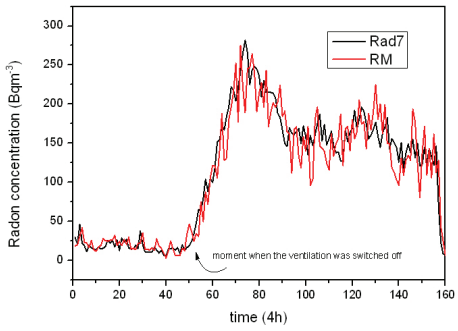

Fig. 1 Radon measurement inside and outside the lead shielding of the VGe detector

3. Measurements and results

The gamma-ray background was measured simultaneously using two germanium detectors, VGe (35% relative efficiency) and MGe (13%), both without any passive shielding. The germanium detectors were mutually separeted about 4 meters while the MGe was positioned near wall, the VGe was about 1.5 meters far of the side walls. The both with vertical dipstick of cryostat configuration stayed on the ground with active detectore volume positioned about 80cm above the ground. In the same time, RM has monitored radon in position close to the VGe, figure 2.

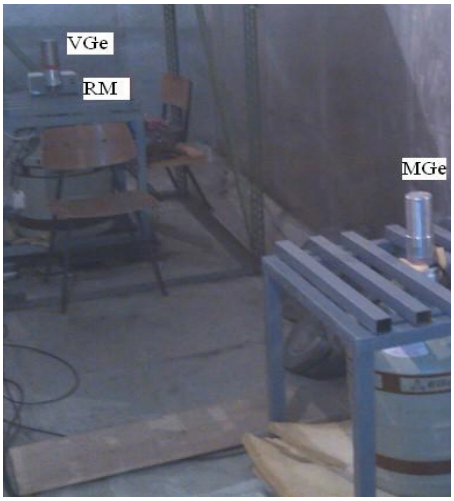

Fig. 2 Positions of detectors inside the UL

The RM, model SN1029, is used by readings on every thirty minutes, which was the same time chosen for sampling intensities of postradon lines in time series of germanium detectors.
Correlation between radon concentration and postradon line intensites during ventilation on and off regimes was analyzed. One cycle of two consecutive ventilation regimes, on then off, presented on figure 3. Here are presented just two most intensive ones at 352keV from Pb-214 and at 609keV from Bi-214.

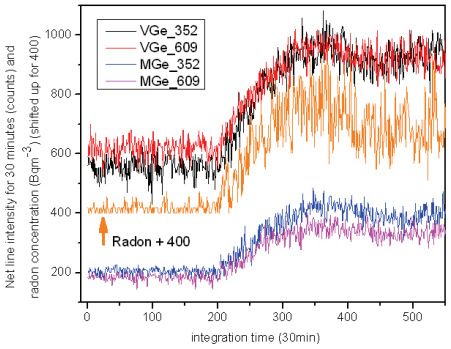

Fig. 3 Radon concentration and postradon line intensities variations inside the UL

On the figure 3, radon concentration values are shifted up for 400 to emphasize similarity of variations, especially between radon and radon progenies measured by VGe. Due to smaller detection efficiency of smaller MGe detector, one can expect better correlation between the VGe and the RM, additioanally because of spatial radon distribution and separeted positions of germanium detectors. The other postradon lines which have smaller intensities do not show obvious variation even in rising part of radon, during a tree days after ventilation was switched off.

When the ventilation was switched on, both radon concentartion and postradon line intensites had almost constant values. For the chosen sampling time of 30 minutes, detection sensitivity of the RM is too low to register non zero values, when the ventilation is on and the mean value of radon concentartion is only about 10 Bqm^{-3}.

When the ventilation was in “on” regime there was no significant variation in radon and postradon measured values. From the figure 2 is obvious that postradon values follows each other, more for the same germanium detectors, and less comparing to radon data. When radon concentration achieved saturation in “off” regime, expected daily variation of both values can not be proved using even sophisticated Lomb-Scargle periodogram analysis, [2], because of a short measuring period. A poor statistics is reason, too, why any time lag effect between 609 keV (from Bi-214) and 352 keV (from Pb-214) did not registered.

Pearson correlation coefficient (Pcc) determined for every combination of variables in rising part of ventilation “off” regime, table 1.

Table 1 Pcc for every combination of variables in rising part of ventilation “off” regime

Pcc	Radon	VGe 352	VGe 609	MGe 352	MGe 609
Radon	1	0.78	0.77	0.70	0.69
VGe-352	0.78	1	0.88	0.76	0.79
VGe-609	0.77	0.88	1	0.78	0.80
MGe-352	0.70	0.76	0.78	1	0.76
MGe-609	0.69	0.79	0.80	0.76	1

Slightly smaller correlation coefficient for radon and MGe lines combination compared to that between radon and VGe lines can be caused by difference in radon concentration on the two different positions of germanium detectors. On the contrary, there is a strong correlation for the same postradon line detected by both Ge detectors. Similarly, the Pcc value for 352 vs. 609 combination of the MGe detector is slightly smaller than that of the VGe detector, which can be caused by the same reason mentioned above. Obviously, there is a need for further investigations for getting better explanation with better statistics.

In another ventilation “on/off” cycle after short period in ventilation “off” regime, radon concentration drops down immediately when ventilation was switched on. Then, the surfaces of both germanium detectors was cleaned thoroughly by alcohol, but in a new cycle the differences in postradon line intensities did not detected. As the both germanium detectors were in lead shielding before, for a long time period, we can conclude indirectly that attachment rates of aerosol particles on detector surfaces, measured via postradon progenies, have small values.

4. Conclusions

Correlation between daily gamma-ray background and radon variability was tested in the underground low-level laboratory in Belgrade using two unshielded germanium detectors and single radon monitor.

Pearson correlation coefficients are determined for every combination of variables in rising part of ventilation “off” regime. Daily variations in radon and postradon lines did not registered in ventilation “on” regime, as well as in saturated radon atmosphere during ventilation “off” regime. Hence, there is a need for further investigations for getting better statistics to explain radon behavior inside the underground laboratory.

The majority of commercial available active radon detectors have sensitivity threshold of radon detection about 10 Bqm^{-3}. Radon atmosphere inside the underground laboratory with long-term low radon concentration seems to be suitable place for some kind of radon chamber.

Acknowledgement: *This work is supported by the Ministry of Education, Science and Technological Development of Republic of Serbia under project III43002.*

References

1. R. Banjanac *et al.*, “Daily variations of gamma-ray background radiation and radon concentration”, Rom. Journ. Phys., Vol. 58, Supplement, P. S14–S21, Bucharest, 2013
2. V. Udovičić *et al.*, “Radon problem in an underground low-level laboratory”, Radiat. Meas. , Volume 44, Issues 9–10, October–November 2009, Pages 1009–1012, Proceedings of the 24th International Conference on Nuclear Tracks in Solids
3. N. Stevanovic, V.M. Markovic, D. Nikezic, “Relationship between deposition and attachment rates in Jacobi room model”, Journal of Environmental Radioactivity 101 (2010) 349-352

Stopped cosmic-ray muons in plastic scintillators on the surface and at the depth of 25 m.w.e

2013 J. Phys.: Conf. Ser. 409 012142

(http://iopscience.iop.org/1742-6596/409/1/012142)

Journal of Physics: Conference Series **409** (2013) 012142 doi:10.1088/1742-6596/409/1/012142

Stopped cosmic-ray muons in plastic scintillators on the surface and at the depth of 25 m.w.e.

D Maletić[1], A Dragić[1], R Banjanac[1], D Joković[1], N Veselinović[1], V Udovičić[1], M Savić[1], J Puzović[2] and I Aničin[1]

[1] Institute of Physics, University of Belgrade, Serbia
[2] Faculty of Physics, University of Belgrade, Serbia

E-mail: maletic@ipb.ac.rs

Abstract. Cosmic ray muons stopped in 5 cm thick plastic scintillators at surface and at depth of 25 m.w.e are studied. Apart from the stopped muon rate we measured the spectrum of muon decay electrons and the degree of polarization of stopped muons. Preliminary results for the Michel parameter yield values lower than the currently accepted one, while the asymmetry between the numbers of decay positrons registered in the upper and lower hemispheres appear higher than expected on the basis of numerous earlier studies.

The laboratory spaces and the apparatus used in this work are described in detail in [1]. Here we first determine the number of stopped positive muons of cosmic-ray origin in our plastic scintillator detectors, which have the vertical thickness of 5 cm and an area of 1 m^2. The pulses from the PMTs are recorded in the event-by-event mode by their amplitude and time of occurrence, with 10 ns resolution. From such a list it is thus possible, among other things, to form the series of time intervals between successive pulses from a single detector. The signature of positive muons which stop and decay in the detector is the succession of pulses – the start pulse which is due to the stopped muon, and the stop pulse which is due to the positron emitted in its decay, which does not necessarily loose all of its energy in the detector (figure 1). The intervals between these start and stop pulses are distributed exponentially, with the constant corresponding to the lifetime of the muon. This distribution sits on another exponential distribution that corresponds to the Poisson count of the through-going muons, with the constant reciprocal to the rate of these events, which is of the order of 100 Hz, and which in the region where the first distribution is present (up to some 20 μs), appears flat (figure 2). In these measurements the dead time of the system was from 1 to 4 μs, and these portions of our time spectra are missing. Integrating this time distribution that corresponds to the stopped and decayed muons, and correcting for the missing events due to the dead time, we obtain the number of stopped muons in the ground level based and in the underground laboratory as:

$$N_{GB}(\mu_{stop}) = 6 \cdot 10^{-2}\ \mathrm{m}^{-2}\ \mathrm{s}^{-1} \quad \text{and} \quad N_{UG}(\mu_{stop}) = 1.5 \cdot 10^{-2}\ \mathrm{m}^{-2}\ \mathrm{s}^{-1}$$

the errors on these numbers being below the significant figures presented here. Next, we find the amplitude spectra of all the start and of all the stop pulses from two different time intervals – one at the very beginning of the time spectrum (marked I in figure 2), and the other of the same width at the

time when the muon decay distribution has practically died out (marked II in figure 2). We now subtract the spectrum of starts that corresponds to region II from that which corresponds to region I, to obtain the true spectrum of starts, which is the spectrum of muon energy losses until they stop in the detector (spectrum designated as "Stopped muons" in figure 3). We thus recover the spectrum of energies that stopped muons have prior to entering our detector. We do the same with the spectra of stops, what produces the spectrum of positron energy losses until they either stop within the detector or until they leave it (the spectrum designated as "Decay positrons" in figure 3). For the purposes of comparison we present in the same figure the much more intense spectrum of energy losses of through-going muons (marked as "Singles"), which peaks at about 10 MeV. It is seen that the spectrum of stopped muons peaks, in spite of the shorter path within the detector, at an energy higher than that at which peak the through-going muons, what is to be expected on the grounds that the muons of energies sufficiently low to stop in the detector have higher specific ionization than the high energy through-going ones, which are practically the minimum ionizing particles. Figure 3b presents the same results for the identical setup situated in the underground laboratory. Comparison between figure 3a and 3b shows the rather unexpected and significant differences between both the spectra of stopped muons and decay positrons on the surface and underground. The differences might be caused by the differences in low-energy parts of the muon spectrum at the two locations and possibly by the different degree of polarization of the stopped muons. This would, by virtue of parity non-conservation in the weak interactions involved, lead to different angular distributions of decay positrons, what would in turn result in the observed differences in their corresponding energy-loss spectra.

To check the above assumption we arranged the triple sandwich arrangement of plastic scintillator detectors, the big plastic detector (1 m^2) sandwiched between the two small ones (0.125 m^2), the pulses from each detector being recorded by their amplitudes and time of occurrence, with 10 ns resolution. All relevant combinations of off-line coinciding and anti-coinciding between the detectors yielded the information that we discuss in what follows.

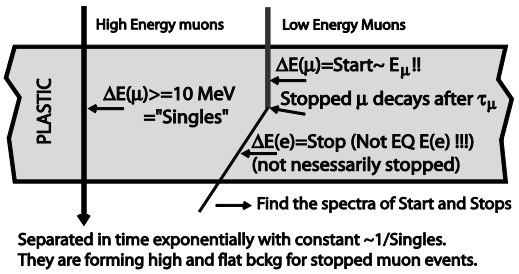

Figure 1. Definitions of the quantities involved in the study of CR muons which stop and decay in plastic scintillator detectors 5 cm thick.

Since the angular distribution of the incoming muons is wide, and the overall geometry of the events included into these spectra is complex, it is not possible to interpret and draw meaningful quantitative conclusions from the significant differences that exist between the two spectra (figure 4). It is, however, evident that the ratio of the number of positrons that are emitted into the upper hemisphere and those that are emitted into the lower hemisphere is significantly bigger than that which might be expected on the basis of the multitude of earlier measurements of this asymmetry (e.g. see [2]). The only possible reason for that might be the different character of the stopping medium, that appears to be different from those used in any of earlier studies. The results of the same measurement underground still do not have sufficient statistics for meaningful conclusions, and the measurements go on.

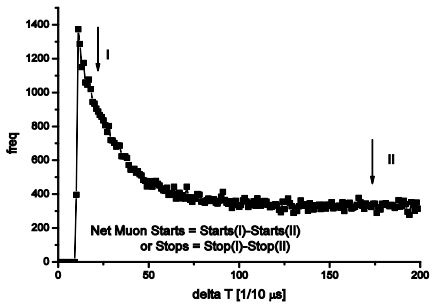

Figure 2. Distribution of time intervals between successive pulses from the 1 m^2 plastic scintillator detector. Region I contains majority of the stopped muon decays, while region II contains only the "background" composed only of time intervals between the through-going high-energy muons.

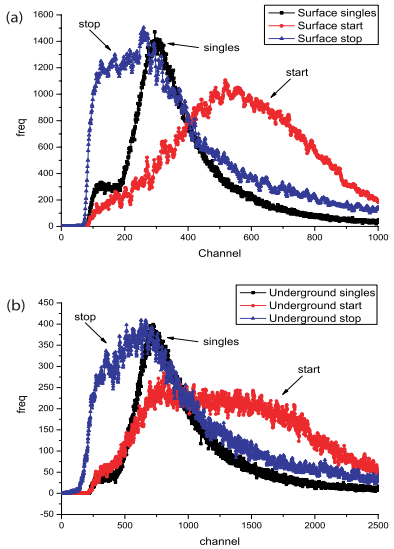

Figure 3. (a) The spectra of through-going muons (Singles), of stopped muons (Starts, or Stopped muons) and of decay positrons (Stops, or Decay positrons), all in the ground level based laboratory (Surface). (b) Same, in the underground laboratory (Cavern).

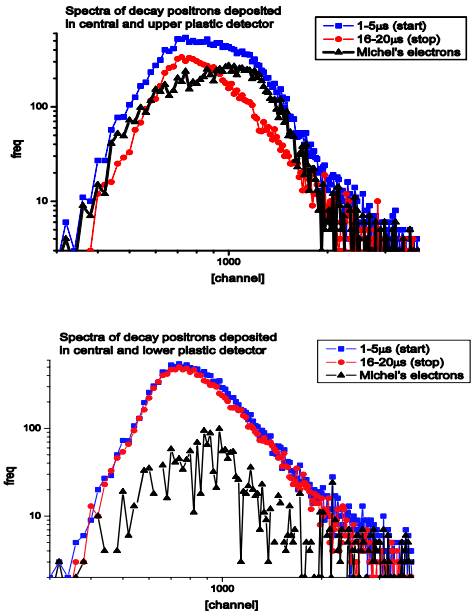

Figure 4. Preliminary results of measurements with the triple sandwich detector arrangement in the ground based laboratory. Spectrum of decay positron energy losses (triangles) in the upper detector (upper image) and in the lower detector (lower image).

References

[1] Dragić A, Udovičić V I, Banjanac R, Joković D, Maletić D, Veselinović N, Savić M, Puzović J, Aničin I V, 2011 The new set-up in the Belgrade Low-level and Cosmic-ray laboratory *Nuclear Technology and Radiation Protection* **26** 181-192

[2] Bradt H V and Clark G W 1963 *Phys. Rev.* **132** 1306–1316

Some Peculiarities of Digital Gamma-ray Spectroscopy with Germanium Detectors Performed in Presence of Neutrons

Article *in* Physics Procedia · November 2014

DOI: 10.1016/j.phpro.2014.10.010

CITATION
1

READS
76

9 authors, including:

Nikola Veselinović
Institute of Physics Belgrade
24 PUBLICATIONS **54** CITATIONS
SEE PROFILE

Dimitrije M Maletić
Institute of Physics Belgrade
110 PUBLICATIONS **4,158** CITATIONS
SEE PROFILE

Dejan Joković
University of Belgrade
59 PUBLICATIONS **355** CITATIONS
SEE PROFILE

Vladimir Udovičić
Institute of Physics Belgrade
59 PUBLICATIONS **193** CITATIONS
SEE PROFILE

Available online at www.sciencedirect.com

ScienceDirect

Physics Procedia 59 (2014) 63 – 70

Physics Procedia

GAMMA-2 Scientific Workshop on the Emission of Prompt Gamma Rays in Fission and Related Topics

Some peculiarities of digital gamma-ray spectroscopy with germanium detectors performed in presence of neutrons

N. Veselinović[a*], D. Maletić[a], D. Joković, R. Banjanac[a], V. Udovičić[a], M. Savić[a], , J. Puzović[b], I.V. Aničin[a] and A.Dragić[a+]

[a]*Institute of Physics, Pregrevica 118, 11080 Belgrade,Serbia*
[b]*Faculty of Physics, Studentski trg 12, 11000 Belgrade, Serbia*
[+]*on leave at Joint Research Centre, Geel, Belgium*

Abstract

We measured the time-differentiated spectrum of the ^{252}Cf source as seen by an high-purity germanium detector triggered by the NE213 liquid scintillator detector. The detectors are off-line coincided from the event-by-event list formed with 10 ns resolution by the quad FADC unit of the CAEN N1728B type. The signatures of the processes induced by fast and slow neutrons, both within the detector itself and in its environment, appear completely separated. The processes induced by fast neutrons are found in the prompt part of the time spectrum and those induced by thermal neutrons in the long tail of delayed coincidences. We analyse the time behaviour of spectral structures at 692 keV, which are the signatures of inelastic neutron scattering on Ge-72, and comment on its suitability for determination of the fast neutron flux in general, and in the digital gamma-ray spectroscopy in particular.

Selection and peer-review under responsibility of Guest Editor: Mr. Stephan Oberstedt - stephan.oberstedt@ec.europa.eu

Keywords: background spectra; neutrons; germanium; Cf-252

* Corresponding author: Tel.: +381 113713000
Email-address: veselinovic@ipb.ac.rs

Selection and peer-review under responsibility of Guest Editor: Mr. Stephan Oberstedt - stephan.oberstedt@ec.europa.eu
doi:10.1016/j.phpro.2014.10.010

1. Introduction

Neutrons induce a number of nuclear reactions on stable isotopes of germanium, which produce characteristic signatures in the spectra of germanium detectors. These have been studied in great detail with the aim to either improve on the knowledge of background spectra of germanium detectors, or for determination of neutron fluxes at the position of the detector (Stelson et al., 1972; Škoro et al., 1992; Wordel et al., 1996; Fehrenbacher et al., 1996, 1997; Gete et al., 1997; Siiskonen and Toivonen, 2005; Ljungvall and Nyberg, 2005; Abt et al., 2007; Ataç et al., 2009; Jovančević et al., 2010). Some of the studies dealt with environmental neutrons of cosmic-ray origin while some used different neutron sources, mostly with the fission spectrum. The findings were quite similar, irrespective of the origin of the neutrons. We undertook the time-differentiated study of some of these processes induced by ^{252}Cf fission neutrons in order to gain some insight into the dynamics of neutron-induced background in the detectors themselves, as well as in their usual environments.

2. The experiment

Our experimental setup consists of a small volume (2 litres) liquid scintillator (NE213) detector placed in a steel container and a 15% efficiency coaxial high-purity germanium (HPGe) detector, positioned as schematically presented in Fig. 1.

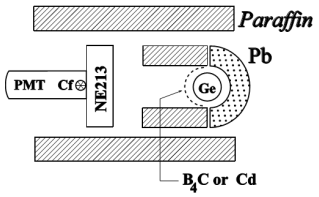

Fig. 1. The layout of the experiment (view from above)

The materials, which surround the detectors in the experiments, include lead, paraffin (hydrogen), boron, cadmium, aluminium and iron. The encapsulated ^{252}Cf source had a strength of about 2000 neutrons in 4π sr/s. On their way towards the HPGe detector the neutrons traverse the 7 cm thick layer of NE213. The distance between the end-cap of the NE213, which faces the HPGe detector, and the closest point of the HPGe detector is 10 cm. Fast neutrons with energies higher than 1 MeV, which leave the NE213 detector towards the HPGe detector, take less than 10 ns to reach this detector, while the neutrons which start as thermal take about 50 μs. Majority of neutrons, which slow down on their way towards the detector, take something in between these two values, but certainly closer to the lower one. The preamplifier outputs of both detectors are fed to the two out of four identical inputs of the flash ADC unit of the CAEN N1728B type. It can perform like a digital spectrometer capable to operate in the list, or the event-by-event mode. For every analysed event the time of its appearance over the triggering level is recorded with 10 ns resolution, while its amplitude is digitized and recorded in one of the available 32 k channels. This enables to off-line coincide the events of given amplitudes with 10 ns resolution. The software that produces and analyses the time spectra, which are equivalent to hardware TAC spectra, is entirely homemade.

3. The results

The singles spectrum of NE213 serves practically only as a trigger for the HPGe spectrum. The singles spectrum of the in this case lightly shielded germanium detector consists of the correspondingly rich environmental background spectrum, of the gamma rays given off by the californium source, and of the different features induced by fission neutrons of californium in the HPGe detector and in the surrounding materials. It stretches up to some 8 MeV. We shall here deal only with some interesting portions of this spectrum that are coincident with different delay times with the NE213 spectrum.

3.1. Effects in the environment

The time structure of the signatures of the effects, which neutrons induce in surrounding materials in our HPGe spectra, is particularly simple and illustrative. All the effects induced by fast neutrons which we see (mostly the inelastic scattering) tend to fall into the prompt peak of our time spectrum, while the effects induced by slow neutrons (mostly capture reactions) fall into the (very long) tail of delayed coincidences. The completeness of this separation is perhaps best illustrated by the cases of boron and iron. Fig.2a presents the portion of the HPGe spectrum that contains the 478 keV Doppler–widened line from the (n,α) reaction on ^{10}B, while Fig.2b depicts the part of the spectrum with the 847 keV line from (n, n') reaction on ^{56}Fe (found mostly in the NE213 casing). The first reaction has the high cross section for thermal neutrons, while the second is induced by neutron energies higher than about 1 MeV. The difference between the two cases is striking; the 478 keV structure is present only in the spectrum of delayed coincidences and on its place in the prompt spectrum the weak lines from the decay of californium appear, while the strong line of 847 keV exists only in the prompt spectrum and is completely absent in the delayed spectrum.

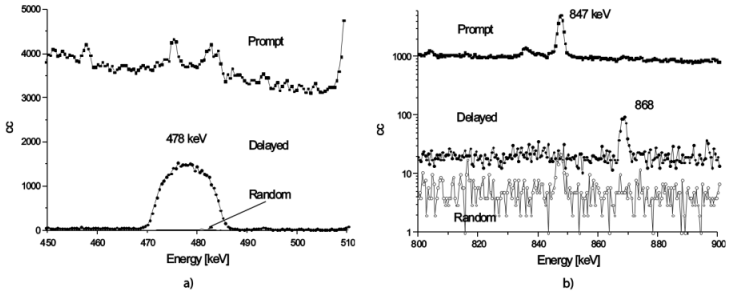

Fig. 2. The prompt, delayed (up to 1 μs) and random coincidence spectra of the 478 keV line from the reaction on boron (**a**), and of the 847 keV line from the reaction on iron (**b**). The line at 868 keV is from neutron capture on ^{73}Ge. Note that the first scale is linear while the second one is logarithmic.

Now the case of cadmium becomes instructive. Figure 3 is same as Fig. 2, but for the portion of the spectrum containing the most prominent line of 558 keV from the assumed thermal neutron capture on ^{113}Cd.

The prompt line is much more intense than the delayed one, implying that for the somewhat harder neutron spectrum, which we have in this case as compared to the one in the case when the boron absorber is present, the (n, n') reaction on ^{114}Cd contributes much more to the intensity of the 558 keV line, than the commonly assumed neutron capture by ^{113}Cd.The ratio of the prompt and delayed intensities could thus in principle serve as a simple estimate of the relative hardness of the neutron spectrum.

3.2. The structure at E_γ = 692 keV

The quasi-triangular structure starting at 692 keV, which is due to inelastic neutron scattering on the first excited state of ^{72}Ge, has been studied many times and in greatest detail [3-6]. The 692 keV state is an isomeric state, with a half-life of 444 ns, and the depopulating radiation is pure E0, meaning that detection efficiency for the 692 keV radiation is practically always 100%. This transition energy sums with the recoil energy from neutron scattering, which depends on the incident neutron energy and the scattering angle, and is reduced by the pulse-height defect. The shape of the resulting spectral distribution has been studied in detail, mostly because the intensity of this distribution has been frequently used to estimate the fast neutron flux at the position of the detector (Škoro et al., 1972; Wordel et al., 1996; Fehrenbacher et al., 1996; Jovančević et al., 2010).

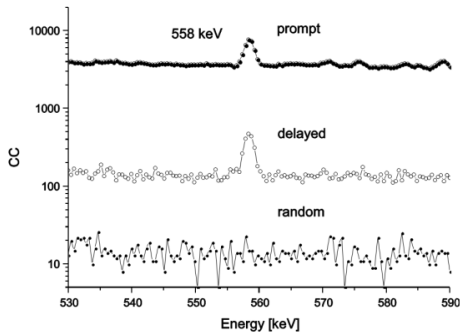

Fig. 3. Same as Fig. 2, but for the 558 keV line induced by neutrons on ^{113}Cd

The time structure of the 692 keV distribution can be seen in Fig. 4. It is seen that in the prompt spectrum, where the spectral background is quite high, the time interval narrow and the intensity of the 692 keV radiation consecutively low, the structure is barely discernible. On the other hand, in the delayed spectrum (here up to 1 μs), where the spectral background is virtually absent, the structure has the pronounced and typical triangular form.

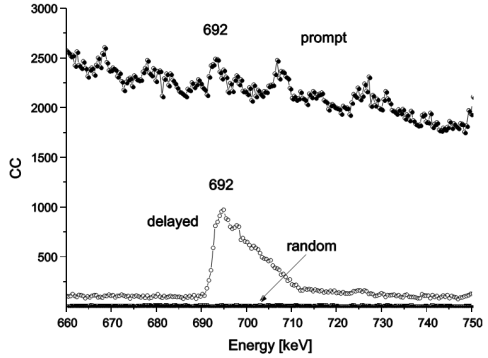

Fig. 4. Spectra of prompt, delayed, and random coincidences (practically negligible) containing the structure of 692 keV from inelastic neutron scattering on ^{72}Ge

Now, if we take the 30 keV-wide software gate, so as to fully embrace this structure (cf. Fig. 5), and find the corresponding time spectrum of coincidences with the entire NE213 spectrum, we obtain the time spectrum presented in Fig. 6a.The time spectrum is corrected for amplitude walk according to the procedure described in (Puzović and Aničin, 2007). The fit through the nicely exponential tail of delayed coincidences (Fig. 6b) yields at the 68% CL the half-life of 459(11) ns, which compares satisfactorily with the established value of 444 ns. This justifies the use of the intensity of this distribution for fast-neutron flux estimation in the case of digital spectroscopy as well. The treatment of the below-the-triggering-level pulses in a given digital spectroscopy system is essential in this respect. The condition is that the threshold is high enough, to let all the recoil pulses sum with the 692 keV pulses.

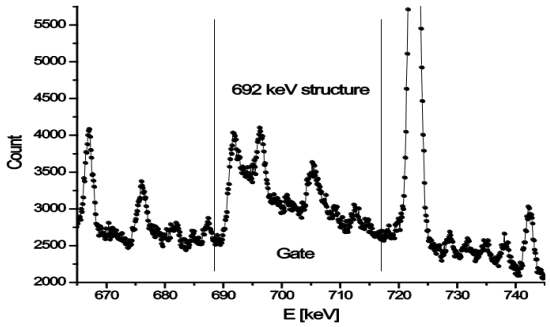

Fig. 5. The "triangular" structure at E_γ = 692 keV in the non-gated HPGe spectrum from the inelastic neutron scattering on ^{72}Ge. The position of the 30 keV-wide software gate, which is used to produce the time spectrum, shown in Fig. 6, is also shown.

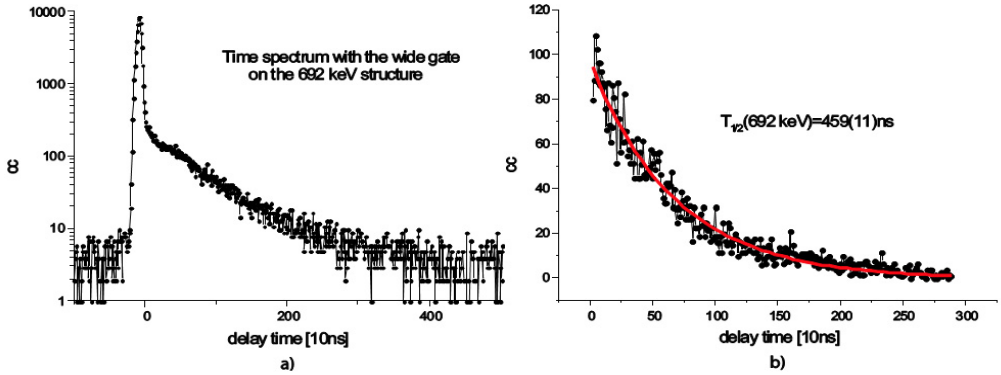

Fig. 6. Time spectrum of delayed coincidences of the 692 keV structure within the gate shown in Fig. 5 with the entire NE213 spectrum (a), which yields the half-life of the 692 keV state of 459(11) ns as shown in (b).

Finally, we took and analysed the direct HPGe californium spectrum in the so-called oscillogramme mode, when the pulses are sampled at 10 ns intervals, starting at the given number of points before the defined trigger level. To illustrate, we present in Fig. 7 the pulse with the amplitude that corresponds to 692 keV, preceded by its corresponding recoil pulse. Firstly, we produced the distribution of time intervals between the appearance of the recoil and 692 keV pulses.

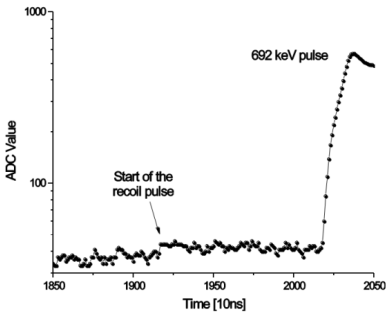

Fig.7. The joint pulses due to the recoil of the excited ^{72}Ge and the de-exciting 692 keV radiation, separated on the average for the mean lifetime of the 692 keV state. The distribution of these time intervals yields 442 to 446 ns for the half-life of this state, in excellent agreement with the accepted value.

We produce the spectrum in the 692 keV region, by the algorithm that defines the baseline after subtracting the corresponding recoil pulse. This, for the first time, produces the normal line at 692 keV, instead of the common summing structure (Fig.8, to be compared with Fig.5). The integral of the line equals the integral of the structure, This additional analysis validates our earlier conclusions concerning the suitability of the 692

keV structure for the determination of the fast neutron flux at the position of the detector.

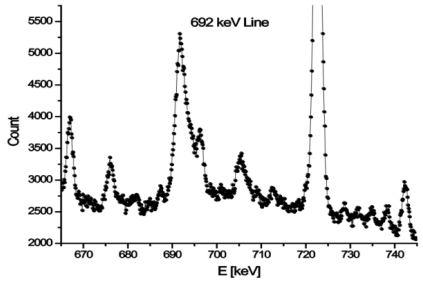

Fig. 8. The spectral line at 692 keV, from the de-excitation of the first excited state of ^{72}Ge, obtained by subtraction of the adjoined recoil pulses. This compares with the structure in Fig. 5, which results from the standard digital spectroscopy algorithm for baseline correction. In both cases the integral of the distributions contains all the events induced by fast neutrons on ^{72}Ge.

4. Conclusion

We measured the time-differentiated spectrum of the ^{252}Cf source as seen by an HPGe detector triggered by the NE213 liquid scintillator detector. The detectors were off-line coincided from the event-by-event list formed with 10 ns resolution by the quad FADC unit of the CAEN N1728B type. We tested the workings of the system on a number of effects generated by neutrons and found the time resolution satisfactory for the purpose. The signatures of the processes induced by fast and slow neutrons, both within the detector itself and in its environment, appear completely separated. The processes induced by fast neutrons are found in the prompt part of the time spectrum and those induced by thermal neutrons in the long tail of delayed coincidences. We find the intensity of the structure at 692 keV structure remains suitable for this purpose even in digital spectroscopy, if the threshold is higher than some 25 to 30 keV, and the germanium recoil pulses are let to sum with the 692 keV pulses.

Acknowledgments

The work is supported by the Ministry of “Education, Science and Technological Development” of the Republic of Serbia, under the Project No. 171002.

References

Abt, I. et al., arXiv:0711.2255v1 [nucl-ex] 14 Nov 2007
Ataç, A. et al., Nucl. Instr. Meth. A607 (2009) 554.
Fehrenbacher, G., Meckbach, R. and Paretzke, H.G., Nucl. Instr. Meth. A372 (1996) 239.
Fehrenbacher, G., Meckbach, R. and Paretzke, H.G., Nucl. Instr. Meth. A377 (1997) 391.
Gete, E. et. al., Nucl. Instr. Meth. A388 (1997) 212.
Jovančević, N. et al., Nucl. Instr. Meth. A612 (2010) 303.
Ljungvall, J. and Nyberg, J., Nucl. Instr. Meth. A550 (2005) 379.
Puzović, J. and Aničin, I., Nucl. Instr. Meth. A572 (2007) 926.
Siiskonen, T. and Toivonen, H., Nucl. Instr. Meth. A540 (2005) 403.
Škoro, G. et al., Nucl. Instr. Meth. A316 (1992) 333.

Stelson, P.H. et al., Nucl. Instr. Meth. 98 (1972) 481.
Wordel, R. et al., Nucl. Instr. Meth. A369 (1996) 557.

Applied Radiation and Isotopes 87 (2014) 70–72

Contents lists available at ScienceDirect

Applied Radiation and Isotopes

journal homepage: www.elsevier.com/locate/apradiso

Variations of gamma-ray background in the Belgrade shallow underground low-level laboratory

Radomir Banjanac [1,*], Aleksandar Dragić, Vladimir Udovičić, Dejan Joković, Dimitrije Maletić, Nikola Veselinović, Mihailo Savić

Institute of Physics, University of Belgrade, Belgrade 11080, Serbia

HIGHLIGHTS

- Time variability of Ge detector background was measured in two laboratories.
- Variations of cosmic ray intensity and radon concentration were tested.
- Advantage of an underground laboratory compared to a ground level one was proved.

ARTICLE INFO

Available online 1 December 2013

Keywords:
Underground low-level laboratory
Cosmic rays
Radon variability

ABSTRACT

During the last three years we investigated the variations of background simultaneously in two laboratories, the ground level (GLL) and the underground laboratory. The Forbush-like effect from March 2010 was observed in the GLL using a Ge detector and plastic veto scintillator. The underground plastic scintillator saw the same effect but the coincident veto spectrum did not detect the decrease of cosmic-ray intensity. Using a time series analysis of prominent post-radon lines, a significant radon daily variability was detected in the Ge detector background spectrum, but only in the GLL.

1. Introduction

Any long and even short-term gamma-ray background measurement is subject to certain temporal variations due to time variability of two prominent contributors to background—cosmic-ray intensity and radon concentration. The duration of background measurements may be anything from one day to several months, depending on the wanted final statistical accuracy of the envisaged measurements. These measurements, however, yield only average values of the background, what in principle may lead to systematic errors in later measurements, especially of NORM samples.

Radon concentrations are known to vary considerably, depending on many parameters that determine this concentration in every particular case. This includes the deposition of radon progenies on the walls of lead castles and detectors themselves, what makes even the traditional radon suppression method by flushing the interior of the sample chamber with nitrogen potentially ineffective.

On the other side, effective protection of Ge detectors from cosmic-rays is provided by active veto shielding using convenient large area detectors, although all significant periodic and aperiodic variations of cosmic ray intensity can usually be neglected since contributions to background, apart from the annihilation line, lie in the continuum.

2. Description of the laboratories and equipment

The Belgrade underground low-level laboratory (UL), located at a depth of 25 m. w. e (meter water equivalent) is equipped with ventilation system which provides low radon concentration of 13 (5) Bq/m^3, the mean value being obtained from more than two years long-term measurement. The UL is presented in more detail by Antanasijević et al. (1999), and the especially designed ventilation system for radon reduction in the laboratory has been described by Udovičić et al. (2009). This system consists of two "radon shields"—the passive and the active one. The passive shield consists of 1 mm thick aluminum foil which completely covers all the wall surfaces inside the laboratory, including floor and ceiling. It is hermetically sealed with a silicon sealant to prevent diffusion of radon from surrounding soil and concrete walls of the laboratory. As the active radon shield the laboratory is continuously ventilated with fresh air, filtered through one rough filter for dust elimination

* Corresponding author. Tel.: +381 11 3161274.
E-mail address: banjanac@ipb.ac.rs (R. Banjanac).
[1] Postal address: Pregrevica street, number 118, 11080 Belgrade, Serbia.

0969-8043/$ - see front matter © 2013 Elsevier Ltd. All rights reserved.
http://dx.doi.org/10.1016/j.apradiso.2013.11.091

followed by active charcoal filters (cross-section of 60 cm × 60 cm, weight of 40 kg) for radon adsorption.

The UL has an area of 45 m^2 and volume of 135 m^3 what required the rate of air inlet adjusted to 800 m^3/h. This huge amount of fresh air contributes to greater temperature variations and the long-term mean value of temperature inside the UL is 19 (4)°C. On the other side the rate of air outlet (700 m^3/h) was adjusted to get an overpressure of about 2 hPa over the atmospheric pressure, what prevents radon diffusion through eventual imperfections in the aluminum layer. The pressure buffer corridor to the laboratory (18 m^2) ensures almost constant value of this overpressure. Relative humidity is controlled by a dehumidifier device, what provides that the relative humidity in the underground laboratory does not exceed 60%.

All the measurements presented in this work which were performed in the underground laboratory were performed in the ground level laboratory (GLL) as well. The GLL is air-conditioned and represents a typical ground level laboratory. This laboratory is situated in two joined standard transportation containers with iron sheet walls, but furnished with quality thermal insulation. The GLL has an area of 30 m^2 and volume of 75 m^3. It is air-conditioned (average radon concentration of 50(30) Bq/m^3).

The low-level background detector system in the UL includes an intrinsically low-radioactivity level Ge detector (35% relative efficiency, named Ge1) and a plastic veto scintillator (1 m^2, named PS1) situated coaxially above the Ge1 detector. Comparative background study is performed in the GLL which is equipped with a Ge detector (18% relative efficiency and not intrinsically low-radioactivity level, named Ge2) and a small plastic scintillator (0.125 m^2, named PS2) in veto position.

Radon monitoring inside the laboratories was performed by radon monitor, model RM1029 manufactured by Sun Nuclear Corporation, NRSB approval-code 31822. The device consists of two diffused junction photodiodes as a radon detector, and is furnished with sensors for temperature, barometric pressure and relative humidity. The user can set the measurement intervals from half an hour to 24 h. The device has no online option (direct access to data) but the data are stored in the internal memory of the device and transferred to the personal computer after the measurement interval. The data obtained from the radon monitor (RM) for the temporal variations of the radon concentrations over a long period of time enable the study of the short-term periodical variations simultaneously with Ge detectors (Bossew, 2005).

Two flash analog to digital converters (FADC), made by C.A.E.N (type N1728B), which sample at 10 ns intervals into 2^{14} channels were used to analyze spectra from Ge detectors. User-friendly software was developed to analyze the C.A.E.N data with the possibility to choose the integration time for further time-series analysis that correspond to integration time of the radon monitor.

3. Results and discussion

For routine measurements of NORM samples the simplest arrangement of a Ge detector system is required due to frequent samples exchanges.

As the emphasis was on realistic conditions of radon and cosmic-ray influences on the Ge background neither any additional radon suppression method nor the full (2π coverage) veto arrangement were applied.

3.1. Cosmic-ray influence on the Ge detector background spectrum

The periodicities in cosmic-ray intensity variations (1-day and 27-days) are known to have small amplitudes. The Ge detectors can not see these variations neither in the annihilation line nor in the entire spectrum, mostly due to their small active area. Aperiodic variations of cosmic-ray intensity have greater amplitudes like a Forbush effect which typically lasts for several days. During simultaneously background measurements using two veto shielded Ge detectors the most intensive cosmic-ray variation occurred in March 2010. The decrease of cosmic-ray intensity, which lasted about four days, was very similar to characteristic decrease during a real Forbush effect, hence this event is appointed as a Forbush-like effect. Characteristic variation (decrease) of cosmic-ray intensity remains after cosmic-ray data correction on pressure variation (real Forbush effect) or vanishes after this correction (Forbush-like effect). A Ge detector does not recognize the cause of these cosmic-ray variations but it can detect them. The Forbush-like effect from March 2010 was registered in both single PS2 and single PS1 detectors inside the GLL and the UL, respectively. The cosmic-ray intensity decrease was relatively small, about 4% in the GLL and 2.5% as measured in the UL. Even small, it seems that a certain variation in number of coincidences between PS2 and Ge2 was registered, and both spectra followed each other during four days (Fig. 1). Integration time in the time series of the coincidence spectrum was chosen to be 6 h to emphasize the similarity between the two spectra. Strictly speaking it is only the time variation of the well-defined annihilation line, mostly caused by cosmic-ray pair-production, that can reflect the cosmic-ray changes, but its count rate is too low. Similarly, statistics is poor even for the high-energy continuous part of the Ge spectrum. The coincidence veto spectrum in Fig. 1 has no energy cuts and includes all gamma-ray lines what corresponds to the real condition of background measurement without a priori selected energy intervals. The single cosmic-ray spectrum was not corrected for atmospheric pressure and temperature because this represents the realistic situation in a typical ground level laboratory, which is probably without a veto shield.

The big plastic scintillator PS1 inside the UL registered the same Forbush-like effect, but the coincidence spectrum does not show any corresponding changes, Fig. 2. At a depth of 25 m.w.e, the mean energy of cosmic-ray muons is about 5 GeV higher than that of ground level muons, which is why they feel all solar modulation effects far less than the cosmic-rays particles on the ground level.

3.2. Radon influence on the Ge detector background spectrum

The significance of the other time variable background component was tested in simultaneous measurements of radon concentration by RM and gamma-ray background by the Ge detector. Inside the sample chamber (SC) of the Ge detector, in the space between the lead shield and the detector, radon concentration is influenced by the radon distribution outside the SC, when the SC is

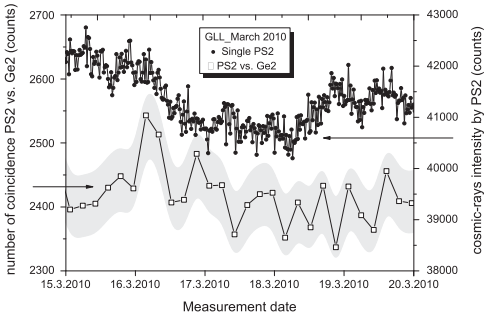

Fig. 1. Single cosmic-ray spectrum (circles) of PS2 and coincidence veto spectrum between PS2 and Ge2 (squares) inside the GLL during the Forbush-like effect in March 2010. The coincidence spectrum includes the error bars (1σ-B-spline).

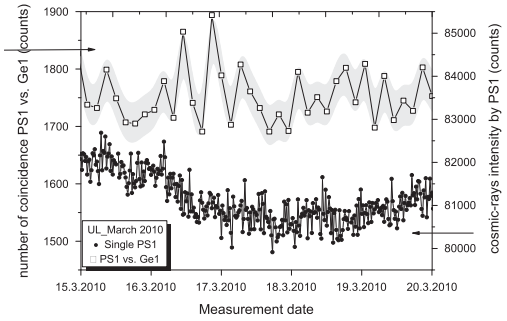

Fig. 2. Single cosmic-ray spectrum (circles) of PS1 and coincidence veto spectrum between PS1 and Ge1 (squares) inside the UL during the Forbush-like effect in March 2010. The coincidence spectrum includes the error bars (1σ-B-spline).

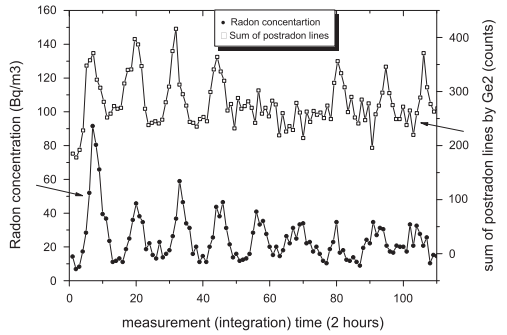

Fig. 3. Variability of radon concentration measured by RM inside the sampling chamber of the Ge2 detector (circles) and the sum of four post-radon lines (squares) measured by Ge2 inside the GLL.

not hermetically sealed. The Ge detector can see the radon daughters (^{214}Pb and ^{214}Bi) not only from the air inside SC but also from surface depositions on the detector and its passive shield.

Fig. 3 presents how the summed intensity of the four most prominent radon daughter lines (295.2 keV and 351.9 keV from ^{214}Pb, 609.3 keV and 1120.3 keV from ^{214}Bi) varies with time, as seen by the small shielded Ge detector (Ge2) inside the air-conditioned GLL. This follows closely the readings of the radon monitor positioned inside the SC (air volume of 1 dm^3). Here, we used the summed intensity of post-radon lines since the detector is small, but for high-efficiency detectors every single line should manifest the same behavior.

The radon monitor recorded radon and atmospheric parameters readings every 2 h and the integration in the time series of post-radon lines was chosen accordingly. This is sufficient to show clearly the one-day radon periodicity (Fig. 3).

Inside the UL, the radon concentration is kept at the low value under stable atmospheric parameters. The variability of radon concentration in the fresh air on the ground level is maximally suppressed in the UL by the ventilation system. The value of the summed post-radon lines inside the UL is almost constant as well as is the radon concentration.

The issue of stability of the gamma-ray background requires special attention when low-level ^{226}Ra measurements are performed by Ge detectors due to radon variability in ground level laboratories and sampling chambers of Ge detectors. Even a small Ge detector can see significant changes of background, if the mean radon concentration in ambient air is of the order or above 10 Bq/m^3 and some kind of radon suppression method inside a sample chamber must be applied (Neumaier et al., 2009).

Acknowledgements

The authors wish to thank Prof. Ivan Aničin for constant interest and support.

This work is supported by the Ministry of Education, Science and Technological Development of Republic of Serbia under project OI 171002.

References

Antanasijević, R., Aničin, I., Bikit, I., Banjanac, R., Dragić, A., Joksimović, D., Krmpotić, Đ., Udovičić, V., Vuković, J., 1999. Radon measurements during the building of a low-level laboratory. Radiat. Meas. 31, 371–374.

Bossew, P., 2005. A very long-term HPGe-background gamma spectrum. Appl. Radiat. Isot 62, 635–644.

Neumaier, S., Wojcik, M., Dombrowski, H., Arnold, D., 2009. Improvements of a low-level gamma-ray spectrometry system at the underground laboratory "UDO". Appl. Radiat. Isot 67, 726–730.

Udovičić, V., Grabež, B., Dragić, A., Banjanac, R., Joković, D., Panić, B., Joksimović, D., Puzović, J., Aničin, I., 2009. Radon problem in an underground low-level laboratory. Radiat. Meas. 44, 1009–1012.

Status of the Belgrade CR laboratory and some preliminary results

I.V. Aničin, J. Puzović*, A. Dragić, V. Udovičić, R. Banjanac, D. Joković, N. Veselinović, M. Savić*

Institute of Physics, Pregrevica 118, Belgrade, Serbia

**Faculty of Physics, Belgrade University, Studentski trg 16, Belgrade, Serbia*

dragic@ipb.ac.rs

Abstract

The Belgrade CR Laboratory, http:\\ www.ipb.ac.rs\~cosmic, (44°51′ N, 20°23′ E; vertical rigidity cut-off: 5.3 GV, altitude 78 m a.s.l.) is described. The existing equipment is presented. Current activities and some preliminary results are reported. The plans for future and scientific potential of the laboratory is discussed.

Laboratory description

• The CR laboratory of the Institute of Physics, Belgrade consists of two separate, corridor connected laboratory spaces, about 25 m apart. One laboratory is located on the ground level (GLL), while the other one is a shallow (25 mwe) underground laboratory (UL). Both laboratories are equipped with identical instrumentation.

• Each of the setups consists of a single bigger 100x100x5 cm plastic scintillator detector furnished with four PMTs directly coupled to the corners bevelled at 45°, and an independent single smaller 50x25x5 cm plastic scintillator detector with a single PMT looking at its longest side via a Perspex light guide tapering to the diameter of a PMT. The analyzers are the two fast ADC units with four independent inputs each, made by CAEN, of the type N1728B. These are sophisticated instruments capable of working in the energy histogram mode, when they perform like digital spectrometers, or/and in the oscillogram mode, when they perform like digital storage oscilloscopes. In both modes they sample at 10 ns intervals, into 2^{14} channels. Every analyzed event is fully recorded in the same PC which controls their workings. This enables to off-line coincide the events at all four inputs, prompt as well as arbitrarily delayed, with the time resolution of 10 ns, as well as to analyze the time series not only of all single inputs, but also of arbitrary coincidences, with any sample period from 10 ns up. The two N1728 units are externally synchronized, what makes possible to coincide/correlate the events recorded in the two laboratories. The flexible software that performs all these off-line analyses is entirely homemade. The preamplifier outputs of the PMTs of bigger detectors are paired diagonally, the whole detector thus engaging the two inputs of the FADC. The output of the PMT of the smaller detector is fed into the third input. It serves as a control of regularity of operation of bigger detector, but also for investigations of development of local EM showers and decoherence measurements. The fourth input remains free, and is put to different use in the two laboratories. In GLL a (3x3) NaI detector is at present used to scan the response of the bigger detector as a function of the position of the interaction point, while in the UL a 35% efficiency radiopure HPGe detector is positioned right below the center of the bigger detector in order to study in detail the effects of cosmic rays on the background spectra in low-level high-resolution gamma-ray spectroscopy.

•The UL is kept in a radiopure environment. Laboratory walls are sealed with 1mm tick aluminium and lab space is 2-3 mb overpressured to prevent intrusion of radon. Radon concentration is typically at $\sim 10 Bq/m^3$ level.

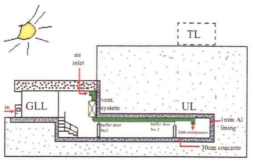

Fig. 1 *Cross sectional view of the laboratory*

Preliminary results

Muon flux and its variations

• Muon flux is measured with smaller plastic scintillators during entire year 2002 at both GL and UL. Muon flux and vertical intensity are:
-at ground level:

$$J_{1G} = (1.37 \pm 0.03) \cdot 10^{-2} s^{-1} cm^{-2}$$

$$I_{vG} = (8.4 \pm 0.2) \cdot 10^{-3} s^{-1} cm^{-2} sr^{-1}$$

-underground:

$$J_{1U} = (4.5 \pm 0.2) \cdot 10^{-3} s^{-1} cm^{-2}$$

$$I_{vU} = (2.5 \pm 0.2) \cdot 10^{-3} s^{-1} cm^{-2} sr^{-1}$$

.

• At cosmic-ray energies relevant for our experiment (primaries with several tens of GeV), cosmic radiation is strongly subjected to solar modulation. In the list of periodicities identified in muon time series in the period 2002-2007 (based also on the measurements with smaller detectors), majority coincides with the established periodicities of solar activity parameters:
- at ground level:

T	5.3	8.4	13.6	20.5	22	27	34.6	37	57	90	194	240	350
ΔT	5 · 10 $^{-4}$	0.05	0.1	0.2	0.2	0.3	1	0.6	2.5	3.5	16	24	53

- underground

T	1	8.7	13.6	20.5	25.4	26.5	34.5	37	57	90	162	194	240	350
ΔT_u	5 · 10 $^{-4}$	0.03	0.1	0.2	0.3	0.3	1	0.6	2.5	3.5	11.5	16	24	53

• If we concentrate on diurnal variation, and organize data in local solar time, with the raw data amplitude of diurnal variation in the ground detector data is $1.96(7) \times 10^{-3}$ and semi-diurnal $7.4(7) \times 10^{-4}$. At the same time amplitude of diurnal variation in the underground detector data is $9(1) \times 10^{-4}$ and semi-diurnal $6(1) \times 10^{-4}$

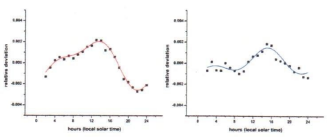

Fig. 2 *Diurnal + semidiurnal variations of muon flux at ground level (left) and underground (right).*

CR induced events in low-level gamma spectroscopy

• To illustrate capabilities of present setup we present spectra of triple coincidences between two PMT pairs at plastic scintillator corners and HPGe detector. An event registered by both PMT pairs is most likely to be a muon (low energy background is effectively suppressed) and a consequent coincidence with HPGe detector represent a muon induced event.

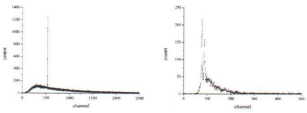

Fig. 3 *Coincident spectra between plastic scintillator and HPGe: prompt (left panel) and delayed (right panel).*

• Dominant feature in the prompt coincident spectrum is annihilation line at 511 KeV, and X-rays from the lead shield surrounding HPGe detector in the spectrum of delayed coincidences.

• Neutrons generated from muons are especially interesting. They represent inconvenient source of background in deep underground experiments. With present day setup in UL, the rate of those events is rather small and can be studied only in a long term program. To test the response of our detectors to neutron events, we triggered a HPGe detector, placed in GLL, with neutrons from a neutron source (*Cf-252*). A portion of the coincident spectrum is shown in Figure 4, with the structure around 692KeV originating from the inelastic neutron scattering on *Ge-72*. Peculiar triangular shape of the line is a result of summing of the transition energy and the recoil energy of the emitting nucleus. From the distribution of time intervals between trigger detector and HPGe, the lifetime of the excited 692KeV state in *Ge-72* is easily determined. It is our intention to use this line shape to determine neutron energy spectrum.

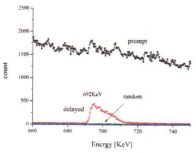

Fig. 4 *The effect of inelastic neutron scattering on Ge-72 seen in delayed coincident spectrum.*

MERENJE KONCENTRACIJE RADONA I PROCENA IZLOŽENOSTI U BOGOVINSKOJ PEĆINI

Vladimir UDOVIČIĆ [1], Mihailo SAVIĆ [1], Dejan JOKOVIĆ [1], Dimitrije MALETIĆ [1], Radomir BANJANAC [1], Nikola VESELINOVIĆ [1], Marina ŽIKIĆ [2]

1) Institut za fiziku, Univerzitet u Beogradu, Srbija, udovicic@ipb.ac.rs

2) Turistička organizacija Boljevac, Boljevac, Srbija

SADRŽAJ

Merenja koncentracije radona urađena su u Bogovinskoj pećini u istočnoj Srbiji. Dobijeni rezultati su analizirani i na osnovu njih je procenjena efektivna doza za zaposlene radnike i turiste, koja potiče od radona iz vazduha. Srednja vrednost koncentracije radona je ~3000 Bqm^{-3}, što je približno srednjoj svetskoj vrednosti koncentracije radona u pećinama. Procenjene efektivne doze su 9.45 mSv za zaposlene, odnosno 9.45 μSv za posetioce, što je oko dva puta manje od granične vrednosti za zaposlene i znatno ispod preporučenih vrednosti za posetioce.

1. Uvod

Merenja koncentracije radona na mestima kao što su podzemni rudnici ili pećine su važna zbog procene radiološke opasnosti prouzrokovane izloženošću radnika i posetilaca. Sa jedne strane, nivo radona u kraškim sistemima zavisi od velikog broja faktora, i spoljašnjih i unutrašnjih, kao što su razlika spoljašnje i unutrašnje temperature, brzina vetra, varijacija atmosferskog pritiska i vlažnosti, zatim osobine stena (karsta), geomorfologija, poroznost i sadržaj radijuma u sedimentima i stenama. Šta više, geološke i morfološke karakteristike pećine igraju važnu ulogu u identifikovanju koncentracije radona. Kompleksna dinamika radona u prirodnim podzemnim prostorima čini da je kontinuirano praćenje koncentracije radona korisno, pa čak i neophodno u pećinama sa stanovišta zaštite od zračenja. Nivo radona u pećinama najviše zavisi od pravca i intenziteta vazdušnih struja. Neka opšta predviđanja koncentracije radona i njene varijacije su moguća ukoliko je poznato kako promene temperature utiču na prirodno provetravanje. Ipak, bilo kakav pokušaj preciznijeg predviđanja koncentracije radona na osnovu poznavanja konkretnih uslova je veoma komplikovano i rezultat neminovno prati značajna greška. Posledica je da je za dobijanje pouzdanijih rezultata i procenu nivoa i apsorbovane doze neophodno vršiti neposredna merenja.

Ovu potencijalnu radiološku opasnost prepoznale su Međunarodna komisija za zaštitu od zračenja (ICRP) i Međunarodna agencija za atomsku energiju (IAEA), koje su dale preporuku i sigurnosni standard za radon i njegove potomke. Prema ovim preporukama, godišnja efektivna doza za posetioce u pećinama ne treba prelaziti 3 mSv, a za zaposlene (radnike na održavanju, turističke vodiče) 20 mSv, usrednjeno u petogodišnjem razdoblju [1].

Merenja vršena u Velikoj Britaniji u većem broju pećina i rudnika pokazala su da postoje velike varijacije koncentracije u zavisnosti od tipa i topologije pećina, odnosno rudnika. Srednja koncentracija u uređenim pećinama je iznosila i do 22500 Bqm^{-3}, sa maksimalnim koncentracijama do 30000 Bqm^{-3}. U nekim pećinskim sistemima te vrednosti su iznosile 30000 Bqm^{-3} i 35000 Bqm^{-3} [2].

Hakl i saradnici su sistematizovali izmerene koncentracije radona u pećinama širom sveta te su zaključili da im je distribucija približno log-normalna, sa aritmetičkom sredinom 2800 Bqm^{-3}, a vrednosti su bile u rasponu od 100 do 20000 Bqm^{-3} [3].

2. **Metod i merenja**

Merenja koncentracije radona vršena su u Bogovinskoj pećini, koja se nalazi u selu Bogovina, 1,5 km od centra sela, na teritoriji opštine Boljevac, u istočnoj Srbiji. Ulaz, na visini od 268 m n.m, je na jugoistočnom obodu masiva Malinika, koji je deo velikog karstnog masiva Južni Kučaj. Pećina je udaljena 6 km od magistralnog puta Paraćin – Zaječar i 14 km od Boljevca.

Vremenske serije merenih koncentracija radona, temperature i relativne vlažnosti u Bogovinskoj pećini dobijene su pomoću uređaja SN1029 (proizvođača Sun Nuclear Corporation). To je merni uređaj jednostavne konstrukcije i primene u praksi. U suštini, radi se o brojaču sa dodatkom senzora za merenje meteoroloških parametara. Nedostatak uređaja je nemogućnost merenja koncentracije radona u zemljištu i vodi. Operater može podesiti vremenske sekvence od 0.5 sati do 24 sati. Jedan ciklus merenja može trajati 1000 sati ili ukupno 720 vremenskih sekvenci (broj sukcesivnih merenja, odnosno tačaka u vremenskoj seriji). S obzirom na očekivane visoke koncentracije radona, uređaj je podešen da radi u vremenskoj sekvenci od 0.5 sati. Jedan ciklus merenja po mernom mestu trajao je 24 sata, kako bi se snimila jednodnevna periodika u varijaciji koncentracije radona. Simultano su mereni temperatura, vazdušni pritisak i vlažnost. Prednost uređaja SN1029 je u velikoj osetljivosti i mogućnošću merenja u uslovima velike vlažnosti vazduha.

Izboru mernih pozicija prethodilo je merenje ambijentalnog doznog ekvivalenta u pećini. Tom prilikom je detaljno snimljena i topologija pećine. Na osnovu toga su izabrana dva merna mesta. Prvo se nalazilo dublje u pećini u jednom užem hodniku, na oko 350 metara od ulaza, dok je za drugo merno mesto izabrana pozicija u većoj dvorani, na oko 100 metara od ulaza (slika 1.).

Slika 1. Jedno od dva merna mesta, na udaljenosti oko 350 od ulaza u pećinu

3. Rezultati

Rezultati merenja koncentracije radona u Bogovinskoj pećini predstavljeni su grafički na slici 2. i u tabeli 1.

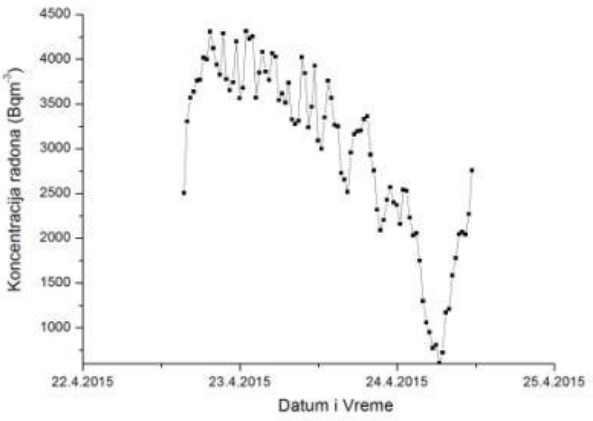

Slika 2. Vremenska serija koncentracije radona u Bogovinskoj pećini

Tabela 1. Statistika rezultata merenja koncentracije radona u Bogovinskoj pećini

	Koncentracija radona [Bqm^{-3}]				
	Srednja vrednost	**Standardna devijacija**	**Minimum**	**Medijana**	**Maksimum**
Merno mesto 1	3723.9	377.6	2505.6	3761.4	4313.2
Merno mesto 2	2164.5	776.2	610.8	2250.0	3363.2

Izmerena srednja vrednost koncentracije radona za oba merna mesta iznosi 2982 Bqm^{-3}. Na osnovu dobijenih rezultata, korišćenjem formule za računanje efektivne doze *E*:

$$E\ [\mathrm{mSv}] = 7{,}923 \cdot 10^{-6} \cdot F \cdot c\ [\mathrm{Bqm^{-3}}] \cdot t\ [\mathrm{h}],$$

gde su *F* ravnotežni faktor (*F*=0.4), *c* koncentracija radona i *t* vreme ekspozicije. Uz pretpostavku da radna sezona u Bogovinskoj pećini traje šest meseci (sa osmočasovnim radnim danom), a da je vreme posete pećini jedan sat, procenjena efektivna doza za zaposlene iznosi 9.45 mSv na godišnjem nivou, odnosno efektivna doza za posetioce iznosi 9.45 μSv na godišnjem nivou.

Takođe, izmerene su temperatura i vlažnost vazduha u pećini. Rezultati su predstavljeni na slikama 3. i 4., kao i u tabeli 2.

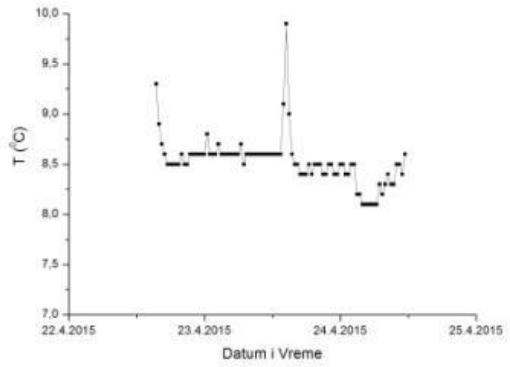

Slika 3. Temperatura vazduha u Bogovinskoj pećini.

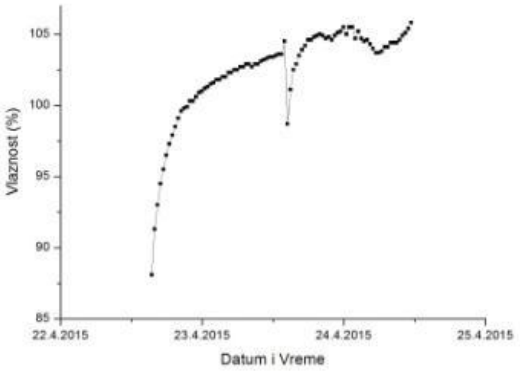

Slika 4. Vlažnost vazduha u Bogovinskoj pećini.

Tabela 2. Statistika rezultata merenja temperature i vlažnosti vazduha

	Srednja vrednost	**Standardna devijacija**	**Minimum**	**Medijana**	**Maksimum**
Temperatura [ºC]	8.5	0.2	8.1	8.5	9.9
Vlažnost vazduha [%]	102.4	3.2	88.1	103.4	105.8

4. Zaključak

Merenja koncentracije radona u Bogovinskoj pećini pokazala su da je izmereni nivo radona, 2982 Bqm^{-3}, gotovo jednak srednjoj svetskoj koncentraciji radona u pećinama. Takođe, primetna je razlika u koncentracijama radona na dva merena mesta, što je očekivano obzirom na izbor njihovih lokacija. Veća koncentracija izmerena je na mernom mestu koje je udaljenije od ulaza u pećinu, u odnosu na merno mesto bliže ulazu. Temperatura i vlažnost u Bogovinskoj pećini su skoro konstantni i iznose 8.5 ºC i 102.4 %, respektivno.

Na osnovu izmerene koncentracije radona, izračunata je i efektivna doza, uz pretpostavljenu radnu sezonu u Bogovinskoj pećini od šest meseci, sa osmočasovnim radnim danom, i pretpostavljeno vreme turističke posete pećini od jednog sata. Ove vrednosti su 9.45 mSv na godišnjem nivou za zaposlene, odnosno 9.45 μSv na godišnjem nivou za posetioce. Dobijene vrednosti su oko dva puta manje od granične vrednosti za zaposlene i znatno ispod preporučenih vrednosti za posetioce, a na osnovu granica koje su propisale međunarodne organizacije koje se bave zaštitom od zračenja.

5. Literatura

[1] International Commission on Radiological Protection (ICRP). Protection against Radon-222 at Home and at Work. ICRP Publication 65. (1994). Pergamon Press.

[2] Hakl, J., Csige, I., Hunyadi, I., Várhegyi, A., and Géczy, G.: Radon transport in fractured porous media – Experimental study in caves, *Environ. Int.* 22 (1996) 433–437.

[3] J. Hakl, I. Hunyadi, I. Csige, G. Géczy, L. Lénárt, A. Várhegyi. Radon transport phenomena studied in karst caves – International experiences on radon level and exposures. *Radiat. Meas.* 28 (1997) 675-684.

RADON MEASUREMENTS AND EXPOSURE ESTIMATES IN BOGOVINA CAVE

Vladimir UDOVIČIĆ[1], Mihailo SAVIĆ[1], Dejan JOKOVIĆ[1], Dimitrije MALETIĆ[1], Radomir BANJANAC[1], Nikola VESELINOVIĆ[1], Marina ŽIKIĆ[2]

1) Institute of Physics, University of Belgrade, Serbia, udovicic@ipb.ac.rs

2) The Tourism Organization of Boljevac, Boljevac, Serbia

ABSTRACT

Measurements of radon concentration were done in Bogovina cave in the region of eastern Serbia. The obtained results were analysed and effective dose, due to radon from the air, is estimated for employees and tourists. Mean value of radon concentration is ~3000 Bqm^{-3}, approximately to world mean of radon concentration in caves. Estimated effective doses are 9.45 mSv for employees and 9.45 μSv for tourist visitors, which is well below the recommended values for caves.

KORELACIONA I REGRESIONA ANALIZA VARIJABILNOSTI RADONA PRIMENOM MULTIVARIJANTNIH METODA

Jelena FILIPOVIĆ, Vladimir UDOVIČIĆ, Dimitrije MALETIĆ, Radomir BANJANAC, Dejan JOKOVIĆ, Mihailo SAVIĆ, Nikola VESELINOVIĆ
Institut za fiziku Beograd, Univerzitet u Beogradu, Beograd, Srbija, jecafi@gmail.com

SADRŽAJ

Multivarijantni metodi omogućavaju ispitivanje korelacija velikog broja meteoroloških parametara i koncentracije radona. Pokazano je da multivarijantne metode za klasifikaciju i regresiju daju dobre rezultate koji su značajni pri proučavanju varijacje radona u zatvorenim prostorijama. Od 12 različitih metoda BDT se pokazao kao najefikasniji. U okviru ovog rada biće više reči o toj metodi.

1. Uvod

Radioaktivne emanacije, radon (^{222}Rn) i toron (^{220}Rn) predstavljaju predmet intenzivnih istraživanja, od otkrića 1900. godine sve do današnjih dana. U širem smislu, ova istraživanja spadaju u domen radijacione fizike, međutim od pre nekoliko decenija predmet istraživanja radioaktivnih emanacija obuhvata veći broj naučnih disciplina (geofizika, seizmologija, medicinska fizika, dozimetrija, zaštita od zračenja) što celoj problematici daje jedan multidisciplinaran karakter. Istraživanja dinamike radona u različitim sredinama, naročito u zatvorenim prostorijama, imaju veliki značaj kako sa aspekta zaštite od jonizujućih zračenja tako i sa projektovanjem mera za njegovu redukciju. To predstavlja dosta složen zadatak. Dosadašnji rezultati i mnogobrojni modeli ponašanja radona u zatvorenim prostorijama ukazuju na svu kompleksnost, pre svega u predviđanju varijabilnosti radona, iz prostog razloga što u toj zavisnosti učestvuje veliki broj parametara. Koncentracija radona unutar zatvorenih prostorija zavisi od velikog broja faktora koji pored meteoroloških parametara uključuje lokalnu geologiju, permeabilnost zemljišta, građevinski materijal od koga je izgrađen objekat kao i same životne navike ljudi. Svi ovi faktori utiču na varijacij koncentracije radona, pa je s toga važno proučiti njihovu korelaciju. Do danas je razvijeno nekoliko modela koji opisuju ponašanje radona u zatvorenim prostorijama [1], [2], [3]. Varijacija koncentracije radona zavisi od varijacije više meteoroloških parametara. U ovom radu biće reči o najefikasnijem metodu u okviru TMVA (Toolkit for Multi Variate Analysis) koji na najbolji način određuje korelaciju koncentracije radona unutar zatvorenih prostorija i različitih klimatskih varijabli. U prethodnim radovima prikazan je način na koji je odredjen najefikasniji metod [4]. Primenom regresione analize u okviru istog TMVA paketa, moguće je sa prihvatljivom tačnošću predviđanje varijabilnosti koncentracije radona, a na osnovu varijacije meteoroloških parametara.

2. Kratkotrajna merenja koncentracije radona u laboratorijskim i realnim uslovima

Postoji veliki broj metoda za određivanje koncentracije radona u vazduhu, vodi i zemljištu. Metode merenja se mogu klasifikovati na različite načine u zavisnosti od primenjenih kriterijuma. Pogodno je uzeti podelu u zavisnosti od načina i dužine trajanja merenja koncentracije radona.

1. Trenutno uzorkovanje izvodi se u kratkom vremenskom periodu (nekoliko minuta) u poređenju sa vremenskim rasponom fluktuacije koncentracije radona.
2. Kontinualno i aktivno uzorkovanje vrši se automatski u kratkim vremenskim intervalima tokom jednog dužeg vremenskog perioda.
3. Integralno uzorkovanje bazira se na prikupljanju svih događaja koji su se desili tokom dužeg vremenskog perioda koji može biti između nekoliko dana i nekoliko meseci.

Za potrebe odredjivanja najboljeg metoda iskorišćeni su rezultati dobijeni merenjima u niskofonskoj laboratoriji Instituta u Zemunu i u jednoj porodičnoj kući. Vremenske serije merenih koncentracija radona, temperature, atmosferskog pritiska i relativne vlažnosti dobijene su pomoću uređaja SN1029 (proizvođača Sun Nuclear Corporation). To je merni uređaj jednostavne konstrukcije i primene u praksi. U suštini, radi se o brojaču sa dodatkom senzora za merenje meteoroloških parametara. Nedostatak uređaja je nemogućnost merenja koncentracije radona u zemljištu i vodi. Operater može podesiti vremenske sekvence od 0.5 sati do 24 sati. Jedan ciklus merenja može trajati 1000 sati ili ukupno 720 vremenskih sekvenci (broj sukcesivnih merenja, odnosno tačaka u vremenskoj seriji).

Od 2008. godine, rade se kratkotrajna merenja koncentracije radona u niskofonskoj podzemnoj laboratoriji u Institutu za fiziku u Zemunu. Ova metoda se koristi za dobijanje vremenskih serija koncentracija radona u datoj sredini. Dobijeni rezultati su publikovani u nekoliko radova u međunarodnim naučnim časopisima [5], [6], [7]. Tokom merenja radila je ventilacija i može se reći da su meteorološki parametri u laboratoriji bili mnogo stabilniji nego u kući. Meteorološki podaci izmereni za taj vremenski interval preuzeti su sa meteorološke stanice koja je locirana 4 km od laboratorije.

Merenje koncentracije radona vršeno je i u dnevnoj sobi porodične kuće koja je izgradjena od standardnih materijala (cigla, beton, malter) i izolovana je stiroporom. Merenje je izvršeno u periodu od 3. juna do 3. jula 2013. godine pri čemu je merena koncentracija radona, temperatura, pritisak i relativna vlažnost vazduha u samoj prostoriji. Vrednosti meteoroloških faktora u tom periodu dobijene su iz automatske meteorološke stanice locirane 400 m od kuće u kojoj je vršeno merenje. U obzir su uzeti sledeći meteorološki parametri: spoljašnja temperatura vazduha, pritisak i vlažnost vazduha, zračenje sunca, brzina vetra na visini od 10 m iznad površine zemlje, padavine, isparavanja i temperatura i vlažnost zemlje na dubinama od 10 cm, 20 cm, 30 cm i 50 cm.

3. **Korelaciona i regresiona analiza dobijenih rezultata**

Pri obradi podataka korišćene su MVA analize koje su implementirane kao deo programskog paketa ROOT [8]. ROOT sadrži, pored programa za analizu podataka, i programe za multivarijantnu analizu (The Toolkit for Multivariate Analysis - TMVA) [9]. Sve multivarijantne tehnike u TMVA pripadaju familiji algoritama "nadgledanog učenja". Nadgledano učenje rezultira u dobijanju algoritma za "mapiranje" (aproksimiranje) izlazne funkcionalne zavisnosti. Put do dobrog algoritma je učenje treniranjem, a srž treniranja je korišćenje skupa ulaznih varijabli (npr. atmosferske varijable) sa poznatim izlaznim vrednostima (npr. koncentracijom radona). Rezultujuća izlazna funkcionalna zavisnost može biti, jednostavno, skup "odluka", tj. uslova na vrednosti ulaznih podataka, kojim klasifikujemo izlazne vrednosti. Češće, traga se za nekom aproksimativnom funkcionalnom zavisnošću, sa uslovom da ova zavisnost daje izlazne vrednosti sa nekom proizvoljnom tačnošću. Određivanje korelacionih

koeficijenata služi kako bi bili u mogućnosti da odaberemo varijable koje imaju najjaču korelaciju sa koncentracijom radona. U tabeli 1 navedene su neke od meteoroloških varijabli poređane po njihovoj važnosti.

Tabela 1. Rangiranje BDT ulaznih varijabli

Variable	**Variable importance**
Temperatura zemljišta na dubini od 10cm	$1{,}37\ 10^{-1}$
Temperatura spoljašnjeg vazduha	$7{,}40\ 10^{-2}$
p(spolj) - p(radon monitor)	$6{,}51\ 10^{-2}$
Vlažnost spoljašnjeg vazduha	$6{,}40\ 10^{-2}$
Temperatura zemljišta na dubini od 50cm	$4{,}68\ 10^{-2}$
Brzina vetra na visini od 10m	$3{,}87\ 10^{-2}$

Multivarijantnim metodama unutar paketa TMVA u ROOT-u može se tragati za multivarijativnom aproksimacijom funkionalne zavisnosti koncentracije radona i meteoroloških varijabli klasifikacijom odbroja radona. Pri obradi podataka korišćeno je nekoliko multivarijantnih metoda od kojih se najbolje pokazao BDT (Boosted Decision Tree), što se može videti na slici 1.

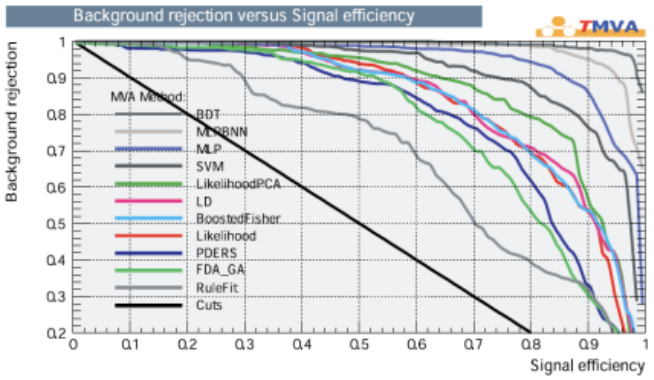

Slika 1. ROC-Krive za različite MVA metode

BDT se pokazao kao najefikasniji metod za klasifikaciju ulaznih podataka i u slučaju podataka dobijenuh iz kuće kao i onih dobijenih merenjem u podzemnoj niskofonskoj laboratoriji. Najbolji multivarijantni regresioni metod je takodje u oba slučaja BDT.
Na slici 2 može se videti korelaciona matrica u kojoj je prikazana korelacija izmedju svih parametara.

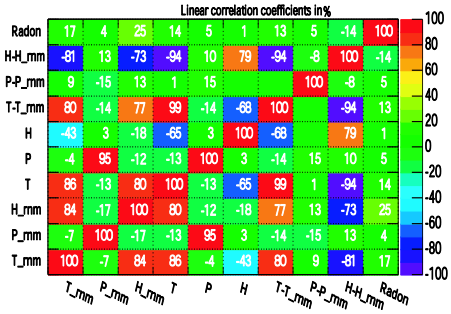

Slika 2. Korelaciona matrica radona i meteo varijabli u podzemnoj niskofonskoj laboratoriji

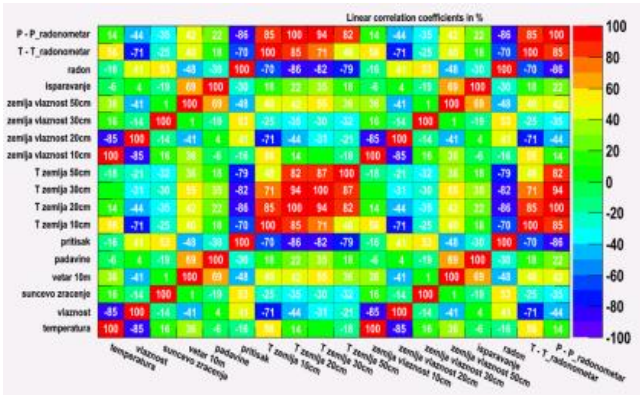

Slika 3. Korelaciona matrica radona i meteo varijabli u porodičnoj kući

Primenom regresione analize u okviru istog TMVA paketa, a za isti skup merenih koncentracija radona i meteo parametara u niskofonskoj podzemnoj laboratoriji i porodičnoj kući u Srbiji, dobijeni su rezultati koji su prikazani na slici 4.

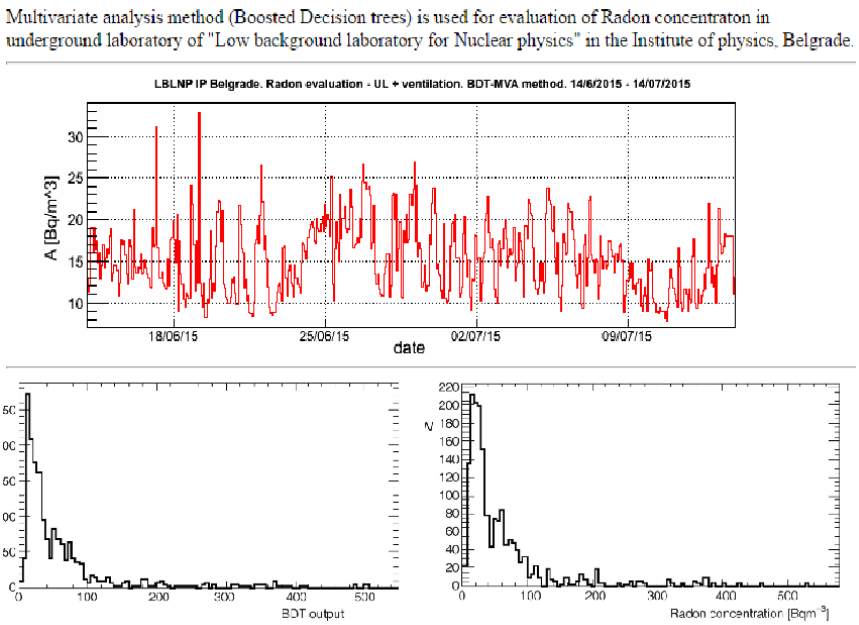

Slika 4. Predviđanje koncentracije radona na osnovu meteo parametara korišćenjem regresione analize u okviru TMVA paketa u niskofonskoj podzemnoj laboratoriji (gore) i porodičnoj kući (dole)

4. Zaključak

Korelaciona i regresiona analiza varijabilnosti radona primenom multivarijantnih metoda, realizovana u softverskom paketu TMVA, primenjena na analizu varijacije koncentracije radona sa klimatskim varijablama u niskofonskoj podzemnoj laboratoriji i porodičnoj kući u Srbiji, pokazala je potencijalnu korisnost ovih metoda. Čini se da se metoda može koristiti sa dovoljnom tačnošću (oko 15 %) za predviđanje koncentracije radona, a na osnovu meteoroloških parametara dobijenih iz obližnjih meteoroloških stanica.

5.Literatura

[1] B. P. Jelle et al. Implementation of radon barriers, model development and calculation of radon concentration in indoor air. *Journal of Building Physics* (2010) 195-222.

[2] B. P. Jelle et. al. Development of a model for radon concentration in indoor air. *Science of the Total Environment* 416 (2012), 343–350.

[3] Font, Ll., Baixeras, C. The RAGENA dynamic model of radon generation, entry and accumulation indoors. Science of the Total Environment 307 (2003) 55–69.

[4] D. M. Maletić et al. Comparison of multivariate classification and regression methods for indoor radon measurements. *Nuclear Technology and Radiation Protection* 29 (2014) 17-23.

[5] V. Udovičić, B. Grabež, A. Dragić, R. Banjanac, D. Joković, B. Panić, D. Joksimović, J. Puzović, I. Aničin. Radon problem in an underground low-level laboratory. *Radiation Measurements.* 44 (2009) 1009-1012.
[6] V. Udovičić, I. Aničin, D. Joković, A. Dragić, R. Banjanac, B. Grabež, N. Veselinović. Radon Time-Series Analysis in the Underground Low-Level Laboratory in Belgrade, Serbia. *Radiation Protection Dosimetry.* 145 (2-3) (2011) 155-158.
[7] R. Banjanac, V. Udovičić, A. Dragić, D. Joković, D. Maletić, N. Veselinović, B. Grabež. Daily Variations of Gamma-Ray Background and Radon Concentration. *Romanian Journal of Physics.* Volume 58, Supplement (2013) S14-S21.
[8] R. Brun and F. Rademakers, ROOT - An Object Oriented Data Analysis Framework. *Nuclear Instruments and Methods in Physics Research. A* 389, (1997) 81
[9] A. Hoecker, P. Speckmayer, J. Stelzer, J. Therhaag, E. von Toerne, and H. Voss. TMVA - Toolkit for Multivariate Data Analysis. PoS ACAT 040 (2007) arXiv:physics/070303

CORRELATION AND REGRESSION ANALYSIS OF VARIABILITY OF RADON CONCENTRATION APPLYING MULTIVARIATE METHODS

Jelena FILIPOVIĆ, Vladimir UDOVIČIĆ, Dimitrije MALETIĆ, Radomir BANJANAC, Dejan JOKOVIĆ, Mihailo SAVIĆ, Nikola VESELINOVIĆ
Institute of Physics, University of Belgrade, Belgrade, Serbia

ABSTRACT
Multivariate methods provide testing the correlation of a large number of meteorological parameters and concentrations of radon. It is shown that multivariate methods for classification and regression give good results, which are important for the study of indoor radon variation. BDT has proven to be the most effective method of 12 different methods that have been tested. In this work, there will be more to say about this method.

МОНТЕ КАРЛО СИМУЛАЦИЈА КРЕИРАЊА КОСМОГЕНИХ РАДИОНУКЛИДА У ЛЕСУ

Димитрије МАЛЕТИЋ, Никола ВЕСЕЛИНОВИЋ, Дејан ЈОКОВИЋ, Владимир УДОВИЧИЋ, Радомир БАЊАНАЦ, Михаило САВИЋ и Александар ДРАГИЋ

Институт за физику, Земун,Београд, Србија, veselinovic@ipb.ac.rs

САДРЖАЈ

Коришћењем Монте Карло симулационог пакета Corsika симулиран је флукс космичког зрачења на површини . Простирање и интеракција космичог зрачења кроз земљиште ,као и креирање радионуклида у земљишту је затим симулирано коришћењем Geant4 симулационог пакета. Дистрибуција и концентрација радионуклида у зависности од дубине земљишта је приказана при чему је и зависност од брзине таложења земљишта узета у обзир. Могућност експерименталног мерења радионуклида у Нискофонској лабораторији Института за физику у Земуну је дискутована.

1. Увод

Космички зраци (КЗ) су енергичне честице које долазе из спољног свемира после интеракције са Соларним и Земљиним магнетним пољем до атмосфере. Интеракција ових, примарних КЗ са атмосфером доводи до стварања каскаде секундарних честица: хадрона, електрона, миона, неутрина и гама зрачења. Ове честице могу да дођу и до тла па и да продру у тло. Најчешће честице које продиру у тло су миони, због своје релативне стабилости и малог пресека за реакције као и слабо интерагујући неутрини. Производ интеракције КЗ са земљиштем је велики број различитих изотопа, како стабилних тако и радиоактивних који се стварају у тлу на одређеној дубини. Ови изотопи се називају *космогени нуклиди и радионуклиди,* респективно. Неки од њих настају спалацијом или фрагментацијом а други су резултат нуклеарних реакција [1]. Табела 1 приказује најчешће космогене изотопе нађене у метеоритима што одговара и изотопима нађеним у земљишту или стени.

Космогени нуклиди се акумулирају на месту настанка тако да концентрација ових нуклида је интегрални податак настао од тренутка њиховог формирања до мерења узорка. Поред тога морају се узети и ерозије и таложења тла као фактори који могу утицати на концентрацију космогених нуклида.

Концентрација космогених радионуклида C је функција дубине z и времена t у земљишту или стени [3]:

$$\frac{\partial C(z,t)}{\partial t} = P(z) + \epsilon \frac{\partial C(z,t)}{\partial z} - \lambda C(z,t) \qquad (1.1)$$

и

$$P(z) = P_0 e^{-\frac{\rho z}{\Lambda}} \qquad (1.2)$$

Где је $C(z,t)$ концентрација изотопа, z дубина, t време, ϵ брзина ерозије, λ константа распада, P(z) брзина продукције атома на дубини z, P_0 брзина продукције на површини а ρ густина и Λ атенуациона дужина. Ова једначина (1.1) има аналитичко решење уколико су испуњени наколико услова, као што су:

земљиште или стена су затворени систем тј,. нема мешања са спољним материјалом, Таложење или раст стене мора бити константан или познате временске зависности. Атенуациона дужина мора бити константна и позната. Ови услови нису увек испуњени па се овом проблему може прићи и преко симулације.

Табела1. Неки од космогених нуклиди нађених у метеоритима [2]

нуклиди	**Полуживот (у годинама)**	**Мете из којих су настали**
^{3}H	**12,3**	**O,Mg, Si, Fe**
^{3}He, ^{4}He	**Стабилан**	**O,Mg, Si, Fe**
^{10}Be	**$1,6 \cdot 10^{6}$**	**O,Mg, Si, Fe**
^{14}C	**5730**	**O,Mg, Si, Fe**
^{20}Ne, ^{21}Ne, ^{12}Ne	**Стабилан**	**Mg, Al, Si, Fe**
^{22}Na	**2,6**	**Mg, Al, Si, Fe**
^{26}Al	**$7,1 \cdot 10^{5}$**	**Al, Si, Fe**
^{36}Cl	**$3,0 \cdot 10^{5}$**	**Fe, Ca,K,CL**
^{36}Ar, ^{38}Ar	**Стабилан**	**Fe,Ca,K**
^{37}Ar	**35 дана**	**Fe,Ca,K**
^{39}Ar	**269**	**Fe,Ca,K**
^{40}K	**$1,3 \cdot 10^{9}$**	**Fe**
^{39}K, ^{41}	**стабилан**	**Fe**
.		
.		
.		

2. Симулација креирања радионуклида

Београдска нискофонска лабораторија се налази у Институту за физику у Земуну. Географске координате лабораторије су: 44° 51'N географске ширине и 20°23'E географске дужине, са надморском висином од 78 метара. У односу на геомагнетно поље координате су следеће: B_x= +22,6 nT, B_y = +1,7 nT, B_z = +42,1 nT, гранична вертикална геомагнететна чврстоћа 5,3 GV. Лабораторија се састоји од две дела, надземног и плитко укопаног подземног дела. Изнад подземне лабораторије се налази 12 метара леса (густине 1,8-2,1 g/cm^3, састоји се претежно од SiO_2 и Al_2O_3). Зидови подземне лабораторије су од армираног бетона, дебљине 30 cm који су са унутрашње стране обложени алуминијумом дебљине од 1 mm. Ефективно, апсорпциони слој изнад подземне лабораторије износи 25 m.w.e (25 hg/cm^3). Та дубина је довољна да је практично присутна само мионска компоненета секундарног КЗ.

Симулација пљуска КЗ у надземном и подземном делу лабораторије урађено је коришћењем Монте Карло симулационих пакета CORSIKA и Geant4 [4,5]. CORSIKA је Монте Карло код који симулира интеракцију КЗ са атмосфером. Као производ, даје спектар секундарног КЗ на заданој надморској висини. За сумулирање проласка КЗ кроз тло, честице секундарног КЗ, добијених из CORSIKA-е, са њиховим карактеристикама као што су просторни положај, импулс и енергија су почетне су улазне вредности Geant4 симулације проласка кроз земљиште.

3. Резултати симулације

Услед губитка енергије услед проласка у подземни део лабораторије, испод леса, доспевају само миони који имају довољно енергије као и извесно гама зрачење (слика 1), док су електрони и хадрони апсорбовани. Неутрини, као веома слабо интерагујуће честице нису разматрани.

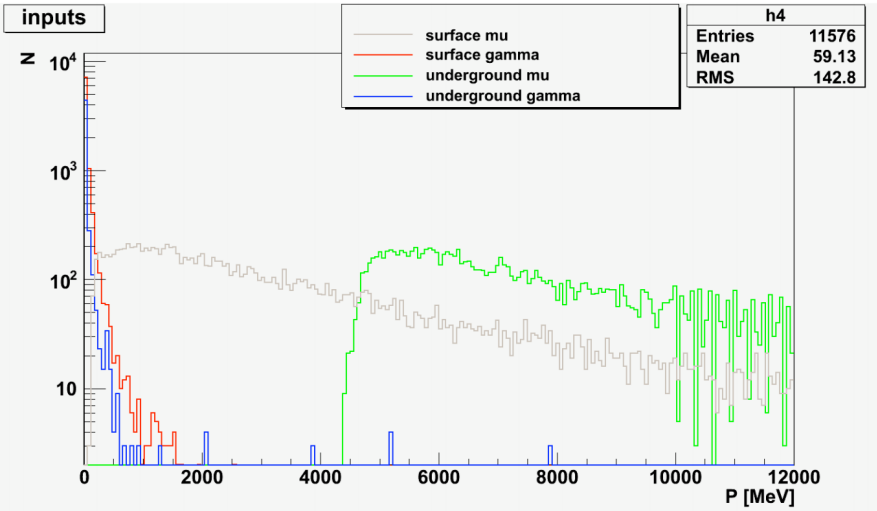

Слика1: Симулациони спектар миона и гама зрачења на површини и испод 12 m леса

У интеракције миона из КЗ са земљиштем, после проласка кроз слој леса, у подземном делу лабораторије се јављају протони, неутрони и језгра деутеријума који излазе у атмосферу подземне лабораторије (слика 2.). Они даље могу интераговати са инструментима и тако допринети повећању шума мерења.

Количина новонасталих изотопа је интегрална вредност у земљишту за улазне честице КЗ. Коришћењем симулације, за 100000 примарних честица на врху атмосфере,што одговара времену од 50 секунди, имамо тачан број креираних изотопа у земљишту између надземног и подземног дела лабораторије(табела 2).

Поред овог интегралног броја честица у целој запремини могуће је, симулацијом, одредити и место у којем се стварају ови нуклиди. Симулација нам омогућава да у прорачун просторне концентрације нуклида урачунамо и таложење леса, што је познати природни феномен. Знајући брзину производње радионуклида , њихов полуживот и брзину раста земљишта можемо наћи концентрацију тих радионуклида у земљишту (слика 3). Овде смо користили, због брзине процесирања, периоде од по 10 хиљада година тако да би са права концентрација одговарала линији која повезује максимуме суме.

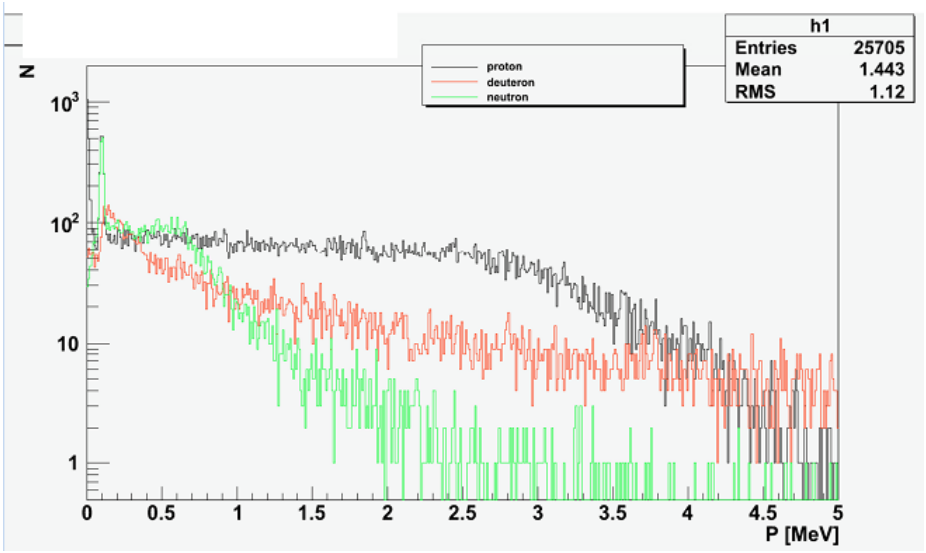

Слика 2. Спектар протона, неутрона и деутерона на дубини од 12 m леса

Табела 2: Нуклиди и честице произведене у 12 m леса

100 Ne21	**365 Mg24**	**21649 mion-**
105 Ar37	**399 Na24**	**25384 e-**
111 P31	**427 Mg27**	**25705 proton**
117 P32	**482 Cl36**	**33353 neutrino_mu**
129 B12	**498 K39**	**34888 mion+**
162 Ne22	**724 Na23**	**37631 alpha**
183 S34	**950 Al26**	**45606**
187 N16	**1002 N15**	**anti_neutrino_mu**
188 Na22	**1321 Al28**	**45703 neutrino_e**
198 K40	**1324 Mg25**	**58560 gamma**
284 Cl35	**1934 Mg26**	**5065 tricium**
310 Ar38	**3624 Al27**	**9255 neutron**
324 B11	**744 e+**	**9980 deuteron**
		16941 anti_neutrino_e

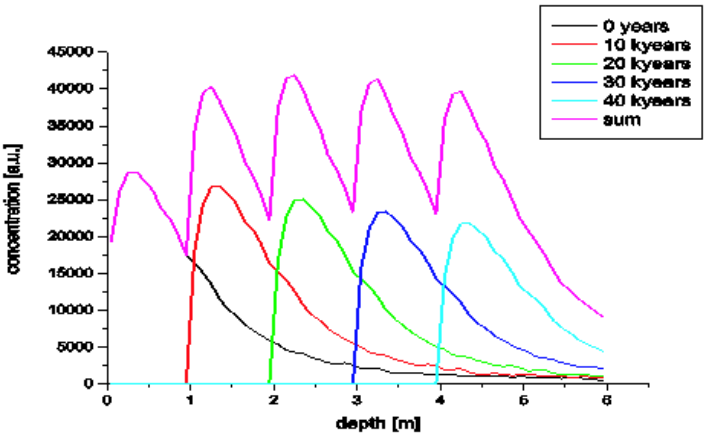

Слика 3: Дистрибуција креираних дугоживећих радионуклида у односу на дубину леса. Претпостављено је да је брзина раста леса ~ 100mm на 1000 година и 10^5 година полуживот нуклида

4. Дискусија и закључак

Из овога се види да производ симулације одговара експериментално нађеним нуклидима (Табела 1) што нам омогућује да, познајући флукс миона на површини и у подземљу [6], израчунамо стварну брзину стварања и обилност ових нуклида од којих се активност радиоактивних може мерити у лабораторији. Исто тако, знајући из симулације, и дистрибуцију радионуклида могуће је то искористити за датирање земљишта. У ову симулациону анализу нису ушли други процеси који делују на лес као што је ерозија, подземне воде и остали феномени тако да је детаљније анализа потребна. Концентрације космогених радионуклида добијених овом симулацијом су врло мале тако да, са садашњом опремом у Нискофонској лабораторији у Земуну је немогуће измерити активност космогених нуклида у узорцима леса са различитих дубина.

5. Захвалница

Овај рад је реализован уз подршку Министарства просвете, науке и технолошког развоја Републике Србије у оквиру пројекта под бројем ОИ171002.

6. Литература

[1] P. Grieder. *Cosmic rays at Earth*. (2001) 975-983.
[2] M.W. Caffe, J.N. Goswami, C.M.Hohenberg, K. Marti and R.C.Reedy. Meteorites and the Early Solar System,1988. The University of Arizona Press.
[3] J. Beer. Neutron Monitor Records in Broader Historical Context, *Space Sci. Rev.* 93 (1-2) (2000) 107-119.
[4] D. Heck et al. CORSIKA: a Monte Carlo code to simulate extensive air showers, *Report FZKA 6019*, 1998. Forschungszentrum Karlsruhe.
[5] S. Agostinelli et al. GEANT4—a simulation toolkit. *Nucl. Instrum. Methods Phys. Res. A.* 506 (2003) 250-303.

[6] A. Dragić, V. Udovičić, R. Banjanac, D. Joković, D. Maletić, N. Veselinović, M. Savić, J. Puzović, and I.V. Aničin. The New Setup in the Belgrade Low-Level and Cosmic-Ray Laboratory, *Nucl. Technol. Radiat. Prot.*Vol. 26, No. 3 (2011) 181-192.

MONTE CARLO SIMULATION OF THE COSMOGENIC NUCLEI PRODUCTION IN LOESS

Dimitrije MALETIĆ, Nikola VESELINOVIĆ, Dejan JOKOVIĆ, Vladimir UDOVIČIĆ, Radomir BANJANAC, Mihailo SAVIĆ, Aleksandar DRAGIĆ
Institute of Physics, University of Belgrade, Belgrade, Serbia
veselinovic@ipb.ac.rs

ABSTRACT
Monte Carlo simulation program CORSIKA is used to simulate the propagation of Cosmic rays through atmosphere to the ground surface. The propagation and interaction of cosmic rays with the soil - loess, including also the simulation of creation of cosmogenic radionuclides in soil is done using Monte Carlo simulation program Geant4. The distribution by depth of concentrations of produced radionuclides obtained from the simulations is presented, also for changing of soil thickness. The possibility of detection of these cosmogenic radionuclides created in soil, especially using our laboratory equipment, is discussed.

ГЛЕДАЊЕ У КУГЛУ-25 ГОДИНА ПОСЛЕ

Радомир БАЊАНАЦ, Александар ДРАГИЋ, Владимир УДОВИЧИЋ, Дејан ЈОКОВИЋ, Димитрије МАЛЕТИЋ, Никола ВЕСЕЛИНОВИЋ, Михаило САВИЋ

Институт за физику, Универзитет у Београду, Србија, banjanac@ipb.ac.rs

САДРЖАЈ

Велики течни сцинтилациони детектор, сфера од нерђајућег челика пречника 100cm са 12 фотомултипликатора и последично велике ефикасности детекције неутрона, и после 25 година показује знаке живота. Велики неутронски, али и детектор свеприсутног амбијенталног зрачења, кога из очигледних разлога зовемо Кугла, прелиминарно је тестиран у циљу провере његових главних карактеристика које су га красиле у експерименту потраге за супертешким елементом са 113 протона. Досадашња тестирања наговештавају да Кугла још није за музеј нуклеарне инструментације.

1. Увод

Крајем осамдесетих година прошлог века било је могуће у Институту за физику направити релативно велики сингл детектор који је по пројекту имао само једну намену. У конфигурацији са силицијумским детектором фисионих фрагмената који је, смештен у унутрашњем каналу Кугле, тригеровао велики сцинтилатор, Кугла је бројала неутроне. По теоријским претпоставкама за фисију супертешких елемената, из узорка руде лорандита која је садржавала екаталијум, из једног акта спонтане фисије хипотетичког елемента екаталијума ($Z=113$) требало је да се емитује већи број неутрона него код трансурана нпр. калифорнијума *Cf-252*. Сам експеримент је имао високу осетљивост и дуго време мерења, али је ипак коначан резултат био негативан, па се могла само проценити граница обилности траженог елемента. Детаљи експеримента описани су у докторату колеге Александра Зарића под менторством професора Ђуре Крмпотића и руководством др. Радована Антанасијевића, [1], док је млађим сарадницима Лабораторије преостало да анализирају софистицираност реализованог мерења и баштине употребљену опрему.

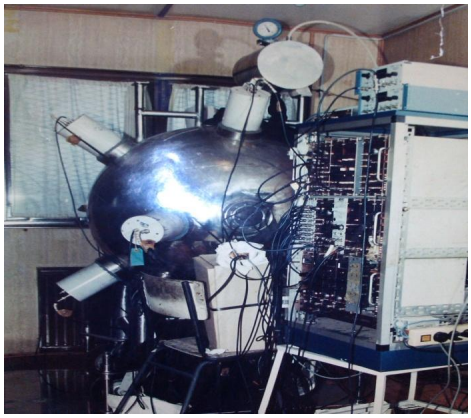

Слика 2. Кугла и припадајућа електроника за велики експеримент

Фотографија Кугле у окружењу неопходног хардвера за велики експеримент прикана је на слици 1.
У међувремену, како је смештена у близину инсталације Плазма фокус експеримента, Кугла је послужила и за одређивање укупног приноса неутрона из деутеријумског Плазма фокуса, [2]. На жалост, због ограничених хардверских ресурса, њено напајање високим напоном расходовано је за потребе великих пластичних сцинтилатора и мерење космичког зрачења.

2. Техничке карактеристике детектора

Кугла је због своје велике запремине (600 литара) мета и за свеприсутно зрачење из околине пре свега продорно гама и космичко зрачење. Фон Кугле је зато велики, ако је сматрамо доминантно детектором неутрона, због адитива у виду гадолинијума. Поред поменутих компоненти фона, присутни су и сами неутрони из хадронске компоненте космичког зрачења и из околине (α,n реакције и фисије урана), па је очекивани фон свих неутрона реда $100/m^2s$.
Детекциона осетљивост Кугле се повећава у коинцидентним мерењима, као и на примеру трагања за супертешким елементом. Ово се још једноставније постиже применом савремених дигиталних анализатора који временску спектрометрију стављају у први план.
Ипак, Кугла је доминантно детектор неутрона, како брзих тако и термалних. Ови први, ако су почетних енергија до око 10MeV, расејањем на протонима и језгрима угљеника који чине сцинтилациону течност, са великом вероватноћом се термализују у великом детектору. На крају њиховог пута унутар сцинтилатора чекају их језгра гадолинијума 155 и 157, којим је *NE343* сцинтилатор допиран, на којима се због великог пресека за захват термални неутрони захватају, а потом језгра гадолинијума деексцитирају емисијом каскадног гама зрачења широког опсега енергија. Пропагацијом кроз течност сцинтилатора, гама зрачење се (због малог Z течности) са највећом вероватноћом Комптоновски расејава и од Комптоновских електрона се ствара сцинтилациона светлост која доспева до великог броја правилно распоређених великих фотомултипликатора. На овај се начин у великом детектору постиже велика ефикасност детекције неутрона, али је спектрални одзив континуиран. На примеру неутрона из фисијоног спектра уранијума и за пречник детектора од 100cm, применом симулационог програма *ДЕНИС* добијена је ефикасност детекције од 85%.
Имајући у виду да је енергија неутрона за доступан извор *Am-Be* до око 10MeV, са средњим слободним путем кроз сцинтилациону течност од око 20cm, симулација је проценила ефикасност детекције 10MeV-ских неутрона од око 65%.
Дванаест фотомултипликатора (*Hamamatsu R1215*, пречника 5 инча (127mm)), селектовано је из базе од 16 за ову намену купљених ПМТ-ова, који имају уједначене одзиве (напонске сигнале) за идентичну светлосну побуду.
За смештање тригер детектора, силицијумског детектора са површинском баријером за фисијоне фрагменте, или како ћемо видети мало касније неког другог, као и узорка лорандита, Кугла по свом пречнику има канал дужине 100cm и пречника 100mm.
Детаљнији опис, за велики експеримент, употребљене аналогне нуклеарне електронике овде није релевантан, али су детаљи описани у [1].
На жалост, у докторату је само поменуто да се течност сцинтилатора "повремено барботира аргоном" у циљу елиминације кисеоника временом раствореног у

сцинтилатору. Овај технички проблем се сматра највећим у дуготрајној употреби течних сцинтилатора.

3. Прелиминарна мерења

Досадашња искуства са другим течним сцинтилаторима, посебно *NE213* који има особину дискриминације неутрона од гама зрачења по времену пораста сигнала, нису давала наду у оживљавање Кугле. Проблем код течних сцинтилатора старијих од неколико година представља присуство кисеоника који, као електронегативан гас, захвата електроне и гаси сцинтилације. Ово је посебно карактеристично код *NE213* сцинтилатора који се мора потпуно заменити новом течношћу након две године када изгуби главно својство *n-гама* дискриминације. Кугла је ипак затворен систем са експанзионом посудом на врху, слика 1, која јој је потребна због екстремног ширења растварача (толуола) на вишој температури, па је тако онемогућен улазак кисеоника, али сметњу представља и кисеоник растворен у сцинтилатору који такође доприноси гашењу сцинтилација.

Друга непознаница је постојаност хемије гадолинијума у растварачу тј. одрживост изотропне расподеле гадолинијума током 25 година.

Оно што се најједноставније могло проверити је одзив фотомултипликатора и то је најпре тестирано.

У оригиналној поставци великог експеримента, Кугла је калибрисана и на гама зрачење. Како је радило свих 12 ПМТ-ова, колекција светла је била максимална, па је калибрациони извор кобалта 60, довољно велике активности и смештен у центар Кугле, као одзив дао спектар са два "пика". Први је један или други сингл (1173 или 1332keV) јер је резолуција сцинтилатора недовољна за њихово раздвајање, а други је њихов суминг на 2505keV. Ово мерење нисмо били у прилици да поновимо, макар због недостајућих напајања за свих 12 ПМТ-ова, па је тестиран сваки ПМТ засебно.

На радном напону од -1000V, са слабоактивним тачкастим извором кобалта 60, у идентичној геометрији за сваки ПМТ, одређивана је амплитуда излазног сигнала осцилоскопом. Резултати су, изненађујуће, репродуцибилни и потпуно се по односу амплитуда слажу са мерењима, која су спроведена током селекције и уједначавања 12 ПМТ-ова, [1].

Наредни тест је дотицао одзив гадолинијума. Пресек за захват термалног неутрона посебно је велики (254kBarn) код обилније присутног (у природном гадолинијуму) изотопа гадолинијума 157. Након захвата, побуђено језгро *Gd-158* деексцитира се емисијом мноштва гама зрака. У припреми великог експеримента, у коинцидентном мерењу са детектором фисијоних фрагмената у циљу редукције неутронског фона, и извором неутрона *Cf-252*, добијен је одзив Кугле на гама зраке из гадолинијума. Максимум континуиране расподеле је на око 4MeV са вишком на месту 6750keV што одговара гама зраку са највећим интензитетом.

Како су енергије емитованог и Куглом детектованог гама зрачења изнад енергија фонског гама зрачења, осмишљена је конфигурација са *NaI* сцинтилатором који је смештен у центар канала Кугле. За извор неутрона коришћен је *AmBe*, чији су се неутрони (који добацују до око 10MeV) додатно термализовали у бурету са водом у коме се извор чува, у контактној геометрији *AmBe* буре-Кугла. Непријатност у детекцији високоенергетског гама зрачења од *Gd* за овај извор неутрона представљају фотони енергија 4.44MeV који се, по природи интеракције америцијума и берилијума у самом *AmBe* извору, емитују у односу један на један

са емитованим неутронима. У добијеном прилично линеарном спектру *NaI*, због његове лоше резолуције, није било могуће раздвојити појединачно гама зрачење из гадолинијума, али су поред слабашних фонских линија (511, 1461, 2614keV) јасно уочљиви пикови на 2223 и 4443keV и њихови припадајући једноструки и двоструки одбегли пикови, слика 2.

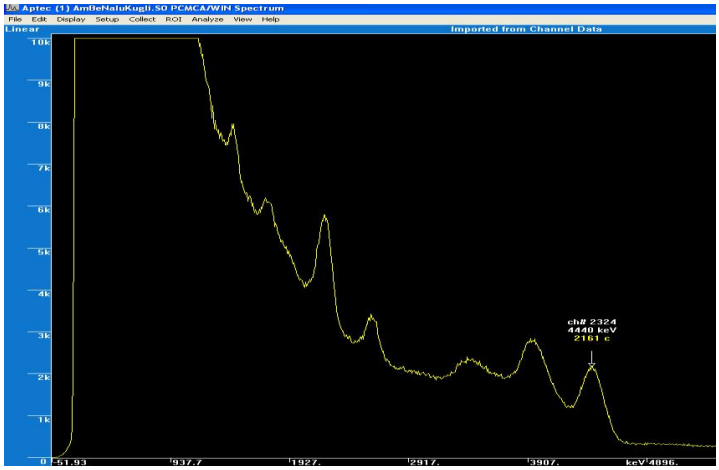

Слика 2. Спектар *NaI* за извор *AmBe* до 5keV

Следећа слика 3, приказује исти спектар на енергијама вишим од 4.44MeV-ског пика, где се очекују структуре које се једино могу идентификовати као гама зрачење од гадолинијума након захвата неутрона.

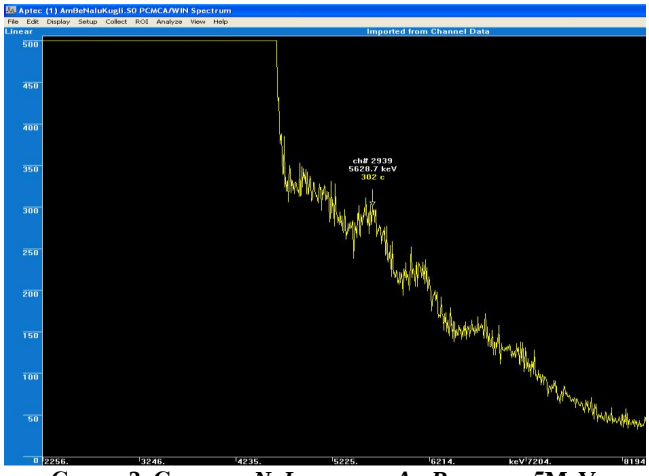

Слика 3. Спектар *NaI* за извор *AmBe* изнад 5MeV

Анализом библиотеке линија гама зрачења из *Gd-158* у областима 4 до 5 "пикова", који се разазнају на слици 3, редом од 4770 до 5350, од 5350 до 5870, од 5870 до 6350, од 6340 до 6890 и од 6890 до 7400keV, њихови сумарни релативни интензитети се слажу са измереним нет интегралима. Ово важи претпостављајући благи пад ефикасности детекције у области енергија где доминира креација парова као механизам интеракције гама зрачења. Детаљнија квантитативна анализа је могућа уз помоћ симулације одзива детектора на гама зрачење високих енергија у конкретној геометрији извор-детектор.

Ипак, описани *NaI* спектар само доказује присуство гадолинијума у Кугли, и могуће га је детаљније истражити временском спектроскопијом знајући да због времена термализације неутрона "гадолинијумско" гама зрачење касни за промптним гама зрачењем од 4.44MeV. Ипак, главни доказ да је Кугла и после 25 година оперативна мора бити спектар космичког зрачења и неутрона.

4. Резултати мерења космичког зрачења и неутрона

У последње описаној конфигурацији, анализа је обављена *C.A.E.N.* дигиталним анализатором, који је поред *NaI* добијао сигнале и са два ПМТ-а са Кугле.

Због ограничених хардверских ресурса (4 независна улаза у *C.A.E.N.* и *HV* модули), поред *NaI* радила су у простору блиска два ПМТ-а повезана на исти *HV* модул. Миони из космичког зрачења су значајан високоенергетски део фонског спектра Кугле, који није једноставно искључити хардверском поставком вето заштите због широке угаоне дистрибуције површинских миона и димензија саме Кугле. Њихово детектовање је са друге стране корисно у смислу енергијске калибрације Кугле. Планирана је и *GEANT 4* симулација одзива Кугле на космичко зрачење, која у првој поставци није неопходна јер се "спектар неутрона" из *AmBe* извора добија одузимањем фонског (мионског) спектра. Поред миона, на ниским енергијама се очекује детекција нискоенергетског космичког зрачења (фотона и електрона), које се успешно анулира коинцидентним мерењем са два ПМТ-а. Ово је поуздано доказано дуговременским мониторингом космичког зрачења у Нискофонској лабораторији Института за физику, пластичним сцинтилаторима (100cm X 100cm X 5cm) који су опремљени са 4 ПМТ-а у смештеним у ћошковима детектора, [3]. Детаљније тестирање геометрије Кугле биће спроведено упаривањем различито позиционираних ПМТ-ова.

Додатни проблем интерпретације доприноса само од неутрона је присуство интензивног гама зрачења из самог извора (4.44MeV). У том смислу тестирање Кугле неутронским извором *Cf-252,* довољно велике активности, било би једноставније интерпретирати.

Природа интеракције неутрона у Кугли је посредна, преко гама зрачења из гадолинијума, али је у поступку дискриминације од промптног гама зрачења (4.44MeV), кашњење реда 10μs, што би се једноставно раздвојило избором закаснелих догађаја из временске криве. У описаној поставци, додатна могућност је коинцидирање са *NaI* подацима.

Мерење фона Кугле и мерење са извором *AmBe*, статистички значајно, добија се брзо после неколико дана због велике ефикасности детекције Кугле. Управо је велики фон Кугле највећи проблем екстраховања корисних података, јер значајно подиже захтеве за капацитетом хард дискова рачунара. Ово би било додатно изражено ако би оперативни били сви ПМТ-ови (у поставци великог експеримента сигнали су сабирани и миксовани за 4 групе од по 3 ПМТ-а).

То је и био случај код ових мерења посебно што се аквизиција података реализовала у моду осцилоскопа (што додатно троши HDD ресурсе). На слици 4 је приказан концидентни спектар фона Кугле (са два ПМТ-а) у коме доминира мионски ΔE пик на око 150MeV. Вишак од *AmBe* извора у односу на мионски фон је свега 6% и он је континуирано размазан на нижим енергијама. На вишим енергијама (мионски пик) слагање два мерења је потпуно.

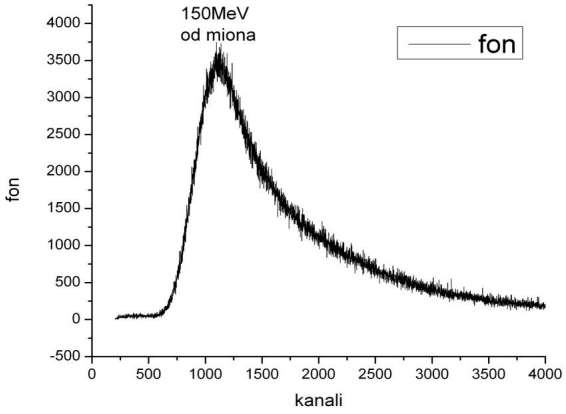

Слика 4. Фонски спектар Кугле

Детаљнија временска спектроскопија закаснелих коинциденција тек ће, у наредном периоду, решити проблем високофонског одзива Кугле и пружити одговоре о самом неутронском спектру Кугле, имајући у виду природу интеракције неутрона:
- када неутрон уђе у Куглу он се термализује (успорава) сукцесивним еластичним расејањем на протонима и у мањој мери језгрима угљеника. Време до захвата на *Gd* језгрима траје до неколико десетина микросекунди. Постављањем гејта на регистрован догађај детекције рикојла (протона) са временом кашњења до тих неколико десетина микросекунди, регистроваће се сумарно фон и гама зрачење емитовано после захвата неутрона на *Gd*. Фон се екстрахује из дела временског спектра након захвата, па се разликом последња два добија чисти спектар из неутронског захвата. Додатна корекција на ометајуће 4.44MeV-ско гама зрачење је такође неопходна (коинциденцијом са *NaI* детектором).

5. Закључак

После 25 година од великог експеримента потраге за супертешким елементом, у коме је велики течни сцинтилатор (Кугла) играо највећу улогу, извршена је серија тестова његових актуелних перформанси.

Иако предстоје још детаљније анализе посебно применом временске спектроскопије и евентуално мерења са другим изворима неутрона, досадашњи резултати карактеристика ПМТ-ова, интеракције гадолинијума и одзива сцинтилатора на високоенергетске мионе наговештавају да “гледање у Куглу” има научну перспективу.

6. Захвалница

Овај рад је реализован уз подршку Министарства просвете, науке и технолошког развоја Републике Србије у оквиру пројекта под бројем ОИ171002.

7. Литература

[1] Александар Зарић, *Истраживање супертешких елемената у геолошким узорцима*, Докторска дисертација, Физички факултет Универзитета у Београду, 1992.

[2] В. Удовичић *et al*., Scaling of the neutron yield with peak discharge current in the deutherium plasma focus device. 23rd Summer School and International Symposium on the Physics of Ionized Gases, (2006) 527-530.

[3] А. Драгић *et al*., The new set-up in the Belgrade low-level and cosmic-ray laboratory. *Nucl. Techn. & Radiat. Protect.* 26 (3) (2011) 181-192.

LOOKING INTO THE SPHERE-25 YEARS AFTER

Radomir BANJANAC, Aleksandar DRAGIĆ, Vladimir UDOVIČIĆ, Dejan JOKOVIĆ, Dimitrije MALETIĆ, Nikola VESELINOVIĆ, Mihailo SAVIĆ

Institute of Physics, Pregrevica 118, University of Belgrade, Belgrade, Serbia,
banjanac@ipb.ac.rs

ABSTRACT

The SPHERE, big liquid scintillator is neutron detector, NE343 gadolinium loaded, has the shape of sphere with diameter of one meter and equipped with twelve (5inch) photomultipliers. The SPHERE was the main detector in high-sensitivity searching for hypothetic super-heavy (Z=113) element, twenty five years ago. In this work the preliminary test of its actual performances was obtained by analyzing photomultipliers voltage outputs, interaction of gadolinium on neutrons, as well as response to cosmic muons. High energy gamma-rays which following gadolinium 157 captured slow neutrons were detected using NaI (3inch x 3inch) scintillator situated inside the SPHERE. Some information is provided using AmBe neutron source, but its intensive 4.44MeV gamma-rays and high detector efficiency producing high background require detailed time spectroscopy to resolve neutron response itself. Even without it, the obtained performances seem satisfactory now in order to the SPHERE could be useful detector using the same “detecting-alive” but old liquid.

ОДРЕЂИВАЊЕ ТЕМПЕРАТУРСКОГ ПРОФИЛА АТМОСФЕРЕ МЕРЕЊЕМ ИНТЕНЗИТЕТА КОСМИЧКОГ ЗРАЧЕЊА НА ПОВРШИНИ ЗЕМЉЕ

Михаило САВИЋ, Димитрије МАЛЕТИЋ, Дејан ЈОКОВИЋ, Никола ВЕСЕЛИНОВИЋ, Александар ДРАГИЋ, Радомир БАЊАНАЦ, Владимир УДОВИЧИЋ

Институт за Физику, Универзитет у Београду, Србија, msavic@ipb.ac.rs

САДРЖАЈ

Методи за корекцију одброја миона из космичког зрачења на метеоролошке параметре, пре свега на барометарски и температурски ефекат, добро су познати. Ови методи, осим временских серија миона, принципијелно захтевају познавање временских серија притиска као и временских серија целокупног температурског профила атмосфере. Познавање температорског профила атмосфере је омогућено појавом савремених нумеричких модела атмосфере. У овом раду је демонстрирана провера супротног приступа, односно одређивања температурског профила атмосфере на основу познавања временских серија миона. Представљена је и дискусија разултата, разматрање могуће примене овог приступа одређивања температорског профила као и могући правци усавршавања овог метода.

1. Увод

Нискофонска лабораторија Института за Физику Универзитета у Београду посвећена је мерењима ниских активности и на проучавању мионске и електромагнетске компоненти космичких зрака на површни земље и у плиткој подземној лабораторији. Надземни део лабораторије налази се на 75 м надморске висине и у подножју вертикалне литице од леса, висине око 10 метара. Подземни део лабораторије, корисне површине 45 m^2, укопан је у подножју литице са укупном висином леса изнад лабораторије од око 12 метара, што је еквивалентно висини од 25 метара воде. [1]

Пластични сцинтилаторски детектори [1m x 1m x 5cm] користе се за континуална мерења спектра космичког зрачења од 2008. године. Један сцинтилациони детектор се налази у надземној а други у подземној лабораторији. Сваки сцинтилациони детектор је опремљен са четири фотомултипликатора директно везане на угловма сцинтилатора. Сцинтилационе детекторе је произвела фирма Амцрис-Х из Харкова, Украина. У срцу система за прикупљање података су два брза аналогно-дигитална претварача (FADC), произвођача CAEN (тип N1728B). Ови инструменти могу да раде у такозваном хистограмском моду, када функционише као дигитални спектрометар или, у осцилограмском моду, када функционише као дигитални осцилоскоп. [1]

Сатне временске серије континуалног мерења секундарног космичког зрачења, односно космичког зрачења које стиже на површину земље, производе се током обраде података и користе се за анализу представљену у овом раду. Овакви одброји космичког зрачења највећим делом су одброји мионске компоненте космичког зрачења које детектују сцинтилациони детектори.

2. Корекције одброја космичког зрачења

Зависност одброја секундарних миона из космичког зрачења од метеоролошких параметара добро је позната. То подразумева да варијација одброја миона зависи од варијације апсолутне дебљине атмосфере тј. притиска (барометарски ефекат), затим температуре (температурски ефекат), влажности и других параметара.

Теорија која формално описује ове зависности дата је у [2] и принципијелно омогућује корекцију одброја на варијацију метеоролошких параметара. Услов за корекцију је да су, упоредо са временским серијама миона, доступне и временске серије поменутих параметара. У пракси су ове корекције могуће када су у питању притисак и температура, док су за остале метеоролошке параметре тешко изводљиве.

За подручје Београда, подаци за притисак доступни су из више метеоролошких станица и редовно се освежавају у бази Нискофонске лабораторије. На слици 1 приказана је зависност одброја миона од варијације притиска за временски период од 2009. до 2015. године. На основу линеарног фита ове зависности одређени су параметри који се даље могу користити за корекцију на притисак.

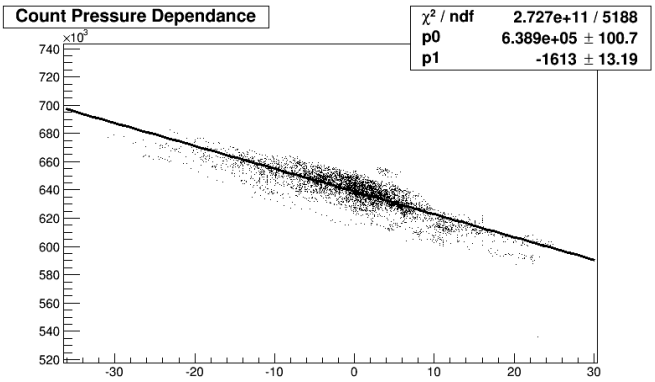

Слика 1. Зависност одброја миона од варијације притиска за временски период од 2009. до 2015. године.

Зависност одброја миона од температуре одн. температурски ефекат, описана је изразом [2]:

$$\frac{\delta I}{I} = \int_0^{h_0} W_T(h)\delta T(h)\,dh$$

где је W_T коефицијент температурске зависности, δT варијација температуре у односу на базну температуру за дати ниво а h дебљина атмосфере у g/cm^2.

Да би се израчунала варијација одброја миона која потиче од температуре потребно је познавати температурски профил за дату локацију као и варијацију истог. Ови подаци су доступни захваљујући Глобалном прогностичком систему (GFS – Global Forecasing System) америчког Националног прогностичког центра (NCEP - National Centers for Environmental Prediction – USA) у оквиру кога је

развијен модел температурских профила [3]. Резултати овог модела нам дају вредност температуре за 26 изобарних нивоа који одговарају следећим вредностима, датим у g/cm^2: 10, 20, 30, 50, 70, 100, 150, 200, 250, 300, 350, 400, 450, 500, 550, 600, 650, 700, 750, 800, 850, 900, 925, 975, 1000, 1013 и то за времена 0, 6, 12 и 18 часова. Интерполацијом могуће је добити сатне температурске профиле. Љубазношћу опсерваторије Измиран (http://cr0.izmiran.rssi.ru) ови подаци доступни су за Београд. То омогућава, уз познавање температурских коефицијената, корекцију одброја миона на температурски ефекат.
Оба типа корекција (на притисак и на температуру) се успешно примењују у Нискофонској лабораторији.

Међутим, овде желимо да на основу познатог одброја миона и познатих коефицијената зависности одредимо температуру датог изобарног нивоа. У ту сврху не користимо теоријски срачунате коефицијенте већ, претпостављајући њихову међусобну линеарну независност, исте одређујемо на основу фита експерименталних података. На следећим сликама 2а, 2б, 2ц представљене су зависности температуре од одброја за свих 26 изобарних нивоа. Такође, приказани су параметри линеарних фитова датих зависности. Одброј је претходно коригован на притисак. У обзир су се узимали само подаци у данима ниске активности сунца (International Quiet Days).

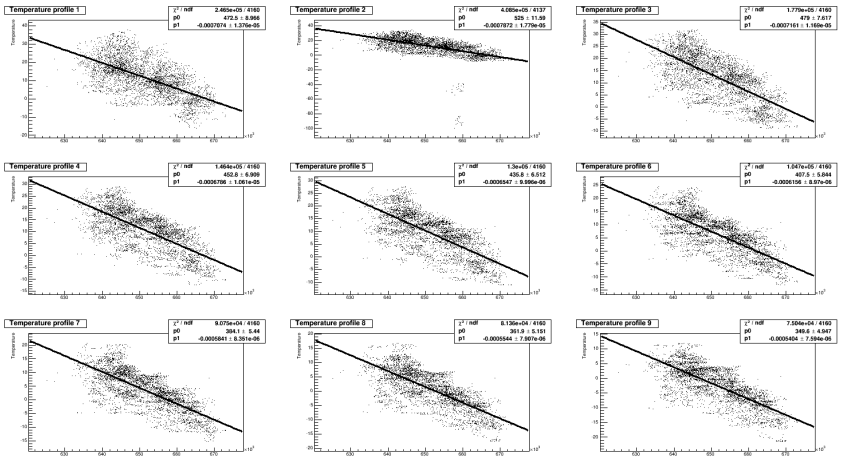

Слика 2а. Зависности температуре од одброја са параметрима линеарних фитова датих зависности за температурске профиле 1-9 (700-1013 g/cm^2).

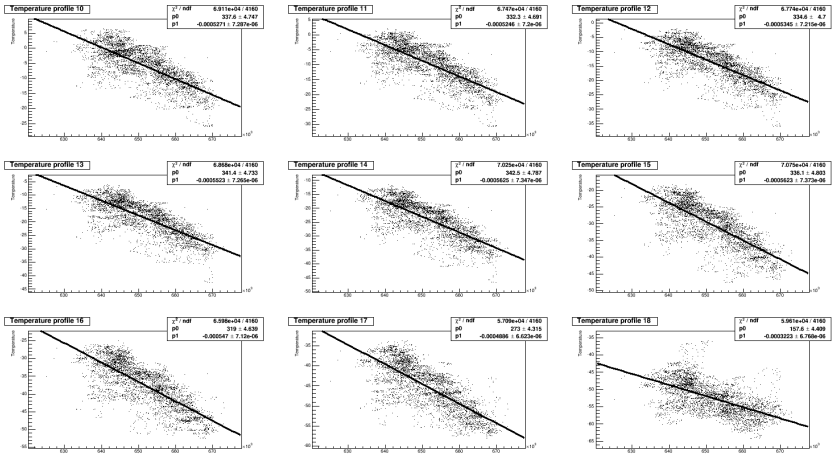

Слика 2б. Зависности температуре од одброја са параметрима линеарних фитова датих зависности за температурске профиле 10-18 (250-650 g/cm^2).

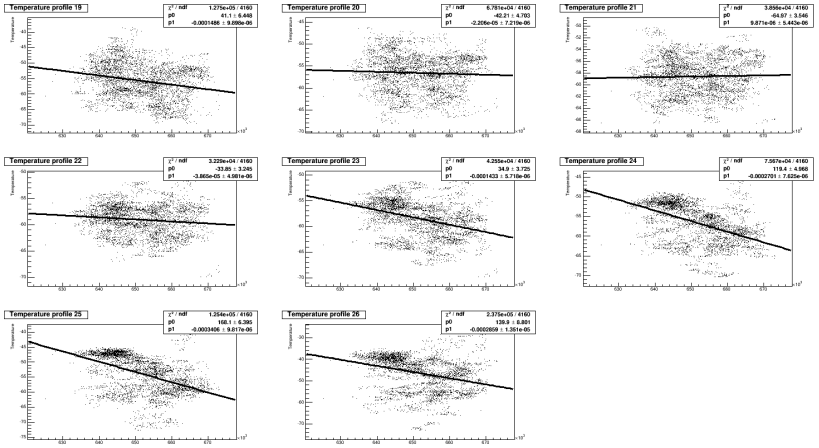

Слика 2ц. Зависности температуре од одброја са параметрима линеарних фитова датих зависности за температурске профиле 19-26 (10-200 g/cm^2).

На основу добијених параметара сада је могуће дати предикцију температуре за дати изобарни ниво на основу познатог одброја миона. На сликама 3а, 3б и 3ц, за три различита изобарна нивоа, приказано је упоређење временских серија овако предвиђених температура и температура израчунатих на основу GFS модела. Због упоређења, изабрани су изобарни нивои различитих вредности коефицијената линеарног фита.

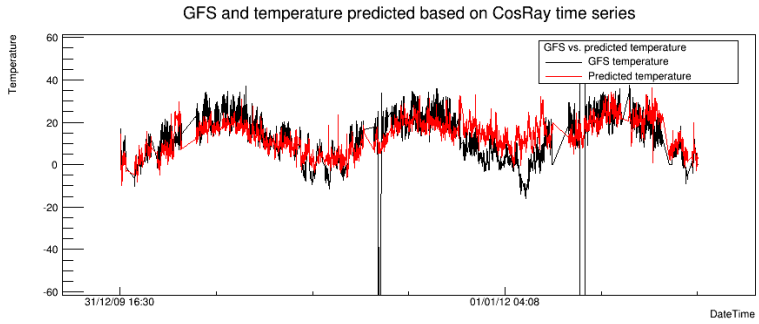

Слика 3а. Поређење временских серија предвиђених температура и температура израчунатих на основу GFS модела за изобарни ниво близак површини земље.

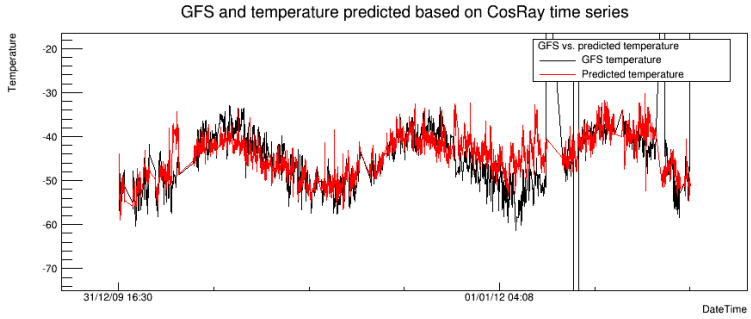

Слика 3б. Поређење временских серија предвиђених температура и температура израчунатих на основу GFS модела за изобарни ниво средње висине у атмосфери.

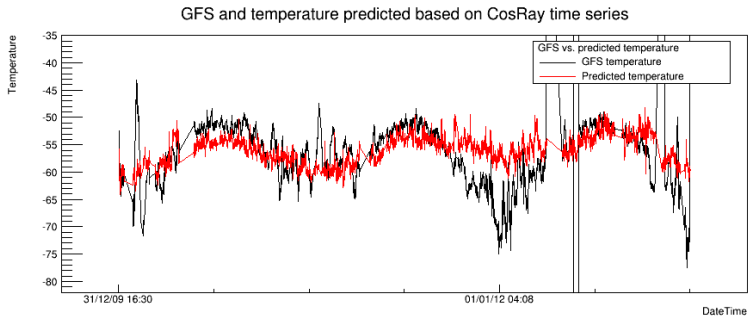

Слика 3ц. Поређење временских серија предвиђених температура и температура израчунатих на основу GFS модела за изобарни ниво високо у атмосфери.

Може се видети да је слагање најбоље у случају када је и линеарна зависност најбоље дефинисана, као што би се и могло очекивати. Даља неодређеност методе би у том случају била одређена мером одступања дистрибуције од линеарне, што може бити условљено чињеницом да коефицијенти нису нужно линеарно независни.

3. Закључак

Методи за корекцију одброја миона из космичког зрачења на метеоролошке параметре, пре свега на барометарски и температурски ефекат, добро су познати. Они, осим временских серија миона, принципијелно захтевају познавање временских серија притиска као и временских серија целокупног температурског профила атмосфере. Нарочито познавање ових других је омогућено појавом савремених нумеричких модела атмосфере. Ти подаци такође омогућавају проверу супротног приступа, односно предвиђања температурског профила атмосфере на основу познавања временских серија миона. У овом раду је дата добра индикација да је то у принципу могуће, чак и најједноставнијим приступом. На основу тога, вероватно је да би софистицираније методе дале још поузданије резултате.

4. **Напомена**

Овај рад је урађен уз помоћ Министарства просвете, науке и технолошког развоја Републике Србије унутар пројекта основног истраживања под ознаком ОИ171002.

5. Литература

[1] Dragic Aleksandar, Udovicic Vladimir, Banjanac Radomir, Jokovic Dejan, Maletic Dimitrije, Veselinovic Nikola, Savic Mihailo, Puzovic Jovan, Anicin Ivan. The New Set-Up in the Belgrade Low-Level and Cosmic-Ray Laboratory, *Nucl. Technol. Radiat. Prot.* 26 (3) (2011) 181-192.

[2] Dorman, Cosmic Rays in the Earth's Atmosphere and Underground

[3] M. Berkova , A. Belov, E. Eroshenko, and V. Yanke, Temperature effect of muon component and practical questions of how to take into account in real time, *Astrophys. Space Sci. Trans.* 8 (2012) 41-44.

DETERMINATION OF THE TEMPERATURE PROFILES OF THE ATMOSPHERE BY MEASURING THE INTENSITY OF THE COSMIC RAY AT SURFACE LEVEL

Dimitrije MALETIĆ, Dejan JOKOVIĆ, Mihailo SAVIĆ, Aleksandar DRAGIĆ, Radomir BANJANAC, Vladimir UDOVIČIĆ, Nikola VESELINOVIĆ
Institute of Physics, Univeristy of Belgrade, Serbia, maletic@ipb.ac.rs

ABSTRACT
Method for correction of Cosmic ray' muon counts on meteorological parameters, especially for barometric and temperature-effects are well known. These methods, in addition to the time series of muons, in principle, require knowledge of the time series of pressure as well as the entire time series of temperature profiles of the atmosphere. Knowledge of temperature profile of the atmosphere is possible by the advent of modern numerical models of the atmosphere. In this study check the opposite approach is demonstrated, i.e. the determination of temperature profiles of the atmosphere based on the knowledge of muon time series. Discussion of the results is presented considering the possible application of this approach of determination of temperature profile of the atmosphere and possible ways to improve this method.

AUTOMATSKA OBRADA PODATAKA KOSMIKE I EVALUACIJA KONCENTRACIJE RADONA NA INTERNET (WEB) SERVERU

Dimitrije MALETIĆ, Dejan JOKOVIĆ, Mihailo SAVIĆ, Aleksandar DRAGIĆ, Radomir BANJANAC, Vladimir UDOVIČIĆ, Nikola VESELINOVIĆ
Institut za fiziku, Univerzitet u Beogradu, Srbija, maletic@ipb.ac.rs

SADRŽAJ

U ovom radu je opisana automatska obrada podataka, na internet (web) serveru, kontinualnog merenja intenziteta kosmičkog zračenja i evaluacije koncentracije radona u Niskofonskoj laboratoriji Instituta za fiziku Univerziteta u Beogradu. Podaci o merenju kosmičkog zračenja sakupljaju se u podzemnoj i nadzemnoj laboratoriji i obradjuju se dnevno. Evaluacija koncentracije radona u podzemnoj laboratoriji takođe se obradjuje dnevno, skupljajući meteorološke podatke, satno, i koristeći ih za evaluaciju radona korišćenjem implementacije multivatijantne regresione analize. Ovim podacima se prilazi preko laboratorijskog sajta www.cosmic.ipb.ac.rs .

1. Uvod

Niskofonska laboratorija Instituta za fiziku Univerziteta u Beogradu sastoji se od dve laboratorije: nadzemne i podzemne laboratorije. U obe laboratorije se vrše kontinuirana merenja intenziteta kosmičkog zračenja [1]. Nabavkom CAEN brzih analogno-digitalnih konvertera, hardver za kontinualna merenja intenziteta kosmičkog zračenja dobija svoj konačan oblik 2008 godine. Poslednja verzija programa za analizu podataka završena je 2012 godine, a sledeće godine pokreće se web server koji služi za prikazivanje i automatsku analizu merenih podataka. Tokom rada niskofonske laboratorije, nekoliko godina (u periodu od 2008 do 2011) je kontinuirano monitorisana koncentracija radona u podzemnoj laboratoriji. Na osnovu rezultata merenja radona uradjena je multivarijantna regresiona analiza, koja je za rezultat dala aproksimativnu više-parametarsku funkciju koja služi za evaluaciju koncentracije radona u podzemnoj laboratoriji sa uključenim sistemom za ventilaciju [2]. Za dobijanje evaluacije radona, program na internet (web) sajtu satno uzima meteorološke podatke koje se kontinualno mere na meteorološkoj stanici u neposrednoj blizini Niskofonske laboratorije.

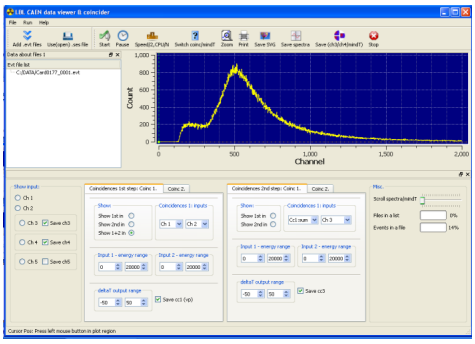

Slika 1. Izgled programa za analizu podataka kontinualnog merenja kosmičkog zračenja u podzemnoj i nadzemnoj laboratoriji.

2. Programi za obradu podataka

Kako je kontinualno merenje intenziteta kosmičkog zračenja davalo sve više podataka, tako se javila potreba za specijalizovanim programom za analizu. Program za analizu razvijan je u C++ jeziku. Finalna verzija softvera za analizu podataka sa vizuelizacijom prikazana je na slici 1. Postoji veliki broj opcija pri analizi podataka, ali ne postoji mogućnost automatske obrade podataka. Kako se podaci sakupljaju na radnim računarima blizu detektora u podzemnoj i nadzemnoj laboratoriji, podaci se kopiraju na File Transfer Protocol (FTP) server na kome se nalazi i web server. Odlučeno je da je najbolje da se razvije linux verzija softvera za analizu koja radi bez vizuelizacije i koja može da radi na linux web serverima. Ovo je otvorilo vrata da se automatizuje analiza podataka kontinualnog merenja kosmičkog zračenja koristeći linux program za automatizaciju: „crontab“ program.

Programi i skripte za evaluaciju koncentracije radona u podzemnoj laboratoriji razvijene su posle analize varijacije radona u podzemnoj laboratoriji korišćenjem programskog paketa TMVA [2] unutar ROOT [3] paketa. TMVA pogramski paket nam omogućuje da se rezultati multivarijantne regresione analize, sadržani u rezultujućoj aproksimativnoj vise-parametarskoj funkciji, prenesu (kompajliraju) u izvršni linux program, koji se može pozvati iz linux programa za automatizaciju “crontab” na web serveru.

3. Internet stranica automatske mionske stanice i evaluacije radona u podzemonoj laboratoriji

Ovim internet stranicama možete pristupiti preko linkova na laboratorijskoj internet stranici: www.cosmic.ipb.ac.rs . Kako je kontinualno merenje intenziteta kosmičkog zračenja davalo sve više podataka, tako je potreba za automatsku kontrolu merenja i analizu podataka rasla. Za automatizaciju je odabrano da se podaci iz laboratorija koncentrišu na linux FTP server, koji je ujedno i web server. Automatskim pristupom podacima programom „crontab“, (shell) skriptovima otpočinje otpakivanje prenetih fajlova putem FTP-a, a potom sledi pokretanje linux verzije programa za analizu podataka Niskofonske laboratorije. Posle obrade podataka, pokreće se ROOT skript za proizvodnju slika vremenskih serija za poslednjih mesec dana. (Slika 2).

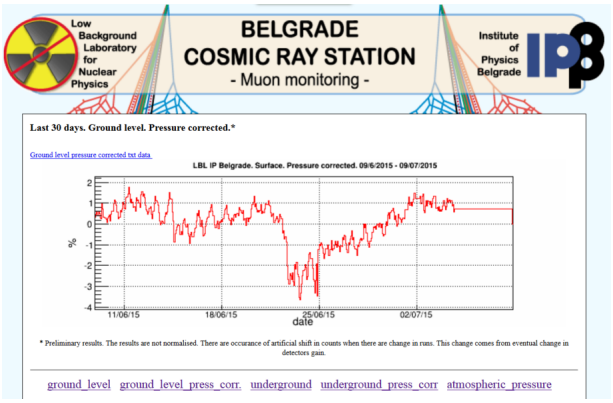

Slika 2. Izgled internet stranice automatske mionske stanice. Svakodnevno se prikazuju najnoviji rezultati koji su uspesno prebačeni na FTP server.

Pored mogućnosti pregleda vremenskih serija kontinualnog merenja intenziteta kosmičkog zračenja, pomoću (CGI) skriptova napisanih u programskom jeziku perl, omogućeno je da se proizvoljno odaberu vremenske serije od interesa, i to za vremenske serije podzemne ili nadzemne laboratorije, sa mogućnošću promene vremenske rezolucije od 1h vremenskih serija na serije sa 5-o minutnom rezolucijom. Postoji pogodnost pregleda korigovanih vremenskih serija, i to korigovanih na pritisak i korigovanih na temperaturu. (Slika 2.)

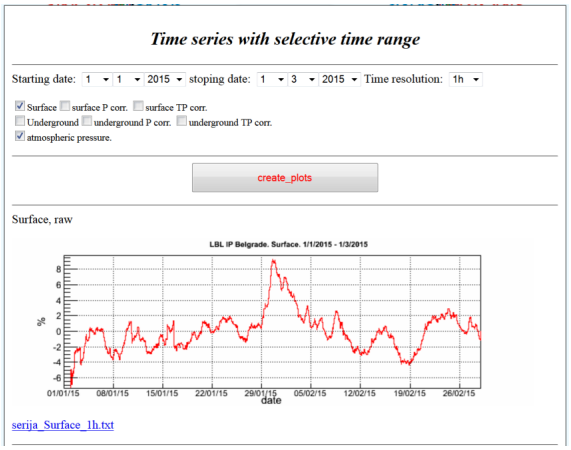

Slika 2. Izgled internet stranice automatske mionske stanice sa mogućnošću izbora intervala vremena za prikaz vremenskih serija.

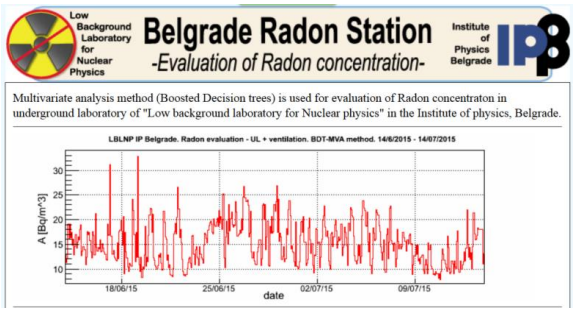

Slika 3. Izgled internet stranice evaluacije koncentracije radona u podzemnoj laboratoriji.

Pored pregleda kontinualnog merenja intenziteta kosmičkog zračenja, na istom internet (web) serveru nalazi se stranica koja prikazuje evaluaciju koncentracije radona u podzemnoj laboratoriji. (Slika 3.) Kako su rezultati multivarijantne regresione analize, sadržani u rezultujućoj aproksimativnoj višeparametarskoj funkciji, preneti

(kompajlirani) u izvršni linux program, potrebno je da se ovaj program periodično pokreće kao i da ima ulazne varijable, gde se izlazne vrednosti ove funkcije prikazuju na server za proteklih mesec dana sa satnom rezolucijom. Vrednosti ulaznih varijabli sa satnom rezolucijom dobijaju se sa stranice meteorološke stanice u blizini Niskofonske laboratorije. Meteorološki podaci se preuzimaju sa meteorološke stanice skriptom kojeg takođe pokreće linux program za automatizaciju "crontab", ali svakog sata, za razliku od procesa obrade podataka i prikaza rezultata koji se pokreći jednom dnevno.

4. Zaključak

Opisana je automatska obrada podataka na internet serveru i to kontinualnog merenja kosmičkog zračenja kao i evaluacije koncentracije radona u Niskofonskoj laboratoriji. Podaci o merenju kosmičkog zračenja sakupljaju se u podzemnoj i nadzemnoj laboratoriji i obradjuju se dnevno. Evaluacija koncentracije radona u podzemnoj laboratoriji takođe se obradjuje dnevno, skupljajući meteorološke podatke satno i koristeći ih za evaluaciju radona korišćenjem implementacije multivatijantne regresione analize koristeći program TMVA implementiran u programskom paketu ROOT. Softver za analizu u Niskofonskoj laboratoriji, napisan u c++, prerađen je da radi na linuxu i bez vizuelizacije, tako da se obrada podataka može odraditi direktno na internet serveru. Automatizacija na linux internet serveru se postiže korišćenjem programa „crontab". Osobina biranja proizvoljnog intervala za koji se prikazuje vremenska serija intenziteta kosmičkog zračenja napisana je kao (CGI) skript korišćenjem programskog jezika perl. Dobijeni rezultati pomažu saradnicima niskofonske laboratorije da prate stabilnost instrumenata koji vrše kontinualno merenja intenziteta kosmičkog zračenja kao i da prate da li je došlo do značajnije promene u intenzitetu kosmičkog zračenja koje pada na zemljinu površinu ili u podzemlju.

5. Napomena

Ovaj rad je urađen uz pomoć Ministarstva prosvete, nauke i tehnološkog razvoja Republike Srbije unutar projekta osnovnog istraživanja pod oznakom OI171002.

6. Literatura

[1] Dragic Aleksandar, Udovicic Vladimir, Banjanac Radomir, Jokovic Dejan, Maletic Dimitrije, Veselinovic Nikola, Savic Mihailo, Puzovic Jovan, Anicin Ivan. The New Set-Up in the Belgrade Low-Level and Cosmic-Ray Laboratory, *Nucl. Technol. Radiat*. 26/3 (2011) 181-192

[2] A. Hoecker, P. Speckmayer, J. Stelzer, J. Therhaag, E. von Toerne, and H. Voss. TMVA - Toolkit for Multivariate Data Analysis. PoS ACAT 040 (2007), arXiv:physics/070303

[3] R. Brun and F. Rademakers. ROOT - An Object Oriented Data Analysis Framework. *Nucl. Inst. Meth. in Phys. Res*. A 389, 81, 1997

AUTOMATIC DATA PROCESSING OF COSMIC RAY DATA AND EVALUATION OF RADON CONCENTRATION ON WEB SERVER

Dimitrije MALETIĆ, Dejan JOKOVIĆ, Mihailo SAVIĆ, Aleksandar DRAGIĆ, Radomir BANJANAC, Vladimir UDOVIČIĆ, Nikola VESELINOVIĆ
Institute of Physics, Univeristy of Belgrade, Serbia, maletic@ipb.ac.rs

ABSTRACT
This paper describes the automatic processing of data on the Internet (Web) server, of continuous measurements of Cosmic rays and evaluation of radon concentration in Low background laboratory of the Institute of Physics, University of Belgrade. Data on measurements of Cosmic ray intensities are collected from underground and above-ground laboratories and processed daily. Evaluation of the concentration of radon in the underground laboratories is also handled daily, and the gathering of meteorological data, hourly. Meteorological data for evaluation of radon concentration is used as an input variables of implementation of multivariate regression analysis. These data are accessed through laboratory site www.cosmic.ipb.ac.rs.

KORIŠĆENJE MOBILNOG TELEFONA ZA TESTIRANJE I OPTIMIZACIJU LABORATORIJSKIH MERENJA FOTOMULTIPLIKATORIMA

Dimitrije MALETIĆ, Dejan JOKOVIĆ, Radomir BANJANAC, Nikola VESELINOVIĆ, Mihailo SAVIĆ, Aleksandar DRAGIĆ, Vladimir UDOVIČIĆ
Institut za fiziku, Univerzitet u Beogradu, Srbija, maletic@ipb.ac.rs

SADRŽAJ

Ubrzani razvoj telekomunikacionih uređaja omogućava korišćenje ovakvih uređaja pri testiranjima i optimizaciji laboratorijskih merenja. U ovom radu prikazujemo primer korišćenja modernih mobilnih telefona pri testiranjima i optimizaciji fotomultiplikatora koji se koriste u kontinuiranim merenjima kosmičkog zračenja u Niskofonskoj laboratoriji Instituta za fiziku Univerziteta Beogradu. Plastični sciltilatori često imaju direktnu spoljnu vezu fotomultiplikatora sa spoljašnošću scintilacionog detektora putem optičkog kabla. Ovakva direktna veza se koristi za periodičnu kalibraciju mernih uređaja u cilju da se dobije stabilnost prilikom kontinuiranih merenja. Korišćenjem aplikacija za prikazivanje slika na mobilnom telefonu moguće je na ulaz optičkog kabla dovesti svetlost raznog intenziteta i talasnih dužina. U ovom radu su prikazani prvi rezultati odziva fotomultiplikatora na razne intenzitete i talasne dužine svetla. Periodične kalibracije upadnom svetlošću omogućavanju da se odredi potrebna korekcija visokog napona koje napaja fotomultiplikatore ili koriguje odbroj scintilacionog detektora u cilju stabilizacije kontinuiranog merenja.

1. Uvod

Niskofonska laboratorija Instituta za fiziku Univerziteta u Beogradu sastoji se od dve laboratorije; nadzemne i podzemne laboratorije. U obe laboratorije se vrše kontinuirana merenja intenziteta kosmičkog zračenja korišćenjem plastičnih scintilatora.[1] Svetlosni signal dobijen scintilacijom prilikom prolaska čestica kosmičkog zračenja sakuplja se na fotomultiplikatoru. Često se u realizaciji scintilacionih detektora na fotomultiplikator dovodi i optički kabl čiji se drugi kraj izvede iz scintilacionog detektora. Prilikom svakodnevnog rada, ovaj optički kabl je izolovan od spoljašnje svetlosti. Ovakva izvedba veze fotomultiplikatora i spoljašnjosti plastičnog scintilacionog detektora koristi se za kalibraciju scintilacionog detektora, odnosno samog fotomultiplikatora. Kalibracija se izvodi periodično i daje nam informaciju o stabilnosti fotomultiplikatora, njegovoj osetljivosti na intenzitet ulazne scintilacione svetlosti i na varijacije visokog napona koji napaja fotomultiplikator. Periodične kalibracije upadnom svetlošću omogućavanju da se odredi potrebna korekcija visokog napona koje napaja fotomultiplikatore ili da se koriguje odbroj scintilacionog detektora u cilju dobijanja stabinijeg kontinuiranog merenja kosmičkog zračenja. Pri ovakvoj svetlosnoj kalibraciji mogu da se koriste razne izvedbe svetlosnih izvora, od kojih neke mogu biti veoma skupe. Ubrzanim razvojem telefonskih uređaja dobili smo veoma dobar i fleksibilan uređaj koji može da se koristi u svrhu monitorisanja promene osobina fotomultiplikatora tokom vremena. Jednostavnim pokretanjem aplikacije za prikaz fotografija, moguće je na ulaz optičkog kabla dovesti svetlost raznih intenziteta i talasnih dužina. Na ovaj način se može pratiti kako se menja osetljivost fotomultiplikatora na razne talasne dužine i intenzitete svetla tokom vremena.

2. Kalibraciona postavka

Scintilacioni detektor je postavljen vertikalno kako bi se učestalost signala koji dolazi od kosmičkog zračenja do fotomultiplikatora minimizovao. Na kraju optičkog kabla, koji se nalazi van scintilacionog detektora, postavlja se mobilni telefon na udaljenost od 10 cm. Optički kabl i telefon se zatim optički izoluju od spoljnog svetla crnim zastorom. Pre postavljanja telefona, na njega se snima gupa od 80 fotografija. Prvo idu 10 fotografija od bele do crne sa po 10% povećanja zatamnjenja. Posle ove sekvence idu sekvence od po 10 crvene, zelene i plave boje gde se od crne boje po 10% uvećava zasićenost boje (slika 1. donji deo). Sledeća sekvenca je smanjenje crne boje u CMYK formatu, a potom idu dugine boje, osnovni set od 8 boja, za kojima sledi istih 8 duginih boja odjednom na istoj fotografiji (ukupno bela svetlost). Mobilni telefon je postavljen da menja slike svakih 10s, a signal sa fotomultiplikatora se snimao u sekundnoj vremenskoj seriji. Ova sekundna vremenska serija prikazana je na slici 1.

3. Rezultati

Odgovor fotomultiplikatora sniman je u sekundnoj vremenskoj seriji, a ulazno svetlo dolazilo je sa mobilnog telefona na kome su se fotografije raznih boja i intenziteta menjale svakih 10s (slika 1).

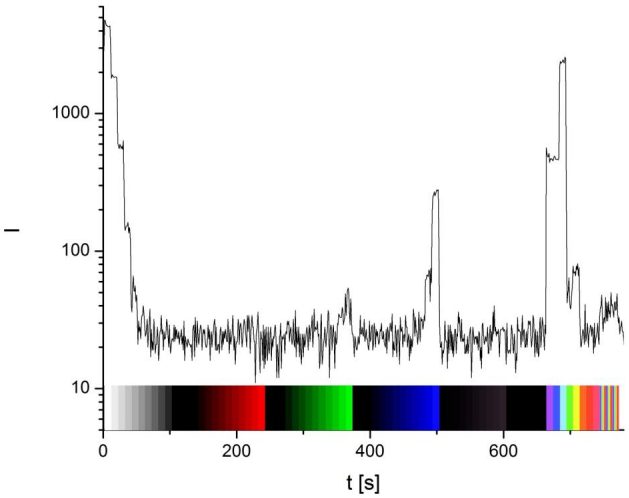

Slika 1. Odgovor fotomultiplikatora na promenu slika na mobilnom telefonu u toku vremena. Slike su menjane svakih 10s.

Kako je cilj da periodično merimo odgovore fotomultiplikatora za poređenje merenja u različitim vremenskim periodima, na primer svake nedelje, prvo mogu da se porede mereni intenziteti bele svetlosti, kod kojih se svakih 10s menja zatamnjenje za po 10% (slika 2). Na slici 2 se vidi kako se odbroji na fotomultiplikatoru menjaju sa povećanjem zatamnjenja i ono ima eksponencijalni pad.

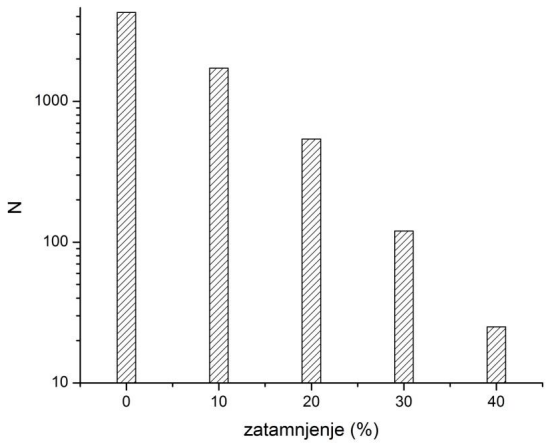

Slika 2. Odgovor fotomultiplikatora na promenu intenziteta bele svetlosti. Promena počinje od 0% zatamnjenja i svaka sledeća je 10% više zatamnjena.

Interesantnija je promena efikasnosti fotomultiplikatora na razne boje svetlosti, odnosno talasne dužine tokom vremena. Ovu informaciju dobijamo kada na ulaz optičkog kabla dovodimo svetlost u različitim duginim bojama. Na slici 3 vidi se zavisnost odbroja fotomultiplikatora od talasne dužine upadne svetlosti. Kako se samo 8 boja koristilo u preliminarnim merenjima, sa slike 3 se vidi da je potrebno povećati broj boja u okolini boje kod koje fotomultiplikator daje najbolji odziv, tj, ima najveću efikasnost, a to je plava svetlost. U sledećoj iteraciji razvoja sistema za proveru varijacije efikasnosti fotomultiplikatora broj boja oko plave boje se mora povećati za red veličine.

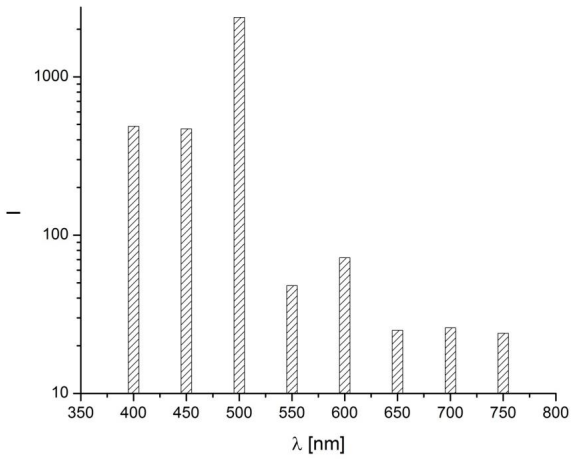

Slika 3. Odgovor fotomultiplikatora na promenu boje slike.

4. Zaključak

U ovom radu je prikazan primer korišćenja modernih mobilnih telefona pri testiranjima i optimizaciji fotomultiplikatora koji se koriste u kontinuiranim merenjima kosmičkog zračenja u Niskofonskoj laboratoriji Instituta za fiziku u Beogradu. Prikazani su prvi rezultati odziva fotomultiplikatora na razne intenzitete i talasne dužine svetla. Ovakav metod za proveru efikasnoti i varijacije odbroja fotomultiplikatora veoma je lako postaviti. Dodatna poboljšanja su moguća i to ako povećamo broj tačaka za određivanje promene efikasnosti odbroja fotomultiplikatora u zavisnosti od talasne dužine upadne svetlosti, posebno oko boje za koju dobijamo najveći odbroj fotomultiplikatora, a to je plava boja. Uvođenjem periodične kalibracije upadnom svetlošću omogućavaju da se odredi potrebna korekcija visokog napona koje napaja fotomultiplikatore ili koriguje odbroj scintilacionog detektora u cilju stabilizacije kontinuiranog merenja.

5. Napomena
Ovaj rad je urađen uz pomoć Ministarstva prosvete, nauke i tehnološkog razvoja Republike Srbije unutar projekta osnovnog istraživanja pod oznakom OI171002.

6. **Literatura**

[1] Dragic Aleksandar, Udovicic Vladimir, Banjanac Radomir, Jokovic Dejan, Maletic Dimitrije, Veselinovic Nikola, Savic Mihailo, Puzovic Jovan, Anicin Ivan. The New Set-Up in the Belgrade Low-Level and Cosmic-Ray Laboratory, *Nucl. Technol. Radiat. Prot.* 26 (3) (2011) 181-192.

THE USEAGE OF MOBILE TELEPHONE FOR TESTING AND OPTIMISATION OF MEASUREMENTS WITH PHOTOMULTIPLIRES

Dimitrije MALETIĆ, Dejan JOKOVIĆ, Radomir BANJANAC, Nikola VESELINOVIĆ, Mihailo SAVIĆ, Aleksandar DRAGIĆ, Vladimir UDOVIČIĆ
Institute of Physics, Univeristy of Belgrade, Serbia, maletic@ipb.ac.rs

ABSTRACT
The rapid development of telecommunication devices enables the use of such devices in testing and optimization of laboratory measurements. This paper shows an example of modern mobile phones use in testing and optimization of photomultiplier used in continuous measurements of cosmic radiation in Low background laboratory of the Institute of Physics University of Belgrade. Plastic scintillators often have direct external connection to the outside of photomultiplier scintillation detector via optical cable. This direct connection is used for periodic calibration of measuring devices in order to gain stability of continuous measurement. Using applications for displaying images on a mobile phone it is possible to input light of various intensity and wavelength to the optic cable. This paper presents the first results of the photomultiplier response to various wavelengths and intensities of light directing from mobile telephone. Periodic calibration using light source enable us to determine the required correction of high voltage which powers a photomultiplier or correct count rate of scintillation detector in order to stabilize the continuous measurement.

ВАРИЈАЦИЈЕ РАДОНА И КОСМИЧКОГ ЗРАЧЕЊА КАО ИЗВОРИ ВРЕМЕНСКЕ ВАРИЈАЦИЈЕ ФОНА ГАМА ЗРАЧЕЊА У НИСКОФОНСКОЈ ГАМА СПЕКТРОМЕТРИЈИ

Р. Бањанац[1)], А. Драгић[1)], В. Удовичић[1)], Д. Јоковић[1)], Д. Малетић[1)], Н. Веселиновић[1)], М. Савић[1)], Б. Грабеж[1)], И. Аничин[1)], Ј. Пузовић[2)]

1) Институт за Физику, Универзитет у Београду, Прегревица 118, 11080 Београд
2) Физички факултет, Универзитет у Београду, Студентски трг 12, 11000 Београд
e-mail: banjanac@.ipb.ac.rs

Апстракт. Упоређена је временска варијација фона гама зрачења симултано са варијацијом концентрације радона и варијацијом интензитета космичког зрачења у типичној надземној као и нискофонској подземној лабораторији. У реалним условима варијације фона показује се значајна предност стабилности фона остварене у подземној лабораторији Института за Физику, посебно у случају нискофонске гама спектрометрије НОРМ узорака радијума 226.

1. УВОД

Заједничка особина врло ретких (маловероватних) фундаменталних појава, као што су распад протона и безнеутрински двоструки бета распад, и апликативних мерења малих активности радиоактивних узорака јесте техника мерења. У оба случаја она се базира на условима ниског фона свих врста зрачења чији интензитет одређује осетљивост мерења. Редукција интензитета космичких миона за фактор већи од милион пута неопходна је за реализацију фундаменталних експеримената али је већ локација плитко укопаних подземних лабораторија (до око 50м.в.е) адекватна за довољно повећање осетљивости примењених мерења. Флукс космичких миона у плитким подземним лабораторијама, који је у односу на локације на површини редукован само неколико пута, довољно је велики за статистички поуздану анализу ефеката којима миони генеришу нове компоненте фона. Једну од њих представљају терцијарни неутрони који настају интеракцијом миона на језгрима олова, а који природом своје интеракције чине главну сметњу у откривању честица тамне материје у експериментима у дубоким подземним лабораторијама (неколико хиљада м.в.е).

Поред потребе постизања услова минималног фона ништа мање значајан није захтев за стабилизацијом (ниског) нивоа фона у времену, јер се одређена статистичка тачност резултата, односно повећање осетљивости, постиже дуготрајним мерењима [1]. Резултати мерења фона, међутим, представљају само средње вредности фона што у принципу производи систематску грешку посебно

код НОРМ узорака. Како се гама зрачење најчешће користи као сигнатурно зрачење ретких процеса и мерења малих активности и пошто је германијумски (Ге) детектор најчешће коришћен спектрометар у студијама ових процеса, акценат се ставља на нискофонску Ге гама спектрометрију. Подразумева се да је сама локација за нискофонску лабораторију изабрана на терену са минималном концентрацијом природних радионуклида, да сам спектрометар припада категорији нискофонских чије компоненте садрже минималне концентрације радиоактивних нечистоћа што треба да важи и за употребљену пасивну заштиту детектора. Варијација фона гама зрачења током времена последица је варијације временски промењивих компоненти фона, космичког зрачења и радона. Детаљна анализа варијације фона садржај је дисертације [2], а главни резултати мерења реализовани у Нискофонској подземној лабораторији Института за Физику у Земуну су овде представљени.

2. ОПИС ЕКСПЕРИМЕНТА

Надземна лабораторија (НЛ) и подземна (ПЛ, 25м.в.е) лабораторија Института за Физику описане су детаљно у [3], као и систем за дигиталну аквизицију података неопходан за каснију анализу временских серија. Климатизована НЛ може се сматрати типичном надземном лабораторијом која испуњава нискофонске услове (<3 одброја у секунди у енергетском интервалу амбијенталног фонског гама зрачења) што је посебно испуњено за ПЛ (<0.5cps) у којој вентилациони систем обезбеђује ниску концентрацију радона (око 10 Bqm^{-3}) и у којој је површински флукс миона редукован око 4 пута [4].

За симултано мерење интензитета космичких миона и фона гама зрачења су у НЛ коришћени пластични сцинтилатор (МП) димензија 50cm x 23cm x 5cm и германијумски детектор (МГе) релативне ефикасности 13% у вето конфигурацији. Слично, у ПЛ у истој конфигурацији мерили су пластични сцинтилатор (ВП, 100 cm x 100cm x 5cm) и нискофонски Ге детектор (ВГе, 35%). Како су амплитуде периодичних варијација космичких миона реда неколико процената, [5], најчешће се њихов утицај на фон гама зрачења занемарује имајући посебно у виду да се, са изузетком анихилационе линије, космичко зрачење у Ге детекторима детектује у континууму фона. Посебна пажња у мерењима је посвећена апериодичним променама флукса миона који су већих амплитуда и у којима доминира тзв. Форбушов ефекат смањења интензитета галактичког космичког зрачења (до 30%) услед заклањања планете Земље међупланетарним шоком или појавом соларног ветра.

Мониторинг радона реализован је радонмонитором РМ, силицијумском диодом као детектором алфа честица, који истовремено мери амбијенталне параметре температуру, релативну влажност и притисак. Сам уређај РМ смештен је унутар коморе за узорке у непосредну близину Ге детектора и као и сам Ге детектор оклопљен је оловном пасивном заштитом. Амплитуде дневне варијације концентрације радона у зависности од промена атмосферских

параметара могу бити веома велике, а сам радон се у фону гама зрачења идентификује преко многобројних и јасно издвојених пострадонских линија.

3. РЕЗУЛТАТИ И ДИСКУСИЈА

Форбушов ефекат регистрован је пластичним сцинтилаторима ВП и МП, док је коинцидентни спектар одговарајућих сцинтилатора и Ге детектора детектован интегрално, и респективно од I до IV приказан је на слици 1.

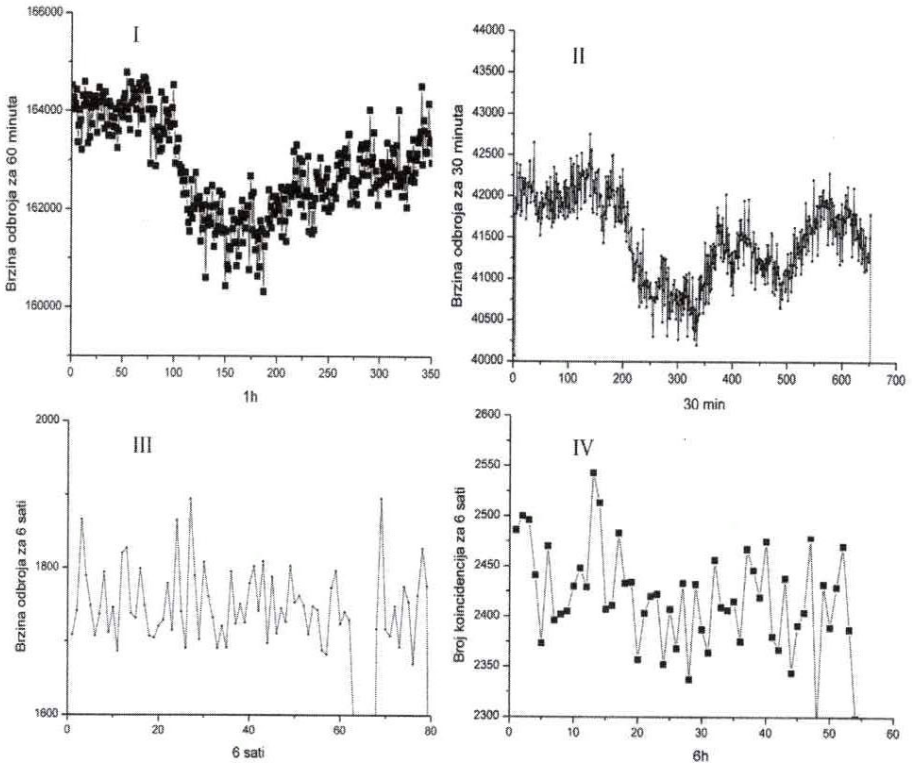

СЛИКА 1. Форбушов ефекат из марта 2010. године виђен пластичним сцинтилаторима (ВП-I и МП-II) и германијумским детекторима (ВГе-III и МГе-IV) у ПЛ (I и III) и НЛ (II и IV).

Имајући у виду да је у октобру 2003. године у НЛ регистрован Форбушов ефекат три пута веће амплитуде у односу на ефекат из 2010. године, као и да постоје и друге краткотрајније али интензивније промене интензитета космичког зрачења, може се закључити да би сваки германијумски детектор смештен у типичну надземну лабораторију осетио интегралну промену фона. Једини поуздан начин корекције промене фона на промену интензитета космичког

зрачења јесте обавезна вето заштита Ге детектора пластичним сцинтилаторима који у антиконцидентном режиму мерења додатно редукују фон.

Дневна промена концентрације радона јасно се види у пострадонским линијама Ге детектора у НЛ. Како је МГе мале релативне ефикасности, слика 2 приказује коинцидентне дневне варијације радона и суме 4 најинтензивније пострадонске линије МГе детектора мерених у НЛ. Ефекат дневне варијације радона и последично пострадонских линија у фону је занемарив у ПЛ, [6], што је за разлику од типичне НЛ чини адекватнијим амбијентом за нискофонска мерења НОРМ узорака радијума 226 у којима велике дневне варијације радона доприносе значајном систематском грешком мерења таквих узорака.

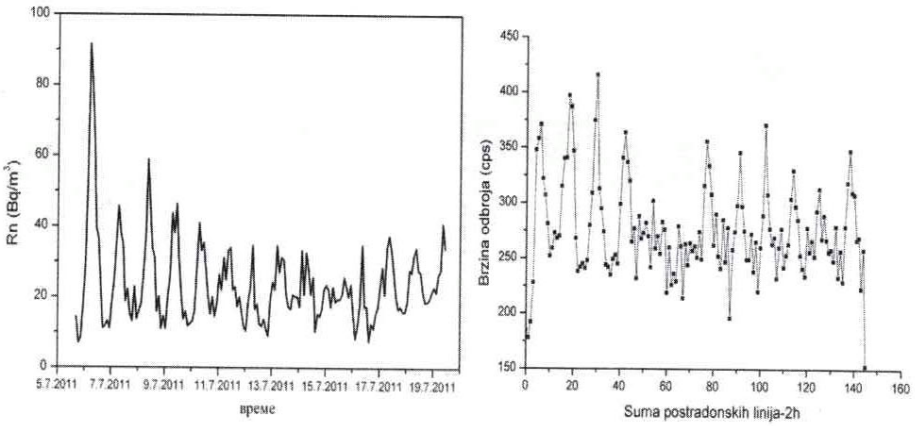

СЛИКА 2. Дневна варијација радона (лево) и суме пострадонских линија (десно) у типичној надземној нискофонској лабораторији.

ЗАХВАЛНИЦА

Овај рад је спроведен уз подршку Министарства за просвету, науку и технолошки развој Републике Србије, у оквиру пројекта ОИ171002.

ЛИТЕРАТУРА

[1] A. Mann, *Nature*, **471**, 433-435, (2011)
[2] Р. Бањанац, "Временски променљиве компоненте фона у нискофонској подземној лабораторији", докторска дисертација, Физички факултет Универзитета у Београду (2011), http://cosmic.ipb.ac.rs/repository.html
[3] А. Драгић *et al.*, *Nucl. Techn. & Radiat. Protect.*, **26**, No. 3, 181-192 (2011)
[4] А. Драгић *et al.*, *Nucl. Instr. and Meth. in Phys. Reas. A.*, **591**, 470-475 (2008)
[5] А. Драгић *et al.*, *Int. J. Mod. Phys. A* **20**, 6953-6955 (2005)
[6] В. Удовичић *et al.*, Radiat. Prot. Dosimetry **145**(2-3) 155-158 (2011)

О СВУДА ПРИСУТНОМ ФОНСКОМ ГАМА ЗРАЧЕЊУ КОНТИНУИРАНОГ СПЕКТРА

Р. Бањанац, Д. Малетић, Д. Јоковић, Н. Веселиновић, А.Драгић, В. Удовичић, И. Аничин

Институт за физику, Универзитет у Београду, Прегревица 118, 11000 Београд
e-mail: banjanac@ipb.ac.rs

Апстракт. Апсорпционим мерењима је утврђено да највећи део континуума у фонским спектрима незаштићених германијумских детектора, и у локалитетима на површини и на дубини од 25 метара воденог еквивалента, потиче од зрачења истог таквог континуираног спектра која пристижу из горње хемисфере. Интеграли тог континуума дају у површинској лабораторији флукс од око 8000 фотона/m^2.s.2π srad а у подземној око 5000 фотона/m^2.s.2π srad, средњих енергија око 150 keV, што по грубим проценама у површинским ткивима производи дозе од око 1.5 nSv/h и 1 nSv/h респективно. Симулације одговарајућих експерименталних ситуација пакетима GEANT4 и CORSIKA показују да је ово расејано и деградирано зрачење двојаког порекла – космичког и терестријалног, у односу кога још треба одредити.

1. УВОД

Фонски спектри незаштићених германијумских детектора потичу првенствено од гама зрачења дискретних енергија из природних радиоактивности присутних у околини а затим и од космичког зрачења. Гама зрачење дискретних енергија одговорно је за линијску компоненту фонског спектра, али и за његов континуум, који је сачињен од комптонских расподела гама зрачења дискретних енергија које је избегло потпуну детекцију. Миони космичког порекла производе континуирани спектар губитака енергије који има максимум интензитета на високим енергијама, реда десетина MeV, док мека компонента деградираним енергијама високоенергетских фотона и електрона свакако производи известан континуум. Све ово резултује у инструменталним фонским спектрима у којима је доминантна компонента, која носи и далеко највећи део инструменталног интензитета, континуирани спектар са изразитим максимумом, у зависности од величине детектора, у близини 100 keV. У овом раду је апсорпционим мерењима испитивано фонско зрачење које долази из горње хемисфере, које се може сматрати извором овог континуираног спектра, са циљем одређивања интензитета, природе и порекла тог зрачења.

2. ПОСТАВКА ЕКСПЕРИМЕНТА

Мерења су вршена радио-чистим германијумским детектором ефикасности 35% у магнезијумском кућишту, потпуно заштићеним оловом од зрачења која долазе из доње хемисфере а потпуно отвореним за она из горње хемисфере, како у површинској лабораторији тако и у подземној на 25 m.w.e. Урађен је и низ апсорпционих мерења са низом оловних фолија које су блокирале пут зрачењима из горње хемисфере. Фонски спектри из оваквих мерења приказани су на Сл.1

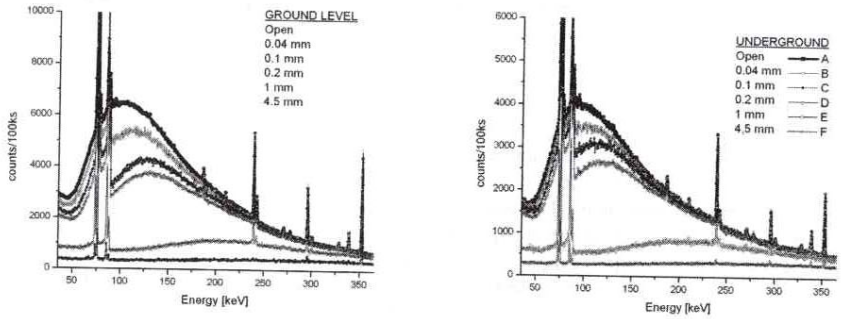

СЛИКА 1. Фонски спектри германијумског детектора отвореног према горњој хемисфери, па затим и са различитим дебљинама оловних апсорбера, у површинској лаборато рији (лево) и у подземној лабораторији на 25 m.w.e. (десно).

3. РЕЗУЛТАТИ И ДИСКУСИЈА

Већ визуелна инспекција апсорпционих спектара са Сл. 1. омогућава неколико занимљивих квалитативних закључака: **1.** Велика је сличност између ових спектара на површини и у подземљу, при чему је интегрални интензитет континуума у подземљу око 1.75 пута мањи. Истовремено, интензитет космичких миона је у подземљу мањи око 3.5 пута [1], **2.** Са повећањем дебљине апсорбера долази до померања максимума интензитета континуума ка вишим енергијама, што је типична карактеристика континуираних спектара, позната као «отврдњавање спектра», **3.** Дисконтинуитет у апсорпционим спектрима на енергији K_β X-зрака олова (88 keV) одражава чињеницу да је инструментални континуирани спектар највећим делом истовремено и стварни спектар долазећих зрачења, а да није последица непотпуне детекције зрачења дискретних енергија, **4.** Почетни пораст интензитета флуоресцентног X-зрачења олова са порастом дебљине апсорбера такође указује да се долазеће зрачење апсорбује фотоефектом, те да је стварни спектар тог зрачења идентичан са инструменталним спектром, и да је то тако бар до енергија реда 200 keV, докле још фотоапсорпција доминира у односу на комптоновску, **5.** Извесне разлике у

карактеру апсорпције на површини и у подземљу су последица нужно различите композиције зрачења и његове различите угаоне расподеле на те две локације.

Ови квалитативни закључци су потврђени квантитативном анализом апсорпционих кривих за енергије у различитим областима континуума. На Сл.2 су као илустрација приказане апсорпционе криве за одброј у каналу у континууму који одговара енергији од 89 keV (најближе апсорпционој ивици).

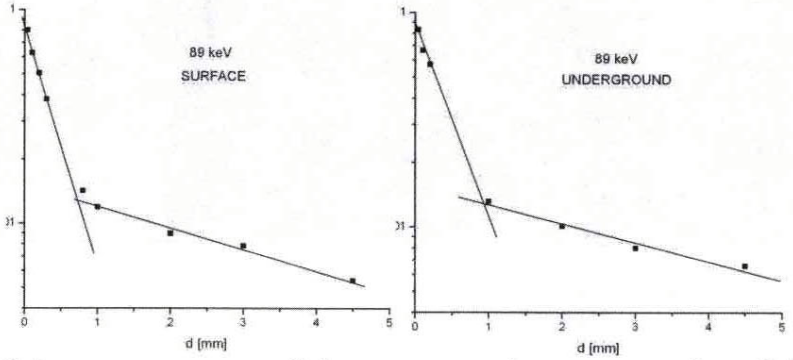

СЛИКА 2. Апсорпционе криве за одброј у континууму који одговара енергији од 89 keV, у површинској лабораторији (лево) и у подземној лабораторији на 25 m.w.e. (десно). Види се постојање две битно различите компоненте, једне која по апсорпционим особинама одговара тој енергији и друга, знатно продорнија, која по тим особинама одговара енергији од око 500 keV.

На слици су уочљиве две компоненте потпуно различитих апсорпционих особина – мање продорна која по апсорпционим особинама добро одговара енергији од 89 keV, и друга знатно продорнија али и знатно мањег интензитета, која по апсорпционом коефицијенту одговара енергији од око 500 keV. Ова прва компонента очигледно представља зрачење континуираног спектра, истих енергија на којима се оно и појављује у инструменталном спектру, док ова друга представља комптонске расподеле од зрачења виших енергија које се апсорбују као јединствено зрачење средње енергије око 500 keV. Са слика се такође види да нискоенергетска компонента континуираног спектра бива практично апсорбована већ дебљином од око 1 mm олова, те да одузимање спектра зрачења које пролази кроз апсорбер те дебљине (видети Сл.1) од спектра потпуно отвореног детектора оставља практично чист спектар зрачења континуираног спектра, онако како га види дати детектор. Такви спектри су приказани на Сл.3.

Интеграли тих спектара, грубо кориговани на детекциону ефикасност, дају за флуксеве овог зрачења континуираног спектра, које долази из горње хемисфере и има средњу енергију око 150 keV, вредности од око 8000 фотона/m^2.s.2π srad на површини и око 5000 фотона/m^2.s.2π srad у подземној лабораторији. Претпоставка да је овакво зрачење по својим јонизационим особинама слично зрачењу Co-57 доводи до грубе процене за дозе које оно саопштава површинским ткивима, од око 1.5 nSv/h на површини и око 1 nSv/h у подземљу

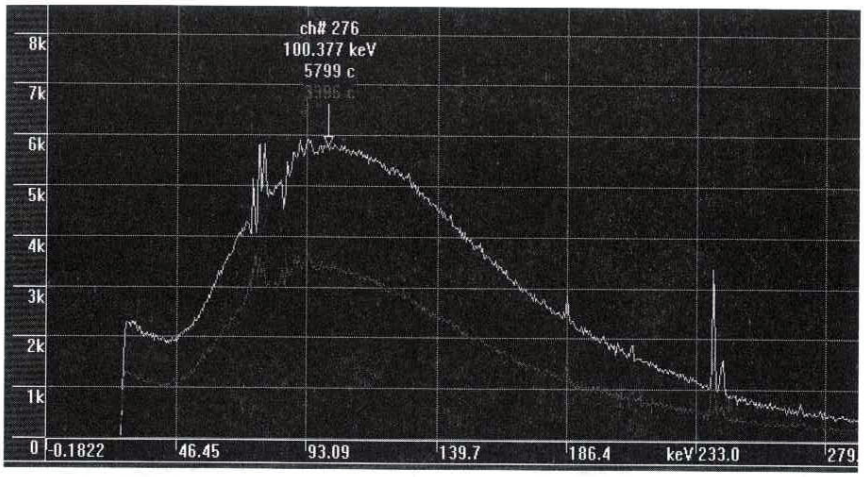

СЛИКА 3. Чисти инструментални спектри фонског зрачења континуираног спектра које долази из горње хемисфере, у површинској лабораторији (горњи) и у подземној лабораторији на 25 m.w.e. (доњи). Интегралне брзине бројања у њима су око 21 и 12 cps респективно.

Експерименталне ситуације које резултују у оваквим фонским спектрима детаљно су симулиране програмским пакетима GEANT4 и CORSIKA. Закључено је да је то зрачење континуираног спектра двојаког порекла – једним делом оно представља расејано и деградирано зрачење електромагнетне компоненте космичког зрачења, док другим делом представља од целокупне околине расејано зрачење терестријалног порекла, често познатог под називом "skyshine radiation" [1]. И поред велике сличности збирног спектра на обе локације, јасно је да је релативни удео ове две компоненте веома различит на две испитиване локације, и тај релативни удео још треба одредити.

ЗАХВАЛНИЦА

Овај рад је реализован уз подршку Министарства за просвету, науку и технолошки развој Републике Србије, у оквиру пројекта ОИ 171002.

ЛИТЕРАТУРА

[1] Dragić A. *et. al. Nucl. Instr. and Meth. in Phys. Res.* **A591** 470-475 2008
[2] Swarup J. *Nucl. Instr. and Meth.* **172** 559-566 1980

О ВЕЗИ ИЗМЕЂУ ИНТЕНЗИТЕТА КОСМИЧКОГ ЗРАЧЕЊА И КЛИМЕ НА ЗЕМЉИ

А. Драгић, Н. Веселиновић, Д. Малетић, Д. Јоковић, Р. Бањанац, В. Удовичић, И. Аничин

Институт за физику, Универзитет у Београду, Прегревица 118, 11000 Београд
e-mail: dragic@ipb.ac.rs

Апстракт. Испитиване су корелације између краткотрајних варијација интензитета космичког зрачења до сада поуздано забележених од стране неутронских монитора и девијација од очекиваних вредности дневног опсега температура дефинисаних универзумом температурских података за Европу у том истом периоду. Нађене корелације и интензитетом и фазним односима наговештавају постојање тражене везе, на скромном нивоу поверења, који је одређен статистиком догађаја у базама података о космичком зрачењу. Утврђено је и постојање извесног ширинског ефекта, што даје додатну тежину овом закључку, чија сигнификантност може значајно порасти само протоком времена, и консекутивним обогаћењем база података о варијацијама интензитета космичког зрачења.

1. УВОД

Дуготрајна расправа о могућој вези између космичког зрачења и климе на Земљи центрирана је око плаузибилне претпоставке да јонизација атмосферских гасова од стране космичког зрачења значајно утиче на процес формирања облака, па затим и око контроверзне евиденције у прилог те претпоставке. Проблем је у томе што су обе величине, и глобална облачност и интензитет космичког зрачења, у средњем константне. Неке анализе постојећих података о глобалној облачности и дуготрајним варијацијама интензитета космичког зрачења (КЗ) изгледа да потврђују почетну хипотезу [1], мада је проблем још далеко од решења [2]. Недавни први резултати јединог контролисаног експеримента од стране CLOUD колаборације у CERN-у [3], који испитује механизме формирања аеросола у присуству јонизујућег зрачења, наговештавају постојање позитивне корелације. Резултати наше анализе података о краткотрајним варијацијама интензитета КЗ и метеоролошких параметара, који су овде приказани, такође указују на могућност постојања извесне узрочне везе.

2. МЕТОД АНАЛИЗЕ

Новост приступа састоји се у коришћењу локалног дневног опсега температура (разлика максималне и миинималне дневне температуре, на даље ДОТ) као проксија за локалну облачност, за кога је показано да је овој инверзно

пропорционалан [4]. Облачност није најпогоднији параметар за квантитативне анализе а његова мерења су на глобалном нивоу почела тек са сателитском ером. ДОТ се међутим са великом поузданошћу мери у довољно густој просторној мрежи током целог периода у коме је интензитет КЗ континуирано мониторисан. Примењен је метод познат као анализа суперпонираних епоха, који је погодан за детекцију апериодичних рекурентних догађаја у временским низовима који поседују шум поредљиве амплитуде. У конкретном случају он се своди на следеће [5]. Лоше дефинисан појам глобалне облачности овде је замењен универзумом очекиваних вредности ДОТ за територију Европе. Прво је на основу педесетогодишњих мерења за сваку од 210 изабраних метеоролошких станица формиран локални образац годишње варијације ДОТ, који за сваку станицу, за сваки датум у години, дефинише интервал у коме са на датом нивоу поверења очекује појава вредности ДОТ. Затим су из низова вредности интензитета космичких неутрона са погодних мониторских станица, за период од 1955 до 2000 године, екстраховане карактеристичне појаве смањења интензитета КЗ, познате као Форбушова смањења (FD), и појаве великог али краткотрајног повећања интензитета (GLE), које амплитудом превазилазе типичан ниво шума у подацима, а које леже на иначе мирним сегментима временског низа (такозвани «мирни дани»). Затим су за сваки дан из интервала око дана у коме је дати појединачни догађај започео («нулти дан») нађена одступања од очекиване вредности ДТО, за сваку од 210 изабраних станица, па су та одступања усредњена по свим станицама у једно средње одступање за сваки дати дан датог догађаја. Коначно су, центрирано на нулти дан, преклопљени сви догађаји истог типа и за сваки дан усредњена сва средња одступања по укупном броју изабраних догађаја. Екстерна статистичка грешка на сваком дану отуд првенствено зависи од броја догађаја који улазе у ово последње усредњавање.

Резултати овакве анализе приказани су у графичкој форми на Сл.1, за случајеве опадања интензитета космичког зрачења, FD, и на Сл.2. за случајеве пораста интензитета, GLE. На горњим сликама приказане су вредности флукса космичког зрачења, а на доњим одговарајуће средње вредности одступања вредности дневног опсега температура.

3. РЕЗУЛТАТИ И ДИСКУСИЈА

Из анализе ових резултата следи неколико важних закључака. Прво, види се да су одступања од очекиваних вредности ДОТ у извесној мери пропорционална амплитуди промене интензитета космичког зрачења, а затим и да су та одступања, како је и очекивано, у противфази са варијацијама интензитета КЗ. Такође је очигледно да реакција инертне атмосфере у случају опадања интензитета космичког зрачења треба више да касни у односу на почетак те промене но у случају раста тог интензитета, што ови резултати и наговештавају. Амплитуда одступања вредности ДОТ од очекиваних вредности је, међутим,

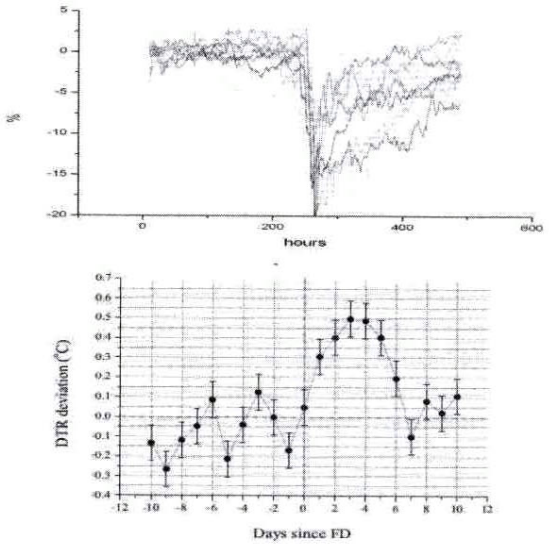

СЛИКА 1. Форбушова смањења интензитета КЗ већа од 10% (горња слика) и одговарајућа средња одступања ДОТ од очекиваних вредности на основу педесетогодишњих просека.

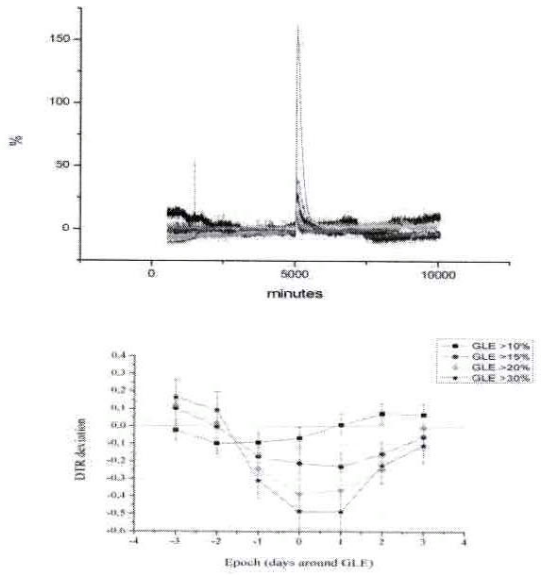

СЛИКА 2. Повећања интензитета КЗ (GLE) већа од 30% (горња слика) и одговарајућа средња одступања ДОТ од очекиваних вредности на основу педесетогодишњих просека. Приметите да на Сл.1 временска скала обухвата 20 дана, а на Сл.1 6 дана.

мала, и не превазилази неколико процената ни у случају највећих постојећих промена интензитета КЗ. Оволика одступања налазе се довољно често у низовима података и некорелирано са дефинисаним варијацијама интензитета космичког зрачења [6]. Отуд горњим закључцима расте значајност углавном због коинцидирања понашања у случајевима варијација интензитета КЗ супротног знака. Ово постаје тим убедљивије ако се погледа зависност ефекта од географске ширине, која је иначе карактеристична за све појаве везане за КЗ. На Сл.3 је приказана ова интервална зависност само за случајеве FD, где статистика дозвољава ову врсту анализе. У оквиру те скромне статистике назире се постојање очекиваног ефекта. Оваква случајна «трипла коициденција» је свакако мало вероватна. Коначно, иако ови резултати сугерирају постојање узрочне везе између космичког зрачења и климе на Земљи, повећање значајности тог закључка се може очекивати само кроз обогаћивање база података монитора космичког зрачења.

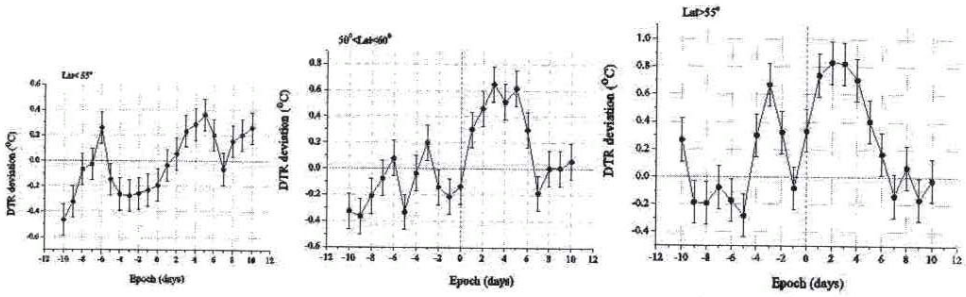

СЛИКА 3. Ширински ефекат за случајеве FD

ЗАХВАЛНИЦА

Овај рад је реализован уз подршку Министарства за просвету, науку и технолошки развој Републике Србије, у оквиру пројекта ОИ171002.

ЛИТЕРАТУРА

[1] Svensmark H. *Phys. Rev. Lett.* **81** 5027–5030, 1998
[2] Kristjansson J.E. Kristiansen J. & Kaas E. *Advances in Space Research* **34** 407–415, 2004
[3] Kirkby J *Surveys in Geophysics* **28** 333–375 2007
[4] Dai, A., Trenberth, K. E., and Karl, T. R., *J. Climate*, **12**, 2451–2473, 1999
[5] Dragić A. et. al. *Astrophys. Space Sci. Trans.*, **7**, 315-318, 2011
[6] Erlykin A.D. Wolfendale A.W. arXiv 1212.2766v1, 12 Dec 2012

ИНДЕКС ДЕВИЈАЦИЈЕ DTR И КОСМИЧКИ ЗРАЦИ

А. Драгић[1)], Д. Малетић[1)], Р. Бањанац[1)], Д. Јоковић[1)], В. Удовичић[1)], Б. Грабеж[1)], Н. Веселиновић[1)], М. Савић[1)], Ј. Пузовић[2)], И. Аничин[1)]

1) Институт за физику, Универзитет у Београду, Прегревица 118, 11000 Београд
2) Физички факултет, Универзитет у Београду, Студентски трг 12, 11000 Београд
e-mail: dragic@ipb.ac.rs

Апстракт. Дневни опсег температура (Diurnal Temperature Range, DTR) је искоришћен као показатељ облачности. Температурни подаци из великог броја метеоролошких станица на северној хемисфери Земље су употребљени за дефинисање индекса варијације DTR. Временске серије овог индекса су посматране у корелацији са варијацијама космичких зрака (КЗ) у настојању да се тестира хипотеза утицаја КЗ на формирање облачности.

1. УВОД

Идеја о могућем утицају КЗ на атмосферске процесе и климу потиче још од половине прошлог века [1,2]. Многе студије, публиковане последњих година, говоре у прилог ове тезе [3,4]. Физички процес, предложен да објасни допринос КЗ стварању облака, је јонима индуковано стварање центара кондензације (ion-induced nucleation) [5,6]. Пролазећи кроз атмосферу, честице КЗ губе енергију јонизационим процесима. КЗ је највећи извор атмосферских јона у области атмосфере од 1 км па све до преко 50 км надморске висине. Концентрација ових јона индукованих КЗ се регуларно мери у Физичком Институту Лебедева [7] и до сада је предложено неколико модела процеса [8,9,10]. Јонизација индукована КЗ производи нове аеросоле. Неки аеросоли могу формирати молекуларне кластере веће од критичних и тако послужити као основ за кондензацију облака. Овај процес стварања облака добија потврду, у контролисаним лабораторијским условима, у експерименту CLOUD у CERN-у [11].

Резултати великог броја студија везе КЗ и климе су контрадикторни, делимично и због комплексности феномена. Неки радови говоре у прилог ове везе [12,13] док друге студије је доводе у питање [14,15,16].

Критика неких радова који говоре у прилог везе је усмерена на податке о облачности са ISCCP-а (International Satellite Cloud Climatology Project). Тешкоће у мерењу облачности укључују маскирање ниске облачности високом, дрифтовима током дугог периода мерења, калибрације инструмената итд.

2. ПОСТАВКА ЕКСПЕРИМЕНТА

Наша намера је била да се спроведе анализа зависности облачности од КЗ користећи независтан скуп података на који наведени проблеми не утичу. Дневни опсег температуре тј. разлика између максималне и минималне дневне температуре, DTR = T_{max} - T_{min}, је за ову потребу корисна величина јер је у антикорелацији са облачношћу [17]. Кад постоји висока облачност више соларног зрачења бива рефлектовано у току обданице у свемир и T_{max} је смањена. Ноћу, мање инфрацрвеног зрачења бива емитовано у свемир са површине Земље па је T_{min} повећана. Додатна предност је и то што подаци о температури сежу далеко у прошлост, а сателитски подаци о облачности постоје тек од 1983. године.

Дефиниција δ DTR

Наша анализа је заснована на индексу девијације DTR (δ DTR) којег треба прво дефинисати. На било којој локацији на Земљи DTR зависи од много фактора (влажности земље и ваздуха, водене паре итд.). Да би се ови локални ефекти редуковали и побољшали квалитет информације о облачности, подаци са укупно 634 станице са северне хемисфере из *World Data Center for Meteorology* (http://www7.ncdc.noaa.gov/CDO/cdo) су коришћени за дефинисање δ DTR. Сезонска варијација DTR је најочитија у овим подацима. Средњи годишњи профил DTR неколико метеоролошких станица за период од око 50 година је дат на слици 1.

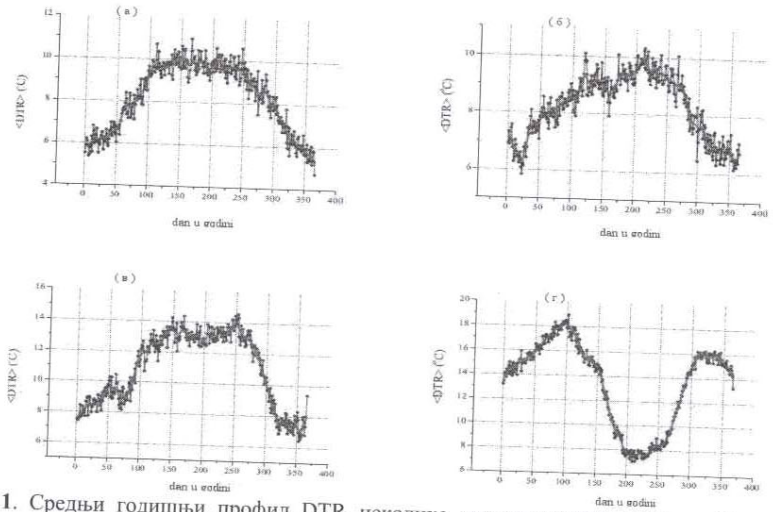

СЛИКА 1. Средњи годишњи профил DTR неколико метеоролошких станица: Лондон (а), Ванкувер (б), Аралско море (в) и Лакнау (г) добијени усредњавањем података о DTR током година укључујући и фит података кубним сплајном.

Многе европске станице имају трапезоидални облик овог профила са релативно равним платоом у летњим месецима који скоро линеарно опада ка вредностима у зимским месецима. Ово није универзално и разликује се од станице до станице.

Овај профил дефинише очекиване вредности DTR за сваку станицу и за сваки дан у години. За к-ту станицу і-тог дана очекивана вредност ће бити дефинисана као < DTR(k, DoY(i))> , где је DoY(i) дан у години за і-ту вредност. Нас ће интересовати разлика DTR од ове очекиване. Та разлика, нормализована са стандардном девијацијом ће бити тражени индекс девијације.

$$\delta\, DTR(k,i) = \frac{DTR(k,i) - < DTR(k, DoY(i)) >}{\sigma_{k,DoY(i)}} \tag{1}$$

Индекс девијације DTR се, на крају, формира усредњавањем локалних вредности δDTR(k,i) кроз све станице:

$$\delta\, DTRI(i) = \frac{1}{N}\sum_{k=1}^{N} \delta\, DTR(k,i) \tag{2}$$

Временска серија δ DTR је формирана за период од 1.1.1 1950 до 31.12.2011.

3. РЕЗУЛТАТИ И ДИСКУСИЈА

Спроведена је хармонијска анализа временских серија δ DTR. Израчунат је Lomb-Scargle периодограм одакле су идентификовани статистички значајни квази-периодични сигнали за цео период, што је и приказано на слици 2.

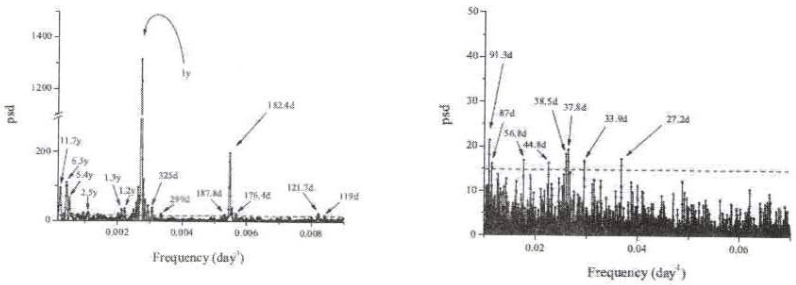

СЛИКА 2. Периодограм δ DTR. Испрекидана линија представља ниво сигнификантности од 0,01

Најуочљивији је пик за период од 1 године. Како следи, дефиниција δ DTR не успева да укључи и годишње варијације DTR. Остали значајни хармоници су на 182,4 дана, 121,7 дана и 91,3 дана. Периодичност корелисана са варијабилношћу

Сунца и КЗ је такође утврђена. На ово указују, у подацима за δ DTR, периодичност соларног циклуса од 11,7 година и ротација Сунца од 27,2 дана. Пик на 33,9 дана је близу пика од 34,5 дана уочен у подацима мионске активности у Београду [18] и 35 дана у Climax NM подацима [18]. Пик од 37 дана је присутан у подацима из неутонских монитора, осим у Хуанкају, у Перуу. Пик на 57 дана се такође појављује и у Београдским мионским подацима сакупљеним у периоду од 2002 до 2004 године. Периодичност од 300 и 323 дана је уочена у соларној активности. Мали део пика од 1 године може се приписати КЗ. Индиректна потврда овога је и пик на 1,3 године. Помак са 1 на 1,3 године је уочен, током соларног минимума, у подацима са неутронских монитора Хуанкајо и Climax.

Закључак је да се варијабилност соларне активности очитује на δ DTR и да се то може утврдити применом ове анализе. Међутим, разлика између индиректног утицаја сунчеве активности на климу кроз модулацију КЗ, и директног утицаја кроз осунчаност, захтева финију анализу.

ЗАХВАЛНИЦА

Овај рад је реализован уз подршку Министарства за просвету, науку и технолошки развој Републике Србије, у оквиру пројекта ОИ171002.

ЛИТЕРАТУРА

[1] Ney E P, *Nature*, 183, 1959, pp451-452,.
[2] Dickinson R E, *B. Am. Meteorol. Soc.*, 56, 1975, pp. 1240-1248,.
[3] Svensmark H, Friis-Christensen E, *J. Atmos. Solar Terr. Phys.*, 59, 1997, pp. 1225-1232,.
[4] Pudovkin M I, Veretenenko S N, *J. Atmos. Solar Terr. Phys.*, 57, 1995, pp. 1349-1355,.
[5] Yu F, Turco R, *Geophys. Res. Lett.*, 27, 2000, pp. 883-886,
[6] Yu F, Turco, J. Geophys. Res., 106, 2001, pp. 4797-2814,.
[7] Stozhkov Yu I, Svirzhevsky N S, Bazilevskaya G A, Kvashnin A N, Makhmutov V S, Svirzhevskaya A K, *Advances in Space Research*,44, 2009, pp.1124-1137
[8] Usoskin I G, Kovaltsov G A, *J. Geophys. Res.*, 111, 2006, D21206,
[9] Desorgher L, Flckiger E O, Gurtner M, Moser M R, Btikofer R, *Int. J. Modern Phys.* A, 2005, 20, 68026804.
[10] Velinov P, Mishev A, *C. R. Acad. Bulg. Sci.*, 2007,60, 493500,.
[11] Kirkby J et al, *Nature*, 476, 2011,429.
[12] Usoskin I G, Marsh N D, Kovaltsov G A, Mursula K, Gladysheva O G, *Geophys. Res. Lett. 31:L16109*, 2004
[13] Harrison R G, Stephenson D B, Proc R Soc A., 2006,1628.
[14] Kristjansson J E and Kristiansen J, *J. Geophys. Res.*, 2000.
[15] Čalogović J, Albert C, Arnold F, Beer J, Desorgher L , Flueckiger O, *Geophys. Res. Lett.*, 37, L03802, 2010.
[16] Laken B, Kniveton D, Wolfendale A, *J. Geophys. Res.*, 116, 2011, D09201,.
[17] Dai A, Trenberth K E, and Karl T R, *J. Climate*, 12, 1999, pp2451–2473,.
[18] Dragić A, Banjanac R, Udovičić V, Joković D, Puzović J and Aničin I, *Proceedings of 21 ECRS*, 368, Košice, 2008.
[19] Caballero R, and Valde-Galicia J F, *Sol. Phys.* 213, 2003, pp. 413-426.

ПРОДУКЦИЈА НЕУТРОНА МИОНИМА ИЗ КОСМИЧКОГ ЗРАЧЕЊА НА ДУБИНИ ОД 25 M.W.E

А. Драгић[1)], Д. Малетић[1)], Р. Бањанац[1)], Д. Јоковић[1)], В. Удовичић[1)], Б. Грабеж[1)], Н. Веселиновић[1)], М. Савић[1)], Ј. Пузовић[2)], И. Аничин[1)]

1) Институт за физику, Универзитет у Београду, Прегревица 118, 11000 Београд
2) Физички факултет, Универзитет у Београду, Студентски трг 12, 11000 Београд
e-mail: yokovic@.ipb.ac.rs

Апстракт. У подземној лабораторији, на дубини од 25 m.w.e испод површине Земље, налази се гама спектрометријски систем који се састоји од HPGe детектора и пластичног сцинтилационог вето детектора. Као пасивна заштита HPGe детектора користи се олово. Миони из космичког зрачења производе неутроне у олову, који уносе неизбежну додатну компоненту фона. У коинцидентном режиму рада два детектора одређен је флукс брзих неутрона произведених мионима из космичког зрачења у оловној заштити HPGe детектора. Неутрони су идентификовани из структуре гама линије од 692 keV у спектру закаснелих коинциденција, која потиче од нееластичног расејања неутрона на изотопу ^{72}Ge. Измерена брзина продукције брзих неутрона је $3{,}1(5)\cdot10^{-4}$ n/cm^2·s.

1. УВОД

Миони су јако пенетрирајуће честице, присутне чак и дубоко испод површине Земље. Миони, као и секундарно зрачење индуковано мионима, важан су извор фона у гама спектрометријским експериментима. Посебан проблем представљају неутрони створени у интеракцијама миона са језгрима у земљи или материјалу околине детектора. У експериментима у којима се трага за тамном материјом неутрони могу произвести узмачне сигнале у детекторима, сличне очекиваним сигналима WIMP-ова. Такође, у експериментима двоструког бета распада, неутрони кроз реакцију (n,n'γ) у олову могу продуковати гама зрачење од 2041 keV, која је блиска Q вредности безнеутринског двоструког бета распада изотопа ^{76}Ge [1].

Наша мерења урађена су у плиткој подземној лабораторији, али такође су и релевантна за експерименте у дубоким подземним лабораторијама [2].

2. ОПИС ЕКСПЕРИМЕНТА

Нискофонска лабораторија Института за физику у Београду има подземну лабораторију укопану на дубини од 12 m испод површине Земље. Просечна густина земљишта изнад лабораторије је 2,0(2) g/cm^3, што даје ефективни апсорпциони слој од 25 m.w.e. Више детаља о лабораторији може се наћи у [3].

Експериментална поставка састоји се од германијумског детектора и пластичног сцинтилационог детектора који раде у коинцидентном режиму. Сцинтилациони детектор (Amcrys-H) је облика паралелопипеда димензија 100x100x5 cm, и на његовим угловима су четири фотомултипликатора. Радиочисти HPGe детектор (ORTEC), активне запремине 149 cm^3 и релативне ефикасности 35 %, налази се испод средишта сцинтилатора.

Аквизиција података врши се дигиталним системом у чијој основи је брзи четвороканални аналогно-дигитални конвертор (FADC), модел CAEN N1728B. Сигнали у FADC-у узоркују се у 2^{14} канала са временском резолуцијом од 10 ns. Два канала су резервисана за сцинтилациони детектор а један за HPGe детектор. Претпојачавачки сигнали са фотомултипликатора на истој дијагонали сцинтилатора сабирају се у један улазни сигнал у FADC; сумирани сигнал са друге дијагонале је други улазни сигнал у FADC. Подаци о сваком сигналу изнад постављеног нивоа прага, редни број тригера, време и амплитуда, снимају се у листу свих догађаја. То омогућује *off-line* анализу коинцидентних догађаја, како промптних тако и закаснелих.

Пластични сцинтилациони детектор мониторише временске промене интензитета миона из космичког зрачења. Германијумски детектор је типични нискофонски гама спектрометар. У антикоинцидентном режиму рада два детектора сцинтилациони детектор има функцију мионског ветоа за HPGe детектор. Са друге стране, коинцидентни режим два детектора омогућује изучавање ефеката у HPGe детектору индукованих космичким зрачењем. Наш конкретан интерес у овом случају био је одређивање флукса неутрона продукованих мионима из космичког зрачења.

3. РЕЗУЛТАТИ И ДИСКУСИЈА

Идентификација неутронских догађаја заснована је на процесу нееластичног расејања неутрона на изотопу ^{72}Ge, у активној запремини германијумског детектора, које побуђује језгро ^{72}Ge у стање од 692 keV. У изотопском саставу природног Ge изозопа ^{72}Ge има 27,7 %. Енергијско стање 692 keV је изомер, са временом полуживота од 444 ns, а депопулациони прелаз је чисти E0, што значи да је ефикасност детекције овог зрачења, односно догађаја, практично 100 %.

Довољна количина података скупљена је након 35 милиона секунди (400+ дана) мерења. Спектар германијумског детектора у коинциденцији са сцинтилационим детектором, пореклом од закаснелих коинцидентних догађаја у временском опсегу од 500 ns до 2 μs, приказан је на Сл. 1. Он показује две карактеристике, анихилациону линију услед распада позитивних миона заустављених у олову, и троугласту структуру на 692 keV услед нееластичног расејања неутрона на језгрима ^{72}Ge. Оваква троугласта спектрална линија резултат је сабирања енергије прелаза од 692 keV и енергије узмачног језгра ^{72}Ge. Ова структура проучавана је у више случајева [4, 5, 6, 7].

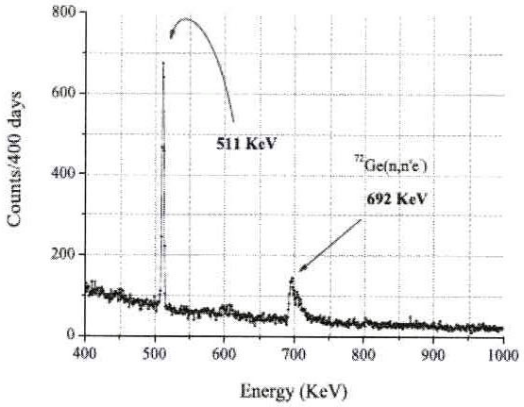

СЛИКА 1. Спектар закаснелих коинциденција германијумског детектора и пластичног сцинтилационог детектора, у временском опсегу од 100 ns до 2 μs, са јасно видљивим карактеристичним линијама на 511 и 692 keV.

Временски спектри, односно расподеле временских интервала између старт и стоп сигнала, са софтверским *gate*-ом за дате две спектралне линије од 692 keV и 511 keV, потрђују претходни исказ (Сл. 2). На тај начин одређено је време полуживота побуђеног стања ^{72}Ge, из временског спектра за линију од 692 keV, као и средње време живота миона, из временског спектра за линију од 511 keV. За време полуживота побуђеног стања ^{72}Ge добијено је 500(50) ns. Средње време живота миона је 2,24(9) μs.

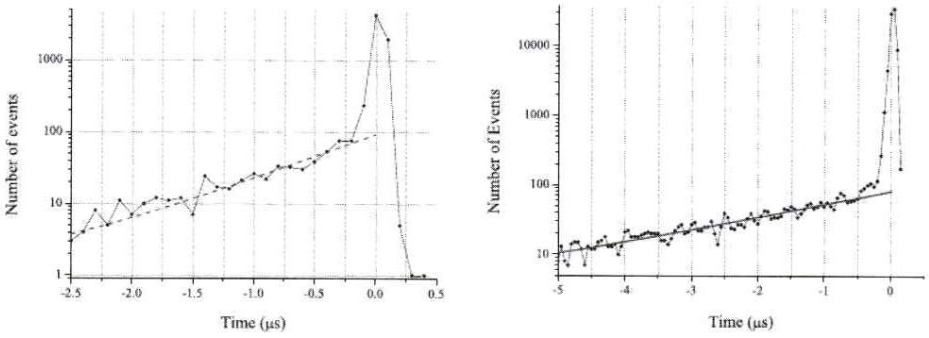

СЛИКА 2. Лево. Временска расподела догађаја који припадају структури на 692 keV. Фит кроз реп закаснелих коинциденција даје време полуживота побуђеног стања ^{72}Ge од 500(50) ns. **Десно.** Временска расподела анихилационих догађаја. Фит кроз реп закаснелих коинциденција даје средње време живота миона од 2,24(9) μs.

Флукс брзих неутрона може се одредити из интензитета спектралне структуре на 692 keV, из емпиријске релације $\Phi=k\cdot I/V$ [8]. I је брзина одброја спектралне линије 692 keV у cps, V је активна запремина у cm^3 и k је параметар који има вредност (900±150) cm.

Ова релација је често коришћена у аналогној спектроскопији, где су интеграционе константе велике и где се енергије узмачних језгара увек сабирају са енергијом прелаза из побуђеног стања језгра ^{72}Ge од 692 keV. У дигиталној спектроскопији, међутим, облик и интензитет ове линије зависи од постављеног нивоа тригера. Ако је ниво тригера виши од амплитуде узмачног сигнала, овај сигнал и сигнал од 692 keV сабирају се практично у потпуности. Ако је ниво тригера нижи од амплитуде узмачног сигнала, он ће окинути FADC и изазвати *pile-up* на сигналу од 692 keV; на тај начин ће дати догађај бити одбачен. У нашем случају ниво тригера је постављен довољно високо, и, следствено томе, интензитет спектралне линије од 692 keV може се поуздано користити за одређивање флукса брзих неутрона. Добијена вредност за флукс неутрона, са енергијом већом од 1 MeV, продукованих у ≈800 kg олова мионима из космичког зрачења на дубини од 25 m.w.e, је $3{,}1(5)\cdot10^{-4}$ n/cm^2·s.

ЗАХВАЛНИЦА

Овај рад је урађен уз подршку Министарства за просвету, науку и технолошки развој Републике Србије, у оквиру пројекта ОИ171002.

ЛИТЕРАТУРА

[1] Mei, D. M., Elliott, S. R., Hime, A., Gehman, V., and Kazkaz, K., *Phys. Rev. C* **77**, 054614 (2008)
[2] Ryazhskaya, O., *Proc. of the 20th ECRS*, Lisbon (2008)
[3] Dragić, A., Udovičić, V., Banjanac, R., Joković, D., Maletić, D., Veselinović, N., Savić, M., Puzović, J., and Aničin, I., *Nucl. Technol. Radiat.* **26**, 181-192 (2011)
[4] Wordel, R., Mouchel, D., Altzitzoglou, T., Heusser, G., Quintana Arnes, B., and Meynendonckx, P., *Nucl. Instrum. Meth. A* **369**, 557-569 (1996)
[5] Fehrenbacher, G., Meckbach, R., and Paretzke, H. G., *Nucl. Instrum. Meth. A* **372**, 239-245 (1996)
[6] Fehrenbacher, G., Meckbach, R., and Paretzke, H. G., *Nucl. Instrum. Meth. A* **397**, 391-398 (1997)
[7] Gete, E., Measday, D. F., Moftah, B. A., Saliba, M. A., and Stocki, T. J., *Nucl. Instrum. Meth. A* **388**, 212-219 (1997)
[8] Škoro, G., Aničin, I., Kukoč, A., Krmpotić, Dj., Adžić, P., Vukanović, R., and Župančić, M., *Nucl. Instrum. Meth. A* **316**, 333-336 (1992)

ВРЕМЕ ЖИВОТА МИОНА КОСМИЧКОГ ЗРАЧЕЊА ЗАУСТАВЉЕНИХ У ОЛОВУ

А. Драгић, Д. Малетић, Д. Јоковић, Р. Бањанац, Н. Веселиновић, В. Удовичић, И. Аничин

Институт за физику, Универзитет у Београду, Прегревица 118, 11000 Београд
e-mail: banjanac@ipb.ac.rs

Апстракт. Посматрани су догађаји које у два пластична сцинтилатора, који су постављени један испод другог, са слојем олова између њих, производе миони космичког зрачења. Догађаји се амплитудом и временом појављивања са резолуцијом од 10 ns уписују у листу из које се касније погодним софтвером могу произвољно обрађивати. Промптне коинциденције између догађаја из два детектора садрже мионе који скрозирају детекторе док закаснеле коинциденције садрже мионе који су заустављени у олову и у њему су се или распали (позитивни миони) или били захваћени од стране језгара олова и узроковали њихов распад (негативни миони). Прелиминарне анализе временских кривих за живот позитивних миона дају контролни резултат од око 2 μs, док се за живот негативних миона добија вредност од око 110 ns.

1. УВОД

Већина негативних миона који се заустављају у материјалним срединама, пре но што се спонтано распадну, бивају захваћени од стране атома средине и притом формирају такозване мионске атоме, где се после низа каскадних прелаза нађу у 1s стању. Прекривање овог стања са функцијама стања језгра тим је веће што је језгро теже, те вероватноћа за слабу интеракцију миона са протонском расподелом, и за реализацију реакције

$$\mu_- + p \rightarrow n + \nu_\mu \qquad (1)$$

брзо расте са порастом редног броја језгра, скоро као Z^4. Ова зависност је добро задовољена у лакшим језгрима, те се мерење живота негативних миона у релативно лаким срединама успешно користи у специфичној методи активационе анализе [1]. У тежим језгрима, међутим, ова је правилност, првенствено због ефеката поларизације вакуума, значајно нарушена. Такође, будући да реакција (1) ослобађа неутрон енергије знатно веће од енергија веза нуклеона, реализација те реакције бива праћена емисијом низа других зрачења као и формирањем нових изотопа, често радиоактивних, што се испоставља као значајан извор фона у фундаменталним експериментима који се изводе и у најдубљим нискофонским лабораторијама. Отуд је мерење живота негативних миона у тешким срединама и од теоријског и од практичног интереса.

2. ПОСТАВКА ЕКСПЕРИМЕНТА

Мерење живота миона космичког зрачења у олову је вршено системом од два пластична сцинтилатора димензија 50x25x5 cm са оловном плочом дебљине 4 mm, истих димензија, између њих. Излази из претпојачавача фотомултипликаторских сонди воде се у два (од четири) независна улаза брзог ADC уређаја типа CAEN N1728B. Сваки догађај се од стране системског софтвера записује у за сваки улаз независну листу која садржи амплитуду одговарајућег претпојачавачког импулса, дигитализовану у највише 32000 канала, и тренутак у коме предња ивица импулса прелази постављени напонски ниво, са резолуцијом од 10 ns. Софтвер који је локално развијен за потребе off-line анализе овако записаних догађаја за сваки улаз производи амплитудске спектре, као и спектре временских интервала између догађаја који чине те амплитудске спектре. Такође је могуће постављати произвољне услове на догађаје из оваквих спектара, те добијати или амплитудске спектре под датим временским условима (спектре промптно или различито закаснелих коинциденција), или временске, под датим амплитудским условима. Живо праћење формирања свих тих спектара из листа омогућава контролу стабилности детекторских система.

3. РЕЗУЛТАТИ И ДИСКУСИЈА

Временски спектар између свих догађаја два детектора поред веома интензивне промптне временске криве садржи и далеко мање интензивну криву закаснелих коинциденција. Коинцидентни спектри под условом промптног коинцидирања, које производе миони који пролазе кроз оба детектора, се суштински не разликују од некоинцидентних појединачних спектара губитака енергије високоенергетских миона, који имају карактеристичан максимум на енергији око 10 MeV. Ови спектри детаљније су описани у [2]. Коинцидентни спектар горњег детектора под условом закаснелог коицидирања, међутим, има максимум на енергији око 13 MeV, што одговара већим губицима енергије нискоенергетских миона који ће бити заустављени у олову. Ту ће се они или као слободни распасти (доминантно позитивни миони) и дати електрон (позитрон) енергије до 50 MeV, кога закаснело може да види или доњи или горњи детектор, или бити захваћени од атома олова (негативни миони) и, у овом случају другачије закаснело, довести до распада језгра атома олова чији ће продукти распада опет бити регистровани или доњим или горњим детектором.

Горе описана временска крива приказана је на слици 1. Упркос лоше статистике, јер су ова прелиминарна мерења вршена само током два дана, из криве се добијају два релативно добро дефинисана времена живота: од око 110 ns, које одговара средњем животу негативних миона заустављених у олову и захваћених од стране атома олова (природног изотопског односа), и оно од око 2

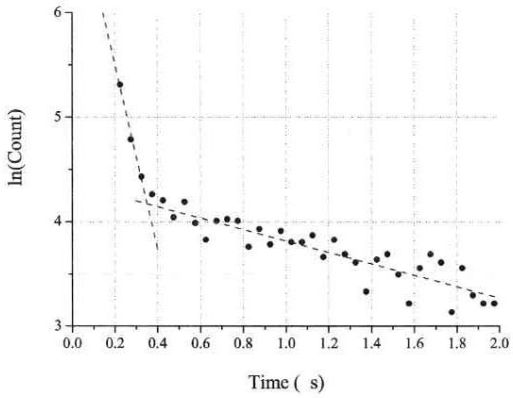

СЛИКА 1. Спектар временских интервала између догађаја у два телескопски распоређена пластична сцинтилатора, са оловном плочом између њих. Виде се два дистинктна времена живота – краће, од око 110 ns, које се може приписати животу негативних миона захваћених од стране атома олова, и дужи, од око 2 μs, који одговара животу слободних миона (доминантно позитивних) заустављених у олову.

μs, које одговара времену живота слободних миона (углавном позитивних) такође заустављених у олову. Првом слободном приликом ова ће мерења бити настављена са циљем побољшања статистике и смањења грешака добијених средњих живота, а затим ће бити проширена мерењем са зауставним оловним плочама различитих дебљина како би се добио спектар нискоенергетских космичких миона, који још увек није задовољавајуће познат.

ЗАХВАЛНИЦА

Овај рад је реализован уз подршку Министарства за просвету, науку и технолошки развој Републике Србије, у оквиру пројекта ОИ 171002.

ЛИТЕРАТУРА

[1] Hosoi, Y. *et al. Br. J. Radiol.*, **68**, pp. 1325-1338, 1995
[2] Dragić A. *et. al. Nucl. Tech. & Rad. Prot.*, Vol. **XXVI**, No. 3, 181-192 December 2011 .

ПАКЕТ ПРОГРАМА ЗА СПЕКТРАЛНУ И ВРЕМЕНСКУ АНАЛИЗУ ПОДАТАКА У ДИГИТАЛНОЈ НУКЛЕАРНОЈ И СПЕКТРОСКОПИЈИ КОСМИЧКОГ ЗРАЧЕЊА

Д. Малетић[1)], А. Драгић[1)], Р. Бањанац[1)], Д. Јоковић[1)], Н. Веселиновић[1)], В. Удовичић[1)], Б. Грабеж[1)], М. Савић[1)], Ј. Пузовић[2)], И. Аничин

1) Универзитет у Београду – Институт за физику, Прегревица 118, 11000 Београд
2) Универзитет у Београду - Физички факултет, Студентски трг 12, 11000 Београд
e-mail: maletic@.ff.bg.ac.rs

Апстракт. Описан је програмски пакет за анализу података у савременој дигиталној спектроскопији. Овај програмски пакет је иницијално развијан за потребе анализе података у Нискофонској лабораторији Института за физику у Београду. При описивању програма приказиване су могућности програма и реални примери анализа података. Имплементиране опције и алгоритми за анализу података омогућавају да програми постају флексибилни за рад, као и да могу да се користе за компликованије анализе података у дигиталној спектроскопији.

1. УВОД

У Нискофонској лабораторији за нуклеарну физику у Институту за физику врше се врло разноврсна мерења из области нуклеарне физике и физике космичког зрачења. Набавком нове опреме за прикупљање података са детектора, базиране на брзим аналогно-дигиталним претварачима произвођача CAEN, типа N1728B, појавила се потреба за развојем програма који би вршили сложене анализе добијених података, и тиме значајно повећали количину информација које се из њих могу добити, у односу на класичну спектроскопску рутину. Више информација о мерењима и самој лабораторији у којој се мерења одвијају могу се наћи у референци [1]. Најважнија особина коју омогућавају нови брзи ADC уређаји јесте могућност записа података у облику догађај-по-догађај листа. За сваки претпојачавачки импулс који се појави на неком од четири независна улаза у анализатор може се записати ампитуда, која се дигитализује у највише 32000 канала, и тренутак у коме узлазна ивица импулса пресеца задати ниво окидања, са разлагањем од 10ns. На тај начин се у off-line анализи подаци са четири независна детектора могу индивидуално спектрално анализирати али и коинцидирати у произвољном редоследу, промптно, као и произвољно закаснело, без коришћења било какве додатне класичне нуклеарне електронике. Различите експерименталне поставке се сада могу реализовати само променама просторног распореда различитих детектора, али и различитих начина обраде података из детектора у истом просторном распореду. Например,

листа догађаја из великог пластичног сцинтилатора који се налази изнад германијумског детектора, а три метра удаљен од другог пластичног сцинтилатора, истовремено може да се користи за добијање антикоинцидентног спектра германијумског детектора, промптног или закаснелог, када се из догађаја које германијумски детектор региструје елиминишу, у првом случају, догађаји директно изазвани космичким мионима, а у другом, неутронима космичког порекла, затим коинцидентни спектар са удаљеним пластичним сцинтилатором, када се региструју догађаји електромагнетних пљускова космичког зрачења, итд.

Програми су писани у програмском језику C++, а посебно треба нагласити да је доста труда уложено да се оптимизира графичко окружење и приступачност за коришћење програма. Постоје три компоненте програмског пакета. Основни, **DataViewer**, који даје најшири спектар основних апликација почев од могућности екстраховања спектара, два нивоа коинциденција као и добијање коплетних листа догађаја – амплитуда+време појављивања догађаја, такође ту је и могућност креирања листе скуцесивних догађаја, итд. Потом следи програм **TimeTools**, везан завременску анализу података и производњу временских спектара, и коначно **Syncronization** – програм за синхронизацију података са два независна ADC-а као и, једнако важна апликација, за додатно, вишеструко коинцидирање и антикоинцидирање.

2. ПРОГРАМ DATAVIEWER

Овај програм служи за исчитавање фајлова у evt формату који долази из CAEN-овог аквизиционог софтвера. Графички интерфејс овог програма подељен је на неколико целина. Поред разних менија, постоји део намењен за графички приказ спектара (Слика 1 горе), као и менији који омогућавају задавање параметара при обради података (Слика 1 доле). Ови менији су груписани у три степена (Слика 1 доле). Први степен омогућава прегледавање улаза CAEN-а, други степен за анализу служи за задавање параметара коинциденције основ улаза CAEN-а (улаза из првог степена). Даље, трећи степен има могућност мало сложенијих коинциденција и то улаза дефинисаних у првом степену и изалаза из коинцидентних кола у другом степену анализе.

Као излази из овог програма, тј. подаци који могу да буду доступни за даљу обраду и презентацију резултата су сви спектри – основни и коинцидентни, затим могу да се снимају листе коинцидентних догађаја. Листа коинцидентних догађаја садржаће информације времена доласка сигнала, амплитуде првог улазног сигнала у коинциденцији, као и амплитуда другог сигнала, а на послетку следи и временска разлика између времена појављивања ових сигнала. Овакав начин записивања даје велику флексибилност у даљој обради података и садржи све информације које би могле бити од користи у каснијој анализи, без икаквих губитака и потребе каснијег враћања и домеравања у експерименту. Коначно,

постоји могућност снимања и сукцесивних догађаја, са истом количином информација као и код претходног начина записивања податка. Последњи начин записивања података је додан програму како би постојала могућност одређивања средњег живота у распадима.

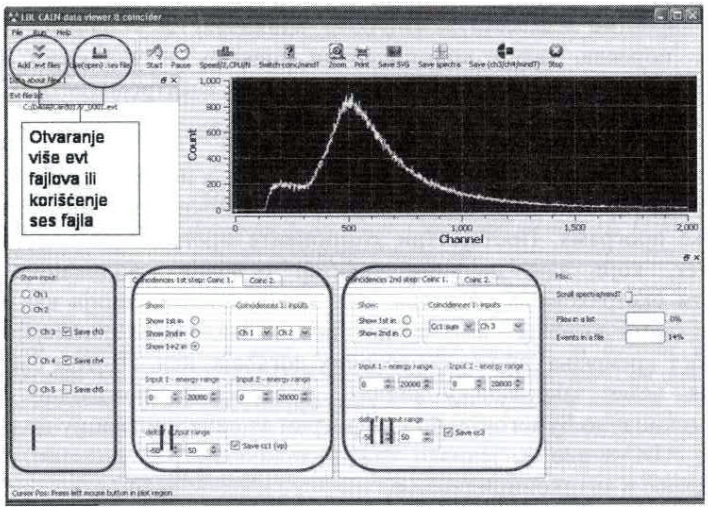

СЛИКА 1. Изглед прозора основног програма развијеног за анализу података у дигиталној спектроскопији у Нискофонској лабораторији Института за физику.

3. ПРОГРАМ TIMETOOLS

Овај програм служи временској анализи коинцидентних и сукцесивних догађаја, тј. користи за добијање временских серија произвољних података (канала). Овде треба напоменути могућности које се добијају анализом листа догађаја. Како у листи сваки догађај садржи информације о амплитудама сигнала који су у коинциденцији, као и временске разлике међу сигналима у коинциденцији, могуће је графички представити криву минималних временских разлика међу сигналима у коинциденцији – овде названу minDT кривом, или прецизније – Time to Amplitude (TAC) кривом минималних временских разлика времена појављивања сигнала у коинцидентим догађајима. Као пример флексибилности и могућности комплекснијег коришћења програма, напомињемо да програм даје могућности екстракције појединих спектралних линија и њихових minDT кривих, које могу да служе за одређивања времена живота одговарајућих нуклеарних стања. Други пример из области космичког зрачења би би одређивање сатних временских низова одброја пластичних сцинтилатора, у циљу испитивања временске структуре интензитета космичког зрачења.

4. ПРОГРАМ SYNCRONIZATION

Овај најновије развијен програм служи за коинцидирање и одређивање временске разлике међу улазним фајловима користећи синхронизациони сигнал на једном од улазних канала на уређају за аквизицију података - CAEN-у. Што се тиче коинцидирања, овај програм служи као проширење основног програма DataViewer. Наиме, Како DataViewer има ограничене могућности за коинцидирање и антикоиндицирање, овај програм нуди неограничене могућности и комплексност у овом домену. Ако је, на пример, жељени резулујући сигнал комбинација неколико брзих коинциденција и неколико антикоинциденција у закаснелим спектрима, ово је избор програма. Ова флексибилност проистиче из тога што је могуће сваки степен у коинциденцији / антикоинциденцији снимити у виду листа догађаја, и поново користити за следећи степен анализе овим програмом.

ЗАКЉУЧАК

Програмски пакет је развијан за потребе Нискофонске лабораторије и у потпуности је одговорио свим захтевима за анализом добијених података. Развијени алгоритми као и програми, међутим, довољно су општи да се могу користити у свим областима нуклеарне и честичне спектроскопије, амплитудске и временске, те се може очекивати њихова примена и у другим нуклеарним и честичним лабораторијама.

ЗАХВАЛНИЦА

Овај рад је реализован уз подршку Министарства за просвету, науку и технолошки развој Републике Србије, у оквиру пројекта ОИ 171002 .

ЛИТЕРАТУРА

[1] Dragić A. *et. al. Nucl. Tech. & Rad. Prot.*, Vol. **XXVI**, No. 3, 181-192 December 2011

ПОЛАРИЗАЦИЈА МИОНА КОСМИЧКОГ ЗРАЧЕЊА НА ПОВРШИНИ ЗЕМЉЕ И У ПОДЗЕМНОЈ ЛАБОРАТОРИЈИ

Д. Малетић[1)], А. Драгић[1)], Р. Бањанац[1)], Д. Јоковић[1)], Н. Веселиновић[1)], В. Удовичић[1)], Б. Грабеж[1)], М. Савић[1)], Ј. Пузовић[2)], И. Аничин

1) Универзитет у Београду – Институт за физику, Прегревица 118, 11000 Београд
2) Универзитет у Београду - Физички факултет, Студентски трг 12, 11000 Београд
e-mail: maletic@ipb.ac.rs

Апстракт. Проучавани су миони из космичког зрачења који се заустављају у пластичним сцинтилаторима на површини и подземној лабораторији. Поред одређивања брзине бројања одређиван је и спектар електрона из распада и степен поларизације заустављених миона. Прелиминарни резултати за Мишелов параметар дају вредности ниже него вредности у литератури, док је примећена асиметрија броја електрона из распада у горњој и доњој хемисфери значајнија од раније опсервиране, што указује на потпуну поларизацију миона из космичког зрачења.

1. УВОД

Детаљан опис лабораторије и апаратуре коришћене у овом раду налази се у [1]. Прво је одређен број заустављених позитивних миона из космичког зрачења у коришћеним детекторима - пластичним сцинтилаторима дебљине 5 cm. Сигнали из ових детектора су записивани у листу, односно записивани су амлитуда и време појављивања сигнала, за сваки догађај посебно, са резолуцијом од 10ns. Програмом који је развијен за обраду овакве врсте података из листе догађаја су екстраховани временски интервали између сукцесивних догађаја. Сигнатура позитивних миона који се заустављају и распадају је сукцесија сигнала – старт сигнал који се добија од заустављања миона и стоп сигнал који следи од детектовања електрона из распада миона, који не морају да депонују сву своју енергију у детектору (Слика 1.). Интервали између ових старт и стоп сигнала су дистрибуирани експоненцијално, са константом која одговара животу миона од 2.2 μs. Ова дистрибуција наседа на још једну експонеуиалну дистрибуцију која одговара Поасоновском одброју миона који пролазе кроз детектор, са константом реципрочном брзини бројања ових догађаја, која је реда 100 Hz. Ова друга расподела изгледа као константна у пределу прве расподеле и то до 20μs (Слика 2). Током ових мерења мртво време детектора је било или 1 или 4 μs, тако да овај део спектра времена између сукцесивних догађаја недостаје. Интеграљењем временске дистрибуције која одговара заустављеним и распаднутим мионима, и кориговање за недостајуће догађаје због мртвог

времена, добија се број заустављених миона на површини и у подземној лабораторији:

$$N_{GB}(\mu_{stop}) = 6\times10^{-2}m^{-2}s^{-1} \quad \text{и} \quad N_{UG}(\mu_{stop}) = 1.52\times10^{-2}m^{-2}s^{-1}$$

Затим се налазе амплитски спектри свих старт и стоп сигнала за два различита временска интервала – један на самом почетку временског спектра (означен као I на слици 2), и другог на самом крају, када је дистрибуција сигнала који долазе од мионског распада готово нестала (означен са II на слици 2). Разлика спектра стоп (II) интервала од старт (I) интервала сада даје прави спектар старт интервала који одговара спектру губитка енергије миона до њиховог заустављања (спектар означен као „Заустављени миони" на слици 3.). Иста процедура за стоп спектроне даје спектар губитака енергија позитрона који се или зауставе или изађу из детектора (спектар означен као „позитрони из распада" на слици 3.) За потребе упоређивања на истој слици је представљен много интензивнији спектар пролазећих миона (означен као Singles), чији спектар има максимум на вредсности око 10MeV. Примећено је да спектар заустављених миона, без обзира што има краћи пут у детектору, има максимум на вишој енергији него код миона који пролазе кроз детектор, што је и за очекивати и базирано је на чињеници да миони, који имају довољно ниске енергије да би се зауставили у детектору, имају вишу специфичну јонизацију од миона виших енергија који пролазе кроз детектор, који су практично минимално јонизујуће честице. Слика 3б представља резултате идентичног детектора постављеног у подземној лабораторији. Поређење слика 3а и 3б показује да спектар депоноване енергије миона у подземљу има максимум на нешто више од 20 MeV, док је маскимум спектра заустављених миона на површини на нешто нижој енергији.

Разлика између спектара позитрона из распада миона на површини и у подземљу је изражена. Спектар губитака енергије позитрона из распада на површини показује комплексу структуру; део спектра нижих енергија нестаје на око 4 MeV; више енергије имају максимум на око 7 MeV, а још више депоноване енергије имају нижи интензитет који се протеже до 50 MeV. Одговарајући спектар у подземљу нема овакву троструку структуру. На нижим енергијама интензитет има максимум на око 6 MeV, а више енергије досежу до 50 MeV. Могуће је да ова разлика међу ниско-енергетским деловима ова два спектра долази од различитог степена поларизације заустављених миона, с тим да су у подземљу вероватно скоро потпуно деполаризовани, а на површини још увек задржавају значајан степен поларизације. Ово ће, због особина неодржања парности у слабим интеракцјама, дати различиту угаону расподелу позитрона из мионских распада, што ће утицати на примећену разлику у одговарајућим енергетским спектрима.

Како би се горње претпоставке провериле постављљен је троструки сендвич од пластичних сцинтилационих детектора, велики пластични детектор (1 m2) усендвичен је међу два мања (0.125 m2), док су сигнали из свих детектора снимани бележењем њихових амплитуда и времена појављивања са 10 ns резолуцијом на три независна канала анализатора CAEN N1728B. Све релевантне комбинације коинцидирања и анти-коинцидирања међу детекторима дају информације које se користе у дискусији која следи.

СЛИКА 1. Дефиниције величина које се користе при изучавању миона космичког зрачења који се заустављају и распадају у 5 cm дебелом пластичном сцинтилатору

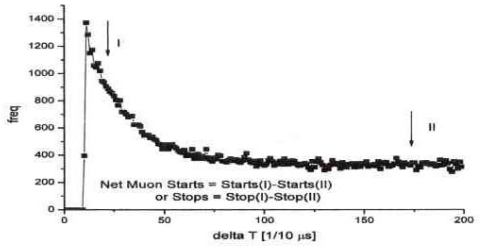

СЛИКА 2. Дистрибуција временских интервала између сукцесивних догађаја великог пластичног сцинтилатора (1 м2). Регион I садржи већину распада заустављених миона, док регион II садржи само «фон» који се састоји од временских интервала између пролазећих високо-енергетских миона.

Како је угаона дистрибуција упадних миона широка, а геометрија догађаја који су укључени у спектар комплексна, није могуће интерпретирати и извући смислени квантитативни закључак из значајне разлике која постоји између два спектра. Међутим, евидентно је да је број позитрона који се емитује у горњу хемисферу значајно већи од броја који се емитује у доњу хемисферу. Ово показује да миони који стижу на површину земље имају значајну поларизацију, која је преостала од процеса њихове креације из распада одговарајућих поларизованих пиона. Ова поларизација је већа од очекиване на основу резултата више ранијих мерења (нпр. види [2]). Једни могући разлог за ову разлику је различит материјал у коме се миони космичког зрачења заустављају јер пластични материјали имају знатно нижи средњи редни број од раније коришћених

зауставних средина. У току су иста мерења у подземној лабораторији, где још увек нема довољно статистике за коначан закључак.

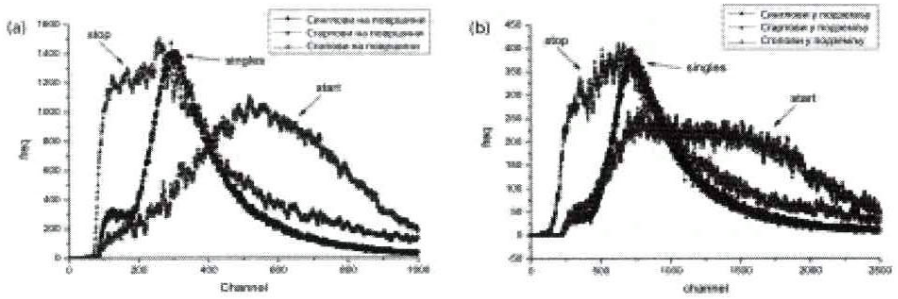

СЛИКА 3. а) Спектар пролазећих миона (Синглови), заустављьних миона (старт) и позитрона из распада миона (стоп) сви на површини, б) У подземљу.

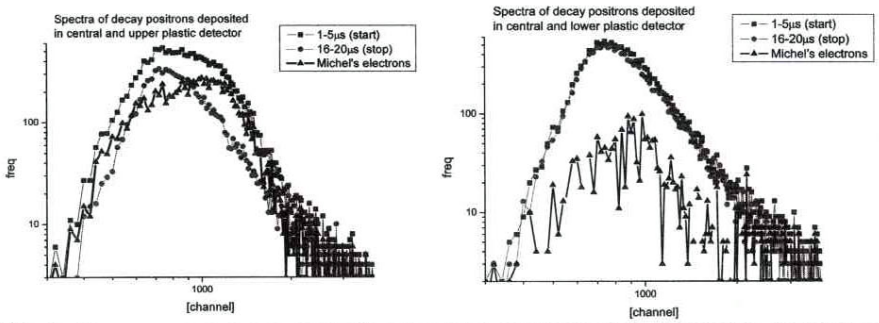

СЛИКА 4. Спектар депоноване енергије позитрона у централном детектору, сумиран са депонованом енергијом у детектору у ком се заустављају – горњем или доњем. Видљива је драстична разлика у броју позитрона регистрованих у горњој и доњој хемисфери.

ЗАХВАЛНИЦА

Овај рад је реализован уз подршку Министарства за просвету, науку и технолошки развој Републике Србије, у оквиру пројекта ОИ 171002 .

ЛИТЕРАТУРА

[1] Dragić A. *et. al. Nucl. Tech. & Rad. Prot.*, Vol. **XXVI**, No. 3, 181-192 December 2011
[2] Bradt H V and Clark G W *Phys. Rev.* **132** 1306–1316 1963

СЕМИ-ЕМПИРИЈСКА СИМУЛАЦИЈА ПРИРОДНОГ ФОНА У ПОДЗЕМНОЈ ЛАБОРАТОРИЈИ

Д. Малетић[1)], В. Удовичић[1)], Р. Бањанац[1)], А. Драгић[1)], Д. Јоковић[1)], Н. Веселиновић[1)], Б. Грабеж[1)], М. Савић[1)], Ј. Пузовић[2)], И. Аничин[1)]

1) Универзитет у Београду – Институт за физику, Прегревица 118, 11000 Београд
2) Универзитет у Београду - Физички факултет, Студентски трг 12, 11000 Београд
e-mail: maletic@ipb.ac.rs

Апстракт. У раду се описује метод за припрему симулационих података који могу да се користе као улазни узорци за произвољну Монте Карло симулацију. Претпостављамо да се спектар природног фона састоји од амбијенталног гама зрачења које се уводи семи-емпиријски, на основу анализе мереног природног фона германијумског детектора. Спектар космичког зрачења добија се коришћењем симулационог пакета CORSIKA. За добијање космички индукованог спектра за подземну лабораторију потребно је увести додатни корак у МК симулацијама (користећи Geant4) који служи за симулацију пропагације космичкког зрачења кроз земљу под којом се налази подземна лабораторија. Овако припремљени подаци користе се за Монте Карло симулације пластичних сцинтилатора и германијумских детектора окружених различитим материјалима.

1. УВОД

Метод који описујемо развијен је приликом изградње сендвич детектора (сцинтилатор-олово-сцинтилатор) с циљем добијања детектора који би био у могућности да раздваја доприносе радијационом спектру на оне који долазе од космичког зрачења од оних који долазе од зрачења амбијенталних радионуклида. За оптимизацију рада овог детектора потребна је добра Монте Карло (МК) симулација, односно добро дефинисан спектар долазећих зрачења.

За добијање узорка спектра природне радиоактивности користимо семи-емпиријски метод. Овај се метод базира на анализи линијског спектра реалног фона HPGe детектора који потиче од зрачења радионуклида из околине детектора.

За симулацију космичког зрачења користи се CORSIKA (COsmic Ray Simulation for KAskade) симулационог пакета. Овај програм симулира пропагацију примарног космичког зрачења и пљускова, који су индуковани овим примарним зрачењем, кроз атмосферу Земље.

2. СЕМИ-ЕМПИРИЈСКА СИМУЛАЦИЈА ПРИРОДНЕ РАДИОАКТИВНОСТИ

Овај метод називамо семи-емпиријски зато што користимо експерименталне податке како би одредили композицију спектра природне радиоактивности. Важан корак је идентификација и одређивање интензитета спектралних линија у фонском спектру HPGe детектора. Познавање криве ефикасности детектора тада омогућава да се у МК генератору догађаја користе реални интензитети у спектру присутних зрачења (Слика 1.).

Треба напоменути да при креацији финалног МК узорка на један начин третирамо радионуклиде из околине а на други радон и његове потомке, због претпоставке да се радон налази доминантно у ваздуху у околини детектора, док се потомци таложе на материјалима око детектора, зидовима и поду.

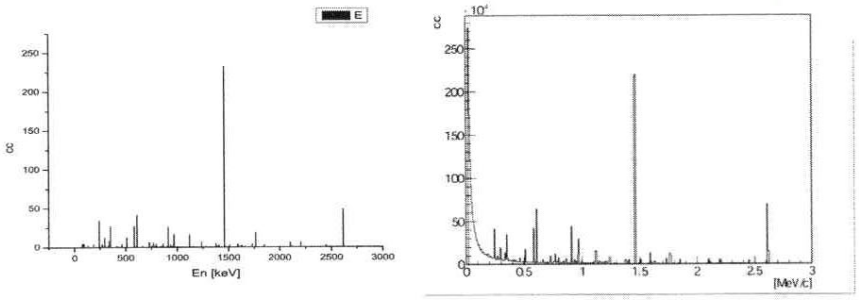

Слика 1. Идентификковане гама линије иницијалног HPGe спектра, и резултујући симулирани спектар природног фона.

За добијање финалног МК узорка коришћен је симулациони пакет Geant4, који се користи за симулације пропагације свих врста честица кроз материју. Користећи овај програм дефинисали смо геометрију детектора и његову околин као и њихов састав, претпостављајући да у околини постоји земљана облога дебљине 30 cm као и бетонски зид.

Радионуклиди су наусмично распоређени у земљи и бетону одакле се симулира пропагација емитованог гама зрачења у свим правцима. Када примарна или секундарна честица доспе до детектора, догађај се записује. Запис садржи информацију о врсти честице, њеној депонованој енергији и инцидентном импулсу.

Овако записани догађаји представљају први део МК узорка. Други део долази од симулације космичког зрачења.

3. СИМУЛАЦИЈА КОСМИЧКОГ ЗРАЧЕЊА

Спектар космичког зрачења, који долази до површинске лабораторије, симулиран је коришћењем програмског пакета CORSIKA који симулира интеракцију примарног космичког зрачења, као и пљускова које оно индукује, са атмосфером. Симулација укључује моделовање електромагнетске, хадронске и мионске компоненте космичког зрачења. Као излаз добијамо догађаје на опсервационој равни (на произвољној надморској висини) са назначеном врстом честица, позицијом на опсервационој равни и вектором импулса.

За потребе ових симулација развијена је симулација пропагације космичког зрачења кроз земљу. Ова симулација је урађена коришћењем Geant4 симулационог пакета (Слика 2.).

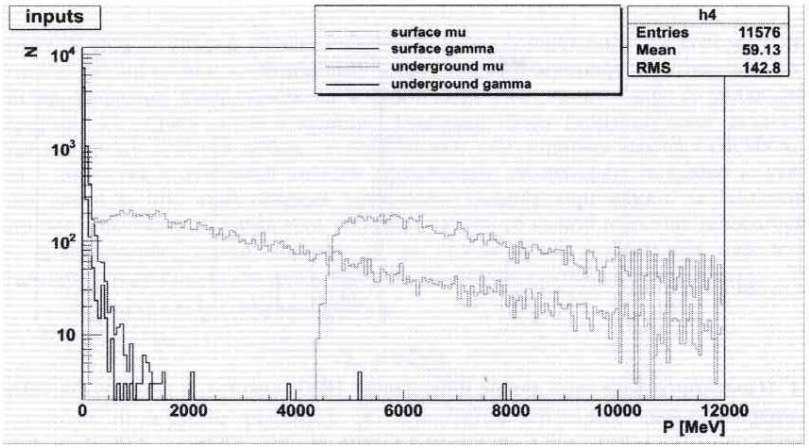

СЛИКА 2. Спектри космичког зрачења на површини и у подземној лабораторији.

4. КОРИШЋЕЊЕ И ТЕСТОВИ МК УЗОРКА

Овако добијен МК узорак догађаја природног фона и космичког зрачења тестиран је на разним детекторима, а као најважније, искоришћен је за оптимизацију дизајна сендвич детектора у изградњи. Поред овога, извршене су и симулације за пластичне сцинтилаторе на површини и у подземљу и симулације HPGe детектора са оловном заштитом. Најбољи доказ да су припремљени узорци добро дефинисани и да се МК симулације које користе овако припремљене МК узорке добро слажу са експериментом је поређење МК симулација и реалних података за спектре сцинтилационих детектора (Слика 3).

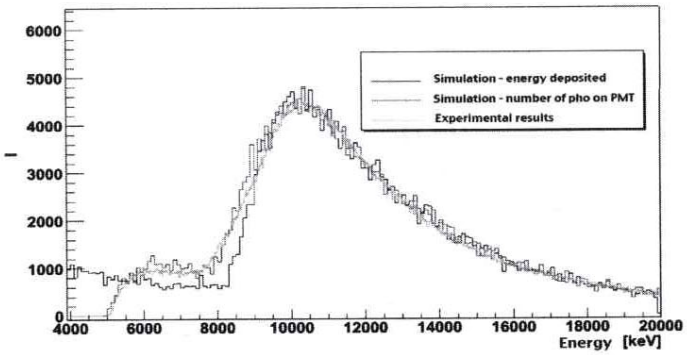

СЛИКА 3. Поређење МК симулација и мереног спектра пластичног сцинтилатора. Црна линија – симулација – само депонована енергија, црвена број фотона који долазе на фотомултипликаторе, зелено – експериментални подаци.

Наставак рада на усавршавању овог метода је неопходан како би се симулације фона на површини и у подземним лабораторијама додатно унапредиле, нарочито у погледу квалитета репродукције континуираних компоненти фонских спектара.

ЗАХВАЛНИЦА

Овај рад је спроведен уз подршку Министарства за просвету, науку и технолошки развој Републике Србије, у оквиру пројекта ОИ171002 .

ЛИТЕРАТУРА

[1] Dragić A. *et. al. Nucl. Tech. & Rad. Prot.*, Vol. **XXVI**, No. 3, 181-192 December 2011
[2] D. Heck, J. Knapp, J.N. Capdevielle, G. Schatz, T. Thouw, CORSIKA: A Monte Carlo Code to Simulate Extensive Air Showers, Forschungszentrum Karlsruhe Report FZKA 6019, 1998
[3] S. Agostinelli et. al., Geant4 - a simulation toolkit , *Nuclear Instruments and Methods in Physics Research* **A506**, 250-303, 2003

NA61/SHINE ЕКСПЕРИМЕНТ И ДЕТЕКТОРСКИ СИСТЕМ

Ј. Пузовић[1)], Б. Грабеж[2)], Д. Малетић[2)], Д. Јоковић[2)], М. Савић[2)], Д. Манић[1)]

1) Универзитет у Београду – Физички факултет, Студентски трг 12, 11000 Београд
2) Универзитет у Београду – Институт за физику, Прегревица 118, 11080 Земун
e-mail: jovan.puzovic@cern.ch

Апстракт. Преглед NA61/Shine експеримента. Експериментална поставка и циљеви. Опис детектора и подсистема.

1. NA61/SHINE ЕКСПЕРИМЕНТ И ЦИЉЕВИ

NA61/SHINE [1] (SPS Heavy Ion and Neutrino Experiment) је експеримент са фиксном метом на SPS акцелератору у CERN-у. Базиран је на свом претходнику, екперименту NA49, од кога је наследио и основну поставку. Значајан део детекторских система у међувремену је унапређен и осавремењен. Програм истраживања подразумева систематично мерење продукције хадрона у протон-протон, протон-језгро и језгро-језгро сударима у функцији енергије и маса честица пројектила и мете. Резултати ових мерења имају следеће циљеве: (1) потрагу за критичном тачком и проучавање продукције хадрона у граничном случају заробљености кваркова (onset of deconfinement) у релативистичким сударима јона, (2) боље разумевање продукције честица са високим трансверзалним импулсом у протон-протон и протон-језгро интеракцијама (high p_t particle supression ефект), (3) високо прецизна мерења хадрон-језгро судара чији резултати се користе у моделовању процеса у неутринским (T2K) и експериментима који проучавају интеракције космичких зрака са атмосфером (Pierre Auger, KASCADE) [2, 3, 4].

2. ДЕТЕКТОР

NA61/SHINE детектор представља спектрометар велике аксептансе (приближно 50% за $p_t \leq 2.5$ GeV), врло добре резолуције за импулс ($\sigma(p)/p^2$ је реда $10^{-4}(\text{GeV/c})^{-1}$) и осталих високих перформанси. Омогућава проучавање финалних хадронских стања продукованих у сударима разних честица пројектила (π, p, јони) са различитим фиксним метама у интервалу енергија снопова доступних на SPS акцелератору (импулса 13-158GeV/c по нуклеону).

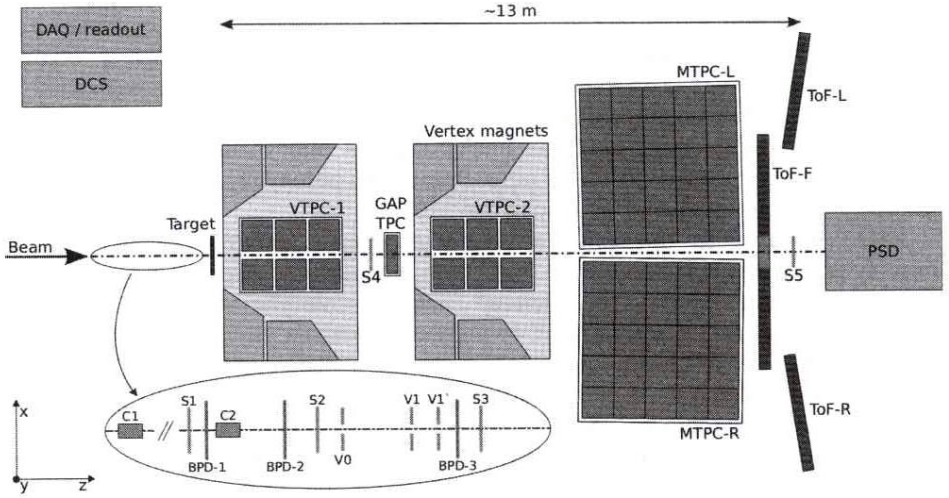

СЛИКА 1. Шематски приказ детектора NA61/Shine

Снопови честица које користи NA61/SHINE детектор потичу из SPS акцелератора. Примарни сноп честица који је прошао стандардни циклус убзавања (proton source, RFQ2, LINAC2, PSB, PS, SPS за протоне одн. ECR, RFQ, LINAC3, LEIR, PS, SPS за Pb јоне), судара се са фиксном примарном метом. Након селекције, жељене честице се транспортују дуж H2 линије до секундарне фиксне мете и главног детектора.

Дуж ове линије налази се више колиматора, бројача и детектора који служе за колимацију и усмеравање, контролу квалитета снопа и селекцију жељених честица пројектила. Међу овима најбитнији су CEDAR, Z и A детектори као и три BPD детектора.

Главни део система за детекцију трагова чине четири Time Projection коморе. Две мање (VTPC-1 и VTPC-2 димензија 2.0x2.5x0.67 m^3) налазе се у магнетном пољу. Две веће коморе (MTPC-L и MTPC-R димензија 3.9x3.9x1.1 m^3) се налазе низводно, постављене симетрично у односу на сноп. Такође, између два VTPC-а накнадно је додата једна мала комора (GTPC) која омогућава бољу реконструкцију трагова у екстраполацији ка примарном вертексу као и хелијумска цев која доприноси редукцији δ-електрона. Све коморе су напуњене мешавином аргона и угљен диоксида (у односу 95/5 за TPC и односу 90/10 за VTPC и GTPC). Магнети који обезбеђују магнетно поље су два идентична суперпроводна дипола са максималном моћи савијања од $9Tm$ при струји од 5000 ампера [5]. Овај систем је у стању да прати и до 1000 трагова честица у догађајима високог мултиплицитета. За сваки траг је са високом прецизношћу доступна информација о позицији и dE/dx информација.

Детектори времена прелета (TOF – Time Of Flight) се налазе иза главних MTPC комора. Укупно постоје три поддетектора или зида: TOF-L, TOF-R и TOF-F. TOF-L и TOF-R се састоје од по 891 сцинтилатора и укупне су површине $4,4m^2$

сваки. Постављени су симетрично у односу на сноп. Између њих се налазио (у периоду 2007.-2012.) TOF-F који се састоји од 80 сцинтилатора у облику вертикално орјентисаних плоча. У најновијој поставци TOF-F је уклоњен како би се омогућила инсталација PSD детектора. Информација добијена из TOF детектора у комбинацији са dE/dx информацијом омогућава одређивање масе честице, односно идентификацију исте. Временска резолуција за TOF-L и TOF-R износи око 90ps док за TOF-F износи око 110ps.

PSD представља последње велико унапређење детекторског система. У питању је хадронски калориметар [6, 7] чији је задатак да мери енергију честица посматрача (спектатора), на основу чега је могуће вршити селекцију централности судара. Састоји се од 44 модула (16 мањих унутрашњих и 28 већих спољашњих). Сваки модул се са стоји од 60 олово/сцинтилатор слојева. За колекцију светла задужени су силиконски фотомултипликатори (SiMP тј. Micro-pixel Avalanche Photodiodes – MAPD).

LMPD је део детекторског система од 2012. године и служи за детекцију протона ниског импулса. Број таквих честица носи додатну информацију о централности судара. Основу овог детектора чине две мале Time Projection коморе унутар којих се налази више неизменично постављених детекционих и апсорпционих слојева.

На NA61/SHINE експерименту користи се велики број различитих мета. Типови мета варирају од течног водоника, преко металних мета различите дебљине до реплика угљеничних мета које се користе у неутринским и експериментима са космичким зрачењем.

Аквизиција података је под надзором савременог DAQ система док је у току рада помоћу DCS апликације могуће пратити стање система за гас, високе и ниске напоне као и рад PSD детектора.

Као софтверска подршка целом систему развијено је потпуно ново и савремено софтверско окружење, које се по аналогији са именом експеримента такође зове *SHINE*. Његова улога је да омогући потпуну интеграцију свих алата за реконструкцију, симулацију и обраду података на јединствен и систематичан начин.

3. БЕОГРАДСКИ SHINE ТИМ

Београдски SHINE тим је члан NA61/SHINE колаборације од 2011. године. Група је ангажована на свим нивоима активности на експерименту, а међу тренутним задужењима се налазе: одржавање и надгледање TOF детектора (неколико чланова групе су expert-on-call за дати систем), унапређење и развој HV система на TOF детектору, координација и имплементација новог TOF read-out система, продукција података, развој софтвера везаног за TOF у Shine окружењу, анализа продукције барионских резонанци, анализа продукције K^0 мезона у протон-протон интеракцијама.

ЗАХВАЛНИЦА

Овај рад је спроведен уз подршку Министарства за просвету, науку и технолошки развој Републике Србије, у оквиру пројекта ОИ171002.

ЛИТЕРАТУРА

[1] *NA61/SHINE homepage* [http://na61.web.cern.ch]
[2] N. Antoniou et al. (NA61/SHINE Collaboration), *Report No. CERN-SPS-2007-004*, 2007
[3] N. Abgrall et al. (NA61/SHINE Collaboration), *Report No. CERN-SPS-2008-018*, 2008
[4] B. Popov, *Nuclear Physics B Proceedings Suplement 00*, 1-8 (2012)
[5] S. Afanasiev at al., *Nucl. Instr. And Meth. A* **430**, 210 (1999)
[6] G.A. Alekseev at al., *Nucl. Instr. And Meth. A* **461**, 381 (2001)
[7] J. Fuyii, *Nucl. Instr. And Meth. A* **453**, 237 (2000)

ЗАВИСНОСТ ПРИНОС НЕУТРОНА ОД ПРИТИСКА РАДНОГ ГАСА У УРЕЂАЈУ ПЛАЗМА ФОКУС

В. Удовичић[1)], Н. Веселиновић[1)], А. Драгић[1)], Р. Бањанац[1)], Д. Јоковић[1)], Д. Малетић[1)] и Д. Јоксимовић[2)]

1) Институт за физику, Универзитет у Београду, Прегревица 118, 11000 Београд
2) Факултет за послове студије, Мегатренд универзитет, Гоце Делчева 8, 11000 Београд
e-mail: udovicic@ipb.ac.rs

Апстракт. У оквиру Нискофонске лабораторије за нуклеарну физику, Института за физику у Земуну већ двадесетак година са доста успеха одвијају се експериментална и теоријска истраживања на уређају плазма фокус. До сада је створена велика база података, на основу бројних серија мерења од којих је у овом раду посебно анализирана зависност приноса неутрона од притиска деутеријума у комори плазма фокуса. Добијени резултати су упоређивани са резултатима других аутора, као и најсвеобухватнијим моделом који описује све најзначајније фазе и процесе у плазма фокусу, моделом Lee-a.

1. УВОД

Контролисана термонуклеарна фузија представља у последњих педесетак година велики изазов за истраживаче. Главни циљ, а уједно и основни проблем је постизање услова за паљење плазме и с тим у вези изградња економичног и еколошки прихватљивог реактора. Параметар који карактерише услов паљења је производ $R = n\tau_E T_i$ (реактивност плазме), где је n концентрација јона плазме, τ_E време одржавања (конфинирања) и T_i температура јона у плазми, а чија вредност мора бити већа од 3×10^{21} $m^{-3}s$ keV. Временом су се развили разни уређаји за магнетно конфинирање плазме на основу два различита приступа. У прву групу уређаја спадају јакострујна импулсна електрична пражњења праћена пинч-ефектом у различитим геометријама (линеарни или з-пинч, тороидални пинч, тета-пинч, плазма фокус, ...). Друга група уређаја се заснива на употреби разних магнетних клопки, код којих се магнетна поља потребна за конфинирање плазме постижу спољашњим струјама (уређај са минимумом-Б, стеларатор, токамак, ...).

Тема овог рада јесу управо уређаји у којима се генерише фузиона плазма у импулсним електричним пражњењима, прецизније један од њих а то је плазма фокус. У оквиру Нискофонске лабораторије за нуклеарну физику, Института за физику у Земуну већ неких двадесетак година са доста успеха раде се експериментална и теоријска истраживања на плазма фокусу пројектованом и изграђеном у Институту за физику, Земун.

Плазма фокус реализован у Нискофонској лабораторији Института за физику у Земуну спада, по својим карактеристикама и депонованој енергији у ред

мањих машина. Овај уређај је могуће оптимизовати, у зависности од радног гаса, да даје оптималан принос X зрака или да даје принос неутрона реда 10^7 неутрона по циклусу. Неутрони настају фузијом деутеријума као радног гаса. Они се детектују помоћу сцинтилационог детектора а струјни параметри уређаја се прате преко осцилоскопа. Током година рада добијена је значајна база података, при чему је у овом раду приказана зависност приноса неутрона од притиска радног гаса, у овом случају деутеријума. Посебно је анализирана добијена зависност и упоређена са најсвеобухватнијим моделом који описује све најзначајније фазе и процесе у плазма фокусу, Lee модел (http://www.plasmafocus.net/).

2. ПОСТАВКА ЕКСПЕРИМЕНТА

Схема плазма фокус уређаја у Нискофонској лабораторији за нуклеарну физику, Института за физику у Земуну дата је на Сл. 1.

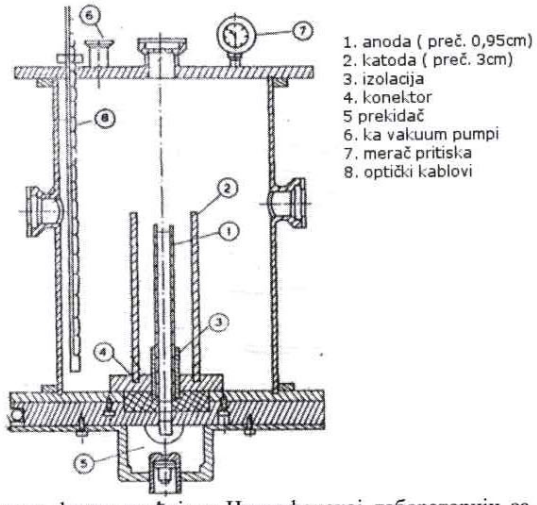

СЛИКА 1. Схема плазма фокус уређаја у Нискофонској лабораторији за нуклеарну физику, Института за физику у Земуну.

Главни део система за прикупљање података је дигитални осцилоскоп Tektronix TDS540A. Мерење напона врши са са високо напонском сондом (Tektronix P 6015A) са несигурношћу од 1%. Роговски калем, смештен између проводних бакарних трака, снима извод струјног сигнала. Добро фокусирање се добије ако се коинцидира време када је струја у пику са доласком струјног листа плазме на врх централне електроде. У овом случају, осцилограм показује сигнал са јаким електромагнетним сметњама (ЕМИ) које интерферирају близу максималне вредности струје. Постојање ЕМИ импулса који следи после сваког фокуса плазме снажно утиче на коришћење електронских дијагностичких

инструмената. Због осетљивости наших нуклеарних електронских инструмената на ЕМИ, сигнали из фотомултипликатора се мешају и евидентирају се на осцилоскопу. Мерења укупног приноса неутрона су спроведена помоћу великог (600 литара) течног сцинтилационог детектора допираног са гадолинијумом Gd-155 и Gd-157 (NE343). Систем детекције је у стању да детектује Д-Д фузионе неутроне емитоване истовремено у широком временском интервалу (око 40 μs) са ефикасношћу детекције појединачног неутрона од око 80%. Калибрација детектора на импулсном извору неутрона, као што су плазма фокуса уређаји, потпуно је описан у [1].

За нумеричку симулацију плазма фокус уређаја у Земуну коришћен је нумеричка симулација развијена од стране Lee (http://www.plasmafocus.net/) и то верзија File7RADPF05.15b. Ова симулација омогућује реалистичну симулацију свих параметара плазме користећи временски профил струјног сигнала.

3. РЕЗУЛТАТИ И ДИСКУСИЈА

За упоређивање експерименталног приноса неутрона и симулираног користили смо, у симулацији, исте параметре као у експерименту; индуктивност, капацитативност кондензатора, радни напон уређаја, радни притикак деутеријума као и дужину и пречник електрода. Експериментални резултати зависности приноса неутрона од притиска као и поређење са резултатима симулације су приказани на Сл 2.

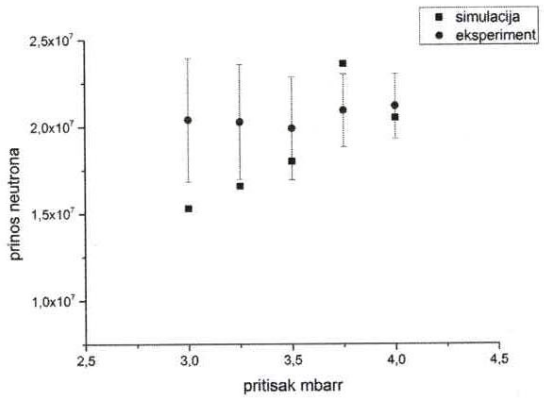

СЛИКА 2. Зависност експерименталног и симулираног приноса неутрона од притиска

Принос неутрона добијен Lee-јевом нумеричком симулацијом показује добро поклапање са експериментално добијеним приносима. Стога, Lee-јева симулација [2], [3] се може користити за оптимизовање плазма фокус уређај у Нискофонској лабораторији у Земуну. Уз бољу заштиту од ЕМИ импулса и

реорганизовањем кондензаторких батерија могуће је остварити учесталија пражњења плазме. Овај плазма фокус уређај се онда може користити за неутронску активацију и продукцију краткоживећих изотопа или као извор високо енергетских X-зрака за индустријске примене.

ЗАХВАЛНИЦА

Овај рад је спроведен уз подршку Министарства за просвету, науку и технолошки развој Републике Србије, у оквиру пројекта ОИ171002.

ЛИТЕРАТУРА

[1] В. Удовичић, Приноси нуклеарних реакција лаких јона у плазми импулсних електричних пражњења, Докрторска дисертација, Универзитет у Београду (2006).
[2] S Lee ,S H Saw, Neutron Scaling Laws from Numerical Experiments, Journal of Fusion Energy 27, pp. 292-295 (2008).
[3] S. Lee, S.H. Saw, L. Soto, S.V. Springham, S.P. Moo, Numerical experiments on plasma focus neutron yield versus pressure compared with laboratory experiments, Plasma Physics and Controlled Fusion 51, 075006 (2009).

Универзитет у Београду
Физички факултет

Михаило Р. Савић

Моделовање утицаја атмосфере на мионску компоненту секундарног космичког зрачења

Докторска дисертација

Београд, 2019. године

University of Belgrade
Faculty of Physics

Mihailo R. Savic

Modeling of atmospheric effect on muon component of secondary cosmic rays

Doctoral Disertation

Belgrade, 2019

Ментор:
Виши научни сарадник
Др Димитрије Малетић
Институт за физику, Универзитет у Београду

Чланови комисије:

Редовни професор
др Миодраг Крмар
Департман за физику, Природно-математички факултет,
Универзитет у Новом Саду

Ванредни професор
др Марија Димитријевић-Ћирић
Физички факултет, Универзитет у Београду

Доцент
др Душко Латас
Физички факултет, Универзитет у Београду

У Београду 2019. године

Ова докторска дисертација урађена је у оквиру Нискофонске лабораторије за нуклеарну физику "Др Радован Антанасијевић" Института за физику у Београду и представља део напора да се пружи што комплетнија слика проблематике детекције космичког зрачења земаљским детекторима

Постоји низ људи без чијег доприноса рад на овој дисертацији не би био могућ. Ту пре свега мислим на мог ментора др Димитрија Малетића, као и колегу др Александра Драгића, чије идеје представљају значајну инспирацију за велики део овог рада. Такође, велику захвалност дугујем сарадницима из Нискофонске лабораторије др Владимиру Удовичићу, др Радомиру Бањанцу, др Дејану Јоковићу, др Николи Веселиновићу и Давиду Кнежевићу, као и Владимиру Савићу, од којих је свако дао посебан и незаменљив допринос.

Речима је тешко описати значај који је за мене и многе друге проф др Иван Аничин имао као научник, ментор, мотиватор и изнад свега човек. Увек ћемо га се сећати са пуно љубави.

Коначно, хвала Аки, Невени, Милени и Вери на безграничној љубави, подршци и стрпљењу.

Моделовање утицаја атмосфере на мионску компоненту секундарног космичког зрачења

Резиме

Моделовање утицаја метеоролошких ефеката на флукс космичких миона осим фундаменталног има и практичан значај. Корекцијом датих ефеката повећава се осетљивост мионских монитора на варијације неатмосферског порекла.

У раду се уводе два нова метода за анализу и корекцију флукса космичких миона. Оба су у потпуности емпиријска и захтевају познавање атмосферског притиска и температурског профила атмосфере. Први метод заснива се на техници декомпозиције на основне компоненте. Други метод се базира на примени алгоритама за мултиваријантну регресију.

Корекција метеоролошких ефеката на основу уведених метода значајно смањују варијансу и амплитуду годишње варијације флукса миона. Методи су универзално применљиви и омогућавају екстензију на већи број улазних варијабли.

Кључне речи: космичко зрачење, миони, метеоролошки ефекти, декомпозиција на основне компоненте, мултиваријантна анализа
Научна област: Физичке науке
Ужа научна област: Физика језгара и честица

Modeling of atmospheric effects on cosmic ray muons

Abstract

Varying conditions in the atmosphere affect the propagation of cosmic ray muons. Adequate description of variations induced by meteorological effects is necessary for understanding the variations of non-atmospheric origin.

Two novel methods for analysis of meteorological effects are introduced. Both are fully empirical and require knowledge about atmospheric pressure and temperature profile of the atmosphere. First method is based on principal component analysis, while second is based on multivariate regression algorithms.

Muon count time series thusly corrected for meteorological effects have significantly smaller variance and reduced amplitude of annual variation. Methods are universally applicable and allow for easy extension of the set of input variables.

Key words: cosmic rays, muons, meteorological effects, principal component decomposition, multivariate analysis
Scientific field: Physics
Narrow scientific field: Nuclear and particle physics

Садржај

Увод

Историјат физике космичког зрачења почиње чувеним експериментима Виктора Хеса (*Victor Francis Hess*) из 1912. године. Он је тада, у серији летова балоном, показао да интензитет непознатог извора јонизације ваздуха расте са висином, те да исти не може бити земаљског порекла. Након што је тако утврђено да је ово зрачење неатмосферског порекла, названо је "космичким". Вишегодишња дебата о природи космичког зрачења разрешена је на основу неколицине експеримената изведених током друге половине тридесетих година прошлог века. Мерењем интензитета космичког зрачења на различитим географским ширинама, Комптон (*Compton*) и други недвосмислено су показали да постоји зависност. То је значило да се космичко зрачење мора у највећој мери састојати од наелектрисаних честица и да није електромагнетне природе, мада се име до тада већ уврежило.

У својој најранијој фази, физика космичког зрачења се пре свега бавила природом и особинама детектованих честица, па је најближе била повезана са честичном физиком. Међутим, када су честична физика и теорија поља већ биле у стању да адекватно опишу већину интеракција честица космичког зрачења, централна питања дисциплине постала су порекло и природа модулације. Да би одговорила на ова питања, физика космичког зрачења морала је да изађе изван оквира честичне физике. Питање порекла честица космичког зрачења залази у домен астрофизике, док питање модулација залази у домен физике плазме и геомагнетизма. Стога се физика космичког зрачења данас налази на размеђи свих ових дисциплина.

Данас, више од једног века након првих експеримената, истраживања у оквиру физике космичког зрачења не само да не посустају, већ чак добијају

и нови замах. Иако су углавном познати механизми и развијени пратећи модели који адекватно описују већину феномена, постоји и даље велики број питања на која модерна физика космичког зрачења покушава да дâ што прецизнији одговор. Нека од њих су: порекло и механизми убрзања и пропагације примарних честица, састав и природа примарног космичког зрачења, интеракција космичког зрачења са магнетним пољима (галактичким, хелиомагнетним, геомагнетним) и атмосфером, интеракција космичког зрачења са живим организмима и друга.

Већина поменутих феномена тиче се примарног космичког зрачења, односно високоенергетских честица пореклом ван нашег соларног система. Интензитет ових честица модулисан је варијацијама магнетних поља кроз која пролазе, те је на основу мерења истог могуће индиректно проучавати феномене у хелиосфери и магнетносфери.

У интеракцији примарног космичког зрачења са језгрима атома атмосфере долази до продукције већег броја секундарних честица, односно секундарног космичког зрачења. Ово секундарно космичко зрачење се, након проласка кроз атмосферу, детектује земаљским детекторима. Променљиви услови у атмосфери утичу на пропагацију секундарног космичког зрачења, па тиме и на варијацију детектованог интензитета. Стога, што боље познавање ових метеоролошких ефеката је, осим од директног интереса, значајно и за уклањање варијација атмосферског порекла, како би се олакшало проучавање варијација неатмосферског порекла земаљским детекторима.

У последње време, све више експеримената је засновано на детекторима инсталираним на сателитима, како би се што директније мериле карактеристике примарног космичког зрачења. Међутим, ограничена величина и комплексност ових детектора условљавају максималне енергије које се тако могу детектовати. Због тога земаљски детектори и даље имају велики значај. Иако најпознатије експерименте представљају велике мреже детектора, и даље два најбројнија типа земаљских детектора су неутронски и мионски монитори. Ови други се базирају на детекцији мионске компоненте секундарног космичког зрачења и за њих су нарочито значајни метеоролошки ефекти, пре свега барометарски и

температурски.

У Нискофонској лабораторији за нуклеарну физику Института за физику у Београду, између осталог мери се и интензитет мионске компоненте секундарног космичког зрачења. Актуелна експериментална поставка састоји се од два идентична мионска монитора, од којих се један налази у надземном делу лабораторије (на нивоу тла), док се други налази у подземној лабораторији (на дубини од $12m$) и континуално мери флукс миона од 2009. године.

Ова докторска дисертација се бави проучавањем и моделирањем метеоролошких ефеката на мионску компоненту секундарног космичког зрачења, као и применом корекција на дате ефекте на основу различитих модела. Анализа се базира на подацима мереним мионским мониторима у оквиру Нискофонске лабораторије за нуклеарну физику, као и моделованим и мереним метеоролошким параметрима. Полази се од описа и примене постојећих, да би се затим демонстрирала два потпуно нова модела и асоцирани методи корекције метеоролошких ефеката.

Текст дисертације је подељен на седам поглавља, од којих прво представља овај увод.

У другом поглављу представљени су извори и механизми убрзања, неке основне карактеристике (хемијски састав, енергетски спектар и др.), главни механизми модулације и асоциране варијације интензитета примарног космичког зрачења. Такође, описани су неки основни процеси у оквиру честичне физике значајни за формирање и пропагацију каскада секундарног космичког зрачења, дат преглед главних карактеристика пропагације ових каскада, као и неке особине мионске компоненте.

У трећој глави су представљени различити емпиријски и теоријски модели метеоролошких ефеката на мионску компоненту секундарног космичког зрачења, методи за корекцију развијени на основу датих модела, као и резултати примене ових метода на подацима мереним у Нискофонској лабораторији.

У четвртом поглављу је описана експериментална поставка, формат и основне технике процесирања мерених података, као и извори и обрада метеоролошких параметара неопходних за анализу.

У петом поглављу се уводи емпиријска анализа метеоролошких ефеката применом технике декомпозиције на основне компоненте и демонстрира ефикасност одговарајуће корекције.

У шестом поглављу се уводи емпиријска анализа метеоролошких ефеката применом метода за мултиваријантну регресију имплементираних у TMVA пакету, у оквиру ROOT окружења за анализу.

Седмо поглавље представља закључак који сумира и пореди уведене методе.

Резултати представљени у овој дисертацији објављени су у три рада у референтним међународним часописима и презентовани на две међународне конференције.

Космичко зрачење

Космичко зрачење у ужем смислу се најчешће дефинише као флукс честица које из свемира долазе до Земљине атмосфере [1]. Некада се користи и строжија дефиниција која подразумева само наелектрисане честице пореклом ван сунчевог система [2]. Ипак, често се под космичким зрачењем (КЗ) у ширем смислу подразумева сво зрачење које долази до Земље, као и честице које настају у интеракцији горе поменутог космичког зрачења са језгрима атома атмосфере. Тада се уводи подела на *примарно космичко зрачење (ПКЗ)*, које се односи на компоненту присутну изнад атмосфере и *секундарно космичко зрачење (СКЗ)*, које се односи на компоненту присутну у атмосфери [3].

2.1 Примарно космичко зрачење

Примарно космичко зрачење можемо дакле најшире дефинисати као честице и фотоне са енергијом бар неколико редова величине вишом од термалне енергије позадинске плазме дате средине [4]. По пореклу и врсти најзначајнијих интеракција, проблематика ПКЗ се се може поделити у две одвојене групе питања. Прва се бави процесима настанка и транспорта ПКЗ, као и структуром енергетског спектра ПКЗ у близини Земље, где главну улогу имају процеси који се одвијају ван соларног система. Друга се бави варијацијама и процесама који модулишу интензитет ПКЗ, где доминирају процеси унутар соларног система.

2.1.1 Порекло и енергетски спектар

Примарно космичко зрачење се углавном састоји од протона, у мањој мери од језгара хелијума и у малом проценту тежих језгара, електрона, позитрона и

осталог зрачења. Иако су извори и процеси настанка примарног космичког зрачења још увек непотпуно познати, једна од могућих подела на основу порекла била би подела примарног космичког зрачења на [4]:

Екстрагалактичко, обично врло високих енергија (до 10^{21} eV), пореклом из различитих објеката ван наше галаксије, као што су радио галаксије, квазари и други извори интензивног зрачења у васиони.

Галактичко, енергија већих од $10^{15} - 10^{15}$ eV, које углавном потиче из експлозија и остатака експлозија супернових, магнетосфера пулсара и система двоструких звезда, ударних таласа у међузвезданом простору и сл.

Соларно, са енергијама до 15-30 GeV, које настаје у соларној корони током интензивних соларних бакљи.

Интерпланетарно, са енергијама 10-100 MeV, генерисано интензивним интерпланетарним и рубним ударним таласима у хелиосфери.

Магнетосферно, са енергијом до 30 keV, које настаје у Земљиној магнетосфери.

Иако је знање о могућим изворима, механизмима убрзања и пропагације примарног космичког зрачења и данас у одређеној мери непотпуно, рад на дубљем познавању ових процеса се наставља и општа слика постаје све комплетнија. Детаљни подаци о хемијској обилности елемената који сачињавају примарно космичко зрачење, изотропност, студија временских варијација, развој магнетне хидродинамике и оптичке и радио-астронимије већ је почетком друге половине двадесетог века показао да је примарно космичко зрачење најмање галактичког порекла. Тада су развијени и основни модели који су описивали процесе инјекције, убрзања и интеракције са међузвезданим гасом [5].

Прецизнија мерења обилности језгара појединих елемената у примарном космичком зрачењу, јаснија слика њихових интеракција са међузвезданим гасом као и одсуство антијезгара показала су да су највероватнији процеси у којима настаје ПКЗ експлозије супернових и убрзавање честица међузвезданог гаса, пре свега унутар наше галаксије, уз могуће изворе ван-галактичког порекла [6]. Поред тога, указала су на различите транспортне процесе у којима учествује ПКЗ, као што су: јонизациони губици (углавном значајни за протоне и тежа

језгра), спалациони процеси, радиоактивни распади, синхротронско зрачење и инверзни Комптонов ефекат (значајни за електроне и позитроне), интеракције са нехомогеним магнетним пољима и слично, а такође укључила и додатне могуће изворе као што су црне рупе и активна галактичка језгра [7].

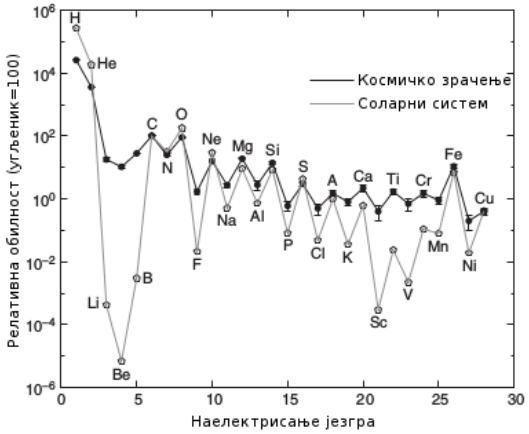

Слика 2.1: Релативна обилност језгара у примарном космичком зрачењу, мерена у околини Земље (пуни кругови), у поређењу са обилношћу језгара у Сунчевом систему (празни кругови), у односу на претпостављену обилност за угљеник 100 [8]

.

Савремена истраживања су потврдила већи део поменутих претпоставки и дала кохерентнију општу слику, иако нека питања и даље остају отворена. Питање порекла примарног космичког зрачења се стога састоји од три повезана али донекле посебна питања: питање порекла честица ПКЗ, питање извора енергија убрзања и питање области у којој до убрзања долази [9].

На основу посматрања дифузног гама зрачења енергија виших од 100 MeV, које углавном потиче из распада неутралних пиона продукованих у интеракцији ПКЗ са међузвезданим гасом, закључује се да је највећи део умеренорелативистичких честица ПКЗ галактичког порекла, док структура енергетског спектра и жиро-радијус који би одговарао високоенергетским честицама указују на њихово вангалактичко порекло. Релативна обилност језгара ПКЗ се

поклапа са обилношћу језгара међузвезданог гаса, односно обилношћу језгара у нашем Сунчевом систему (слика 2.1), а одступања се у највећој мери могу објаснити добро познатим процесима у којима ПКЗ учествује у току пропагације кроз међузвездани простор. На основу тога се закључује да практично све честице ПКЗ потичу из међузвезданог гаса, а не из неких егзотичних процеса.

Процењено је да се снага која одговара опаженој луминозности ПКЗ у нашој галаксији налази у интервалу од 6×10^{33} W до 3×10^{34} W. Једини извори енергије унутар галаксије способни да произведу такву снагу, а који се такође могу асоцирати са процесима убрзања наелектрисаних честица, представљају експлозије супернових. Што се вангалактичких извора тиче, најбоље кандидате представљају активна галактичка језгра, мада постоји и низ других претпостављених извора као што су: експлозије гама зрака (*gamma bursts*), акрециони ударни таласи црних рупа [7] и група галаксија [10] и други. Као највероватнији процес убрзања честица ПКЗ издваја се модел убрзања путем дифузије унутар ударног таласа (*difussion shock acceleration - DSA*), који представља један облик Фермијевог модела убрзања. Ударни таласи унутар којих би такав процес био могућ типично прате експлозије супернових. Механизам је најефикаснији када остаци експлозије супернове уђу у Тејлор-Седов фазу, односно неколико стотина година након експлозије. Слични процеси су могући и код ударних таласа који прате поменуте вангалактичке могуће изворе ПКЗ.

Енергетски спектар свих честица ПКЗ, независно од масе или наелектрисања, покрива распон енергија већи од десет редова величине, почев од енергија испод 1 GeV до енергија већих од 10^{11} GeV. Интензитет зрачења се обично изражава у јединицама GeV по језгру.

На слици 2.2 приказан је енергетски спектар свих честица примарног космичког зрачења у интервалу енергија од 1 MeV до преко 100 EeV (10^{20} eV). Нискоенергетски део спектра, енергија до 10 GeV, са израженим седлом и грбом, јако варира услед интеракције са сунчевим ветром (о чему ће бити више речи касније). Зато неки аутори сматрају да је практично немогуће знати нешто поузданије о спектру галактичког ПКЗ на енергијама нижим од 300 MeV [7].

На енергијама изнад 10 GeV, приказан на логаритамско-логаритамској ска-

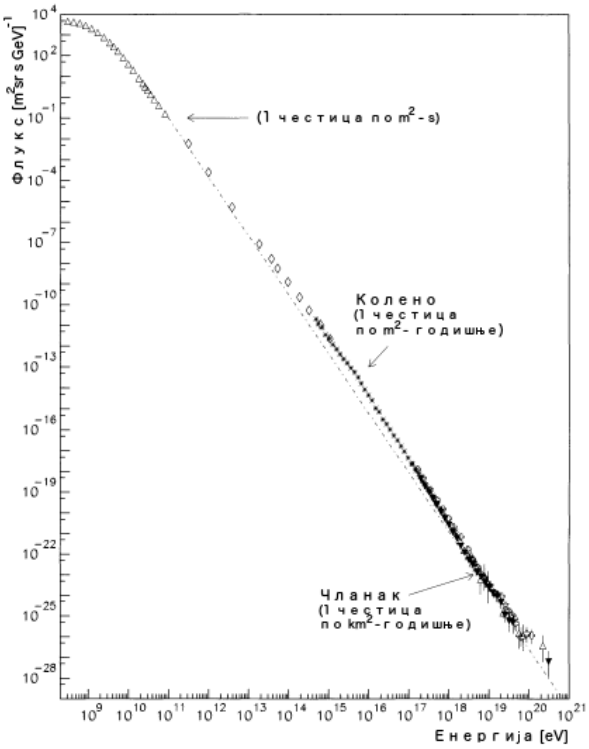

Слика 2.2: Диференцијални енергетски спектар свих честица примарног космичког зрачења [11].

ли, спектар ПКЗ је малтене константног нагиба, осим благе промене до које долази на енергији блиској 3×10^{15} eV, где се формира такозвано *колено*. Спектар је у том интервалу добро описан експоненцијалном зависношћу облика:

$$j(E) \sim E^{-\gamma_{1,2}}, \tag{2.1}$$

где се експонент $\gamma_1 = 2.68$ (≈ 2.7) односи на интервал лево од колена, а експонент $\gamma_2 = 3.15$ (≈ 3.1) на интервал десно од колена [1]. Природа колена и даље није сасвим разјашњена. Иако на енергијама блиским енергији колена долази до промене експерименталних техника које се користе, односно преласка са непосредних мерења на мерења помоћу мреже земаљских детектора, искључена

је могућност да је узрок опажене промене нагиба систематска експериментална грешка [12]. Релативне обилности појединих језгара зависе од енергије те самим тим и хемијски састав интегралног спектра ПКЗ није исти на различитим енергијама. Стога је једно могуће објашњење да је колено последица сумирања парцијалних спектара, донекле различитих нагиба (повећан допринос језгара хелијума [13] или других тежих елемената, као што су угљеник, азот, кисеоник или гвожђе [1]). Друга објашњења претпостављају вишестепене механизме убрзања или већи допринос вангалактичких извора ПКЗ [12].

Сличне идеје се користе да би објасниле поновну промену нагиба до које долази на енергији реда величине 10^{19} eV, када се вредност нагиба смањује и поново бива $\gamma \approx 2.7$. Део спектра на коме долази до ове промене назива се *чланак*. Примарно космичко зрачење енергија значајно изнад чланка било би у супротности са очекиваним Грајзен-Зацепин-Кузмин (ГЗК) ефектом, који предвиђа да, услед интеракције са позадинским макроталасним зрачењем, енергија примарног космичког зрачења мора бити ограничена и процењује вредност ове границе на $(3-5) \times 10^{19}$ eV. Упркос ранијим негативним резултатима, најновији подаци Пјер Оже (Pierre Auger) опсерваторије у Аргентини потврђују да на ултрависоким енергијама заиста долази до очекиваног пада интензитета [9].

2.1.2 Временска варијација и ефекти модулације

Интензитет примарног космичког зрачења у близини Земље није сталан већ је временски и просторно зависан. Ово се нарочито односи на честице енергија у интервалу од 10^8 eV до 10^{11} eV [14]. Временске варијације су углавном везане за ефекте у области у којој је доминантно интерпланетарно магнетно поље - *хелиосфери*, чија динамика зависи од интензитета сунчеве активности и различитих догађаја на Сунцу. Просторне варијације су пре свега последица ефеката у области у којој доминира Земљино магнетно поље - *магнетносфери*. Интензитет интерпланетарног магнетног поља на растојању од Сунца које одговара орбити Земље је око 5 nT (50 μG), док на површини Земље интензитет магнетног поља варира између 30 μT (0.3 G) и 60 μT (0.6 G). За потпуније разумевање порекла варијација ПКЗ је пре свега непоходно што боље познавање ове две групе

ефеката, као и асоцираних процеса.

Ефекти у хелиосфери

Хелиосфера представља сфероидну област у интерпланетарном простору, пречника процењеног на око 200 астрономских јединица (1 АЈ = удаљеност Земље од Сунца), у којој је притисак соларног ветра доминантан у односу на притисак плазме међузвезданог простора. Постоје бар два ефекта у хелиосфери која су значајна за космичко зрачење: ефекат модулације КЗ енергија мањих од 10^{12} eV и чињеница да у самој хелиосфери настају честице енергија реда GeV [15].

Соларни ветар представља ток плазме који настаје у горњим слојевима Сунчеве короне и креће се радијално у смеру од Сунца, брзинама између 300 и 600 km/s. Настаје услед хидродинамичког ширења короне, загреване нижим слојевима. Корона, која се загрева до температура реда 10^6 K (око 100 пута веће него у фотосфери), под дејством јаке Сунчеве гравитације губи стабилност и шири се у околни простор [16]. Каже се да је коронално магнетно поље "замрзнуто" у овој плазми која га повлачи са собом. Поље је са друге стране везано за Сунце које ротира и услед поменутог ширења обликује структуру сличну Архимедовој спирали, а која се назива *Паркерова спирала* (слика 2.3). На довољно великом растојању од Сунца радијална компонента магнетног поља постаје занемарљива, док је азимутална доминантна и постаје приближно кружна [2]. Магнетно поље у хелиосфери се историјски назива *интерпланетарно магнетно поље*.

Особине соларног ветра варирају због променљиве природе Сунчевог магнетног поља. Ове промене могу бити дугорочне, као оне везане за 11-годишњи циклус Сунчевих пега, односно 22-годишњи циклус инверзије полова Сунчевог магнетног поља, или краткорочне, које се огледају у појавама као што су соларне бакље и коронални експлозије.

Сунчеве пеге представљају области на Сунцу које су тамније и хладније од околине, што је последица интеракције концентрисаних соларних магнетних поља и соларне плазме [18]. Број Сунчевих пега варира са периодом од 11 година, прати интензитет Сунчеве активности и највећи је у периоду соларног максимума. Ова периодика је последица инверзије поларитета Сунчевог маг-

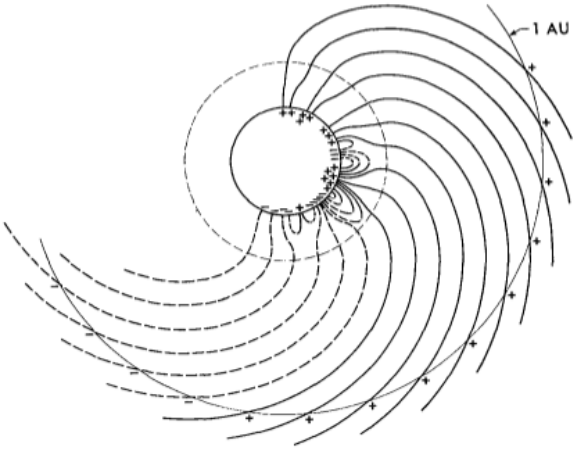

Слика 2.3: Структура Паркерове спирале према једном од модела короналног магнетног поља [17].

нетног поља, које се у периоду соларног минимума може апроксимирати магнетним диполом, док у периоду соларног максимума, када долази до инверзије, има комплекснију структуру услед значајнијег доприноса магнетних момената виших редова [19]. Према томе, пун циклус Сунчевог магнетног поља траје два соларна циклуса, односно 22 године.

Соларне бакље и *коронални експлозије* (*Coronal Mass Ejection - CME*) су блиско повезани, али у бити различити феномени. Обе појаве представљају ерупције које прате деформације Сунчевог магнетног поља и често су асоциране са Сунчевим пегама. Насупрот ранијем мишљењу, данас преовладава становиште да соларне бакље представљају ерупцију претежно X и γ зрачења, док при короналним експлозијама долази до избацивања и убрзавања плазме из Сунчеве короне. Иако су корналне експлозије често праћене соларним бакљама, 30%-50% се јавља независно [20]. Мада то питање и даље донекле остаје отворено [21], следи да само у ударним таласима који прате коронални екплозије долази до убрзавања неких честица до енергија реда 10 до 30 GeV (*соларни космички зраци*), као и да је утицај соларних бакљи, иако и даље битан за многе процесе у Земљиној атмосфери, за модулацију КЗ много мање значајан.

И данас актуелну теорију транспорта ПКЗ кроз соларни ветар први је предложио Паркер 1965. године узимајући у обзир неколико различитих ефеката. Услед релативно ниске густине честица које чине соларни ветар, сматра да се честичне интеракције могу занемарити и да ПКЗ превасходно интерагује са магнетним пољем соларног ветра. Честице ПКЗ се крећу двојако: прецесирају око спиралних линија магнетног поља, док се у исто време крећу паралелно са њима. Неправилности у магнетном пољу могу насумично расејати ове честице и оне дифундују релативно у односу на соларни ветар. Такође, плазма соларног ветра се или шири, док се удаљава од Сунца, или сажима, у ударним таласима. Услед тога се релативна растојања међу нехомогеним структурама у магнетном пољу повећавају или смањују, због чега честице ПКЗ подлежу "адијабатском" загревању или хлађењу. Коначно, обзиром да је механизам прецесије око спиралних линија магнетног поља најчешће бржи од механизма расејања, честице дрифтују услед просторних варијација спиралног магнетног поља. Паркерова теорија је и даље основа за највећи број интерпретација транспорта наелектрисаних честица у току космичке плазме [15]

Ефекти у магнетосфери

Земљина магнетосфера (слика 2.4) настаје као резултат интеракције Земљиног магнетног поља са соларним ветром. Земљино магнетно поље се, у првој апроксимацији, може представити као магнетни дипол чија се оса грубо поклапа са осом ротације Земље. Кључну улогу у овој интеракцији има интерпланетарно магнетно поље чија структура је заробљена у соларном ветру. Трећа компонента значајна за ову интеракцију је Земљина јоносфера. *Јоносфера* је горњи слој атмосфере који се налази приближно на висини од 100 km. Делимично је јонизован X и виосокоенергетским UV зрачењем и представља секундарни извор плазме у магнетосфери [22].

Мерења која је двадесетих година прошлог века холандски физичар Клеј спроводио на свом путу бродом од Јаве до Холандије показала су да је у близини полутара интензитет космичког зрачења мањи за више од 10% [23]. Овај резултат је пре свега показао да се космичко зрачење бар у некој мери састоји од

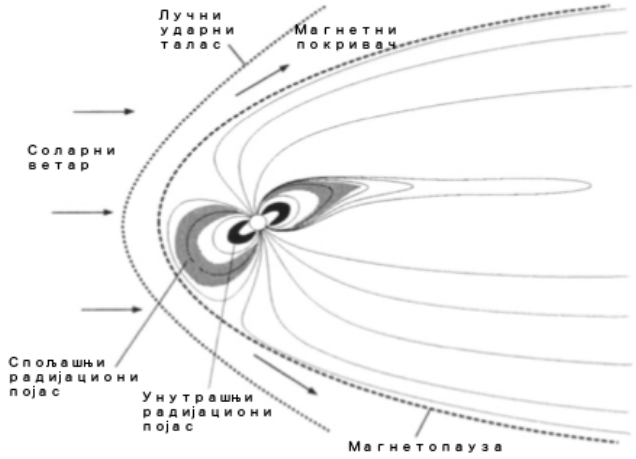

Слика 2.4: Оријентација магнетосфере у односу на соларни ветар. Као резултат интеракције јављају се области лучног ударног таласа, магнетног покривача и магнетопаузе, као и радијациони појасеви [1].

наелектрисаних честица (а не од високоенергетских гама зрака као што је тада било преовлађујуће мишљење), а затим и да су неопходна прецизнија мерења као и теоријска интерпретација кретања честица ПКЗ у Земљином магнетном пољу.

Експерименти који су уследили потврдили су постојање геомагнетног ширинског ефекта, али такође указали и на додатна два: дужински геомагнетни ефекат, који представља мање интензивну варијацију флукса КЗ дуж геомагнетног полутара, а такође и на ефекат асиметрије интензитета у односу на правац исток-запад. Први је последица измештености Земљиног магнетног дипола у односу на центар Земље (у 2015. години ова раздаљина је износила приближно 577 km [24]), као и локалних магнетних аномалија [1]. Други ефекат је последица чињенице да је наелектрисање честица примарног космичког зрачења скоро искључиво позитивног знака.

У то време већ је постојала основа теорије кретања наелектрисаних честица

у Земљином магнетном пољу, коју је развио Стермер како би објаснио феномен поларне светлости, а која се без губитка општости могла применити на пропагацију ПКЗ. Стермер полази од претпоставке да се Земљино магнетно поље у првој апроксимацији може представити као дипол, магнетног момента $M_E = 8. \times 10^{22}$ Am^2, нагнут у односу на Земљину осу ротације под углом од 11.5° и померен у односу на центар Земље (претходни пасус). Иако су касније уведене додатне поправке, ова теорија је и даље релевантна јер, са нешто мањом тачношћу, описује велики број ефеката утицаја геомагнетног поља на ПКЗ који постоје и у реалном магнетном пољу (ширински и ефекат исток-запад асиметрије, израчунавање граничних чврстоћа, области полусенке, настанак радијационих појасева и сл.) [23].

Стермер је пре свега покушавао да утврди које трајекторије честица су дозвољене, а које забрањене за дату географску локацију. Погодна величина за описивање датог критеријума је магнетна чврстоћа, која представља однос импулса и наелектрисања честице и типично се изражава у гигаволтима (GV). За сваку тачку на Земљи се може одредити вредност граничне магнетне чврстоће за честицу која долази под одређеним зенитним, односно азимуталним углом, испод које честица неће стићи до Земље. Стермер је извео следећи интеграл кретања који описује могуће трајекторије наелектрисане честице у диполном магнетном пољу [14]:

$$2\gamma = R\cos\lambda\sin\theta + \frac{\cos^2\lambda}{R}, \tag{2.2}$$

где је γ константа пропорционална параметру судара за честицу која се налази у бесконачности, λ је геомагнетна ширина, θ је угао између правца вектора брзине честице и меридијалне равни, док R представља радијално растојање од дипола. R се изражава у Стермеровим јединицама, где је једна Стермерова јединица једнака $\sqrt{\frac{M}{P}}$. M је диполни момент, а $P = \frac{pc}{Ze}$ представља магнетну чврстоћу.

За честицу која долази вертикално у односу на магнетни дипол тада се може израчунати минимална чврстоћа која омогућава да честица стигне до Земље - *вертикална гранична чврстоћа*:

$$P = \frac{M}{4r_e^2}\cos^4\lambda = 14.9\cos^4\lambda GV, \tag{2.3}$$

где је r_e полупречник Земље.

Леметр и Валарта уводе прву поправку Стермерове теорије, узимајући у обзир да Земља као тело може да се нађе на путу честица ПКЗ [25], док Квенби и Вебер урачунавају и недиполне чланове Земљиног магнетног потенцијала [14]. Резултат ових поправки је да се у простору може дефинисати више класа конуса унутар којих леже различите трајекторије честица: дозвољени конус - одређен углом унутар кога леже све дозвољене трајекторије које не пресецају Земљу, забрањени конус - одговара углу у коме се налазе све забрањене путање, и област полусенке (*пенумбра*) - садржи комплексну структуру дозвољених и забрањених трајекторија. На слици 2.5 приказане су ове области за произвољну вредност магнетне чврстоће и произвољну локацију честице у магнетном пољу дипола.

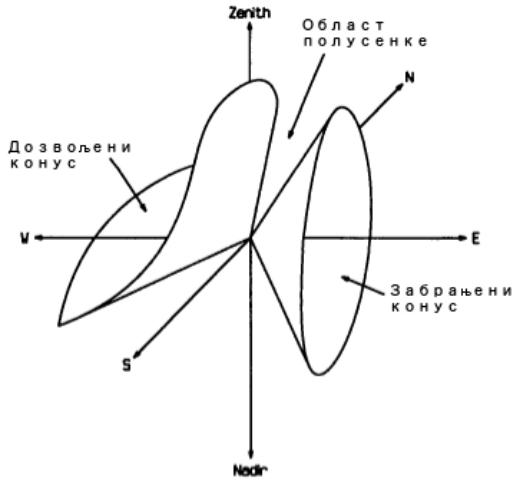

Слика 2.5: Дозвољени и забрањени конус и област полусенке у простору, приказани за произвољне вредности магнетне чврстоће и координате наелектрисане честице у пољу магнетног дипола [1].

Модерна израчунавања користе методу "рачуна уназад" (*backtracking*) и реалистичније моделе Земљиног магнетног поља. Овај приступ прати трајекторију

честице супротног наелектрисања која полази са датих координата и под датим угловима са Земље. Уколико се трајекторија завршава у области у којој више није могуће заробљавање честице у Земљином магнетном пољу, сматра се да је у питању дозвољена путања [2]. Један такав модел је IGRF [26].

Варијације примарног космичког зрачења

Иако приближно константан, интензитет примарног космичког зрачења у непосредној близини Земље варира услед здруженог утицаја ефеката у хелиосфери и магнетосфери. Варијације могу бити просторне или временске.

Просторне варијације су углавном везане за геомагнетне, односно ефекте у магнетосфери, и најзначајнији су:

Ширински ефекат који представља смањење интензитета од полова ка екватору и директно је повезан са граничном магнетном чврстоћом асоцираном са честицама ПКЗ у Земљином магнетном пољу. У случају енергија до 15 GeV, за честице које долазе из вертикалног правца, на средњим ширинама, ове варијације могу износити и до 20% интензитета [1]. Важно је напоменути да се овај ефекат односи на геомагнетну, а не на географску ширину.

Дужински ефекат који се огледа у промени интензитета са променом геомагнетне дужине и објашњава се измештеношћу центра Земљиног магнетног дипола у односу на центар Земље, у правцу Индијског океана. Релативно у односу на географску дужину интензитет космике може варирати и до 15% [1].

Асиметрија исток-запад се односи на разлику интензитета у датом правцу и последица је чињенице да је наелектрисање честица ПКЗ углавном позитивног знака. Интензитет је већи из правца запада и ефекат расте од полова ка екватору, а такође и са порастом надморске висине [23].

Временске варијације највише зависе од ефеката у хелиосфери, односно Сунчеве активности. Могу бити периодичне и апериодичне и најзначајније су:

Соларна дневна варијација се односи на промене интензитета са периодом од једног соларног дана. Соларни дан представља време од поднева до поднева, односно време једне пуне ротације Земље релативно у односу на Сунце. Варијација је последица интеракције соларног ветра, односно магнетног поља

које носи са собом, са примарним космичким зрачењем. Поменуто магнетно поље ротира заједно са Сунцем, а ту ротацију прате и нискоенергетске честице ПКЗ које прецесирају око линија магнетног поља. Стога је флукс честица које се крећу у истом правцу као и Земља на својој орбити за око 0.4% већи од флукса честица које се крећу у супротном смеру.

Блиска по периоду је сидерална варијација, чији период је један сидерални дан или временски интервал који одговара једној ротацији Земље од 360°, односно пуној ротацији релативно у односу на центар галаксије. Постојање овакве варијације би указало на анизотропију и евентуално открило могуће изворе ПКЗ. Неки савременији експерименти су имали позитивне резултате, али је слагање са теоријским предвиђањима и даље недовољно за јасну интерпретацију [27].

27-одневна варијација је последица комбинованог ефекта ротације Сунца (са периодом ротације од 27 дана) и различитих процеса на Сунцу као што су активне регије, Сунчеве пеге, коротирајући брзи млазеви и сл. Како ове структуре обично трају неколико Сунчевих ротација, долази до квазипериодичне модулације физичких параметара интерпланетарног простора, са приближним периодом од 27 дана, а која даље утиче на интензитет ПКЗ. Модулација је квазипериодична услед стохастичне природе соларне активности и параметара као што су брзина соларног ветра, структура магнетних поља и сл. У међупланетарном простору варијација интензитета ПКЗ може достићи 10% [16].

11-огодишња варијација је повезана са 11-огодишњим циклусом Сунчевих пега, односно соларне активности. Интензитет ПКЗ је антикорелисан са соларном активношћу тако да максимуму соларне активности одговара минимум интензитета примарног космичког зрачења. Постоји више модела који задовољавајуће описују ову корелацију и пратеће ефекте. Једна од основних претпоставки је да је варијација интензитета пропорционална релативној учестаности аномалних догађаја на Сунцу, односно пропагацији пратећих ударних таласа у равни еклиптике. Други значајан фактор представља утицај коротирајућих интерагујућих области на ПКЗ. *Коротирајуће интерагујуће области (Corotating Interacting Regions - CIR)* су структуре у интерпланетарном маг-

нетном пољу које настају у интеракцији бржег са споријим соларним ветром, док први пристиже други. Како се удаљавају од Сунца, ови токови се стапају и на већим растојањима стварају концентричне љуске сабијеног магнетног поља, са израженијим флуктуацијама, које се простиру радијално [28].

22-огодишња варијација је ефекат вишег реда у односу на једанаестогодишњу варијацију и прати периодику 22-огодишњег Сунчевог магнетног циклуса. Већ је поменуто да је интензитет примарног космичког зрачења антикорелисан са интензитетом соларне активности. Један од ефеката 22-одишње варијације се видљив у промени облика сукцесивних максимума ПКЗ, односно наизменичној смени оштријих и мање оштрих профила. Такође, и релативни интензитет ових максимума се мења на сличан начин, наизменичном сменом профила мање и веће амплитуде. Сматра се да, будући да су честице ПКЗ скоро искључиво позитивног наелектрисања, Сунчево магнетно поље другачије утиче на дрифт ових честица у интепланетарном магнетном пољу у зависности од конкретне оријентације [28].

Форбушев ефекат (Forbush decrease) се односи на класу догађаја који представљају апериодичне краткотрајне падове детектованог интензитета космичког зрачења, где се најчешће подразумева да се детектор налази на Земљи. Само смањење интензитета се дешава брзо и типично траје неколико сати, док је време потребно да се интензитет врати на релативну вредност пре пада најчешће неколико дана. Промена интензитета варира од неколико до 20 процената [1]. Форбушеви догађаји су последица короналних експлозија, односно интеракције примарног космичког зрачења са структурама у интерпланетарном простору које прате овакве експлозије.

До смањења интензитета долази или у простору турбулентног поља који прати линију ударног таласа, уколико избачени материјал (*ејекта*) има довољну брзину да креира ударни талас, или унутар самог избаченог материјала услед затворене структуре поља [20]. У случају да су оба механизма присутна, догађај се назива класичним и већина интензивнијих догађаја је овог типа. Структура ових догађаја у временским серијама космике је карактеристична и јасно се виде обе фазе. Један такав догађај приказан је на слици 2.6.

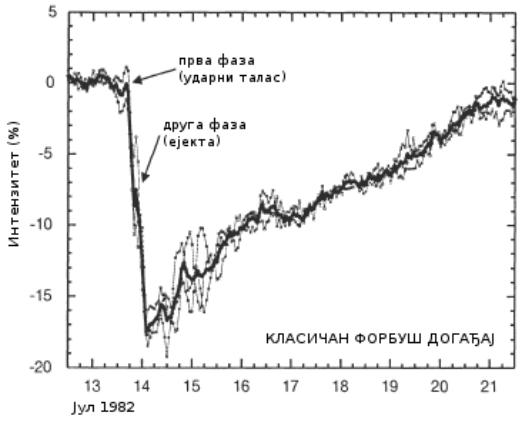

Слика 2.6: Процентуално смањење одброја три, приближно једнако лонгитудинално удаљена, неутронска монитора (Deep River, Mt.Wellington, Kerguelen). Тамнија линија приказује средњу вредност одброја и представља приближну меру изотропног интензитета [20].

Потпун скуп варијација ПКЗ је шири и обухвата ефекте као што су сидералне варијације (значајне за детекцију анизотропија ПКЗ), дугорочне варијације (везане за споре промене Сунчеве активности и геомагнетног поља) и други, али су ти ефекти од мањег значаја за остатак излагања у овој дисертацији и стога су изостављени.

2.2 Секундарно космичко зрачење

Честице примарног космичког зрачења које долазе до Земље интерагују са језгрима и електронима атома ваздуха у највишим слојевима атмосфере. У случају да поседују довољну енергију, резултат ове интеракције ће бити креација каскаде, односно *пљуска* честица која пропагира даље ка површини Земље и који се назива *секундарно космичко зрачење*. За тему ове дисертације нарочито је значајна мионска компонента оваквих пљускова. Да би се потпуније разумели ефекти везани за пропагацију ове компоненте неопходно је најпре нешто изложити о основним процесима који доводе до формирања оваквих каскада, као и главним карактеристикама пљускова секундарних честица.

2.2.1 Процеси значајни за интеракцију космичког зрачења са атомима атмосфере

Процеси који доминирају у формирању пљускова секундарног космичког зрачења по својој природи могу се поделити у три главне категорије: хадронске интеракције, распади честица и електромагнетне интеракције. Иако је потпун скуп процеса бројан, овде ћемо представити само најзначајније.

Хадронске интеракције

Честица примарног космичког зрачења са језгрима атома атмосфере интерагује путем јаке интеракције. Већ са енергијом већом од неколико GeV, ови судари могу бити нееластични и иницирати развој пљуска секундарних честица [1]. Да би креација неке честице била могућа, неопходно је да енергија у систему центра масе (CM) буде већа од збира маса мировања дате честице и маса честица пројектила и мете. Енергија у систему центра масе се изражава преко Манделштамове варијабле s, која је Лоренц-инваријантна величина дефинисана као:

$$s = (\mathbf{P}_a + \mathbf{P}_b)^2 = \left[(E_a + E_b)^2 - (\mathbf{p}_a + \mathbf{p}_b)^2\right], \tag{2.4}$$

па је $\sqrt{s} = E_{CM}$. У случају да је мета масе m_b фиксна, а пројектил масе m_a у лабораторијском систему има енергију E_a, енергија у систему центра масе биће:

$$\sqrt{s} = \left(m_a^2 + m_b^2 + 2m_b E_a\right)^{1/2}. \tag{2.5}$$

Када је енергија честице пројектила значајно већа у односу на масе честица пројектила и мете, може се сматрати да је $\sqrt{s} \approx \sqrt{2m_b E_a}$.

На високим енергијама процеси креације честица, у нееластичним сударима путем јаке интеракције, добро су описани теоријом квантне хромодинамике. Међутим, на нижим енергијама то није случај и тада се прибегава феноменолошком приступу [2]. Такође, различити механизми креације честица доминирају у зависности од енергије.

На најнижим енергијама, у интервалу од прага за креацију честица до $\sqrt{s} = 1 - 2GeV$, преовлађују процеси креације и распада хадронских резонанци, те се овај интервал енергија зове *област резонанци*. У овој области мултиплицитет честица у финалном стању је познат, са обзиром да резонанце имају јасно дефинисане канале распада. Пресеци за интеракцију и дистрибуција секундарних честица из распада резонанци се могу описати *изобар* моделима, који се базирају на одржању изоспина и ангуларног момента [8].

На вишим енергијама, до $\sqrt{s} \sim 100GeV$, се налази *област скалирања*, у којој типично долази до креације већег броја секундарних честица. Средњи мултиплицитет секундарних честица у овој области приказан је на слици 2.7.

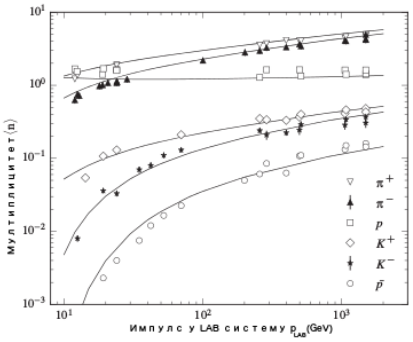

Слика 2.7: Средњи мултиплицитет секундарних честица. Подаци са експеримената са фиксном метом ISR у CERN-у и протон сихнротрона у FERMILAB-у. Израчунате вредности добијене су на основу DPMJET III модела [8].

Име за овај интервал енергије потиче од претпоставке да, на енергијама довољно већим од маса честица које учествују у интеракцији, пресек за нееластичну интеракцију постаје приближно константан. Такође, претпоставка је да расподеле физичких величина од значаја (нпр. лонгитудиналне или трансверзалне компоненте импулса) не зависе од енергије доступне у систему центра масе, већ се скалирају у зависности од бездимензионих кинематичких величина (као што је x_F у случају Фајнмановог скалирања).

На енергијама изнад $\sqrt{s} \sim 100GeV$ хипотеза скалирања престаје да важи. Наиме, не само да је средња вредност трансверзалне компоненте импулса секун-

дарних честица ($p_\perp$) већа од оне предвиђене хипотезом скалирања, већ и дистрибуције трансверзалног импулса на нижим и вишим енергијама имају различите расподеле. Ово је у складу са чињеницом да се хадрони састоје од кваркова. У случају малих вредности $p_\perp$ интеракције су периферне и конституентни кваркови колективно учествују у њима. У случају дубоке нееластичног расејања на партонима, у интеракцији учествују појединачни конституентни кваркови и долази до продукције секундарних честица високог $p_\perp$, које су груписане у хадронске *млазове* (*jets*). Ово представља основу *minijet* (миницет) модела, а самим тим и овај интервал енергија назива се *област minijet-ова*. У оквиру овог модела пресек за интеракцију на ниским енергијама се рачуна одвојено од пресека за креацију *minijet*-ова, за чије израчунавање се може применити формализам пертурбативне квантне хромодинамике.

Будући да су у примарним интеракцијама ПКЗ честице мете свакако језгра атома, а да то у мањем проценту случајева могу бити и честице пројектила, један део хадронских интеракција може представљати *нуклеарна фрагментација*. То је процес у коме се језгро дели на два или више фрагмената. Енергија неопходна да до сепарације дође, у најједноставнијој интерпретацији, једнака је разлици енергија везе иницијалног језгра и енергија везе језгара продуката фрагментације, уз урачунавање разлике у Кулоновој интеракцији [2].

Највећи број хадрона креираних у свим поменутим интеракцијама представљају π мезони (*пиони*) који су врло значајни за развој различитих компоненти пљуска секундарних честица, о чему ће више речи бити у одељку 2.2.2.

Распади честица

Распади нестабилних честица су изузетно значајни за развој пљуска секундарног космичког зрачења. То се пре свега односи на распад неутралних пиона, одговоран за развој електромагнетне компоненте пљуска, као и распад наелектрисаних пиона који је одговоран за развој мионске компоненте пљуска.

Распад наелектрисаних пиона. Наелектрисани π мезони спадају у категорију лаких мезона. Кварковска структура π^+ мезона је $u\bar{d}$, док је структура π^- $\bar{u}d$, и стога немају *flavor* ($S = C = B = 0$). Масе су једнаке и износе

$m = 139.57018 \pm 0.00035 MeV$. Спин је 0, а парност је негативна и спадају у класу *псеудоскаларних мезона.*

Наелектрисани пиони су нестабилне честице са средњим временом живота $\tau = (2.6033 \pm 0.0005) \times 10^{-8} s$. Доминантан канал распада, са вероватноћом од $(99.98770 \pm 0.00004)\%$ [29], је:

$$\pi^+ \longrightarrow \mu^+ + \nu_\mu \qquad \pi^- \longrightarrow \mu^- + \bar{\nu_\mu}. \tag{2.6}$$

Вероватноћа за распад у електронски канал, шематски приказан испод, је далеко мања и експериментално утврђена вредност релативно у односу на вероватноћу за мионски канал износи $(1.230 \pm 0.004) \times 10^{-4}$:

$$\pi^+ \longrightarrow e^+ + \nu_e \qquad \pi^- \longrightarrow e^- + \bar{\nu}_e. \tag{2.7}$$

Теоријски је однос ових вероватноћа добро описан и може се свести на израз [30]:

$$\frac{\Gamma(\pi^- \longrightarrow e^- + \bar{\nu_e})}{\Gamma(\pi^- \longrightarrow \mu^- + \bar{\nu_\mu})} = \frac{m_e^2 \left(1 - \frac{m_e^2}{m_\pi^2}\right)^2}{m_{mu}^2 \left(1 - \frac{m_\mu^2}{m_\pi^2}\right)^2} = 1.28 \times 10^{-4} \tag{2.8}$$

Према закону одржања ангуларног момента, лептон у распадима описаним изразима 2.6 и 2.7 морао би да има позитиван хелицитет. Вероватноћа да лептон буде у таквом стању зависи од масе и мања је за лакше честице, што објашњава однос вероватноћа распада у различите лептонске канале [31].

Наелектрисани пиони се распадају путем слабе интеракције и на слици 2.8 приказан је Фајнманов дијаграм за распад позитивног пиона на антимион и мионски неутрино. Већина миона у пљусковима космичког зрачења потиче из распада наелектрисаних пиона.

Распад неутралних пиона. Неутрални π мезон такође спада у лаке мезоне и са наелектрисаним пионима чини изоспински триплет. Кварковска структура је $|\pi^0\rangle = \frac{1}{2}(|u\bar{u}\rangle - |d\bar{d}\rangle)$, те такође немају *flavor*. Маса је нешто мања него масе наелектрисаних пиона и износи $m = 134.9766 \pm 0.0006 MeV$.

Средње време живота неутралног пиона је $\tau = (8.52 \pm 0.18) \times 10^{-17} s$ и пре-

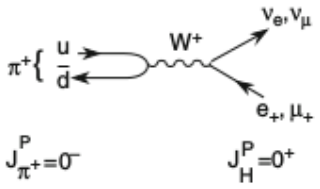

Слика 2.8: Фајнманов дијаграм за распад $\pi^+ \longrightarrow \mu^+\nu_\mu$ [32].

васходно се распада на два гама зрака са вероватноћом од $(98.823 \pm 0.034)\%$. Неки мање вароватнији канали распада су Далицов ($\pi^0 \longrightarrow e^+e^-\gamma$) и двоструки Далицов ($\pi^0 \longrightarrow e^+e^-e^+e^-$) распад.

Неутрални пиони су веома значајни за развој електромагнетне компоненте пљуска секундарног космичког зрачења, јер већина високоенергетских гама зрака који иницирају електромагнетну каскаду потиче из распада π^0.

Распад миона. Миони су наелектрисани лептони друге генерације и самим тим су у питању фермиони спина $\frac{1}{2}$. Маса миона је $m = 105.6583745 \pm 0.0000024 MeV$. Нестабилна је честица са средњим временом живота $\tau = (2.1969811 \pm 0.0000022) \times 10^{-6} s$. Ово релативно дугачко средње време живота значи да ултрарелативистички космички миони, настали у атмосфери, стижу до површине Земље пре него што се распадну.

Негативни миони се распадају скоро искључиво на електроне. Закон одржања лептонског броја налаже да се у распаду креирају мионски неутрино и електронски антинеутрино (односно одговарајуће коњуговане честице у случају распада позитивног антимиона). Распад се одвија путем слабе интеракције и на слици 2.9 приказан је Фајнманов дијаграм распада позитивног миона.

Више детаља о особинама миона и развоју мионске компоненте секундарног космичког зрачења биће наведено у одељку 2.2.3.

У пљусковима секундарног космичког зрачења долази до креације многих других нестабилних честица, чији распади у принципу могу допринети развоју пљуска, али будући да су у питању честице са релативно мањим пресецима за продукцију (K^+, K^-, резонанце, ...) или честице дужег средњег живота

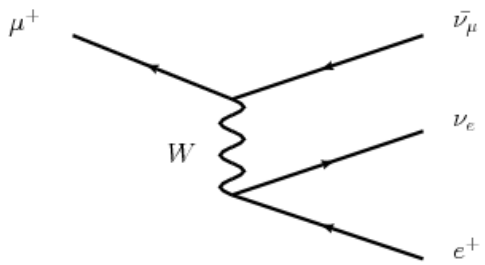

Слика 2.9: Фајнманов дијаграм за распад $\mu^+ \longrightarrow e^+\bar{\nu}_\mu\nu_e$ [33].

(неутрони), имају мање значајну улогу и стога их нећемо детаљније помињати.

Електромагнетне интеракције

Електромагнетне интеракције су значајне за развој електромагнетне компоненте пљуска секундарног космичког зрачења, односно развој електромагнетне каскаде. Овде ћемо поменути најбитније.

Кулоново расејање. Једну од најосновнијих електромагнетних интеракција представља еластично расејање наелектрисане честица у спољашњем, стационарном електромагнетном пољу, односно Кулоново расејање. Сила којом два наелектрисане честице делују једна на другу је дата изразом [2]:

$$F = \frac{q_1 q_2}{R^2}\mathbf{n}, \tag{2.9}$$

где су q_1 и q_2 респективна наелектрисања честица, R је њихово међусобно растојање, а n јединични вектор истог правца као и растојање.

У нерелативистичком случају, дифренцијални ефикасни пресек за расејање честице пројектила наелектрисања ze, на честици мети наелектрисања Ze, под углом θ, описан је Радерфордовом формулом [34]

$$\frac{\mathrm{d}\sigma}{\mathrm{d}\Omega} = \sigma_R(\Theta) = \frac{\alpha^2 z^2 Z^2}{16T^2 \sin^4 \frac{\Theta}{2}}, \tag{2.10}$$

где је T кинетичка енергија честице пројектила.

У случају релативистичких честица неопходна је поправка, па је диференцијални ефикасни пресек за расејање електрона, у пољу тачкастог наелектрисања

Ze, описан Мотовом формулом:

$$\sigma_R(\Theta) = \frac{Z^2\alpha^2}{4p^2\beta^2 \sin^4 \frac{\Theta}{2}}(1 - \beta^2 \sin^2 \frac{\Theta}{2}), \tag{2.11}$$

која се у нерелативистичкој апроксимацији своди на Радерфордову формулу.

Наелектрисана честица ће се при проласку кроз материју углавном расејавати радерфордовски, што подразумева велики број расејања под малим угловима који ће имати Гаусову расподелу. Међутим, повремено ће се расејати и под утицајем јаке интеракције, а расподела углова таквих расејања није Гаусова. Теоријску интерпретацију која успешно уједињује ове ефекте дао је Молијер, а касније допунио Бете [29]. Накнадно је Молијерова теорија успешно примењена на расејање електрона у плазми [35]. На основу ове теорије је могуће израчунати *Молијеров полупречник* који је значајан параметар апсорбера и представља меру трансверзалног ширења електромагнетног пљуска.

Јонизациони губитак енергије. При проласку кроз материју тешке наелектрисане честице пре свега губе енергију у нееластичним интеракцијама са електронским омотачем атома средине, односно у процесима ексцитације или јонизације.

Класичну теоријску формулу за губитак енергије дао је Бор, док је квантномеханичку интерпретацију развио Бете, примењујући Борнову апроксимацију (у првом реду) на процесе судара тешких наелектрисаних честица са електронима у атомском омотачу. Блох је увео поправку која је усагласила класичну и квантномеханичку слику и дала коректне изразе у респективним апроксимацијама [36]. Касније су уследиле додатне поправке које укључују више редове у Борновој апроксимацији (објашњава различит губитак енергије позитивних и негативних наелектрисања или *Баркасов ефекат*) [37], ефекат екранирања захваћених електрона (на нижим енергијама) [38], густински ефекат услед поларизације [39] и друге. Стога се, у зависности од тога који од поменутих ефеката се узимају у обзир, у литератури израз за јонизациони губитак енергије појављује у различитим облицима.

Јонизациони губитак енергије се најчешће изражава помоћу величине $\frac{dE}{dx}$, односно *масене заустављне моћи*. Један често навођен облик формуле за масену

зауставну моћ представља израз за средњи губитак енергије умерено релативистичке тешке наелектрисане честице [29]:

$$\left\langle -\frac{\mathrm{d}E}{\mathrm{d}x} \right\rangle = 4\pi N_A r_e^2 m_e c^2 z^2 \frac{Z}{A}\frac{1}{\beta^2}\left[\frac{1}{2} ln \frac{2m_e c^2 \beta^2 \gamma^2 W_{max}}{I^2} - \beta^2 - \frac{\delta(\beta\gamma)}{2}\right], \qquad (2.12)$$

где је N_A Авогадров број, m_e маса електрона, $r_e = e^2/4\pi\epsilon_0 m_e c^2$ класични полупречник електрона, z наелектрисање честице пројектила, Z атомски број мете, A масени број мете, I средња енергија ексцитације, W_{max} максималан трансфер енергије на електрон у једном судару и $\delta(\beta\gamma)$ поправка услед густинског ефекта.

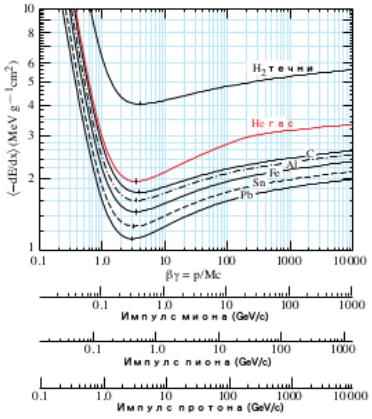

Слика 2.10: Средњи губитак енергије у течном водонику, гасовитом хелијуму, угљенику, алуминијуму, гвожђу, калају и олову. Приказана је такозвана "Бетеова" област и нису укључени радијациони губици, значајни за мионе и пионе. Радијациони губици за мионе у гвожђу престају да буду занемарљиви за вредност $\beta\gamma > 1000$, а за апсорбере већег атомског броја на још нижим вредностима импулса [29].

Вредност овако дефинисане масене зауставне моћи се мало мења за различите апсорбере и полако опада са растућим атомским бројем (слика 2.10).

У случају великог трансфера енергије, расејање електрона на електронима назива се Мелеровим расејањем. Пошто се ради о неразличивим честицама, зауставна моћ се по конвенцији рачуна за бржи од два електрона, и дата је

изразом [29]:

$$\left\langle -\frac{\mathrm{d}E}{\mathrm{d}x} \right\rangle = \frac{1}{2} K \frac{Z}{A} \frac{1}{\beta^2} \left[ln \frac{m_e c^2 \beta^2 \gamma^2 \{m_e c^2 (\gamma - 1)/2\}}{I^2} + (1 - \beta^2) - \frac{2\gamma - 1}{\gamma^2} ln2 + \frac{1}{8} \left(\frac{\gamma - 1}{\gamma} \right)^2 - \delta \right]. \quad (2.13)$$

Израз за зауставну моћ у процесу расејања електрона на позитрону, односно Баба расејање, је нешто компликованији, са обзиром на чињеницу да честице које се расејавају нису идентичне:

$$\left\langle -\frac{\mathrm{d}E}{\mathrm{d}x} \right\rangle = \frac{1}{2} K \frac{Z}{A} \frac{1}{\beta^2} \left[ln \frac{m_e c^2 \beta^2 \gamma^2 \{m_e c^2 (\gamma - 1)\}}{2I^2} + 2ln2 - \frac{\beta^2}{12} \left(23 + \frac{14}{\gamma + 1} + \frac{10}{\gamma + 1}^2 + \frac{4}{\gamma + 1}^3 \right) - \delta \right]. \quad (2.14)$$

Закочно зрачење. Емисије фотона при расејању електрона на атому назива се закочним зрачењем (нем. bremsstrahlung). До емисије долази пре свега због интеракције електрона са Кулоновим пољем језгра атома на коме долази до расејања. Електронски омотач атома такође доприноси ефекту и има двојаку улогу: у случају расејања на језгру, електронски омотач екранира поље језгра, што ефективно смањује пресек за емисију фотона, док се у процесу расејања на електронском омотачу електрони понашају као индивидуалне честице и тада говоримо о електрон-електрон ефекту [40].

Процес је у принципу могућ за било коју наелектрисану честицу. За честицу масе M и наелектрисања ze, која интерагује са пољем језгра атомског броја Z, убрзање је пропорционално zZ/M. Према класичној електродинамици, интензитет емитованог зрачења биће пропорционалан z^2Z^2/M^2. Стога је закочно зрачење много мање значајан ефекат за мезоне, а нарочито протоне, него за електроне, за које представља значајан механизам губитка енергије већ на енергијама од неколико MeV, посебно у апсорберима високог Z [41].

За високоенергетске електроне закочно зрачење представља доминантан ме-

ханизам губитка енергије и диференцијални ефикасни пресек за овај процес (у случају урачунавања потпуног ефекта екранирања) дат је изразом [29]:

$$\begin{aligned}\frac{\mathrm{d}\sigma}{\mathrm{d}k} &= (1/k)4\alpha r_e^2\{(\frac{4}{3}-\frac{4}{3}y+y^2[Z^2(L_{rad}-f(Z))+ZL_{rad}^{'}] \\ &\quad +\frac{1}{9}(1-y)(Z^2+Z)\},\end{aligned} \tag{2.15}$$

где је $y = k/E$ део енергије електрона који односи израчени фотон.

Губитак енергије услед закочног зрачења за електроне је директно пропорционалан енергији електрона, док губици услед јонизације зависе логаритамски од енергије. Вредност енергија за коју се губици услед ових процеса изједначавају назива се *критична енергија*.

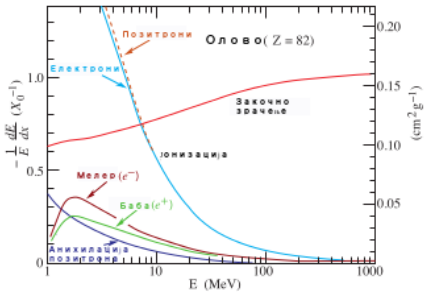

Слика 2.11: Парцијални губитак енергије по радијационој дужини у олову као функција енергије електрона (позитрона). Нелеастично расејање електрона (позитрона) карактеришемо као јонизацију ако је губитак енергије по судару мањи од 0.255 MeV. У случају већег трансфера енергије сматрамо да је у питању Мелерово (Баба) расејање [29].

На слици 2.11 приказани су парцијални губици енергије у олову за различите процесе, у функцији енергије електрона, односно позитрона. Губици су изражени по радијационој дужини, која карактерише апсорбер и представља средњу дужину (изражену у $g\,cm^{-2}$) након које енергија високоенергетског електрона износи $1/e$ његове првобитне енергије, док је остала енергија израчена путем закочног зрачења.

За мионе, пресек за емисију закочног зрачења занемарљив је на енергијама

до 2 TeV, али постаје значајан са порастом енергије [42].

Креација парова и Комптоново расејање. На слици 2.12 приказани су ефикасни пресеци, у зависности од енергије, за различите облике интеракције фотона са материјом. На нижим енергијама фотони доминатно губе енергију у процесу атомског фотоефекта (емисија електрона из атомског омотача услед апсорпције фотона). Одређен допринос имају и Рејлијево расејање (еластично расејање фотона) и Комптоново расејање (нееластично расејање фотона на електрону).

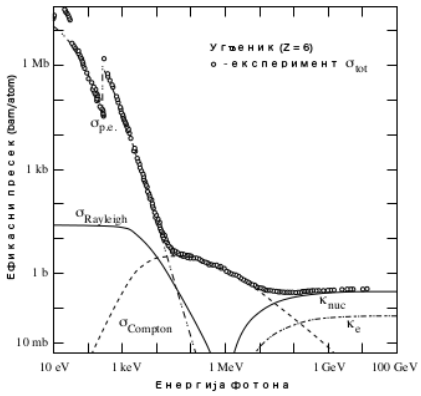

Слика 2.12: Укупни диференцијални ефикасни пресек фотона у функцији енергије за угљеник. Приказани су доприноси различитих процеса [29]:
σ_{tot} - укупни ефикасни пресек, $\sigma_{p.e.}$ - атомски фотоефекат, $\sigma_{Rayleigh}$ - Рејлијево расејање, $\sigma_{Compton}$ - Комптоново расејање, κ_{nuc} - креација парова (поље језгра), κ_e - креација парова (поље електрона).

На вишим енергијама, које су значајније за формирање пљускова секундарног космичког зрачења, доминира процес креације парова (где фотон у Кулоновом пољу креира пар честица-анти честица, најчешће пар електрон-позитрон), али Комптоново расејање и даље може да има значајан допринос.

Ефикасни пресек за креацију електрон-позитрон пара, у случају урачунавања свих ефеката екранирања, дат је изразом [2]:

$$\sigma_{pp}(k,E) = \frac{4Z^2\alpha r_e^2}{k}[1 + 4y(y-1)/3]ln(191Z^{-1/3}) - y(1-y)/9, \qquad (2.16)$$

где је $y = k/E$ однос енергије упадног фотона и енергије једне честице креираног пара.

Ефикасни пресек за Комптоново расејање фотона енергије k описан је изразом:

$$\sigma_C(k) = \frac{\pi r_e^2}{q} \times \left[\left(1 - \frac{2(q+1)}{q^2} \right) ln(2q+1) + \frac{1}{2} + \frac{4}{q} - \frac{1}{2(2q+1)^2} \right], \qquad (2.17)$$

где је q енергија упадног фотона, изражена у јединицама масе електрона ($q \equiv k/m_e c^2$).

Наведени скуп електромагнетних интеракција свакако није потпун, и детаљнији опис неких процеса (као нпр. Черенковљевог зрачења, анихилације позитрона и др.) је изостављен, са обзиром да имају мање значајан допринос развоју пљускова секундарног космичког зрачења.

2.2.2 Пљускови секундарног космичког зрачења

Већ је поменуто да интеракција честице ПКЗ са атомима атмосфере може довести до развоја каскаде (пљуска) секундарних честица, нарочито ако честица има енергију већу од неколико GeV. До примарне интеракције обично долази у горњим слојевима атмосфере, типично на висинама изнад $20km$. Будући да је у питању јака интеракција, највећи број креираних честица представљаће мезони, док ће примарна честица наставити да пропагира ка површини Земље. Високоенергетска примарна честица (протон или фрагмент језгра) наставиће да интерагује са језгрима атома атмосфере, производећи нове секундарне хадроне и тиме доприносити развоју хадронске каскаде, која се често назива *нуклеонска компонента*.

Највећи број овако креираних секундарних честица представљаће π мезони, а у мањем броју и други хадрони. Високоенергетски наелектрисани пиони ће са великом вероватноћом интераговати са језгрима атома атмосфере и доприносити даљем развоју хадронске каскаде, док на нижим енергијама расте вероватноћа за распад на мионе и одговарајућа неутрина. За мезон-мион кас-

каду се користи назив *тврда компонента*.

Неутрални пиони се скоро одмах распадају на два гама зрака и иницирају развој електромагнетне каскаде кроз процесе креације парова и закочног зрачења - *мека компонента*.

У случају да примарна честица има довољно велику енергију, велики број секундарних честица може скоро истовремено доћи на раван која се налази у близини површине Земље и нормална је на правац кретања примарне честице, покривајући велику површину која може бити реда величине хиљада квадратних метара. У том случају говоримо о *широком (екстензивном) атмосферском пљуску* (*extensive air shower*) секундарног космичког зрачења. На слици 2.13 шематски су приказани неки од поменутих процеса за један такав пљусак.

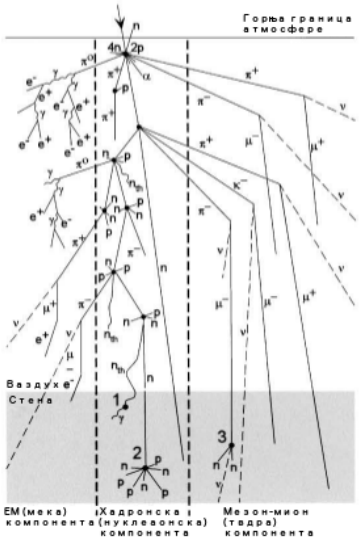

Слика 2.13: Главне компоненте и основни процеси у развоју и пропагацији екстензивног атмосферског пљуска секундарног космичког зрачења кроз атмосферу и стену [43].

У наредна два одељка биће описане најзначајније карактеристике хадронске и електромагнетне каскаде, док је мионска компонента секундарног космичког зрачења од ужег значаја за тему дисертације и биће детаљније описана у одељку 2.2.3. Неутринска компонента се због изузетно малих пресека за интеракцију

и специфичности неутринских експеримената типично не разматра у анализи развоја пљускова СКЗ.

Хадронска каскада

Средњи слободни пут за интеракцију честице се дефинише као [1]:

$$\lambda_i = \left[\frac{N_A}{A}\sigma_i\right]^{-1}, \tag{2.18}$$

где је N_A Авогадров број, A масени број језгра мете, σ_i ефикасни пресек за одговарајућу интеракцију, а изражава се у јединицама g/cm^2.

Ефикасни пресек за интеракцију примарног протона, енергије $10^{14}eV$, са језгром атома ваздуха, средњег масеног броја $A = 14.5$ је приближно $290mb$ ($b = 10^{-24}cm^2$), што одговара средњем слободном путу од приближно $80g/cm^2$ [44]. Према томе, на путу до површине Земље, такав протон у средњем може доживети 12 интеракција. У случају да је примарна честица језгро масеног броја $A = 25$, вредност за средњи слободни пут интеракције била би приближно једнака $23g/cm^2$, што би значило да би таква честица доживела 50 интеракција на путу до површине Земље. На основу тога је јасно да је вероватноћа да таква примарна честица буде детектована на нивоу мора практично занемарљива [1].

Већ је поменуто да највећи број секундарних хадрона у хадронској каскади представљају пиони. Вероватноћа за продукцију различитих пиона је једнака, па је однос наелектрисаних према неутралним пионима приближно $2 : 1$.

Средњи слободни пут за распад неутралног пиона може се изразити као $l_d = \gamma_{\pi^0} \times 2.51 \times 10^{-6}cm$, што значи да се сви, осим изузетно високоенергетских неутралних пиона, распадају у вертексу примарне интеракције и иницирају електромагнетну каскаду [2].

Средњи слободни пут за распад наелектрисаних пиона је значајно већи и дат је изразом $l_d = \gamma_{\pi^\pm} \times 780cm$. Секундарни наелектрисани пиони могу даље интераговати са језгрима атома ваздуха или се могу распасти. Однос вероватноћа за ова два процеса обрнуто је пропорционалан односу одговарајућих средњих путева, односно дат је изразом $\frac{\beta\gamma c\tau}{\lambda_i/\bar{\rho}}$, где је $\bar{\rho}$ средња густина ваздуха

[45]. Знајући да је средњи слободни пут за интеракцију наелектрисаних пиона приближно $120 g/cm^2$ и да је средња густина ваздуха на висинама на којима типично долази до креације миона реда величине $10^{-4} g/cm^3$, може се закључити да за вредности $\gamma > 10^4$ ($E_{\pi^\pm} > 100 GeV$) процеси интеракције почињу да бивају доминантни.

Хадронска каскада ће се развијати док год енергија хадрона не падне испод прага за креацију пиона. Уколико користимо GeV као јединице за енергију, средњи број честица креираних у свакој хадронској интеракцији честице пројектила енергије E дат је са $n = \ln E$. Ако уведемо скалирану варијаблу $\nu = x/\lambda_i$, за енергију прага узмемо $E_{prag} \approx 2m_\pi \approx 0.28 GeV$ и претпоставимо да се каскада развија све док енергија хадрона не падне испод енергије прага (односно престане продукција пиона), енергију e и и број честица у ν-тој генерацији можемо описати као [46]:

$$e(\nu) = \frac{E}{n^\nu} \qquad e(\nu_{max}) = E_{prag}, \tag{2.19}$$

одакле се добија:

$$n^{\nu_{max}} = \frac{E}{E_{prag}} \implies \nu_{max} = \frac{ln\left(\frac{E}{E_{prag}}\right)}{\ln n}. \tag{2.20}$$

Најчешће, о структури хадронске компоненте пљуска секундарног космичког зрачења закључујемо посредно, углавном преко мионске компоненте. То је последица чињенице да иако одређен број мезона и нуклеона стиже на опсервациону раван, укупан број хадрона ће скоро увек бити значајно мањи него број секундарних миона, електрона и гама зрака [2].

Електромагнетна каскада

Већ је поменуто да је електромагнетна каскада иницирана високоенергетским фотонима који потичу из распада неутралних пиона. Они односе приближно трећину енергије хадронске каскаде у сваком степену развоја. Фотони учествују у развоју каскаде кроз процесе креације парова и Комптоновог расејања (на нижим енергијама), док тако креирани електрони и позитрони доприносе про-

дукцији следеће генерације фотона у интеракцији са језгрима атома ваздуха путем закочног зрачења. У доста мањој мери фотони могу учествовати у хадронским интеракцијама у ком случају се део енергије враћа из електромагнетне у хадронску каскаду.

Са сваком следећом генерацијом електромагнетне каскаде укупан број честица се повећава а њихова енергија опада. Продукција честица ће се наставити докле год њихова енергија не падне испод критичне енергије ϵ, када почиње да опада пресек за креацију парова а расту пресеци за јонизацију и ексцитацију. Једноставан модел развоја електромагнетне каскаде предложио је Хајтлер. Модел се заснива на претпоставци да свака честица, након што пређе неко константно растојање пропорционално радијационој дужини, продукује пар честица [47] (слика 2.14).

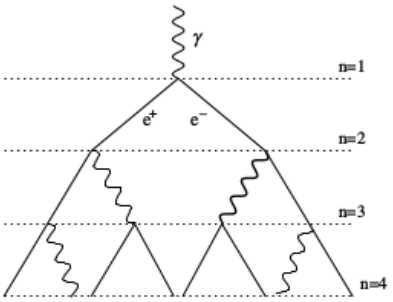

Слика 2.14: Електромагнетна каскада иницирана фотоном, према поједностављеном Хајтлеровом моделу [47].

Зависност од природе апсорбера може се уклонити ако се дефинишу скалиране варијабле [46]:

$$t = x/X_0 \qquad\qquad y = E/\epsilon, \tag{2.21}$$

где је E енергија фотона или електрона (позитрона) који иницира каскаду а X_0 је дужина која одговара једној генерацији мултипликације електромагнетне каскаде. Након t генерација број и енергија честица t-те генерације биће:

$$n(t) = 2^t \qquad e(t) = E/2^t. \tag{2.22}$$

Каскада достиже максималан развој када је $e \approx \epsilon$, и тада ће број и енергија честица бити:

$$n(t_{max}) = E/\epsilon = y \qquad t_{max} \sim \ln(E/\epsilon) = \ln y. \tag{2.23}$$

У даљем развоју каскаде електрони критичне енергије прелазе пут мањи од X_0. Каскада се стога практично састоји само од фотона чији интензитет (а тиме и енергија каскаде) опада по експоненцијалном закону.

Иако представља врло упрошћену слику релевантних процеса, овај модел је у стању да успешно предвиди најбитније карактеристике електромагнетне каскаде. Једна од значајнијих мана је прецењен број електрона у односу на фотоне, пре свега због чињенице да се у процесу закочног зрачења често израчује више од једног фотона.

Високоенергетске секундарне честице су релативно уско колимисане око основне осе дуж које се простире електромагнетна каскада. 90% енергије је локализовано унутар цилиндра око основне осе, одређеног Молијеровим радијусом, који се назива "језгром" каскаде. За типичан пљусак вредност Молијеровог радијуса је $R_M \approx 60m$. Ипак, нискоенергетки фотони и електрони се могу расејати и неколико километара далеко од основне осе и чине облак нискоенергетских честица који наставља да се шири докле год "језгро" остаје активно [48].

Симулација атмосферских пљускова секундарних честица

Иако једноставнији модели имају одређену применљивост, за прецизнију анализу су неопходни детаљни модели имплементирани у симулационе пакете.

Вероватно најпознатији и најупотребљаванији симулациони пакет у физици космичког зрачења је CORSIKA (**CO**smic (R)ay **SI**mulation for **KA**skade) [49], развијен за потребе KASKADE (**KA**rlsruhe **S**hower **C**ore and **A**rray **DE**tector) [50] експеримента. У питању је Монте Карло (Monte Carlo) код за детаљну симулацију екстензивних атмосферских пљускова секундарног космичког зрачења.

На слици 2.15 приказан је CORSIKA симулација развоја атмосферског пљуска секундарних честица, иницираног различитим честицама примарног космичког зрачења.

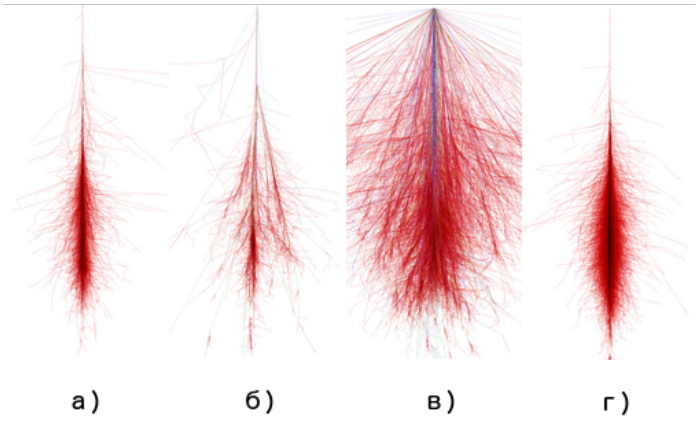

Слика 2.15: Симулирани атмосферски пљусак секундарних честица, иницираn а) фотоном, б) протоном, в) језгром гвожђа и г) мионом (симулациони пакет CORSIKA) [49].

У симулацији, примарне честице које иницирају пљусак могу бити лака језгра (закључно са гвожђем), фотони и друге честице. Честице се прате кроз атмосферу до интеракције или евентуалног распада у случају нестабилних честица.

Пет различитих модела се користи како би се описале хадронске интеракције на високим енергијама. VENUS, QGSJET и DPMJET су засновани на Грибов-Реге теорији, SIBYLL је минијет модел, док је HDPM генератор који користи феноменолошки приступ и непрекидно се унапређује на основу најновијих експерименталних резултата. На нижим енергијама хадронске интеракције су описане GHEISHA моделом, у случају да је неопходна детаљна симулација, или ISOBAR моделом за случај да је довољан једноставнији приступ.

За описивање распада честица, урачунавају се сви канали распада са вероватноћом већом од 1% . За симулацију електромагнетних интеракција користи се пакет EGS4, а такође је могуће укључити и NKG опцију која користи аналитички приступ за праћење развоја електромагнетне компоненте, што уз нешто

мању тачност смањује захтеве за ресурсима . Постоје опције и за симулацију Черенковљевог зрачења и пропагације и интеракције неутрина [42].

Укључен је реалистичан опис атмосфере са дефинисаних 5 слојева, како би се описала варијација густине у зависности од висине, а такође је имплементиран и модел геомагнетног поља и асоцираних ефеката. Могуће је урачунати и ефекте нуклеарне фрагметације (иако се показало да то мало утиче на крајњи резултат).

CORSIKA адекватно описује атмосферске пљускове космичког зрачења до енергија примара од $100EeV$. Користи се на већем броју експеримената у области физике космичког зрачења (AUGER и KASKADE међу значајнијима), а са великим успехом се примењује у оквиру Нискофонске лабораторије за нуклеарну физику.

2.2.3 Мионска компонента секундарног космичког зрачења

1937. године, мерећи губитак енергије честица у електромагнетним пљусковима космичког зрачења, Андерсен и Недермајер открили су класу честица чији се губитак енергије није понашао у складу са предвиђањима на основу Бете-Хајтлерове теорије за електроне или позитроне. Чинило се да ове новооткривене честице једва губе енергију при проласку кроз плочу од платине, као и да нису асоциране са електромагнетним пљусковима. Стога је ова класа названа "продорном" компонентом космичког зрачења.

На основу резултата ових енсперимената претпостављено је да се ради о честицама тежим од електрона. Накнадна мерење су показала да је то заиста случај и да је њихова маса већа од масе електрона за два реда величине (односно ред величине мања од масе протона). Након периода у коме се сматрало да су ове честице кандидат за тада предвиђени Јукавин преносилац нуклеарне интеракције, на основу чињенице да је у лаким апсорберима долазило до распада негативних честица (уместо предвиђене нуклеарне интеракције са језгрима), постало је јасно да то никако не могу бити Јукавине честице већ да се ради о новој класи честица које су назване *миони* [51].

Данас знамо да су миони лептони друге генерације, односно да су у питању

фермиони спина $\frac{1}{2}$. Маса износи $m = 105.6583745 \pm 0.0000024 MeV$ а средње време живота је $\tau = (2.1969811 \pm 0.0000022) \times 10^{-6} s$. Главни канал распада, са вероватноћом од приближно 100%, је $\mu^- \to e^- \bar{\nu}_e \nu_\mu$ (са коњугованим честицама у случају распада позитивног антимиона) [29].

Интеракција космичких миона са материјом

Миони (и антимиони) у секундарном космичком зрачењу углавном потичу из распада наелектрисаних пиона, а у мањој мери и распада наелектрисаних K мезона и других мање вероватних процеса. Како је у питању двочестични распад, а једна продукована честица је неутрино (односно антинеутрино), следи да су продуковани миони поларизовани.

Са језгрима атома ваздуха интерагују путем слабе интеракције због чега су пресеци за интеракцију мали, што донекле објашњава продорност мионске компоненте секундарног космичког зрачења [52]. Енергију углавном губе јонизујући атоме средине, а могу се распасти, према раније описаној шеми, било у лету или након што се зауставе. Нискоенергетски антимиони се распадају док нискоенергетски миони могу заменити један од електрона у атому и формирати такозвани "мионски атом". Када се мион нађе у $1s$ стању, може се распасти или бити захваћен од стране једног од протона везаног у језгру [53]. Шема овакве реакције захвата је:

$$p + \mu^- \longrightarrow n + \nu. \tag{2.24}$$

Осим за веома лака јазгра вероватноћа за захват је већа од вероватноће за распад (приближно је једнака за $Z = 11$) [52].

Главни процеси у којима миони губе енергију у интеракцији са материјом су процеси јонизације и ексцитације, продукција парова, закочно зрачење и нуклеарне интеракције [54].

Губитак енергије миона се пре свега одвија кроз процесе јонизације и ексцитације. Јонизација је добро описана Бетеовом формулом, на основу које се закључује, са обзиром на масу упадне честице, да миони занемарљиво мало

дивергирају у односу на оригинални правац. Избачени електрони се називају δ електронима (у случају да се њихове енергије налазе у интервалу $10 - 100keV$), односно *knock-on* електронима (у случају енергија реда MeV).

На вишим енергијама расту ефикасни пресеци за остале процесе. Директна продукција парова представља процес у коме мион губи енергију тако што долази до креације електронско-позитронског пара у интеракцији са Кулоновим пољем. Такође, у интеракцији са Кулоновим пољем језгра мион може емитовати закочно зрачење. Ефикасни пресек за овај процес је значајно мањи него у случају електрона (услед веће масе миона) али није занемарљив за мионе високих енергија. Електромагнетне каскаде, детектоване под великим упадним угловима у пљусковима секундарног космичког зрачења, су иницране фотонима који потичу из ових процеса [55].

Осим тога, високоенергетски миони имају незанемарљив пресек за нееластичне сударе са језгрима. Сматра се да је у питању процес апсорпције виртуелних фотона (асоцираних са мионом) од стране језгра и зато се често назива "фотонуклеарном" интеракцијом миона. На слици 2.16 приказан је допринос поменутих процеса укупном губитку енергије миона у гвожђу, у зависности од енергије упадне честице, а на основу симулације у програму Geant4.

Већина миона који стижу до нивоа мора имају енергија реда GeV. Доминантни процес кроз који ови миони губе енергију је јонизација. Губитак енергије путем јонизације слабо зависи од енергије миона. У првој апроксимацији се може сматрати да је константан и износи приближно $2MeV$ по g/cm^2 [2].

Мионска компонента у атмосфери

Да би се адекватно описао очекивани флукс миона на различитим атмосферским дубинама, неопходно је урачунати горе поменуте процесе. Више аутора је дало изразе који, иако се донекле разликују, адекватно описују флукс миона у атмосфери. У наредној глави ће бити представљено формално извођење Дормановог резултата, од кога полази теорија метеоролошких ефеката, док ћемо овде, без детаљнијег извођења, навести Гајзеров крајњи резултат.

Гајзер претпоставља да је енергетски спектар продукованих секундарних че-

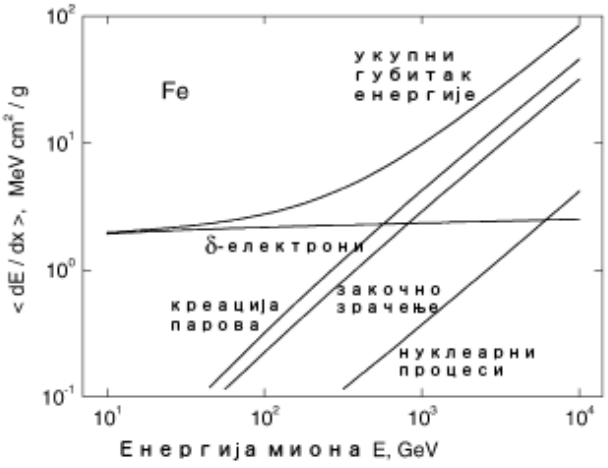

Слика 2.16: Допринос различитих процеса укупном губитку енергије миона у гвожђу на основу симулације у пакету Geant4 [56].

стица типа i, на некој дубини атмосфере, одређен сумом која укључује распаде свих честица типа j који могу продуковати честице типа i:

$$\mathcal{P}_i(E,X) = \sum_j \int_{E_{min}}^{E_{max}} \frac{\mathrm{d}n_i(E,E')}{\mathrm{d}E} \mathcal{D}_j(E',X)\mathrm{d}E', \tag{2.25}$$

где су $\mathrm{d}n_i(E,E')/\mathrm{d}E$ инклузивни спектар секундарних честица типа i продукованих у распадима честица типа j, $E_{min} \geq E$ и E_{max} минимална и максимална енергија честице типа j, док $\mathcal{D}_j(E',X)$ представља диференцијални спектар честица типа j.

На основу горњег израза, за спектар атмосферских миона добија се:

$$\frac{dN_\mu}{dE_\mu} \approx S_\mu(E_\mu)\frac{N_0(E_\mu)}{1-Z_{NN}}\Big[\mathcal{A}_{\pi\mu}\frac{1}{1+\mathcal{B}_{\pi\mu}\cos\theta E_\mu/\epsilon_\pi} + 0.635\mathcal{A}_{K\mu}\frac{1}{1+\mathcal{B}_{K\mu}\cos\theta E_\mu/\epsilon_K}\Big], \tag{2.26}$$

где су:

$$\mathcal{A}_{\pi\mu} \equiv Z_{N\pi}\left[1-(r_\pi)^{\gamma+1}\right](1-r_\pi)^{-1}(\gamma+1)^{-1} \tag{2.27}$$

и

$$\mathcal{B}_{\pi\mu} \equiv \frac{\gamma+2}{\gamma+1}\frac{1-(r_\pi)^{\gamma+1}}{1-(r_\pi)^{\gamma+2}}\frac{\Lambda_\pi-\Lambda_N}{\Lambda_\pi \ln(\Lambda_\pi/\Lambda_N)}, \tag{2.28}$$

док је:

$$S_\mu = \int_0^{X_0/\cos\theta}\frac{\mathrm{d}X}{\Lambda_N}\left(\frac{X\cos\theta}{X_0}\right)^{p_1} \times\left(\frac{E_\mu}{E_\mu+\alpha(X_0/\cos\theta-X)}\right)^{p_1+\gamma+1} exp\left[-\frac{X}{\Lambda_N}\right] \tag{2.29}$$

такозвани фактор супресије [8]. Изрази за $_{K\mu}$ и $\mathcal{B}_{K\mu}$ се добијају ако се у горњим једначинама маса пиона замени масом каона.

Величине у горњим изразима су: E_μ енергија миона, $N_0(E)$ флукс примара у зависности од енергије, Z_{ij} отежињени моменти који карактеришу продукцију честица типа j у распадима честица типа i, Λ_i атенуационе дужине, $\epsilon_\pi = \frac{m_\pi c^2}{\tau_\pi}\frac{RT}{Mg}$ (M - моларна маса ваздуха), r_i однос квадрата масе честице типа i и квадрата масе миона, док је X дубина атмосфере у g/cm^2. За експонент γ се обично подразумева вредност од 1.7.

Ако се коефицијенти у горњем изразу израчунају за случај високих енергија, када такође важи да је $S_\mu \longrightarrow 1$, добија се израз:

$$\frac{\mathrm{d}N_\mu}{\mathrm{d}E_\mu} \approx 0.14E_\mu^{-2.7}\left[\frac{1}{1+\frac{1.11E_\mu\cos\theta}{115GeV}}+\frac{0.054}{1+\frac{1.11E_{mu}\cos\theta}{850GeV}}\right]. \tag{2.30}$$

Експериментално добијени спектри су резултат комбинованих мерења земаљским детекторима (на различитим надморским висинама) и мерења високо у атмосфери (помоћу балона или авиона). Један такав комбинован резултат приказан је на слици 2.17.

На ниским енергијама (где важи $E_\mu << \epsilon_\pi$) спектар миона прати облик спектра честица примарног космичког зрачења, док на вишим енергијама постаје

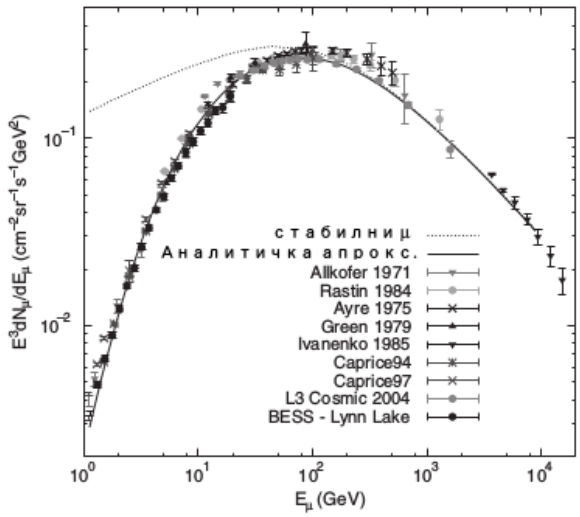

Слика 2.17: Поређење експериментално мереног флукса миона и флукса израчунатог на основу једначине. Испрекидана линија описује флукс у случају претпоставке да су миони стабилне честице 2.26 [8].

стрмији са обзиром да високоенергетски наелектрисани пиони не стижу да се распадну у атмосфери [2].

Однос броја позитивно и негативно наелектрисаних миона, енергија реда GeV, у горњим слојевима атмосфере је већи од јединице и одсликава састав примарних честица. Међутим, већина миона ових енергија који стижу на ниво мора је продукована на мањим висинама, где се у каснијој фази каскаде веза са примарним честицама губи а поменути однос смањује.

Мионска компонента на нивоу мора

Миони, уз фотоне и неутрина, представљају најбројније честице секундарног космичког зрачења на нивоу мора. То је последица чињенице да је вредност $c\tau = 658.6384m$ [29], односно да већ миони енергија већих од $2.5GeV$, продуковани у атмосфери на висини од $15km$, могу бити детектовани на нивоу мора.

Вредност ескпериментално мереног интензитета миона разумљиво зависи од различитих ефеката, које ћемо поменути касније, али за референцу можемо

навести Алкоферов резултат за интегрални вертикални интензитет тврде компоненте (односно за космичке мионе импулса већег од $0.35GeV/c$), који износи [1]:

$$I_v = (0.94 \pm 0.05) \times 10^{-2}[cm^2 s^{-1} sr^{-1}]. \tag{2.31}$$

Енергетски спектар је већ приказан на слици 2.17, где су узета у обзир и мерења земаљским детекторима. Вреди напоменути да је детекција миона највиших енергија могућа само у случају да је правац миона скоро хоризонталан, због чега је неопходно да земаљски детектор буде дирекционо осетљив. Услов је последица чињенице да је средњи слободни пут за распад наелектрисаних пиона, енергија довољно високих да продукују високоенергетске мионе, већи од дебљине атмосфере у вертикалном правцу, те је неопходно да пиони пређу већи пут како би се распали.

Такође, вероватноће за интеракцију односно распад пиона и каона зависе од упадног угла. Градијент промене густине атмосфере је мањи за веће упадне углове и као последица тога вероватноћа за распад пиона расте у односу на вероватноћу за интеракцију, резултујући сразмерно већим детектованим интезитетом високоенергетских миона [1].

Зависност интезитета од зенитног угла се за нискоенергетске мионе може описати изразом:

$$I(\theta) = I(0^\circ) \cos^n(\theta), \tag{2.32}$$

где n зависи од импулса. За мионе импулса $1GeV$, $n = 1.85 \pm 0.10$. Међутим, на енергијама реда $100GeV$ ова угаона расподела постаје практично константна [57].

На слици 2.18 приказана је зависност од зенитног угла за мионе различитог импулса, нумерички израчуната на основу Монте Карло симулације.

Раније поменути ширински ефекат, који је последица различите вредности граничне магнетне чврстоће на различитим геомагнетним ширинама, утиче на нискоенергетске секундарне мионе са енергијама до $5GeV$, а самим тим и на

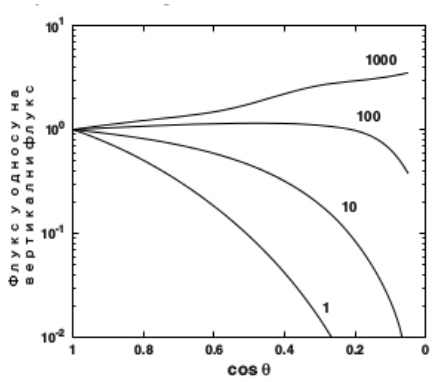

Слика 2.18: Однос флукса честица, које долазе под углом у односу на вертикални флукс, у зависности од зенитног угла θ. Уз сваку криву је наведен одговарајући импулс честица у јединицама GeV/c (на основу Монте Карло симулације) [2].

интегрални флукс. Величина која описује овај ефекат је дефинисана као:

$$L = I(\lambda_1, p)/I(\lambda_2, p), \tag{2.33}$$

где су $I(\lambda_i, p)$ интензитети на i-тој, односно j-тој геомагнетној ширини.

На слици 2.19 ширински ефекат илустрован је променом детектованог флукса миона (енергија већих од $70MeV$) за различите вредности граничне магнетне чврстоће. Експериментално мерене вредности су упоређене са вредностима израчунатим на основу Монте Карло симулације.

Флуксу миона на нивоу мора такође доприноси део миона који се расејава уназад од тла. Ова компонента може имати незанемарљив допринос фону у нискофонским експериментима, нарочито уколико су у питању експерименти у плитком подземљу.

Још увек отворено питање представља вишак секундарних миона детектованих у пљусковима индукованим честицама ПКЗ ултрависоких енергија. Наиме, у таквим пљусковима експериментално је дектовано $30 - 60\%$ миона више него што се може очекивати на основу продукције хадрона чијим распадом настају, како то предвиђају савремени генератори хадронских догађаја. Ови генератори су усаглашени са експериментима на великом хадронском сударачу (Large

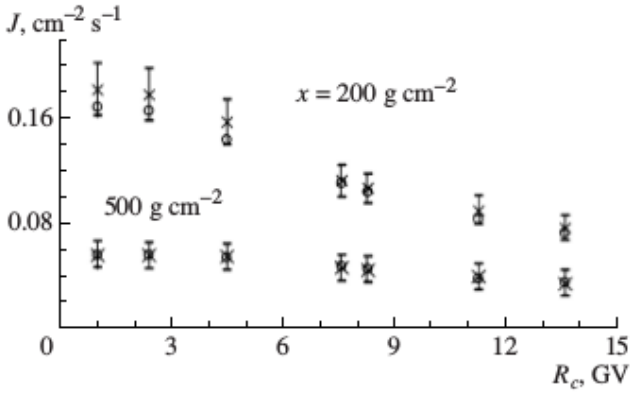

Слика 2.19: Зависност флукса космичких миона од граничне магнетне чврстоће, приказана за две дубине атмосфере: $200g/cm^2$500 и g/cm^2. Експериментално мерене вредности су приказане крстовима ($\times$) а израчунате вредности круговима($\circ$) [58].

Hadron Collider) у CERN-у. Примећено неслагање, на енергијама које су за ред величине веће од највећих тренутно доступних на акцелераторским експериментима, може указати на наше непотпуно познавање хадронских интеракција [59].

Мионска компонента испод земље

Секундарно космичко зрачење је могуће детектовати и испод земље. Међутим, док се највећи део електромагнетне и хадронске компоненте брзо апсорбује, миони (а нарочито неутрина) могу проћи кроз релативно дебеле слојеве земљишта и бити детектовани дубоко под земљом.

Уколико се претпостави вредност густине Земљине коре од $2.65g/cm^3$ (*стандардна стена*), дубини целе атмосфере одговара дубина стене тек нешто мања од 4 метра. Стога, вероватноћа за нуклеарне интеракције нестабилних хадрона је много већа од вероватноће за распад, док стабилни хадрони или интерагују или брзо губе енергију услед великих пресека за јонизацију. Електромагнетна каскада се такође врло брзо развија и апсорбује на малим дубинама у стени.

Како састав земљишта и стена варира у зависности од локације, дубина стене

се често изражава у еквивалентној дебљини воде. Јединице које се користе су *метар воденог еквивалента* (meter water eqivalent, $1m.w.e = 100g/cm^2$), односно *километар воденог еквивалента* ($1km.w.e = 10^5 g/cm^2$).

За мионе енергија реда GeV-а главни механизам путем кога губе енергију у атмосфери је јонизација. У подземљу други, раније поменути, процеси почињу да имају значајнију улогу. Јонизациони губици слабо зависе од енергије и у првој апроксимацији се може сматрати да су приближно константни и износе $\approx 2MeV$ по g/cm^2. Са друге стране, радијациони губици су пропорционални енергији миона, те се укупни губитак енергије миона може изразити као:

$$\frac{\mathrm{d}E_\mu}{\mathrm{d}x} = -a - bE_\mu, \tag{2.34}$$

где је a пропорционалан јонизационим губицима енергије, а $b = b_{br} + b_{pp} + b_{ph}$ представља збирни губитак енергије кроз радијационе процесе закочног зрачења, продукције парова и фотонуклеарне интеракције. За вредност $\epsilon = a/b \approx 500GeV$ јонизациони и радијациони губици енергије миона су приближно једнаки, па је јасно да у лимиту $E_\mu >> \epsilon$ доминирају јонизациони, а у уколико важи $E_\mu << \epsilon$ доминирају радијациони губици енергије. Решавањем горње једначине добијамо израз за енергију миона, почетне енергије E_μ^0, у зависности од пута X (у јединицама g/cm^2) у стени:

$$E_\mu = (E_\mu^0 + \epsilon) \times exp(-bX) - \epsilon, \tag{2.35}$$

односно израза за енергију миона на површини у зависности од дубине стене:

$$E_\mu^0 = (E_\mu + \epsilon) \times exp(bX) - \epsilon. \tag{2.36}$$

Уз услов $E_\mu = 0$ добија се израз за минималну енергију коју треба да има мион на површини како би дошао до дубине стене X:

$$E_\mu^{min} = \epsilon[exp(bX) - 1]. \tag{2.37}$$

На малим дубинама, за које важи $bX << 1$ односно $X << 1/bg/cm^2$ миони

доминантно губе енергију кроз процес јонизације и може се рећи да је $E_\mu^{min} \approx aX$. Према томе енергетски спектар миона у подземљу је пропорционалан спектру миона на површини, осим за вредности енергије испод $E_\mu^{min} \approx aX$ где постаје приближно једнак нули. На великим дубинама, где је $X >> 1/bg/cm^2$, спектар је скоро константан до вредности енергије $E_\mu \approx \epsilon$, да би на вишим енергијама постајао стрмији [2].

Спектар миона у подземљу се типично описује зависношћу интегралног вертикалног интензитета од дубине. Ако се за интензитет миона на површини претпостави облик AE_μ^γ, а минимална енергија миона који може да стигне на дубину X је одређена једначином 2.37, интегрални вертикални интезитет у зависности од дубине биће дат изразом:

$$F_\mu^{vert} = \frac{A\epsilon^{-(\gamma-1)}}{\gamma-1} e^{-(\gamma-1)bX}(1-e^{-bX})^{-(\gamma-1)} \tag{2.38}$$

Први терм је константа и одсликава спектар миона на површини Земље. Трећи терм је увек већи од један и на великим дубинама постаје приближно једнак јединици. Други терм се може представити у облику $exp(-X/X_0)$, где је $X_0 = [b(\gamma-1)]^{-1}$, и одређује облик зависности интензитета од дубине на великим дубинама.

На слици 2.20 приказана је ова зависност, као и референтни резултати неких експеримената.

За боље слагање са експерименталним резултатима неопходно је узети у обзир да јонизациони и радијациони губици зависе од енергије, као и урачунати флуктуације у губитку енергије миона.

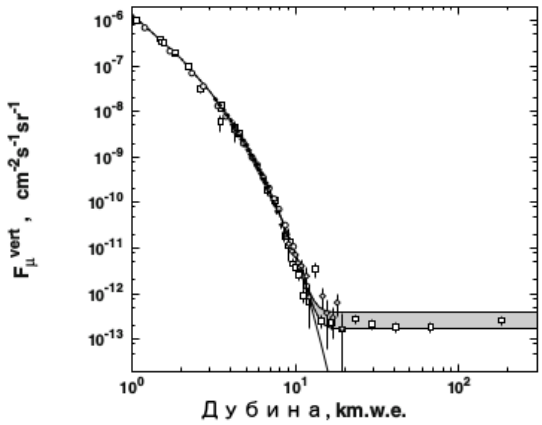

Слика 2.20: Зависност интегралног вертикалног интензитета миона од дубине - упоређење предвиђеног и експериментално мереног. Неке од тачака су добијене тако што је флукс миона мерен под различитим угловима прерачунат у одговарајући вертикални [2].

Метеоролошки ефекти на мионску компоненту секундарног космичког зрачења

Секундарно космичког зрачење на путу до површине Земље простире се кроз апсорбер - атмосферу. Атмосфера је динамичан систем, те је неопходно проучити да ли и како метеоролошки параметри и њихове варијације утичу на пропагацију различитих компоненти СКЗ. Нарочито је значајан утицај метеоролошких параметара на неутронску и мионску компоненту будући да већина дектора КЗ спада у категорију неутронских, односно мионских монитора. За неутронске мониторе се показало да постоји корелација детектованог флукса са атмосферским притиском - *барометарски ефекат*, док за мионску компоненту постоји и значајна корелација са температуром атмосфере - *температурски ефекат*.

Педесетих година 20. века развијена је и теорија метеоролошких ефеката која, полазећи од основних интеракција честица СКЗ у атмосфери, даје изразе за варијацију интензитета мионске компоненте у зависности од атмосферских параметара.

Будући да за проучавање модулација примарног космичког зрачења неатмосферског порекла ови секундарни ефекти представљају фонски процес, развијено је неколико метода за корекцију метеоролошких ефеката. Неки су базирани на емпиријском док се други ослањају на теоријски приступ.

3.1 Историјат открића метеоролошких ефеката

Најранији експерименти у физици космичког зрачења указали су на постојање флуктуација интезитета космичког зрачење. Мерења интензитета космике, која је Гокел (Gockel) 1915. године спроводио у Алпима на висини од 2200 метара, показала су да је интензитет флуктуација видно већи него у случају мерења при сличним условима у низији. Флуктуације су биле неправилне и релативни интензитет видно се мењао из дана у дан.

Колхорстер (Kolhörster) је, у мерењима које је 1923. и 1924. године вршио на глечеру на Јунгфраујоху (Jungfraujoch), поред постојања периодичних, уочио и апериодичне флуктуације. Периодичне флуктуације су имале период од једног дана и амплитуду која је износила 15 процената средњег интензитета космике и претпоставка је била да су последица Земљине ротације и неједнаке дистрибуције космичког зрачења у свемиру. Са друге стране Колхорстер је апериодичне флуктуације приписао инструменталним грешкама.

Мисковски (Мысовский) и Тувим су 1927. године, мерећи интензитет космичког зрачења у делти Неве, приметили да постоји веза између апериодичних флуктуација космике и атмосферског притиска. Показало се да промене детектованог интензитета космичког зрачења линеарно зависе од флуктуација атмосферског пристиска, односно да је ефекат последица варијације у апсорпцији космичког зрачења у атмосфери [60]. Накнадна мерења су потврдила ове резултате [61] и ефекат је назван *барометарским*.

Једну од првих анализа опаженог смањења интензитета продорне компоненте секундарног космичког зрачења, при порасту атмосферске температуре, дао је Блекет (Blackett) 1938. године. За ту компоненту се тада сматрало да се превасходно састоји од *баритрона*, честица који настају на висини од приближно 16 километара ($\sim 8 cmHg$). Те честице су заиста били миони, тада још увек погрешно идентификовани као претпостављени Јукавини (Yukawa) преносиоци јаке интеракције (уствари 10 година касније откривени пиони). Блекет је претпоставио да се детектовани ефекат може објаснити ширењем атмосфере при повећању темепературе, услед чега се повећава пут који баритрони (миони)

морају да пређу од нивоа на коме настају до нивоа на коме се детектују.

1947. године, мерећи интензитет космичког зрачења у руднику на дубини од $470m$ (око $1000m.w.e$), Форо (Forró) је утврдила да се детектована варијација интензитета услед температуре не може објаснити само постојањем већ уоченог *негативног* температурског ефекта (поменутог у претходном пасусу), већ да мора постојати и *позитивни* температурски ефекат који постаје нарочито значајан на дубинама већим од $300m.w.e$ [62].

Дуперијер (Duperier) је 1944. године израчунао висину нивоа атмосфере за који је претпостављено да представља ниво генерације миона [63] и [64]. Затим је 1949. године показао да модификована формула за варијацију интензитета миона, која претпоставља зависност само од атмосферског притиска (барометарски ефекат) и висине нивоа генерације (негативни температурски ефекат), не може коректно да опише експерименталне резултате, те да мора постојати најмање још један фактор. Дуперијерова анализа показује да миони доминантно настају у области атмосфере који налази између изобарних нивоа са вредностима $100mb$, односно $200mb$, и док је интензитет миона негативно корелисан са висином овог слоја, корелација са температуром овог слоја је позитивна. Тиме Дупериер квантитативно утврђује постојање позитивног температурског ефекта [65].

Такође, 1947. године идентификовани су наелектрисани пиони, као и да миони настају у распадима ових честица [66]. Стога је Дуперијер предложио да је позитивни температурски ефекат последица смањене вероватноће пиона за нуклеарне интеракције, односно веће вероватноће за распад на мионе. До овог смањења вероватноће долази услед локалног смањења густине атмосфере у околини нивоа генерације, а које је последица локалног повећања температуре. Две године касније утврђује да, осим варијације температуре слоја који се налази између изобарних нивоа $100mb$ и $200mb$, значајан допринос за позитивни температурски ефекат има и варијација температуре виших нивоа (између $50mb$ и $100mb$) [67].

1953. Олберт (Olbert) даје теоријску интерпретацију која узима у обзир чињеницу да се миони континуално продукују у слоју атмосфере ширем од оног

који Дуперијер узима у обзир. Такође, његова анализа узима у обзир јонизационе губитке миона у атмосфери, који нису били третирани у емпиријском моделу. У једначини која описује варијацију интензитета миона услед променљивих услова у атмосфери добија термове који зависе од атмосферског притиска и висине једног нивоа атмосфере (претпостављени доминантни ниво генерације миона), а који одговарају барометарском односно негативном температурском ефекту. Трећи терм, који одговара позитивном температурском ефекту, зависи од средње температуре целе тропосфере, за разлику од Дуперијеровог који зависи само од температуре слоја ниске стратосфере [68].

1956. Мурајама (Murayama) и сарадници користе теоријски приступ сличан Олбертовом али посматрају негативни температурски ефекат засебно у вишим и нишим слојевима атмосфере. Добијају једначину са четири терма чији облик је једноставнији за упоређење са Дуперијеровим експерименталним резултатима [69].

Настављајући рад који је започео Фајнберг (Фейнберг), Дорман је током педесетих година двадесетог века, паралелно са неколицином других аутора, развио теорију метеоролошких ефеката, коју је у интегралном облику објавио у својој монографији о космичког зрачењу 1972. године [4]. Иако су други аутори у каснијем периоду модификовали или допуњавали ову теорију, Дорманова интерпретација и данас представља једну од најчешће цитираних. Представља свеобухватну анализу, третира све значајне ефекте, применљива је на различите компоненте секундарног космичког зрачења, добро се слаже са експерименталним подацима и чини основу интегралног метода за корекцију флукса миона на метеоролошке ефекате.

Други аутори, као на пример Маеда (Maeda) и Вада (Wada), су у овом периоду и каснијим годинама дали свој допринос теорији метеоролошких ефеката. Поправке су се односиле на коришћење реалистичнијег средњег температурског профила атмосфере, узимање у обзир доприноса K мезона и друге. Међутим, главни резултати се тиме нису битно променили и за овај рад није неопходно детаљно навођење ових доприноса.

3.2 Теорија метеоролошких ефеката

3.2.1 Увод и рани резултати

Теорија метеоролошких ефеката свој приближни данашњи облик добила је средином педесетих година 20. века. У периоду од открића појединих ефеката до формулације теорије у зрелој форми развијено је више емпиријских и теоријских модела. Овде ћемо представити неке од најважнијих корака у овом развоју.

Као што је поменуто у претходном одељку, Мисовски и Тувим су открили корелацију атмосферског притиска са интензитетом продорне компоненте космичког зрачења. Сматрали су да је та корелација (барометарски ефекат) последица апсорпције продорне компоненте у атмосфери и да сходно томе мора зависити од укупне дебљине апсорбера, односно од атмосферског притиска мереног на опсервационом нивоу. Зависност интензитета зрачења од апсорпције у атмосфери описали су једначином:

$$J_{\theta=90^\circ} = \frac{1}{2} J f(\mu_{air} H) \tag{3.1}$$

где висина H варира пропорционално атмосферском притиску израженом у милиметрима живиног стуба. Мисовски и Тувим нашли су да варијацији притиска од $1mm$ одговара варијација интензитета космичког зрачења од $0.47 \pm 0.03\%$ [60].

Проучавајући негативну корелацију интензитета продорне (претежно мионске) компоненте космичког зрачења, Блекет је претпоставио да је детектовани негативни температурски ефекат последица ширења атмосфере при повећању температуре, односно повећања ефективне висине на којој миони настају. Предложио је следећи израз за температурски коефицијент којим се може описати дато смањење интензитета:

$$\alpha = -\delta z / L \delta\theta. \tag{3.2}$$

У горњем изразу δz представља повећање висине нивоа генерације баритро-

на а до кога долази услед повећања средње температуре атмосфере $\delta\theta$, док је L средњи слободни пут за распад баритрона који је, рачунат на основу тадашње процена средњег времена живота ових честица ($\tau_0 = 2.7 \times 10^{-6}s$), износио $32km$. Температурски коефицијент који је Блекет израчунао ($\alpha = -0.16\%$) доста добро се слагао са тада актуелним експерименталним резултатима ($\alpha = (0.180 \pm 0.011)\%$) [70].

Касније аутори су ова два ефекта обично обједињавали у следећем изразу:

$$\delta I = \mu \delta B + \mu' \delta H, \tag{3.3}$$

где су I релативни интензитет (изражен у процентима), B вредност притиска, μ вредност апсорпционог коефицијента, H висина референтног изобарног нивоа атмосфере и μ' вероватноћа за распад миона по јединици пређеног пута. Референтни изобарни ниво представља ниво атмосфере у околини кога се доминантно креирају секундарни миони.

Пажљивом статистичком анализом Дуперијер је утврдио да овај модел није у сагласности са експерименталним подацима. У то време већ је постојала индикација о позитивном температурском ефекту ([62]) и Дуперијер је сматрао да је неопходно узети у обзир додатни фактор. Претпоставио је да је овај додатни фактор густина атмосфере у околини нивоа генерације миона, односно да на варијацију интензитета миона утиче варијација густине атмосфере у слоју између референтног нивоа P и нивоа $P + 100mb$. Будући да је температура инверзно пропорционална густини, а ради се о величини која је директно мерљива, предлаже следећи израз којим би се описала варијација интензитета миона услед метеоролошких ефеката:

$$\delta I = \mu \delta B + \mu' \delta H + \alpha \delta T, \tag{3.4}$$

где додатни члан у односу на једначину 3.3 описује допринос варијације средње температуре слоја између P и $P + 100mb$.

На основу анализе парцијалних корелационих коефицијената Дуперијер идентификује изобарни ниво од $100mb$ као референтни ниво генерације. Према томе,

осим варијације атмосферског притиска, на варијацију интензитета миона утичу варијација висине нивоа P као и варијације температуре слоја који се налази између P и $P + 100mb$. За вредности одговарајућих коефицијената добија [65]:

$$\begin{aligned}
\mu &= -(0.77 \pm 0.12) \times 10^{-}3cm^2/g \\
\mu' &= -(3.90 \pm 1.10)\%/km \\
\alpha &= (0.123 \pm 0.024)\%/^{\circ}C
\end{aligned} \tag{3.5}$$

Касније, на основу прецизнијих метеоролошких сондирања, утврђује да је за позитиван температурски ефекат значајна варијација температуре у слоју који се налази између изобарних нивоа од $50mb$ и $200mb$ [67].

Један од раних покушаја да се дâ теоријска интерпретација метеоролошких ефеката потиче од Олберта [68]. Он полази од израза за вероватноћу да мион (у даљем тексту се подразумева да се то односи и на антимионе) креиран на висини z и који се брзином $\beta\gamma$ креће вертикално наниже стигне на опсервациони ниво који се налази на висини z_0:

$$w = exp\left[-\int_{z_0}^{z} \frac{(1-\beta)^{1/2}}{c\tau\beta}\mathrm{d}z'\right], \tag{3.6}$$

где је τ средње време живота миона.

Релевантне варијабле могу се изразити у зависности од атмосферске дубине x', односно резидуалног домета, дефинисаног као $R' = R + x_0 - x'$, где се примоване величине односе на ниво продукције, а величине са индексом нула на ниво опсервације. Тада се израз 3.6 трансформише у:

$$w(x, R) = exp\left[-\frac{\mathcal{R}}{c\tau Mg}\int_{x}^{x_0} \frac{T(x')}{x'}\Big(\frac{B}{x_e - x'} - \kappa\Big)\right], \tag{3.7}$$

где је $\mathcal{R}$ универзална гасна константа, M моларна маса ваздуха, g гравитационо убрзање, а $x_e = x_0 + R + b$. Константе у изразу имају следеће вредности: $B = 53.5gcm^{-2}$, $b = 56gcm^{-2}$ и $\kappa = 2.07 \times 10^{-3}$.

Варијација вероватноће услед варијације температуре може се даље изрази-

ти као:

$$\delta_T w(x,R) = w_{Av}(x,R)\left[\alpha_H \delta H(x) + \alpha_K \delta K(x,R)\right], \tag{3.8}$$

где су:

$$\alpha_H(R) = -\frac{1}{c\tau}\Big(\frac{B}{x_e - \kappa}\Big) = -\frac{\mu}{\tau p(x_0+R)'} \tag{3.9}$$

и

$$\alpha_K(R) = -\mathcal{R}B/Mgc\tau x_e^2, \tag{3.10}$$

док су:

$$\delta H(x) = \frac{\mathcal{R}}{Mg}\int_x^{x_0} \frac{\delta T(x')}{x'}\mathrm{d}x' \tag{3.11}$$

и

$$\delta K(x,R) = x_e \int_x^{x_0} \frac{\delta T(x')}{x_e - x'}\mathrm{d}x', \tag{3.12}$$

а w_{Av} представља средњу вероватноћу да мион стигне до опсервационог нивоа.

Варијација диференцијалног интензитета миона услед температурског ефекта се стога може представити као:

$$\delta_T i_v(R) = \int_0^{x_0} [\alpha_H \delta H(x) + \alpha_K \delta K(x,R)]\Phi(x,R)\mathrm{d}x, \tag{3.13}$$

где је $\Phi(x,R) = G(R_s)e^{-x/L}(w)_{Av}(x,R)$, односно:

$$G(R_s) = \frac{7.31\times 10^4}{(520+R_s)^{3.58}}(g^{-2}cm^2sec^{-1}sterad^{-1}). \tag{3.14}$$

Сличним поступком добија израз за варијацију диференцијалног интензитета миона услед варијације атмосферског притиска:

$$\delta_P i_v/i_v = a_p(R)\delta x_0. \tag{3.15}$$

У горњој једначини коефицијент a_p представља барометарски коефицијент и дат је изразом:

$$a_P(R) = \frac{3.58}{x_0 + R - x_2 + 520} + \gamma \frac{\partial \alpha_H}{\partial x_0} H(x_1) + \alpha_H \frac{\mathcal{R}T}{Mgx_0} + \frac{\partial}{\partial x_0}[\alpha_K K(x_2), R], \quad (3.16)$$

где су:

$$x_1 = \int_0^{x_0} x \ln(x_0/x)\Phi(x,R)\mathrm{d}x \Big/ \int_0^{x_0} \ln(x_0/x)\Phi(x,R)\mathrm{d}x, \quad (3.17)$$

$$x_2 = \int_0^{x_0} x\Phi(x,R)\mathrm{d}x \Big/ \int_0^{x_0} \Phi(x,R)\mathrm{d}x \quad (3.18)$$

и

$$\gamma = \Big[\int_0^{x_0} \ln(x_0/x)\Phi(x,R)\mathrm{d}x\Big] \Big/ \Big[\ln(x_0/x_1)\int_0^{x_0} \Phi(x,R)\mathrm{d}x\Big]. \quad (3.19)$$

Увођењем горња три израза у 3.13, једначина за диференцијални интензитет миона се може представити као:

$$\delta i_v/i_v = a_H \delta H(x_1) + a_K(R)[\delta T(x_2)]_{Av}, \quad (3.20)$$

где су:

$$\begin{aligned} a_H(R) &= \alpha_H(R)\gamma(R), \\ a_K(R) &= \frac{\mathcal{R}B}{Mgc\tau x_e} \ln\Big(x_e - x_2 x_e - x_0\Big), \\ [\delta T(x_2)]_{Av} &= \frac{1}{x_0 - x_2}\int_{x_2}^{x_0} \delta T(x')\mathrm{d}x'. \end{aligned} \quad (3.21)$$

За варијацију интегралног интензитета миона I_v услед метеоролошких ефеката Олберт добија израз:

$$\delta I_v/I_v = A_H \delta H(\bar{x}_1) + A_K[\delta T(\bar{x}_2)]_{Av} + A_P \delta X_0, \quad (3.22)$$

где су:

$$
\begin{aligned}
A_{H,K}(R_0) &= \frac{1}{I_v(R_0)} \int_{R_0}^{\infty} a_{H,K}(R) i_v(R) \mathrm{d}R, \\
\bar{x}_1 &= x_1(R_1), \quad \bar{x}_2 = x_2(R_2), \\
R_{1,2} &= \int_0^{\infty} a_{H,K} i_v \mathrm{d}R = \int_{R_0}^{\infty} R a_{H,K} i_v \mathrm{d}R, \\
A_P(R_0) &= \frac{1}{I_v(R_0)} \int_{R_0}^{\infty} a_P(R) i_v(R) \mathrm{d}R.
\end{aligned} \tag{3.23}
$$

Олбертова једначина 3.22 упоредива је са изразом 3.4 који је дао Дуперијер. Први и други терм у Дуперијеровој једначини односе се на варијацију интензитета миона услед варијације атмосферског притиска и висине ефективног нивоа генерације миона (негативни температурски ефекат) и одговарају трећем и првом терму у Олбертовој једначини. Преостали члан се код Дуперијера односи на варијацију температуре нивоа генерације (позитивни температурски ефекат), док је Олберт показао да је због јонизационих губитака неопходно узети у обзир и варијацију температуре нижих слојева атмосфере.

Израчунате вредности коефицијената у једначини 3.22 су:

$$
\begin{aligned}
A_H &= -3.15\%/km \\
A_K &= -0.059\%/^{\circ}C \\
A_P &= -1.79\%/cmHg.
\end{aligned} \tag{3.24}
$$

Вредности коефицијената који се односе на барометарски ефекат и висину негативни температурски ефекат добро се слажу са експериментално утврђеним вредностима. Вредност коефицијента који се односи на позитивни температурски ефекат је нешто теже упоредити будући да не постоји директна коресподенција. Такође, теоријски израчуната вредност ефективне вредности притиска нивоа генерације од $115 g cm^{-2}$ је сагласна са експериментално утврђеном вредношћу од приближно $100 g cm^{-2}$.

Мурајама и сарадници полазе од сличних претпоставнки као Олберт али уводе неколико новина [69]. Негативни температурски ефекат третирају одвојено у горњем и доњем делу атмосфере. За границу ова два дела узимају изобарни ниво од $300mb$. Негативни температурски ефекат у горњем делу атмосфере корелишу са варијацијом температуре овог слоја а не са висином нивоа генерације. Негативни температурски ефекат у доњем делу атмосфере се, као и код Олберта, односи на јонизационе губитке миона, али је јасно издвојен. Позитивни температурски ефекат је везан за варијацију изобарног нивоа од $20mb$ и директније упоредив са Дуперијеровим резултатима.

Према томе, варијација интегралног интензитета миона услед варијације атмосферских параметара дата је изразом:

$$\delta I/I = A_1\delta T_1 + A_2\delta T_2 + A_3\delta T_3 + A_p\delta p, \tag{3.25}$$

где су T_1 температура слоја у коме се доминира пионизација, док δT_2 и δT_3 представљају варијацију температуре горњег односно доњег дела атмосфере.

За вредности одговарајућих коефицијената израчунате су следеће вредности:

$$\begin{aligned} A_1 &= +.0568\%/^\circ C \\ A_2 &= -0.305\%/^\circ C \\ A_3 &= -0.157\%/^\circ C \\ A_p &= -0.072\%/mb. \end{aligned} \tag{3.26}$$

Вредност коефицијента за негативни температурски ефекат се добро слаже са Дуперијеровим резултатима док је вредност коефицијента који описује позитивни температурски ефекат мања него експериментално утврђена.

Резултати Олберта и Мурајаме не само да су помогли у квантитативној интерпретацији емпиријски утврђених корелација интензитета космичких миона са атмосферским параметрима, већ представљају значајне кораке у развоју пот-

пуније теорије метеоролошких ефеката. Зрелој форми те теорије је допринело више аутора који су раније већ поменути. Свакако један од најзначајнијих и најутицајнијих је био Дорман те ће у следећем одељку у главним цртама бити представљена теорија метеоролошких ефеката у форми коју је он објавио 1972. године, те цитирао у каснијим публикацијама [4]. Посебна пажња ће бити посвећена температурском ефекту на мионску компоненту, где Дорман демонстрира да он зависи не само од распада миона већ и од распада пиона, као и функције дистрибуције продукције пиона у нуклеарним интеракцијама честица ПКЗ са атомима атмосфере.

3.2.2 Теорија метеоролошких ефеката у једнодимензионалној апроксимацији

Нека је $f_\pi(E_\pi, h_1, Z)$ функција која описује продукцију $\pi^\pm$ мезона у зависности од дубине атмосфере која одговара притиску h_1, укупне енергије E_π и зенитног угла Z (егзактан облик функције ће бити наведен касније). Део наелектрисаних пиона ће бити захваћен од стране језгара атома ваздуха, што ће резултовати продукцијом већег броја секундарних честица. Међутим, миони продуковани у оваквим интеракцијама неће имати довољну енергију да стигну до површине Земље. Наелектрисани пиони који нису интераговали се распадају и продукују мионе.

Ако је l средњи слободни пут пиона за нуклеарне интеракције, тада ће $\mathrm{d}h/(l\cos Z)$ представљати део пиона захваћених у слоју атмосфере дебљине $\mathrm{d}h$. Ако са m_π и τ_π означимо масу и средње време живота пиона у миру, део пиона који се распада у слоју дебљине $\mathrm{d}h$ биће $\mathrm{d}\tau/\tau$, где је $\mathrm{d}\tau = \mathrm{d}h(c\rho(h)cosZ)^{-1}$ време потребно да пион прође кроз слој $\mathrm{d}h$, $\rho(h)$ густина ваздуха на нивоу h, c брзина светлости (којом се у овом случају може апроксимирати брзина пиона), док $\tau = \tau_\pi E_\pi/(m_\pi c^2)$ представља средње време живота наелектрисаних пиона у референтном систему везаном за Земљу.

Према томе вероватноћа да наелектрисани пиони неће бити захваћени, односно да се неће распасти у слоју између h_1 и h_2 дата је изразом:

$$\phi_\pi(E_\pi, h_1, h_2, Z) = \exp\left(-\frac{h_2 - h_1}{l\cos Z}\right)\exp\left(-\frac{m_\pi c}{\tau_\pi E_\pi cosZ}\int_{h_1}^{h_2}\frac{\mathrm{d}h}{\rho(h)}\right). \tag{3.27}$$

Како продукција пиона почиње од највиших слојева атмосфере ($h_1 = 0$), интензитет пиона на висини h_2 биће:

$$N_\pi(E_\pi, h_2, Z) = \int_0^{h_2} f_\pi(E_\pi, h_1, Z)\phi_\pi(E_\pi, h_1, h_2, Z)\mathrm{d}h_1. \tag{3.28}$$

Може се сматрати да миони настају скоро искључиво у распадима наелектрисаних пиона. Правац простирања продукованих миона је практично исти као и пиона у чијим распадима настају. У том случају број миона креираних распадом пиона енергије E_π у слоју између h_2 и $h_2 + \mathrm{d}h_2$ биће:

$$f_\mu(E_\pi, h_2, Z)\mathrm{d}h_2 = \frac{\mathrm{d}\tau}{\tau}N_\pi(E_\pi, h_2, Z) = \frac{m_\pi c}{\tau_\pi E_\pi}\frac{N_\pi(E_\pi, h_2, Z)\mathrm{d}h_2}{\rho(h_2)\cos Z}\mathrm{d}f. \tag{3.29}$$

Може се показати да је апроксимативни однос енергија миона и пиона у чијем распаду је настао дат као $\langle E_\pi\rangle \approx E_\mu\alpha$, где је $\alpha = m_\mu/m_\pi$. Тада ће мион енергије $E_\mu = \alpha E_\pi$, продукован на нивоу h_2 у распаду пиона енергије E_π, на нивоу h имати енергију $\alpha E_\pi - a(h-h_2)/\cos Z$, где је a енергију коју мион изгуби пролазећи кроз $1g/cm^2$ ваздуха ($a = 2MeV/(g/cm^2)$ за релативистичке честице јединичног наелектрисања).

Са обзиром да миони скоро да не интерагују са језгрима атома ваздуха, интензитет миона се смањује само путем њихових распада на електроне и одговарајућа неутрина, па се вероватноћа да мион продукован на нивоу h_2 стигне на опсервациони ниво h_0 може изразити као:

$$\phi_\mu(E_\pi, h_2, h_0, Z) = \exp\Big(-\frac{m_\mu c}{\tau_\mu}\int_{h_2}^{h_0}\frac{\mathrm{d}h}{\rho(h)}(\alpha E_\pi\cos Z) - a(h-h_2)^{-1}\Big). \tag{3.30}$$

Како се миони продукују од највишег слоја атмосфере ($h_2 = 0$), за интензитет миона на опсервационом нивоу h_0 добија се израз:

$$N_\mu(h_0, Z, E_{\mu_{min}}) = \int_{E_{\pi_{min}}}^{\infty} \mathrm{d}E \int_0^{h_0} f_\mu(E_\pi, h_2, Z)\phi_\mu(E_\pi, h_2, h_0, Z)\mathrm{d}h_2, \qquad (3.31)$$

где је $E_{\pi_{min}}$ минимална енергија пиона чијим распадом настаје мион који у тренутку продукције има енергију $E_{\mu_{min}}$. За план-паралелни детектор релација ове две енергије је $E_{\pi_{min}} = (a(h_0 - h_2) + E_{\mu_{min}})/\alpha \cos Z$.

Коначно, за интензитет миона на опсервационом нивоу h_0 добија се израз:

$$N_\mu(h_0, Z, E_{\mu_{min}}) = \int_{E_{\pi_{min}}}^{\infty} \mathrm{d}E_\pi \int_0^{h_0} \mathrm{d}h_2 \int_0^{h_2} \mathrm{d}h_1 F(E_\pi, h_1, h_2, h_0, Z), \qquad (3.32)$$

где је

$$F(E_\pi, h_1, h_2, h_0, Z) = \frac{m_\pi c f_\pi(E_\pi, h_1, Z)}{\tau_\pi E_\pi \rho(h_2) \cos Z} \exp\left(-\frac{m_\pi c}{\tau_\pi E_\pi \cos Z} \int_{h_1}^{h_2} \frac{\mathrm{d}h}{\rho(h)}\right)$$
$$\times \exp\left(-\frac{h_2 - h_1}{l \cos Z}\right) \exp\left(-\frac{m_\mu c}{\tau_\mu} \int_{h_2}^{h_0} \frac{\mathrm{d}(h)}{\rho(h)} (\alpha E_\pi \cos Z - a(h - h_2))^{-1}\right). \qquad (3.33)$$

Ако једначину 3.32 варирамо по свим варијаблама које зависе од метеоролошких параметара $(E_{\pi_{min}}, h_0, \rho(h))$, за варијацију интензитета миона услед метеоролошких ефеката добијамо:

$$\delta N_\mu(h_0, Z, E_{\mu_{min}}) = -\delta E_{\pi_{min}} \int_0^{h_0} \mathrm{d}h_2 \int_0^{h_2} \mathrm{d}h_1 F(E_{\pi_{min}}, h_1, h_2, h_0, Z)$$
$$+ \delta h_0 \int_{E_{\pi_{min}}}^{\infty} \mathrm{d}E_\pi \exp\left(-\frac{h_2 - h_1}{l \cos Z}\right) \left\{ \int_0^{h_0} \mathrm{d}h_1 F(E_\pi, h_1, h_2, h_0, Z) \right.$$
$$\left. - \frac{m_\mu c}{\tau_\mu \rho(h_0)} \int_0^{h_0} \mathrm{d}h_2 \int_0^{h_2} \mathrm{d}h_1 \frac{F(E_\pi, h_1, h_2, h_0, Z)}{\alpha E_\pi} \cos Z - a(h_0 - h_2) \right\}$$
$$- \int_{E_{\pi_{min}}}^{\infty} \mathrm{d}E_\pi \int_0^{h_0} \mathrm{d}h_2 \frac{\delta\rho(h_2)}{\rho(h_2)} \int_0^{h_0} \mathrm{d}h_1 F(E_\pi, h_1, h_2, h_0, Z)$$
$$+ \int_{E_{\pi_{min}}}^{\infty} \mathrm{d}E_\pi \int_0^{h_0} \mathrm{d}h_2 \int_0^{h_2} \mathrm{d}h_1 F(E_\pi, h_1, h_2, h_0, Z)$$
$$\times \left\{ \frac{m_\pi c}{\tau_\pi E_\pi \cos Z} \int_{h_1}^{h_2} \frac{\mathrm{d}h \delta\rho(h)}{\rho^2(h)} + \frac{m_\mu c}{\tau_\mu} \int_{h_2}^{h_0} \frac{\mathrm{d}h}{\rho^2(h)} \frac{\delta\rho(h)}{\alpha E_\pi \cos Z - a(h_0 - h_2)} \right\}. \quad (3.34)$$

Први члан у једначини 3.34 односи се на апсорпциони ефекат услед варијације $E_{\pi_{min}}$. Други терм има два члана. Први је позитиван и одражава додатну продукцију пиона услед повећања укупне дебљине атмосфере (овај члан је доминантан на великим висинама где је барометарски ефекат позитиван, али је занемарљиво мали на нивоу мора). Други члан је негативан због повећања броја миона који се распадају. Ово повећање је последица веће висине нивоа на коме се продукују миони а до кога долази због веће дебљине атмосфере h_0. Трећи четврти члан су последица локалне варијације густине атмосфере која утиче на вероватноћу распада наелектрисаних пиона и миона продукованих у њиховим распадима.

Густина се може изразити на следећи начин:

$$\rho(h) = \frac{g\bar{h}}{R(h)T(h)}, \quad (3.35)$$

где су g Земљино гравитационо убрзање, $\bar{h}$ је маса ваздуха у вертикалном цилиндру попречног пресека $1cm^2$, $R(h)$ гасна константа ваздуха (која је у првој апроксимацији једнака гасној константи сувог ваздуха R_0 али у општем случају зависи од влажности ваздуха), а $T(h)$ апсолутна температура ваздуха. Тада варијације везане за густину ваздуха можемо изразити као:

$$\frac{\delta\rho(h)}{\rho(h)} = \frac{\delta g}{g} - \frac{\delta R(h)}{R(h)} - \frac{\delta Th}{T(h)}; \quad \frac{\delta\rho(h)}{\rho^2(h)} = \frac{\delta g}{\rho(h)g} - \frac{T(h)}{gh}\delta R(h) - \frac{R(h)}{gh}\delta T(h). \quad (3.36)$$

Да бисмо се израчунала варијација интензитета миона на основу једначине 3.34 неопходно је познавање функције продукције пиона у атмосфери, $f_\pi(E_\pi, h_1, Z)$. Ова функција се апроксимативно може изразити као:

$$f_\pi(E_\pi, h_1, Z) = AE_\pi^{-(2+\gamma)} \exp\left(-\frac{h_1}{L\cos Z}\right), \quad (3.37)$$

где је A константа, $0 < \gamma < 1$, а L је средњи слободни пут за апсорпцију нуклеонске компоненте примарног космичког зрачења у чијим интеракцијама долази до продукције наелектрисаних пиона.

Израз који се добија за варијацију интензитета миона услед метеоролошких ефеката је доста комплексан али се може раздвојити на основу различитих типове метеоролошких ефеката. То су: такозвани *снежни* ефекат (везан за варијацију минималне енергије миона услед апсорпције), барометарски ефекат, температурски ефекат, ефекат влажности и гравитациони ефекат (везан за апсорпцију и распад пиона и миона).

У овом раду се превасходно бавимо температурским и барометарским ефектом те није неопходно цитирати теорију метеоролошких ефеката у пуном обиму. Штавише, барометарски ефекат се типично третира емпиријски па ће овде аналитички облик бити наведен само у најопштијој форми. Међутим, за примену интегралног метода корекције интензитета космичких миона на метеоролошке ефекте (о коме ће бити више речи у одељку 3.4.2) неопходно је температурски ефекат навести у потпунијој аналитичкој форми.

Пре него што наведемо изразе за ова два ефекта увешћемо функцију:

$$\Phi(E_\pi, h_1, h_2, h_0, Z, E_{\mu_{min}}) = F(E_\pi, h_1, h_2, h_0, Z)/N_\mu(h_0, Z, E_{\mu_{min}}), \quad (3.38)$$

где је израз за $N_\mu(h_0, Z, E_{\mu_{min}})$ дат у једначини 3.32 а за $F(E_\pi, h_1, h_2, h_0, Z)$

у једначини 3.33.

Барометарски ефекат се сада може изразити као:

$$\left.\frac{\delta N_\mu(h_0,Z,E_{\mu_{min}})}{N_\mu(h_0,Z,E_{\mu_{min}})}\right|_{bar} = \delta h_0 \times \{-a\alpha^{-1}\int_0^{h_0}\mathrm{d}h_2\int_0^{h_2}\mathrm{d}h_1\Phi(E_{\pi_{min}},h_1,h_2,h_0,Z,E_{\mu_{min}}) - \frac{m_\mu c}{\tau_\mu\rho(h_0)}\int_{E_{\pi_{min}}}^{\infty}\mathrm{d}E_\pi\int_0^{h_0}\mathrm{d}h_2\int_0^{h_2}\mathrm{d}h_1\frac{\Phi(E_\pi,h_1,h_2,h_0,Z,E_{\mu_{min}})}{\alpha E_\pi\cos Z - a(h_0-h_2)} + \int_{E_{\pi_{min}}}^{\infty}\mathrm{d}E_\pi\int_0^{h_2}\mathrm{d}h_1\Phi(E_\pi,h_1,h_2,h_0,Z,E_{\mu_{min}})\}. \quad (3.39)$$

Три члана у једначини 3.39 везани су за процесе апсорпције, распада и продукције миона респективно.

Температурски ефекат, који је последица процеса распада и нуклеарних интеракција пиона, као и распада и губитака енергије миона услед јонизације, има облик:

$$\left.\frac{\delta N_\mu(h_0,Z,E_{\mu_{min}})}{N_\mu(h_0,Z,E_{\mu_{min}})}\right|_{temp} = \int_{E_{\pi_{min}}}^{\infty}\mathrm{d}E_\pi\int_0^{h_0}\mathrm{d}h_2\int_0^{h_2}\mathrm{d}h_1\Phi(E_\pi,h_1,h_2,h_0,Z,E_{\mu_{min}})\times \left\{\frac{\delta T(h_2)}{T(h_2)} - \frac{R_0 m_\pi c}{gE_\pi\tau_\pi\cos Z}\int_{h_1}^{h_2}\frac{\mathrm{d}h\delta T(h)}{h} - \frac{R_0 m_\mu c}{g\tau_\mu}\int_{h_2}^{h_0}\frac{\mathrm{d}h}{h}\frac{\delta T(h)}{\alpha E_\pi\cos Z - a(h-h_2)}\right\}. \quad (3.40)$$

Параметар a се односи на јонизациони губитак енергије миона у атмосфери. У горњим једначинама се претпоставља да је a константа, што је тачно за мионе енергија $\alpha E_\pi < 10^{10}eV$. У том интервалу енергија приближно важи $a = 2\times10^6 eV/(gcm^{-2})$. На енергијама већим од $10^{11}eV$ овај параметар није константан, али тада и јонизациони губици енергије постају занемарљиви у односу на укупну енергију миона.

Уколико енергију пиона и миона изразимо у јединицама $2GeV$, а дубину атмосфере у јединицама atm, где је $1atm = 1000gcm^{-2}$, параметар a има вредност $a = 1$.

Да би се израчунале очекиване вредности величина које фигуришу у изразима за коефицијенте који се односе на различите метеоролошке ефекте, користи се приближни температурски профил атмосфере дефинисан као:

$$T(h) = \begin{cases} 220, & h \leq 0.2atm, \\ 204 + 80h, & h > 0.2atm. \end{cases} \tag{3.41}$$

Сада се очекивани интензитет миона на опсервационом нивоу, као и његова релативна варијација услед варијације температуре, могу изразити као:

$$N_\mu(h_0, Z, E_{\mu_{min}}) = A(\alpha \cos Z)^{1+\gamma} N_\gamma(h_0, Z, E_{\mu_{min}}), \tag{3.42}$$

$$\left.\frac{\delta N_\mu(h_0, Z, E_{\mu_{min}})}{N_\mu(h_0, Z, E_{\mu_{min}})}\right|_{temp} = \int_0^{h_0} W_T(h, h_0, E_{\mu_{min}}, Z)\delta T(h)\mathrm{d}h, \tag{3.43}$$

где је

$$W_T(h, h_0, E_{\mu_{min}}, Z) = W_T^\pi(h, h_0, E_{\mu_{min}}, Z) + W_T^\mu(h, h_0, E_{\mu_{min}}, Z) \tag{3.44}$$

и

$$N_\gamma(h_0, Z, E_{\mu_{min}}) = \int_0^{h_0} \frac{\exp(-h2/L\cos Z)\phi_\gamma(s, \nu)\mathrm{d}h_2}{(h_0 - h_2 + E_{\mu_{min}})^{1+\gamma}}, \tag{3.45}$$

$$W_T^\pi(h, h_0, E_{\mu_{min}}, Z) = \frac{h\exp(-h/L\cos Z)\chi_\gamma(s, \nu)}{\alpha\lambda b_\pi(h)T(h)(h_0 - h_2 + E_{\mu_{min}})^\gamma N_\gamma \cos Z}, \tag{3.46}$$

$$W_T^\mu(h, h_0, E_{\mu_{min}}, Z) = \frac{m_\mu c R_0}{\tau h N_\gamma} \int_0^h \frac{\exp(-h_2/L\cos Z) f_\gamma(s, k, \nu)\mathrm{d}h_2}{(h_0 - h_2 + E_{\mu_{min}})^{2+\gamma}}. \tag{3.47}$$

У једначинама 3.45 - 3.47 коришћене су следеће помоћне функције:

$$\phi(s,\nu) = \int_0^1 t^{1+\gamma}(t+s)^{-1}e^{\nu t}\mathrm{d}t,$$
$$\chi(s,\nu) = \int_0^1 t^{1+\gamma}(t+s)^{-2}e^{\nu t}\mathrm{d}t,$$
$$f_\gamma(s,k,\nu) = \int_0^1 kt^{2+\gamma}(t+s)^{-1}(k-t)^{-1}e^{\nu t}\mathrm{d}t, \tag{3.48}$$

где су

$$s = \frac{h_2(h_0 - h_2 + E_{\mu_{min}})}{\alpha\lambda b_\pi(h_2)\cos Z}, \quad t = \frac{E_{\pi_{min}}}{E_\pi} = \frac{E_{\mu min} + h_0 - h_2}{\alpha E_{pi}\cos\theta}$$
$$k = \frac{h_0 - h_2 + E_{\mu_{min}}}{h - h_2}, \quad \lambda = lL(L-l)^{-1} \tag{3.49}$$

$$\nu = \begin{cases} \dfrac{\eta_{\mu_1}\ln\left[\dfrac{h_2}{h_0}\left(1 - \dfrac{t(h_0-h_2)}{h_0-h_2+E_{\mu_{min}}}\right)\right]}{h_0 - h_2(1-t) + E_{\mu_{min}}}, & \text{за } h_0 \le 0.2atm \\ \dfrac{\eta_{\mu_1}\ln\left[\dfrac{0.2}{h_2}\left(1 - \dfrac{t(h_0-h_2)}{h_0-h_2+E_{\mu_{min}}}\right)\right]}{h_0 - h_2(1-t) + E_{\mu_{min}}} + \dfrac{\eta_{\mu_3}}{t}\ln\left(\dfrac{1 - \dfrac{t(h_0-h_2)}{h_0-h_2+E_{\mu_{min}}}}{1 - \dfrac{t(0.2-h_2)}{h_0-h_2+E_{\mu_{min}}}}\right), \\ \quad + \dfrac{\eta_{\mu_2}\ln\left[\dfrac{0.2}{h_0}\left(1 - \dfrac{t(h_0-h_2)}{h_0-h_2+E_{\mu_{min}}}\right)\left(1 - \dfrac{t(0.2-h_2)}{h_0-h_2+E_{\mu_{min}}}\right)^{-1}\right]}{h_0 - h_2(1-t) + E_{\mu_{min}}}, \\ \qquad\qquad \text{за } h_0 > 0.2atm, h_2 \le 0.2atm, \\ \dfrac{\eta_{\mu_2}\ln\left[\dfrac{h_2}{h_0}\left(1 - \dfrac{t(h_0-h_2)}{h_0-h_2+E_{\mu_{min}}}\right)\right]}{h_0 - h_2(1-t) + E_{\mu_{min}}} + \dfrac{\eta_{\mu_3}}{t}\left(\dfrac{t(h_0-h_2)}{h_0-h_2+E_{\mu_{min}}}\right), \\ \qquad\qquad \text{за } h_2 > 0.2atm. \end{cases} \tag{3.50}$$

У горњим једначинама коришћени су следећи помоћни изрази:

$$b(\pi) = \begin{cases} \eta_{\pi_1}, \text{за } h \leq 0.2atm, \\ \eta_{\pi_2} + h\eta_{\pi_3}, \text{за } h > 0.2atm, \end{cases} \tag{3.51}$$

где су:

$$\begin{array}{l} \eta_{\pi_1} = 220R_0 m_\pi c\tau_\pi^{-1} g^{-1}, \eta_{\pi_2} = 204R_0 m_\pi c\tau_\pi^{-1} g^{-1}, \eta_{\pi_3} = 80R_0 m_\pi c\tau_\pi^{-1} g^{-1} \\ \eta_{\mu_1} = 220R_0 m_\mu c\tau_\mu^{-1} g^{-1}, \eta_{\mu_2} = 204R_0 m_\mu c\tau_\mu^{-1} g^{-1}, \eta_{\mu_3} = 80R_0 m_\mu c\tau_\mu^{-1} g^{-1} \end{array}. \tag{3.52}$$

Овим завршавамо преглед теорије метеоролошких ефеката на мионску компоненту СКЗ, са обзиром да постоји неопходна основа за разумевање метода за корекцију детектованог флукса.

3.3 Методи за корекцију метеороloших ефеката

Већ је поменуто да се модулација примарног космичког зрачења различитим процесима у хелиосфери и друге варијације ПКЗ огледају и у промени флукса секундарног космичког зрачења. За проучавање ових процеса земаљским детекторима, као што су неутронски и мионски монитори, варијације СКЗ услед променљивих услова у атмосфери представљају фонски процес. Стога је развијено неколико метода за корекцију флукса неутрона и миона на метеоролошке ефекте. Будући да се у Нискофонској лабораторији за нуклеарну физику мери мионски флукс (поставка експеримента је детаљније описана у секцији 4.1), описаћемо методе који се односе на корекцију овог флукса на атмосферске ефекте. Наведени методи базирају се на емпиријским и теоријским моделима представљеним у претходној секцији и то су: метод ефективног нивоа продукције, интегрални метод, метод усредњене температуре и метод ефективне температуре.

Метод ефективног нивоа продукције и метод средње температуре истовремено третирају температурски и барометарски ефекат. Остали наведени методи се односе само на корекцију температурског ефекта, док се коефицијент за

барометарски ефекат утврђује накнадно линеарном регресијом зависности мионског флукса од атмосферског притиска. Мерени флукс се претходно коригује на температурски ефекат.

3.3.1 Метод ефективног нивоа продукције

Метод ефективног нивоа продукције заснива се на Дуперијеровом моделу метеоролошких ефеката на флукс космичких миона. Као што је раније поменуто, Дуперијер варијацију мионског флукса описује помоћу једначине:

$$\delta I = \mu \delta B + \mu' \delta H + \alpha \delta T. \tag{3.53}$$

Висина H представља висину референтног нивоа који одговара слоју атмосфере у коме долази до продукције највећег броја миона. Највећи број аутора који користе ову методу сматра да је то слој приближно између $100mb$ и $200mb$, те се за висину H узима висина нивоа од $100mb$ (приближне вредности су условљене доступним метеоролошким подацима који се мере за стандардно утврђене изобарне нивое). Такође, будући да се у стратосфери температура слабо мења са променом висине, сматра се да је температура тог слоја добро апроксимирана температуром која одговара нивоу од $100mb$.

Температура референтног нивоа се мери метеоролошким балонима. За неке локације, нарочито у урбанијим срединама, ова мерења стандардно врше локалне или јавне метеоролошке службе. Међутим, за удаљеније локације то често није случај и тада се морају вршити наменска мерења метеоролошким балонима или користити моделоване температуре (о чему ће детаљније бити речено у одељку 4.2.1). Вредности атмосферског притиска за дату локацију су лако доступне, *in situ* мерењима или на основу података јавних метеоролошких сервиса. Висина референтног нивоа се може израчунати на основу формула као што су хипсометријска или барометарска.

Одговарајући коефицијенти у изразу 3.53 утврђују се на основу вишеструке линеарне регресије, односно представљају коефицијенте линеарне регресије реазидуалних вредности две варијабле од интереса, након корекције на зависност

од осталих варијабли у вишеструкој регресији.

Компаративне предности овог метода су једноставност примене, мали скуп независних варијабли које је неопходно мерити, доста добра ефикасност и једноставна интепретација резултата. Са друге стране, чињеница да се не узима у обзир целокупни температурски профил атмосфере ограничава ефикасност метода и смањује применљивост, нарочито када је у питању проучавање ефеката мањег интензитета.

3.3.2 Интегрални метод

Интегрални метод се заснива на теоријски добијеном изразу за варијацију мионског флукса услед варијације температуре атмосфере. Ова варијација је дата следећом једначином:

$$\delta I_T = \int_0^{h_0} \alpha_T(h)\delta T(h)\mathrm{d}h, \tag{3.54}$$

где δI_T релативна варијација флукса космичких миона, $W_T(h)$ температурски коефицијент а $\delta T(h) = T_B(h) - T(h)$, односно варијација температуре $T(h)$ у односу на неку базну температуру $T_B(h)$ за дати изобарни ниво h. $W_T(h)$ је интегрални температурски коефицијент и представља директан збир позитивног ($W_T^{\pi}(h)$) и негативног ($W_T^{\mu}(h)$) температурског коефицијента.

За примену овог метода неопходно је потпуно познавање температурског профила атмосфере што је у пракси немогуће. Међутим, метеоролошка сондирања атмосфере, односно подаци добијени на основу модела, дају вредности температуре за довољан број нивоа да се у пракси за израчунавање варијације мионског флукса услед температурског ефекта може применити модификована једначина 3.54:

$$\Delta I_T = \sum_{i=0}^{n} \alpha_T(h_i)\Delta T(h_i)\Delta h_i, \tag{3.55}$$

где су h_i нивои за које су доступна мерења. Типично n се креће од 10 до 30 а температурски коефицијент умерено до слабо варира у зависности од висине, те прелазак на суму представља добру апроксимацију.

Више аутора је вршило упоређења интегралног и Дуперијеровог метода и већина се слаже да је интегрални метод ефикаснији у корекцији флукса космичких миона [71, 72, 73], мада има и аутора који су сматрали да разлика није значајна [74]. Због тога се интегрални метод често узима као референтни, а чињеница да се теоријски температурски коефицијент одређује независно представља највећу компаративну предност овог метода у односу на Дуперијеров метод.

Ипак, примена је нешто компликованија јер захтева израчунавање температурског коефицијента и нужно детаљније познавање температурског профила атмосфере. Овај други захтев је дуго био разлог за мање раширену примену интегралног метода, међутим у последњих пар деценија доступни су модели атмосфере који доста коректно описују велики скуп атмосферских параметара, као што је температура, и у многоме олакшавају примену интегралног метода.

3.3.3 Метод усредњене температуре

Метод усредњене температуре заснива се на апроксимацији интегралног метода. Наиме, температурски коефицијент не варира много у зависности од дубине атмосфере па су неки аутори [75] сматрали да се без већег губитка ефикасноти може претпоставити да је вредност температурског коефицијента константна.

У том случају једначина 3.54 се своди на облик:

$$\delta I_T = \bar{\alpha}_T \int_0^{h_0} \delta T(h) \mathrm{d}h = \bar{\alpha}_T^* \sum_{i=0}^{n} \frac{h_i - h_{i+1}}{h_0} \bar{T}_i = \bar{\alpha}_T^* \delta T_m, \tag{3.56}$$

где су $\bar{\alpha}$ средња вредност температурског коефицијента у интервалу $(0, h_0)$, $\bar{\alpha}_T^*$ вредност коефицијента помножена дубином целокупне атмосфере, а δT_m температура атмосфере усредњена по маси.

Овај метод је нешто једноставнији за примену јер не захтева израчунавање температурског коефицијента. За израчунавање отежињене температуре довољно је само познавање температурског профила атмосфере а температурски коефицијент се затим добија линеарном регресијом зависности детектованог флукса миона од отежињене температуре.

Упоређења са другим методима су показала да је овај метод приметно ефикаснији од метода ефективног нивоа продукције а тек нешто мало мање ефикасан од интегралног метода [76]. Стога, у случају да су доступни неопходни атмосферски подаци, овај метод има значајну практичну примену.

3.3.4 Метод ефективне температуре

Последњи метод ћемо описати само у најопштијим цртама. Обично се примењује за корекцију флукса миона високих енергија детектованих на већим дубинама ($\approx 1000 m.w.e$), те је од мањег значаја за примену на податке Београдске мионске станице и овде је поменут пре свега због комплетности.

Претпоставка на којој се овај метод базира је да је негативни температурски ефекат на мионе који имају довољно велике енергије да стигну у дубоко подземље занемарљив, односно да је за такве мионе значајан пре свега позитивни температурски ефекат [77]. Будући да је варијација интензитета миона услед варијације температуре атмосфере мала, детаљан температурски профил атмосфере се може заменити ефективном температуром. Ефективна температура представља температуру изотермалне атмосфере која би продуковала исти интензитет миона као и у случају атмосфере чија температуру има дистрибуцију у зависности од висине.

Тако је релативна варијација интензитета космичких миона услед релативне варијације ефективне температуре дата изразом:

$$\delta I_T = \alpha_T \Delta T_{eff}, \tag{3.57}$$

где је α_T температурски коефицијент, а T_{eff} ефективне температуре која се може изразити као [78]:

$$T_{eff} = \frac{\int_0^{h_0} T(h) \frac{\mathrm{d}h}{h} \left(e^{-\frac{h}{\lambda_\pi}} - e^{-\frac{h}{\lambda_n}} \right)}{\int_0^{h_0} \frac{\mathrm{d}h}{h} \left(e^{-\frac{h}{\lambda_\pi}} - e^{-\frac{h}{\lambda_n}} \right)} \tag{3.58}$$

где су λ_π средњи слободни пут за интеракцију наелектрисаних пиона, а λ_n средњи слободни пут за интеракцију нуклеона у чијим интеракцијама настају

пиони.

Показано је [79] да је примена овог метода на земаљске детекторе ограничена са обзиром да се у изразу за ефективну температуру већа тежина даје температурама виших слоја атмосфере.

3.4 Корекција барометарског и температурског ефекта постојећим методима

У овој секцији ће бити представљени резултати корекције флукса мионске компоненте секундарног космичког зрачења на барометарски и температурски ефекат претходно представљеним методима. Резултати корекције ће представљати референцу за нове методе које ће бити уведене у каснијим поглављима.

Експериментални подаци на којима ће корекције бити примењене су мерени у оквиру Нискофонске лабораторије за нуклеарну физику (НИЛНФ) Института за физику у Земуну. Детаљан опис лабораторије, детектора, система за аквизицију и складиштење података, као и карактеристике мереног мионског флукса ће бити дати у одељку 4.1, док ће експериментални подаци овде бити представљени као интегрални одброј мерен у надземној и подземној лабораторији НИЛНФ.

Као што је раније поменуто, за анализу метеоролошких ефеката и примену одговарајућих корекција, поред мионског флукса неопходно је познавање метеоролошких параметара. Метеоролошки подаци коришћени у овој анализи представљају комбинацију моделованих и директно мерених података. Референтни временски интервал изабран за анализу представља период од годину дана, почев од 01.06.2010. а завршно са 31.05.2011. године. У следећим одељцима ће бити дате само најнужније референце, док ће о доступним изворима, избору, обради метеоролошких података као и аргументацији за избор овог интервала бити детаљније изложено у секцији 4.2.

Метод ефективног нивоа продукције и метод средње температуре симултано третирају температурски и барометарски ефекат. Интегрални метод коригује само температурски ефекат, те ће корекција барометарског ефекта за овај метод

бити представљена на крају.

3.4.1 Корекција методом ефективног нивоа продукције

Метод ефективног нивоа продукције заснива се на Дуперијеровој једначини 3.53, коју ћемо овде представити у следећој нотацији:

$$\delta I = a_P \Delta P + a_T \Delta T_{100} + a_H \Delta H_{100}, \tag{3.59}$$

где су δI релативна варијација интензитета космичких миона (рачуната на основу детектованог броја), ΔP варијација атмосферског притиска, ΔT_{100} и ΔH_{100} варијације температуре, односно геопотенцијалне висине атмосферског нивоа који одговара притиску од $100mb$, док су a_i одговарајући коефицијенти. Варијације су рачунате у односу на средње годишње вредности варијабли.

На слици 3.1 приказана је зависност одброја космичких миона од атмосферског притиска, као и температуре и висине референтног изобарног нивоа за надземну лабораторију НИЛНФ.

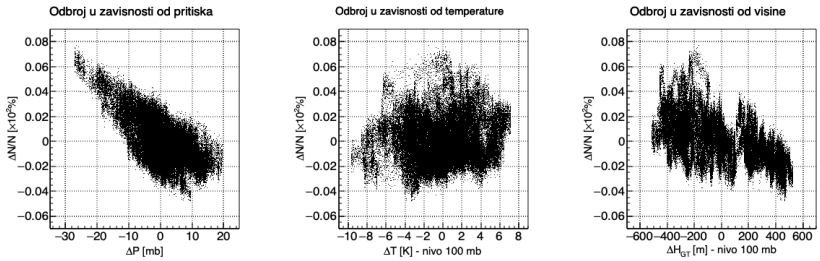

Слика 3.1: Зависност одброја космичких миона детектованог у надземној лабораторији од атмосферског притиска, односно температуре и геопотенцијалне висине изобарног нивоа од $100mb$.

Табела 3.1 приказује елементе корелационе матрице за горе поменуте варијабле.

Анализа коефицијената показује да постоји незанемарљива корелација између метеоролошких параметара, где је нарочито значајна корелација атмосферског притиска и висине нивоа продукције. Стога су за оцену значаја зависности одброја од појединих атмосферских варијабли индикативнији парцијални

Табела 3.1: *Корелациона матрица за одброј космичких миона у надземној лабораторији.*

	$\delta I[\%]$	$\Delta P[mb]$	$\Delta T_{100}[^\circ C]$	$\Delta H_{100}[m]$
$\delta I[\%]$	1.0000000	-0.8901752	0.2549857	-0.8846057
$\Delta P[mb]$	-0.8901752	1.0000000	0.1773757	-0.8151721
$\Delta T_{100}[^\circ C]$	0.2549857	0.1773757	1.0000000	0.2718952
$\Delta H_{100}[m]$	-0.8846057	-0.8151721	0.2718952	1.0000000

Табела 3.2: *Парцијални корелациони коефицијенти за одброј космичких миона у надземној лабораторији.*

	$\Delta P[mb]$	$\Delta T_{100}[^\circ C]$	$\Delta H_{100}[m]$
$\delta I[\%]$	-0.8901752	0.216529	-0.5821504

корелациони коефицијенти. Ови коефицијенти описују корелацију одброја са изабраним метеоролошким варијаблама у случају да је међусобна корелација метеоролошких варијабли уклоњена. Вредности одговарајућих коефицијената приказане су у табели 3.2.

Са обзиром да атмосферске варијабле нису линеарно независне, коефицијенти зависности детектованог одброја од ових варијабли одређени су помоћу вишеструке линеарне регресије и добијене су следеће вредности:

$$\begin{aligned} a_P &= (-1.782e-03 \pm 4e-06)[\%/mb], \\ a_T &= (5.45e-04 \pm 8e-06)[\%/^\circ C], \\ a_H &= (-4.403e-05 \pm 8e-08)[\%/m]. \end{aligned} \tag{3.60}$$

За израчунавење корелационих коефицијената и вишеструку линеарну регресију коришћене су процедуре имплементиране у програмском језику R [80]. На основу овако одређених коефицијената, помоћу следеће формуле може се одредити одброј миона коригован на метеоролошке ефекте:

$$I_{corr} = \frac{I}{1 + a_P \Delta P + a_T \Delta T_{100} + a_H \Delta H_{100}}. \tag{3.61}$$

На слици 3.2 приказане су некоригована временска серија одброја космичких миона детектованог у надземној лабораторији и временске серија одброја коригованог на барометарски, односно барометарски и температурски ефекат.

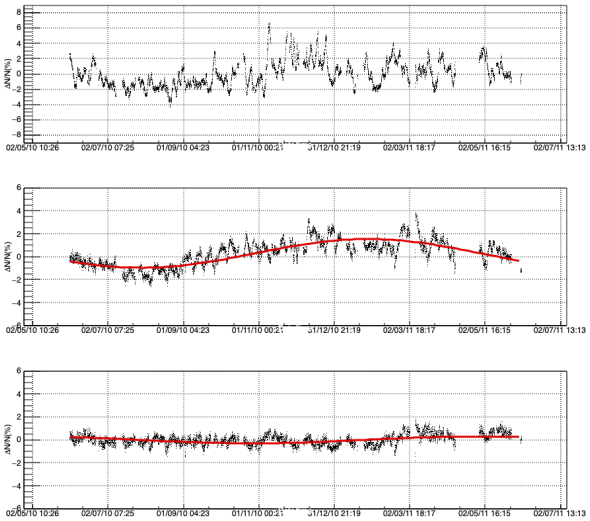

Слика 3.2: Метод ефективног нивоа продукције: временске серије одброја космичких миона за надземну лабораторију: некоригована (горе), коригована на барометарски (у средини) и коригована на барометарски и температурски ефекат (доле).

Процедура за корекцију барометарског ефекта на основу које је продукована временска серија коригована на притисак биће детаљније описана у одељку 3.4.4. Након корекције на барометарски ефекат у временским серијама космике долази до изражаја годишња варијација којој највише доприноси температурски ефекат. Један начин за упоређење различитих метода корекције је управо ефикасност са којом поједини методи уклањају годишњу варијацију. Стога се временска серија коригована на притисак и временска серија коригована на притисак и температуру фитују функцијом облика:

$$f(t) = a + b * sin(c + d * t), \tag{3.62}$$

где параметар t представља време. Коефицијент d је фиксиран и одговара

Табела 3.3: *Корелациона матрица за одброј космичких миона у подземној лабораторији.*

	$\delta I[\%]$	$\Delta P[mb]$	$\Delta T_{100}[^\circ C]$	$\Delta H_{100}[m]$
$\delta I[\%]$	1.00000000	-0.47733573	-0.03239227	-0.35519850
$\Delta P[mb]$	-0.47733573	1.0000000	-0.08880243	-0.22632853
$\Delta T_{100}[^\circ C]$	-0.03239227	-0.08880243	1.0000000	0.06873177
$\Delta H_{100}[m]$	-0.35519850	-0.22632853	0.06873177	1.0000000

периоду од годину дана, док коефицијент b представља амплитуду годишње варијације.

Амплитуда годишње варијације након корекције на барометарски ефекат, а одређена на основу фита приказаног на слици 3.2, износи $(1.25 \pm 0.02)\%$. Након корекције на оба метеоролошка ефекта вредност амплитуде износи $(-0.298 \pm 0.008)\%$. На основу ових вредности јасно је да корекција уклања велики део годишње варијације. Како се један од главних фокуса овог рада тиче упоређивања различитих метода за корекцију метео ефеката, овде нећемо улазити у анализу природе и евентуалних извора резидуалне годишње варијације.

Слика 3.3 приказује зависност одброја космичких миона од атмосферског притиска као и температуре и висине референтног изобарног нивоа за надземну лабораторију НИЛНФ.

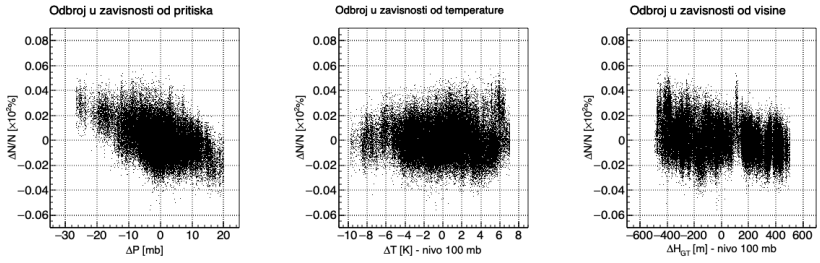

Слика 3.3: Зависност одброја космичких миона детектованог у подземној лабораторији од атмосферског притиска, односно температуре и геопотенцијалне висине изобарног нивоа од $100mb$.

Табела 3.3 приказује корелациону матрицу за подземну лабораторију док су у табели 3.3 дати одговарајући парцијални корелациони коефицијенти.

Вишеструком линеарном регресијом добијени су следећи коефицијенти:

Табела 3.4: *Парцијални корелациони коефицијенти за одброј космичких миона у подземној лабораторији.*

	$\Delta P[mb]$	$\Delta T_{100}[^{\circ}C]$	$\Delta H_{100}[m]$
$\delta I[\%]$	-0.4773357	0.0114211	-0.2889568

$$
\begin{aligned}
a_P &= (-8.27e-04 \pm 6e-06)[\%/mb], \\
a_T &= (-1.1e-04 \pm 2e-05)[\%/^{\circ}C], \\
a_H &= (-1.51e-05 \pm 2e-07)[\%/m],
\end{aligned} \tag{3.63}
$$

на основу којих је одређена временска серија коригованог одброја за подземну лабораторију приказана на слици 3.4.

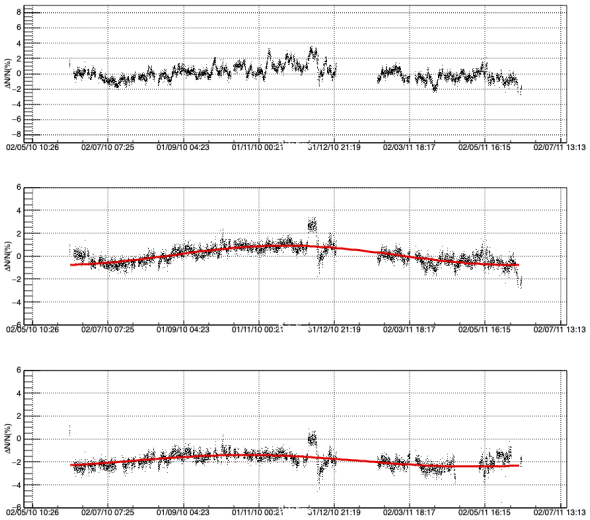

Слика 3.4: Метод ефективног нивоа продукције: временске серије одброја космичких миона за подземну лабораторију: некоригована (горе), коригована на барометарски (у средини) и коригована на барометарски и температурски ефекат (доле).

Амплитуда годишње варијације након корекције на притисак је (0.84±0.02)%, док након корекције и на температуру вредност амплитуде износи (0.51±0.03)%.

На основу ових резултата можемо да закључимо да овај метод доста добро описује метеоролошке ефекте и ефикасно уклања њихов допринос. Корекција очекивано има већи ефекат на одброј у надземној лабораторији. Поред тога, једноставност анализе и примене и мали скуп метеоролошких варијабли на коме се заснива показују зашто се и даље користи упркос чињеници да су од његовог увођења развијени софистицираније методи.

3.4.2 Корекција интегралним методом

Интегрални метод полази од једначине 3.55. Као што је већ изложено у одељку 3.2.2, температурски коефицијент α_T представља збир позитивног и негативног температурског ефекта који су описани једначинама 3.46 и 3.47 респективно.

Да би се избегле додатне апроксимације, интеграција ових израза је рачуната нумерички, Монте Карло методом. Коришћен је Марсен Твистер (*Marsenne Twister*) генератор псеудослучајних бројева у оквиру ROOT пакета за анализу података [81].

Вредности различитих параметара у интеграцији су: $\gamma = 0.7$, $L = 0.12 g/cm^2$, $l = 0.06 g/cm^2$, $h_0 = 1.0208 g/cm^2$. Минимална енергија миона износи $E_{min} = 0.4 GeV$ за надземну, односно $E_{min} = 6.4 GeV$ за подземну лабораторију.

На сликама 3.5 и 3.6 приказане су функције позитивног, негативног и збирног диференцијалног температурског коефицијента у зависности од упадног угла миона за надземну, односно подземну лабораторију.

Интегрални температурски коефицијент за мионе на површини земље приказан је на слици 3.7, док је за мионе на дубини од $25 m.w.e.$ приказан на слици 3.8.

Помоћу добијених функција густине температурског коефицијента израчунате су одговарајуће варијације одброја миона према једначини 3.55. На основу израчунатих варијација одређене су временске серије одброја миона кориговане на температурски ефекат. Одброј овако коригован на температурски ефекат је потом коришћен за одређивање барометарског коефицијента, што је детаљније описано у одељку 3.4.4.

На сликама 3.9 и 3.10 упоредно су приказане временске серије некориго-

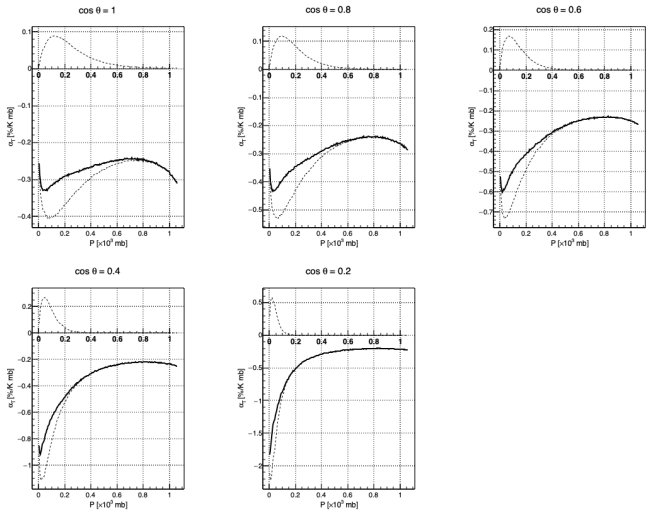

Слика 3.5: Позитивни, негативни и укупни диференцијални температурски коефицијент за различите вредности азимуталног угла за мионе који стижу на површину земље (надземна лабораторија).

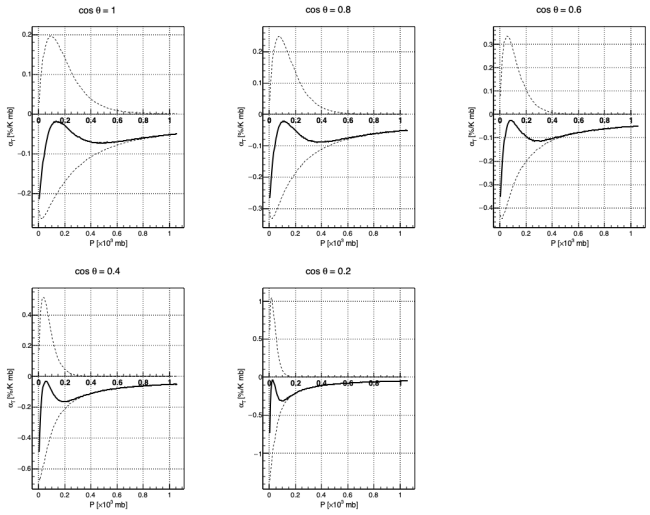

Слика 3.6: Позитивни, негативни и укупни диференцијални температурски коефицијент за различите вредности азимуталног угла за мионе који стижу на дубину од $25 m.w.e.$ (подземна лабораторија).

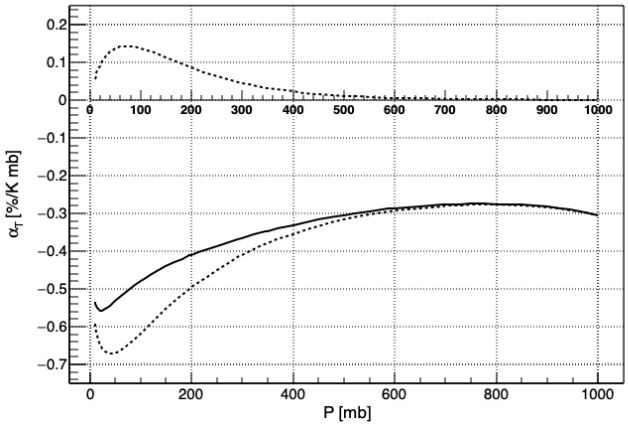

Слика 3.7: Позитивни, негативни и укупни температурски коефицијент за мионе који стижу на површину земље (надземна лабораторија).

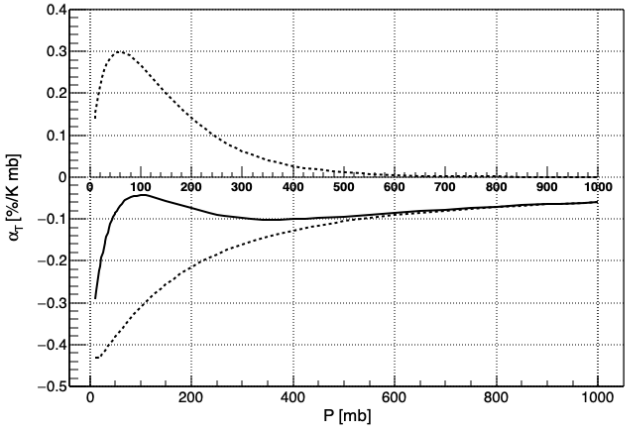

Слика 3.8: Позитивни, негативни и укупни температурски коефицијент за мионе који стижу на дубину од $25 m.w.e.$ (подземна лабораторија).

ваног, коригованог на барометарски и одброја коригованог на барометарски и температурски ефекат интегралним методом.

Амплитуда годишње варијације након корекције на барометарски и температурски ефекат износи $(-0.40\pm0.04)\%$ за надземну и $(0.576\pm0.009)\%$ за подземну лабораторију.

Упоређењем са резултатима метода ефективног нивоа продукције, чини се да је за дати период интегрални метод приближне, али ипак нешто мање, ефикасности у отклањању метеоролошких ефеката када су и питању подаци из надземне лабораторије, док је упоредиве ефикасности када су у питању подаци из подземне лабораторије. Међутим, будући да је метод ефективног нивоа продукције у основи статистичке природе, коефицијенти који описују допринос појединих ефеката могу да варирају у зависности од временског периода који се посматра. Ове варијације могу бити сезонске или везане за дуже временске периоде и повећавају неодређеност резултата [65, 82].

Већина аутора се због конзистентности и једноставније интерпретације одлучује за интегрални метод као референти. До развоја нових метода које ће бити представљене касније, већина анализа и публикованих резултата Нискофонске лабораторије за нуклеарну физику у домену физике космичког зрачења ослањала се на податке кориговане на метеоролошке ефекте интегралним методом [83, 84, 85]. Овако кориговани подаци омогућили су јаснији увид у различите трендове временских серија космике (као што је промена интензитета), анализу резидуалних периодичних ефеката неатмосферског порекла, значајно повећали осетљивост на апериодичне ефекте као што су Форбушева смањења и повећали прецизност одређивања величина као што су медијана и гранична вредност магнетне чврстоће [86, 87].

Додатну предност интегралног метода представља могућност корекције временских серија космике у реалном времену [76] где би употреба било ког емпиријског метода представљала екстраполацију и самим тим уносила додатну неодређеност.

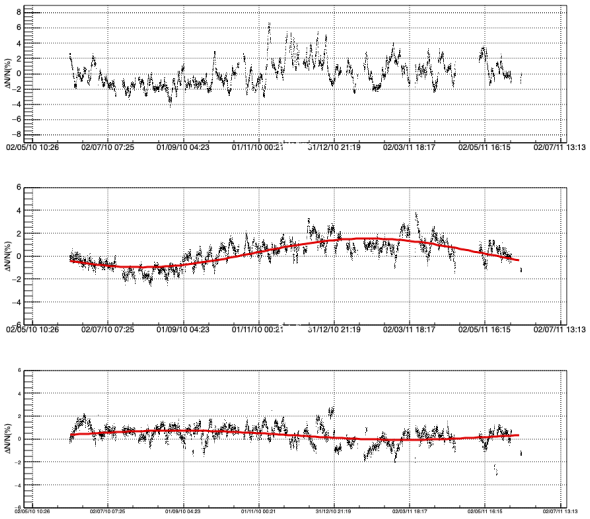

Слика 3.9: Интегрални метод: временске серије одброја космичких миона за надземну лабораторију: некоригована (горе), коригована на барометарски (у средини) и коригована на барометарски и температурски ефекат (доле).

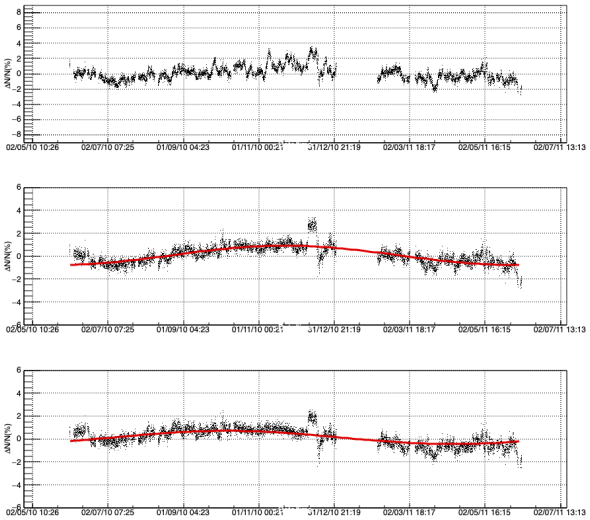

Слика 3.10: Интегрални метод: временске серије одброја космичких миона за подземну лабораторију: некоригована (горе), коригована на барометарски (у средини) и коригована на барометарски и температурски ефекат (доле).

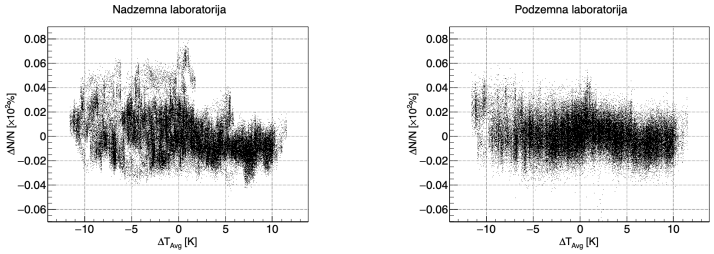

(a) (b)

Слика 3.11: Зависност релативне варијације интензитета космичких миона од атмосферске температуре усредњене по маси за: а) надземну б) подземну лабораторију.

3.4.3 Корекција методом усредњене температуре

Као што је раније поменуто, метод усредњене температуре представља апроксимацију интегралног метода, где се претпоставља да је температурски коефицијент приближно константан. Тада се зависност релативне варијације интензитета космичких миона може представити као производ температурског коефицијента и температуре атмосфере усредњене по дебљини апсорпције, односно како је неки аутори називају, усредњене по маси.

Температурски коефицијент се утврђује емпиријски, међутим као и у случају осталих емпиријских метода, не може се третирати одвојено од осталих метеоролошких варијабли, односно пре свега притиска. Стога се релативна варијација интензитета космичких миона може представити једначином:

$$\delta I = a_P \Delta P + a_T \Delta T_m, \tag{3.64}$$

где су P и T_m атмосферски притисак и атмосферска температура усредњена по маси, а a_i одговарајући коефицијенти.

Зависност релативног одброја од усредњене температуре за надземну и подземну лабораторију приказана је на слици 3.11.

Коефицијенти у једначини 3.64 одређују се вишеструком линеарном регресијом на сличан начин како је описано у одељку 3.4.1. За надземну лабораторију добијене су следеће вредности коефицијената:

$$a_P = (-2.165e-03 \pm 4e-06)[\%/mb],$$
$$a_T = (-1.967e-03 \pm 4e-06)[\%/^\circ C], \tag{3.65}$$

док су за подземну лабораторију добијене следеће вредности:

$$a_P = (-9.5e-04 \pm 1e-05)[\%/mb],$$
$$a_T = (-8.2e-04 \pm 2e-05)[\%/^\circ C]. \tag{3.66}$$

На основу ових коефицијената, а помоћу једначине:

$$I_{corr} = \frac{I}{1 + a_P \Delta P + a_T \Delta T_m}, \tag{3.67}$$

израчунат је коригован интензитет космичких миона. Временске серије коригованог одброја за обе лабораторије приказане су на сликама 3.12 и 3.13.

Амплитуда годишње варијације након корекције на барометарски и температурски ефекат износи $(0.15 \pm 0.05)\%$ за надземну и $(0.48 \pm 0.02)\%$ за подземну лабораторију.

Упоређењем са осталим представљеним методама, ако се као критеријум ефикасности узме редукција амплитуде годишње варијације детектованог одброја, за дати период у надземној лабораторији може се чинити да је овај метод најефикаснији. Међутим, исте замерке које се односе на остале емпиријске методе важе и у овом случају, те интерпретација резултата није тривијална. Ефекат корекције у доњој лабораторији није значајно већи него кад су у питању остале методе.

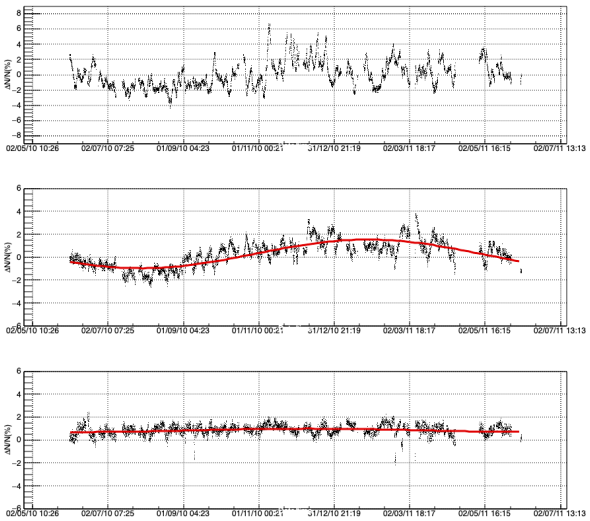

Слика 3.12: Метод усредњене температуре: временске серије одброја космичких миона за надземну лабораторију: некоригована (горе), коригована на барометарски (у средини) и коригована на барометарски и температурски ефекат (доле).

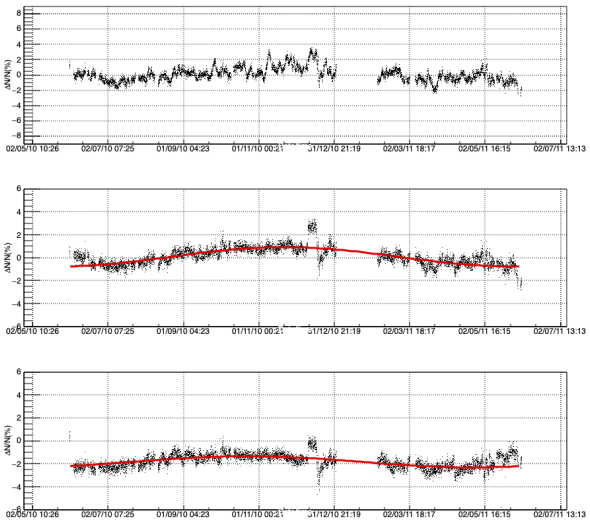

Слика 3.13: Метод усредњене температуре: временске серије одброја космичких миона за подземну лабораторију: некоригована (горе), коригована на барометарски (у средини) и коригована на барометарски и температурски ефекат (доле).

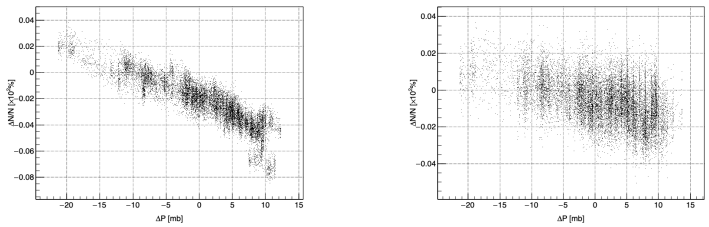

(a) (b)

Слика 3.14: Зависност релативне варијације интензитета космичких миона од атмосферског притиска за: а) надземну б) подземну лабораторију.

3.4.4 Корекција барометарског ефекта

Метод ефективног нивоа продукције и метод усредњене температуре истовремено третирају барометарски и температурски ефекат. Када је интегрални метод у питању, корекције су независне. Иако је барометарски коефицијент у принципу могуће израчунати теоријски, у пракси се најчешће одређује на основу линеарне регресије одброја претходно коригованог на температурски ефекат.

Одброј космичких миона је коригован на температурски ефекат, као што је описано у одељку 3.4.2. Затим се барометарски коефицијент одређује на основу линеарне регресије зависности релативног одброја космичких миона од варијације атмосферског притиска. Како би се смањила статистичка грешка услед варијације одброја космике, у обзир се узимају само геомагнетно мирни дани. Геомагнетно мирне дане представља десет дана са најнижим Kp индексом у сваком месецу. Kp индекс мери пертурбацију геомагнетног поља соларним ветром. Листа геомагнетно мирних дана преузета је од Немачког центра за геонауке (*GeoForschungsZentrum - GFZ*) у Потсдаму [88].

Како се средња вредност интензитета миона мења током соларног циклуса услед промене Сунчеве активности, барометарски коефицијент се одређује за сваку календарску годину. На слици 3.14 приказана је зависност релативне варијације одброја космичких миона од варијације притиска, за податке обе лабораторије из 2010. године.

На слици 3.15 приказане су вредности барометарског коефицијента у пери-

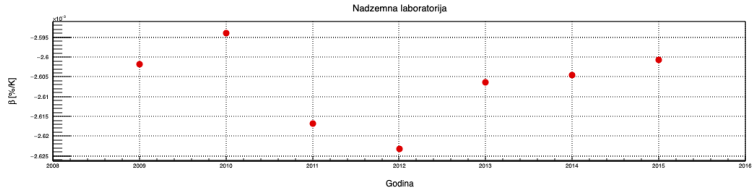

(a)

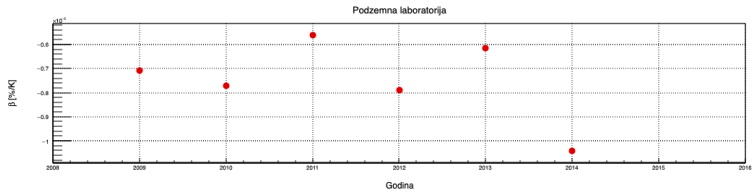

(b)

Слика 3.15: Вредности барометарског коефицијента за период 2009-2015. године за: а) надземну б) подземну лабораторију.

оду $2009 - 2015$. године, покривајући највећи део 24. соларног циклуса.

Резултати корекција одброја космичких миона постојећим методама презентовани у овом одељку немају за циљ квантитативно упоређење ефикасности ових метода, са обзиром да је неколицина аутора је већ презентовала такве компарације [74, 71, 76, 72, 73]. Радије, циљ је да се представи какав ефекат постојеће методе имају примењене на одброј детектован специфичном експерименталном поставком у Нискофонској лабораторији за нуклеарну физику и да се успостави што општија и прегледнија референца за нове методе које ће бити уведене у каснијим поглављима.

Експериментални подаци

Основни задатак физике космичког зрачења представља проучавање карактеристика примарног космичког зрачења. Најнепосреднију експерименталну слику са минималним пертурбацијама би дали детектори који би се налазили ван хелиосфере, или макар ван Земљине атмосфере. Због објективних тешкоћа искључиво директан начин проучавања ПКЗ није остварив, те индиректна детекција земаљским детекторима и даље има значајну улогу. Тако ова два комплементарна приступа дају пуну експерименталну слику.

ПКЗ се директно проучава помоћу сателита који орбитирају око Земље или помоћу балона (који ипак подразумевају минималну пертурбацију у највишим слојевима атмосфере). Очигледна предност оваквог приступа је директна детекција честица ПКЗ, односно минимална потреба за корекцијом услед интеракције ПКЗ са атмосфером.Ману представљају ограничене димензије, односно маса детектора, што ограничава највише енергије ПКЗ које се могу детектовати. Осим тога, ове експерименте прате различити технолошки проблеми (потреба за редундантним системима, отежана измена топлоте, специфичност неопходне опреме), што се посебно односи на детекторе инсталиране на сателитима [89]. Примери детектора у орбити су PAMELA (*Payload for Antimatter Matter Exploration and Light-nuclei Astrophysics*) и FGST (*Fermi Gamma-ray Space Telescope*), док су примери експеримената који користе балоне у високим слојевима атмосфере JACEE (*Japanese American Collaborative Emulsion Experiment*) и RUNJOB (*Russian-Nippon Joint Balloon*).

Земаљски експерименти детектују секундарно космичко зрачење и нужно формирају посредну слику о ПКЗ. За ове експерименте је стога битно да у што већој мери елиминишу ефекте пропагације СКЗ кроз атмосферу, како би што

тачније рекреирали карактеристике примарних честица. Са друге стране, земаљски детектори могу у принципу бити произвољно велики или комплексни, па је немају ограничења поменута у претходном пасусу. За посредну детекцију ПКЗ највиших енергија неопходно је да детектори покривају велику површину и стога су често у облику мреже мањих детектора. Примери оваквих експеримената су AUGER у оквиру Pierre Auger опсерваторије и ICECUBE.

За посредну детекцију ПКЗ средњих енергија и даље значај имају земаљски детектори мањих димензија, као што су неутронски и мионски монитори. Експеримент у оквиру Нискофонске лабораторије за нуклеарну физику спада у ову другу категорију.

У овом поглављу представићемо експерименталну поставку за детекцију мионске компоненте секундарног космичког зрачења у оквиру НИЛНФ, неке технике анализе и обраде које повећавају употребљивост сирових података, као и изворе и процедуре процесирања метеоролошких података неопходних за анализу метеоролошких ефеката на космичке мионе.

4.1 Нискофонска лабораторија за нуклеарну физику

Нискофонска лабораторија за нуклеарну физику у оквиру Института за физику у Београду пројектована је и изведена пре свега за потребе мерења процеса ниске активности. Осим тога, једну од значајних активности представља и континуално мерење мионске компоненте секундарног космичког зрачења. Мерење космике је двоструко значајно и то због праћења и редукције фонских процеса индукованих космичким мионима (нарочито значајних за мерења у подземљу), као и различитих процеса у оквиру физике космичког зрачења на које је конкретна експериментална поставка осетљива.

Лабораторија се налази на око $100m$ од обале Дунава у Земуну. Географске координате су $44°51'N$ за ширину, односно $20°23'E$ за географску дужину, док је вредност граничне вертикалне геомагнетне чврстоће $5,3GV$.

Састоји се од надземног и подземног дела (шематски приказано на слици

4.1). Надземна лабораторија се налази на $75m$ надморске висине у подножју лесне литице, док је подземна лабораторија укопана у подножје литице и налази се на крају ходника дугачког приближно $10m$, а на дубини од $12m$. Пасивну заштиту од продора радона из околног земљишта представља алуминијумски лим којим је лабораторија обложена изнутра. Поред поменутог слоја леса и $30cm$ армираног бетона, ефективна дебљина вертикалног апсорбера износи приближно $25m.w.e.$.

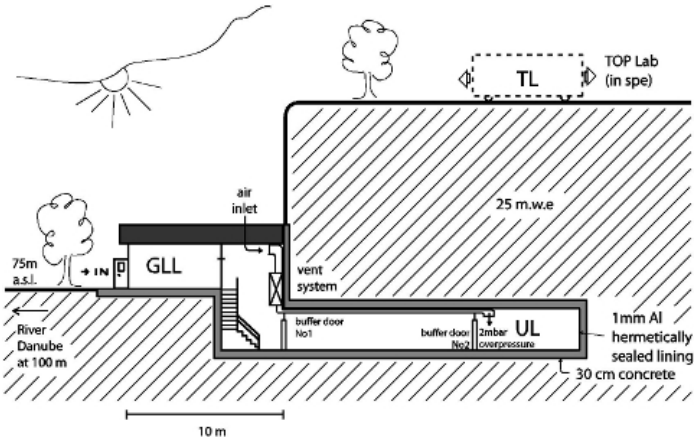

Слика 4.1: Шематски приказ попречног пресека Нискофонске лабораторије за нуклеарну физику [90].

Овде ћемо изоставити остале спецификације лабораторије, са обзиром да се директно тичу постизања што нижег фона, те нису од непосредносг значаја за мерење космике.

4.1.1 Експериментална поставка, спектри и временске серије мионске компоненте

Експериментална поставка намењена мерењу флукса мионске компоненте СКЗ у обе лабораторије је практично идентична. Састоји се од пластичног сцинтилационог детектора димензија $100cm \times 100cm \times 5cm$ са четири фотомултипликатора, директно постављена на ћошкове зарубљене под углом од $45°$. Сцинтилациони детектор је произведен од стране украјинске фирме $Amcrys - H$

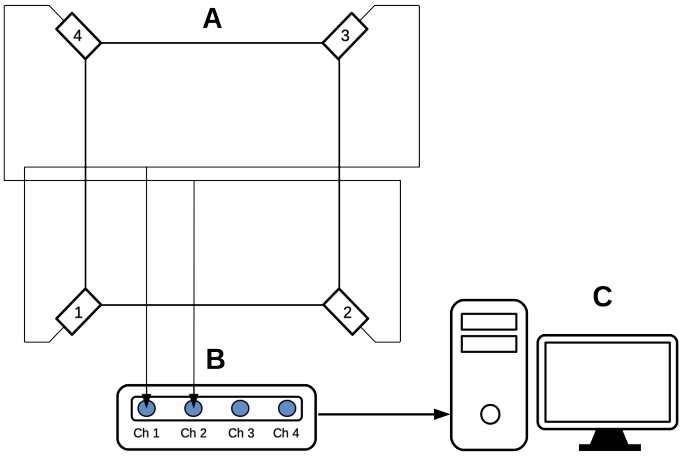

Слика 4.2: Шематски приказ експерименталне поставке: А) сцинтилациони детектор (пластик), Б) брзи аналогно-дигитални конвертер, Ц) рачунар.

из Харкова. Након првог степена појачања у предпојачавачима, сигнали фотомултипликатора који се налазе на истој дијагонали (парни, односно непарни фотомултипликатори у оквиру компоненте А на слици 4.2) директно се сумирају и прослеђују систему за аквизицију.

Систем за аквизицију се састоји од брзог аналогно-дигиталног конвертера и рачунара за обраду и складиштење података (компоненте Б и Ц на слици 4.2). Брзи аналогно-дигитални конвертери (FADC - *Flash Analog to Digital Converter*) модел $N1728B$ произведени су од стране италијанске фирме CAEN. Ови уређаји имају четири улаза, 2^{14} канала и узоркују сигнал сваких $10ns$. Могуће је селектовати мод у коме уређаји раде као дигитални спектрометри. За сваки догађај се снимају амплитуда и време детекције, па је могуће накнадно (*offline*) комбиновање и анализа догађаја снимљених у различитим каналима, са временском резолуцијом од $10ns$.

Сумирани сигнал две дијагонале се води на један од улаза аналогно-дигиталног конвертера и независно складишти. Тако је могуће формирати спектре и временске серије појединачних дијагонала. Такође је могуће формирати спектре и временске серије коинцидентних догађаја, односно догађаја које су забележили

Табела 4.1: *Својства флукса примарног космичког зрачења у Нискофонској лабораторији за никлеарну физику.*

	Минимална енергија $[GeV]$	Енергија максимума $[GeV]$	Медијана енергије $[GeV]$
Надземна лабораторија	5 ± 2	17	59 ± 2
Подземна лабораторија	12 ± 3	42	137 ± 5

фотомултипликатори на обе дијагонале. Коинцидирање сигнала две дијагонале уклања практично сав нискоенергетски део у спектрима (до $3MeV$) који углавном потиче од амбијенталног зрачења. Тако у спектрима остају само догађаји са високим губитком енергије, индуковани космичким мионима или електромагнетним пљусковима [90]. Овакви коинцидентни спектри имају максимум на енергији од приближно $10MeV$ за надземну лабораторију и $10.9MeV$ за подземну. За ове потребе, као и за друге неопходне процедуре припреме података, користи се софтвер наменски развијен у оквиру лабораторије.

На слици 4.3 приказани су спектри појединачних дијагонала и коинциденти спектар за надземну, односно подземну лабораторију.

На основу поређења симулација и мерених података утврђено је да су коинцидентни догађаји у надземној лабораторији углавном изазвани космичким мионима, уз контаминацију електромагнетном компонентом (углавном електронима) од око 30%. Након елиминације EM компоненте, измерени флукс миона износи $(1,37 \pm 0,06) \times 10^{-2} cm^{-2} s^{-1}$. У подземној лабораторији коинцидентни спектри представљају практично чисте мионске спектре, а флукс износи $(4,46 \pm 0,04) \times 10^{-3} cm^{-2} s^{-1}$ [91].

Такође, позната је функција одзива детекторског система на примарно космичко зрачење у обе лабораторије. На основу те функције могуће је одредити спектар енергија ПКЗ на које су одговарајући детектори осетљиви. У табели 4.1 приказане су вредности минималне, енергије максимума расподеле и медијане за надземну и подземну лабораторију [92].

Континуална мерења космике у Нискофонској лабораторији постојећом експерименталном поставком врше се од 2008. године. Временске серије јавно су доступе и могу се наћи на страници Београдске мионске станице (*Belgrade Cosmic*

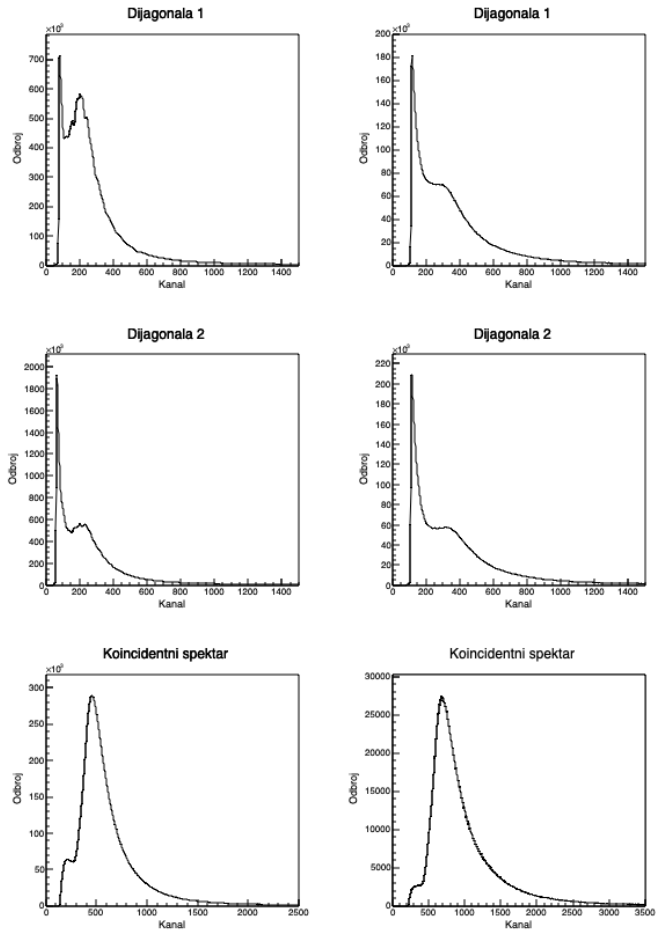

Слика 4.3: Спектри појединачних дијагонала и коинцидентни спектри за надземну (лево) и подземну лабораторију (десно).

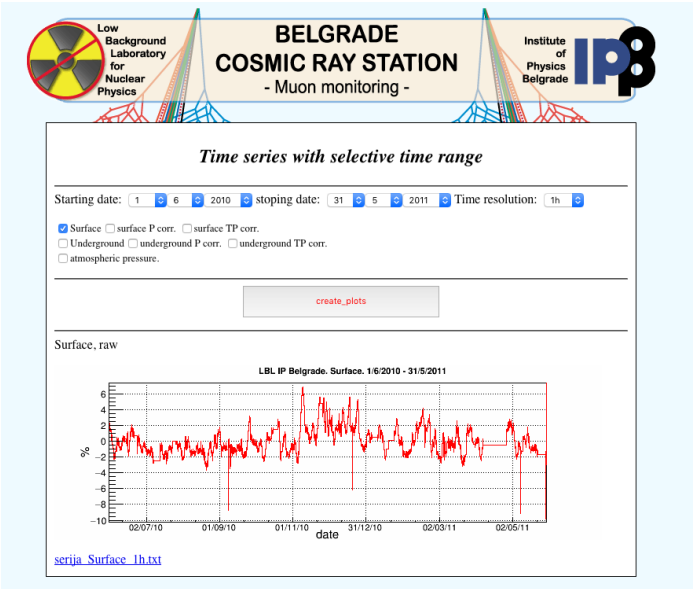

Слика 4.4: Кориснички интерфејс на страници Београдске мионске станице.

Ray Station [93]). Кориснику је омогућено да креира плотове временских серија и преузме одговарајуће податке у жељеном интервалу и временској резолуцији (5 минута или сат времена). Такође, доступни су подаци кориговани на барометарски или барометарски и температурски ефекат. За корекцију температурског ефекта користи се интегрална метода. На слици 4.4 приказан је кориснички интерфејс странице.

4.1.2 Корекција и нормализација података

Одржати стабилан рад апаратуре при дуготрајним континуалним мерењима је нетривијалан задатак. Постоји читав низ параметара који утичу на стабилност мерења и пре свега могу бити амбијенталне или инструменталне природе.

Амбијентални услови у Нискофонској лабораторији су релативно стабилни. Познатно је да ефикасност фотомултипликатора може да зависи од варијације температуре, те је стога посебна пажња посвећена постизању стабилне радне температуре. Надземна лабораторија је климатизована док је у подземној ла-

бораторији варијација температура условљена фреквенцијом измене ваздуха вентилационог система. У обе лабораторије постоје грејна тела неопходна у зимском периоду. Са друге стране, у подземној лабораторији повећана влажност има значајнију улогу, због чега је инсталиран одвлаживач који ради у садејству са вентилационим системом.

Температура и влажност се континуално мере и прате специјализованим уређајем. Резултат је да је варијације температуре у надземној лабораторији око $2°C$, док је у подземној $4°C$ [94], а влажност у подземној лабораторији не прелази 70% у летњем, односно 30% зимском периоду.

Инструменталне нестабилности могу бити узроковане различитим ефектима: нестанцима у напајању електричном енергијом, нестабилностима и отказима високонапонских система за напајање фотомултипликатора, променама радних карактеристика опреме током дужих временских периода, променом вредности хардверских прагова система за аквизицију. Овакве нестабилности се директно огледају у дискретним променама одброја детектоване космике, односно скоковима у временским серијама.

Како у великом броју ових случајева, или није у потпуности могуће одредити тачан разлог који је довео до нестабилности система, или је немогуће егзактно квантификовати везу истог са променом одброја, један начин да се промене коригују је детекција и корекција скокова на основу статистичке анализе.

За процедуру детекције скокова одабрана је адаптација Кени (*Canny*) алгоритма, који се превасходно користи за детекцију контура на дигиталним сликама. Контуре се детектују на основу области у којима постоји велики локални градијент интензитета. У општем случају ивице контура нису јасно дефинисане, већ постоји дисторзија слике, односно шум. Алгоритам стога треба да задовољи два донекле опречна захтева: (1) да ублажи ефекат шума, и да (2) одреди ивицу са што већом прецизношћу. Елиминисање шума (*smoothing*) типично смањује осетљивост детекције ивице, те се мора наћи равнотежа ова два процеса [95].

Кени алгоритам се заснива на првом изводу гаусијана и лоцирању великог локалног градијента у равни. За детекцију скока у временским серијама космике коришћена је врло упрошћена једнодимензионална адаптација, која подра-

зумева конволуцију података гаус филтером (*gaussian smoothing filter*), одређивања првог извода резултујуће временске серије и локализацију екстремних вредности градијента.

Овако изоловани скокови у временским серијама су затим кориговани. За референтни део временске серије узет је део након скока средњег одброја, а одброј у делу временске серије пре скока се коригује за неку вредност. Ова вредност (*shift*) се одређује на основу разлике средњег одброја за неки број тачака пре и после скока:

$$\Delta N = \bar{N}_{>} - \bar{N}_{<}. \tag{4.1}$$

Затим се одброј у делу временске серије пре скока коригује на ову вредност. На слици 4.5 приказан је један пример рада алгоритма.

Да би се проценила грешка ове процедуре, урађена је једноставна симулација. У временским серијама реалних података коригованих на притисак и температуру вештачки је креиран скок одређене вредности. Затим је на основу горе описаног алгоритма одређена вредност за коју је потребно кориговати податке. Поступак је понављан довољан број пута да се формира расподела израчунатих вредности. На слици 4.6 приказана је ова расподела за симулирану вредност скока одброја у горњој лабораторији од 5000 и прекид у подацима од једног дана. Корекција је рачуната на основу разлика средњих вредности пре и после скока у временском прозору од 5 дана.

Може се видети да је разлика средње вредности расподеле и симулиране вредности скока врло мала. Како у случају реалних корекција не знамо праве вредности скокова, апроксимативно можемо сматрати да се семплују из дистрибуција сличних приказаној, па за процену статистичке грешке узети ширину дате расподеле. Са обзиром да је систематска грешке занемарљива, укупна грешка коју процедура корекције уноси је одређена стандардном девијацијом расподеле израчунатих корекција одброја.

На слици 4.7 приказана је временска серија детектованог одброја космике у надземној лабораторији, кориговања на барометарски и температурски ефекат, са интервалом од једне стандардне девијације расподеле израчунатих скокова

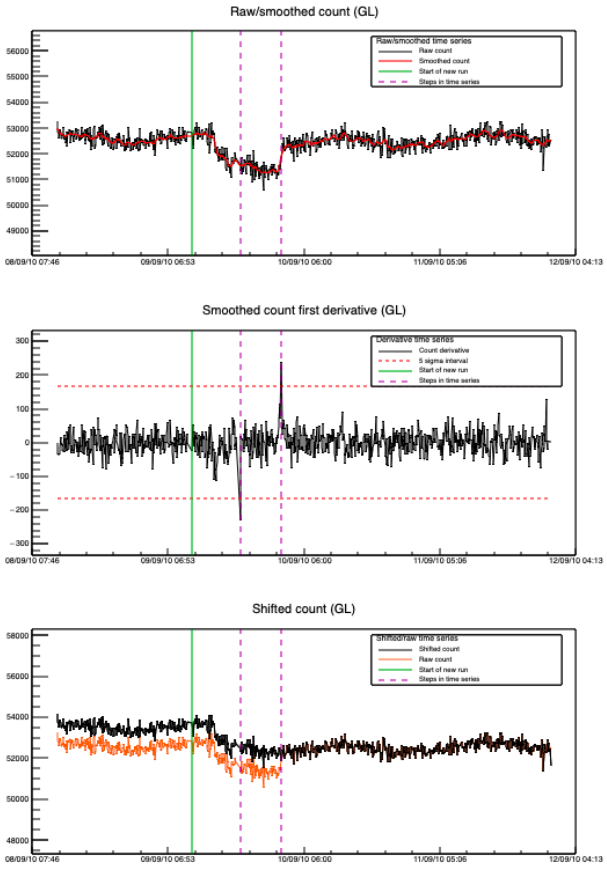

Слика 4.5: Пример рада адаптираног Кени алгоритма за корекцију скокова одброја у временским серијама космике: некоригована и ”смутована” временска серија (горе), временска серија првог извода (у средини) и коригована временска серија (доле).

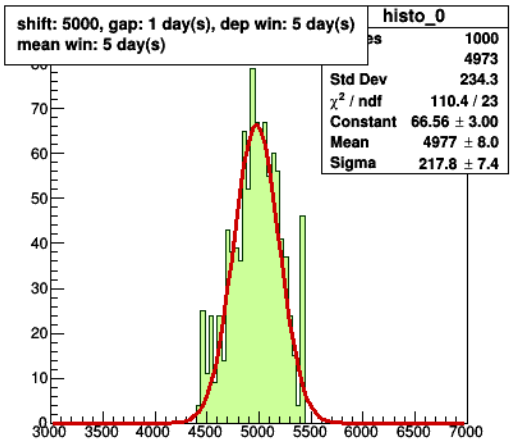

Слика 4.6: Расподела разлика симулиране и израчунате вредности скока одброја.

одброја. Због упоређења, приказани су интервали од једне, односно две стандардне девијације средњег одброја рачунатог у периоду од једног дана који претходи свакој тачки.

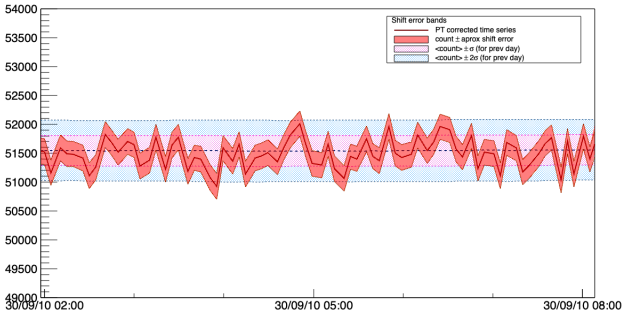

Слика 4.7: Временска серија одброја у надземној лабораторији, коригована на притисак и температуру, са интервалом процењене грешке алгоритма за одређивање скокова одброја

У случају када постоје дужи прекиди у мерењима, систематска грешка алгоритма за одређивање скока почиње да расте. Тада је коришћен нешто другачији приступ за одређивање вредности скока одброја. Тај приступ се ослања на ре-

ферентни одброј неког другог детектора (мионски детектор у комплементарној лабораторији или неутронски монитор са приближном вредношћу географске ширине и граничне вертикалне геомагнетне чврстоће). Резултати су нешто бољи али је процена грешке и дискусија резултата нешто сложенија.

Још једна нестабилност у раду апаратуре која може утицати на детектовани одброј представља засићење система за аквизицију. Обично до засићења долази због презаузетости рачунара који прихвата податке. Ефекат је краткотрајан и огледа се у смањеном забележеном петоминутном одброју. У анализи која користи петоминутне одброје овакве тачке нису узимане у обзир. У случају да су у анализи коришћене сатне суме, одређен је минималан број (најчешће 10) коректних вредности сумираних на 5 минута који мора постојати да би се формирао сатни одброј. Таква умањена сума је затим нормирана на пун сатни одброј. Грешка која се тиме уноси је занемарљива у односу на већ поменуте статистичке грешке процењене у анализи која користи сатне одброје космике.

За анализу представљену у овом раду биран је временски интервал са што мање прекида у мерењима и што већом стабилношћу података. Да би се избегла сезонска зависност, референтни интервал такође треба да представља пун умножак периода од годину дана.

Интервал који најбоље задовољава ова два захтева и који је на крају изабран за анализу је период од 01.06.2010. године до 31.05.2011. године. Основна временска резолуција података је 5 минута. Поред петоминутних одброја (одређивање различитих зависности, корекције и сл.) у анализи су такође коришћени и сатни одброји (временске серије, одређивање периодичности и сл.).

4.2 Метеоролошки подаци

За анализу и корекцију метеоролошких ефеката неопходно је познавање атмосферских параметара. У овом раду третирамо барометарски и температурски ефекат, па минимални скуп метеоролошких података подразумева познавање атмосферског притиска и температуре на нивоу тла, као и температурског профила атмосфере (слика 4.8) за географске координате које одговарају локацији

лабораторије. За температурски ефекат су нарочито значајне температуре у тропосфери, тропопаузи и ниској стратосфери.

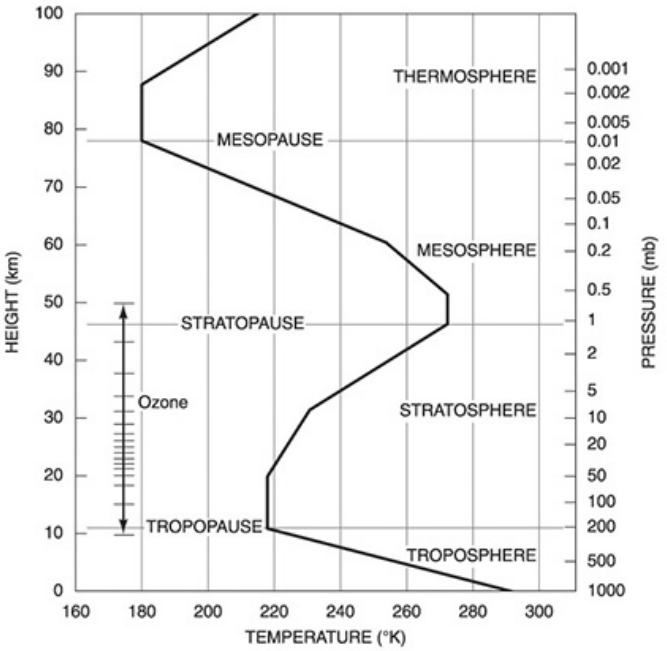

Слика 4.8: Температурски профил атмосфере.

Иако не постоје *in situ* мерења атмосферског притиска и температуре ваздуха, на територији Београда и у околини постоји већи број аутоматских метеоролошких станица чији подаци су јавно доступни. Апсолутне вредности се могу нешто разликовати од станице до станице, али варијација мерених параметара која је од главног интереса за анализу је приближно иста.

Подаци о температурском профилу атмосфере у принципу су доступни од стране Републичког хидрометеоролошког завода Србије (РХМЗ) [96], који врши мерења метеоролошким балонима. Међутим, фреквенција и континуитет мерења нису довољни за потребе корекције метеоролошких ефеката и стога се анализа у овом раду ослања на моделоване температуре.

4.2.1 Моделовани метеоролошки подаци

У свету је развијен већи број атмосферских модела способних да са великом прецизношћу симулирају кретања ваздушних маса. Сложени нумерички модели узимају у обзир велики број параметара којима се описује атмосфера и дају поуздана предвиђања њихових вредности.

Један од најпознатијих модела је Глобални прогностички модел (*Global Forecast System - GFS*) [97] развијен од стране Америчке националне агенције за атмосферска и океанографска истраживања (*National Oceanic and Atmospheric Administration - NOAA*) [98].

У Нискофонској лабораторији за нуклеарну физику смо се одлучили за овај модел као извор атмосферских температура и других атмосферских параметара. Као што ће бити показано, GFS добро моделује атмосферске температуре за локацију лабораторије. Такође, други аутори су већ успешно користили овај модел [99] за сличне анализе, што је значајно због евентуалних компарација.

GFS даје прогнозу вредности великог броја атмосферских параметара до 16 дана унапред. Осим прогностичких података, доступни су и резултати настали накнадним укључивањем реалних података (мерених у оквиру светске мреже метеоролошких станица) у модел. Ови подаци се продукују дан касније у односу на мерења. Доступни су за четири различита времена у току дана: $00:00, 06:00, 12:00$ и $18:00$ часова, са просторном резолуцијом од $0.5°$ географске ширине, односно дужине.

Атмосферска температура је израчунава за следеће изобарне нивое: 10, 20, 30, 50, 70, 100, 150, 200, 250, 300, 350, 400, 450, 500, 550, 600, 650, 700, 750, 800, 850, 900, 925, 950, 975 и $1000mb$.

Моделоване вредности, селектоване за координате најближе координатама лабораторије, упоређене су са мерењима које је РХМЗ спроводио метеоролошким балонима. На слици 4.9 приказан је профил разлика мерених и моделованих температура за различите нивое, у периоду од јануара 2009. године до августа 2015..

Са слике се види да је слагање моделованих и мерених вредности углавном добро и да значајно одступа само за ниво $1000mb$. Стога је за слој између $975 -$

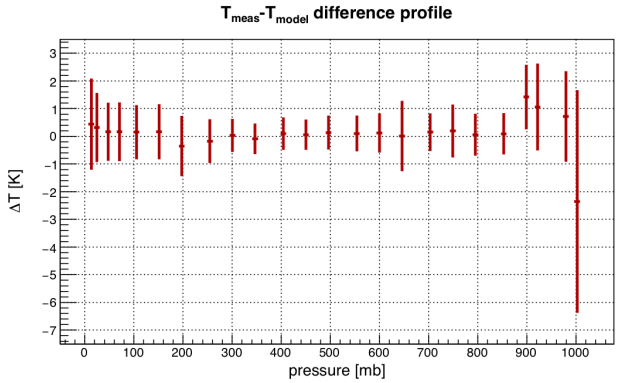

Слика 4.9: Профил разлика мерених и моделованих вредности температуре за различите нивое.

$1000mb$ у анализи коришћена локално мерена температура на нивоу тла.

Како би се добила финија временска резолуција, основни сет података је интерполиран. Упоређено је више алгоритама за интерполацију (кубни, квинтни и акима сплајнови) и најбоље се показала интерполација кубним сплајном, што се слаже са резултатима других аутора [99]. На слици 4.10 приказан је резултат интерполације за температуру једног изобарног нивоа на одабраном интервалу. Сплајн функција је евалуирана на сваких 5 минута, на основу чега је формиран коначан скуп података.

4.2.2 Локално мерени метеоролошки подаци

Подаци о атмосферском притиску и температури на нивоу тла употпуњују скуп метеоролошких варијабли. Превасходно се преузимају од мануелних и аутоматских мерних станица РХМЗ у Београду и околини (Карађорђев парк, Кошутњак, Панчево), мада су коришћени и други доступни извори (мерне станице београдског аеродрома, АМС на Трошарини и лабораторије за физику животне средине ИФ).

Метеоролошке станице су уређене по поузданости и доступности података. Затим је формирана јединствена временска серија, узимајући увек податак најпоузданије доступне станице. Подаци су нормирани на вредности референтне

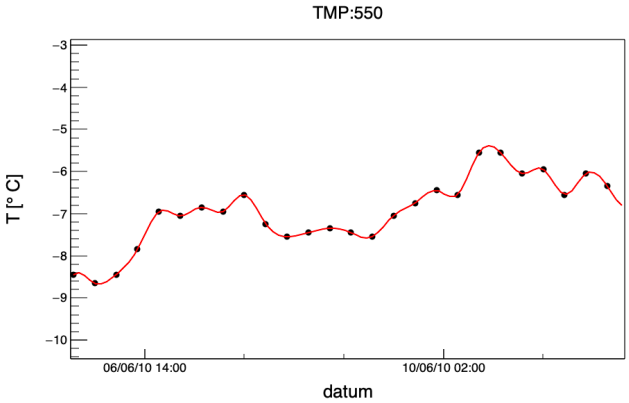

Слика 4.10: Температура нивоа од 550mb: вредности GFS модела (тачке) и интерполација (црвена линија).

мерне станице - Карађорђевог парка. Због веће густине података, интерполација сплајном је давала слабије резултате, па су подаци интеполирани линеарном функцијом.

На слици 4.11 приказане су временске серије изабраних метеоролошких параметара након интерполације: атмосферских температура за изобарне нивое од 10, 100, 200, 400 и 700mb, температуре на нивоу тла и атмосферског притиска.

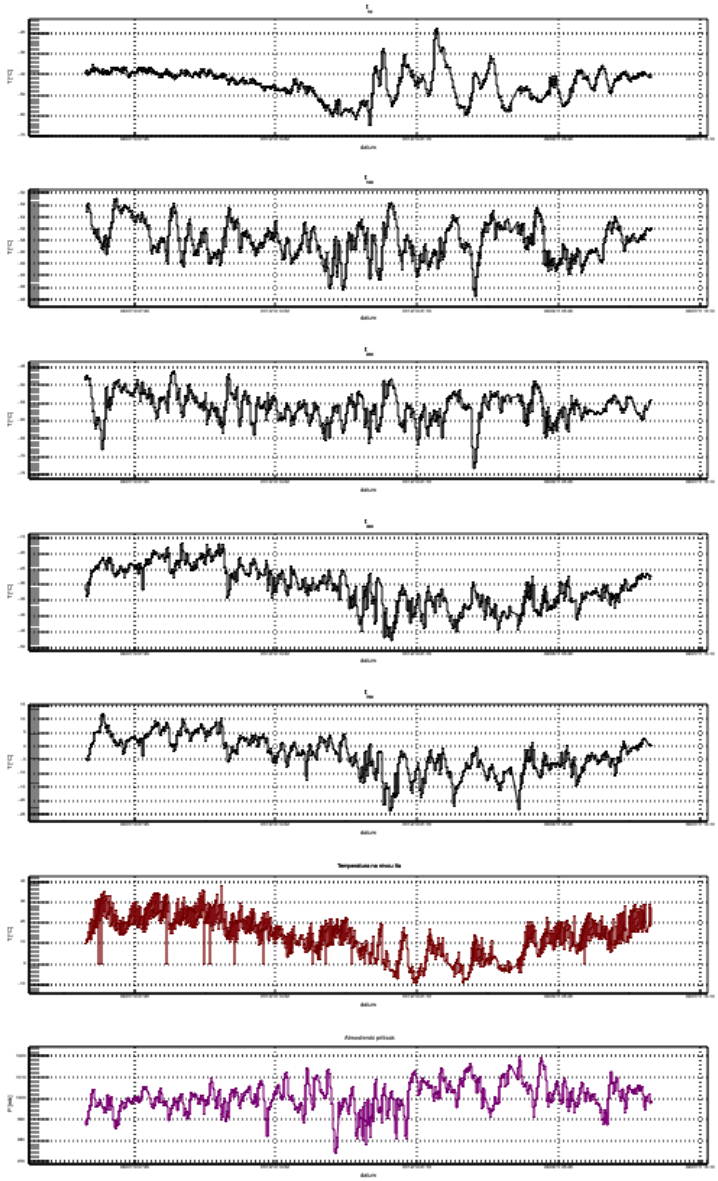

Слика 4.11: Временске серије изабраних метеоролошких параметара. Одозго на доле: температуре нивоа од 10, 100, 200, 400 и 700mb, температура на нивоу тла и атмосферски притисак.

Анализа и корекција метеоролошких ефеката применом декомпозиције на основне компоненте

До сада представљене методи за корекцију метеоролошких ефеката на мионску компоненту космичког зрачења имају нека ограничења. Теоријски методи су донекле апроксимативног карактера, док емпиријски методи не узимају обавезно у обзир потпун скуп матеоролошких варијабли. За унапређење теоријског приступа нема превише простора. међутим то није случај са емпиријским приступом. Такође, предност емпиријских метода је једноставност примене и универзалност приступа.

Дуперијеров метод, односно метод ефективног нивоа продукције (представљен у одељку 3.3.1), је један од најпознатијих и најчешће коришћених емпиријских метода. Овај приступ претпоставља да се миони доминантно продукују у једном слоју атмосфере (типично се узима $100 - 200mb$), па се у примени узима у обзир само утицај температуре овог слоја. Главна замерка овом методу је превелика неодређеност коју оваква апроксимација уноси, као и чињеница да се не узимају у обзир јонизациони губици при пропагацији миона кроз атмосферу.

На слици 5.1 приказана је расподела броја генерисаних миона у зависности од висине, односно дубине атмосфере. Расподела је продукована применом пакета за симулацију космичких пљускова CORSIKA.

Види се да се миони продукују континуално на свим висинама, односно ду-

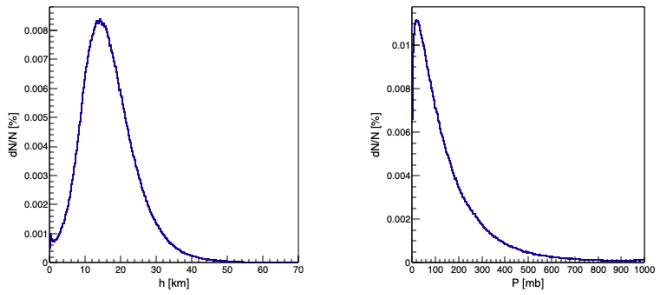

Слика 5.1: Расподела броја продукованих миона у зависности од геопотенцијалне висине (лево) и датог нивоа притиска (десно) (симулација пакетом CORSIKA).

бинама атмосфере, те да се у анализи метеоролошких ефеката мора узети у обзир целокупни температурски профил атмосфере.

Како су доступне моделоване температуре за довољан број нивоа атмосфере (одељак 4.2.1), у принципу је могуће наћи зависност детектованог одброја од температуре за различите нивое и одредити коефицијенте зависности на основу регресије. Помоћу тако одређених коефицијената затим је могуће кориговати одброј и уклонити допринос температурског ефекта.

Препреку оваквом приступу представља чињеница да температуре различитих слојева атмосфере нису независне, већ могу бити значајно корелисане у ком случају коефицијенти одређени на горе описан начин нису линеарно независни.

На слици 5.2 приказана је корелациона матрица за атмосферски притисак и температуре различитих нивоа атмосфере. Атмосферски притисак и температура на нивоу тла су мерене, док су температуре преосталих нивоа атмосфере моделоване (одељак 4.2.1). Види се висока корелација температура у тропосфери као и нешто мања корелација температура у тропопаузи и стратосфери. Такође, постоји незанемарљива корелација температуре неких нивоа са атмосферским притиском.

Овај проблем може да се превазиђе преласком са скупа корелисаних варијабли на скуп некорелисаних варијабли, а погодан начин да се то оствари представља декомпозиција на основне компоненте (*Principal Component Analysis* -

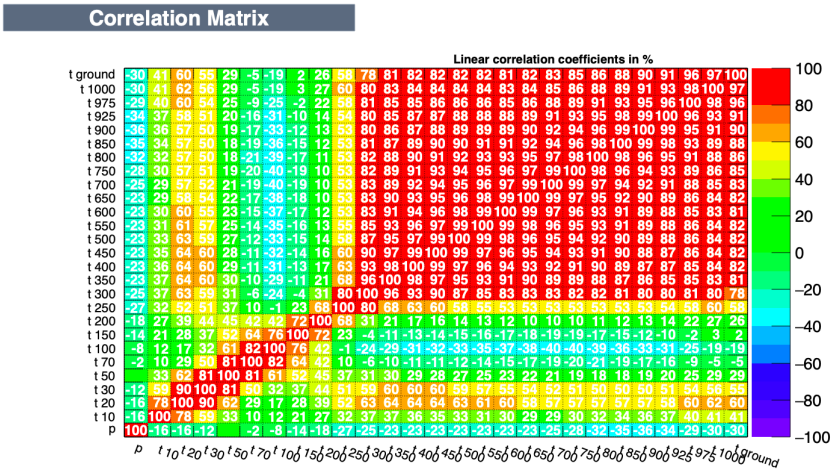

Слика 5.2: Корелациона матрица метеоролошких параметара на основу података за 2010. и 2011. годину.

PCA). Додатно, нови скуп би тако био одређен да првих неколико компоненти садржи највећи део варијације основног скупа варијабли. Тако је могуће смањити димензионалност скупа података а очувати највећи део варијације. Метода декомпозиције на основне компоненте је стога добар кандидат за моделовање и анализу метеоролошких ефеката на мионску компоненту космичког зрачења.

Потенцијална мана оваквог приступа је да се губи директна веза са почетним скупом варијабли, па физичка интерпретација резултата није увек једноставна.

5.1 Основе декомпозиције на основне компоненте

Основни задатак декомпозиције на основне компоненте (ДОК) је двојак: (1) са основног скупа корелисаних варијабли прећи на нови скуп некорелисаних варијабли (основне компоненте) и (2) у новом скупу издвојити што мањи подскуп варијабли које су статистички сигнификантне. Додатни услов да нове варијабле представљају линеарну комбинацију основних у многоме поједностављује овај задатак. Овде ћемо у главним цртама изложити формалну основу методе.

Нека је $\mathbf{x}$ вектор који репрезентује вредности m варијабли. Први корак у

одређивању скупа основних компоненти представља налажење решења једначине:

$$\mathbf{p_1^T x} = p_{11}x_1 + p_{12}x_2 + \cdots + p_{1m}x_m = \sum_{i=1}^{m} p_{1i}x_i, \tag{5.1}$$

по $\mathbf{p_1}$, тако да функција $\mathbf{p_1^T x}$ има максималну варијансу [100].

Ова варијанса се може изразити као $var[\mathbf{p_1^T x}] = \mathbf{p_1^T}\Sigma\mathbf{p_1}$, где Σ представља корелациону матрицу за полазни скуп варијабли $\mathbf{x}$. У пракси корелациона матрица за популацију (Σ) углавном није позната, али се може заменити корелационом матрицом за узорак (S). Да би се варијанса ограничила мора се увести додатни услов $\mathbf{p_1^T p_1} = 1$.

Горњи израз се може максимизирати применом Лангражевих множитеља, односно максимизацијом израза:

$$\mathbf{p_1^T}\Sigma\mathbf{p_1} - \lambda_1(\mathbf{p_1^T p_1} - 1), \tag{5.2}$$

где је λ_1 Лагранжев множитель. Диференцијација овог израза по p_1 даје:

$$\Sigma\mathbf{p_1} - \lambda_1\mathbf{p_1} = 0, \tag{5.3}$$

односно

$$(\Sigma - \lambda_1 I_m)\mathbf{p_1} = 0, \tag{5.4}$$

где I_m представља јединичну матрицу димензије m. Види се да је λ_1 својствена вредност, а $\mathbf{p_1}$ својствени вектор за матрицу Σ. На основу следеће релације можемо да одредимо ком од својствених вектора одговара максимална вредност варијансе:

$$\mathbf{p_1^T}\Sigma\mathbf{p_1} = \mathbf{p_1^T}\lambda_1\mathbf{p_1} = \lambda_1\mathbf{p_1^T p_1} = \lambda_1. \tag{5.5}$$

Видимо да се проблем максимизације варијансе $var[\mathbf{p_1^T x}]$ своди на налажење највеће својствене вредности и одговарајућег својственог вектора корелационе матрице Σ. Тиме је одређена прва основна компонента.

За одређивање следеће компоненте неопходно је максимизирати $var[\mathbf{p_2^T x}]$, уз услов да је функција $\mathbf{p_2^T x}$ некорелисана са $\mathbf{p_1^T x}$. Захтев је еквивалентан услову да је коваријанса $cov[\mathbf{p_1^T x}, \mathbf{p_2^T x}]$ једнака нули. На основу:

$$cov[\mathbf{p_1^T x}, \mathbf{p_2^T x}] = \mathbf{p_1^T}\Sigma\mathbf{p_2} = \mathbf{p_2^T}\Sigma\mathbf{p_1} = \mathbf{p_2^T}\lambda_1\mathbf{p_1} = \lambda_1\mathbf{p_2^T p_1} = \lambda_1\mathbf{p_1^T p_2}, \tag{5.6}$$

види се да је то еквивалентно услову $\mathbf{p_1^T p_2} = \mathbf{p_2^T p_1} = 0$. Према томе, одређивање следеће компоненте се своди на максимизацију израза:

$$\mathbf{p_2^T}\Sigma\mathbf{p_2} - \lambda_2(\mathbf{p_2^T p_2} - 1) - \phi_2\mathbf{p_2^T p_1}, \tag{5.7}$$

где су λ_2 и ϕ_2 Лагранжеви множитељи. Диференцијација по $\mathbf{p_2}$ и множење са $\mathbf{p_1^T}$ са леве стране дају:

$$\mathbf{p_1^T}\Sigma\mathbf{p_2} - \lambda_2\mathbf{p_1^T p_2} - \phi_2\mathbf{p_1^T p_1} = 0. \tag{5.8}$$

Уз претпостављену ортогоналност и $\phi = 0$, максимизација за другу компоненту се своди на $\Sigma\mathbf{p_2} - \lambda_2\mathbf{p_2} = 0$, односно $(\Sigma - \lambda_2 I_m)\mathbf{p_2} = 0$, уз услов да је у питању следећа највећа својствена вредност.

Другим речима, основне компоненте су редови ортогоналне матрице која дијагонализује корелациону матрицу полазних варијабли, односно представљају својствене векторе корелационе матрице. Одговарајуће својствене вредности представљају њихове варијансе на основу чијих опадајућих вредности је скуп основних компоненти уређен.

Проблем одређивања скупа основних компоненти се стога своди на решавање својственог проблема корелационе матрице скупа полазних варијабли и уређивање скупа својствених вектора на основу опадајуће вредности одговарајућих својствених вредности. Општији приступ одређивања скупа основних компоненти ослања се на сингуларну декомпозицију матрица (*Singular Value Decomposition - SVD*), али овде нећемо улазити у детаље те процедуре.

5.2 Декомпозиција метеоролошких параметара

У наредна два одељка представићемо резултате декомпозиције на основне компоненте полазног скупа метеоролошких параметара, као и критеријуме за селекцију подскупа значајних компоненти.

5.2.1 Процедура декомпозиције

Први корак у анализи методом ДОК подразумева одређивање скупа основних компоненти. За декомпозицију је коришћена рутина у програмском језику *R* [80].

Полазни скуп варијабли су представљале моделоване температуре 24 нивоа атмосфере и локално мерени температура на нивоу тла и атмосферски притисак. Пре декомпозиције полазне варијабле су центриране и нормиране.

Резултат је новодобијени скуп од 26 компоненти. Декомпозиција није једнозначна јер зависи од корелационе матрице, па према томе и од интервала у ком су мерени подаци. Из разлога наведених у одељку 4.1.1, интервал коришћен за анализу је 01.06.2010. – 31.05.2011. године.

На слици 5.3 приказана је корелациона матрица добијених основних компоненти на основу које се види да након декомпозиције не постоји значајна корелација између појединих компоненти.

На слици 5.4 графички је приказана композиција, док су у табели 5.1 дати параметри ротација за првих 9 основних компоненти које садрже 98% варијансе полазног скупа метеоролошких варијабли.

Може се видети да прве две компоненте зависе скоро сасвим од температуре. Прва компонента највећим делом представља комбинацију температура у тропосфери (нивои $250 - 1000mb$), које учествују са скоро једнаким тежинама. Друга компонента је највећим делом линеарна комбинација температура нивоа $10 - 250mb$, где доминантан допринос дају температуре у тропопаузи.

Компоненте 3-6 представљају комбинацију атмосферског притиска и температура различитих нивоа атмосфере. Притисак нарочито значајно доприноси компонентама 3, 4 и 6. Ово указује на корелацију атмосферског притиска и тем-

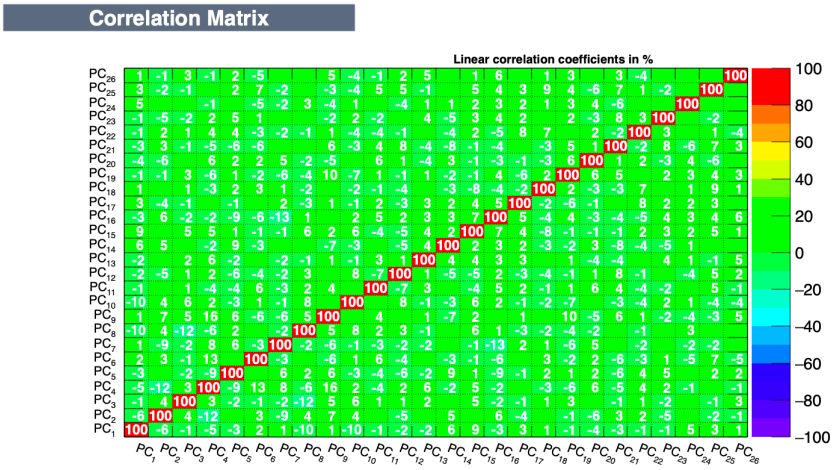

Слика 5.3: Корелациона матрица основних компоненти добијених декомпозицијом метеоролошких података за 2010. и 2011. годину.

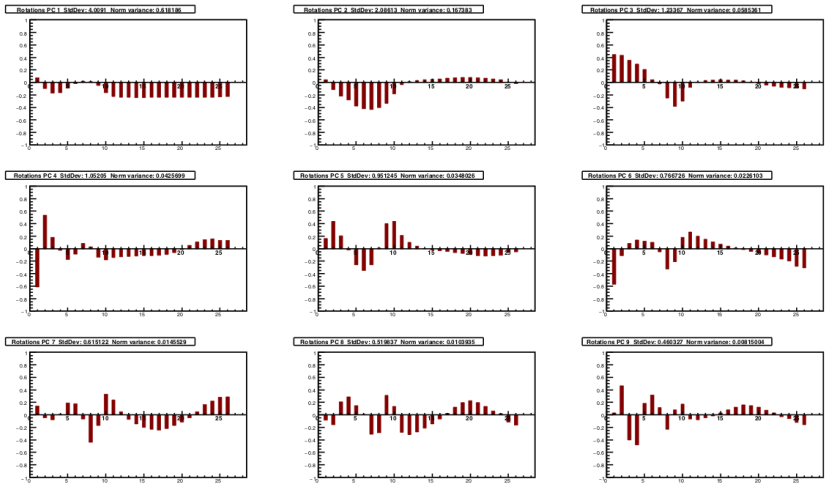

Слика 5.4: Композиција првих девет основних компоненти уређених на основу опадајућих вредности варијансе. На X-оси су приказане метеоролошке варијабле и то: притисак (1), моделоване атмосферске температуре почев од нивоа $10mb$ (2) до нивоа $975mb$ (25) и температура на нивоу тла (26). На Y-оси су одговарајуће ротације.

Табела 5.1: *Композиција првих девет основних компоненти.*

Meteo varijable	Osnovne komponente								
	PC1	PC2	PC3	PC4	PC5	PC6	PC7	PC8	PC9
p	0.07699	0.04117	0.44694	-0.61285	0.16301	-0.57121	0.14028	-0.08106	0.03443
t_{10}	-0.0947	-0.11603	0.43488	0.5344	0.43741	-0.11036	-0.04499	-0.15825	0.46469
t_{20}	-0.16947	-0.21766	0.35754	0.18029	0.20527	0.08546	-0.07719	0.20635	-0.40309
t_{30}	0.16476	-0.27825	0.29593	-0.02505	-0.02204	0.14134	0.00634	0.28574	-0.47812
t_{50}	-0.09124	-0.37682	0.20969	-0.17322	-0.25798	0.12084	0.19349	0.14645	0.18493
t_{70}	-0.01483	-0.42304	0.04507	-0.08651	-0.3472	0.09965	0.18155	0.01024	0.31886
t_{100}	0.02192	-0.43132	-0.02451	0.08228	-0.25692	-0.04937	-0.06464	-0.3103	0.1183
t_{150}	0.01487	-0.40127	-0.24673	0.03037	0.012	-0.32566	-0.43658	-0.28393	-0.23316
t_{200}	-0.04737	-0.33404	-0.38636	-0.13563	0.40141	-0.2069	-0.16852	0.31181	0.07995
t_{250}	-0.16218	-0.17984	-0.29739	-0.18123	0.43708	0.18013	0.32866	0.13662	0.17389
t_{300}	-0.22473	-0.03266	-0.07561	-0.14073	0.21179	0.26504	0.23807	-0.27931	-0.06785
t_{350}	-0.2369	0.01439	0.00488	-0.12991	0.0998	0.1988	0.05306	-0.31612	-0.0771
t_{400}	-0.23956	0.03362	0.02958	-0.12159	0.04075	0.14932	-0.06959	-0.27189	-0.04852
t_{450}	-0.24028	0.04271	0.0402	-0.11503	0.00384	0.10744	-0.14772	-0.21165	-0.01823
t_{500}	-0.24005	0.04935	0.0428	-0.11304	-0.02187	0.07218	-0.19893	-0.14512	0.03068
t_{550}	-0.23958	0.05695	0.03965	-0.11295	-0.03254	0.0388	-0.23263	-0.06843	0.08056
t_{600}	-0.23881	0.06549	0.03681	-0.10649	-0.04369	0.01102	-0.24562	0.02401	0.12499
t_{650}	-0.23854	0.07279	0.0236	-0.09184	-0.06132	-0.01542	-0.21788	0.12597	0.15977
t_{700}	-0.23835	0.0801	0.00429	-0.06052	-0.07601	-0.04668	-0.16785	0.19559	0.14932
t_{750}	-0.23842	0.08071	-0.01837	-0.01332	-0.09245	-0.07308	-0.11295	0.22563	0.12401
t_{800}	-0.23814	0.07557	-0.03907	0.05036	-0.10989	-0.09943	-0.04696	0.19596	0.07735
t_{850}	-0.23701	0.0675	-0.06202	0.1081	-0.11988	-0.12745	0.04989	0.13672	0.0304
t_{900}	-0.23535	0.05462	-0.07977	0.14776	-0.11454	-0.16955	0.16551	0.06204	-0.02952
t_{925}	-0.23414	0.04606	-0.08313	0.15641	-0.10257	-0.19925	0.21877	0.01715	-0.05804
t_{975}	-0.23108	0.00789	-0.08827	0.13022	-0.05888	-0.28046	0.284	-0.11523	-0.12249
t_{ground}	-0.22494	-0.01582	-0.10092	0.13401	-0.04977	-0.30749	0.28553	-0.16516	-0.15908

пературе атмосфере, што је у складу са претпоставком да се дневна и полудневна варијација атмосферског притиска могу објаснити као последица загревања горњих слојева атмосфере под утицајем Сунчевог зрачења [101].

Такође, ова корелација може да објасни зашто није могуће издвојити једну компоненту којом доминира атмосферски притисак. Можда је значајна паралела са теоријским изразом за барометарски ефекат, који је представљен као сума три независна ефекта: ефеката апсорпције, распада и продукције (једначина 3.39). Коначно, ова корелација указује на то да емпиријски методи који независно третирају барометарски и температурски ефекат могу продуковати прецењене вредности корекционих коефицијената.

5.2.2 Селекција сигнификантних компоненти

Други задатак декомпозиције на основне компоненте представља редукција добијеног скупа како би се у анализи задржале само статистички сигнификантне компоненте. Не постоји један општи критеријум на основу ког се скуп редукује, већ избор варира у зависности од карактеристика декомпозиције или нахођења аутора. Представићемо овде неколико различитих, који се могу поделити у две категорије: критеријуми на основу варијансе и критеријуми на основу функције аутокорелације и спектралне анализе.

Критеријуми на основу варијансе

Идеја овог приступа је да се у даљој анализи користе само компоненте које су сачувале значајну варијацију почетног скупа варијабли. Основни и често коришћени критеријум за редукцију броја компоненти се ослања на анализу релативне кумулативне варијансе. Наиме, задржава се најмањи број компоненти такав да њихова кумулативна варијанса није мања од неког унапред одређеног прага. Праг се дефинише преко процента укупне варијансе и обично варира између 70% и 90%. Вредност прага може бити и ван овог интервала, у зависности од конкретног случаја. Уколико су једна или две компоненте доминантне, вредност прага може бити и већа од 90%. Са друге стране, ако се на основу критеријума добија превелик подскуп, непрактичан за анализу, праг се може спустити.

На слици 5.5 приказане су релативна варијанса и кумулативна релативна варијанса за добијене основне компоненте (*Principal Components - PC*).

Видимо да варијанса прве две компоненте чини скоро 80% укупне (где прва компонента доминантно учествује). Ако се на основу горњег критеријума за праг за кумулативну варијансу узме вредност од 95%, скуп основних компоненти се редукује на 6 компоненти са највећом варијансом.

Други начин за одређивање редукованог скупа компоненти поставља постављање прага на апсолутну вредност варијансе. Према Кајзеровом (*Kaiser*) правилу, из анализе треба изоставизи све компоненте чија варијанса је мања од 1, јер садрже мање информација него почетне варијабле (чија варијанса је

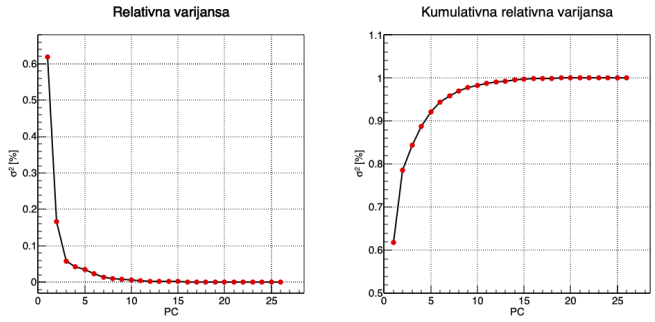

Слика 5.5: Релативна варијанса (лево) и кумулативна релативна варијанса (десно) за скуп основних компоненти.

нормирана). Неки аутори [100] сматрају да је овако одређен праг превисок, јер постоји могућност изостављања доприноса варијабле која је слабо корелисана са осталим варијаблама. Таква варијабла би могла да даје доминантан допринос једној компоненти, која би ипак имала варијансу мању од 1 те би била елиминисана из анализе. На основу резултата симулација, ти аутори су предложили нижу вредност прага за прихватљиву варијансу, од 0.7.

У табели 5.2, осим релативне и кумулативне релативне варијансе, приказане су и апсолутне вредности варијанси за добијени скуп компоненти. На основу вредности у табели видимо да првих шест компоненти задовољава овај релаксирани критеријум.

Донекле сличан је критеријум по коме треба задржати компоненте чије варијансе су веће од средње вредности. Тај критеријум задовољава првих седам компоненти.

Остали тестови су дали потцењен број варијабли (критеријум "сломљеног штапа" - *brocken stick*) или нејасну интерпретацију (скри плот - *scree plot*).

Критеријуми на основу аутокорелације и спектралне анализе

Нешто дугачији приступ за редукцију почетног скупа компоненти се ослања на идеју да корелација сукцесивних вредности и спектралне карактеристике временских серија компоненти морају бити различите од карактеристика насумичних расподела (*white noise*). Овај приступ је често коришћен у примени

Табела 5.2: *Апсолутна, релативна и кумулативна варијанса свих* 26 *основних компоненти.*

Komponenta	Svojstvena vrednost	Relativna varijansa (%)	Kumulativna varijansa (%)
1	4.0091	0.618186	0.618186
2	2.08613	0.167383	0.785569
3	1.23367	0.0585361	0.844105
4	1.05205	0.0425699	0.886675
5	0.951245	0.0348026	0.921478
6	0.766726	0.0226103	0.944088
7	0.615122	0.0145529	0.958641
8	0.519837	0.0103935	0.969034
9	0.460327	0.00815004	0.977184
10	0.382006	0.00561263	0.982797
11	0.32832	0.00414592	0.986943
12	0.294489	0.00333553	0.990278
13	0.247876	0.00236317	0.992642
14	0.239462	0.00220546	0.994847
15	0.206157	0.00163465	0.996482
16	0.184453	0.00130857	0.99779
17	0.144657	8.04834E-4	0.998595
18	0.119676	5.5086E-4	0.999146
19	0.0938189	3.38538E-4	0.999485
20	0.0739496	2.10328E-4	0.999695
21	0.0586253	1.32189E-4	0.999827
22	0.0414996	6.62391E-5	0.999893
23	0.0338811	4.41511E-5	0.999937
24	0.0281359	3.04472E-5	0.999968
25	0.0219102	1.84637E-5	0.999986
26	0.0188263	1.36319E-5	1

ДОК у физици атмосфере [102].

Прва квалитативна оцена се може дати на основу плотова временских серија компоненти. На слици 5.6 приказане су временске серије првих девет компоненти. У временским серијама првих шест компоненти недвосмислено се виде сезонске варијације.

Квантитативнија оцена се може дати на основу аутокорелационих функција појединих компоненти. Заснива се на Бокс-Пирсовом тесту (*Box-Pierce*). Посматра се такозвана "закаснела" корелација временске серије $a_j(t)$ (за j-ту компоненту), где је $t = 1, ..., n$, односно аутокорелациона фукција (ACF) дефинисана као:

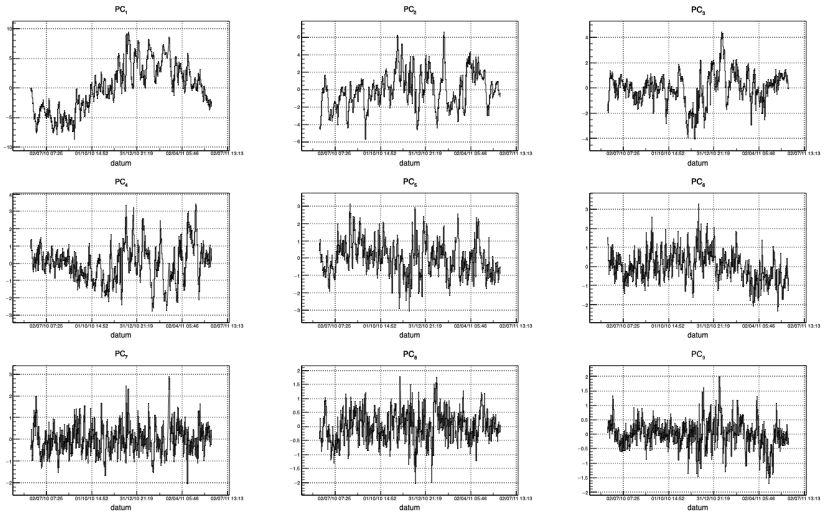

Слика 5.6: Временске серије првих девет компоненти.

$$r_j(l) = \frac{\sum_{t=l+1}^{n} a_j(t)a_j(t-l)}{\sum_{t=1}^{n} a_j^2(t)}, \tag{5.9}$$

где је l временски интервал "кашњења" који задовољава $l = 1, ..., n-1$.

Аутокорелациона функција насумичног шума има гаусову расподелу, средње вредности нула и варијансе дате са:

$$var[r_j(l)] = \frac{n-l}{n(n+2)}. \tag{5.10}$$

Према томе, у случају да нека компонента представља насумични шум, вредности њене аутокорелационе функције би требало да се налазе унутар интервала од приближно две стандардне девијације око нуле, на нивоу поверења од 95%.

На слици 5.7 приказане су аутокорелационе функције за првих девет компоненти. Такође, означен је интервал од 1.96σ око нуле. Види се да је за све компоненте могуће наћи неки интервал кашњења у коме је вредност аутокорелационе функције значајно изван овог интервала.

Још један начин да се утврди сигнификантност компоненти је на основу спектралне анализе. Критеријум за селекцију се ослања на чињеницу да

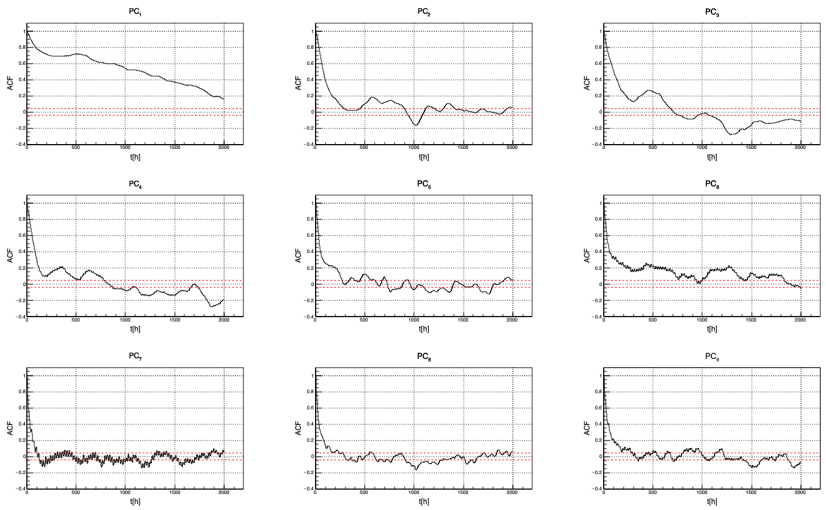

Слика 5.7: Аутокорелациона функција првих девет компоненти. Временско кашњење је дато у сатима (x-оса).

фреквентни спектар значајних компоненти треба да буде различит од спектра насумично дистрибуиране променљиве, односно шума. На слици 5.8 приказана је спектрална густина снаге у зависности од фреквенције за првих девет компоненти.

У фреквентним спектрима скоро свих компоненти јасно се виде неке карактеристичне периодичности, те је додатна квантитативна анализа сувишна. Прва, четврта, пета и шеста компоненте показују дневну периодичност, док компоненте $3, 4, 5$ и 6, које значајније зависе од притиска, показују и полудневну периодичност. Код компоненти 5 и 6 се види и осмочасовна периодичност. Друга компонента нема изразито изражене ове периодичности, али се у периодограму виде структуре које нису насумичне природе

Када се у обзир узму сви поменути критеријуми, на основу варијансе и временске анализе, сигнификантно се издваја првих шест компоненти. Међутим, коначну селекцију је могуће направити тек на основу анализе корелације компоненти са детектованим одбројем миона. Разлог је могућност да нека компонента, која би била на граници да буде одбачена, ипак има значајну корелацију са одбројем и самим тим незанемарљиву предиктивну моћ.

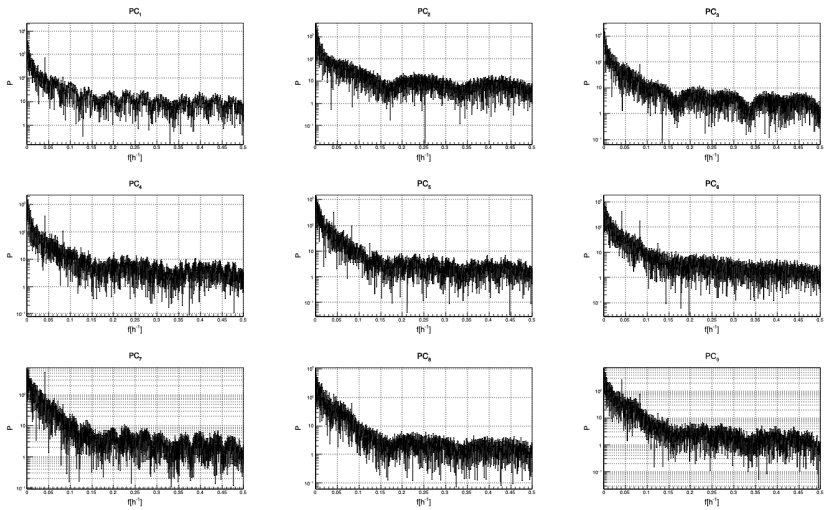

Слика 5.8: Спектрална анализа временских серија првих девет основних компоненти.

5.3 Анализа и корекција метеоролошких ефеката

У табели 5.3 приказани су корелациони коефицијенти за корелацију детектованог одброја у обе лабораторије са потпуним скупом основних компоненти.

Табела 5.3: *Коефицијенти корелације одброја у обе лабораторије са скупом основних компоненти.*

Komponenta	1	2	3	4	5	6	7	8	9	10	11	12	13
Nadzemna	0.43	0.01	-0.37	0.48	-0.55	0.30	-0.01	0.03	-0.01	0.06	0.00	-0.04	0.00
Podzemna	0.26	0.02	-0.48	0.21	-0.19	0.52	0.02	0.04	0.07	0.04	0.01	-0.04	-0.07
Komponenta	14	15	16	17	18	19	20	21	22	23	24	25	26
Nadzemna	0.01	0.02	-0.01	0.00	-0.01	-0.01	0.03	-0.03	0.00	0.02	-0.01	0.04	0.02
Podzemna	0.06	-0.02	-0.05	0.04	0.04	-0.02	0.00	0.00	0.01	0.00	-0.03	0.01	0.01

Види се да постоји значајна корелација одброја у обе лабораторије са компонентама $1, 3, 4, 5$ и 6. Занимљиво је да је корелација космике са компонентом 2, која има значајну варијацију ($16,7\%$ укупне), занемарљиво мала.

Одброј у горњој лабораторији је јаче корелисан са првом компонентом. Она углавном зависи од температура у тропосфери, па је ова зависност у сагласности са интерпретацијом негативног температурског ефекта. Одброј у доњој

лабораторији је нешто јаче корелисан са трећом компонентом, која превасходно зависи од температура у горњим слојевима атмосфере. Ова чињеница би могла да се доведе у везу са позитивним температурским ефектом, који би требало да буде јаче изражен у подземљу. Компоненте 4 и 5 више утичу на одброј у надземној лабораторији, док компонента 6 има већи утицај на одброј у подземној лабораторији. Физичка интерпретација корелације за ове компоненте је нешто компликованија због њихове комбиноване композиције.

Да би се одредили одговарајући коефицијенти, одброј је плотован у зависности од вредности појединих компоненти. На слици 5.9 приказани су графици зависности одброја од првих девет компоненти, за обе лабораторије. Како би се смањила неодређеност, у обзир су узимани само подаци за интернационалне геомагнетно мирне дане (5 најмирнијих дана у сваком месецу).

Зависности су фитоване линеарном функцијом, на основу чега су одређени градијенти, односно коефицијенти зависности. Затим је одброј коригован на барометарски и температурски ефекат, одређен према формули:

$$N_\mu^{(corr)} = N_\mu - \langle N_\mu \rangle \sum_i k_i PC_i, \qquad i = 1, 3, 4, 5, 6, \tag{5.11}$$

где су $N_\mu^{(corr)}$ кориговани одброј, $\langle N_\mu \rangle$ средњи одброј у датом периоду, k_i градијенти а PC_i одговарајуће основне компоненте. На сликама 5.10 и 5.11 приказане су временске серије кориговане на метеоролошке ефекте за надземну, односно подземну лабораторију. Због поређења, дате су и некориговане, односно временске серије кориговане на барометарски ефекат.

Временске серије одброја коригованог на барометарски и одброја коригованог на барометарски и температурски ефекат фитоване су синусоидалном фукцијом с периодом од годину дана. Смањење амплитуде годишње варијације података након коначне корекције у односу на амплитуду података коригованих само на притисак може дати једну меру ефикасности метода.

Амплитуда годишње варијације након корекције на притисак износи $(1.25 \pm 0.02)\%$ за надземну, односно $(0.84 \pm 0.02)\%$ за подземну лабораторију. Након корекције на барометарски и температурски ефекат методом ДОК ове амплитуде

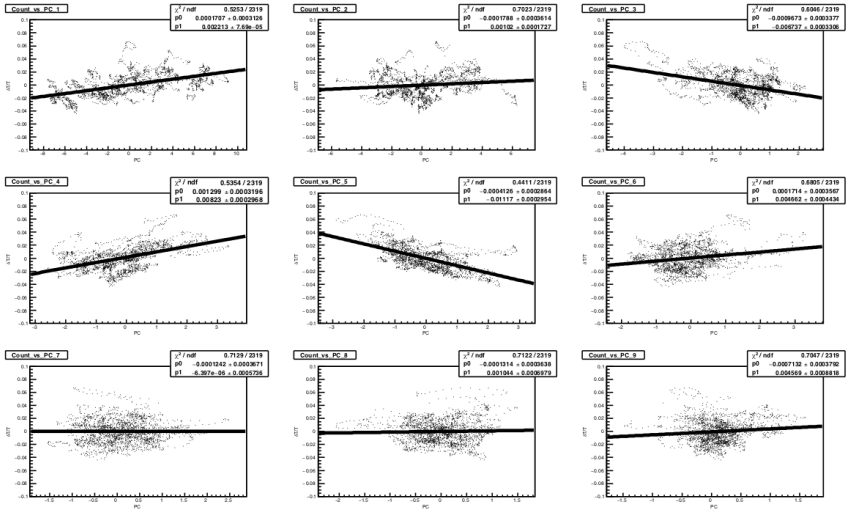

(a)

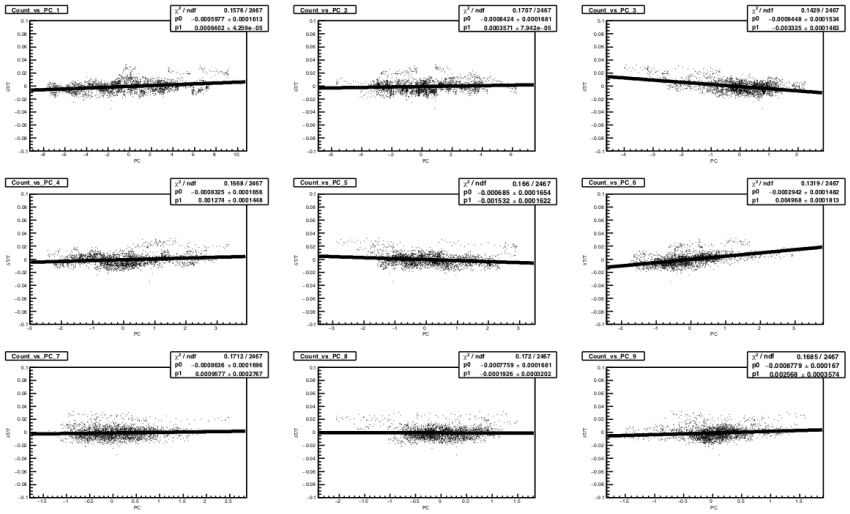

(b)

Слика 5.9: Графици зависности детектованог одброја од првих девет основних компоненти за а) надземну лабораторију и б) подземну лабораторију.

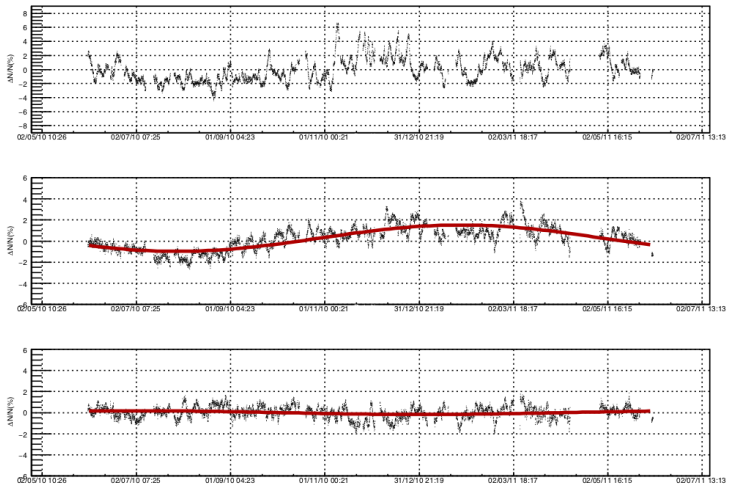

Слика 5.10: Метод декомпозиције на основне компоненте: временске серије одброја космичких миона за надземну лабораторију: некоригована (горе), коригована на барометарски (у средини) и коригована на барометарски и температурски ефекат (доле).

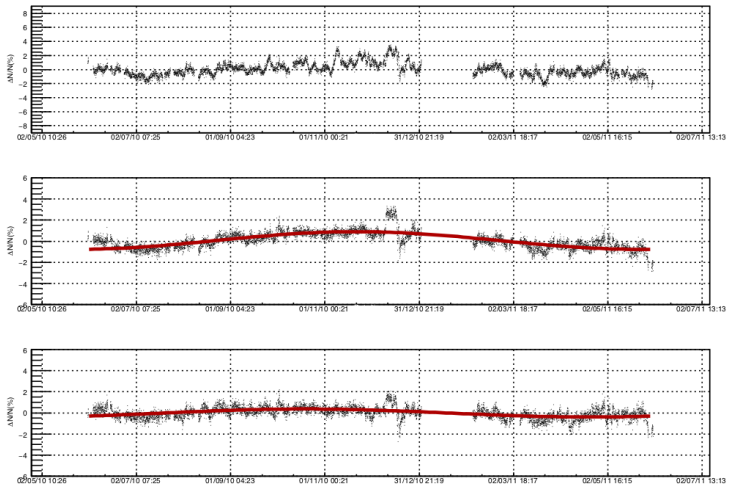

Слика 5.11: Метод декомпозиције на основне компоненте:временске серије одброја космичких миона за подземну лабораторију: некоригована (горе), коригована на барометарски (у средини) и коригована на барометарски и температурски ефекат (доле).

износе $(0.18 \pm 0.05)\%$ за надземну, односно $(0.38 \pm 0.02)\%$ за подземну лабораторију. То даје одговарајуће редукцију годишње варијације од 86%, односно 54.9% респективно.

Још једна илустрација ефикасности метода би могао да буде проценат варијансе који корекција уклања. Тако за надземну лабораторију корекција уклања 64.5%, док за подземну уклања 38.1% варијансе [103].

У поређењу са постојећим методима (представљеним у одељку 3.4.4) метод декомпозиције на основне компоненте је ефикаснији од свих представљених метода, осим метода усредњене температуре примењеном на податке горње лабораторије, када је упоредиве ефикасности. Осим тога, једноставност и универзалност га чине лако применљивим за корекцију метеоролошких ефеката на подацима било ког мионског монитора, независно од локације или конкретне експерименталне поставке, што представља додатну компаративну предност.

Мултиваријантна анализа и корекција метеоролошких ефеката применом пакета TMVA

Методи машинског, односно статистичког машинског учења, користе се у анализи података у науци, индустрији, финансијском сектору и другде. Основни задатак ових техника је да се употребом рачунарских ресурса и флексибилних мултиваријантних алгоритама (углавном заснованих на статистици или функционалној анализи), на основу ограниченог скупа података произведе концизан модел високе предиктивне моћи [104].

Техника учења подразумева да се параметри алгоритма одреде (тренирају) на једном делу података (*training set*), на основу чега се одређује предиктивни модел (*learner*) применљив на нове податке, који предвиђа исход са високом тачношћу.

У случају да постоји једна или више излазних (зависних) варијабли, које покушавамо да предвидимо на основу улазних (независних) варијабли, говоримо о "надгледаном" проблему (*supervised learning problem*). У случају да је циљ да се посматрани систем само карактерише, без конкретних излазних варијабли, говоримо о "ненадгледаном" проблему (*unsupervised learning problem*).

Када се ради о надгледаним проблемима, излазне варијабле могу бити квалитативног или квантитативног карактера. Методу код које је излазна варијабла квалитативног карактера називано **класификацијом**, док методу код које је излазна варијабла квантитативног карактера називано **регресијом**.

Јасно је стога да је за проблем анализе и корекције метеоролошких ефеката

на космичке мионе управо метод мултиваријантне регресије, базиране на статистичком машинском учењу, веома погодан. Идеја је да се као излазна варијабла дефинише одброј миона, док би улазне варијабле представљале атмосферски притисак и температура атмосфере. Након што би модел био адекватно истриниран, давао би предвиђање одброја на основу вредности метеоролошких параметара. Помоћу овако предвиђеног одброја у принципу би било могуће кориговати реално мерени одброј миона и тако ефективно уклонити ефекте атмосферских варијација.

Постоји велики број метода и конкретних имплементација прилагођених различитим дисциплинама, што донекле отежава избор. У овој анализи смо се одлучили за пакет TMVA 4 (*Toolkit for Multivariate Data Analysis with ROOT*) [105] који је могуће опционо инсталирати у оквиру рачунарсног окружења за анализу ROOT [81].

Пакет је развијен пре свега за примену у честичној физици и оптимизован је за издвајање сигнала малог интензитета из велике количине података помоћу различитих алгоритама надгледаног учења. Подржава класификацију и регресију за велики број мултиваријантних техника и садржи додатни сет алата за манипулацију података и оптимизацију алгоритама.

Неки од алгоритама укључених у TMVA су:

- мултидимензионална анализа на основу "лајклихуд" (*likelihood*) функција (PDE, PDE-Foam, kNN)
- анализа на основу линеарних и нелинеарних дискриминантних функција (LD, FDA)
- вештачке неуронске мреже (две различите имплементације)
- алгоритми на основу бинарног гранања (BDT, BDTG)

У наредним одељцима ћемо представити основе неких алгоритама од значаја, процедуру тренирања и тестирања, као и примену изабраних тренираних алгоритама у корекцији метеоролошких ефеката.

6.1 Преглед метода за мултиваријантну регресију

У овом одељку ћемо у најосновнијим цртама представити неке од алгоритама за регресију у оквиру пакета TMVA. Информације о конкретној имплементацији алгоритама углавном се ослањају на кориснички приручник [106].

6.1.1 Методи на основу максималне вредности "лајклихуд" функције

Овај метод се базира на оптимизацији параметара функције густине вероватноће (*Probability Density Function - PDF*). Нека је $Z = z_1, ..., z_N$ скуп података за тренинг. За сваку промењиву тада можемо претпоставити функцију густине вероватноће:

$$z_i \sim g_\theta(z), \tag{6.1}$$

где θ представља један или више параметара који описују дистрибуцију за скуп података за тренинг (нпр. за Гаусову дистрибуцију би било $\theta = (\mu, \sigma^2)$).

"Лајклихуд" функција, дефинисана као:

$$\mathcal{L}(\theta; Z) = \prod_{i=1}^{n} g_\theta(z_i), \tag{6.2}$$

описује колико је изгледно (*likelihood*) да дате варијабле имају баш измерене вредности. Затим се параметри одређују тако да вредност ове функције буде максимална. Процедура максимизације може да захтева налажење првог извода фукнције, па се због поједностављења рачуна често користи логаритам "лајклихуд" функције [107], односно:

$$\ell(\theta; Z) = \sum_{i=1}^{N} \ell(\theta; z_i) = \sum_{i=1}^{N} \log g_\theta(z_i). \tag{6.3}$$

Како је конкретан облик функције густине вероватноће унапред непознат, у оквиру TMVA пакета се за сваку промењиву бира апроксимативна функција на основу расподеле тренинг података. У случају да број улазних варијабли није

превелик и да је количина тренинг података таква да у довољној мери попуни фазни простор, овај метод може бити упоредиве ефикасности са комплекснијим методима.

Алгоритми за мултиваријантну регресију, имплементирани у TMVA, а који се базирају на овом приступу су: PDERS (*PDE range search*), PDE-Foam (*PDE using self-adapting phase-space binning*), kNN (*k-Nearest Naighboor Classifier*).

6.1.2 Методи на основу линеарних и нелинеарних дискриминантних функција

Мултиваријантна анализа помоћу дискриминантних функција се углавном користи за класификацију, али је врло успешно применљива и на проблеме регресије.

Циљ метода је да се дефинише функција улазних варијабли на основу које је могуће извршити ефикасну класификацију, односно регресију. За разлику од неких других метода, функција не мора бити ни у каквој вези са дистрибуцијом улазних варијабли, већ се дефинише од стране корисника и највише зависи од ефикасности примене. Такође, избор функције не мора бити једнозначан.

Фамилија дискриминантних функција се може дефинисати као линеарна комбинација вектора улазних варијабли $\mathbf{x} = (x_1, ..., x_n)^T$ [108]:

$$g(\mathbf{x}) = \mathbf{w}^T\mathbf{x} + w_0 = \sum_{i=1}^{n} w_i x_i + w_0. \tag{6.4}$$

Претпоставимо да тачке $\mathbf{p}_1, ..., \mathbf{p}_c$ репрезентују c различитих класа. Критеријум за припадност $\mathbf{x}$ i-тој класи еквивалентан је услову да је минимално удаљен од вредности $\mathbf{p}_i$. Овај услов се може дефинисати преко квадрата метрике у еуклидском простору:

$$|\mathbf{x} - \mathbf{p}_i|^2 = \mathbf{x}^T\mathbf{x} - 2\mathbf{x}^T\mathbf{p}_i + \mathbf{p}_i^T\mathbf{p}_i. \tag{6.5}$$

Услов за минимално растојање је да израз $\mathbf{x}^T\mathbf{p}_i - \frac{1}{2}\mathbf{p}_i^T\mathbf{p}_i$ има максималну вредност. Тада је i-та дискриминантна функција дата са:

$$g_i(\mathbf{x}) = \mathbf{w}_i^T \mathbf{x} + w_{i_0}, \tag{6.6}$$

где су

$$\mathbf{w}_i = \mathbf{p}_i \quad \text{и} \quad w_{i_0} = -\frac{1}{2}|\mathbf{p}_i|^2. \tag{6.7}$$

Резултат процедуре је разграничење у простору класа хипер-површима које су нормалне на правац најкраћег растојања тачака које дефинишу класе. У случају регресије, класа се замењује конкретном вредношћу излазне варијабле.

У датом примеру дискриминантна функција је линеарна по $\mathbf{x}$, али у општем случају не мора бити и тада говоримо о генералисаним дискриминантним линеарним функцијама.

У пакету TMVA линеарни дискриминантни метод имплементиран је кроз алгоритам LD, док је нелинеарни метод заступљен са четири различите имплементације алгоритма FDA ($FDA\_GA, FDA\_MC, FDA\_MT, FDA\_GAMT$).

6.1.3 Методи на основу вештачких неуронских мрежа

Вештачке неуронске мреже су пре свега биле замишљене као математички модел људског мозга, али су нашле можда и већу примену као ефикасан метод за класификацију и регресију мултиваријантних проблема.

Ако посматрамо проблем класификације n улазних променљивих репрезентованих вектором $\mathbf{x} = (x_1, ..., x_n)^T$, док су резултујуће излазне функције $g_1(\mathbf{x}), ..., g_c(\mathbf{x})$, задатак неуронске мреже је да минимизира квадратну грешку дату изразом [109]:

$$E = \frac{1}{2} \sum_{j=1}^{N} \sum_{i=1}^{c} \left(g_i(\mathbf{z}_j) - \mathcal{I}(\omega_i, y_j) \right)^2, \tag{6.8}$$

где је $\mathbf{Z} = \{\mathbf{z}_1, ..., \mathbf{z}_N\}$ скуп тренинг података, $\mathcal{I}(\omega_i, y_j)$ функција која има вредност 1 ако је за $\mathbf{z}_j$ $y_j = \omega_i$, а вредност нула у супротном, док су ω_i су могуће излазне вредности.

Вештачка неуронска мрежа састоји се од неурона или, како се такође често

зову, чворова (*nodes*). Нека је $\mathbf{u} = (u_0, ..., u_q)^T$ вектор улазних варијабли, а ν излазна вредност за неки чвор. Уводимо *вектор синаптичких тежина* $\mathbf{w} = (w_0, ..., w_q)^T$. На датом ноду имплементира се следећа функција:

$$\nu = \phi(\xi); \quad \xi = \sum_{i=0}^{q} w_i u_i, \tag{6.9}$$

где је ϕ *активациона функција* а ξ *укупна сума.*

Користе се различити аналитички облици функције ϕ: Хевисајдова (степ) функција, сигмоидална, линеарна функција идентитета, хиперболичка тангенс, радијална функција и друге.

Једна специфична имплементација вештачких неурона назива се зове перцептрон (*perceptron*). Када су перцептрони организовани у нивоима (*layers*), таквим да процесирање увек иде од нижег ка вишем нивоу почев од улазног нивоа, говоримо о MLP неуронској мрежи (*Multilayer Perceptron*).

MLP мора имати најмање улазни и излазни ниво, али може имати и више нивоа између ова два, који нису доступни кориснику, односно "скривени" су. MLP је конкретна имплементација која ће бити коришћена за регресију у оквиру TMVA.

6.1.4 Методи на основу бинарног гранања

Фамилија метода који се заснивају на принципу бинарног гранања развијена је касније од већине осталих до сада представљених и најмање се ослања на математички статистички формализам. Идеја овог приступа је да се фазни простор промењљивих подели на много мањих делова (n-димензионалних коцки у случају n-димензионалног простора), на основу којих је могуће предвидети излазне варијабле.

За било коју варијаблу је могуће дефинисати неки критеријум, а затим поделити почетни (тренинг) скуп података на основу тога да ли варијабла задовољава овај критеријум или не. Критеријум може бити категоричан или континуалан. Добијени подскуп података поново се може делити на основу неког новог критеријума. Свака подела дефинише један "чвор" (*node*) на коме се скуп

података "грана". Скуп се увек дели на два подскупа према томе да ли подаци задовољавају критеријум или не, па говоримо о бинарном гранању.

Структура која се формира узастопним гранањем назива се "дрво" (*tree*). Дрво се састоји од грана и листова, који представљају коначне подпросторе у фазном простору варијабли и дају предикцију вредности излазне варијабле. Ако је излазна варијабла категорична ради се о класификацији (*decision tree*), док ако је излазна варијабла континуална говоримо о регресији (*regression tree*).

Постоје различити алгоритми који одређују избор варијабле и критеријум за гранање и овде их нећемо детаљније наводити. Гранање престаје када се постигне неки унапред задати услов.

Алгоритам је релативно нестабилан и осетљив на флуктуације основног скупа података. Тај проблем се превазилази гранањем дрвета на основу различитих подскупова тренинг скупа података, односно креацијом "шуме" (*forest*). За коначни резултат се узима вредност добијена на основу већинског предвиђања појединих дрвета. Ефикасност алгоритма се може додатно повећати отежињавањем удела појединих дрвета (*boosting*).

За потребе мултиваријантне регресије у оквиру TMVA пакета имплементирана су два метода: BDT (*boosted decision tree*) и BDTG(*gradient boosted decision tree*).

6.2 Тренирање метода и селекција оптималних параметара

Први корак у мултиваријантној регресији помоћу TMVA пакета представља дефинисање скупа података који се користи за тренинг. И за ову анализу коришћене су временске серије петоминутних одброја детектованог космичког зрачења из периода 01.06.2010. – 31.05.2011. године. Чињеница да временски интервал износи годину дана требало би да смањи потенцијални утицај сезонских варијација.

За тренинг скуп података селектовани су подаци за 5 геомагнетно најмирнијих дана у сваком месецу. Тако се минимизује део варијације у одброју кос-

мике који потиче од процеса у хелиосфери и повећава се удео, а самим тим и осетљивост на варијације одброја услед метеоролошких ефеката.

Скуп података се тада дели на два дела: део за тренирање (*training*) и део за тестирање метода (*testing*). За потребе тренирања одређено је 1000 насумично одабраних података, док су сви остали подаци коришћени за тестирање. Осим основних услова квалитета (елиминација екстремних вредности), никакви други критеријуми селекције података нису наметани.

Поменуто је да је у оквиру TMVA пакета кориснику на располагању већи број алгоритама за регресију, а који се могу сврстати у четири категорије. Унутар сваке категорије постоји више имплементација сродних алгоритама. За сваки од алгоритама постоји већи број улазних параметара које дефинише корисник, а који утичу на тачност регресије. Како преглед рада свих метода није ни циљ ове анализе, овде ћемо детаљније представити само изабране.

За сваку категорију алгоритама биће представљен један метод који се показао најефикаснијим у моделирању и корекцији метеоролошких ефеката. Критеријум за избор метода представља средње квадратно одступање процењене излазне вредности од мерених вредности података.

Ефикасност метода у многоме зависи од избора улазних параметара. Варирање њихових вредности је значајно побољшало ефикасност појединих алгоритама. У појединим случајевима вредност средњег квадратног одступања се смањила и за неколико редова величине у односу на резултат добијен на основу предефинисаних вредности параметара. Коначно је из сваке категорије изабран репрезентативни метод који се показао најефикаснијим. Ова четири метода су kNN (k-Nearest Neighboor), LD (Linear Discriminant Analysis), MLP (Multilayer Perceptron neural network) и BDTG (Gradient Boosted Decision Tree).

На слици 6.1 приказана је вредност средњег квадратног одступања моделираног одброја мереног у надземној лабораторији, за изабране методе и вредности улазних параметара за које алгоритми имају високу тачност. Плави симболи се односе на целокупан скуп података, док се црни симболи односе на 90% најбоље моделираних података. Празни симболи (само контуре) се односе на подскуп података коришћен за тренинг метода, док се пуни (обојени) симболи

односе на подскуп коришћен за тестирање метода.

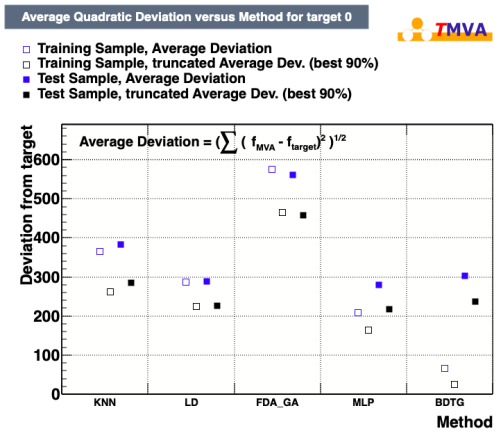

Слика 6.1: Средње квадратно одступање моделиране од мерене вредности одброја за различите методе (подаци из надземне лабораторије).

Овде ћемо укратко представити избор неких главних опција, као и дати илустрацију рада одабраних метода. Већина информација које следе се могу наћи у референци [106].

k-NN алгоритам се базира на максимизацији "лајклихуд" функције. Кад је овај алгоритам у питању, функција густине вероватноће се одређује помоћу емпиријске расподеле формиране на основу предефинисаног броја тачака, најближих суседа у фазном простору тачки која одговара одређеној излазној вредности. Критеријум близине је одређен метриком која је дефинисана у датом простору (у овом случају скалирана Еуклидска метрика).

Да би се познавала емпиријска расподела густине вероватноће потребно је у довољној мери популисати фазни простор променљивих, што у пракси често није могуће. Стога се емпиријска расподела "размазује" (*smoothing*), односно дискретно конволуира неком функцијом. За конволуцију је коришћена Гаусова расподела.

Да би се повећала брзина алгоритма, подаци се пре процесирања сортирају према координатама у фазном простору. Коначни параметри у регресији, који одређују подпросторе фазног простора који одговарају појединим вредностима,

одређују се усредњавањем предвиђања свих тренинг догађаја.

Анализа на основу линеарних дискриминантих функција (**LD алгоритам**) нема улазне параметре доступне кориснику. За мултиваријантну регресију излазна функција је практично еквивалентна процени на основу методе најмањих квадрата.

MLP алгоритам представља вештачку неуронску мрежу која се састоји од одређеног броја неурона типа перцептрон, уређених у нивое, па припада класи *multilayer preceptron* неуронских мрежа. Неурони из једног нивоа могу једносмерно комуницирати само са неуронима из првог вишег нивоа.

Број неурона улазног нивоа одређен је бројем улазних варијабли, док се последњи ниво састоји само од једног излазног неурона. Сви остали нивои су скривени. На слици 6.2 приказан је пример архитектуре MLP неуронске мреже са три скривена нивоа и 20, односно 10 и 10 неурона по нивоу. Већи број нивоа доприноси робусности мреже али захтева веће рачунарске ресурсе. Са друге стране, сматра се да се и са једним скривеним нивоом може постићи произвољна прецизност, уколико је дефинисан довољно велики број неурона за тај ниво, па смо се у овој анализи одлучили за овај други приступ.

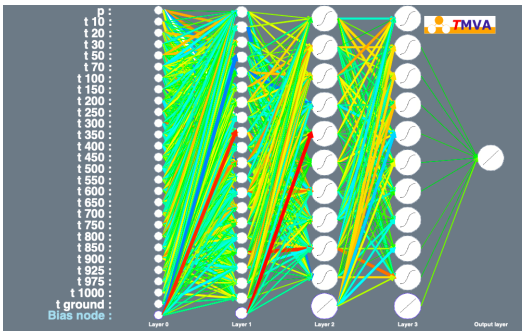

Слика 6.2: Архитектура MLP неуронске мреже са три скривена нивоа. Број неурона у скривеним нивоима је 20, 10 и 10.

Функција одговора неурона представља сложену функцију синаптичке функције (функција која отежињује улазне варијабле за сваки неурон) и активационе функције (функција која мапира излаз неурона). За синаптичку функцију је изабрана проста сума тежина, док је за активациону функцију изабрана хипер-

боличка тангенс функција. За одређивање тежина коришћен је BFGS (*Broyden-Fletcher-Goldfarb-Shannon*) метод.

BDT алгоритам је врло ефикасан како у класификацији, тако и у регресији. Не почива доминантно на некој конкретној статистичкој техници па има једноставну интерпретацију. Већина улазних параметара је интуитивно јасна.

Први значајан параметар представља укупан број дрвета у шуми, што утиче како на стабилност тако и на ефикасност алгоритма. Такође, могуће је дефинисати максималну дубину појединачног дрвећа, односно максималан број гранања. На слици 6.3 приказано је једно дрво са 6 гранања. Плавим су обележени листови који се коначно користе у анализи.

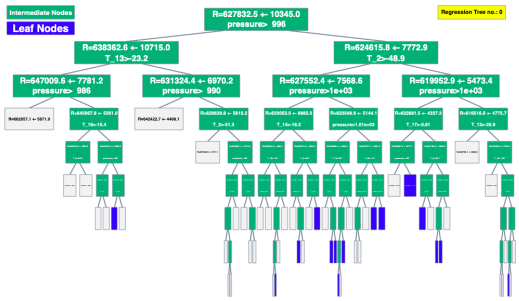

Слика 6.3: Структура једног дрвета, максималне дубине 6 чворова (BDT модел).

Свако гранање се врши на основу неког критеријума за сепарацију. Постоји више различитих критеријума, али будући да нема велике разлике у ефикасности за анализу је коришћен предефинисан критеријум, Џини индекс (*Gini index*).

Да би се у коначној предикцији повећала тежина ефикаснијих дрвета користи се *boosting*. Алгоритам који је коначно коришћен у анализи и који користи градијентни *boost* је BDTG . Одређује се тако да минимизује функцију која описује девијацију моделиране од мерене вредности. У случају градијентног *boost*-а, функција је логаритам биномиалног експоненцијалног одступања (*binomial log-likelihood loss*). Додатно побољшање ефикасности, а нарочито стабилности, даје *bagging* процедура, која подразумева понављано узорковање и тренирање како би расподела вредности података из тренинг подскупа боље репрезентовала

стварну расподелу реалних података.

За одабране методе варирани су улазни параметри тако да средње квадратно одступање има минималну вредност. У табели 6.1 приказане су овако оптимизоване вредности неких од улазних параметара метода изабраних за мултиваријантну регресију на подацима из надземне лабораторије.

Алгоритми су се показали мање осетљиви на варирање улазних параметара при тренирању на подацима из подземне лабораторије, па за ту регресију параметри нису мењани.

Табела 6.1: *Улазни параметри за регресију одабраним мултиваријантним методама.*

Algoritam	Parametri
kNN	broj najbližih suseda = 10 deo događaja na osnovu kojih je računata širina raspodele = 0.8 faktor skaliranja standardne devijacije u gausijanu = 0.3 metod za *smoothing* = Gaus
LD	/
MLP	aktivaciona funkcija = tanh broj iteracija = 20000 broj neurona na skrivenom nivou = 40 metod treniranja = BFGS
BDTG	broj drveta = 100 tip *boost*-a = Grad odnos broja podataka za *bagging* prema ukupnom broju podataka = 0.5 maksimalan broj čvorova = 3

Додатну илустрацију конзистентности и ефикасности појединих алгоритама за регресију представљају хистограми одступања моделоване од мерених вредности у зависности од вредности одброја.

На сликама 6.4 и 6.5 приказане су ови хистограми за изабране методе за надземну лабораторију, односно подземну лабораторију.

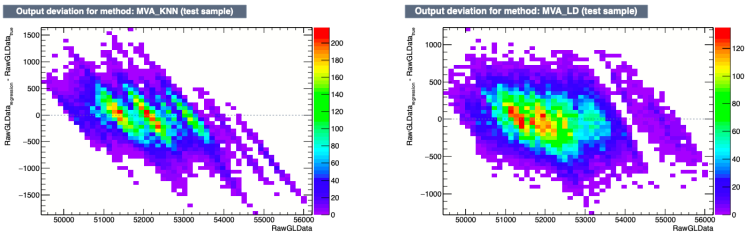

(a) (b)

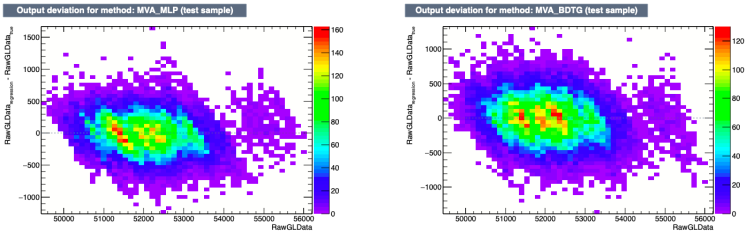

(c) (d)

Слика 6.4: Одступање моделованих од мерених вредности за: а) k-NN б) LD ц) MLP д) BDTG (тест подскуп података за надземну лабораторију).

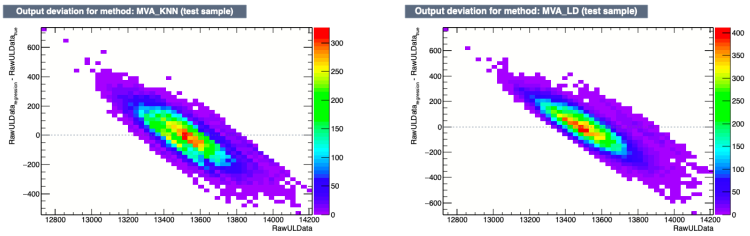

(a) (b)

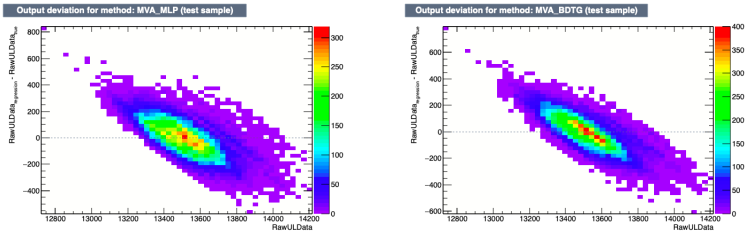

(c) (d)

Слика 6.5: Одступање моделованих од мерених вредности за: а) k-NN б) LD ц) MLP д) BDTG (тест подскуп података за подземну лабораторију).

6.3 Анализа и корекција метеоролошких ефеката

У фази тренирања, односно тестирања, одређују се вредности параметара функције која мапира скуп улазних варијабли на (у овом случају) једну излазну варијаблу. Ова функција може имати егзактан аналитички облик или може бити композитна.

У овој анализи улазне варијабле су представљали локални атмосферски притисак и температура мерени на нивоу тла, као и температуре атмосфере на различитим нивоима. У процесу тренирања као позната излазна варијабла дефинисан је одброј космике. За тренинг мултиваријантних метода су коришћени само подаци за међународне геомагнетно мирне дане. Излазна варијабла мултиваријантне регресије, моделована на основу улазних варијабли, се поредила са реално мереним одбројем. На основу минималног средњег квадратног одступања ове две величине одређени су коначни параметри функција мапирања за различите методе. Претпоставка је да је тиме предвиђена вредност одброја која садржи максималну варијацију услед улазних матеоролошких варијабли.

На основу параметара функција мапирања израчунат је моделован одброј за цео временски период коришћен у анализи. Да би се проценила конзистентност и ефикасност примењених метода, урађена је прелимимнарна квалитативна анализа.

Прва провера се односи на конзистентност метода. Стога су формирани хистограми разлике моделоване и мерене вредности у зависности од мереног одброја за потпун скуп података, еквивалентни хистограмима формираним на основу тренинг подскупа пдоатака, приказаним на сликама 6.4 и 6.5. На слици 6.6 приказане су ове расподеле за податке из обе лабораторије. На основу упоређења одговарајућих хистограма може се закључити да нема видних одступања између расподела за ова два сета података.

Додатну илустрацију квалитета резултата могу да дају хистограми моделованог одброја. На слици 6.7 приказани су ови хистограми за изабране мултиваријантне методе заједно са расподелом мереног одброја, за надземну и подземну лабораторију. Када су у питању подаци из горње лабораторије, може се видети

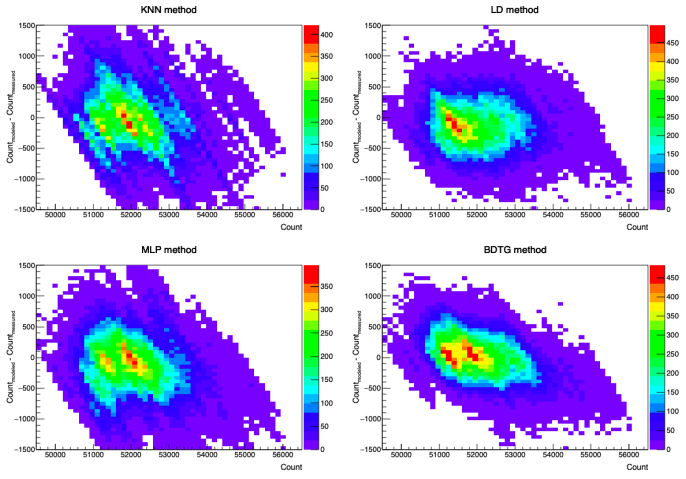

(a)

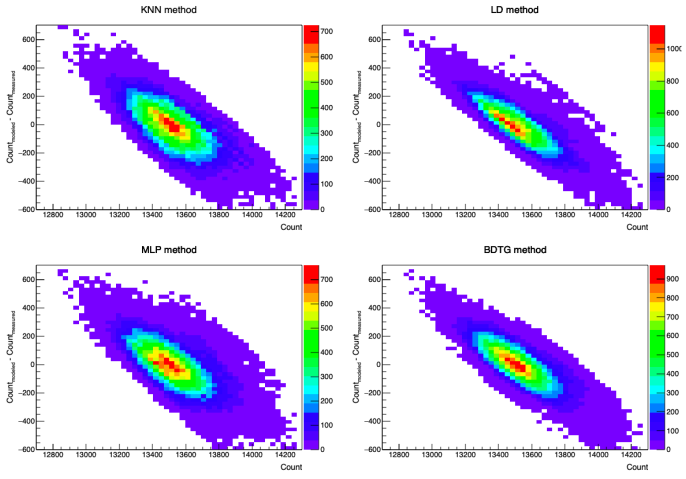

(b)

Слика 6.6: Одступање моделованих од мерених вредности у зависности од одброја након примене корекције барометарског и температурског ефекта изабраним методама за а) надземну лабораторију и б) подземну лабораторију.

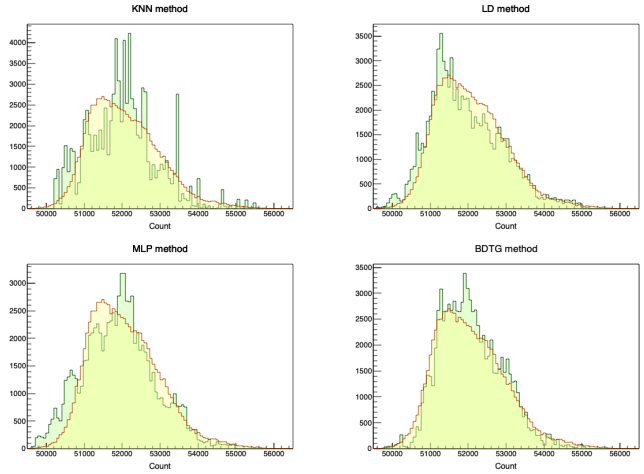

(a)

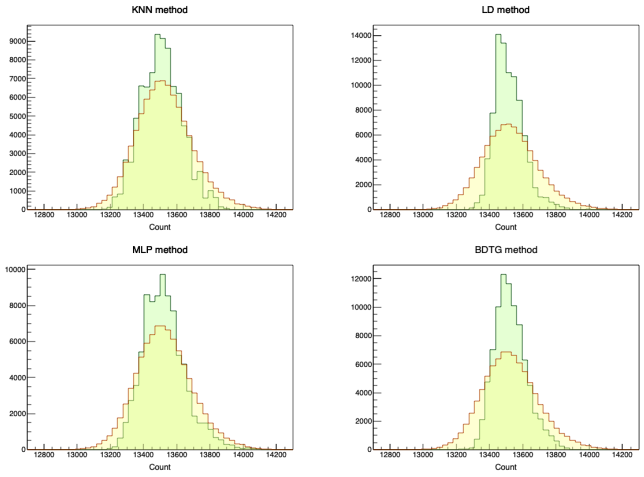

(b)

Слика 6.7: Хистограми мереног (жута боја) и предвиђеног одброја изабраним методама (зелена боја) за а) надземну лабораторију и б) подземну лабораторију.

да постоји боље слагање расподела моделованих и мерених података за методе BDTG и нарочито за LD. Сличан случај је и када је подземна лабораторија у питању, где облик расподеле података моделованих са ова два метода боље одговара расподели мерених података, али је ширина моделованих расподела видно мања.

Како моделован одброј садржи највећи део варијације која потиче од метеоролошких ефеката (барометарског и температурског), разлика моделованог и реално мереног одброја садржи преосталу варијацију, која би требало да доминантно потиче од неатмосферских ефеката.

Према томе, одброј коригован на поменуте метеоролошке ефекте је могуће одредити на основу следеће формуле:

$$N_{\mu}^{(corr)} = \Delta N_{\mu} + \langle N_{\mu} \rangle \,, \tag{6.10}$$

где је

$$\Delta N_{\mu} = N_{\mu}^{(mod)} - N_{\mu} \tag{6.11}$$

разлика моделованог и мереног одброја, а $\langle N_{\mu} \rangle$ представља средњи одброј за дати период.

На сликама 6.8 и 6.9 приказане су временске серије за податке из надземне, односно подземне лабораторије, кориговане изабраним методама. Због референце приказане су и временске серије некоригованих података, односно података коригованих на притисак.

Као и раније, један од критеријума ефикасности изабраних мултиваријантних метода за корекцију метеоролошких ефеката може представљати одговарајућа редукција амплитуде годишње варијације у коригованим временским серијама у односу на исту у временској серији коригованој на притисак. У табели 6.2 приказане су вредности ове амплитуде за различите методе, одређене на основу фита временских серија синусоидалном функцијом облика датог једначином 3.62.

Из табеле 6.2 може се видети да по овом критеријуму највећу ефикасност

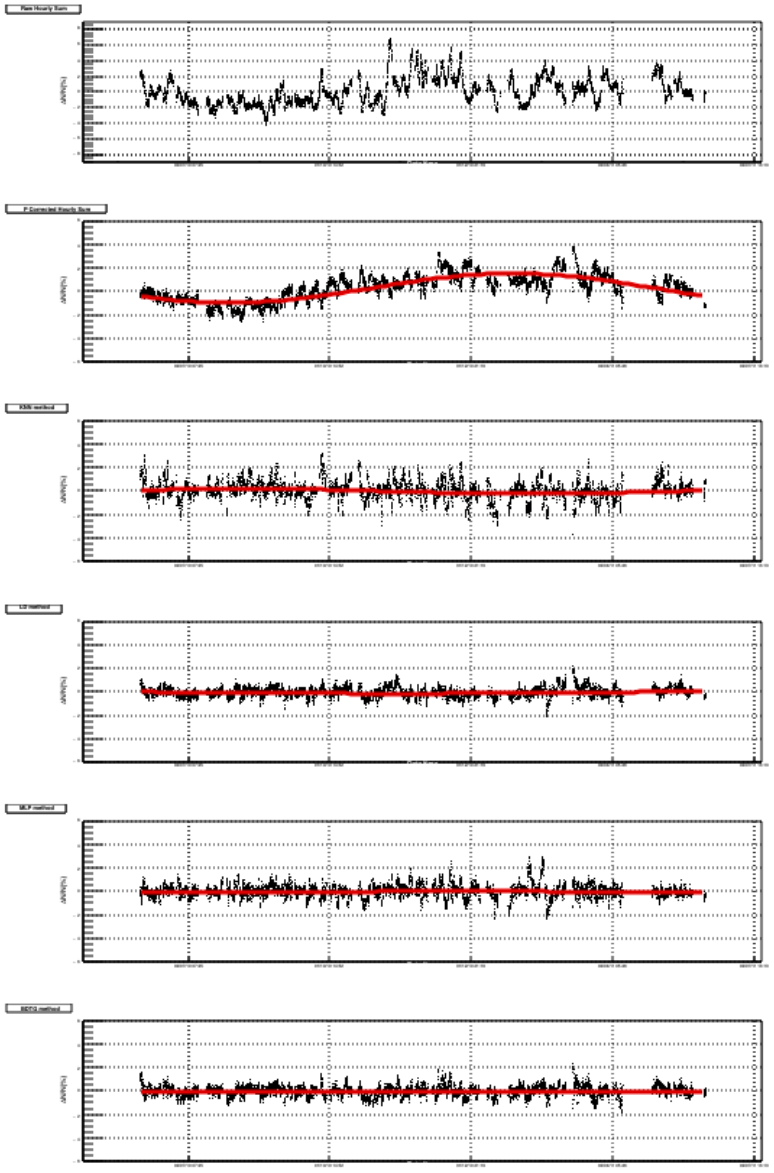

Слика 6.8: Временске серије одброја космичких миона за надземну лабораторију, одозго на доле: некоригована, коригована на притисак, коригована на притисак и температуру методама KNN, LD, MLP, BDTG.

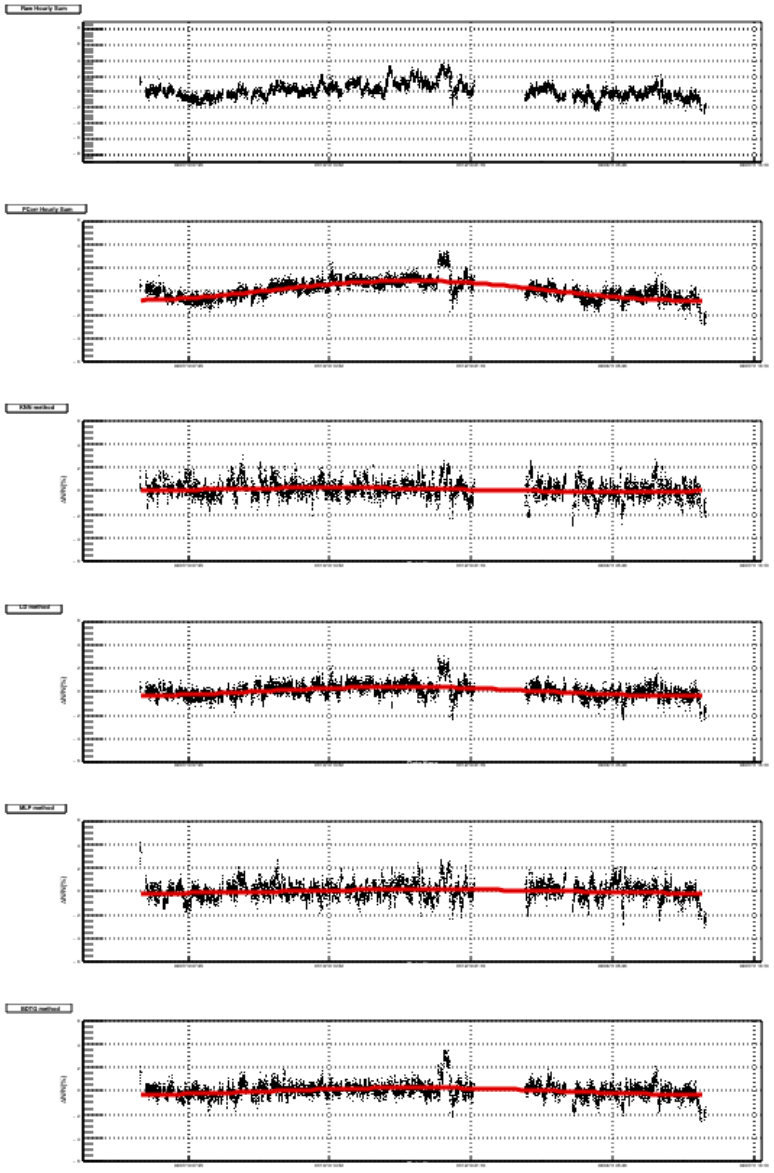

Слика 6.9: Временске серије одброја космичких миона за подземну лабораторију, одозго на доле: некоригована, коригована на притисак, коригована на притисак и температуру методама KNN, LD, MLP, BDTG.

Табела 6.2: *Амплитуде годишње варијације временских серија космике коригованих на метеоролошке ефекте различитим методама.*

Metoda korekcije	Godišnja varijacija [%] (nadzemna laboratorija)	Godišnja varijacija [%] (podzemna laboratorija)
Pritisak	1.25 ± 0.02	0.84 ± 0.02
kNN	0.22 ± 0.02	0.17 ± 0.04
LD	0.07 ± 0.05	0.38 ± 0.02
MLP	0.04 ± 0.05	0.16 ± 0.03
BDTG	0.05 ± 0.03	0.29 ± 0.02

имају методе BDTG и MLP, када су у питању подаци из надземне лабораторије, односно методе MLP и KNN, када су у питању подаци из подземне лабораторије.

Међутим, ако погледамо кориговане временске серије из обе лабораторије, можемо да уочимо да методе MLP, а нарочито KNN, уносе додатне, на око насумичне, флуктуације. То је у складу са опаженим већим ширинама одговарајућих дистрибуција на слици 6.7, нарочито истакнутим када је подземна лабораторија у питању. Ово може указивати на потенцијалну непрецизност или нестабилност алгоритма, која се можда може превазићи другачијим избором параметара у фази тренирања, као и ригорознијим квантитативним тестовима. Могуће је да регресија овим методама даје прецењене параметре услед недовољне или претеране истренираности алгоритма, што се евентуално може превазићи другачијим избором величине тренинг подскупа. Алтернативно, будући да су улазне варијабле приближно гаусовски дистрибуиране, а одговарајуће зависности одброја линеарне, постоји могућност да су ове методе мање подесне за примену у овој проблематици и да су применљивије на неке комплексније, нелинеарне проблеме.

Са друге стране, чини се да методе LD и BDTG коректно коригују одброј космике на метеоролошке ефекте. У овоме се нарочито ова друга показало ефикасном, па би у коначном избору то била предложена метода.

Закључак

Тему ове докторске дисертације представља анализа метеоролошких ефеката на мионску компоненту секундарног космичког зрачења. Ту се пре свега мисли на барометарски и температурски ефекат, који су повезани са утицајем атмосферског притиска, односно температуре атмосфере, на флукс космичких миона.

Осим фундаменталног, изучавање метеоролошких ефеката има и посредан значај. Што се боље моделује утицај атмосфере на флукс миона, то га је могуће ефикасније елиминисати, а то је веома значајно за изучавање варијација флукса неатмосферског порекла.

Циљ дисертације представља увођење два нова емпиријска метода за опис и корекцију метеоролошких ефеката, као и њихово поређење са постојећим емпиријским и теоријским методима.

Пре свега, демонстрирано је овладавање постојећим емпиријским и теоријским моделима. На основу добијених резултата кориговане су временске серије детектованог одброја космичких миона и тиме дефинисане референтне вредности за ефикасност корекције. Када је у питању теоријски метод, функција густине температурског коефицијента је одређена нумерички, док је барометарски коефицијент одређен линеарном регресијом на основу података претходно коригованих на температурски ефекат. У случају емпиријских и семиемпиријских метода, одговарајући коефицијенти добијени су линеарном (метод усредњене температуре) или вишеструком линеарном регресијом (метод ефективног нивоа продукције).

Подаци о одброју космичких миона коришћени у анализи су резултат мерења мионским мониторима у оквиру надземне (ниво тла) и подземне лабораторије (на дубини од $25 m.w.e.$) Нискофонске лабораторије за нуклеарну физику Ин-

ститута за физику у Београду.

За анализу је неопходно познавање метеоролошких параметара и то атмосферског притиска и температуре атмосфере. Подаци о притиску и температури на нивоу тла преузети су из мреже мерних станица локалних и државних метеоролошких служби. Подаци о температурама различитих слојева атмосфере добијени су на основу симулационих модела кретања ваздушних маса. Основни скуп података је интерполиран, одакле је затим било могуће узорковати податке са жељеном временском резолуцијом.

Први од новоуведених метода за анализу и корекцију метеоролошких ефеката базира се на техници декомпозиције на основне компоненте. Полазни скуп корелисаних метеоролошких варијабли је трансформисан у скуп некорелисаних компоненти. Из добијеног скупа издвојен је подскуп сигнификантних компоненти, које садрже највећи део варијације полазног скупа. Коначно, на основу корелације са детектованим одбројем миона издвојен је подскуп коришћен за анализу. Тиме је број улазних варијабли за анализу редукован са 26 на 5. Помоћу линеарне регресије одређени су одговарајући парцијални температурски коефицијенти, на основу којих је детектовани одброј коригован.

Други представљени метод базира се на примени различитих аллгоритама за мултиваријантну регресију имплементираних у пакету TMVA, у оквиру окружења за анализу ROOT. Методи за су тренирани на изабраном подскупу података, где су улазне варијабле представљале атмосферски притисак, температуру на нивоу тла и моделоване температуре различитих слојева атмосфере, док је излазна варијабла била детектовани одброј. За изабране методе одређени су оптимални параметри. Алгоритми дају предикцију одброја космике који садржи варијацију пореклом само од улазних метеоролошких варијабли, помоћу које је израчунат коригован одброј. На основу критеријума ефикасности и конзистентности, коначно су као најбољи кандидати за примену издвојени методи LD (метод линеарних дискриминантних фукција) и BDTG (метод бинарног гранања са градијентним *boost*-ом).

Уведени методи дају карактеристичан допринос по питању ефикасности, односно посебног увида у проблематику. У поређењу са постојећим емпиријским и

теоријским методима, у отклањању варијација флукса космичких миона метеоролошког порекла, показали су се најмање једнако ефикасни, а углавном веће ефикасности.

Методи су применљиви на било који тип мионских монитора, независно од географске локације или дубине на којој се детектор налази. Додатна предност метода декомпозиције на основне компоненте је једноставна и непосредна примена, која омогућава примену корекције са минималним закашњењем. Компаративна предност уведених мултиваријантних метода је флексибилност и могућност додатне софистикације.

Представљени методи омогућавају једноставну екстензију анализе на шири скуп метеоролошких варијабли, чиме би били укључени додатни ефекти (влажност, динамички притисак и сл.). Такође, постоји могућност примене корекција метеоролошких ефеката на друге типове детектора, као што су неутронски монитори, за које не постоји једноставан теоријски или емпиријски модел. Коначно, демонстриране технике су применљиве за анализу различитих варијација космичког зрачења које нису метеоролошког порекла.

Литература

[1] Peter K.F. Grieder. *COSMIC RAYS AT EARTH: Researcher's Reference and Data Book Manual*. Elsevier Science B.V., 2001. ISBN: 0-444-50710-8.

[2] Todor Stanev. *High Energy Cosmic Rays*. Praxis Publishing Ltd, Chichester, UK, 2010. ISBN: 978-3-540-85147-9.

[3] A. W. Wolfendale. "Introductory Cosmic Rays". у: *Origin of Cosmic Rays, Proceedings of the NATO Advanced Study Institute held in Durham, England, August 26-September 6, 1974*. D. Reidel Publishing Company, Dordrecht, 1975, с. 1—12. ISBN: 978-94-010-1814-2. DOI: 10.1007/978-94-010-1812-8.

[4] Lev I. Dorman. *COSMIC RAYS IN THE EARTH'S ATMOSPHERE AND UNDERGROUND*. Springer Science+Business Media New York Originally published by Kluwer Academic Publisher in 2004, 2004. ISBN: 978-94-015-6987-3. DOI: 10.1007/978-1-4020-2113-8.

[5] Philip Morrison. "The Origin of Cosmic Rays". у: *ENCYCLOPEDIA OF PHYSICS: COSMIC RAYS I*. под ред. S. Flugge. Springer-Verlag OHG. Berlin-Gottingen-Heidelberg, 1961, с. 1—87. ISBN: 978-3-642-45966-5. DOI: 10.1007/978-3-642-45964-1.

[6] V. L. Ginzburg. "The Origin of Cosmic Rays". у: *Origin of Cosmic Rays*. International Astronomical Union, 1981, с. 1—6. ISBN: 978-90-277-1272-1. DOI: 10.1007/978-94-09-8475-2.

[7] Peter L. Biermann и Günter Sigl. "Introduction to Cosmic Rays". у: *Physics and Astrophysics of Ultra-High-Energy Cosmic Rays*. под ред. Martin Lemoine и Günter Sigl. Springer, Berlin, Heidelberg, 2001, с. 1—26. ISBN: 978-3-540-42899-2. DOI: 10.1007/3-540-45615-5.

[8] Thomas K. Gaisser, Ralph Engel и Elisa Resconi. *COSMIC RAYS AND PARTICLE PHYSICS*. Cambridge University Press, 2016. ISBN: 978-0-521-01646-9.

[9] Luke O'C. Drury. "Origin of Cosmic Rays". y: *Astroparticle Physics* 39 (2012), с. 52—60. DOI: 10.1016/j.astropartphys.2012.02.006.

[10] Hyesung Kang, Dongsu Ryu и T. W. Jones. "Cluster Accretion Shocks as Possible Acceleration Sites for Ultra High Energy Protons below the Greisen Cutoff". y: *Astrophysical Journal* 456 (1996), с. 422—427. DOI: 10.1086/176666.

[11] S. P. Swordy. "THE ENERGY SPECTRA AND ANISOTROPIES OF COSMIC RAYS". y: *THE ASTROPHYSICS OF GALACTIC COSMIC RAYS, Proceedings of two ISSI Workshops, 18-22 October 1999 and 15-19 May 2000, Bern, Switzerland*. Springer Science+Business Media Dordrecht, 2001, с. 85—94. ISBN: 978-90-481-5862-1. DOI: 10.1007/978-94-017-3239-0.

[12] D. Muller. "COSMIC RAYS BEYOND THE KNEE". y: *THE ASTROPHYSICS OF GALACTIC COSMIC RAYS, Proceedings of two ISSI Workshops, 18-22 October 1999 and 15-19 May 2000, Bern, Switzerland*. Springer Science+Business Media Dordrecht, 2001, с. 105—116. ISBN: 978-90-481-5862-1. DOI: 10.1007/978-94-017-3239-0.

[13] A.D.Erlykin и A.W.Wolfendale. "The nature of the 'knee' in the cosmic ray energy spectrum". y: *Journal of Physics G* 32 (2006), с. 1—8. DOI: 10.1088/0954-3899/32/1/001.

[14] J. J. Quenby. "The Time Variations of the Cosmic Ray Intensity". y: *ENCYCLOPEDIA OF PHYSICS: COSMIC RAYS II*. под ред. S. Flugge. Springer-Verlag OHG. Berlin-Heidelberg, 1967, с. 310—371. DOI: 10.1007/978-3-642-46079-1.

[15] J. R. Jokipii. "Cosmic Rays". y: *From the Sun: Auroras, Magnetic Storms, Solar Flares, Cosmic Rays*. т. 50. the American Geophysical Union, 1998, с. 123—131. ISBN: 0-87590-292-8.

[16] I. N. Toptygin. *COSMIC RAYS IN INTERPLANETARY MAGNETIC FIELDS*. D. Reidel Publishing Company, Dordrecht, Holland, 1985. DOI: 10.1007/978-94-009-5257-7.

[17] K.H. Schatten и Wilcox J.M. Ness. "A model of interplanetary and coronal magnetic fields". y: *N.F. Sol Phys* 6 (1969), с. 442. ISSN: 0038-0938. DOI: https://doi.org/10.1007/BF00146478.

[18] Sami K. Solanki, Bernd Inhester и Manfred Schüssler. "The solar magnetic field". y: *Reports on Progress in Physics* 69 (2006), с. 563—668. DOI: 10.1088/0034-4885/69/3/R02.

[19] Owens Mathew J. и Robert J. Forsyth. "The Heliospheric Magnetic Field". y: *Living Reviews in Solar Physics* 10.1 (2013), с. 5. ISSN: 1614-4961. DOI: 10.12942/lrsp-2013-5. URL: https://doi.org/10.12942/lrsp-2013-5.

[20] Hilary V. Cane. "CORONAL MASS EJECTIONS AND FORBUSH DECREASES". y: *COSMIC RAYS AND EARTH Proceedings of an ISS/Workshop, 21-26 March 1999, Bern, Switzerland*. Springer Science+Business Media Dordrecht, 2000, с. 55—77. ISBN: 978-90-481-5615-3. DOI: 10.1007/978-94-017-1187-6.

[21] Leonty Miroshnichenko. *SolarCosmic Rays, Fundamentals and Applications*. Springer International Publishing Switzerland, 2015. ISBN: 978-3-319-09428-1. DOI: 10.1007/978-3-319-09429-8.

[22] S. W. H. Cowley. "The Earth's Magnetosphere". y: *From the Sun: Auroras, Magnetic Storms, Solar Flares, Cosmic Rays*. т. 50. the American Geophysical Union, 1998, с. 13—22. ISBN: 0-87590-292-8.

[23] Lev Dorman. *Cosmic Rays in Magnetospheres of the Earth and other Planets*. Springer Science+Business Media B.V., 2009. ISBN: 978-1-4020-9238-1. DOI: 10.1007/978-1-4020-9239-8.

[24] Laundal K. M. и Richmond A. D. "Magnetic Coordinate Systems". y: *Space Science Reviews* 206 (2017), с. 27—59. DOI: 10.1007/s11214-016-0275-y.

[25] Manuel Sandoval Vallarta. “Theory of the Geomagnetic Effects of Cosmic Radiation”. y: *ENCYCLOPEDIA OF PHYSICS: COSMIC RAYS I*. под ред. S. Flugge. Springer-Verlag OHG. Berlin-Gottingen-Heidelberg, 1961, с. 88—129. ISBN: 978-3-642-45966-5. DOI: 10.1007/978-3-642-45964-1.

[26] Thébault et al. “International Geomagnetic Reference Field: the 12th generation”. y: *Earth, Planets and Space, a SpringerOpen Journal* 67:79 (2015). DOI: 10.1186/s40623-015-0228-9.

[27] Markus Ahlers и Philipp Mertsch. “Origin of Small–Scale Anisotropies in Galactic Cosmic Rays”. y: *Progress in Particle and Nuclear Physics* 94 (2017), с. 184—216. DOI: 10.1016/j.ppnp.2017.01.004.

[28] D. Venkatesan и Badruddin. “Cosmic-ray intensity variations in the 3-dimensional heliosphere”. y: *Space Science Reviews* 52.1 (1990), с. 121—194. ISSN: 1572-9672. DOI: 10.1007/BF00704241.

[29] C. Patrignani и Particle Data Group. “Review of Particle Physics”. y: *Chinese Physics C* 40.10 (2016), с. 100001. URL: http://stacks.iop.org/1674-1137/40/i=10/a=100001.

[30] R. Mann. *An Introduction to Particle Physics and the Standard Model*. Taylor & Francis, 2011. ISBN: 9781439887608. URL: https://books.google.rs/books?id=cz7hQlot49IC.

[31] W. N. Cottingham и D. A. Greenwood. *An introduction to the standard model of particle physics*. Cambridge University Press, 2007. ISBN: 9780511271366.

[32] Sylvie Braibant, Giorgio Giacomelli и Maurizio Spurio. *Particles and Fundamental Interactions: An Introduction to Particle Physics*. Springer Netherlands, 2012. ISBN: 978-94-007-2463-1. DOI: 10.1007/978-94-007-2464-8.

[33] V. Tishchenko и др. “Detailed Report of the MuLan Measurement of the Positive Muon Lifetime and Determination of the Fermi Constant”. y: *Phys. Rev.* D87.5 (2013), с. 052003. DOI: 10.1103/PhysRevD.87.052003. arXiv: 1211.0960 [hep-ex].

[34] Dragomir Krpić. *Elementarne čestice*. Skripta za predmet Fizika elementarnih čestica na Fizičkom fakultetu u Beogradu.

[35] C. T. Case и E. L. Battle. "Moliere's Theory of Multiple Scattering". у: *Physical Review* 169.1 (1968), с. 201—204.

[36] Hans A. Bethe и Julius Ashkin. "Passage of Radiations through Matter". у: *Experimental Nuclear Physics, Vol. 1.* под ред. Emilio Segre. John Wiley и Sons, 1953. гл. 2, с. 166—251.

[37] L. E. Porter. "The Barkas-Effect Correction to Bethe–Bloch Stopping Power". у: *Advances in Quantum Chemistry* 46 (2004), с. 91—119. DOI: 10.1016/S0065-3276(04)46004-3.

[38] Jens Lindhard и Allan H. Sorensen. "Relativistic theory of stopping for heavy ions". у: *Physical Review A* 53.4 (1996), с. 2443—2456. DOI: 10.1103/PhysRevA.53.2443.

[39] M. J. Berger и др. *Report 49*. 2. 1993. DOI: 10.1093/jicru/os25.2.Report49.

[40] Eberhard Haug и Werner Nakel. *The Elementary Process of Bremsstrahlung*. WORLD SCIENTIFIC, 2004. DOI: 10.1142/5371. eprint: https://www.worldscientific.com/doi/pdf/10.1142/5371. URL: https://www.worldscientific.com/doi/abs/10.1142/5371.

[41] W. E. Burcham. *Nuclear physics: an introduction*. Longman, 1973. ISBN: 0582441102.

[42] D. Heck и др. *CORSIKA: A Monte Carlo Code to Simulate Extensive Air Showers," Report FZKA 6019, Forschungszentrum Karlsruhe*. 1998.

[43] John C. Gosse и Fred M. Phillips. "Terrestrial in situ cosmogenic nuclides: theory and application". у: *Quaternary Science Reviews* 20.14 (2001), с. 1475—1560. ISSN: 0277-3791. DOI: 10.1016/s0277-3791(00)00171-2.

[44] Ho-ming Mok. *Cosmic Rays: Climate, Weather and Applications (Physics Research and Technology)*. Nova Science Pub Inc; UK ed. edition, 2012. ISBN: 978-1622573004.

[45] Giuseppe Cocconi. “Extensive Air Showers”. у: *ENCYCLOPEDIA OF PHYSICS: COSMIC RAYS I*. под ред. S. Flugge. Springer-Verlag OHG. Berlin-Gottingen-Heidelberg, 1961, с. 215—271. ISBN: 978-3-642-45966-5. DOI: 10.1007/978-3-642-45964-1.

[46] Goran P. Škoro. *Uvod u eksperimentalnu fiziku čestica*. Skripta za predmet Fizika elementarnih čestica na Fizičkom fakultetu u Beogradu.

[47] J. Matthews. “A Heitler model of extensive air showers”. у: *Astroparticle Physics* 22.5 (2005), с. 387—397. ISSN: 0927-6505. DOI: 10.1016/j.astropartphys.2004.09.003.

[48] Pierre Billoir. “Phenomenology of Ultra-High-Energy Atmospheric Showers”. у: *Physics and Astrophysics of Ultra-High-Energy Cosmic Rays*. под ред. Martin Lemoine и Günter Sigl. Springer, Berlin, Heidelberg, 2001, с. 1—26. ISBN: 978-3-540-42899-2. DOI: 10.1007/3-540-45615-5.

[49] *CORSIKA – an Air Shower Simulation Program*. 2017. URL: https://www.ikp.kit.edu/corsika/.

[50] *KASCADE - Grande*. 2014. URL: https://web.ikp.kit.edu/KASCADE/.

[51] Robert N. Cahn и Gerson Goldhaber. *The Experimental Foundations of Particle Physics*. 2-е изд. Cambridge University Press, 2009. DOI: 10.1017/CBO9780511609923.

[52] A. Ramakrishnan. *Elementary Particles and Cosmic Rays*. A Pergamon Press book. Macmillan, 1962. URL: https://books.google.rs/books?id=8Dy6AAAAIAAJ.

[53] D. F. Measday. “The nuclear physics of muon capture”. у: *Physics Report* 354 (2001), с. 243—409. DOI: 10.1016/S0370-1573(01)00012-6.

[54] P. J. Hayman, N. S. Palmer и A. W. Wolfendale. “The rate of energy loss of high-energy cosmic ray muons”. у: *Proceedings of the Royal Society of London A: Mathematical, Physical and Engineering Sciences* 275.1362 (1963), с. 391—410. ISSN: 0080-4630. DOI: 10.1098/rspa.1963.0176. eprint: http://rspa.

royalsocietypublishing.org/content/275/1362/391.full.pdf. URL: http://rspa.royalsocietypublishing.org/content/275/1362/391.

[55] P Kiraly, M G Thompson и A W Wolfendale. "Cosmic ray showers produced by muon bremsstrahlung". у: *Journal of Physics A: General Physics* 4.3 (1971), с. 367. URL: http://stacks.iop.org/0022-3689/4/i=3/a=014.

[56] A. G. Bogdanov и др. "Geant4 simulation of production and interaction of muons". у: *IEEE Transactions on Nuclear Science* 53.2 (2006), с. 513—519. ISSN: 0018-9499. DOI: 10.1109/TNS.2006.872633.

[57] J. Kempa и I.MM. Brancus. "Zenith angle distributions of cosmic ray muons". у: *Nuclear Physics B - Proceedings Supplements* 122 (2003), с. 279—281. ISSN: 0920-5632. DOI: 10.1016/s0920-5632(03)80398-5.

[58] V. S. Makhmutov и др. "Latitude Effect of Muons in the Earth's Atmosphere during Solar Activity Minimum". у: *Bulletin of the Russian Academy of Sciences: Physics* 73.3 (2009), с. 350—352. ISSN: 1062-8738. DOI: 10.3103/S1062873809030216.

[59] Alexander Aab и др. "Testing Hadronic Interactions at Ultrahigh Energies with Air Showers Measured by the Pierre Auger Observatory". у: *Phys. Rev. Lett.* 117.19 (2016), с. 192001. DOI: 10.1103/PhysRevLett.117.192001. arXiv: 1610.08509 [hep-ex].

[60] L. Myssowsky и L. Tuwim. "Unregelmäßige Intensitätsschwankungen der Höhenstrahlung in geringer Seehöhe". у: *Zeitschrift für Physik* 39.2-3 (1926), с. 146—150. ISSN: 0044-3328. DOI: 10.1007/BF01321981.

[61] E. Steinke. "Über Schwankungen und Barometereffekt der kosmischen Ultrastrahlung im Meeresniveau". у: *Zeitschrift für Physik* 64.1-2 (1930), с. 48—63. ISSN: 0044-3328. DOI: 10.1007/BF01397427.

[62] M. Forró. "Temperature Effect of Cosmic Radiation at 1000-M Water Equivalent Depth". у: *Physical Review* 72 (1947), с. 868—869. DOI: 10.1103/PhysRev.72.868.

[63] A. Duperier. “A New Cosmic-Ray Recorder and the Air-Absorption and Decay of Particles”. y: *Terrestrial Magnetism and Atmospheric Electricity* 49.1 (), c. 1—7. DOI: 10.1029/TE049i001p00001. eprint: https://onlinelibrary.wiley.com/doi/pdf/10.1029/TE049i001p00001. URL: https://onlinelibrary.wiley.com/doi/abs/10.1029/TE049i001p00001.

[64] A Duperier. “The Temperature Effect on Cosmic-Ray Intensity and the Height of Meson Formation”. y: *Proceedings of the Physical Society* 61.1 (1948), c. 34. URL: http://stacks.iop.org/0959-5309/61/i=1/a=306.

[65] A Duperier. “The Meson Intensity at the Surface of the Earth and the Temperature at the Production Level”. y: *Proceedings of the Physical Society. Section A* 62.11 (1949), c. 684. URL: http://stacks.iop.org/0370-1298/62/i=11/a=302.

[66] C.M.G. LATTES, G.P.S. OCCHIALINI и C.F. POWELL. “Observations on the Tracks of Slow Mesons in Photographic Emulsions”. y: *Nature* 160 (окт. 1947), c. 486—92. DOI: 10.1038/160453a0.

[67] A Duperier. “Temperature of the Upper Atmosphere and Meson Production”. y: *Nature* 167 (1951), c. 312—313. DOI: 10.1038/167312a0.

[68] S. Olbert. “Atmospheric Effects on Cosmic-Ray Intensity Near Sea Level”. y: *Phys. Rev.* 92 (2 1953), c. 454—461. DOI: 10.1103/PhysRev.92.454. URL: https://link.aps.org/doi/10.1103/PhysRev.92.454.

[69] T. Murayama и др. “The Atmospheric Effects on the Intensity of High Energy μ-Mesons”. y: *Progress of Theoretical Physics* 15 (1956), c. 421—430. DOI: 10.1143/PTP.15.421.

[70] P. M. S. Blackett. “On the Instability of the Barytron and the Temperature Effect of Cosmic Rays”. y: *Physical Review - PHYS REV X* 54.11 (1938), c. 973—974. DOI: 10.1103/PhysRev.54.973.

[71] H. Carmichael, M. Bercovitch и J. F. Steljes. “Introduction of meteorological corrections into meson monitor data”. y: *Tellus* 19.1 (1967), c. 143—160. DOI:

10.1111/j.2153-3490.1967.tb01468.x. URL: https://onlinelibrary.wiley.com/doi/abs/10.1111/j.2153-3490.1967.tb01468.x.

[72] A N Dmitrieva и др. "Temperature effect correction for muon flux at the Earth surface: estimation of the accuracy of different methods". у: *Journal of Physics: Conference Series* 409 (2013), с. 012130. DOI: 10.1088/1742-6596/409/1/012130. URL: https://doi.org/10.1088%2F1742-6596%2F409%2F1%2F012130.

[73] R. R. S. De Mendonça и др. "Analysis of atmospheric pressure and temperature effects on cosmic ray measurements". у: *Journal of Geophysical Research: Space Physics* 118.4 (2013), с. 1403—1409. DOI: 10.1029/2012JA018026. URL: https://agupubs.onlinelibrary.wiley.com/doi/abs/10.1029/2012JA018026.

[74] F. Bachelet и A. M. Conforto. "Atmospheric effects on the cosmic ray total intensity at sea level". у: *Il Nuovo Cimento (1955-1965)* 4.6 (1956), с. 1479—1495. ISSN: 1827-6121. DOI: 10.1007/BF02746375. URL: https://doi.org/10.1007/BF02746375.

[75] V. M. Dvornikov, Y. Y. Krestyannikov и A. Sergeev. "Determination of the mass-average temperature on the cosmic ray intensity data". у: *Геомагнетизм и аэрономия* 16 (5 1976), с. 923—925.

[76] M. D. Berkova и др. "Temperature effect of the muon component and practical questions for considering it in real time". у: *Bulletin of the Russian Academy of Sciences: Physics* 75.6 (2011), с. 820—824. ISSN: 1934-9432. DOI: 10.3103/S1062873811060086. URL: https://doi.org/10.3103/S1062873811060086.

[77] Paul H. Barrett и др. "Interpretation of Cosmic-Ray Measurements Far Underground". у: *Rev. Mod. Phys.* 24 (3 1952), с. 133—178. DOI: 10.1103/RevModPhys.24.133. URL: https://link.aps.org/doi/10.1103/RevModPhys.24.133.

[78] M. Ambrosio et al. "Seasonal variations in the underground muon intensity as seen by MACRO". у: *Astroparticle Physics* 7.1 (1997), с. 109—124. ISSN: 0927-6505. DOI: https://doi.org/10.1016/S0927-6505(97)00011-X.

[79] R. R. S. de Mendonça и др. “THE TEMPERATURE EFFECT IN SECONDARY COSMIC RAYS (MUONS) OBSERVED AT THE GROUND: ANALYSIS OF THE GLOBAL MUON DETECTOR NETWORK DATA”. у: *The Astrophysical Journal* 830.2 (2016), с. 88. DOI: 10.3847/0004-637x/830/2/88. URL: https://doi.org/10.3847%2F0004-637x%2F830%2F2%2F88.

[80] *The R Project for Statistical Computing*. URL: https://www.r-project.org/.

[81] *ROOT - Data Analysis Framework*. URL: https://root.cern.ch/.

[82] Abdullrahman Maghrabi и Mohammed Almutayri. “Atmospheric Effect on Cosmic Ray Muons at High Cut-Off Rigidity Station”. у: *Advances in Astronomy* 2016 (2016), с. 1—9. DOI: 10.1155/2016/9620189.

[83] *Low-background Laboratory for Nuclear Physics*. URL: http://www.cosmic.ipb.ac.rs/.

[84] M. Savić и др. “Pressure and temperature effect corrections of atmospheric muon data in the Belgrade cosmic-ray station”. у: *J. Phys. Conf. Ser.* 632.1 (2015), с. 012059. DOI: 10.1088/1742-6596/632/1/012059.

[85] Mihailo Savic и др. “Effect of pressure and temperature corrections on muon flux variability at ground level and underground”. у: *25th European Cosmic Ray Symposium (ECRS 2016) Turin, Italy, September 04-09, 2016*. 2016. arXiv: 1701.00164 [physics.ins-det].

[86] N. Veselinović и др. “An underground laboratory as a facility for studies of cosmic-ray solar modulation”. у: *Nuclear Instruments and Methods in Physics Research Section A: Accelerators, Spectrometers, Detectors and Associated Equipment* 875 (2017), с. 10—15. ISSN: 0168-9002. DOI: https://doi.org/10.1016/j.nima.2017.09.008. URL: http://www.sciencedirect.com/science/article/pii/S0168900217309634.

[87] M Savić и др. “Rigidity dependence of Forbush decreases in the energy region exceeding sensitivity of neutron monitors”. у: *Advances in Space Research* (сент. 2018). DOI: 10.1016/j.asr.2018.09.034.

[88] *GeoForschungsZentrum - GFZ, Potsdam*. URL: https://www.gfz-potsdam.de/en/home/.

[89] Hiroyasu Tajima. "Detectors for cosmic rays on ground and in Space". у: *Nuclear Instruments and Methods in Physics Research Section A: Accelerators, Spectrometers, Detectors and Associated Equipment* 581.1 (2007). VCI 2007, с. 12—24. ISSN: 0168-9002. DOI: https://doi.org/10.1016/j.nima.2007.07.021. URL: http://www.sciencedirect.com/science/article/pii/S016890020701443X.

[90] A Dragić и др. "The new set-up in the Belgrade low-level and cosmic-ray laboratory". у: *Nuclear Technology and Radiation Protection* 26 (янв. 2011). DOI: 10.2298/NTRP1103181D.

[91] Dejan Joković. "Detekcija i spektroskopija miona iz kosmičkog zračenja plastičnim scintilacionim detektorima". дис. ... док. Univerzitet u Beogradu, Fizički fakultet, 2011.

[92] Никола Б. Веселиновић. "Детекција мионских догађаја у подземној лабораторији и енергетски зависна соларна модулација мионске компоненте космичког зрачења". дис. ... док. Univerzitet u Beogradu, Fizički fakultet, 2018.

[93] *Belgrade Cosmic Ray Station*. URL: http://147.91.87.33/cgi-bin/bcrs.

[94] R Banjanac и др. "Daily variations of Gamma-Ray background and Radon concentration". у: *Romanian Reports of Physics* 58 (янв. 2013), S14—S21.

[95] R. Jain и др. *Machine Vision*. Computer Science Series. McGraw-Hill, 1995. ISBN: 9780070320185. URL: https://books.google.rs/books?id=5rucQgAACAAJ.

[96] *Републички хидрометеоролоки завод*. URL: http://www.hidmet.gov.rs/.

[97] *Global Forecast System*. URL: https://www.ncdc.noaa.gov/data-access/model-data/model-datasets/global-forcast-system-gfs.

[98] *National Oceanic and Atmospheric Administration*. URL: https://www.noaa.gov/.

[99] M. Berkova и др. “Temperature effect of the muon component and practical questions of how to take it into account”. у: *Proceedings of the 21 European Cosmic Ray Symposium*. 2008, с. 634.

[100] I.T. Jolliffe. *Principal Component Analysis*. Springer-Verlag New York, 2002. ISBN: 978-1-4419-2999-0. DOI: 10.1007/b98835.

[101] B. Haurwitz. “The diurnal surface-pressure oscillation”. у: *Archiv für Meteorologie, Geophysik und Bioklimatologie, Serie A* 14.4 (1965), с. 361—379. ISSN: 1436-5065. DOI: 10.1007/BF02253483. URL: https://doi.org/10.1007/BF02253483.

[102] R.W. Preisendorfer и C.D. Mobley. *Principal Component Analysis in Meteorology and Oceanography*. Developments in atmospheric science. Elsevier, 1988. ISBN: 9780444430144. URL: https://books.google.rs/books?id=c1YRAQAAIAAJ.

[103] M Savić и др. “A novel method for atmospheric correction of cosmic-ray data based on principal component analysis”. у: *Astroparticle Physics* 109 (2019). DOI: 10.1016/j.astropartphys.2019.01.006.

[104] Ralf Herbrich. *Learning Kernel Classifiers: Theory and Algorithms*. Cambridge, MA, USA: MIT Press, 2001. ISBN: 026208306X.

[105] *TMVA - Tool for Multivariate Data Analysis with ROOT*. URL: http://tmva.sourceforge.net/.

[106] Andreas Hocker и др. “TMVA - Toolkit for Multivariate Data Analysis”. у: (2007). arXiv: physics/0703039 [physics.data-an].

[107] Trevor Hastie, Robert Tibshirani и Jerome Friedman. *The Elements of Statistical Learning*. Springer Series in Statistics. Springer New York Inc., 2001.

[108] A.R. Webb и K.D. Copsey. *Statistical Pattern Recognition*. Wiley, 2011. ISBN: 9781119952961. URL: https://books.google.rs/books?id=WpV9Xt-h3OOC.

[109] Ludmila I. Kuncheva. *Combining Pattern Classifiers: Methods and Algorithms, 2nd Edition*. Wiley, 2014. ISBN: 978-1-118-31523-1.

Слике

Табеле

Биографија

Михаило Савић рођен је 31.12.1975. године у Београду. Дипломирао је 2009. године а затим 2011. године завршио и мастер студије године на Физичком факултету у Београду . Исте године уписао је докторске студије на Физичком факултету Универзитета у Београду.

У периоду од 2009. до 2011. године био је запослен на Физичком факултету у Београду, где је у оквиру катедре за Физику језгра и честица држао рачунске и експерименталне вежбе из неколико предмета. Од 2011. године запослен је на Институту за физику у Београду као члан Нискофонске лабораторије за нуклеарну физику.

Од 2011. до 2014. године, као члан Београдског SHINE Team-а, био је део NA61/SHINE колаборације. Од 2015. године, као члан Београдског MICE Team-а, део је MICE колаборације.

У оквиру Нискофонске лабораторије за нуклеарну физику радио је на анализи временских серија мионске компоненте секундарног космичког зрачења, пре свега на проблемима везаним за утицај атмосферских параметара на ову компоненту као и на проблематици ефикасности мерења исте. У оквиру NA61/SHINE колаборације радио је на анализи продукције барионских резонанци, продукцији података, одржавању и надгледању Time-Of-Flight (TOF) под-детектора, калибрацији TOF података, одржавању и развоју софтвера за калибрацију, реконструкцију и геометрију.

У оквиру MICE колаборације радио је на развоју апликације за визуелизацију догађаја (EventViewer) снимљених у оквиру MICE експеримента.